



**HAL**  
open science

# Nanostructures-based 1.55 $\mu\text{m}$ -emitting Vertical-(External)-Cavity Surface-Emitting Lasers for microwave photonics and coherent communications

Salvatore Pes

► **To cite this version:**

Salvatore Pes. Nanostructures-based 1.55  $\mu\text{m}$ -emitting Vertical-(External)-Cavity Surface-Emitting Lasers for microwave photonics and coherent communications. Optics [physics.optics]. INSA de Rennes, 2019. English. NNT: 2019ISAR0013 . tel-02892844

**HAL Id: tel-02892844**

**<https://hal.science/tel-02892844v1>**

Submitted on 7 Jul 2020

**HAL** is a multi-disciplinary open access archive for the deposit and dissemination of scientific research documents, whether they are published or not. The documents may come from teaching and research institutions in France or abroad, or from public or private research centers.

L'archive ouverte pluridisciplinaire **HAL**, est destinée au dépôt et à la diffusion de documents scientifiques de niveau recherche, publiés ou non, émanant des établissements d'enseignement et de recherche français ou étrangers, des laboratoires publics ou privés.

# THESE DE DOCTORAT DE

L'INSTITUT NATIONAL DES SCIENCES  
APPLIQUEES RENNES  
COMUE UNIVERSITE BRETAGNE LOIRE

ECOLE DOCTORALE N° 596  
*Matière, Molécules, Matériaux*  
Spécialité : Photonique

Par **Salvatore PES**

## **Nanostructures-based 1.55 $\mu\text{m}$ -emitting Vertical-(External)-Cavity Surface-Emitting Lasers for microwave photonics and coherent communications**

Thèse présentée et soutenue à Rennes, le 26 Septembre 2019  
Unité de recherche : Institut FOTON, UMR-CNRS 6082  
Thèse N° : 19ISAR 12 / D19 - 12

### **Rapporteurs avant soutenance :**

**Isabelle SAGNES**

Directrice de recherche CNRS, C2N

**Daniel DOLFI**

Directeur du Groupe de Physique, Thales Research & Technology

### **Composition du Jury :**

**Isabelle SAGNES**

Directrice de recherche CNRS, C2N / Président et rapporteur

**Daniel DOLFI**

Directeur du Groupe de Physique, Thales Research & Technology / Rapporteur

**Mircea GUINA**

Professeur, Tampere University of Technology / Examineur

**Stéphane CALVEZ**

Chargé de Recherche CNRS, LAAS / Examineur

**Philippe ADAM**

Responsable Photonique, DGA-MRIS / Invité

**Christophe LEVALLOIS**

MCF, INSA Rennes / Co-encadrant de thèse

**Cyril PARANTHOËN**

MCF, INSA Rennes / Co-encadrant de thèse

**Mehdi ALOUINI**

Professeur, Université de Rennes 1 / Co-directeur de thèse

**Hervé FOLLIOU**

Professeur, INSA Rennes / Co-directeur de thèse



Intitulé de la thèse :

Nanostructures-based 1.55  $\mu\text{m}$ -emitting Vertical-(External)-Cavity Surface-Emitting Lasers  
for microwave photonics and coherent communications

**Salvatore PES**

En partenariat avec :



*Document protégé par les droits d'auteur*





*"[...] Thus I got my own room in the Physics Institute, which was filled with piles of sensitive optical instruments. I will not bore the reader with the principles and methodology of these experiments, and will mention only the so-called "interferometer", consisting of two half-silvered glass plates which must be kept parallel with the precision of one-millionth of an inch. After adjusting them with great labor, one sneezes and everything comes out of adjustment! I called them the entrance-and-exit devils."*

*(George Gamow, My World Line: An Informal Autobiography, 1970)*

*"One shouldn't work on semiconductors, that is a filthy mess; who knows whether any semiconductors exist."*

*(Wolfgang Pauli)*

*"It's only those who do nothing that make no mistakes, I suppose."*

*(Joseph Conrad, An Outcast of the Islands, 1896)*



## Remerciements

Pendant ma thèse, j'ai eu la chance de travailler avec deux équipes différentes, et de développer donc des connaissances complémentaires dans la physique des semiconducteurs, dans la technologie des composants opto-électroniques et dans la physique des laser. Les travaux présentés dans cette mémoire de thèse, réalisés au sein des équipes de recherche OHM (INSA Rennes) et DOP (Université de Rennes 1) de l'Institut FOTON, n'auraient pas pu être obtenus bien évidemment sans l'aide et la contribution de beaucoup de personnes et sans le soutien financier de la DGA et de la Région Bretagne. Qu'ils trouvent ici l'expression de ma profonde gratitude.

Tout d'abord je remercie mes directeurs de thèse, **Hervé FOLLIOT** et **Mehdi ALOUINI**, pour m'avoir donné la possibilité de poursuivre l'aventure dans le monde des V(E)CSELS que j'avais commencé lors de mon stage de Master 2.

**Hervé**, bien que on n'a pas eu énormément de temps pour discuter pendant la thèse, tu étais toujours disponible quand j'ai eu besoin, et pour ça je te remercie beaucoup. Merci aussi pour tes bons conseils, pour toutes tes remarques pertinentes et tes avis sur le manuscrit, et ta profonde gentillesse.

**Mehdi**, je te remercie profondément de m'avoir appris la rigueur scientifique, de m'avoir éclairé et soutenu dans les moments de doute et de difficulté, et de m'avoir donné goût à la physique des lasers. Je garderai un très bon souvenir de toutes les discussions scientifiques que on a eu ensemble et de tes explications au tableau, toujours données avec une simplicité et une clarté remarquables. Je te remercie pour la confiance que tu m'as témoignée lors de ces années, et d'avoir su m'apprendre à garder confiance en moi.

Je tiens également à remercier **Cyril PARANTHOËN** et **Christophe LEVALLOIS** pour le super-encadrement dont j'ai bénéficié pendant les trois années de thèse, toujours dans la bonne humeur et dans une ambiance agréable. **Cyril** et **Christophe**, grâce à vous j'ai appris énormément de choses sur les procédés de salle blanche, la technologie des semiconducteurs III-V et les dispositifs VCSELS. Un merci énorme aussi pour votre soutien quotidien et votre énorme disponibilité quand j'en ai eu besoin (assez souvent, j'avoue), la relecture soignée du manuscrit et vos conseils lors de la préparation de la soutenance, et toutes les discussions que on a pu avoir autour des sujets scientifiques ou non. Sans vous, la thèse ça aurait été beaucoup plus compliqué pour moi. Pour tout cela, je vous serai toujours reconnaissant.

J'exprime aussi ma reconnaissance à **Isabelle SAGNES** et **Daniel DOLFI**, qui ont accepté d'être rapporteurs de ce manuscrit, et à **Mircea GUINA** et **Stéphane CALVEZ** pour avoir jugé mes travaux de thèse. Je remercie également **Philippe ADAM** d'avoir intégré le jury, et pour les discussions scientifiques qu'on a eu lors de ses visites au laboratoire.

Je remercie tous les partenaires des projets scientifiques HYPOCAMP et IDYLIC, auxquels j'ai eu la chance de participer. En particulier, je tiens à remercier **Véronique BARDINAL** et **Thierry CHAMPS** du LAAS, **Laurent DUPONT** de l'IMT Atlantique, **Sophie BOUCHOLE** du C2N (merci beaucoup pour la croissance métamorphique du DBR GaAs/AlAs sur la puce

QDH-VECSEL!!!) et **Rose-Marie SAUVAGE** de la DGA, pour les nombreuses discussions scientifiques lors des réunions d'avancement du projet ANR-ASTRID HYPOCAMP auxquelles j'ai participé pendant la thèse.

Merci aussi à **Vladimir IAKOVLEV** et à toute l'équipe du LPN-EPFL, pour m'avoir accueilli lors de ma visite à Lausanne pour les tout premiers tests de wafer bonding sur les puces VECSELS à quantum dashes.

Comme j'ai dit, la contribution des plusieurs personnes a été précieuse pour l'accomplissement de cette thèse. Je tiens tout particulièrement à remercier **Julie** et **Karine** pour l'aide en salle blanche, **Cyril** pour les super-montages mécaniques du banc VECSEL, **Steve** et **Ludo** pour votre assistance en électronique et la bonne ambiance au labo (« RUUUUUUUUUU !!! »), **Goulc'hen** pour m'avoir aidé à faire laser un VECSEL un peu timide (« Bienvenue dans le club des laseristes ! ») et aussi pour tes blagues pourries (« Bienvenue dans le club des laseristes ! »), **Antony** pour ton assistance en optique et informatique, **Gwennaël** pour ton aide ponctuel mais précieuse pendant les mesures de largeur de raie du QDH-VECSEL, **Isabelle** pour l'aide administratif et ta bonne humeur.

Merci aussi à tous ceux avec lesquels j'ai discuté et passé un peu de temps pendant les années de la thèse : **Yoan**, c'était toujours un plaisir t'écouter quand tu parlais de physique au tableau. **Laurent**, merci pour l'aide avec Silvaco et d'être venu m'écouter lors des répètes de soutenance. **Mathieu**, merci à toi aussi pour les nombreuses discussions scientifiques qu'on a eu de temps en temps. **Charles** et **Antoine**, les séances de TP avec vous ont été très agréables. **Marco**, dividere l'ufficio con te è stato un piacere.

Je ne peux pas oublier mes compagnons de voyage, les thésards FOTON ! Merci à tous ceux qui ont partagé des moments avec moi, grâce à vous je garderai toujours un très bon souvenir de la thèse. **Kevin** et **François**, j'espère que vous avez continué à pratiquer la langue italienne que je vous ai enseigné. Grazie mille a **Ida** per avermi fatto sentire un po' meno lontano dall'Italia, per le serate a Rennes insieme a **Fabrizio** e per i momenti divertenti durante le pause caffè. **Daniel**, j'espère que maintenant tu arrives à distinguer Place de Bretagne et Place du Parlement, ce n'est pas la même chose ! **Mickael**, je peux te l'avouer maintenant : je faisais express d'être en retard quand on allait au RU juste pour t'embêter ahah. Clin d'œil à **Ronan**, super-collègue de bureau. Je garde un très beau souvenir des discours sur le InP et le GaP qui après finissaient en délire (comme tous nos discours, d'ailleurs !). Une pensée aussi à **Yong**, qui a dû supporter les blagues et les plaisanteries de Ronan et moi. **Gaëlle**, je savais que la manip VECSEL avec toi ne pouvais tomber en meilleures mains ! Merci aussi à tous les autres thésards avec qui j'ai passé moins de temps : **Shinjen**, **Aurélien**, **Marie**, **Romain**, **Alejandro**, **Ang**, **Anwar**.

Infine, vorrei ringraziare la mia famiglia, mia mamma **Antonietta** e mio fratello **Michele**, per avermi sempre sostenuto nelle mie scelte e per essermi stati vicini nei momenti difficili, quando ne avevo più bisogno. Grazie per avermi incoraggiato ad andare avanti e non mollare, ed essere venuti alla discussione. Questo lavoro è anche merito vostro, non sarebbe stato possibile senza il vostro aiuto.

Tore

# TABLE OF CONTENTS

<b>General introduction</b>	<b>1</b>
<b>1 Generalities on VCSELS</b>	<b>5</b>
1.1 Introduction .....	6
1.2 Basic concepts of semiconductor lasers.....	6
1.3 State-of-the-art of VCSEL technology .....	9
1.3.1 Short history of VCSEL development .....	9
1.3.2 Different material systems and applications .....	10
1.4 Characteristics of the VCSEL cavity.....	13
1.4.1 Introduction.....	13
1.4.2 Distributed Bragg Reflectors .....	14
1.4.3 The Fabry-Pérot resonator .....	17
1.4.4 Carrier confinement and transverse mode control in VCSELS.....	24
1.5 Conclusions.....	29
<b>2 Development of VCSEL technology: design, realization and characterization</b>	<b>31</b>
2.1 Development of InP-based VCSELS: technological challenges.....	32
2.1.1 Material for DBRs based on InP system.....	32
2.1.2 Electrical confinement issues.....	37
2.2 A new approach for thermal management: TSHEC process.....	39
2.2.1 Motivations .....	39
2.2.2 Hybrid metal-dielectric DBRs .....	42
2.2.3 TSHEC process development .....	49
2.2.4 Devices characterization .....	54
2.3 Development of the electrical-injected VCSEL technology.....	62
2.3.1 Buried tunnel junction: investigations .....	63
2.3.2 EP-VCSEL cavity design.....	75
2.3.3 Technological process for electrically-injected VCSELS .....	79
2.3.4 Preliminary results on EP-VCSEL tests sample .....	83
2.4 Conclusions.....	84

<b>3</b>	<b><i>Monolithic wide-tunable devices based on liquid crystal micro-cells</i></b>	<b>87</b>
3.1	<b>Optical application of tunable devices</b>	<b>89</b>
3.2	<b>State-of-the-art of vertical-cavity tunable devices</b>	<b>91</b>
3.2.1	Tunable VCSELs	92
3.2.2	Tunable filters and photodiodes	94
3.2.3	Drawbacks of MEMS-based devices	95
3.3	<b>Monolithic approach: the interest of liquid crystals</b>	<b>95</b>
3.3.1	Optical properties of liquid crystals	96
3.3.2	Working principle of liquid crystals: tuning mechanism	98
3.4	<b>Anisotropic gain media: optical and physical properties of self-assembled quantum dashes</b>	<b>101</b>
3.4.1	Epitaxial growth	102
3.4.2	Polarization properties of QDHs	104
3.4.3	Temperature dependence	106
3.4.3	Spectral coverage and (modal) gain of QDHs active media	107
3.4.4	Summary	112
3.5	<b>Devices based on liquid crystal micro-cell technology</b>	<b>113</b>
3.5.1	Accomplished results from the past (2006-2014)	113
3.5.2	The HYPOCAMP project (2014-2019)	113
3.5.3	Tunable p-i-n photodiode	115
3.5.4	Investigation of a tunable LC-VCSELs: preliminary results	121
3.6	<b>Conclusions</b>	<b>127</b>
<b>4</b>	<b><i>VECSELs: basic concepts and advantages</i></b>	<b>129</b>
4.1	<b>Introduction</b>	<b>130</b>
4.2	<b>Key elements of a VECSEL</b>	<b>131</b>
4.2.1	Composition of the cavity	131
4.2.2	Pumping schemes	133
4.3	<b>Mode control in VECSELs</b>	<b>135</b>
4.3.1	Transverse mode selection for power scaling	135
4.3.2	Longitudinal modes	139
4.3.3	...and single-frequency operation	140
4.4	<b>Output power</b>	<b>143</b>
4.4.1	State-of-the-art in multi-mode emission	143
4.4.2	Performance in single-frequency operation	147

<b>4.5 VECSEL cavity architectures and applications .....</b>	<b>148</b>
4.5.1 Cavity geometries .....	148
4.5.2 VECSELS applications.....	150
<b>4.6 Optimization guidelines for VECSEL design .....</b>	<b>152</b>
4.6.1 Thermal management in VECSELS.....	153
4.6.2 Resonant vs anti-resonant configurations and confinement factor .....	159
4.6.3 Optimization of laser threshold and output power.....	162
<b>4.7 Conclusions.....</b>	<b>167</b>
<b>5 <i>Development and characterization of a low noise quantum dashes-based VECSEL on InP</i> .....</b>	<b>169</b>
<b>5.1 Introduction .....</b>	<b>170</b>
<b>5.2 Design and realization of the optically-pumped VECSEL based on quantum dash active medium .....</b>	<b>171</b>
5.2.1 Quantum dash active region design and characterization.....	172
5.4.2 GaAs/AlGaAs DBR metamorphic growth and device integration (C2N).....	176
<b>5.3 Characterization of the OP-QDH-VECSEL in multi-mode regime.....</b>	<b>179</b>
5.3.1 Experimental setup.....	179
5.3.2 Spectral emission and output characteristic .....	181
5.3.3 Preliminary conclusion .....	183
<b>5.4 Low noise Class-A single-frequency operation.....</b>	<b>184</b>
5.4.1 Obtaining the low noise Class-A regime .....	184
5.4.2 Realization of the experimental setup .....	187
5.4.3 Estimation of the thermal impedance.....	189
5.4.4 Single-frequency operation .....	191
5.4.5 Static polarization properties of the QDH-VECSEL .....	194
5.4.6 Class-A regime and RIN .....	195
5.4.7 Spectral purity .....	200
<b>5.5 Conclusions.....</b>	<b>203</b>
<b>6 <i>Preliminary results on direct coupling constant measurements in dual-frequency VECSELS</i> .....</b>	<b>205</b>
<b>6.1 Introduction .....</b>	<b>206</b>
<b>6.2 Coupling in dual-frequency VECSELS.....</b>	<b>211</b>



6.2.1 Coupling: SQWs vs QDHs/QDs .....	211
6.2.2 Measurement principle of the coupling constant between two laser eigenmodes .....	213
<b>6.3 Direct measurement of the coupling constant in dual-frequency VECSELS ..</b>	<b>215</b>
6.3.1 Development of the experimental setup.....	216
6.3.2 Simultaneous dual-frequency emission between two orthogonally-polarized modes of a SQW-VECSELS.....	219
6.3.3 Preliminary results on direct coupling constant measurement in SQW-VECSELS.....	220
<b>6.4 Conclusions.....</b>	<b>223</b>
<b><i>Conclusions and perspectives</i></b>	<b>225</b>
<b><i>Appendices</i></b>	
<b><i>A Gaussian beam waist calculations based on the ABCD matrices method in resonant laser cavities</i></b>	<b>231</b>
<b><i>B Modeling heat transfer in V(E)CSELS</i></b>	<b>235</b>
<b><i>C Semi-empirical model for OP-VECSEL threshold and output power estimation</i></b>	<b>245</b>
<b><i>D Electrical schemes of RIN measurement benches</i></b>	<b>251</b>
<b><i>Résumé des travaux de thèse</i></b>	<b>255</b>
<b><i>Bibliography</i></b>	<b>265</b>
<b><i>List of publications and conferences</i></b>	<b>293</b>

# ***General introduction***

Vertical-Cavity Surface-Emitting Lasers (VCSELs) have shown a growing interest in the scientific community and industry over the last decades, particularly in the domains of data communications (Datacom) and coherent optical systems. Characterized by low power consumptions and high modulation frequencies deriving from their small dimensions, they are ideal candidates to be integrated in optical infrastructures including the 10, 40 and 100 Gbps Ethernet links for LAN and MAN network systems. Additionally, when coupled to a tunable mechanism, VCSELs have been demonstrated to outperform their edge-emitting counterparts in terms of achievable tunable ranges, with emissions over 100 nm without mode hopping. This has paved the way to their integration in Wavelength Division Multiplexing (WDM) systems, Fiber Bragg Grating (FBG) sensors for mechanical deformation monitoring, gas/toxic molecules analysis or Optical Coherent Tomography (OCT) modules for biomedicine applications and many others fields.

Besides that, when coupled with an external cavity, VECSELs (the E standing for “External”) can operate in the so-called “Class-A” regime, which is characterized by the absence of relaxation oscillation phenomena, reaching a noise down at the quantum level. In such a regime, VECSELs become suitable for being integrated in radio-frequency (RF) oscillators for the distribution of highly pure references signals over long distances, atom manipulation and probing experiments, optical pumping apparatus for atomic clocks, high-resolution spectroscopy systems and microwave photonic links. The external architecture of VECSELs also allows the introduction of optical elements inside the cavity, such as saturable absorbers or non-linear or birefringent crystals, to bring new functionalities. In such a way it is possible to achieve a mode-lock operation, frequency-doubled emission or dual-frequency regime.

The work presented in this Ph.D. dissertation, which has been carried out at FOTON Institute (OHM and DOP research teams jointly), involves the development of InP-based VCSELs and VECSELs emitting in the 1.55-1.6  $\mu\text{m}$  wavelength range and integrating active regions based on anisotropic nanostructures like InAs quantum dashes, in order to confer original performance, such as a fixed and stable polarization state of emission, a wide emission range and a lower sensitivity to temperature. Moreover, according to previous observations on conventional semiconductor edge-emitting laser diodes, such nanostructures are expected to be promising candidates for the development dual-frequency devices if integrated on a vertical-cavity device, thanks to their

physical properties arising from their inhomogeneously broadened spectral emission. In this framework, the peculiar physical properties of quantum nanostructures, if coupled to electrical injection schemes, would open multiples opportunities both for fundamental and applied research, especially in the case of 1.55  $\mu\text{m}$ -emitting devices which already benefit from important technology developments.

In this dissertation we will present the design, the technological realization and the experimental characterization of such devices for different applications such as telecom communications and microwaves photonics. For that reason, the manuscript is divided in two main parts, each part consisting in three chapters, which individually address the peculiarities of such devices, respectively. The first part is dedicated to the discussion of the micrometric-long cavity VCSELs, the development of their technology and the optimization of their performance, whereas the second part is focused on the realization and characterization of VECSELs devices in an external cavity configuration, in single-frequency and dual-frequency operations.

In more detail, the manuscript is arranged as follows:

**Chapter 1** introduces the basic concepts of vertical-cavity lasers and its advantages compared to edge-emitting lasers. It also presents a state-of-the-art of VCSELs, together with the description of the basic blocks composing the VCSEL resonator and the technological approach to obtain an efficient carrier confinement in vertical structures.

In **Chapter 2** we address the problem of the thermal management of VCSELs, which represents a severe limitation to reach good output performance in such devices. To this aim, we present a new hybrid process (the TSHEC process, standing for Through Silicon Holes Electroplated Copper), which has been developed at FOTON Institute to improve the temperature dissipation of VCSELs and which is fully compatible with both optical and electrical pumping schemes. We discuss the technological realizations and we show experimental evidences of the effective improvements in performance, obtained in the case of optically-pumped VCSELs. We also present a preliminary design and study of the basic blocks necessary to transfer the TSHEC technology to the case of electrically-injected devices, together with some preliminary tests and characterizations.

In **Chapter 3** we introduce the concept of tunable devices based on liquid crystals micro-cells. After a state-of-the-art of devices based on movable membranes, which currently represents the technique of choice to perform the wavelength tuning in vertical-cavity devices, we describe the advantages of using a fully-monolithic approach based on the electro-optic effect of nematic liquid crystal subjected to an external electric field, and the optical and physical properties of the liquid crystal molecules which are responsible of the tuning mechanism. The advantages of

using an anisotropic gain media based on InAs quantum dashes nanostructures in the active region of the devices in order to efficiently exploit the optical properties of anisotropic liquid crystals are also discussed. We describe the optical and physical properties (polarization, temperature dependence, gain and spectral coverage) of such nanostructured media, and we discuss their integration on the final devices. To validate such an approach, we first present the results of the integration of liquid crystal micro-cells on a tunable PIN photodiode operating in the telecom C-band. The results obtained with such a device show the potentialities of such an approach. We finally conclude the chapter by showing the preliminary results of the integration of liquid crystal micro-cells on a 1.55  $\mu\text{m}$ -emitting VCSEL.

**Chapter 4** summarizes the basic principles of operation and the key elements composing a VECSEL, and the differences and peculiarities with respect to its monolithic counterpart. A state-of-the-art in terms of output performance and applications is also presented. In the chapter we also discuss some technological challenges related to the thermal management of VECSELs, which is again one of the main limitations in the performance of such devices. The last part of the chapter is devoted to present the design rules adopted to realize a 1.6  $\mu\text{m}$ -emitting optically-pumped VECSEL based on quantum dashes nanostructures (OP-QDH-VECSEL), which is the subject of the next chapter.

**Chapter 5**, as said, details the realization and characterization of an InAs quantum dash-based VECSEL on an InP substrate. We focus on the different parts of the laser and the technological steps which have been performed to realize the device. Later, we describe the experimental setups used to characterize the device. Experimental characterizations on multi-mode and single-frequency operation are presented, together with advanced characterizations in terms of Relative Intensity Noise (RIN) and phase noise of the device in low-noise Class-A operation.

Finally, in **Chapter 6** we present the experimental setup which has been developed to perform direct coupling measurements in dual-frequency VECSELs, and which has been inspired by previous works on coupling measurements in solid-state lasers. In particular, such an experiment allows investigating and measuring the intrinsic coupling constant between two orthogonal eigenmodes of an optically-pumped dual-frequency VECSEL. The setup is validated though preliminary results on a 1.54  $\mu\text{m}$ -emitting device based on conventional strained quantum well active media (SQW-VECSEL), but it represents a general procedure which in the future will be applied to devices based on different gain media, such as quantum dashes-based or quantum dot-based VECSELs.



# **Chapter 1**

## **Generalities on VCSELS**

<b>1.1 Introduction .....</b>	<b>6</b>
<b>1.2 Basic concepts of semiconductor lasers.....</b>	<b>6</b>
<b>1.3 State-of-the-art of VCSEL technology .....</b>	<b>9</b>
1.3.1 Short history of VCSEL development .....	9
1.3.2 Different material systems and applications .....	10
<b>1.4 Characteristics of the VCSEL cavity.....</b>	<b>13</b>
1.4.1 Introduction .....	13
1.4.2 Distributed Bragg Reflectors.....	14
1.4.3 The Fabry-Pérot resonator.....	17
1.4.4 Carrier confinement and transverse mode control in VCSELS.....	24
<b>1.5 Conclusions.....</b>	<b>29</b>

## 1.1 Introduction

As already discussed in the *General Introduction*, this chapter deals with the presentation of some general aspects of VCSEL devices. Before describing the architecture of the VCSEL cavity, we will briefly discuss their peculiarities and advantages with respect to their corresponding and more conventional semiconductor laser family represented by ridge lasers. Then we will present the state-of-the-art of these devices with respect to the wavelength emission range and material systems, their main applications and a brief history of VCSELs' development. We will then detail the key elements composing the VCSEL cavity, such as the Distributed Bragg Reflectors (DBR), The Fabry-Pérot resonator and the pumping schemes, which have been developed to confine the carriers in the active region and control the transverse modes of VCSELs.

## 1.2 Basic concepts of semiconductor lasers

Here, we limit the analysis to semiconductor lasers that are based on interband transitions (thus excluding quantum cascade lasers). Those lasers are generally divided in two major configurations, depending on the direction of the laser emission. In edge-emitting lasers (EELs, Fig. 1.1a) the light oscillates in the same plane as the active region, while in Vertical-Cavity Surface-Emitting Lasers (VCSELs, Fig. 1.1b) the light exits normally to the plane defined by the active layers.

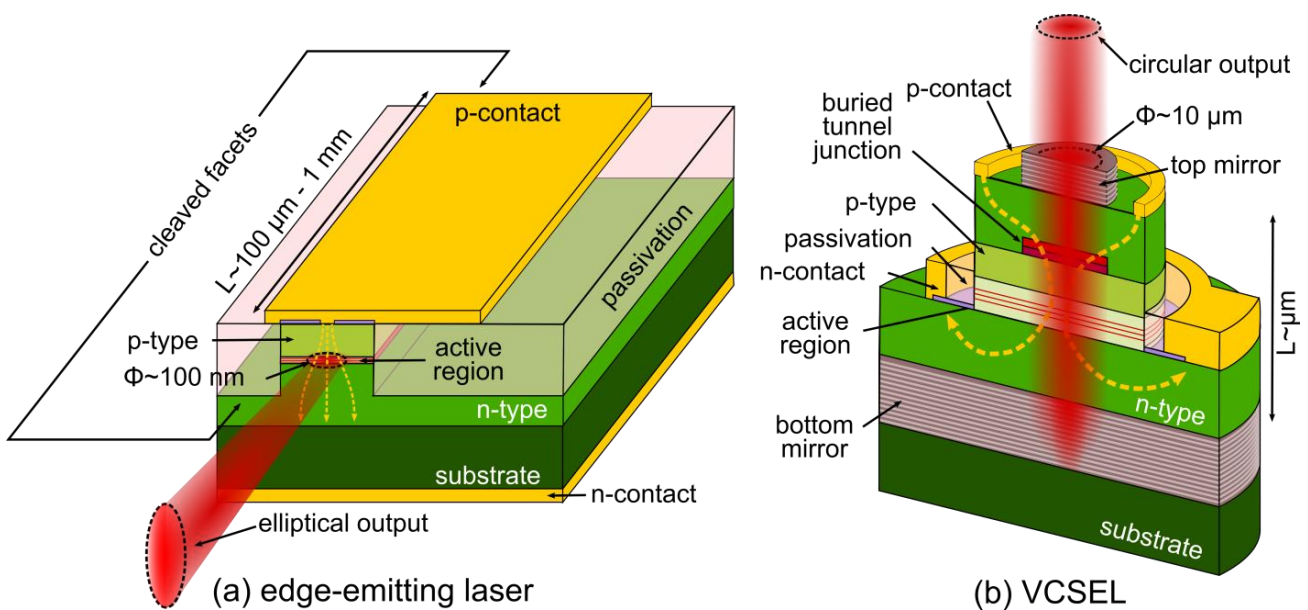


Fig. 1.1 – Two main families of semiconductor lasers: (a) the edge-emitting laser (EEL) and (b) the vertical-cavity surface-emitting laser (VCSEL).

In the simple configuration of edge-emitting lasers, a ridge waveguide acts as carrier injection and light confinement section. The light is extracted from the edge(s) of the laser and the optical cavity is simply formed by the perpendicular cleavage of the vertical facets, which act as plane mirrors. Relying on the fact that the cavity is formed on the plane of the active medium, the gain per photon round-trip is very high and the facet reflectivity, of the order of  $R \sim 30\%$ , is sufficient to establish laser operation. Because of their relatively long cavity (100  $\mu\text{m}$  - 1 mm), EELs have an inherent multi-longitudinal emission, if no filtering mechanisms are implemented (such as in-plane distributed grating sections).

Small waveguide dimensions (some hundreds of nm until few  $\mu\text{m}$ ) are instead necessary to ensure single-transverse mode operation in EELs. The small emitting surface, however, induces a large angular divergence which results in a high elliptic output. For this reason, EELs have a low coupling efficiency with optical fibers, ranging between 30% to 50%, unless complicated beam shaping approaches are used [Tian2013]. On the other hand, EELs typically provide high output powers, ranging from several hundreds of mW in single-mode waveguide configuration, up to several tens of watts in multi-mode waveguide, or even hundreds of watts in the case of multi-stripe arrays.

Conversely, in VCSELs, the optical cavity is perpendicular to the growth plane with a typical thickness of few  $\mu\text{m}$ , so that the optical gain per photon round-trip is considerably lower than in the case of EELs [Michalzik2013]. Thus, to ensure lasing, the optical losses must be minimized by employing thick and high reflective mirrors ( $R \geq 99.5\%$ ), such as Distributed Bragg Reflectors (DBRs). For such a reason, the epitaxial growth and the process of vertical-cavity devices is more time-consuming and expensive with respect to EELs, since it involves the growth of several stacks of multiple layers composing the active region and the top/bottom DBRs, and the integration of a buried tunnel junction (BTJ) or oxides apertures to laterally confine the carriers and get a truly transverse single-mode emission. Nevertheless, the possibility to directly perform burn-in tests on wafers at various stages of the realization process increases the manufacturing yield and contributes to dramatically lower the production costs related to quality assurance and packaging, while their small footprint make them good candidates for mass production. Moreover, the wafer integration of VCSELs is fully compatible with detectors [Kern2013] and other microelectronic circuitry (i.e. CMOS-based driving modules) [Pu1999].

For such devices, the optical aperture offers some advantages with respect to the EEL configuration: the circular micrometer-size aperture results in an efficient coupling with optical fibers (typically  $> 80\%$ ), since it is sufficiently narrow (several  $\mu\text{m}$ ) to ensure a single-transverse mode regime, but at the same time it is sufficiently wide to have a very small diffraction angle. On



the other hand, the micrometric cavity ensures a single-longitudinal mode emission. So that, in the case of VCSELs, nearly circular and symmetric single-frequency emission is typically achieved for smaller values of threshold current with respect to EELs. Unfortunately, the output power of VCSELs is generally low (of the order of few mW) and the heat dissipation is challenging, requiring particular attention to the choice of the device architecture to improve thermal management. As in the case of EELs, increasing the output power of VCSELs can lead to multi-modal emission due to the appearance of higher transverse modes. High values of output power can be achieved with array architectures, which are easy to integrate on the same chip thanks to the in-plane nature of the vertical-emitting devices. Another advantage with respect to EELs, is represented by the low threshold and low power dissipation, which is basically due to the smaller volume of VCSELs. Small dimensions also translates into high modulation speeds, which makes VCSELs good candidates to be integrated in low-power data centers, in order to reduce the costs deriving from the power consumption and the cooling systems.

Table 1.1 summarizes the pro and cons of both technologies.

**Table 1.1 – Advantages and disadvantages of EELs and VCSELs.**

Configuration	Advantages	Disadvantages
<b>EELs</b>	<ul style="list-style-type: none"> <li>- High output power</li> <li>- High power conversion efficiency</li> <li>- Easy and fast fabrication process</li> <li>- Linear polarization easily achieved</li> </ul>	<ul style="list-style-type: none"> <li>- Highly elliptical output (low fiber coupling efficiency)</li> <li>- High power consumption</li> <li>- Single-mode design challenging</li> <li>- More complex packaging</li> </ul>
<b>VCSELs</b>	<ul style="list-style-type: none"> <li>- Circular output (high fiber coupling efficiency)</li> <li>- Inherently single-frequency emission</li> <li>- Low power consumption</li> <li>- High modulation frequencies</li> <li>- Small footprint and high integration yields</li> <li>- Direct on-wafer tests (low costs), simple packaging and high reliability</li> </ul>	<ul style="list-style-type: none"> <li>- Low output power</li> <li>- Long fabrication process</li> <li>- Demanding thermal management</li> <li>- Generally subjected to polarization switching phenomena if no particular solutions are employed</li> </ul>

## 1.3 State-of-the-art of VCSEL technology

### 1.3.1 Short history of VCSEL development

After the first demonstration of a semiconductor edge-emitting laser in 1962 [Hall1962], in 1977 K. Iga of the Tokyo Institute of Technology proposed a different approach based on a vertical structure emitting from the surface. The first VCSEL is demonstrated two years later by the same group [Soda1979]. This device was based on the GaInAsP/InP material system and had an emission at 1.3  $\mu\text{m}$ . Because of the challenging material system chosen to realize this device, laser emission was only possible in pulsed-mode at 77 K with a high current level ( $I_{th} \geq 800$  mA). Improvements on the performance of VCSELs have been achieved in late 1980s, when continuous-wave (CW) operation at room temperature and low threshold current (28-40 mA) was first demonstrated with an 890 nm-emitting GaAs-based VCSEL integrating performant metal/dielectric mirrors [Koyama1989]. A year later, in 1989, Lee and co-workers demonstrated 980 nm-emitting InGaAs/GaAs monolithic VCSELs with thresholds as low as 1.1 mA (average) and 1.3 mA in pulsed and CW operation, respectively [Lee1989]. These two experiments pave the way for the future development and commercialization of VCSELs on GaAs and InP substrates.

Starting from the beginning of 1990s, GaAs-based VCSELs covering the 780, 850 and 980 nm bands have been extensively developed [Geels1990, Lee1991, Wipiejewski1992]. The introduction of the oxide-confinement technique produced a further increasing in the performance of GaAs-based VCSELs [Hayashi1995]. In parallel, InP-based devices benefited from innovative technology concepts, such as the use of deposited dielectric [Baba1993] or wafer-bonded GaAs/Al(Ga)As mirrors [Dudley1994, Babic1995], to improve performance in the 1.3-1.55  $\mu\text{m}$  range as well.

The great effort in pushing the performance and the technological advantages of the GaAs material system, together with the standardization of industrial processes, resulted in the commercialization of a first-generation of GaAs-based VCSELs emitting near 850 nm by Honeywell, in 1996 [Tatum2000]. In the same year, the first GaN-based VCSEL emitting at 365 nm appeared [Redwing1996], increasing the wavelength coverage towards the UV range. One year later, a 2.9  $\mu\text{m}$ -emitting GaSb-based VCSEL was reported [Felix1997].

Starting from 1999, VCSEL-based optical links have been introduced into Gbps Local Area Networks (LANs) and many companies operating in such a field were founded (especially during 1999-2002), aiming to profit by the increasing growth in the optical telecom domain.

In recent years, research on VCSELs technology focused in pushing the limits of the performance of devices based on GaAs and InP on one hand, and optimizing the technology of the GaSb- and GaN-based devices to the other hand. New technologies such as high-contrast gratings (HCG) [Huang2007], tunable MEMS (Micro-Electro-Mechanical Systems) [Haidar2018], photonic crystals (PhC) [Alias2010] and arrays architectures [Moench2016] applied to VCSELs are currently investigated. The worldwide production volume until 2014 was estimated about 1 billion VCSELs with more than 300 million devices in data communication systems [Tatum2014], and the VCSEL market is still growing [ElectroOptics2018, CompoundSemiconductor2018].

### 1.3.2 Different material systems and applications

Thanks to their advantages, VCSELs find several applications, such as telecom systems for short/medium/long haul communications, optical storage, signal processing, power applications, biology/medicine, spectroscopy, sensors and metrology, microwaves, and more.

One of the key point of semiconductor material systems is the versatility offered by the engineering of the emission in terms of spectral coverage, which is not possible or hardly achievable with others laser technologies (i.e. solid-state lasers). According to the different domains and emission wavelengths, different semiconductor material systems are employed. They are summarized in Fig. 1.2, where the well-known semiconductors' constellation map is reproduced.

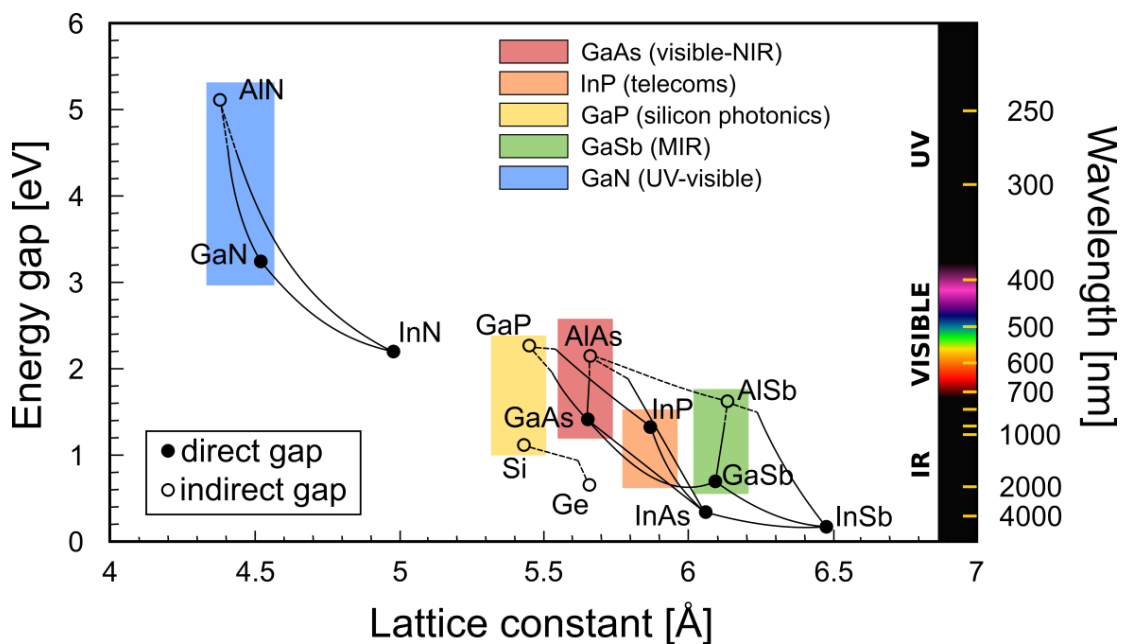


Fig. 1.2 – Energy gap vs lattice constant for different semiconductor compounds families, and their emission wavelength.

Here follows a short description of the material families used in VCSEL technology, together with their main characteristics and range of applications.

## **GaAs**

GaAs-based VCSELs typically cover the 0.7-1  $\mu\text{m}$  band, even if emission at 1.3  $\mu\text{m}$  have been reported from devices incorporating InGaAsN-based quantum wells [Nishida2005] or InAs quantum dots [Chang2006] in their active region. Attempts to further extend the emission range of GaAs-based devices through the 1.55  $\mu\text{m}$  emission range has been made in the past by incorporating antimony on the quaternary InGaAsN [Laurand2006], but the performance of such lasers are lower than their counterparts emitting at the same wavelength and based on InP, which still represents the material system of reference for the optical sources at telecom wavelengths.

Thanks to the good thermal properties of GaAs and related compounds, and the relatively large refractive index contrast between GaAs and AlAs composing the distributed reflector, GaAs-based devices experienced a rapid development. Such devices are able to reach very high modulation speeds in short-distance (1-1000 m) fiber communication systems: 25-28 Gbps for 850 nm-VCSELs are currently in production [Tatum2015], while researchers have demonstrated record speeds of 71 Gbps at 850 nm [Kuchta2015], and 980/1060 nm-VCSELs operating at 50 Gbps [Larisch2016, Larsson2018].

For these reason, nowadays, the VCSEL market is led by GaAs-based devices, which represent roughly 77% of the total market. Their main applications are on the above-mentioned short-haul optical interconnects and storage systems (servers and data centers), informatics/electronics mass products (CD/DVD players, mouse tracking and laser printers), 3D sensing/LIDAR (automotive, laptop/phones, augmented reality, etc.) and power applications (2D arrays for thermal processing or infrared illumination). These laser sources are widely commercialized by several companies worldwide, such as Finisar, IQE, Princeton Optronics, Vixar, Lumentum and Philips Photonics, just to name a few.

## **InP**

InP is the material of choice for telecom applications. Devices based on such a material are capable to emit in the 1.0-1.6  $\mu\text{m}$  wavelength range, in which we found the optical fiber minima in absorption (1.55  $\mu\text{m}$ ) and dispersion (1.3  $\mu\text{m}$ ). The emission range can be eventually extended above 2  $\mu\text{m}$  if active regions integrating type-II quantum wells are employed. With such a method, CW laser emission at 2.5  $\mu\text{m}$  up to 20°C, with maximum single-mode output power above 500  $\mu\text{W}$  in InP-based VCSELs was recently demonstrated [Veerabathran2018]. Despite the enormous technological development of such material system, nowadays the realization of InP-based VCSELs

remains still challenging, due to the poor thermal properties of monolithic grown compounds on InP, which results in lower performance if compared with their GaAs counterparts. Solutions involving the use of buried tunnel junction in combination with high thermal conductive GaAs/Al(Ga)As-based DBRs [Mereuta2015] or hybrid metal/dielectric mirrors [Gründl2013] allowed a significant increasing in the devices' performance. As a result, InP-based single-mode VCSELs is now widely considered as a mature technology, reaching data rates of 30 Gbps at 1270 nm and 25 Gbps at 1310 over 10 km [Müller2012, Caliman2016], 50-56 Gbps at 1530 nm over 200 m-2 km [Kuchta2016, Spiga2017]. For these reasons, some companies (such as Vertilas or Raycan) started to commercialize long-wavelength VCSELs based on InP, which approximately represent 13% of the world market. These devices found application in medium/long-range data transmission systems (WDM networks, FTTH, etc.), in biomedicine (OCT systems), sensors (fiber Bragg grating sensors for stress and deformations monitoring), microwaves (RF links, optical filters), etc.

### **GaSb**

The extension of long-wavelength emission range above 2  $\mu\text{m}$  imposes the use of antimony-based devices, which are largely employed in mid-infrared (MIR) spectroscopic systems for the detection of explosives or pollutants gases having peculiar signatures in this spectral range. However, due to the technological issues and processing difficulties related to antimony, GaSb-based VCSELs are at the very early stage of development. At present, fair performance have been obtained at 2.3-2.6  $\mu\text{m}$  with single-mode output power  $< 300 \mu\text{W}$  in CW operation at room temperature [Arafin2009, Boehm2011], whereas significantly lower CW single-mode output power ( $< 10 \mu\text{W}$ ) has been obtained at low temperature ( $T < 5^\circ\text{C}$ ) in the 3-4  $\mu\text{m}$  range [Andrejew2016, Veerabathran2017]. The use of type-II quantum wells resulted in an improvement of laser performance of long-wavelength emitting VCSELs, enabling the CW laser emission at  $-7^\circ\text{C}$  (and pulsed-mode operation at  $45^\circ\text{C}$ ) with a maximum single mode output up to  $175 \mu\text{W}$  for a 4  $\mu\text{m}$ -emitting GaSb-based device [Veerabathran2018]. Optically-pumped GaSb-based VCSEL operating at room temperature around 3.35  $\mu\text{m}$  and based on type-I InGaAsSb quantum wells have also been recently demonstrated [Jayaraman2018].

### **GaN**

During the past two decades, most of the technological efforts were focused in increasing the performance of red and infrared devices. But for a long time, most of the portion of the visible spectral range had not been covered by VCSELs technology. This was mainly due to the lack of good quality materials adapted for short-wavelength emission, the performance of the gain medium,

and the lack of suitable GaN substrates. Nitride-based VCSELs are promising to cover the near-UV and part of the visible range which is not addressed by the GaAs-based devices (blue-violet, blue and green bands). In 1996 the first optically-pumped GaN-based VCSEL was demonstrated [Redwing1996] and in few years the GaN-VCSEL technology advanced toward electrically-injected devices at low [Lu2008] and room temperature [Higuchi2008]. Anyway, this kind of devices are still at an early stage of development. Several issues must be still solved to achieve high performance CW emission at room temperature, which include the development of good current spreading layers and efficient DBRs, together with improvements of the active region efficiency. Applications of GaN-based VCSELs can include optical storage (Blu-ray disc readers), laser printers, projectors, displays, bio-sensing, etc.

## 1.4 Characteristics of the VCSEL cavity

### 1.4.1 Introduction

A VCSEL is basically composed by a thin micro-cavity in which the gain region, and eventually a carrier confinement section (in the case of electrically-pumped devices), is sandwiched between two highly reflective mirrors, to form the Fabry-Pérot laser cavity with thickness  $L_c$  (cf. Fig. 1.3). The dimension of the micro-cavity is always a multiple of the emission wavelength  $\lambda$ , which corresponds to a typical cavity length in the range of few  $\mu\text{m}$ .

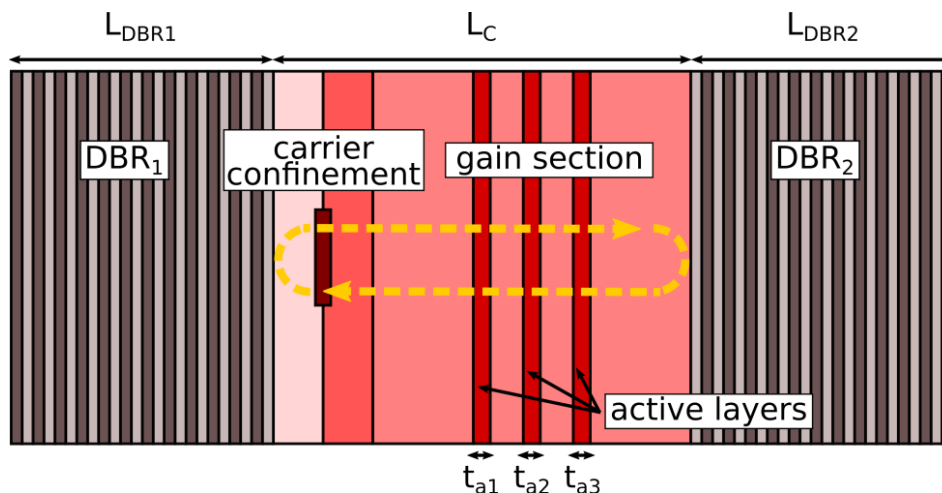


Fig. 1.3 – Main blocks composing the VCSEL cavity (electrically-injected device).

The gain region integrates a finite number  $N_{\text{active}}$  of active sections, such as strained quantum wells or lower dimensional nanostructures (quantum dashes or quantum dots).

Generally, electrical injection is preferred for VCSELs because it makes them compact, although it complicates the fabrication process with additional steps, such as the realization of electrical contacts, carrier confinement and passivation layers. Optical pumping is sometimes used, because it simplifies the process and laser tests, but it requires an additional pump module and optics to be implemented.

The carrier confinement is generally different according to the material system, but the most employed techniques are those based on oxide apertures (typically employed in the GaAs-based devices) and buried tunnel junctions (or BTJ, which are mostly used in the InP system, due to the lack of efficient native oxides). On one hand the carrier confinement allows reducing the laser threshold, and on the other hand it ensures a single-transverse mode emission.

In the following sections, we will present the basic blocks composing vertical-cavity structures, and the principal methods to control the transverse emission on VCSEL devices.

### 1.4.2 Distributed Bragg Reflectors

#### Working principle

As already anticipated, VCSEL devices have a very thin active region which results in a low gain per photon round-trip. Therefore, in order to attain the laser oscillation, high reflective mirrors are needed to reduce the optical losses. VCSELs typically employ specifically designed distributed mirrors, called Distributed Bragg Reflectors (DBRs). The working principle of DBRs is depicted in Fig. 1.4.

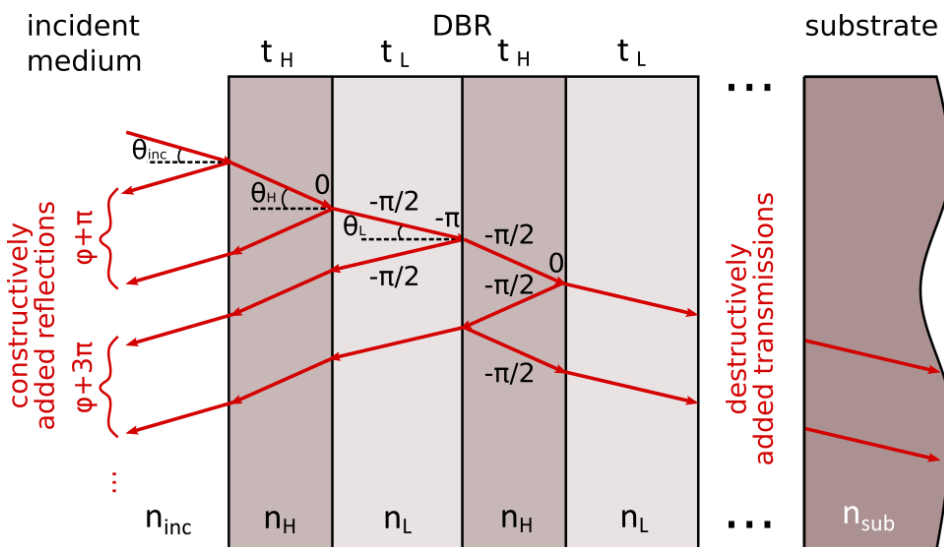


Fig. 1.4 - Standard configuration of a DBR mirror.

A DBR consists in  $N$  periodic stacks of alternative high and low refractive index ( $n_H$  and  $n_L$ ) layers of quarter-wave thickness  $t_i = \frac{\lambda_B}{4n_i}$ , with  $\lambda_B$  the designed Bragg wavelength for which we want to maximize the mirror reflectivity.

The working principle of a DBR can be easily described by considering a propagating wave coming from the incident medium  $n_{inc}$ , which is partially back-reflected at each interface. In particular, no phase shift is introduced when passing from a high index to a low index medium ( $n_H \rightarrow n_L$ ), whereas a phase shift of  $-\pi$  is added otherwise ( $n_L \rightarrow n_H$ ). Moreover, each  $i^{th}$  layer introduces a further phase shift  $\varphi$  equal to  $-\frac{\pi}{2}$  due to the propagation inside that layer.

### Reflectivity and stop-band of a DBR

At the Bragg wavelength, the maximum reflectivity  $R$  for a multilayered structure with  $N$  periods, in the simple case of non-absorbing layers ( $n_i$  are strictly real) and normal incidence ( $\theta_i = 0$ ), is given by [Coldren2012]:

$$R_{even} = \left( \frac{1 - \frac{n_S}{n_{inc}} \left( \frac{n_L}{n_H} \right)^{2N}}{1 + \frac{n_S}{n_{inc}} \left( \frac{n_L}{n_H} \right)^{2N}} \right)^2 \quad R_{odd} = \left( \frac{1 - \frac{n_L n_L}{n_{inc} n_S} \left( \frac{n_L}{n_H} \right)^{2N}}{1 + \frac{n_L n_L}{n_{inc} n_S} \left( \frac{n_L}{n_H} \right)^{2N}} \right)^2 \quad (1.1)$$

which holds for an even ( $2N$ ) or odd number ( $2N+1$ ) of layers, respectively. From Eqs. 1.1, it is clear that the reflectivity increases as the refractive index contrast  $\Delta n = |n_H - n_L|$  rises. In the practice, materials with high values of the refractive index contrast are thus preferred. Eqs. 1.1 also show that the reflectivity of the DBR increases with the number of periods, as clearly expected.

If materials with non-negligible residual absorption are employed for the fabrication of DBRs, an additional contribution which results from the imaginary part of the wave vector related to the propagation losses inside the mirror has to be considered<sup>1</sup>. The presence of a residual absorption of the materials composing the DBR decreases the reflectivity of the mirror. In order to take into account this effect and obtain reliable results, the design of DBRs presented in this Ph.D. thesis is based on the formalism of the Transfer-Matrix Method (TMM). Starting from the definition of the DBR structure, in terms of materials' optical properties (i.e. the complex refractive indices

<sup>1</sup> If the residual absorption is not uniform throughout the mirror (as it is in practical cases), an effective (average) absorption can be considered.



$\tilde{n}_i = n_i + j\kappa_i$ ), thickness of the different layers  $d_i$  and number of periods  $N$  composing the structure, the reflectivity spectra are computed by performing a simple product between the matrices describing the layer stacking. A database of materials' optical properties based on ellipsometry and/or optical transmission measurements on bulk layers has been used to extract the values of complex refractive index  $\tilde{n}_i$ .

To show the effect of increasing the number of pairs  $N$ , we can refer to Fig. 1.5a, which shows the case of a standard GaAs/AlAs-based DBR. As results from the figure, a higher value of pairs  $N$  translates in a higher value of the reflectivity on one hand, but on the other hand it results in a long deposition process and in thicker structures with higher electrical impedances. In practical cases, we also tend to limit the number of pairs to the minimum, because as  $N$  increases, the thermal resistance of the structure increases as well, lowering the heat dissipation of devices from the active region.

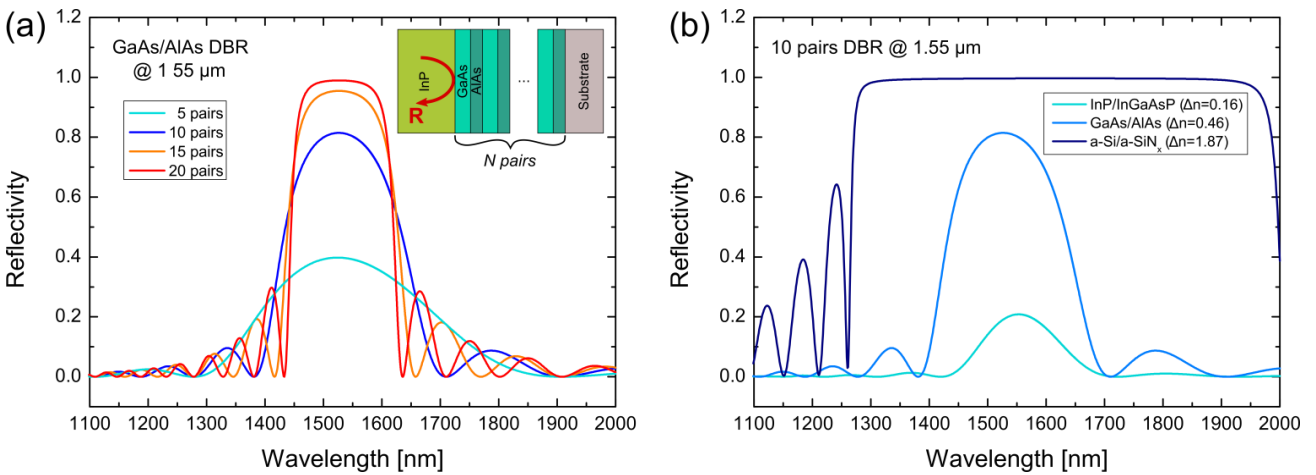


Fig. 1.5 – Evolution of computed reflectivity of a DBR designed at 1.55 μm as a function of (a) the number of GaAs/AlAs pairs  $N$  composing the structure while the mirror composition is fixed, and (b) the index contrast of the layers composing the structure while the number of layer is fixed. The reflectivity has been calculated from inside the VCSEL cavity, i.e. considering the InP as incident material, as sketched in the inset of (a).

It can be possible to limit the number of pairs  $N$  necessary to attain a specific value of reflectivity by using materials with high index contrast. This choice allows reducing the whole thickness of the DBR, while keeping the same value of the reflectivity. Fig. 1.5b shows the comparison of three different DBR designs, which have a fixed number of layers ( $N = 10$  pairs) but different material composition. As attested by the figure, as the refractive index contrast rises, the maximum reflectivity  $R_{max}$  increases from 20% in the case of InP/InGaAsP-based DBR with  $\Delta n = 0.16$ , to 81% using GaAs/AlAs-based DBR ( $\Delta n = 0.46$ ), up to 99.7% when dielectric materials such as a-Si and a-SiN<sub>x</sub> are used ( $\Delta n = 1.87$ ).

Additionally to this, as the refractive index contrast  $\Delta n$  increases, the so-called stop-band  $\Delta\lambda$  (which is the plateau of maximum reflectivity centered on the designed Bragg wavelength  $\lambda_B$ ) increases as well. In literature there are several expressions of the stop-band, according to the approximation used to define it. For instance, it can be roughly estimated by [Babic1992]:

$$\Delta\lambda = \frac{4\lambda_B}{\pi} \sin^{-1} \left( \frac{n_H - n_L}{n_H + n_L} \right) \quad (1.2)$$

A large stop-band plateau is desired in the case of tunable-laser devices, to allow laser operation over a wide range of wavelengths. As we can observe in Fig. 1.5b, among the three different solutions, the a-Si/ a-SiN<sub>x</sub>-based DBR offers the wider stop-band.

However, the index contrast is not the only criterion for the choice of the materials composing the DBR. Thermal conductivity plays an important role as well, to determine the performance of the devices. Indeed, a trade-off between optical and thermal properties is typically chosen, as it will be further discussed in the next chapter.

### 1.4.3 The Fabry-Pérot resonator

#### Resonant field inside a VCSEL cavity

When an optical wave oscillates inside a laser cavity, it generates an internal stationary field, which is characterized by the position of its nodes and antinodes, and its amplitude inside the cavity. In the case of a VCSEL, the Fabry-Pérot cavity is constituted by an active region sandwiched between two DBRs. To properly design a VCSEL, it is fundamental to know the distribution of the optical standing wave inside the cavity. The particularity of a VCSEL is that the internal stationary field is not entirely confined in its cavity, but partially penetrates inside the two DBRs. This partial penetration of the stationary field into the DBR must be considered during the design process of the VCSEL.

Indeed, the knowledge of the resonant stationary field distribution inside the VCSEL cavity helps us to place the gain layers on the antinodes of the resonant stationary field, according to the Resonant Periodic Gain (RPG) configuration [Raja1988], to reduce the laser threshold. Additionally to that, in the case of electrically-injected devices, the highly doped layers composing the buried tunnel junction should be exactly placed on a node of that stationary field, to limit the losses due to free-carrier absorption. The TMM is again useful to this aim.

Fig. 1.6 shows a practical example in a 980 nm-emitting VCSEL based on a GaAs substrate. As it is clear from Fig. 1.6a, the resonant stationary field is resonant inside the cavity, which thickness should be a multiple of a half-wavelength (here we choose an optical thickness equal to  $\lambda$ ). According to that, the structure presents a resonant dip at 980 nm (Fig. 1.6b). The DBRs are designed to have the maximum reflectivity at the emission wavelength and consists in 25 pairs of GaAs/AIAs layers. The penetration of the resonant stationary field inside the DBRs is also noticeable in Fig. 1.6a. In the next section we will see how to evaluate the value of the penetration depth.

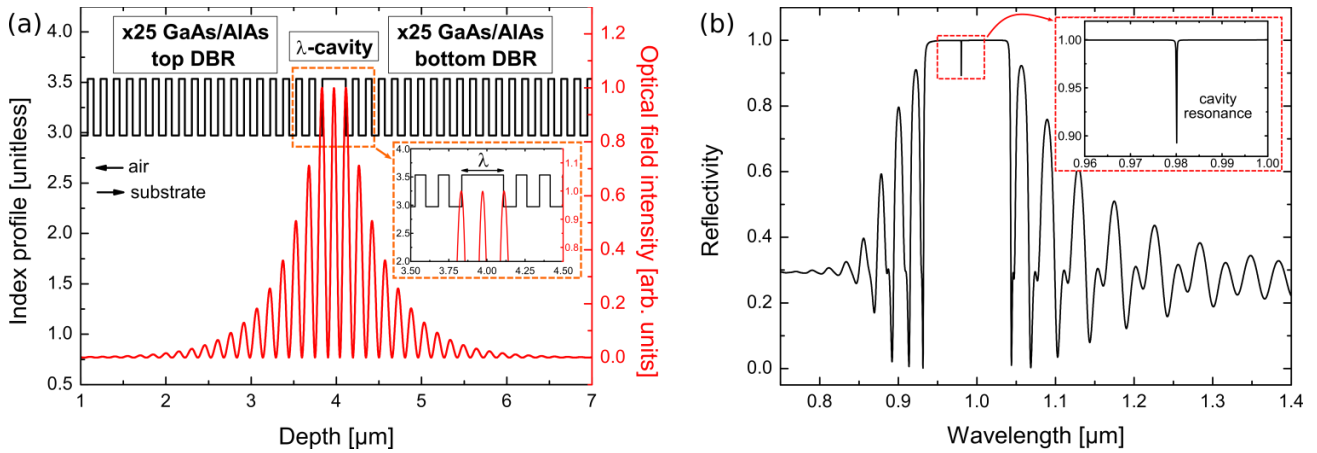


Fig. 1.6 – (a) Computed internal stationary field distribution of a 980 nm-emitting VCSEL cavity formed by two DBRs (25 pairs) and a GaAs cavity with optical thickness equal to  $\lambda$ . (b) Reflectivity spectrum with cavity resonance at 980 nm.

### Penetration depth and mirror dephasing

From a practical point of view, the DBR acts like a distributed plane mirror in which the internal stationary field penetrates for some extent. The penetration of the internal stationary field inside the two DBRs can be taken into account by considering the penetration depth  $L_p$ , which is defined to be [Michalzick2013]:

$$L_p = -\frac{1}{2} \frac{\partial \phi}{\partial k} = \frac{\lambda^2}{4\pi \bar{n}_{gr}} \frac{\partial \phi}{\partial \lambda} \quad (1.3)$$

Here,  $\phi$  is the DBR reflection phase and  $k = \frac{2\pi \bar{n}_{gr}}{\lambda}$  is the wave vector of the incident wave at the DBR wavelength, with  $\bar{n}_{gr}$  the average group index. The penetration of the resonant field inside the DBR depends on the index contrast between the materials composing the Bragg mirror. To limit the penetration depth inside the mirror, here again it is better to use high index contrast DBRs.

The real VCSEL cavity with length  $L_c$  (Fig. 1.7a) can be described by a fictitious cavity (Fig. 1.7b) formed by two effective plane mirrors with the same reflectivity of the respective DBR mirrors, but placed at a distance  $L_{p,i}$  with respect to the real cavity, to take into account the penetration of the stationary field inside the DBR structure. The effective length of the fictitious cavity is then equal to

$$L_{eff} = L_c + L_{p1} + L_{p2} \quad (1.4)$$

In that virtual cavity, the dephasing  $\phi'_i$  is also introduced to obtain the reflected phase equal to the one in the real VCSEL cavity,  $\phi_i$ .

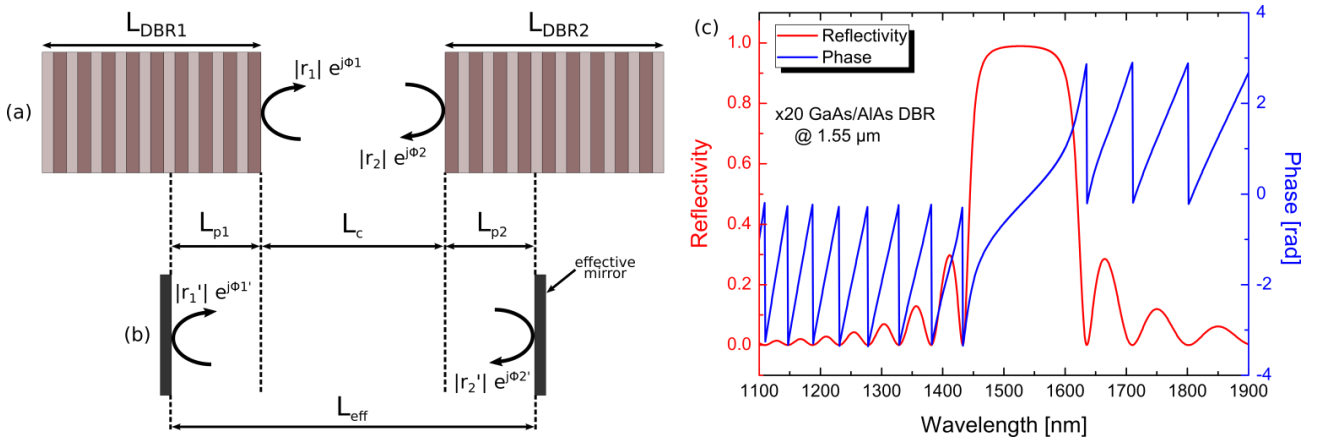


Fig. 1.7 – Definition of penetration length of a DBR: (a) real VCSEL cavity and (b) virtual cavity. (c) Reflectivity and phase spectra of a 20 pairs GaAs/AlAs DBR centered at 1.55  $\mu\text{m}$ .

Around the designed Bragg wavelength  $\lambda_B$  (i.e. in the reflectivity plateau of the DBR, see Fig. 1.7c), the variation of the reflected phase  $\phi_i$  with respect to the wave vector  $k$  is quasi-linear, and it can be approximated by a first-order Taylor development as

$$\phi_i = \phi_{B,i} + (k - k_{B,i}) \left. \frac{d\phi_i}{dk} \right|_{k_{B,i}} \quad (1.5)$$

where  $\phi_{B,i}$  is the dephasing at the Bragg wavelength, and  $k_{B,i} = \frac{2\pi n}{\lambda_B}$  its corresponding wave vector.

### Longitudinal confinement factor and modal gain

As previously seen, the resonance of the optical wave inside the VCSEL micro-cavity produces a stationary field  $E(z,\lambda)$ , which presents nodes and antinodes. The nodes (antinodes) are replicated at

$\Delta z = \frac{\lambda_B}{2\bar{n}_{cav}}$ , where  $\bar{n}_{cav}$  is the average cavity refractive index. The fact that the gain medium in VCSELs is not uniformly distributed over the entire cavity length, together with the fact that the cavity has a very thin thickness ( $\sim \mu\text{m}$ ) if compared with EELs, imposes to adopt a different strategy to assure a sufficient gain to reach the laser oscillation. In order to assure a good coupling with electrons and photons, and thus minimize the laser threshold, the active layers should be periodically accommodated at the antinodes of the resonant field, where its intensity is maximum. The Resonant Periodic Gain configuration also maximizes the overlap between the active layers and the standing-wave pattern  $E(z, \lambda)$ , which can be quantified by considering the longitudinal confinement factor  $\Gamma_z(\lambda)$ , defined as<sup>2</sup>

$$\Gamma_z(\lambda) = \frac{\bar{n}_{active}}{\bar{n}} \frac{\int |E(z, \lambda)|^2 \delta_{active}(z) dz}{\int_{L_c} |E(z, \lambda)|^2 dz} \quad (1.6)$$

where  $\bar{n}_{active}$  and  $\bar{n}$  are the average refractive index in the active section and in the VCSEL cavity, respectively. This expression represents the average optical intensity in the gain region normalized with respect to the total optical intensity in the cavity.

Generally, for simplicity the standing-wave is assumed to have a sinusoidal pattern  $E(z, \lambda) = E_0 \cos(\bar{k}z)$ , with  $\bar{k} = \frac{2\pi\bar{n}}{\lambda}$  the average wave vector inside the cavity. Additionally, the thickness  $t_a$  of the active layers composing the gain medium is designed to be much smaller than the wavelength  $\lambda$  of the standing wave. After integration, we get [Yu2005]

$$\Gamma_z(\lambda) = \underbrace{\frac{t}{L_c} \left[ 1 + \cos\left(\frac{2\pi\bar{n}}{\lambda} z_0\right) \frac{\sin\left(\frac{2\pi\bar{n}}{\lambda} t_a\right)}{\frac{2\pi\bar{n}}{\lambda} t_a} \right]}_{\text{enhancement factor}} = \Gamma_{fill} \Gamma_{enh} \quad (1.7)$$

which holds for a cavity presenting only one active layer.  $\Gamma_{fill}$  is the “fill factor”, and it is the ratio of the total gain sections to the total cavity length.  $\Gamma_{enh}$  is called “gain enhancement factor”, and Fig. 1.8 (next page) shows it as a function of the active section thickness  $t_a$ . The cosine factor

<sup>2</sup> The delta function  $\delta_{active}(z)$  is a function which is equal to 1 at each active layer position ( $z = z_{active}$ ) and 0 elsewhere.

simply takes into account the shift between the active layer center and the standing-wave peak. In the case of a perfectly aligned ( $z_0 = 0$ ) and very thin ( $t_a \rightarrow 0$ ) active section, the gain enhancement factor  $\Gamma_{enh}$  tends to 2, whereas if the active section thickness is a multiple of a half-wave in thickness, then  $\Gamma_{enh} = 1$ . Beside the enhancement of the gain, the RPG configuration also has the advantage to increase the mode selectivity of the designed Bragg wavelength (for which  $\Gamma_{enh} \approx 2$ ) with respect to the other modes off-resonance (where  $\Gamma_{enh} \approx 1$ ).

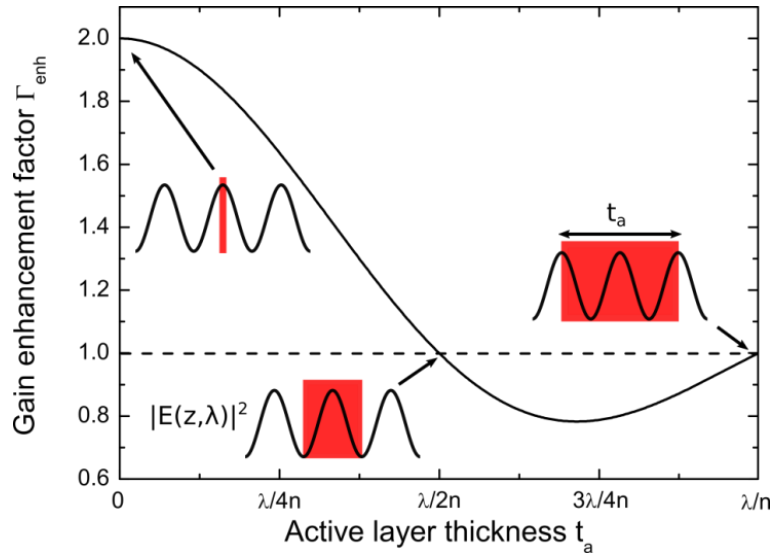


Fig. 1.8 – Gain enhancement factor  $\Gamma_{enh}$  vs active section thickness  $t_a$ , in a VCSEL cavity integrating one active section (here the active section is considered to be centered with respect to a antinode of the resonant field  $E(z, \lambda)$ , so that  $z_0=0$ ).

VCSELs are generally designed to work in a RPG configuration, in order to maximize the gain.

For the same reason, it is common practice to design a VCSEL active region integrating multiples thin gain sections placed on the maximum of the standing wave pattern, rather than a unique thick gain section that extends over several periods of the resonant field.

The total confinement factor  $\Gamma$ , which takes into account both the transverse  $\Gamma_{xy}$  and the longitudinal  $\Gamma_z$  contributions, is defined as

$$\Gamma = \Gamma_{xy} \Gamma_z \quad (1.8)$$

In the case of vertical-cavity devices, the optical field is highly confined in the transverse direction, therefore the transverse confinement factor  $\Gamma_{xy}$  is typically equal to 1. So that, the main contribution to the net modal gain  $g$  is given by the longitudinal confinement factor  $\Gamma_z$ .

The net modal gain of the structure can be expressed as

$$g = \Gamma g_{mat} - \alpha_i - \alpha_m \quad (1.9)$$

Here  $g_{mat}$  is the material gain of the active section composing the gain region,  $\alpha_i$  are the internal losses due to the residual absorption of the layers composing the inner cavity and the DBRs, whereas  $\alpha_m$  are the losses due to the mirror transmission which are distributed along the length of the effective cavity  $L_{eff}$  and eventually a residual absorption term  $\alpha_{abs}$ , according to

$$\alpha_m = \frac{1}{2L_{eff}} \ln \left( \frac{1}{\sqrt{R_1 R_2}} \right) + \alpha_{abs} \quad (1.10)$$

$R_1$  and  $R_2$  being the reflectivity of the top and bottom DBR mirrors, which are defined by the materials composing the Bragg reflectors together with their structure (as described in the previous section).

### Fabry-Pérot cavity parameters

As already seen, the distributed resonator of the VCSEL can be considered as a classic Fabry-Pérot cavity with effective length  $L_{eff}$  and mirror reflectivity  $R_1$  and  $R_2$ , respectively. The resonant electromagnetic field creates an interference pattern characterized by its maxima and minima. Depending on the wavelength of the optical wave, we can have constructive or destructive interference patterns, which give rise to allowed and forbidden cavity modes, as shown in Fig. 1.9a on the next page.

The transmission  $T$  of the Fabry-Pérot cavity, resulting from the multiple allowed reflections inside the optical resonator, can be expressed by the following and well-known formula [[Wilmsen2001](#)]:

$$T = \frac{T_1 T_2}{1 + R_1 R_2 - 2\sqrt{R_1 R_2} \cos \left( \frac{4\pi n L_{eff} \nu}{c} + \phi'_1 + \phi'_2 \right)} \quad (1.11)$$

where  $T_i = 1 - R_i$  is the transmission of the mirrors, in the case of lossless reflectors. Again, it is valid for normal incidence only.

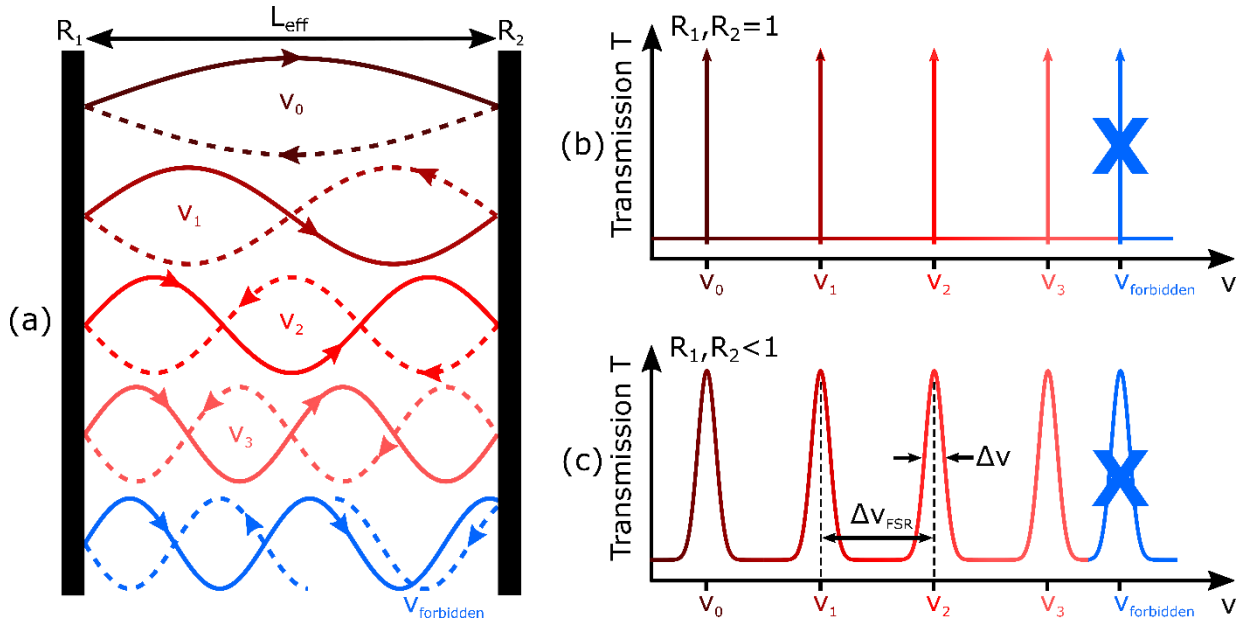


Fig. 1.9 – (a) Constructive/destructive cavity modes inside a Fabry-Pérot resonator, and respective transmission spectra in the case of (b) ideal lossless mirrors ( $R_{1,2} = 1$ ), and (c) real mirrors with a finite residual absorption ( $R_{1,2} < 1$ ).

In resonance conditions, the transmission reaches its maximum (see Fig. 1.9b) and Eq. 1.11 becomes

$$T_{\max} = \frac{T_1 T_2}{1 + R_1 R_2} \quad (1.12)$$

In practical cases, however, the transmission of the Fabry-Pérot cavity is subjected to the residual losses localized in the cavity and DBRs, which translates into a reduction of the maximal transmission value together with a broadening  $\Delta\nu$  of the transmission peaks (cf. Fig. 1.9c). The broadening, which is directly related to the cavity internal losses  $\alpha_i$  and the mirror residual absorption  $\alpha_m$ , can be expressed as follows [Shen2001]:

$$\Delta\nu = \frac{c \left[ \alpha - \frac{1}{L_{eff}} \ln \sqrt{R_1 R_2} \right]}{2\pi\bar{n}} \quad (1.13)$$

where  $\alpha$  takes into account all the above-mentioned total losses encountered during a photon round-trip.



Owing to the thin thickness of the optical cavity, which is comparable with the emission wavelength, in a VCSEL the free spectral range (FSR)  $\Delta\nu_{FSR}$  between the modes is much bigger than in the case of edge-emitting lasers (as schematized in Fig. 1.10).

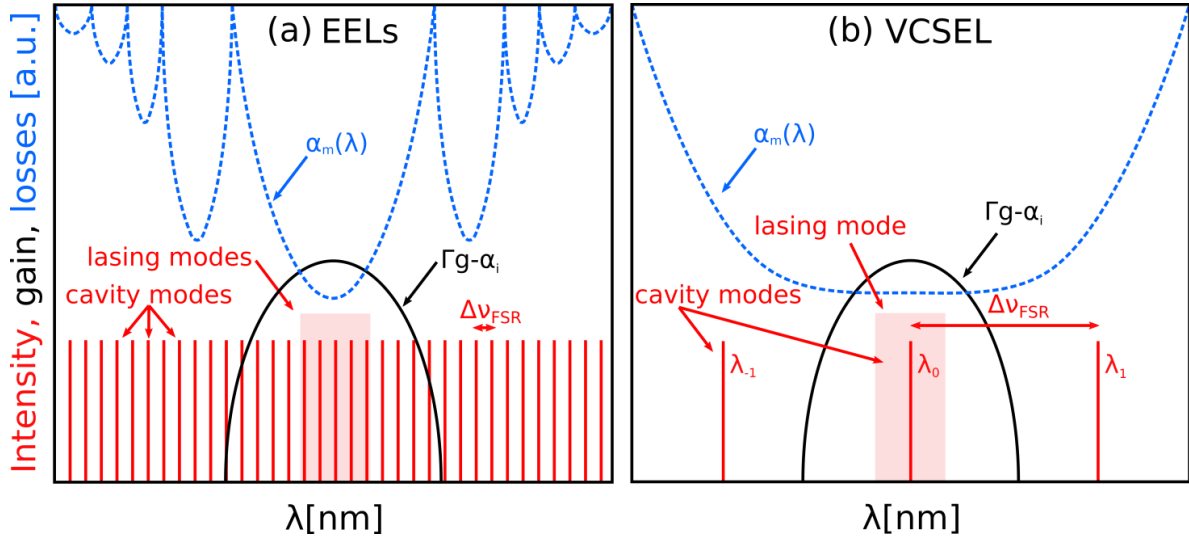


Fig. 1.10 – Longitudinal mode spacing in (a) edge-emitting lasers and (b) vertical-cavity surface-emitting lasers. Net modal gain  $\Gamma g - \alpha_i$  and mirror losses  $\alpha_m$  are reported in both cases.

Since the spectral width of the gain is typically much thinner than the FSR, the short cavity of VCSELs is sufficient to force an inherent single-longitudinal laser operation, which is undoubtedly one of their main advantages of such a class of lasers compared to EELs. This fact, together with an effective control of the transverse modes (as discussed in the next section), is the basis of the single-frequency operation of VCSELs.

#### 1.4.4 Carrier confinement and transverse mode control in VCSELs

Depending on the different material system used for the realization of VCSEL emitters, different strategies can be employed to perform the carrier confinement in the laser active region. The VCSEL is generally designed to assure a low laser threshold by the confinement of carriers in a small recombination section. This section is also involved in the selection of the transverse single-mode operation of the device, while the longitudinal single-mode operation is naturally given by the short cavity of the VCSEL, as discussed above. A single-transverse operation of a laser is necessary to assure an optimal coupling with optical fibers. Thanks to the ability to control the transverse modes, VCSEL assures very high coupling efficiencies, which allows optimal data transfer in optical links, while the single-mode maximum emitted power typically lies in the 1-10 mW range.

In most cases, a single-transverse-mode operation is ensured for confinement surfaces sufficiently small to only support the fundamental Gaussian  $TEM_{00}$  mode, or to highly suppress the higher-

order modes by introducing high optical losses which prevent them to reach the laser threshold. This is typically ensured by confinement surfaces with a diameter of  $\sim 7\text{-}10\ \mu\text{m}$  for VCSEL operating at  $1.55\ \mu\text{m}$ . The carrier confinement section is thus involved in both the path management of the carriers across the semiconductor structure and the lateral confinement of the optical mode. In the following we resume some typical technological approaches developed with the aim of ensuring a single-transverse mode operation. Those involve either optical pumping or electrical injection schemes. In the case of optically-pumped VCSELs, the confinement section is inherently defined by the pump spot dimension, and the optical confinement is ensured by the thermal lens which arises from the thermally-induced change of the refractive index. In the case of electrically-pumped devices, the carrier confinement is achieved by realizing an injection section with low series resistance, surrounded by a highly resistive ring, to confine carriers into a small area in the center of the device. Generally, this requires a more complex design of the VCSEL. Depending on the material system chosen to realize the device, different strategies are employed, as discussed as follows.

### Ion implantation and buried heterostructures

One of the first and simplest techniques for VCSEL single-mode operation involved the use of proton implantation (see Fig. 1.11a) [Orenstein1990]. In this case, the implanted area becomes electrically resistive due to the formation of active defects, forcing the current to flow across a small unimplanted aperture.

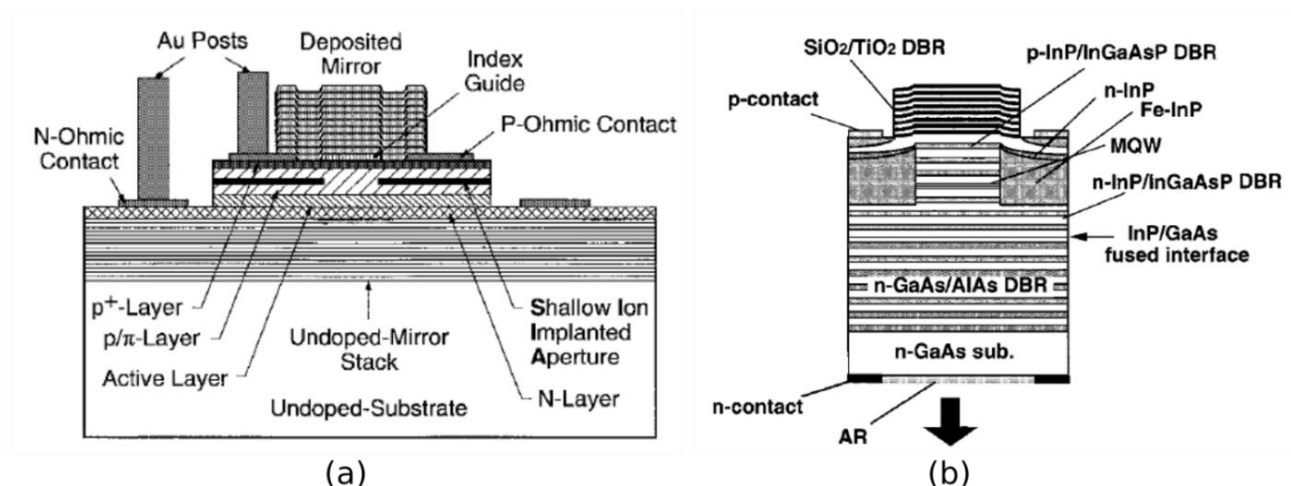


Fig. 1.11 – (a) Electrically-driven 970 nm-emitting VCSEL with proton-implanted aperture (from [Chirovsky1999], © 1999 IEEE) and (b)  $1.55\ \mu\text{m}$  bottom-emitting VCSEL based on buried heterostructure technique (from [Ohiso2002], © 2002 IEEE).

With such an approach, the refractive index variation in the lateral direction is very small, and the transverse optical confinement is weak. The lateral optical confinement is thus mainly due to gain

guiding and thermal lensing phenomena, which are respectively due to the carrier injection along the axis of the device and the heating related to the Joule effect. In particular, such devices are strongly affected by thermal lensing, which may induce the appearance of high-order modes at high injection levels. Truly single-transverse emission, regardless of the injection level, is obtained with aperture diameters of  $\sim 5 \mu\text{m}$  [Chang-Hasnain1990]. Single-mode emission up to 4.4 mW at 945 nm has been reported with such a technique, with apertures of  $8 \mu\text{m}$  [Lear1994].

Buried heterostructures (BH) have been also used to realize single-mode VCSELs. Fig. 1.11b shows an example of this technique, involving the formation of a patterned mesa, with a subsequent epitaxial regrowth. The current confinement is ensured by a semi-insulating regrowth material with high series resistance. The regrowth material can be chosen to assure a sufficient refractive index contrast in order to produce an optical confinement in the transverse direction. An example are Fe-doped epitaxial layers, which have been used to realize VCSELs both emitting at 850 nm and  $1.55 \mu\text{m}$ . However, due to the quality of the regrowth layers, maximum emitted power of less than 1 mW in single-mode has been demonstrated [Ohiso2002].

### Oxide apertures

Significant improvements with respect to the previous techniques are obtained thanks to the oxide confinement method. Such a technique, which has been primarily developed for  $\text{Al}_x\text{Ga}_{1-x}\text{As}$ -based VCSELs, involves the selective oxidation of layers with high aluminum content ( $x > 70\%$ ) to form an aperture (Fig. 1.12). As a result, the oxidized material becomes electrically insulating and the carriers are forced to flow across the central aperture. Furthermore, contrarily to the ion-implanted apertures, a changing in the refractive index appears in oxidized layers, with respect to the non-oxidized ones. The index contrast is such that an efficient optical confinement is additionally obtained.

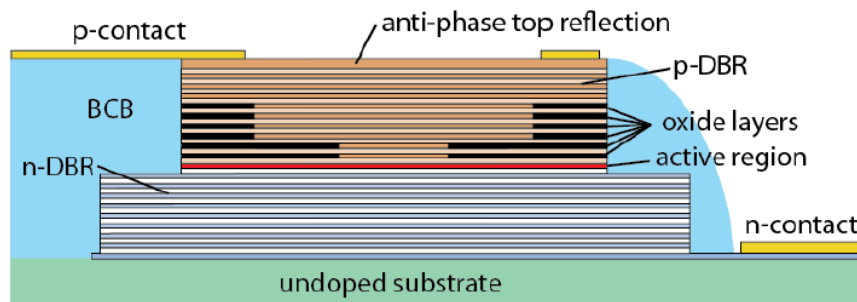


Fig. 1.12 – Cross-view of an 850 nm top-emitting oxide-confined VCSEL (reprinted from [Haglund2012] with permission. Courtesy of Dr. E. Haglund, OptiGOT AB and SPIE).

This technique has also some concerns from a technological point of view, because a precise control of the small aperture size is necessary. Moreover, to improve the current confinement, the oxide

layers are typically placed near the active region. The oxidation can induce a change in the mechanical properties of the layers, which translates into a mechanical stress near the active region of the device. However, nowadays this technique is relatively mature in the VCSEL fabrication industry and was one of the technological breakthroughs in the progress of GaAs-based VCSELs. Single-mode emission power of 4.8 mW at 840 nm can be reached for such technology, with an aperture of 3.5  $\mu\text{m}$  [Jung1997].

### Tunnel junction

The oxidation technology developed for AlGaAs-based VCSELs is not easily transferable to long-wavelength InP- or GaSb-based VCSELs, due to the lack of efficient oxide formation in such material systems. For these devices, a different injection scheme, which involved a buried tunnel junction (BTJ), has been proposed by Amann's group at Walter Schottky Institute in Munich [Ortsiefer2000]. The design of this solution is depicted in Fig. 1.13a.

This solution involves the epitaxial growth of the active region (within a p-n junction) and the n+/p+ tunnel junction, which is patterned afterwards. The tunnel junction is then buried in an n-type layer by a regrowth step. The top reflector can be a semiconductor n-type doped DBR (top contact scheme) or a dielectric DBR (intra-cavity contact scheme), while the bottom reflector is typically a hybrid metal/dielectric DBR.

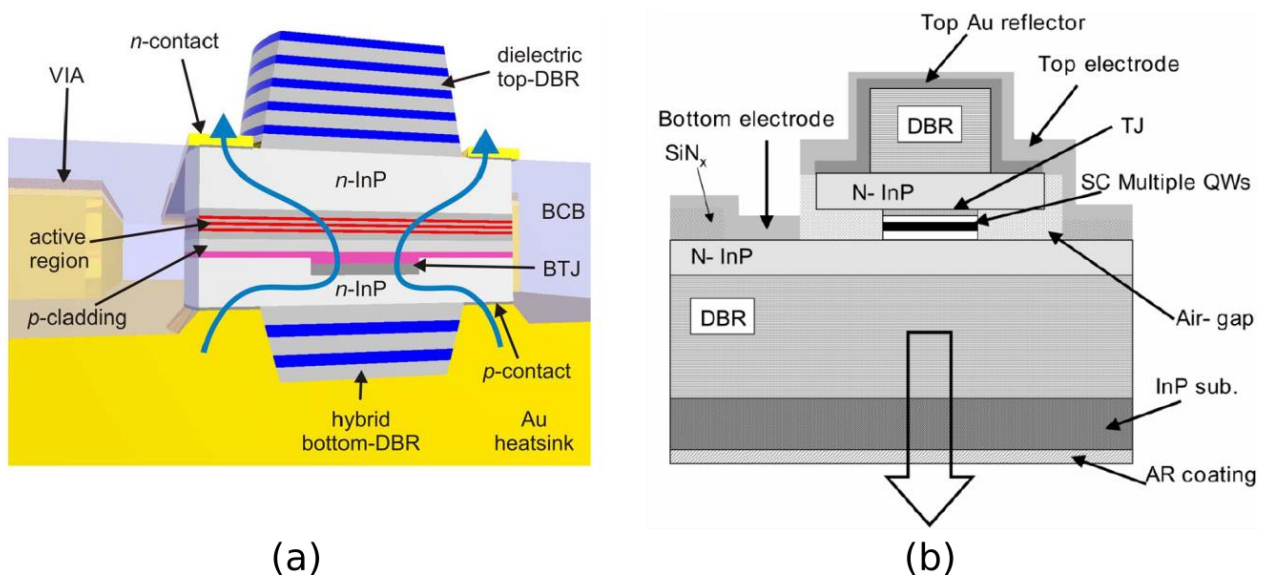


Fig. 1.13 – (a) 1.55  $\mu\text{m}$  top-emitting VCSEL with integrated buried tunnel junction (from [Muller2011], © 2011 IEEE) and (b) Selectively-etched tunnel junction bottom-emitting VCSEL working in the 1.3-1.6  $\mu\text{m}$  range (from [Park2006], © 2006 IEEE).

The transverse current confinement is ensured by the inversely polarized (i.e. blocking) p-n junction surrounding the BTJ, while the optical confinement is due to the refractive index contrast in lateral direction. With small diameters of the BTJ ( $\leq 10 \mu\text{m}$ ), a single-mode emission is obtained. A record

of 7.9 mW in single-mode emission has been demonstrated for 1.55  $\mu\text{m}$ -emitting VCSELs integrating a 7  $\mu\text{m}$ -diameter BTJ [Gründl2013] and 6.8 mW at 1.3  $\mu\text{m}$  ( $d_{BTJ} = 6 \mu\text{m}$ ) [Mereuta2015], whereas for the GaSb-based devices emitting above 2  $\mu\text{m}$  the output power is well below 1 mW ( $d_{BTJ} = 6 \mu\text{m}$ ), as already discussed in Section 1.3.2 [Arafin2009]. Thanks to these results, carrier confinement based on BTJs became the elective approach for the long-wavelength VCSEL based on InP and GaSb substrates.

A different way to pattern a tunnel junction is to use a selective etching method, in order to form an air-gap aperture of 6-8  $\mu\text{m}$ , which ensure the transverse confinement of the current and the optical mode, according to the design shown in Fig. 1.13b. The etching is performed thanks to wet chemical etchants with high selectivity between binary and ternary or quaternary compounds composing the layers, in order to overetch in the lateral direction.

The air/semiconductor index difference produces a high optical confinement, while the electrical injection is ensured by the presence of the tunnel junction. However, carrier recombination process on the lateral surface, together with mechanical stress can limit the performance. With such a design, single-mode emission up to 1-1.6 mW in the 1.3-1.6  $\mu\text{m}$  range has been obtained [Park2006].

### Optical pumping

The previous methods are based on electrical injection of carrier in the active region of VCSELs. Carrier injection can be also performed by optical pumping: in this case carriers are photo-generated by a pump laser which is absorbed by the gain layers. The pumped region is thus defined by the surface of the pumping laser spot. An example of optically-pumped VCSEL is shown in Fig. 1.14.

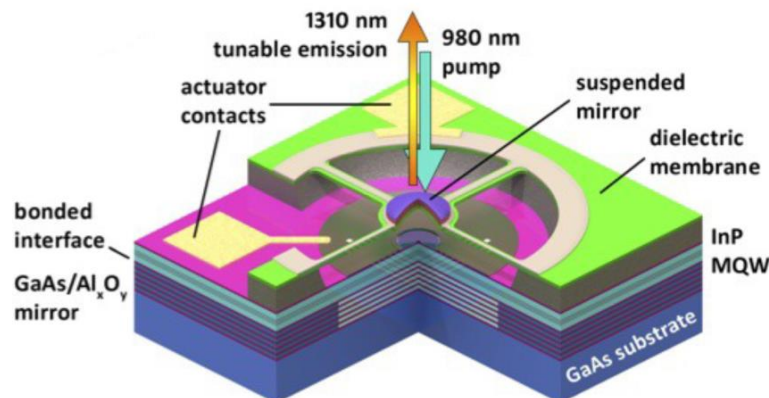


Fig. 1.14 – Optically-pumped tunable VCSEL at 1.3  $\mu\text{m}$  integrating a MEMS movable mirror (reprinted from [Jayaraman2013] with permission. Courtesy of Dr. V. Jayaraman and SPIE).

This method avoids complicated technological steps to realize the VCSEL device, since the realization of the carrier confinement section with highly doped layers, the eventual intra-cavity

current-spreading layers and the electrical contacts can be avoided. On the other hands an optically-pumped device can be more cumbersome with respect to its electrical version because of the presence of the pump module and the focusing optics. Nevertheless, it is useful because it allows fast characterizations of devices in order to validate new technological approaches. Additionally, self-heating effects can be reduced because the carriers are directly generated into the active region, which may result in an increased output power and operating temperature of the device. Typical pump spot diameter is 10-20  $\mu\text{m}$  and the output power is in the mW range.

## 1.5 Conclusions

In this chapter we discussed some key points of the design of VCSEL devices and their working principles.

After a brief comparison between conventional edge-emitting lasers and VCSELs, we emphasized the advantages of the latter technology, such as their power efficiency, the good coupling with optical fibers and the low costs.

Afterwards, **we presented the building blocks of a VCSEL cavity and their design rules**. Firstly, we discussed the working principles of the Distributed Bragg Reflectors. Subsequently, we focused the attention of the architecture of the Fabry-Pérot resonator and their figures of merits, which should be taken into account to realize efficient devices. A brief presentation of the most used technologies for carrier injection and single-mode optical confinement has been done. It allowed comparing these technological solutions, in order to choose the most eligible in the case of an InP-based device, as it is our case.

Indeed, two approaches are suitable:

- The first one, based on **the optical confinement of the carriers, allows a simple development of the VCSEL technology and a fast characterization of the devices**. We choose to use the optical pumping to validate the Through Silicon Holes Electroplated Copper (TSHEC) approach, which is a new process developed at FOTON Institute to realize VCSEL devices integrated in a Silicon host platform. It will be the subject of the next chapter.
- At a later time, **we adopted the buried tunnel junction approach, which allows the electrical injection of the devices** and represented, across the years, the best choice in terms of performance (emitted output power in single-mode emission). Moreover, the TSHEC technology can be adapted to be compatible with the BTJ approach. We will discuss about this point in *Chapter 2* as well.



# ***Chapter 2***

## ***Development of VCSEL technology: design, realization and characterization***

<b>2.1 Development of InP-based VCSELs: technological challenges</b> .....	<b>32</b>
2.1.1 Material for DBRs based on InP system .....	32
2.1.2 Electrical confinement issues.....	37
<b>2.2 A new approach for thermal management: TSHEC process</b> .....	<b>39</b>
2.2.1 Motivations.....	39
2.2.2 Hybrid metal-dielectric DBRs .....	42
2.2.3 TSHEC process development.....	49
2.2.4 Devices characterization.....	54
<b>2.3 Development of the electrical-injected VCSEL technology</b> .....	<b>62</b>
2.3.1 Buried tunnel junction: investigations.....	63
2.3.2 EP-VCSEL cavity design .....	75
2.3.3 Technological process for electrically-injected VCSELs .....	79
2.3.4 Preliminary results on EP-VCSEL tests sample.....	83
<b>2.4 Conclusions</b> .....	<b>84</b>



## 2.1 Development of InP-based VCSELs: technological challenges

As anticipated in *Chapter 1*, during the years InP-VCSELs faced a significant delay with respect to the short-wavelength counterpart based on the GaAs system. This is mainly due to different technological problems inherent to the InP system and its related compounds. Nowadays, the development of cost-efficient VCSELs emitting in the 1.55  $\mu\text{m}$  wavelength range, with relatively high output power ( $> 1 \text{ mW}$ ) and enhanced thermal dissipation is still challenging, but would represent a real breakthrough with important consequences for the industrial and the scientific communities.

In the first part of this chapter we will discuss the main challenges in the development of InP-based devices, together with some technological solutions which have been developed to overcome such limitations.

With respect to this general context, we will present a new technological process for the realization of InP-based VCSELs which has been recently developed at FOTON Institute, which represents our contribution to solve the above-mentioned challenges. This technology, which has been called TSHEC (which stands for “Through Silicon Holes Electroplated Copper”), is based on the use of polymer bonding to integrate a III-V active region onto a silicon host substrate, thanks to copper-filled vias acting as localized micro-heat sinks.

The validation of this approach has been firstly obtained with an optically-pumped version of 1.55  $\mu\text{m}$ -emitting VCSELs based on InGaAsP quantum wells (QWs), integrating thermally-improved buried hybrid metal/dielectric DBRs mirrors. Related characterizations of the devices confirmed a good performance in terms of improved output emission, decreased laser threshold and lower thermal resistance, validating the effectiveness of the approach.

Following these results, the TSHEC technology has been adapted to the development of the electrically-injected version of the device. The basic blocks composing the devices (such as the BTJ or the cavity geometry) have been designed and optimized and a new set of masks have been realized. Preliminary results on test structures allowed validating the new approach.

### 2.1.1 Material for DBRs based on InP system

#### Technological limits of lattice-matched DBRs

Conversely to the GaAs system, thermal efficient DBRs with high refractive index contrast are missing in the case of the InP system. Table 2.1 (next page) summarizes the properties of the main lattice-matched semiconductor materials used to realize the DBRs of InP-based VCSELs, compared

with the GaAs/AlAs system, which represents the semiconductor system of reference in terms of optical and thermal performance. The average thermal conductivity  $k_{t,avg}$  of a pair of layers is calculated in the vertical direction (across the layers) for a reflector designed at  $1.55 \mu\text{m}^1$ .

**Table 2.1 – Refractive index  $n$  and thermal conductivity  $k$  of some semiconductor material systems.**

Substrate	Material 1 / Material 2	$n_1$	$n_2$	$\Delta n$	$k_{t,1}$ [W/m-K]	$k_{t,2}$ [W/m-K]	$k_{t,avg}$ [W/m-K]
InP	InGaAlAs <sub>1,42μm</sub> / InAlAs	3.50	3.21	0.29	4.5	4.5	4.5
InP	InGaAsP <sub>1,44μm</sub> / InP	3.46	3.17	0.29	3.5	68	7
InP	InGaAlAs <sub>1,42μm</sub> / InP	3.50	3.17	0.33	4.5	68	9
InP	AlGaAsSb <sub>1,4μm</sub> / AlAsSb	3.50	3.10	0.40	6.2	5.7	6
GaAs	GaAs / AlAs	3.38	2.91	0.47	53	84	66

Refractive indices  $n_{1,2}$  are given at  $1.55 \mu\text{m}$ .  $k_{t,1}$  and  $k_{t,2}$  is the thermal conductivity of material 1 and 2, respectively.

As evidenced from the table, the optical and/or thermal performance of lattice-matched materials on InP substrates are rather poor. In order to get high reflective DBRs based on such lattice-matched compounds exceeding 99.5% of reflection (generally required to get laser operation of VCSELs), a greater number of pairs would be needed to compensate for the lower index contrast. This finally results in thicker and poorly conductive structures, strongly affected by a severe temperature rise in the gain region, leading to higher laser threshold, limited output power and reduced dynamic characteristic for the devices. Additionally, the large number of pairs needed to realize the top and bottom DBRs in the InP system imposes excessively long growth sequences, implying high risks in layer thicknesses deviation, and thus degradation in DBRs performance.

These are the main reasons why epitaxially-grown DBRs on InP cannot represent the best choice for long-wavelength VCSELs.

### Different approaches for thermal management in InP-based VCSELs

The lack of thermally and optically efficient DBRs in the InP system pushed the community to develop alternative strategies to replace the native lattice-matched reflectors on InP-based VCSELs to improve their reliability and performance. Two main approaches emerged as leading candidates:

- the integration of GaAs/Al(Ga)As-based DBRs;
- the use of thin Bragg reflectors based on dielectric materials.

<sup>1</sup> The value of the average thermal conductivity  $k_{t,avg}$  in the vertical direction is calculated according to [Lee2009]:

$$k_{t,avg} = \frac{\sum_i t_i}{\sum_i \frac{t_i}{k_{t,i}}}, \text{ where } t_i \text{ is the quarter-wave thickness of the } i^{\text{th}} \text{ layer composing the DBR at } 1.55 \mu\text{m}$$

These two approaches are very different, but they have the same goal: decreasing the thermal impedance of the device in order to increase the heat flow from the active region toward the heat-sink. In the case of GaAs-based DBRs, the approach consists in employing highly conductive materials to promote the thermal dissipation across the mirror, while in the case of dielectric materials composing the DBR, the strategy is to minimize the number of layers  $N$  composing the reflector (and thus its total thickness) by using large index contrast materials, and simultaneously to simplify the process.

*a) GaAs/AlAs DBRs: wafer fusion and metamorphic growth approaches*

As the GaAs/AlAs system is characterized by exceptional optical and physical properties, DBRs based on such materials would provide a significant improvement to the performance of InP-based devices too. However, the growth of GaAs and related compounds on InP substrates by standard epitaxial methods is not straightforward, due to the difference in the lattice constant of the two material systems (cf. Fig. 1.2 in *Chapter 1*), and it involves the use of advanced techniques.

One solution is represented by the “wafer fusion” approach, pioneered by J.E. Bowers and colleagues at the University of California Santa Barbara. It consists in the separate growth of the active region on the InP wafer and the GaAs/AlAs DBRs on the GaAs wafer, and then fusing the two substrates together, in order to form a heterostructure [Liau1990, Lo1991, Ram1995]. The fusion is carried out by relative long thermo-compression steps obtained thanks to dedicated equipment [Sirbu2010]. As a result of the process, the two parts are subjected to a plastic deformation and are uniformly bonded together at the nanometric scale, with smooth fused interfaces (Fig. 2.1a, next page). The GaAs substrate is then selectively etched away to complete the process.

With such a technique, CW emission up to 6.8 mW at room temperature (and 2.8 mW at 80°C) was reported on single-mode 1.3  $\mu\text{m}$ -emitting VCSELs based on 5 InAlGaAs/InP multi-quantum wells (MQWs) [Mereuta2015]. On 1.55  $\mu\text{m}$ -emitting VCSELs integrating InAlGaAs strained MQWs, demonstration of room temperature CW emission up to  $\sim 6$  mW (8 mW at 0°C) and device operation up to 115°C was also reported [Caliman2011]. Dynamic characteristics of 1.3  $\mu\text{m}$ -VCSELs employing GaAs-based DBRs are also quite interesting, allowing to reach a direct modulation at  $>25$  Gbps and bandwidths exceeding 11 GHz [Caliman2016].

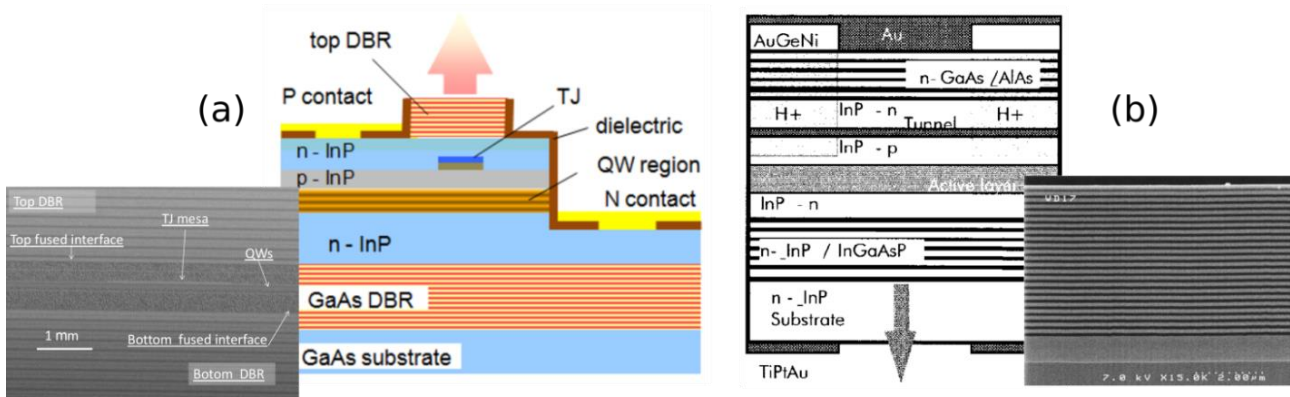


Fig. 2.1 – Schematic structure of (a) a 1.3 μm-emitting VCSEL realized by wafer fusion technique (reprinted with permission from [Merueta2015], © The Optical Society) and (b) a 1.55 μm-emitting VCSEL incorporating metamorphic grown GaAs/AlAs DBRs from [Boucarter1999b], © 1999 IEEE. Insets shows the SEM cross-section of a double-fused heterostructure (reprinted with permission from [Iakovlev2013], courtesy of Pr. E. Kapon and SPIE), and a metamorphic grown GaAs/AlGaAs DBR (reprinted from [Boucarter1999b], © 1999 IEEE).

However, the strict requirements imposed by the wafer fusion technique (i.e. the separate growth of active region and DBRs) increase the technological steps and costs required to realize the devices. Additionally, wafers with high quality surface (i.e. low interfaces roughness) are essential.

A different and completely monolithic approach involving the metamorphic growth of the GaAs-based reflectors on the InP substrate has been developed to simplify the process. In order to avoid the propagation of dislocations, this technique typically implies particular growth conditions (i.e. the integration of buffer layers at the interfaces, low growth temperatures, etc.) to limit the surface roughness and obtain smooth interfaces (Fig. 2.1b) [Boucarter1999a]. The advantages of the monolithic approach are generally at the expenses of a minor performance with respect to the wafer fusion technique. CW emission of devices at room temperature has been demonstrated at 1.55 μm, with multi-mode output levels up to 1 mW (< 0.2 mW in single-mode) and operation up to 47°C on a VCSEL device based on 9 compressively strained InGaAsP QWs [Boucarter1999b].

#### b) Dielectric DBRs: hybrid integration

Although the integration of GaAs-based DBRs assures a good performance of devices, it involves relatively complex techniques. A different and simpler approach consists to realize the DBR mirrors with dielectric materials. Fig. 2.2 on next page shows an example of such an approach.

This solution has the obvious advantage to speed up and simplify the process thanks to plasma-aided deposition techniques (such as PECVD or RF sputtering) with respect to epitaxial growth required for semiconductor-based DBRs. In addition, the use of dielectric materials reduces the realization costs.

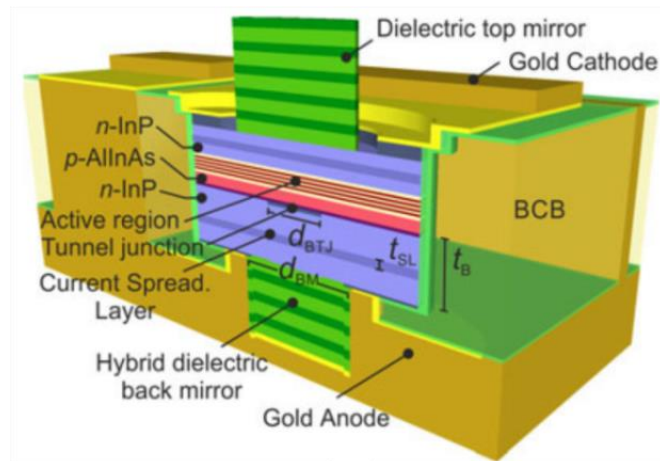


Fig. 2.2 – Schematic structure of a 1.55  $\mu\text{m}$ -emitting VCSEL integrating a 5-pairs top AlF<sub>3</sub>/ZnS dielectric DBR and a 3.5-pairs bottom hybrid AlF<sub>3</sub>/ZnS/Au DBR reprinted from [Spiga2017], © 2017 IEEE.

Table 2.2 resumes the properties of some dielectric materials employed in long-wavelength InP-based VCSELs. The high index contrast offered by dielectrics allows a considerable reduction of the number of layers needed to reach high values of reflectivity, which translates into a reduction of the overall thickness of the structure. However, their poor thermal conductivity (similar to that of ternary and quaternary compounds of the InP system, cf. Table 2.1), represents their main drawback.

Table 2.2 – Properties of most used dielectric materials for DBRs\* (designed at 1.55  $\mu\text{m}$ ).

Dielectric materials		Refractive index			Absorption [ $\text{cm}^{-1}$ ]		Thermal conductivity [ $\text{W/m-K}$ ]			N for $R \geq 99.5\%$
Mat. 1	Mat. 2	$n_1$	$n_2$	$\Delta n$	$\alpha_1$	$\alpha_2$	$k_{t,1}$	$k_{t,2}$	$k_{t,avg}$	
ZnS	CaF <sub>2</sub>	2.29	1.43	0.86	-	-	6.8	1.8	2.5	3.5
AlF <sub>3</sub>	ZnS	1.34	2.29	0.95	-	-	2	6.8	2.7	3.5
TiO <sub>2</sub>	SiO <sub>2</sub>	2.44	1.44	1	20	-	1.2	1.4	1.3	6
SiO <sub>2</sub>	SiC	1.44	2.57	1.13	-	-	1.4	490	2.2	6.5
a-Si	a-SiN <sub>x</sub>	3.7	1.86	1.84	440	-	2.6	1	1.3	5
a-Si	Al <sub>2</sub> O <sub>3</sub>	3.7	1.74	1.96	440	-	2.6	0.7	0.9	5
a-Si	SiO <sub>2</sub>	3.7	1.44	2.26	440	-	2.6	1.4	1.6	4
a-Si	CaF <sub>2</sub>	3.7	1.43	2.27	440	-	2.6	1.8	2	2.5

\*values have been taken from literature [Piprek1995, Shau2001, Ortsiefer2005, Gierl2014a, Gierl2014b]

To partially mitigate this problem, dielectric DBRs are often combined with highly-reflective metallic layers (such as Au) to form hybrid metal/dielectric reflectors [Symonds2004b, Hofmann2010]. The presence of the metal at the end of the mirror is used to boost the mirror's reflectivity and further decrease the number of layers, resulting in improvements in the thermal

resistance of the devices. The metallic pseudo-substrate in which the device is typically embedded acts also as a thermal heat-sink and offers an improved mechanical stability. This strategy, which is quite general, can be applied to GaAs/Al(Ga)As-based DBRs as well. Additionally, a further improvement of the thermal impedance of hybrid DBRs involves the reduction of the lateral dimensions of the reflector to promote the lateral heat flux toward the metallic heat-sink.

Devices integrating such buried hybrid metal/dielectric DBRs integrated in metallic pseudo-substrates have been proved to attain good performance in terms of output power, where a record room temperature single-mode emission of 7.9 mW and laser operation at a temperature as high as 90°C have been obtained with 1.55  $\mu\text{m}$ -emitting VCSELs [Gründl2013], while dynamic response with modulation bandwidth exceeding 21 GHz [Spiga2017] and data rates up to 56 Gbps [Kuchta2016] have been also reported.

An additional advantage of hybrid metal/dielectric reflectors, with respect to their semiconductor counterparts, is the relatively wide stop-band arising from the large refractive index contrast which can be achieved with such materials. This last advantage finds also application in the realization of highly-tunable devices.

## **2.1.2 Electrical confinement issues**

A further problem of InP-based VCSELs is the difficulty to efficiently inject carriers in the gain region of the lasers. As described in the previous chapter, GaAs-based devices benefit from the reliable and simple technique employing the selective oxidation of Al(Ga)As layers to realize low resistive apertures and inject the electrical carriers across very small surfaces. The success of such a technique is one of the reasons of the extensive development of GaAs-based VCSELs across the years, allowing extremely low threshold currents ( $I_{th} \sim 200 \mu\text{A}$ ) [Huffaker1994], with some record examples below  $10 \mu\text{A}$  [Yang1995]. In the past, there have been attempts to reproduce the oxidation technique in the InP system using ternary or quaternary compounds such as InAlAs, InAlAsP or AlGaAsSb [Gebretsadik1998, Linnik2001, Reddy2003]. Particularly, the antimony-based compounds showed acceptable oxidation rates at low temperature. Unfortunately, this compound is unstable, because of the diffusion of Sb during the oxidation process, which gives rise to optical losses due to non-radiative recombination and lateral carrier diffusion phenomena induced by the thin Sb conductive layer, which are responsible to relatively high threshold current levels ( $I_{th} = 60\text{-}300 \text{ mA}$ ) [Reddy2003]. Moreover, complications during the etching steps of Sb-rich layers further limit the use of such materials on InP-based devices.

The practical issues related to the efficient technological transfer of the oxidation technique on the InP material system pushed to the development of new solutions for carrier and optical confinement

in long-wavelength devices. Indeed, the afore-mentioned techniques have been rapidly outperformed by the one based on the buried tunnel junction, and nowadays state-of-the-art devices emitting several mW in single-mode operation at 1.3-1.55  $\mu\text{m}$  currently employs this solution [Gründl2013, Mereuta2015].

To briefly resume the technological progress and the most effective approaches to realize long-wavelength InP-based electrically-pumped VCSELs, Table 2.3 presents the main solutions which have been proposed through the years, together with the best performance reported so far.

**Table 2.3 – State-of-the-art performance of single-mode InP- based EP-VCSELs.**

Approach	DBRs composition	Electrical confinement method	Emission wavelength [ $\mu\text{m}$ ]	Performance				Ref.
				$P_{out}$ [mW]	$I_{th}$ [mA]	$T_{max}$ [ $^{\circ}\text{C}$ ]	$d_{(BTJ)}$ [ $\mu\text{m}$ ]	
Monolithic growth	InGaAsP/InP	Buried heterostructure + TJ	1.32	1.1	< 1	90	5	[Francis2005]
	InAlGaAs/InAlAs	Selectively etched TJ	1.34	1.1	2	80	12	[Park2006]
			1.54	1.6	2.5	80	12	
	AlGaAsSb/AlAsSb	Selectively etched TJ	1.56	0.9	0.8	88	8	[Nakagawa2001]
Metamorphic growth	GaAs/AlAs	H <sup>+</sup> implantation + TJ	1.55	0.2	16.5	47	35	[Boucart1999b]
Double wafer bonding	GaAs/AlGaAs	BTJ	1.3	6.8	0.8	100	6	[Mereuta2015]
			1.54 - 1.58	6	5	115	7	[Caliman2011]
Buried hybrid metal/dielectric deposition	AlF <sub>3</sub> /ZnS + Au	BTJ	1.55	7.9	2.5	115	7	[Gründl2013]

As we can see from the table, the use of (buried) tunnel junctions seems unavoidable to get efficient devices. Among all the presented techniques, those based on double wafer-bonding or buried hybrid metal/dielectric DBRs are by far the best in terms of emitted power and maximum operation temperature.

In the framework of this Ph.D. thesis, the improvement in the performance of InP-based devices emitting in the 1.55-1.6  $\mu\text{m}$  range was one of the main motivations to develop a new technological process which is suitable for the realization of VCSEL integrating hybrid metal/dielectric (a-Si/a-SiN<sub>x</sub>/Au) DBRs mirrors. Such a process, which has been initially

developed in the case of optically-pumped devices, it is also fully compatible with an electrical-injected version of VCSELs. The detailed descriptions of the development of the new process, together with the experimental characterizations of devices, are the subject of the following section.

## **2.2 A new approach for thermal management: TSHEC process**

In the following, we will detail the new technological process developed at FOTON Institute, called Through Silicon Holes Electroplated Copper (TSHEC) process, which allows an efficient integration of electrically-pumped VCSELs based on buried hybrid gold/dielectric bottom mirrors, benefiting from copper micro-heat-sinks to improve their thermal dissipation. Besides that, it also provides a flexible and cost-effective solution to the heterogeneous combination of III-V active regions onto a Si host substrate, allowing the development of photonics and microelectronics co-integration.

This new approach is thus intended to simultaneously provide a solution to the following points:

- possibility of a hybrid integration of III-V active region (or virtually any other material) on a Si platform;
- realization of mechanical stress-induced-free devices;
- significantly improvements in thermal management of VCSELs;
- compatibility with both optical pumping or electrical injection schemes;
- cost-effectiveness and potential industrial scalability;
- simultaneous microelectronics, photonics and microfluidics on-chip integration.

Before detailing such a technique, however, we will focus the attention to the design of the hybrid metal/dielectric DBR and its optical and thermal optimization. This preliminary step, which is presented in the following section, has been crucial for the realization of a thermally-improved version of the bottom reflector, and it acts as a starting point toward the development of the TSHEC technique and the optimization of the VCSEL's performance presented in this Ph.D. dissertation.

### **2.2.1 Motivations**

As discussed above, one of the main limitations for thermal management in InP-based VCSELs is related to the thermal performance of the bottom DBR, through which the heat generated in the



active region is generally evacuated. The different approaches (described in the previous section) used to realize the DBRs in the case of InP-based devices have been studied and compared with the help of a commercial finite element modeling (FEM) software.

**Table 2.4 – Structure and parameters of the optically-pumped VCSEL thermal model.**

OP-VCSEL structure		
Active region description	DBRs composition	DBRs thickness
3 sets of 3×8 nm-thick InGaAsP MQWs separated by 10 nm-thick InGaAsP barriers + InP spacers and an InP phase layer	<b>(a) InP/InGaAsP</b> $k_{i,v} = 6.8 \text{ W/m-K}$ $k_{i,t} = 36.6 \text{ W/m-K}$	TOP: ×75 layers, $t_{top} = 18 \mu\text{m}$
		BOTTOM: ×78 layers, $t_{bottom} = 18.7 \mu\text{m}$
	<b>(b) GaAs/AlAs</b> $k_{i,v} = 66 \text{ W/m-K}$ $k_{i,t} = 69 \text{ W/m-K}$	TOP: ×17.5 layers, $t_{top} = 4.3 \mu\text{m}$
		BOTTOM: ×24.5 layers, $t_{bottom} = 6 \mu\text{m}$
	<b>(c) a-Si/a-SiN<sub>x</sub></b> $k_{i,v} = 1.3 \text{ W/m-K}$ $k_{i,t} = 1.5 \text{ W/m-K}$	TOP: ×4 layers, $t_{top} = 1.3 \mu\text{m}$
		BOTTOM: ×6.5 layers, $t_{bottom} = 2.1 \mu\text{m}$

$k_{i,v}$  and  $k_{i,t}$  are the average thermal conductivities along the vertical ( $z$ ) and the transverse directions ( $x$  and  $y$ ), respectively.

A 2D-axisymmetric thermal model (details on the model can be found in **Appendix B**) has been developed to simulate the case of an optically-pumped VCSELs integrating an InGaAsP-based active region composed by three sets of three 8 nm-thick MQWs emitting at 1.55  $\mu\text{m}$ . The device is fixed onto a metallic pseudo substrate, which acts as a heat-sink, and its temperature is fixed to 300 K. Owing to the vertical design of the VCSEL cavity, it is obvious that the thermal performance of the bottom DBR are crucial to effectively remove the heat generated in the active region.

Different DBRs based on three material systems of reference have been compared: InP/InGaAsP, GaAs/AlAs and a-Si/a-SiN<sub>x</sub> (amorphous silicon and amorphous silicon nitride). The VCSEL structure is resumed in Table 2.4, together with the parameters used in simulations.

In this model, the lateral dimension of DBRs has been set to be equal to the device itself (i.e. 1 mm). The three structures only differ for the thickness of the layers and the materials composing

the Bragg reflectors. In each case, the DBRs have been designed to have the same reflectivity, namely  $R \sim 99\%$  for the top and  $R \sim 99.6\%$  for the bottom reflector. The results of the simulations are shown in Fig. 2.3. They are obtained by considering a dissipated power in the active region equal to 20 mW and a pump spot diameter of 15  $\mu\text{m}$ , resulting in a dissipated power density of  $D_{diss} \sim 11 \text{ kW/cm}^2$ .

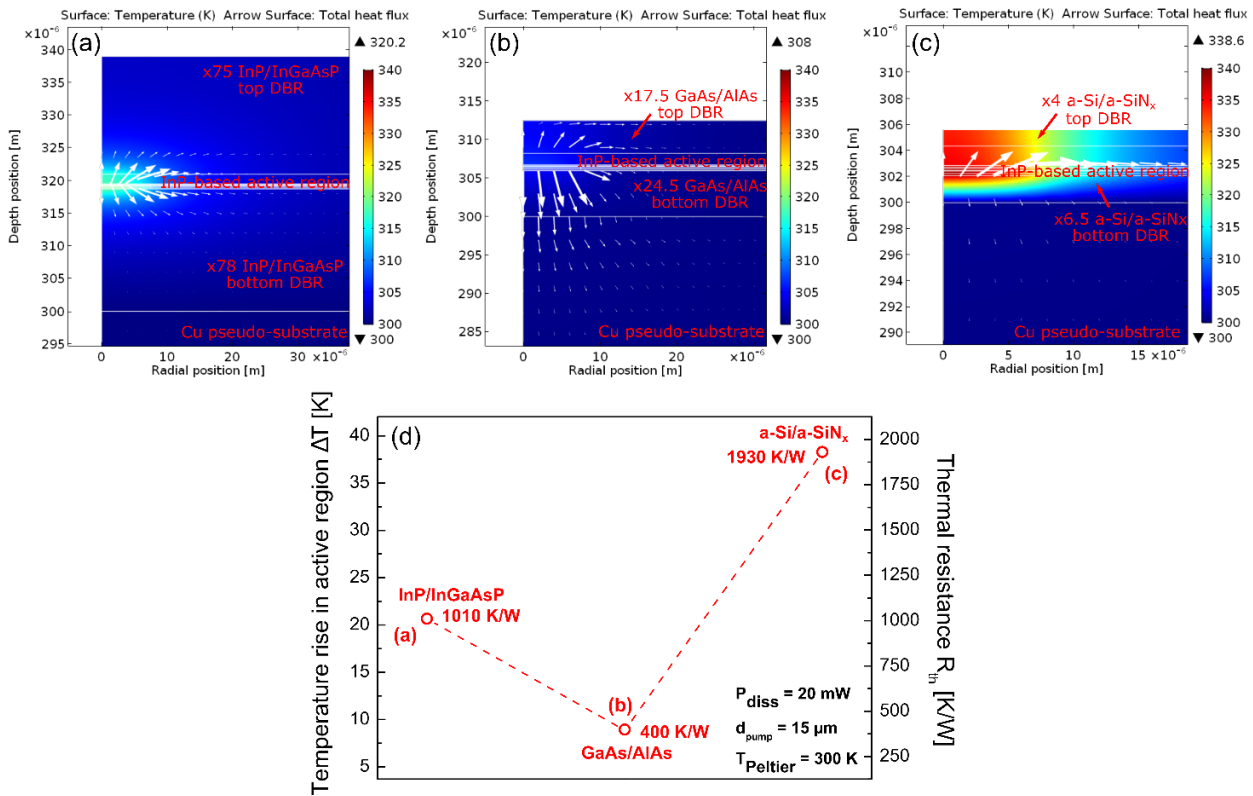


Fig. 2.3 – FEM simulations of an OP-VCSEL integrating (a) InP/InGaAsP, (b) GaAs/AlAs or (c) a-Si/a-SiNx top and bottom DBRs. (d) Temperature rise and thermal impedance related to structures (a), (b) and (c). White arrows represent the total heat flux across the devices. Dissipated power is 20 mW and pump spot diameter is 15  $\mu\text{m}$  (i.e.  $D_{diss} \sim 11 \text{ kW/cm}^2$ ). Dashed red line is a guide for the eyes.

Entirely monolithic InP/InGaAsP DBRs typically present an extremely high number of pairs ( $N \sim 80$ ) to attain such values of reflectivity [Francis2005], which result in very thick structures (see Fig. 2.3a). As a result, main of the heat remains confined in the active region, while a small amount flows laterally across the top InP spreading layer and partially through the DBR. We stress the fact that, in this case, the relatively large lateral dimensions of the device help extracting the heat towards the periphery of the device. In more realistic devices, the lateral mesas are typically smaller, thus temperature rise would be higher because the lateral flow would be reduced.

In the case of a device integrating GaAs/AlAs DBRs, the excellent thermal properties of the materials composing the reflectors are responsible to the efficient spreading of the heat essentially across the bottom mirror towards the heat-sink, as attested by Fig. 2.3b.

Despite their very thin thickness, FEM simulations shows that large area DBRs based on dielectric materials do not offer an optimal solution to heat dissipation, since the bottom reflector acts as a thermal barrier for the heat flow towards the heat-sink, limiting the performance of the devices, as shown in Fig. 2.3c. Lateral heat flow in this case is not sufficient since we do not benefit from thick InP layers on the top of the device, which would help the spreading of the heat.

## 2.2.2 Hybrid metal-dielectric DBRs

Several strategies have been developed to mitigate the impact of dielectric DBR mirrors on the thermal impedance of VCSELs and to obtain low-cost DBRs with performance closer to that of GaAs-based counterpart. In this perspective, InP-based VCSELs can benefit from optimized designs employing thick InP heat spreading layers and efficient packaging involving flip-chip or embedded heat-spreaders approaches [Masabih2017, Kaur2014, Muller2011]. Anyway, InP spreading layers must be limited in thickness because of constraints on the maximum length of the VCSEL cavity, so that this remains a hardly practicable way to improve the performance. A hybrid design of the resonator, together with the localization of the metallic heat-spreader as close as possible to the active region, can be a good solution to limit the temperature rise in the active region of the device [Hofmann2010]. As a result, a very thin bottom dielectric DBR embedded into a metallic host pseudo-substrate can represent the best compromise in terms of a simplified process, cost and optical/thermal performance.

The long experience gained at the lab on the use of low-cost dielectric materials for the realization of DBRs naturally addressed us towards this latter approach. In fact, since the studies of C. Levallois on the use of a-Si and a-SiN<sub>x</sub> for DBRs for the realization of DBR mirrors [Levallois2006a], FOTON Institute has developed a reliable and reproducible process for the deposition of such dielectric materials. In the framework of this Ph.D. thesis, we focused the efforts to minimize the thermal resistance of the bottom reflectors by completing the dielectric DBR with a high-reflective and thermally efficient metallic layer on one hand, and to limit the lateral dimension of the bottom DBR to the other hand, in order to benefit from an improved thermal dissipation through the bottom of the device.

For what concerns the metallic layer, typical metals employed for bottom heat-spreaders are Au or Cu [Gründl2013, Mathine1996], both presenting superior thermal efficiency. Au, for its optical properties, is additionally well adapted to be integrated in hybrid DBRs as high-reflective layer to improve the mirror reflectivity. On the other hand, if compared to gold, Cu is less expensive and has high thermal conductivity, which makes it really attractive to be integrated as efficient heat-

spreader. Moreover, it is widely diffused in microelectronics. An intermediate solution which employs a thin gold layer to boost the reflectivity and a copper heat-spreader to promote the thermal dissipation is particularly interesting, because it allows exploiting the advantages of both materials.

However, regardless of whether Au or Cu is used, metallic pseudo-substrates with large surfaces are not compatible with any realization process involving high temperatures ( $> 85^{\circ}\text{C}$ ), because of the appearance of stress-induced deformations and defects in the epitaxial layers, which are the result of a significantly difference in the thermal expansion between the metal and the semiconductor materials<sup>2</sup>.

In the case of optically-pumped VCSELs, the components are not subject to high temperatures steps after the metal deposition, so that the use of large metallic surfaces is still tolerated. Conversely, the processing of electrically-injected devices is based on high-temperature post-processing steps implying lithographic and thermal annealing procedures, so that this approach is no longer possible. Since our final purpose is to develop electrically-injected devices, a solution which avoids the use of large metallic pseudo-substrates is thus desired. This also was one of the motivations for the development of the TSHEC process, which will be detailed later on.

### Design and optimization of hybrid metal/dielectric DBRs

A hybrid DBR (H-DBR) differs from the standard DBR configuration (Fig. 2.4a) from the fact that a high reflective metallic layer is added at the end of the structure (Fig. 2.4b).

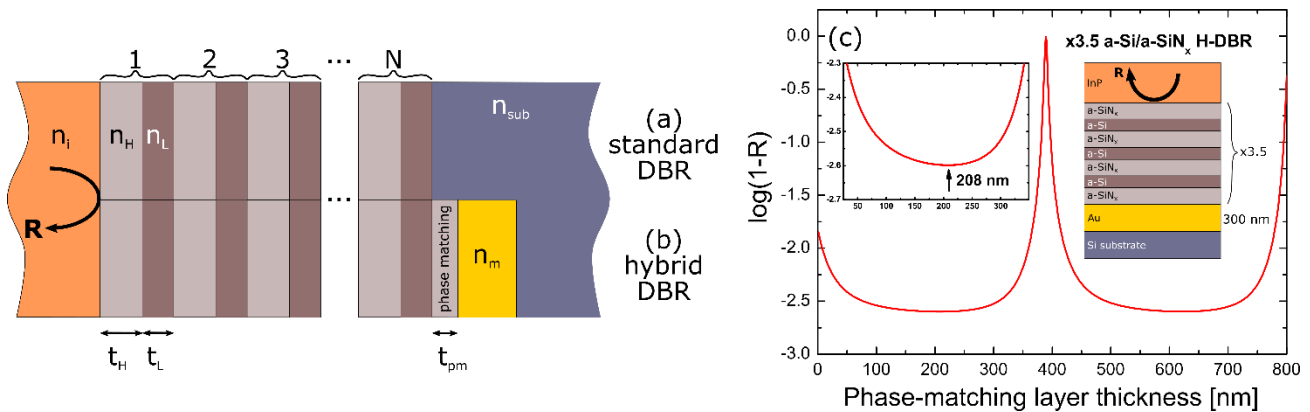


Fig. 2.4 – Distributed Bragg reflectors: (a) Standard and (b) hybrid configuration with  $N$  pairs of alternative layers. (c) Influence of the phase-matching layer thickness on the reflectivity of a H-DBR (designed at  $\lambda_B = 1.55 \mu\text{m}$ ).

<sup>2</sup> Linear thermal expansion coefficients (at 300 K):  $\alpha_{t,Au} = 14.2 \times 10^{-6} \text{ K}^{-1}$ ,  $\alpha_{t,Cu} = 17 \times 10^{-6} \text{ K}^{-1}$ ,  $\alpha_{t,InP} = 4.6 \times 10^{-6} \text{ K}^{-1}$ ,  $\alpha_{t,InGaAsP} = 4.6 - 5.7 \times 10^{-6} \text{ K}^{-1}$ .

At the metallic interface, the presence of the metallic layer induces a phase shift  $\Delta\varphi$  of the optical wave inside the structure. This shift can be compensated by inserting a phase-matching layer with an adaptive thickness  $t_{pm}$ , which can be calibrated by using the TMM method cited in the previous chapter. Our first efforts have been then focused in the optimization of the hybrid DBRs in terms of number of pairs  $N$  and phase-matching layer thickness  $t_{pm}$ .

As already said, Au is regularly employed as metallic layer, eventually in combination with Ti, Ni or Cr to improve its adhesion with dielectric materials, especially in the case of large area depositions. Unfortunately, the adhesion materials introduce a severe optical absorption which limits the maximum achievable reflectivity, even if very thin layers (10-15 nm) are employed. Besides that, the absorption of the optical field in the adhesion layer translates in unwanted thermal heating which also limits the performance of the devices. Benefits on the overall performance of the DBR can be obtained if no adhesion layers are employed, provided that the adhesion of the Au to the dielectric layers is sufficient.

In addition to that, the reflectivity may be also limited by the residual absorption of the materials used to realize the Bragg mirror (in our case, the amorphous silicon being the main responsible). These effects have been taken into account during the design of the hybrid DBRs thanks to experimental FTIR and transmission data on optical properties of the materials used in simulations.

Thanks to the TMM method, the reflectivity spectrum of the DBR is computed. At the same time, the procedure allow optimizing the thickness of the phase-matching layer  $t_{pm}$  to achieve the highest reflectivity at the designed Bragg wavelength  $\lambda_B$ .

The optimization of the phase-matching thickness has a great influence for maximizing the reflectivity at the designed wavelength (in our case  $\lambda_B = 1.55 \mu\text{m}$ ), as attested by Fig. 2.4c. TMM simulations allowed identifying an optimal H-DBR configuration integrating 3.5 pairs of a-Si/a-SiN<sub>x</sub>, with a phase-matching layer of 208 nm in thickness. For such a structure, a theoretical reflectivity of 99.75% has been computed.

Once the optimal structure has been found, the refractive index profile and the stationary optical field intensity inside the structure are computed. The procedure is also able to estimate the effective length  $L_{eff}$ , the average effective absorption  $\alpha_{eff}$  and the effective refractive index  $n_{eff}$  inside the structure.

Fig. 2.5 (on the next page) compares a standard dielectric a-Si/a-SiN<sub>x</sub> DBR and its optimized hybrid version. Both mirrors present the same number of pairs, namely 3.5. The hybrid DBR clearly shows a significantly higher value of the reflectivity. It also provides a wider stop band with respect to a standard dielectric mirror.

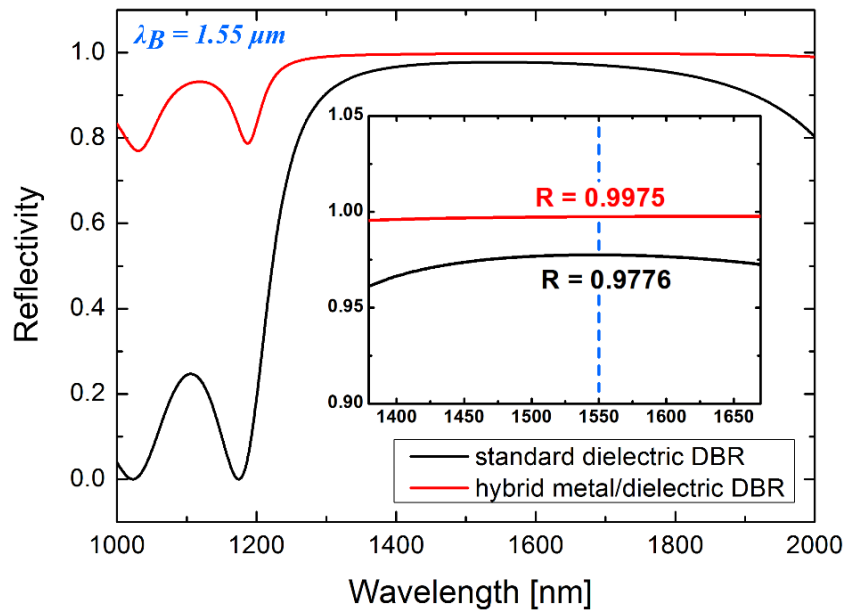


Fig. 2.5 – Comparison between a standard dielectric DBR (black) and its corresponding hybrid version (red). Both mirrors integrate 3.5 pairs of  $a\text{-Si}/a\text{-SiN}_x$  layers and have been designed at  $1.55 \mu m$ .

### Realization and characterization of H-DBRs

In the case of standard dielectric DBRs, the reflectivity is typically obtained by means of transmission measurements of the light across the structure, which is typically deposited on a glass support. This approach cannot be used with hybrid mirrors because of the high absorbing metallic layer at the end of the structure, that prevents the light to be detected on the opposite side of the mirror. In this case, only a study in reflection can be performed.

However, in the case of highly reflective mirror, it is not straightforward to measure the precise value of reflectivity. It is thus extrapolated by simulations, or it is experimentally measured by multi-reflection methods [Berseth1998] or cold-cavity methods [Levallois2006a]. We choose the latter approach, being easier to implement and less sensitive to any spatial inhomogeneity due to the deposition techniques involved in the realization of the dielectric Bragg mirrors.

For this aim, we realized a sample onto a quarter of 2-inches Si wafer by means of RF sputtering deposition. It consists in a half-wave  $a\text{-SiN}_x$  layer sandwiched between two stacks of quarter-wave-thick Bragg mirrors, to form a high quality factor cold-cavity (Fig. 2.6a on the next page). The top mirror of the structure is a standard 4.5 pairs  $a\text{-Si}/a\text{-SiN}_x$  dielectric DBR, whereas the bottom one is a 3 periods hybrid DBR. Both the top and the bottom mirrors have been designed to have a similar value of reflectivity and to be resonant around  $1.55 \mu m$ . Note that a Ti adhesion layer is added in this case, to ensure the perfect adhesion of the Au across the whole surface.

The measurement has two main purposes:

1. it allows extracting a reliable value for the reflectivity of the hybrid DBR;

- it allows estimating the value of the residual absorption of the a-SiN<sub>x</sub> and the a-Si layers, which is generally relatively low.

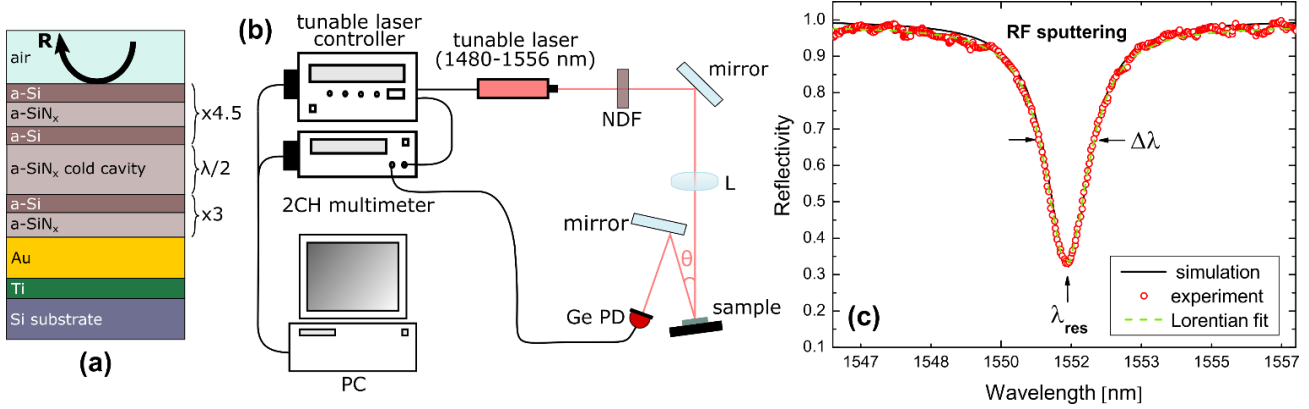


Fig. 2.6 – a-SiN<sub>x</sub> cold cavity: (a) structure of the sample, (b) experimental setup, (c) measurement and simulation results.

The sample has been characterized with the experimental setup shown in Fig. 2.6b. The optical source is represented by a tunable laser (1480-1556 nm range) with a resolution of 0.05 nm and a variable output power between 2 and 7 mW. The laser beam is attenuated by a neutral density filter (NDF) to avoid the saturation of the Ge photodetector. A lens is used to focus the laser beam and to have a small spot diameter on the surface of the sample, to avoid thickness variation effects of the  $\lambda/2$ -thick layer on the measurement of the linewidth of the cavity mode. The tunable laser is automatically controlled by a PC with a LabVIEW<sup>®</sup> virtual instrument [LabVIEW], which also allows acquiring the detected signal from the spectrometer and the tuned wavelength via a dual-channel digital multimeter.

The result of the measurements on the cold cavity is shown in Figs. 2.6c, for an incident power of 3 mW (the results being independent with respect to the incident power).

The reflectivity of the hybrid mirror is related to the quality factor  $Q$  of the cavity through [Shen2001]:

$$Q = \frac{\lambda_{res}}{\Delta\lambda} = \frac{2\pi n_{eff} \lambda_{res}}{c \left[ \alpha_{eff} - \frac{1}{L_{eff}} \ln(R_{top} R_H)^{1/2} \right]} \quad (2.1)$$

$\lambda_{res}$  being the cavity resonant wavelength,  $\Delta\lambda$  the full width at half maximum (FWHM) of the resonant cavity mode,  $c$  the speed of light,  $n_{eff}$ ,  $\alpha_{eff}$ , and  $L_{eff}$  the effective refractive index, the effective absorption and the effective length of the cold-cavity, while  $R_{top}$  and  $R_H$  are the top standard and bottom hybrid DBR reflectivity, respectively. The result of the measurement presented

in Fig. 2.6c allows estimating a quality factor of  $Q \sim 1260$ , which is compatible with that of a VCSEL resonator.

The result of the analysis is resumed in Table 2.5. It provides an estimated reflectivity of 99.45% for the bottom hybrid DBR. These values, which are in good agreement with the theoretical predictions of simulations ( $R_{H,th}$ ), show the potentiality of the hybrid configuration, which ensures a thinner structure while maintaining a high value of reflectivity ( $R \sim 99.5\%$ ), if compared to the expected  $R \sim 97.8\%$  of the standard configuration without the Au layer (cf. previous Fig. 2.5).

**Table 2.5 – Cold cavity parameters.**

$L_c = \lambda/2$ [nm]	414
$n_{eff}$	2.103
$a_{eff}$ [ $\text{cm}^{-1}$ ]	$\sim 36$
$L_{eff}$ [nm]	860
$\lambda_{res}$ [nm]	1552
$\Delta\lambda$ [nm]	1.23
$Q$	$\sim 1260$
$R_{top}$ [%]	99.39
$R_H$ [%]	99.45
$R_{H,th}$ [%]	99.55

### Thermal impedance of H-DBRs

We are now going to show the benefits on the thermal resistance of VCSELs when the standard fully-dielectric bottom DBR is replaced by the hybrid reflector. To this aim, we again consider the thermal FEM models of the optically-pumped VCSEL that we have introduced before.

The top dielectric DBR of the OP-VCSEL is composed by 4 pairs of a-Si/a-SiN<sub>x</sub> in both cases, while the bottom reflector is:

1. a standard fully-dielectric DBR composed by 6 pairs of a-Si/a-SiN<sub>x</sub>, in the first case;
2. a hybrid 3.5 pairs a-Si/a-SiN<sub>x</sub> DBR completed by 200 nm Au layer, in the second case.

Again, to fairly compare the two devices, the bottom mirrors are both designed to have the same reflectivity ( $R \sim 99.6\%$ ).

As shown in Fig. 2.7 on the next page, the result of simulations show an appreciable decrease of the maximum temperature of the device (-7.4 K) when the hybrid configuration is employed, which is associated to an improvement in the thermal resistance, where a value of  $R_{th} = 1560$  K/W has been obtained. This results in a  $\sim 19\%$  improvement with respect to the fully-dielectric DBR, which



shows a thermal resistance of  $R_{th} = 1930$  K/W. Also, from FEM simulations we can notice a slight increase of the thermal flow from the active layer down to the substrate, as the main consequence of the reduction of the thermal resistance, even if most of the dissipation still occurs across the InP spreading layer.

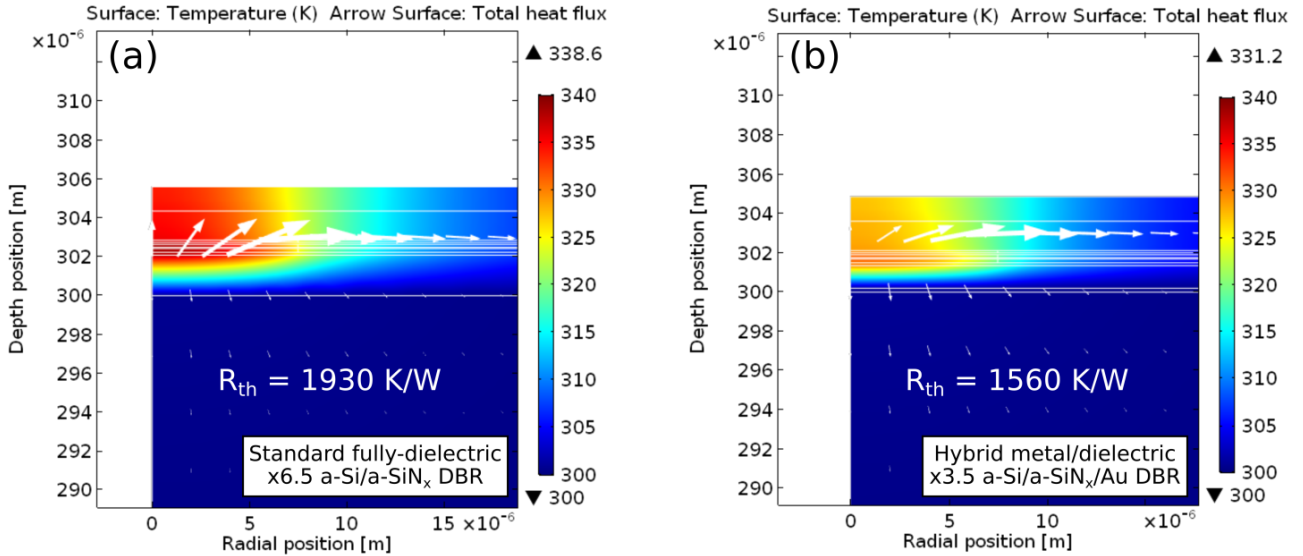


Fig. 2.7 – Comparison between (a) a 6.5 pairs standard dielectric DBR and (b) a hybrid metal/dielectric DBR with 3.5 pairs completed by 200 nm-thick Au layer.  $P_{diss} = 20$  mW and  $d_{pump} = 15$   $\mu$ m.

### Optimization of the lateral dimensions of H-DBRs

To conclude, this study has shown that the use of the hybrid configuration for the bottom mirror is more promising than a fully-dielectric approach. In particular, the high reflectivity offered by the presence of the Au layer in the hybrid version of the a-Si/a-SiN<sub>x</sub> DBR allowed decreasing the number of pairs of the bottom mirror from 6.5 to 3.5, and thus reducing the thermal impedance of the device by 19%, without sacrificing its optical performance ( $R \geq 99.5\%$ ).

Significant thermal improvements could be further achieved if the lateral dimensions of the bottom DBR are reduced, in order to benefit from the direct contact of the metal heat-sink with the gain section, to promote the lateral extraction of the heat generated in the active region and further lower the thermal impedance of the device (see Fig. 2.8a, next page). As shown in Fig. 2.8b, we expect a theoretical improvement of the order of 20% of the thermal resistance if a 20  $\mu$ m-large buried H-DBR is used ( $R_{th} \sim 1250$  K/W) instead of a large area H-DBR ( $R_{th} \sim 1560$  K/W), which results in a significant  $\sim -35\%$  thermal impedance decreasing with respect to the fully-dielectric case ( $R_{th} \sim 1930$  K/W). This becomes even more noticeable ( $\sim -59\%$ ) in the case of a 10  $\mu$ m-large BH-DBR (B stands for buried), for which a value of  $R_{th} \sim 800$  K/W has been obtained. It is worth to notice that this value, although higher, begins to be comparable to that obtained with a GaAs/AlAs-based DBR ( $R_{th} = 400$  K/W). Conversely to the devices integrating BH-DBRs with

lateral dimensions in the range of  $d_{BH-DBR} = 10-30 \mu\text{m}$ , in the case of BH-DBRs with  $d_{BH-DBR} \geq 50 \mu\text{m}$  the benefits are less evident.

Based on the results of FEM simulation, the adoption of the buried hybrid DBR approach has been the starting point for the development of the new technological TSHEC process.

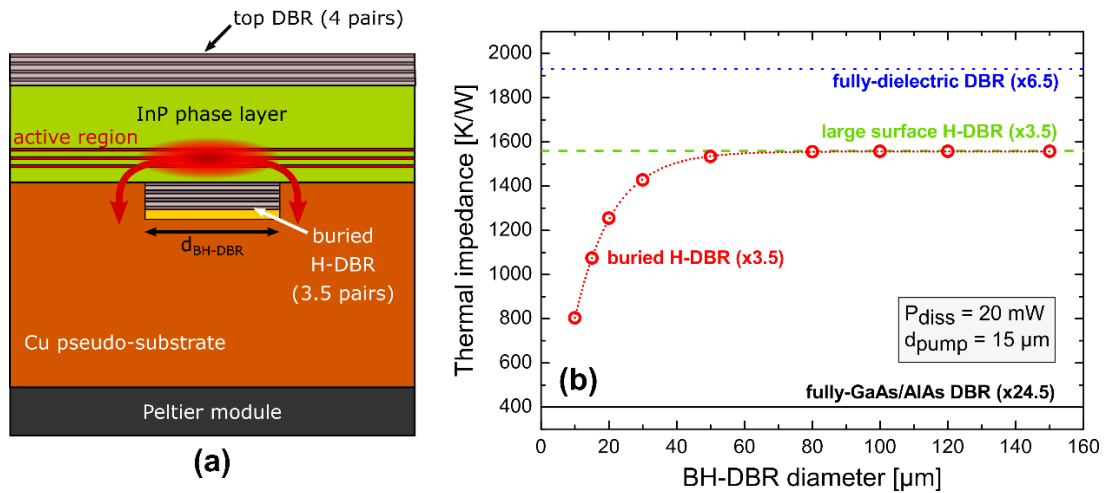


Fig. 2.8 – (a) Section of a VCSEL integrating a 3.5 pairs BH-DBR embedded in a Cu pseudo-substrate and (b) its improvements in terms of the thermal impedance with respect to a 6.5 pairs fully-dielectric DBR (blue-dotted curve) and a large area H-DBR with 3.5 pairs (green-dashed curve). Solid black line is a 24.5 pairs fully-GaAs/AlAs DBR.

## 2.2.3 TSHEC process development

This section describes the TSHEC process flow applied to the fabrication of InP-based optically-pumped VCSELs operating at  $1.55 \mu\text{m}$ . In the next section we will discuss the VCSELs characterization, and we will present experimental evidences showing significant improvements related to the reduction of the thermal impedance of the devices, as expected according to preliminary FEM simulations presented in the previous section. These results evidence the potentialities of the TSHEC process, allowing the hybrid integration of (virtually any) photonic or microelectronic devices on a silicon platform, while guarantying a thermally efficient, cost-effective and relatively simple process.

### Process flow

The complete TSHEC process flow, developed in collaboration with the Institut d'Électronique et de Télécommunications de Rennes (IETR), is resumed in Fig. 2.9a on the next page.

The starting point is represented by the preparation of a 3-inches  $300 \mu\text{m}$ -thick double-side polished silicon wafer. After the oxidation of the Si substrate to grow a thick  $\text{SiO}_2$  layer, a photolithography and a wet etching process is performed to realize a hard mask with  $600 \times 600 \mu\text{m}^2$  squared holes. The silicon is then etched with a 5% diluted Tetramethylammonium hydroxide (TMAH) solution heated at  $80^\circ\text{C}$ , resulting in an anisotropic wet etching of the (100) and (111) planes with a

selectivity ratio of  $\sim 30$  [Sato1999], which produces  $54.7^\circ$ -tilted silicon tranches. Due to the strongly diluted TMAH solution, the process is quite slow (several hours are needed to completely etch the Si substrate), but extremely controlled. This process produces  $3 \times 3$  matrices with  $200 \mu\text{m}$ -side squared holes in the back face of the silicon wafer (Fig. 2.9b). The front and back sides  $\text{SiO}_2$  layers are then removed by a wet etching step.

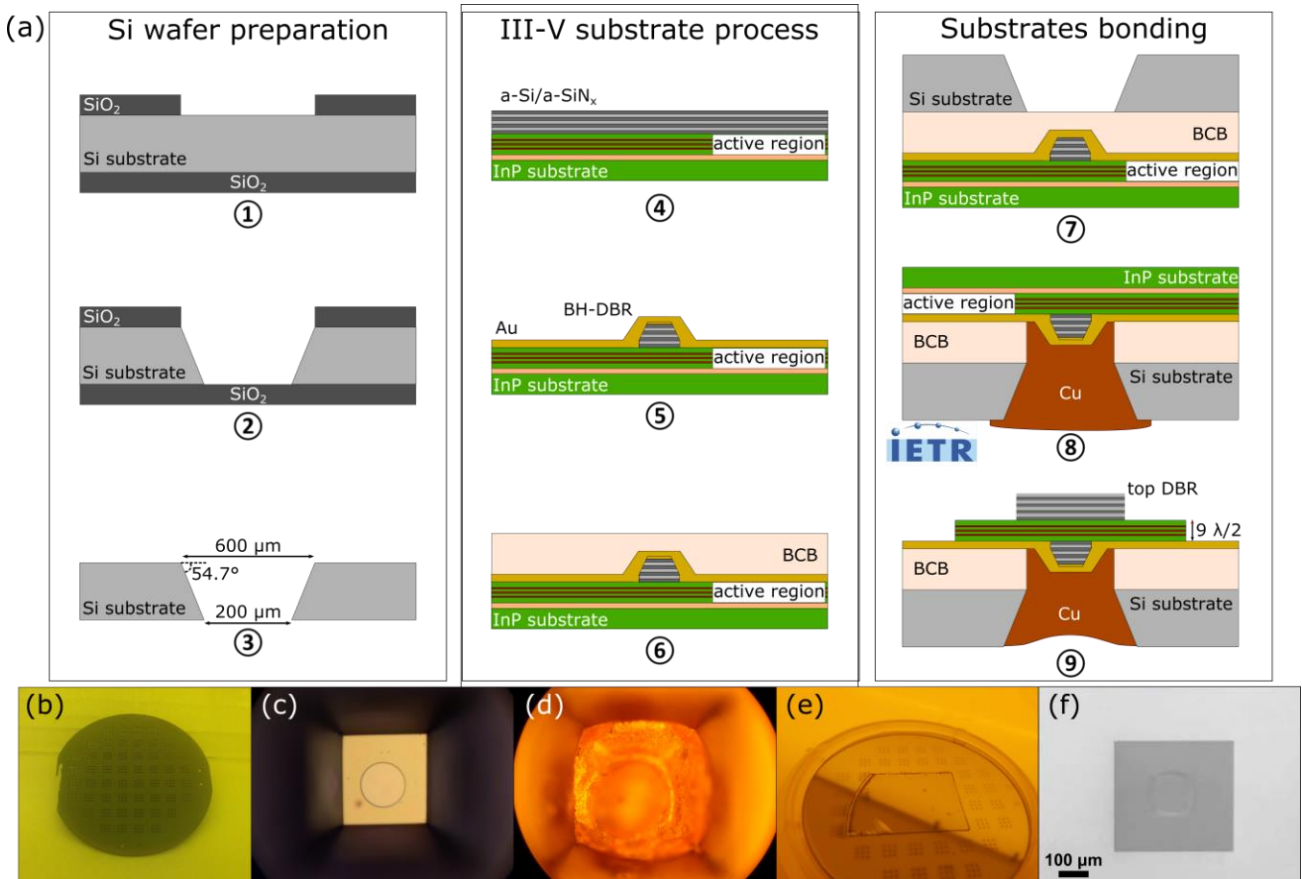


Fig. 2.9 – TSHEC process applied to the realization of  $1.55\mu\text{m}$ -emitting InP-based OP-VCSELs. (a) Process flow: ①  $\text{SiO}_2$  mask preparation, ② Si vias opening, ③  $\text{SiO}_2$  chemical etching, ④ InP-based active region growth and H-DBR deposition, ⑤ H-DBR patterning and Ti/Au contact deposition, ⑥ BCB spin-coating and pre-curing, ⑦ Substrates alignment and bonding, ⑧ Cu heat-sink electroplating, ⑨ InP substrate mechanical/chemical thinning, top dielectric DBR deposition and dies patterning. Pictures representing different realization step of a  $100 \mu\text{m}$ -diameter BH-DBR device: (b)  $3 \times 3$  matrices on Si, (c) BH-DBR view through a Si hole after the BCB bonding and dry etching, (d) Cu electroplating, (e)  $1/4$  of  $2''$  InP substrate after bonding on the Si platform and substrate thinning, (f) SEM image of a final  $400 \times 400 \mu\text{m}^2$  OP-VCSEL die on Si wafer.

In parallel, the VCSEL active region is grown by Gas Source Molecular Beam Epitaxy (GS-MBE), according to the design of the structure defined by the TMM simulation tool. Prior to the actual growth of the structure, dedicated samples are realized to calibrate the GS-MBE growth parameters (one for precisely measuring the InP growth rate, another one for checking the active layer wavelength). If satisfactory, the real active region is then realized immediately afterwards (on the same day). Then, the VCSEL active region can be eventually cleaved in a quarter of wafer, to

simplify the alignment and bonding procedures. Its composition and design will be detailed in the following section.

The process continues with the deposition of the bottom DBR on the InP substrate, consisting in 3.5 periods of a-Si and a-SiN<sub>x</sub> dielectric layers. To improve the mirror adhesion with the InP substrate, the first silicon nitride layer is deposited by PECVD. The following dielectric layers are deposited by RF magnetron sputtering with an additional 200 nm-thick Au layer to realize the H-DBR, which has a theoretical reflectivity of 99.61%. By performing basic scotch-tape peeling tests, we found an acceptable adhesion between the RF sputtered a-Si/a-SiN<sub>x</sub> dielectrics and the deposited Au without the use of any adhesion layer. For these reasons, we chose to avoid its use during the processing of our H-DBRs. Circular mesas with diameters varying from 10 up to 150 μm are subsequently patterned by a combination of a KI+I<sub>2</sub> wet etching for the gold layer and a SF<sub>6</sub> plasma-assisted dry etching for the dielectric layers composing the H-DBR. The dry-etching has been performed using low-energy plasma and a relatively high pressure on the reactive ion etching (RIE) system, in order to obtain a moderate tilt of the etched mirror sides (60°). A Ti/Au metallic layer (15/300 nm) is then deposited on the whole surface. The smooth slope of the H-DBR sides ensures the continuity of this metallic layer, the purpose of which being to act as an electrode for the following electroplating step.

At this point, the two substrates (Si and InP) are ready to be bonded together. To this aim, a 3 μm-thick BCB layer is spin-coated on the processed InP substrate. A first 2 min-long soft-bake step at 140°C allows evaporating most of the BCB solvents. The silicon and the InP substrates are then aligned one to each other to center the H-DBRs within the 200×200 μm<sup>2</sup> wide holes, thanks to a home-made substrate holder and a Karl Suss MJB4 mask aligner. Both substrates are then brought into contact and the BCB is finally hard-baked for 1 h at 250°C under nitrogen atmosphere to complete the curing step. At this point, the two substrates are bonded together. The BCB is then dry etched through the silicon holes thanks to a SF<sub>6</sub> + O<sub>2</sub> mixture, to reveal the underneath H-DBRs covered by the Ti/Au metallic layer (Fig. 2.9c).

By applying a voltage potential via the holes on the edge of the silicon wafer, an electroplating step is performed on such a metallic layer through the Si vias, leading to the filling of the matrices with the copper (Fig. 2.9d, this step has been realized at IETR). The H-DBRs are thus completely buried (in the following they will be indicated as BH-DBR for buried H-DBR). The eventual excess of copper can be removed from the back side by a simple polishing procedure. The copper layer allows a robust mechanical clamping with the silicon substrate while simultaneously promoting the heat spreading from the device, thereby acting as a localized and efficient heat-sink. Additionally, the copper layer can be also used as electrical contact if an electrical injection scheme is

implemented for such devices. After that, the whole InP substrate is removed by a combination of mechanical polishing and wet chemical etching, thanks to an InGaAs stop-etching layer, to reveal the InP-based active region. As a result, a 2  $\mu\text{m}$ -thick InP-based layer remains on the silicon host substrate (Fig. 2.9e). To complete the process, a 4-pairs dielectric a-Si/a-SiN<sub>x</sub> DBR is deposited on top of the active region, to form the VCSEL micrometric cavity. The theoretical reflectivity of the top DBR has been computed to be equal to 99.2%. Eventually, the top DBR and the InP active region can be patterned to form individual dies (Fig. 2.9f).

### InP-based active region

The active region of the devices, which is detailed in Fig. 2.10a, consists in three sets of three 8 nm-thick In<sub>0.78</sub>Ga<sub>0.22</sub>As<sub>0.81</sub>P<sub>0.19</sub> strained multi-quantum wells (MQWs) grown on a (001)-oriented InP substrate. In order to compensate for the thermal redshift due to pump heating and obtain a VCSEL emission around 1.55  $\mu\text{m}$  during room temperature operation, the quantum wells have been deliberately designed to emit near 1.52  $\mu\text{m}$  (i.e. a -30 nm detuning). The QWs belonging to each set are separated by 10 nm-thick In<sub>0.8</sub>Ga<sub>0.2</sub>As<sub>0.435</sub>P<sub>0.565</sub> quaternary alloy layers (indicated as Q<sub>1.18</sub>).

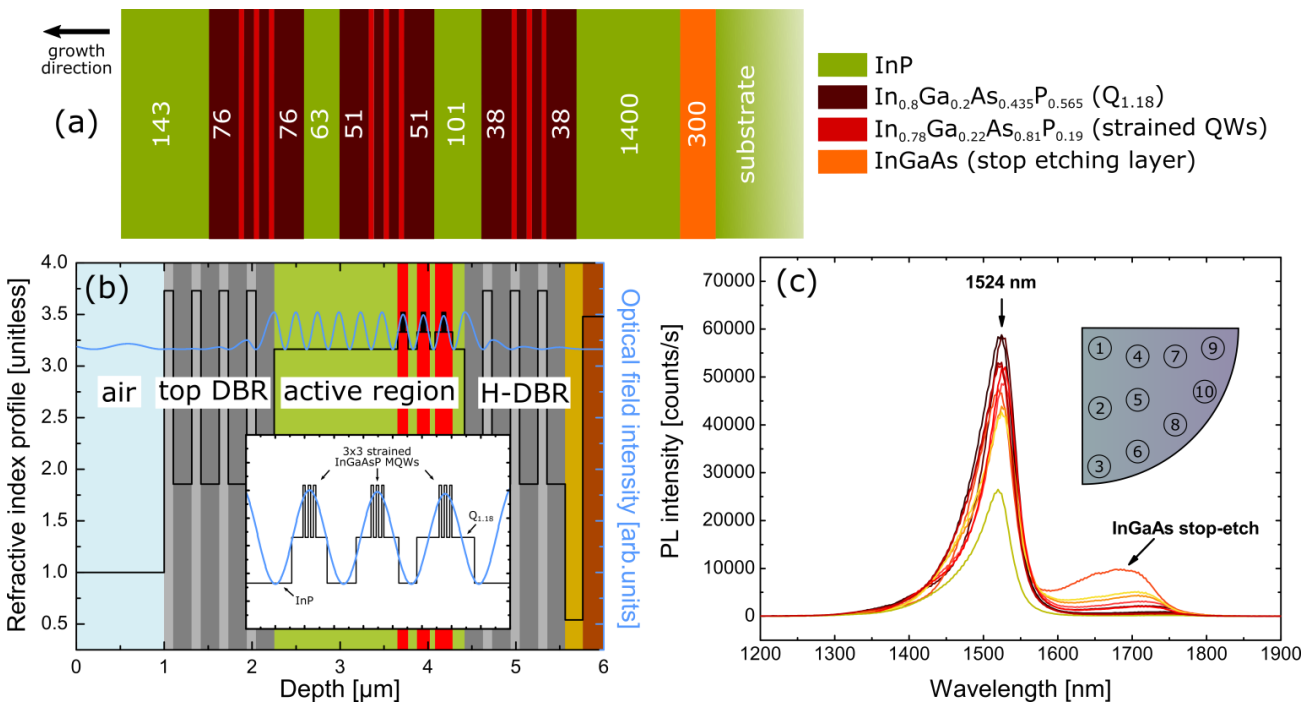


Fig. 2.10 – OP-VCSEL active region: (a) structure (layers thickness in nm), (b) computed optical field intensity inside the structure and (c) room-temperature photoluminescence mapping across the surface of the as grown sample (a quarter of 2" InP wafer).

The sets are then sandwiched between two thicker  $Q_{1.18}$  layers, which have two main purposes:

- they act as barrier to decouple the QWs and confine the carriers inside the active layers;
- they enhance the pump absorption at 980 nm (which would be otherwise only limited to the QWs), leading to a reduction of the laser threshold.

The thickness of the  $Q_{1.18}$  barriers is chosen to provide a uniform carrier injection per set [Geske2004]. Each set is then further separated by InP spacers, the thickness of which has been designed to exactly accommodate the MQWs on the antinodes of the internal optical field (cf. inset of Fig. 2.10b) and maximize the modal gain of the structure once the final device is realized, according to a Resonant Periodic Gain (RPG) configuration.

The structure is completed by a thick InP layer of 1400 nm, which act as phase layer. Before the deposition of the top DBR, the thickness of the InP phase layer can be finely adjusted by a slow rate wet-etching step (20 nm/min) in order to exactly match the wavelength cavity resonance with respect to the designed layers thickness, and thus compensating any possible MBE growth deviation (although in this particular case this was not necessary). To this aim, the resonance of the half-VCSEL cavity is systematically checked by photoluminescence measurements. Additionally, the InP phase layer (together with the InP spacers) contributes to the spreading of the heat generated in the active region, improving the lateral thermal dissipation. As indicated by Fig. 2.10a, a 300 nm-thick  $In_{0.53}Ga_{0.47}As$  layer has been grown before the VCSEL active region to be used as stop-etching layer during the removal of the InP substrate, as previously mentioned.

After the MBE growth of the active region, we cleaved a quarter of the 2-inches wafer, to further process the devices. On such a sample we first proceeded to a mapping to check its photoluminescence efficiency. In agreement with the previous MBE calibration, we observed a relative good homogeneity in terms of signal intensity and peak wavelength (centered at 1524 nm) across the whole surface, with a typical decreasing in intensity near the edges of the sample, as attested by Fig. 2.10c. The low-energy side half width at half maximum (HWHM) has been estimated to 19 nm ( $\sim 10$  meV), indicating rather smooth interfaces between the MQWs and the  $Q_{1.18}$  barriers. The peak around 1700 nm is related to the presence of the InGaAs stop-etching layer, and it will disappear after the substrate removal.

Once the optical quality of the structure has been assessed, we applied the TSHEC process to combine the InP-based VCSEL active region with the previously processed Si substrate.

Before the deposition of the top DBR on the InP active region and the half-VCSEL fabrication, we observed a drastic reduction of the FWHM of the PL spectrum due to the cavity effects, from 50-60 nm down to 20-30 nm (cf. Fig. 2.11a).

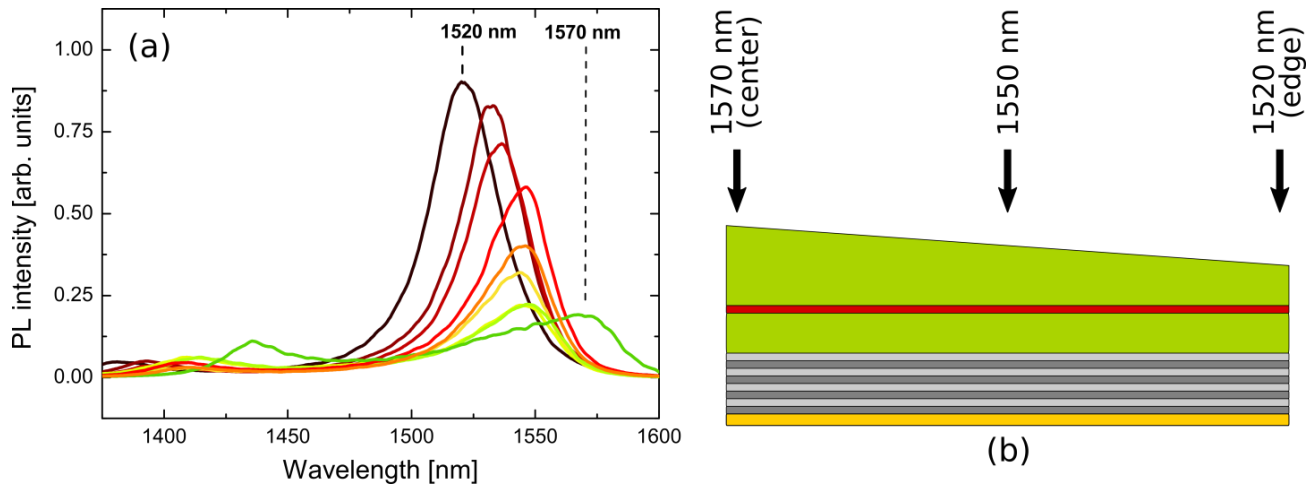


Fig. 2.11 – (a) PL spectra for different positions across the surface of the III-V active region bonded on the Si substrate. (b) Cross-section of the half-cavity  $\frac{1}{4}$ -wafer with a InP phase layer thickness gradient (resonance wavelength is indicated).

Additionally, a distribution of the quasi-resonant PL peak of the cavity ranging between 1520 nm and 1570 nm is observed, depending on different positions in the sample surface. This is related to a gradient in the thickness of the InP phase layer, that is estimated to be  $\pm 3.5\%$  with respect to the nominal value targeted during epitaxy. It is worthwhile to notice that the maximum of the PL intensity occurs at 1520 nm, according to -30 nm detuning considered during the design of the active region.

## 2.2.4 Devices characterization

After the realization of the optically-pumped VCSELs according to the TSHEC process already described, we proceeded to their characterization. The goal of such measurements was double: primarily, we wanted to validate the TSHEC process to realize VCSELs and secondly, we wanted to investigate the influence of the BH-DBR diameter on the performance of the devices.

To investigate the performance of the OP-VCSELs obtained with the TSHEC process, different matrices have been characterized in terms of maximum output power and threshold pump power, to finally recover their thermal performance in terms of thermal impedance. To this aim, we used the experimental setup presented in Fig. 2.12 on the next page.



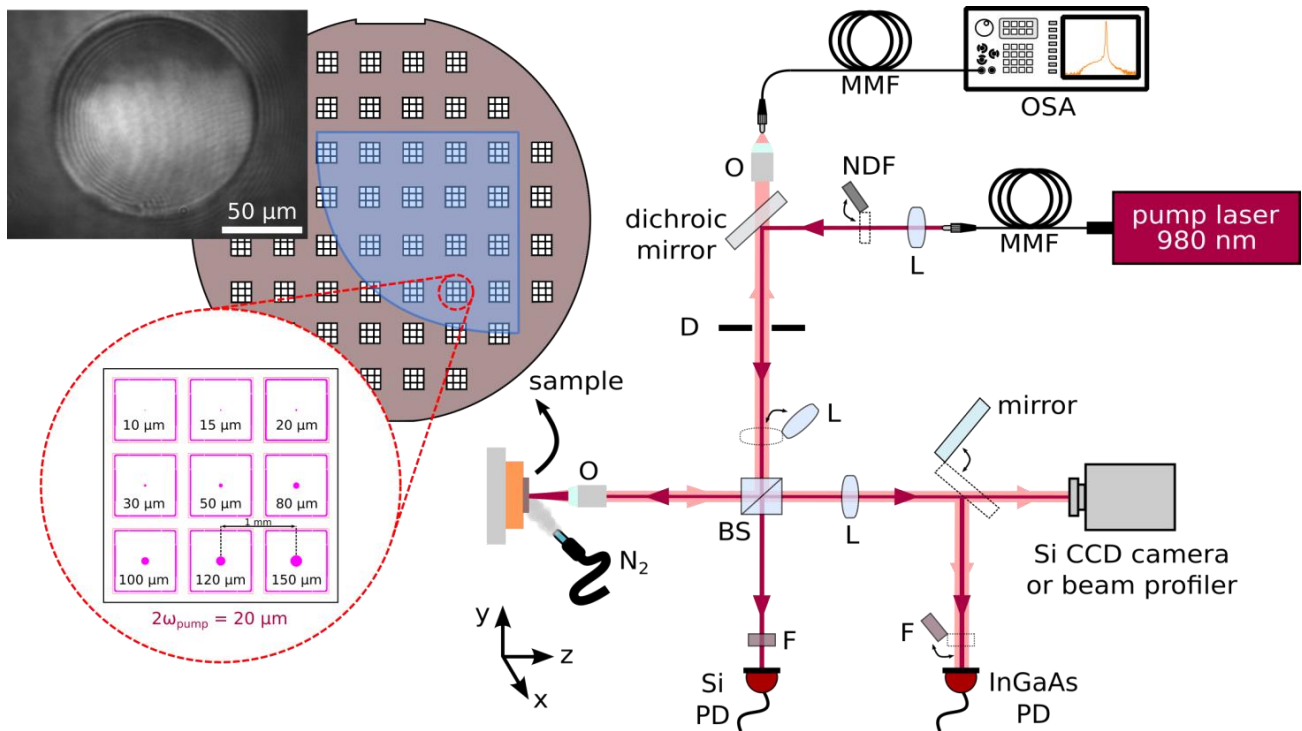


Fig. 2.12 – Experimental setup used to characterize the OP-VCSELs matrices. The insets (left) show a  $3 \times 3$  matrix with the different dimensions of BH-DBRs composing the OP-VCSELs and an enlarged image of a  $120 \mu\text{m}$ -diameter BH-DBR. The distance between each device belonging to the same matrix is  $1 \text{ mm}$ . BS: beam splitter, D: diaphragm, F: low-pass filter, L: lens, MMF: multi-mode fiber,  $N_2$ : nitrogen flow, NDF: neutral density filter, O: objective, OSA: optical spectrum analyzer, PD: photodiode.

The sample is mounted on a copper support with thermal grease, which is then fixed onto a Peltier cell attached on a tri-axis manual stage. The devices are optically-pumped by a continuous-wave 980 nm semiconductor fibered diode laser with a multi-mode optical fiber (MMF). A dichroic mirror (selective with respect to the pump wavelength) is used to reflect the pump beam towards a beam splitter, which directs most of the pump towards the sample through an objective lens, to focus it on the surface of the sample with an estimated spot diameter of  $\sim 20 \mu\text{m}$ . The rest of the incident pump power is sent to a Si photodiode, for input power estimation. Thanks to a high-pass 1200 nm filter and an InGaAs photodiode, it is possible to measure the VCSEL output power, or the reflected pump power when this filter is removed. This, thanks to the input power measurement, enables to calibrate the setup to get a good estimation of the absolute absorbed power. Thanks to the beam splitter, a part of this signal is also collected by a multi-mode optical fiber through the dichroic mirror and a microscope objective, and directed to an optical spectrum analyzer (OSA). The small dimensions of the BH-DBRs imposed to exactly know their position on the sample surface, in order to properly focus the pump spot over them. For that reason, a Si CCD camera has been used. It has been placed in front of the sample, to collect the reflected pump signal (just above threshold) coming from the sample and image its surface. A neutral density filter (NDF) was necessary to avoid the saturation of the camera, and an optical diffuser illuminated the sample with



the 0.98  $\mu\text{m}$  pump, for imaging purposes. The inset of Fig. 2.12 shows the picture of a 120  $\mu\text{m}$ -diameter BH-DBR, seen through the InP-based active region, obtained by the procedure described above. Thanks to this procedure, we were able to focus the pump beam exactly at the center of each device during the characterization. Eventually, a nitrogen flow has been used when measurements at temperatures lower than the dew point have been performed. This was necessary to avoid water condensation on the sample surface. Finally, a PC has been used to control the pump diode and the OSA through a LabVIEW<sup>®</sup> program, and to collect the image from the CCD camera or a beam profiler as well.

### Output power and optical emission spectra at room temperature

As first step, the devices have been characterized at 20°C. Due to the gradient in thickness of the InP phase layer, emissions between 1530 and 1570 nm have been recorded all across the surface of the sample. Since the gain of the devices strongly depends on the resonance wavelength of the micrometric cavity, we selected devices belonging to the same matrix or to two adjacent matrices (within an area of  $< 65 \text{ mm}^2$ ). In this way we limited the effect associated to the variation of the cavity length, being able to fairly relate the optical performance of the devices to their individual thermal efficiency, which is also associated to the different BH-DBR dimensions. As shown in Fig. 2.13a, in the investigated area (near the center of the sample) single-mode emission spectra centered around 1550 nm have been obtained, for different dimensions of the BH-DBR, ranging from 20 to 100  $\mu\text{m}$ .

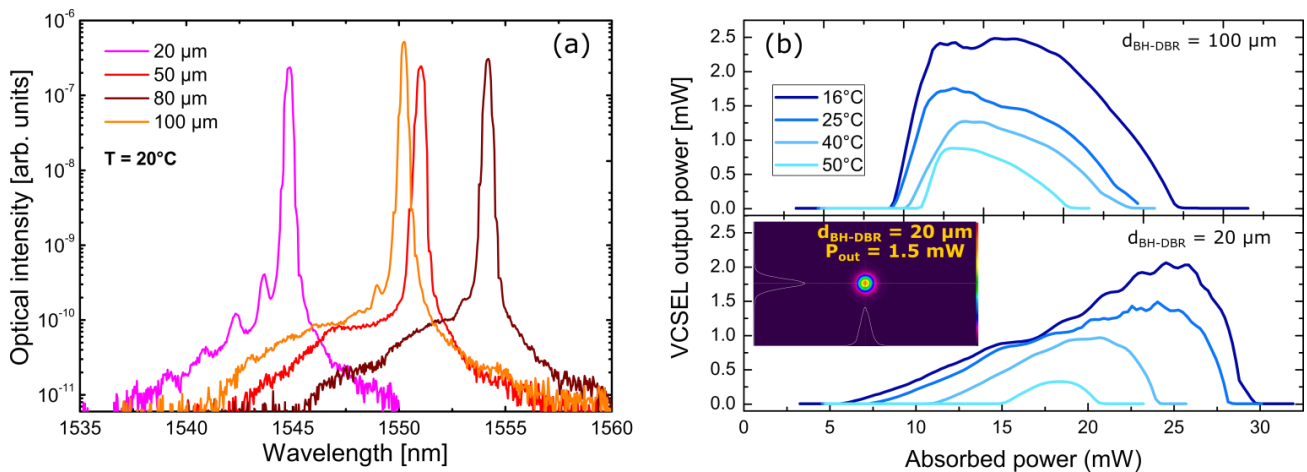


Fig. 2.13 – (a) OSA spectrum of OP-VCSELs for various BH-DBR diameters, recorded at 20°C. (b) L-L characteristics of OP-VCSELs integrating a 100  $\mu\text{m}$ -BH-DBR (top) and a 20  $\mu\text{m}$ -BH-DBR (bottom) at different stage temperatures. Insets show a typical near-field single-mode profile of a 20  $\mu\text{m}$ -diameter BH-DBR device obtained at 1.5 mW of emitted power.

According to the size of the BH-DBR, a red shift of the laser emission as high as 10 nm (1545 nm  $\rightarrow$  1555 nm) has been observed for the investigated devices, which can be directly

related to different values of their thermal impedance. A single-mode suppression ration (SMSR)  $> 27$  dB has been obtained for the 20  $\mu\text{m}$ -diameter BH-DBR device, while it increases to  $> 32$  dB in the case of the bigger BH-DBRs.

The corresponding light-to-light (L-L) curves as a function of the absorbed pump power are presented in Fig. 2.13b. We choose to focus the attention on the comparison of two types of VCSELs integrating a BH-DBR with a notable difference in dimensions, in order to emphasize the role of size of the bottom mirror in the thermal dissipation process.

To this aim, we present the CW L-L characteristics as a function of the absorbed pump power obtained for a Peltier stage temperature in the range 16-50°C for a 100  $\mu\text{m}$ -BH-DBR device (Fig. 2.13b, top curves) and a 20  $\mu\text{m}$ -BH-DBR device (Fig. 2.13b, bottom curves), in order to quantify the improvements in the thermal management of the devices based on the TSHEC process, in particular for those integrating BH-DBRs with small diameters. It is worth to notice that laser operation has been still possible up to 60°C with such devices.

During the measurements a peculiar attention has been paid to the optical excitation of the VCSEL devices, in order to ensure a single transverse mode emission, as evidenced by the OSA spectra of Fig. 2.13a and the inset of Fig. 2.13b representing a typical transverse single-mode near field intensity pattern recorded in the case of a device integrating a 20  $\mu\text{m}$ -diameter BH-DBR emitting 1.5 mW. This peculiar point is important for reliable L-L curves, but also for the estimation of the thermal impedance measurements, which will be presented later on.

Concerning the two devices under test, the 100  $\mu\text{m}$  BH-DBR VCSEL exhibits typical threshold around 9 mW (equivalent to a threshold power density of  $D_{abs} = 2.9 \text{ kW/cm}^2$ ) and a maximal output power of 2.5 mW, measured at 16°C. At 50°C, the threshold slightly increases (11 mW) while the output power drops to 0.9 mW. As the temperature rises, its slope efficiency decreases from 0.6 down to 0.45.

In the case of the 20  $\mu\text{m}$  BH-DBR VCSEL, a smaller threshold of 5.5 mW ( $D_{abs} = 1.8 \text{ kW/cm}^2$ ) is obtained at 16°C together with a 2 mW maximal output power, which decreases to 300  $\mu\text{W}$  while the threshold significantly increases to 15 mW at 50°C. From 16°C up to 50°C, a lower slope efficiency of 0.08 is measured, being constant in the whole temperature range. Anyway, the lower value of the slope efficiency together with a late appearance of the thermal roll-over for the small devices is probably related to the experimental conditions. Indeed, the dimensions of the pump spot achievable within our experimental setup (as a reminder,  $d_{pump} \sim 20 \mu\text{m}$ ) were somehow limiting the operation of the small VCSELs. On one hand, this is the reason why no laser emission has been obtained with devices integrating a buried H-DBR with diameters equal to 10 and 15  $\mu\text{m}$ : in this case, a non-negligible part of the pump spot were most likely located outside the small BH-DBRs,

in close proximity to the metallic layers surrounding the bottom mirrors, causing its absorption by the Ti/Au layers, and resulting in an over-heating of the device which prevents their laser operation. On the other hand, the same effect is also responsible for the lower slope efficiency measured for the 20  $\mu\text{m}$ -diameter device. In this case the pump spot and the device dimensions being comparable, the pumped surface is probably slightly bigger than the cavity surface delimited by the BH-DBR dimension. Although this is not sufficient to prevent the device to work, it definitely translates into an overestimation of the absorbed pump power, which translates into a lower slope efficiency. A further shrink of the pump spot was extremely difficult to achieve in our setup, we thus decided to perform the characterization of the devices under these experimental conditions. Additionally, we point out that the results obtained for devices with BH-DBR diameters ranging from 80  $\mu\text{m}$  up to 150  $\mu\text{m}$  exhibited similar performance than the one integrating a 120  $\mu\text{m}$  BH-DBR. This in accordance with the FEM analysis presented in *Section 2.2.2*, which indicated that devices integrating BH-DBR with diameters  $\geq 50 \mu\text{m}$  evidence a constant thermal resistance.

From the results that have been obtained, we can retain that the 20  $\mu\text{m}$  BH-DBR VCSEL threshold at 16°C is nearly twofold lower, if compared with the 100  $\mu\text{m}$  BH-DBR. The higher threshold and lower output power obtained with the small devices at 40°C-50°C should not be surprising, because this is absolutely compatible with their improved thermal performance. Indeed, for such devices, the heat diffusion is efficient in either direction, i.e. either when they are cooled down or when they are heated up. To confirm this, we plotted the threshold and the maximum achievable output power of the two devices at different stage temperatures, from 50°C down to -15°C. Results are shown in Fig. 2.14.

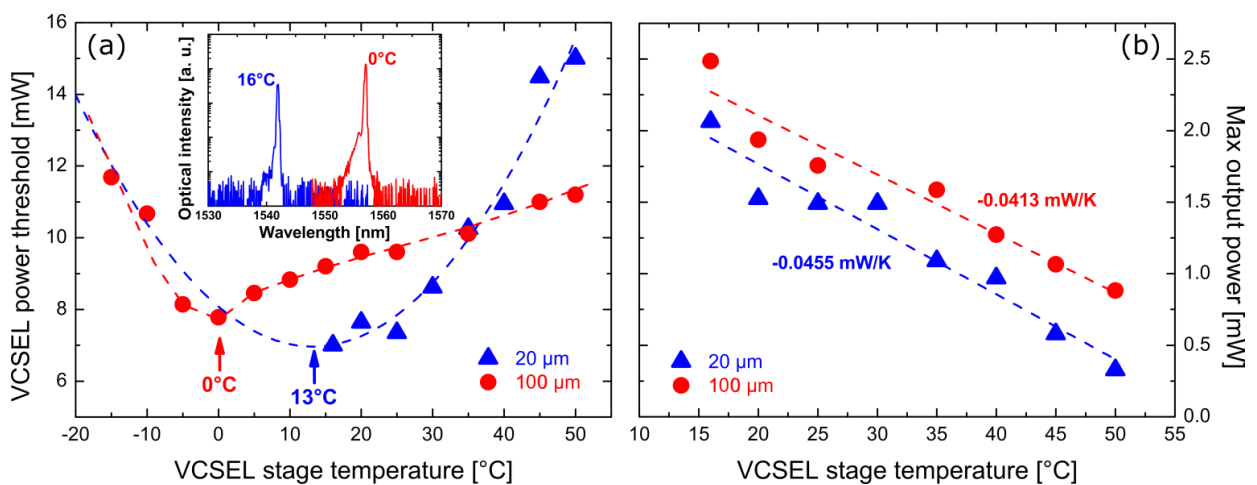


Fig. 2.14 – (a) VCSEL threshold and (b) maximum achieved output power vs stage temperature for the 20 and 100  $\mu\text{m}$  BH-DBR VCSELs (blue triangles and red dots, respectively). Red dashed curve in (a) is only for eye-guiding, the blue dashed curve is a 2<sup>nd</sup> order polynomial fit. In the inset, the emission spectra of the two devices at 0°C and 16°C.

For temperatures lower than the dew point ( $T_{dew} \sim 15^\circ\text{C}$ ), measurements have been performed under a nitrogen flux. Note that in the case of the 20  $\mu\text{m}$  BH-DBR VCSEL, measurements in the low temperature range ( $-15^\circ\text{C} - 15^\circ\text{C}$ ) have not been performed, because such small devices were partly destroyed after an unintended exposure to moisture. We proceed to a simple second order polynomial fit to estimate that the minimum threshold is achieved at a temperature of  $13^\circ\text{C}$  for such a device. For the 100  $\mu\text{m}$  BH-DBR VCSEL, the minimum threshold is measured at a temperature of  $0^\circ\text{C}$ . The inset of Fig. 2.14a shows the optical emission spectra of both VCSELs, measured respectively at  $16^\circ\text{C}$  and  $0^\circ\text{C}$ . The 20  $\mu\text{m}$  BH-DBR VCSEL (blue spectrum) presents a 15 nm blueshift in comparison with the 100  $\mu\text{m}$  one. Both measurements clearly indicate that the VCSEL internal temperature is lower for the device integrating the 20  $\mu\text{m}$  BH-DBR. This translates into a shorter wavelength emission when the matching between the modal gain and the cavity resonance is achieved together with a lower threshold condition. These results are an experimental evidence of the improved heat dissipation generated in the active region of the device when a smaller BH-DBR is combined with the TSHEC process.

Regarding the maximum achievable output power, we observe a similar decreasing in efficiency for the two devices (slopes of  $-0.0455$  mW/K and  $-0.0413$  mW/K, for the 20 and the 100  $\mu\text{m}$  BH-DBR VCSEL, respectively) as attested by Fig. 2.14b, which demonstrate that no particular degradations are observed as a function of the temperature, at least on the range of interest.

### **Thermal impedance of VCSELs and validation of the approach**

To complete this section, we now present the characterization of devices in terms of their thermal resistance. These values are extracted directly from the experimental data, and compared with the FEM thermal model of the VCSELs, to interpret the results.

A standard practice to experimentally determine the thermal impedance  $R_{th}$  of VCSELs is based on the measurement of the wavelength redshift with respect to the dissipated pump power ( $\Delta\lambda/\Delta P_{diss}$ ) and to the heat-sink temperature ( $\Delta\lambda/\Delta T_{hs}$ ), according to [Michalzik2013]:

$$R_{th} = \left( \frac{\Delta\lambda}{\Delta P_{diss}} \right) \left( \frac{\Delta\lambda}{\Delta T_{hs}} \right)^{-1} \quad (2.2)$$

Fig. 2.15 on the next page shows the results of such measurements, obtained on four different devices integrating a 20, 50, 80 and 120  $\mu\text{m}$ -diameter BH-DBR.

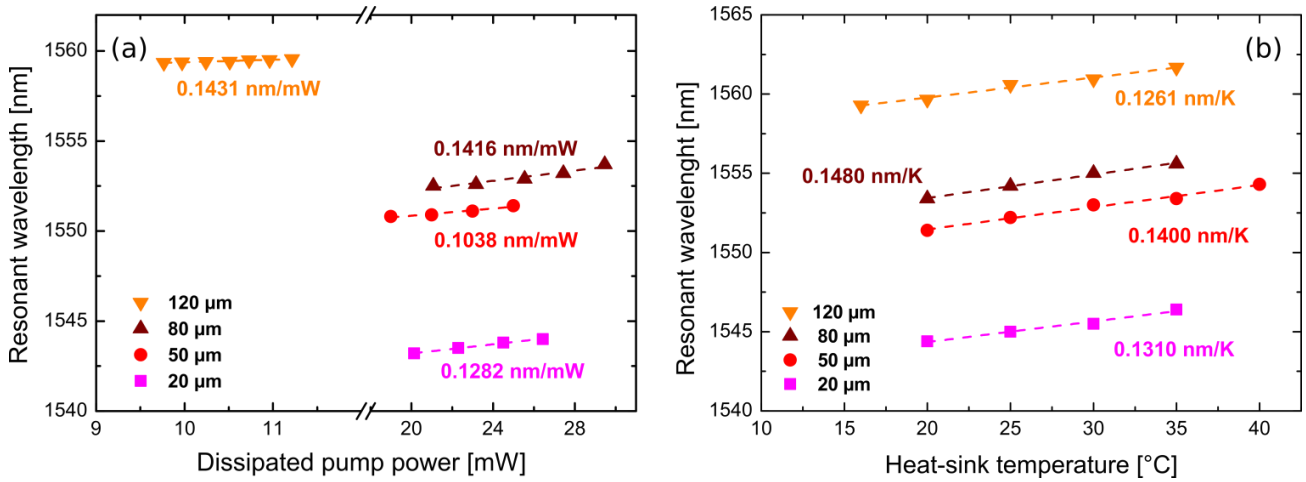


Fig. 2.15 – Lasing wavelength shift with respect to (a) the dissipated pump power  $P_{\text{diss}}$  and to (b) the heat-sink temperature  $T_{\text{hs}}$  of devices with different BH-DBR diameters.

During the measurements, we took care of the experimental conditions to extract a reliable value for the thermal impedance. In the case of the wavelength shift vs dissipated pump power, the measurements have been performed before the appearance of the thermal rollover. Concerning the wavelength shift vs heat-sink temperature, we pumped the devices just above threshold to minimize the internal heating of the devices.

By applying Eq. 2.2 to such measurements we extract the values of the thermal impedance. For large BH-DBR diameters of 80 and 120  $\mu\text{m}$ , we measured a thermal resistance of 957 K/W and 1134 K/W, respectively. For a BH-DBR diameter of 50  $\mu\text{m}$ , a clear decrease of  $R_{th}$  is measured down to 741 W/K, evidencing better heat spreading. It is followed by an increase for the 20  $\mu\text{m}$  BH-DBR, up to 979 K/W. Once again, as previously discussed for such a small BH-DBR diameter, we considered this unexpected increase of the thermal impedance as the consequence of the optical pumping setup. This value has to be considered with precaution, if we take into account the above experimental evidences showing the superior thermal properties of this 20  $\mu\text{m}$  BH-DBR VCSEL.

In an effort to interpret the experimental measurements, we compared them with the results our FEM thermal model, adapted to the case of TSHEC processed devices. According to the OP-VCSEL design already discussed, the thermal impedance is estimated by computing the internal temperature gradient of the VCSEL when the active region of the device is pumped with a 20  $\mu\text{m}$ -diameter spot of a 15 mW power, and a heat-sink temperature of 16°C (standard pumping conditions, see Fig. 2.16 on the next page, black squares).

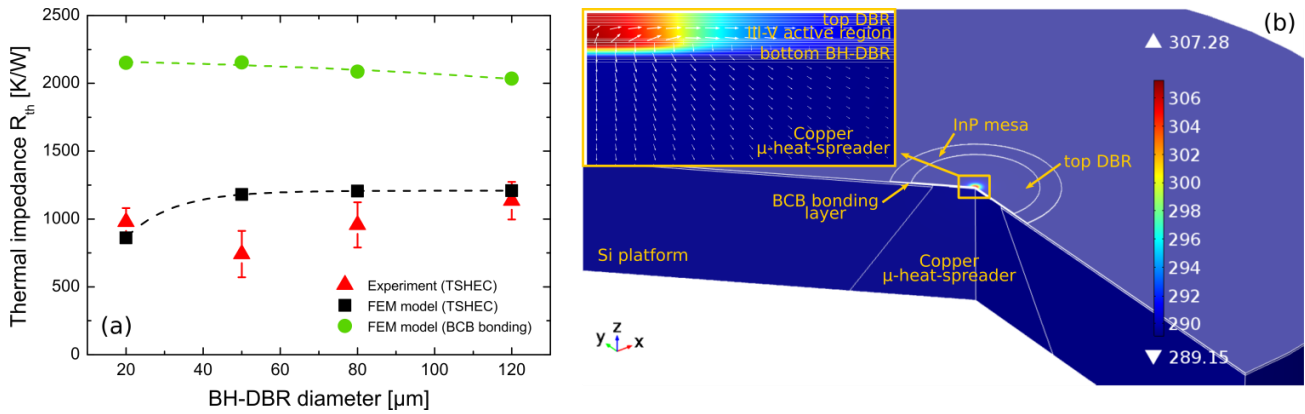


Fig. 2.16 – Thermal impedance  $R_{th}$  of VCSELs realized by the TSHEC process as a function of the BH-DBR diameter: (a) experimental measurements (red triangles) compared with results of FEM simulations (black squares). Green dots represent the results of FEM simulations if a standard bonding technique employing a 5 $\mu\text{m}$ -thick BCB layer is used. (b) FEM model of a TSHEC-OP-VCSEL integrating a 120  $\mu\text{m}$ -diameter BH-DBR.  $P_{diss}=15$  mW,  $d_{pump}=20$   $\mu\text{m}$ ,  $T_{hs}=16^\circ\text{C}$ .

For devices presenting a BH-DBR larger than 50  $\mu\text{m}$ , a constant thermal impedance of  $\sim 1200$  W/K is computed by the FEM model. This value, which is in good agreement with the experimental data related to the 120  $\mu\text{m}$  BH-DBR device, is mainly limited by the BH-DBR thermal impedance, the reflector being almost entirely composed by dielectric materials. The reduction of the BH-DBR diameter below 50  $\mu\text{m}$  promotes the lateral heat flow from the active region towards the copper heat-sink across the InP layers surrounding the pumped area. As a consequence, from these simulations we deduced a decrease of  $\sim 5^\circ\text{C}$  for maximal internal temperature of the 20  $\mu\text{m}$  BH-DBR device in comparison with the 120  $\mu\text{m}$  BH-DBR, resulting in an improvement of the thermal impedance of  $\sim 29\%$  (860 K/W). We verified that this value stay constant at high pumping rates. For a dissipated pump power of 30 mW, we computed almost the same thermal resistance for the two devices, namely 880 and 1240 K/W respectively, resulting again in a difference of  $\sim 29\%$ , while the maximal internal temperature difference is now equal to  $\sim 11^\circ\text{C}$  (not shown). As a first glance then, the overall tendency obtained with our FEM model confirms the experimental results and the assumptions considering a superior thermal performance of the TSHEC process when small diameter BH-DBRs are employed.

To highlight the benefits of the TSHEC process with respect to standard fully polymer bonding techniques currently used in hybrid III-V silicon integration, we analyzed the case in which a 5  $\mu\text{m}$ -thick large-area BCB layer is used to bond our devices on the Si host wafer (green circles in Fig. 2.16). In this case, a large thermal impedance of  $\sim 2000$  W/K is obtained for a 120  $\mu\text{m}$  BH-DBR, which is getting even worse when the BH-DBR diameter is reduced. This is mainly due to the bad thermal conductivity of the BCB, which acts as a very efficient thermal isolation layer, in comparison with the one offered by the combination of the BH-DBR and the localized copper heat-spreader.

To conclude, we investigated the thermal behavior of the VCSEL devices realized with the TSHEC. We observed that devices integrating a BH-DBR with lateral dimension smaller than 50  $\mu\text{m}$  in diameter offer an improved thermal performance with respect to those with large BH-DBRs. In particular, the 20  $\mu\text{m}$ -BH-DBR devices showed a significant improvement of the laser threshold, with no degradation of the output power ( $> 2 \text{ mW}$  at  $16^\circ\text{C}$ ) with respect to the other components. The inconsistencies observed in the measurement of the thermal resistance of small devices have been related to the pumping conditions, since the impinging pump power is very likely overestimated, leading to an overestimation of the thermal resistance for such devices. FEM simulations have provided a useful tool to validate the approach: on one hand they confirmed the advantages of using small BH-DBRs to improve the thermal dissipation, while on the other hand they supported the benefits of the TSHEC approach with respect to standard bonding process.

## 2.3 Development of the electrical-injected VCSEL technology

After showing that TSHEC process works quite well in the case of optically-pumped devices, a legitimate question arises: can we go further towards electrically-pumped (EP) devices? Electrical-injected devices are indeed preferred for a practical use and large commercialization. In fact, despite the simplicity of the technological process required to realize optically-pumped VCSELs, they generally remain at a proof-of-concept stage as they are seen as predecessors to electrically-pumped devices, because of their major drawback inherent to the excitation scheme involving costly and cumbersome pump laser and focusing optics, together with the problems of intensity noise fluctuations transferred from the pump to the VCSELs.

To meet these needs, we thus adapted the TSHEC process for the case of electrically-injected VCSELs.

The investigated EP-VCSEL device is depicted in Fig. 2.17 (on the next page) and it is based on:

1. an InP-based active region, integrating strained InGaAsP MQWs and emitting around  $1.55 \mu\text{m}$ ;
2. a laser cavity formed by a top dielectric a-Si/a-SiN<sub>x</sub> DBR and a bottom BH-DBR;
3. an optical and current confinement section, represented by a buried tunnel junction (BTJ);
4. BCB planarization and adhesion layers;
5. the TSHEC technology, thus benefiting by the heat management and the mechanical solidity offered by such a method.

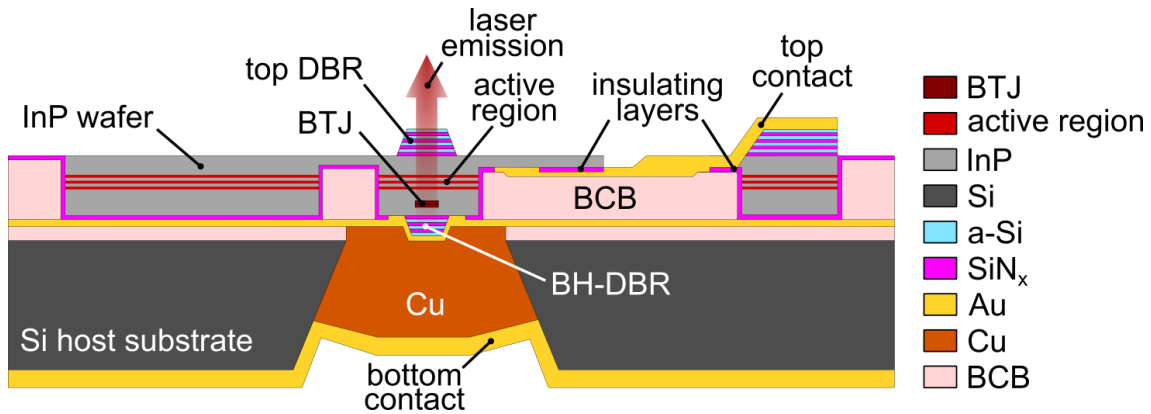


Fig. 2.17 – Scheme of the investigated EP-VCSELs obtained employing the TSHEC process.

In this part we detail the design of the main building blocks composing the device, the mask design, the fabrication steps and some preliminary results we obtained on test samples.

### 2.3.1 Buried tunnel junction: investigations

As already discussed in *Chapter 1*, the lack of efficient oxides in the InP material system imposed to employ buried tunnel junctions acting as current and optical apertures. The use of such technique, applied to long-wavelength ( $> 1.3 \mu\text{m}$ ) VCSELs, has been pioneered by Amann group at Walter Schottky Institute [[Ortsiefer2000](#)].

This approach consists to realize a thin p-n junction ( $\sim 40\text{-}50 \text{ nm}$ ), with heavily-doped layers (typically  $N_{a,d} \geq 10^{19} \text{ cm}^{-3}$ ), to promote the carrier flow through the junction thanks to tunnel effect, in the most transparent way (low applied voltage, low resistance). Additionally, to confine the carriers in a limited injection surface, the tunnel junction is laterally patterned by an etching step, and buried in a reverse biased standard p-n junction, realized after an epitaxial regrowth. The index contrast in the lateral direction results also in the optical confinement of the light.

#### Working principle and advantages of tunnel junctions

The qualitative working principle of a tunnel junction, initially studied by Leo Esaki in 1958 in a germanium p-n junction [[Esaki1958](#)], is sketched in Fig. 2.18 on the next page.



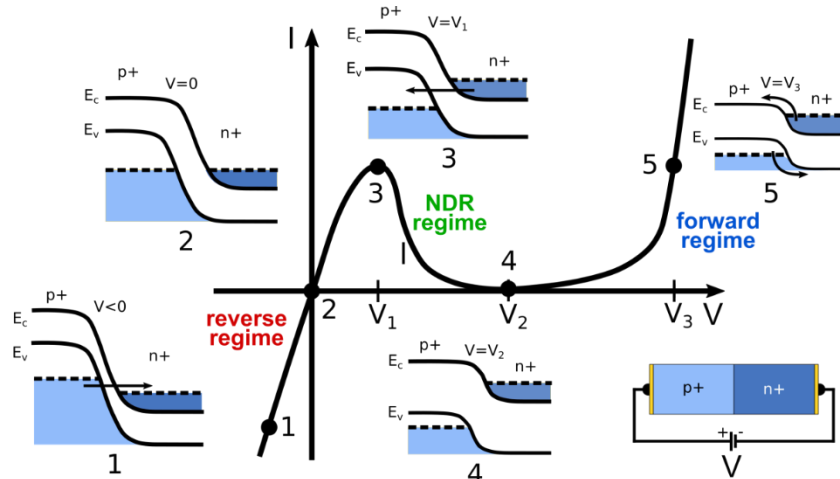


Fig. 2.18 – Qualitative working principle of a tunnel junction.

When the junction is inversely polarized (1), tunneling occurs from occupied states of the valence band ( $E_v$ ) towards empty states of conduction band ( $E_c$ ). Increasing the applied voltage, we reach the equilibrium condition (2), where no current flows. As soon as the junction is directly polarized, the current starts to flow again due to the tunneling process which now takes place in the specular direction (3), until it starts dropping again because of the decreasing of available empty states in the valence band (4). This negative differential resistance (NDR) regime is characteristic of tunneling diodes. For higher applied voltage, the junction behaves as a regular p-n junction and the current increases following the standard exponential law (5) in forward regime.

As qualitatively presented in Fig. 2.18, a tunnel junction is more conductive in the reverse regime. In order to exploit its advantages in VCSEL devices, it is thus typically employed in that region.

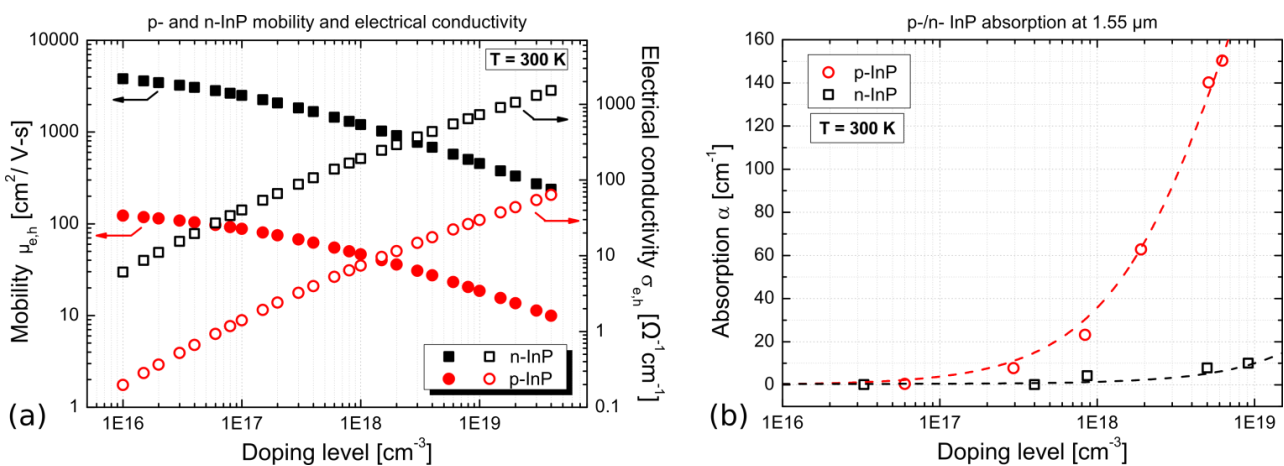


Fig. 2.19 – (a) Electrons/holes mobility  $\mu$  (electrical conductivity  $\sigma$ ) and (b) optical absorption  $\alpha$  at 1.55  $\mu\text{m}$  vs doping levels  $N_d$ ,  $N_a$  in the case of n-type and p-type InP. Values are taken from literature [Wiley1975, Anderson1985, Ballman1983, Casey1984, Bugajski1985].

However, the benefits of tunnel junctions are not only limited to an efficient carrier injection, they also provide advantages in terms of thermal management. In electrically-driven devices, self-

heating is usually associated to Joule effect, due to the electrical impedance which is largely dominated by the p-conducting layers. This effect is related to the higher effective mass  $m_h^*$  (and consequently the lower mobility  $\mu_h$ ) of holes with respect to that of electrons  $m_e^*$  ( $\mu_e$ ). For example, the ratio between electron and holes mobility in n/p-InP is  $\mu_e/\mu_h \approx 25-30$ , as shown in Fig. 2.19a on the previous page. This translates in a lower electrical conductivity  $\sigma$  (i.e. higher resistance) of the current spreading layers used for carrier injection in p-doped materials<sup>3</sup>. Additionally, low resistive metallic contacts on p-doped materials are generally more challenging to achieve.

An additional limiting factor is represented by a significantly larger free-carrier absorption of p-type materials compared with n-type counterparts (see Fig. 2.19b in the case of doped InP), which again limits the performance of the devices.

So that, the use of a buried tunnel junction in InP-based VCSELs simultaneously allows obtaining the following benefits:

- it provides an efficient lateral confinement of both current and transverse optical field in order to promote a transverse single mode emission;
- it converts the confinement layers from p- to n-doped InP, which translates in a lower electrical impedance (i.e. lower heat generation due to lower Joule dissipation) and allows the deposition of n-type electrical contacts on both sides of the VCSEL device (lower contact resistances);
- it also allows minimizing the thickness of the p-doped layers, with consequently reduced optical losses due to free carrier absorption (mainly due to p-doped materials).

### **Materials choice for the tunnel junction**

On the basis of what we have just presented, we are going to discuss about the materials choice for the BTJ. In general, this imposes a trade-off between a low energy gap (to increase the probability of carrier tunneling) but sufficiently high to limit the light absorption at the emission wavelength (in our case at 1.55  $\mu\text{m}$ , which correspond to an energy of 0.8 eV). Moreover, as anticipated, very high doped materials are required to assure low threshold tunnel voltages and high tunnel currents. At the lab, during the work detailed in this manuscript, the available dopants in the GS-MBE system were Si (donor) and Be (acceptor), which can ensure typical doping levels as high as  $10^{19} \text{ cm}^{-3}$ , depending on the material composition.

---

<sup>3</sup> Assuming complete ionization of the donors/acceptors, the electrical conductivity  $\sigma$  is related to the mobility  $\mu$  through the formulas  $\sigma_e = qN_d\mu_e$  (n-type semiconductor) and  $\sigma_h = qN_a\mu_h$  (p-type semiconductor), where  $N_d$  ( $N_a$ ) is the doping level of donors (acceptors).

Fig. 2.20a shows the band gap and band alignment of the commonly used compounds in the InP material system (the values being referred to the vacuum level) available in the GS-MBE system (please note: no Al-based alloys). Except for the InGaAs, all the other materials have a bandgap exceeding 0.8 eV and are thus non-absorbing at 1.55  $\mu\text{m}$ .

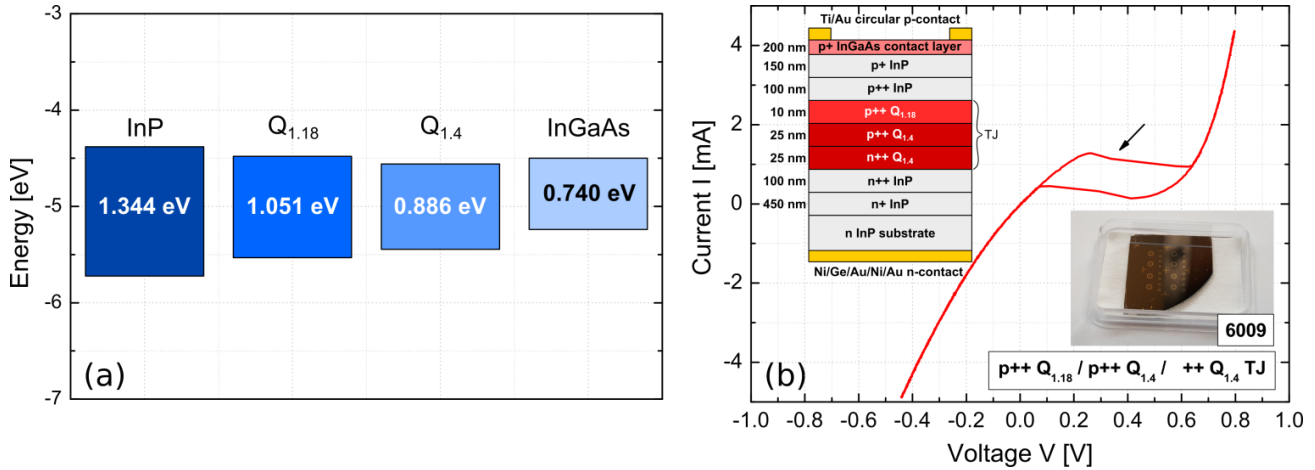


Fig. 2.20 – (a) Room temperature band gap and band alignment of the most used (intrinsic) compounds in the InP material system and (b) I-V characteristic of a  $Q_{1.4}$ -based TJ on InP (the black arrow indicates the NDR region). The insets show the structure of the TJ and a picture of the tested devices.

Initial investigations at FOTON Institute for the integration of BTJs in InP-based EP-VCSELs were addressed to the use of the quaternary alloy  $Q_{1.4}$  ( $\text{In}_{0.66}\text{Ga}_{0.34}\text{As}_{0.73}\text{P}_{0.27}$ ), which was initially selected because of its small band gap (0.886 eV), but large enough to be transparent at designed wavelength of the investigated devices [Lamy2008, Gauthier2011]. To limit the effect of the large barrier arising at the interface between the valence bands of InP and  $Q_{1.4}$ , a thin  $Q_{1.18}$  buffer layer is added. This  $Q_{1.18}$  layer is intended to lower the barrier and promote the holes transport to the active region. This approach has been validated both on simple diode structures (an example of I-V characteristic is shown in Fig. 2.20b on a tunnel diode) and on BTJs embedded in a pn-junction after a regrowth step. However, despite the satisfying performance achieved with those components (characteristic resistance  $R_s \sim 4.7 \cdot 10^{-5} \Omega \cdot \text{cm}^2$  and interface resistance  $R_i \sim 40 \Omega$ ), efficient tunnel junctions based on n+/p+ quaternary alloys such  $Q_{1.4}$  are challenging to realize, because they require very high doping levels ( $\sim 5 \cdot 10^{19} \text{ cm}^{-3}$  for both the n- and p-doping) which are not easily reproducible in practice, especially in the case of p-doping based on Be, because it tends to diffuse rapidly [Ma2017]. Also, reaching high doping levels on quaternary alloys implies a challenging low temperature growth with specific epitaxial conditions, adding more complexity and uncertainty on the already challenging VCSEL growth.

As a result, we re-oriented our choice to the InGaAs. This was justified by the fact that high doping levels and abrupt profiles are easier to achieve in InGaAs, because Be is more easily incorporated

than in InGaAsP (or InP) [Ritter1991, Shamir1998]. Additionally, the lower bandgap of n<sup>++</sup>/p<sup>++</sup> - InGaAs should help in lowering the series resistance of the BTJs. To validate this last assumption, numerical simulations have been performed under Silvaco<sup>®</sup> TCAD (Atlas module) [Silvaco]. To limit the computational cost at a reasonable value, we simulated 15 nm-thick tunnel junctions (7.5 nm p-side + 7.5 nm n-side) with a surface equal to 1×1 μm<sup>2</sup>. A constant doping level of 10<sup>19</sup> cm<sup>-3</sup> has been set for both the p- and n- sides of the junction. Additionally, perfect ohmic contacts for the anode and the cathode have been considered in our model.

In Fig. 2.21, we compared the results obtained for four tunnel junctions based on different materials.

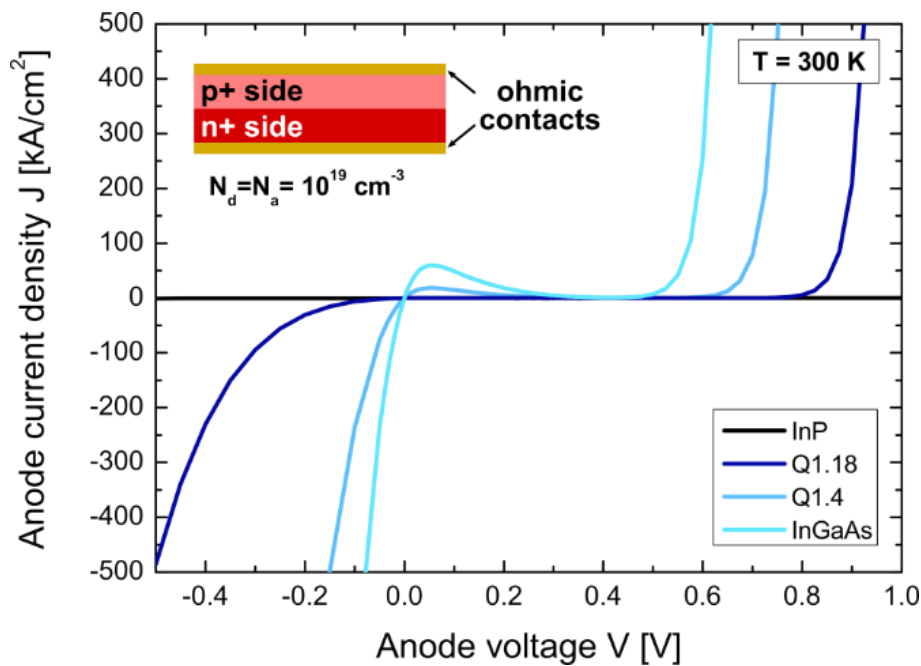


Fig. 2.21 – Simulated I-V characteristic of the tested tunnel homojunctions based on different materials.

As clearly evident, the highest current in the inverse regime are obtained with the InGaAs-based TJ, because of its reduced bandgap (0.74 eV) with respect to the other tested materials (cf. Fig. 2.20a). However, because of the reduced bandgap, InGaAs-TJs are subjected to fundamental bandgap absorption at 1.55 μm (especially for highly p-doped layers). This inconvenient, which may potentially spoil the laser performance of VCSELs, can be partially mitigated by exactly placing the BTJ in a node of the standing optical wave inside the VCSEL cavity and by limiting the total thickness of the BTJ below 50 nm.

### Design and optimization of the InGaAs-based BTJ

On the basis of the previous considerations on ideal TJ (without any InP surrounding layers), we investigated the behavior of different InGaAs-based BTJ structures embedded in an InP pn-junction

by means of our TCAD model, to identify the design which offers the best performance in reverse bias conditions. Similarly to what we have anticipated before for the case of  $Q_{1.4}$ -based TJJs, in order to improve the holes transport is necessary to decrease the interface barrier between the valence bands of InP and InGaAs (being even larger than the previous case) by adding a thin and highly doped quaternary buffer layer.

To test the impact of different designs, we simulated the current density  $J$  versus the applied voltage  $V$  ( $J$ - $V$  characteristics) for several BTJ structures, which differ for the composition of the quaternary buffer layers (whether  $Q_{1.18}$  or  $Q_{1.4}$ ) and the position of these layers (if single- or double-sandwiched configuration) with respect to the simpler case of a fully InGaAs-BTJ embedded in an InP pn-junction, as presented in Fig. 2.22a.

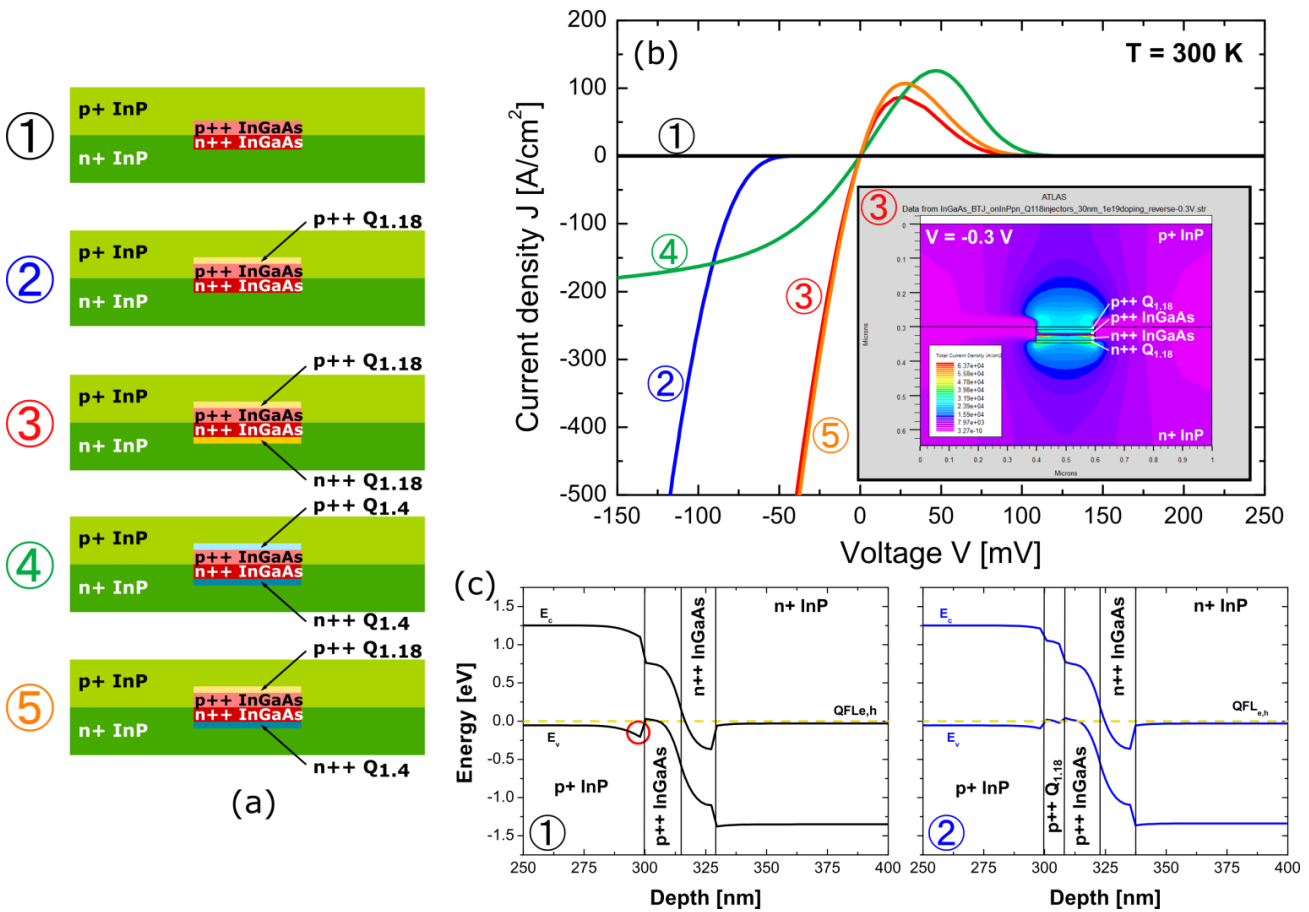


Fig. 2.22 – (a) Simulated BTJ structures and (b) corresponding  $J$ - $V$  characteristics (zoom on the NDR region). The inset shows that the current is efficiently confined across the BTJ (here in the case of structure ③). (c) Room-temperature energy band profiles of structures ① and ② at equilibrium.

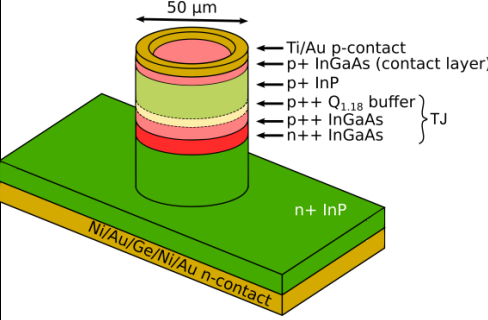
Each structure is constituted by a 30 nm-thick InGaAs BTJ. The thickness of the quaternary buffer layers has been set to 8 nm, while the InP layers thickness (of both n- and p- sides) has been set equal to 300 nm. The net n- and p-doping levels are equal to  $10^{18}$  cm<sup>-3</sup> for the InP and  $10^{19}$  cm<sup>-3</sup> for the  $Q_{1.18/1.4}$  and InGaAs layers. As expected, the result of TCAD simulations show that the

tunneling is inefficient in the case of the simple BTJ entirely composed by InGaAs (structure ①, black curve in Fig. 2.22b). This is mostly due to the appearance of a barrier between the InP and InGaAs valence bands (see Fig. 2.22c-①, red circle), as previously discussed. Adding a thin layer of Q<sub>1.18</sub> quaternary alloy on the p-side of the InGaAs-BTJ helps minimizing that barrier (Fig. 2.22c-②), promoting the tunneling process (structure ②, blue curve in Fig. 2.22b). This effect is even more noticeable if two Q<sub>1.18</sub> buffer layers are added on both sides of the InGaAs-BTJ (structure ③, red curve of Fig. 2.22b). As evidenced by the green curve in Fig. 2.22b, two Q<sub>1.4</sub> buffer layers are less efficient in injecting the carriers through the BTJ (structure ④), because of the aforementioned barrier on the p-side of the valence band is less compensated. Conversely, no significant difference is observed if the Q<sub>1.4</sub> is used instead of the Q<sub>1.18</sub> as n-side buffer (structure ⑤, orange curve of Fig. 2.22b), provided that the p-side buffer is made by Q<sub>1.18</sub>. This confirms also that the hole barrier on the BTJ p-side is the main limiting factor for the tunneling. In forward bias conditions, the result of simulations provides a threshold voltage around 1.1 V for such structures (not shown), mainly related to the InP pn-junction which becomes conductive.

### Experimental validation of the Q<sub>1.18</sub> buffer on macroscopic tunnel diodes

The results of simulations have been experimentally reproduced on macroscopic InGaAs-based tunnel diodes. The diameter of the structures is fixed to 50 μm. Two samples have been realized by epitaxy, whose layers thickness, composition and targeted doping level are detailed in Table 2.6. The main difference between the two samples involves a 10 nm-thick Q<sub>1.18</sub> buffer layer, which is missing in sample #1 (while present in sample #2).

**Table 2.6 – Tunneling diode structures.**

Structure	Layer		Sample #1 (6102)	Sample #2 (6106)
 <p>Scheme of the tunnel diode</p>	Ti/Au	metallic p-contact	20/200 nm	20/200 nm
	InGaAs	p+ contact layer	200 nm $N_a=10^{19} \text{ cm}^{-3}$	200 nm $N_a=10^{19} \text{ cm}^{-3}$
	InP	p+ layer	50nm $N_a=10^{18} \text{ cm}^{-3}$	50 nm $N_a=10^{18} \text{ cm}^{-3}$
	Q <sub>1.18</sub>	p++ buffer	MISSING	10 nm
	InGaAs	p++ TJ layer	25 nm $N_a=10^{19} \text{ cm}^{-3}$	15 nm $N_a=10^{19} \text{ cm}^{-3}$
	InGaAs	n++ TJ layer	25 nm $N_d=5 \times 10^{18} \text{ cm}^{-3}$	15 nm $N_d=5 \times 10^{18} \text{ cm}^{-3}$
	InP	n+ layer	300 nm $N_d=10^{18} \text{ cm}^{-3}$	300 nm $N_d=10^{18} \text{ cm}^{-3}$
	InP	Substrat	$N_d=10^{18} \text{ cm}^{-3}$	$N_d=10^{18} \text{ cm}^{-3}$
	Ni/Au/Ge/Ni/Au	metallic n-contact		

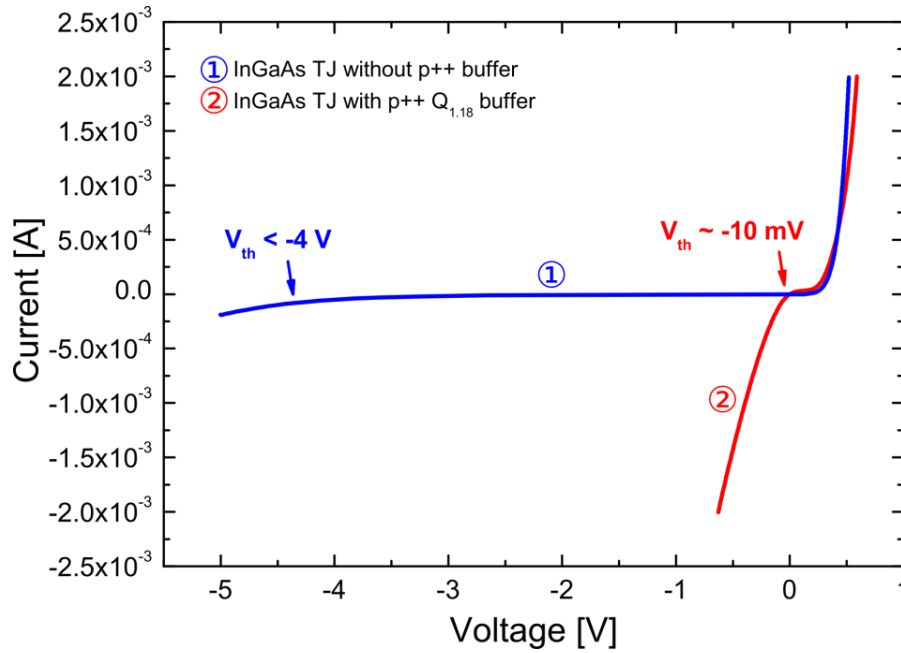


Fig. 2.23 –  $I$ - $V$  characteristics of the two tested tunnel diodes without (①) and with (②)  $p^{++}$   $Q_{1.18}$  buffer layer.

The comparison of the current to voltage ( $I$ - $V$ ) characteristics of the two samples (Fig. 2.23) confirms that the integration of a  $p^{++}$   $Q_{1.18}$  buffer layer between the  $p^{+}$  InP and the  $p^{++}$  InGaAs significantly improves the electrical performance of the tunnel diodes in reverse bias. We observe a decreasing of the threshold voltage from more than 4 V (in absolute value) for standard InGaAs tunnel diodes, to a value of about 10 mV when the buffer layer is integrated. This is in agreement with what obtained by TCAD simulations, and experimentally confirms the benefits brought by the  $Q_{1.18}$  buffer layer in promoting the tunneling process and lowering the resistance of the tunnel diode.

### InGaAs-based BTJ: growth and electrical characterization

The approach involving such a design has been finally applied to the realization of test devices, consisting in BTJ-based infrared LEDs. These devices have almost the same architecture of a VCSEL, except for the DBR-delimited microcavity which is missing here. They also include micrometric InGaAs-BTJs of various sizes (ranging from 3 to 15  $\mu\text{m}$  in diameter), defined by a selective wet etching step, followed by the MBE regrowth of an  $n$ -doped InP layer, an undoped VCSEL active region based on a single set of 6 strained InGaAsP MQWs emitting at 1.5  $\mu\text{m}$ , sandwiched in a  $p$ - $n$  junction. The process is shown in Fig. 2.24a (next page). The top circular metallic mesa has a diameter of 40  $\mu\text{m}$  (Fig. 2.24b).



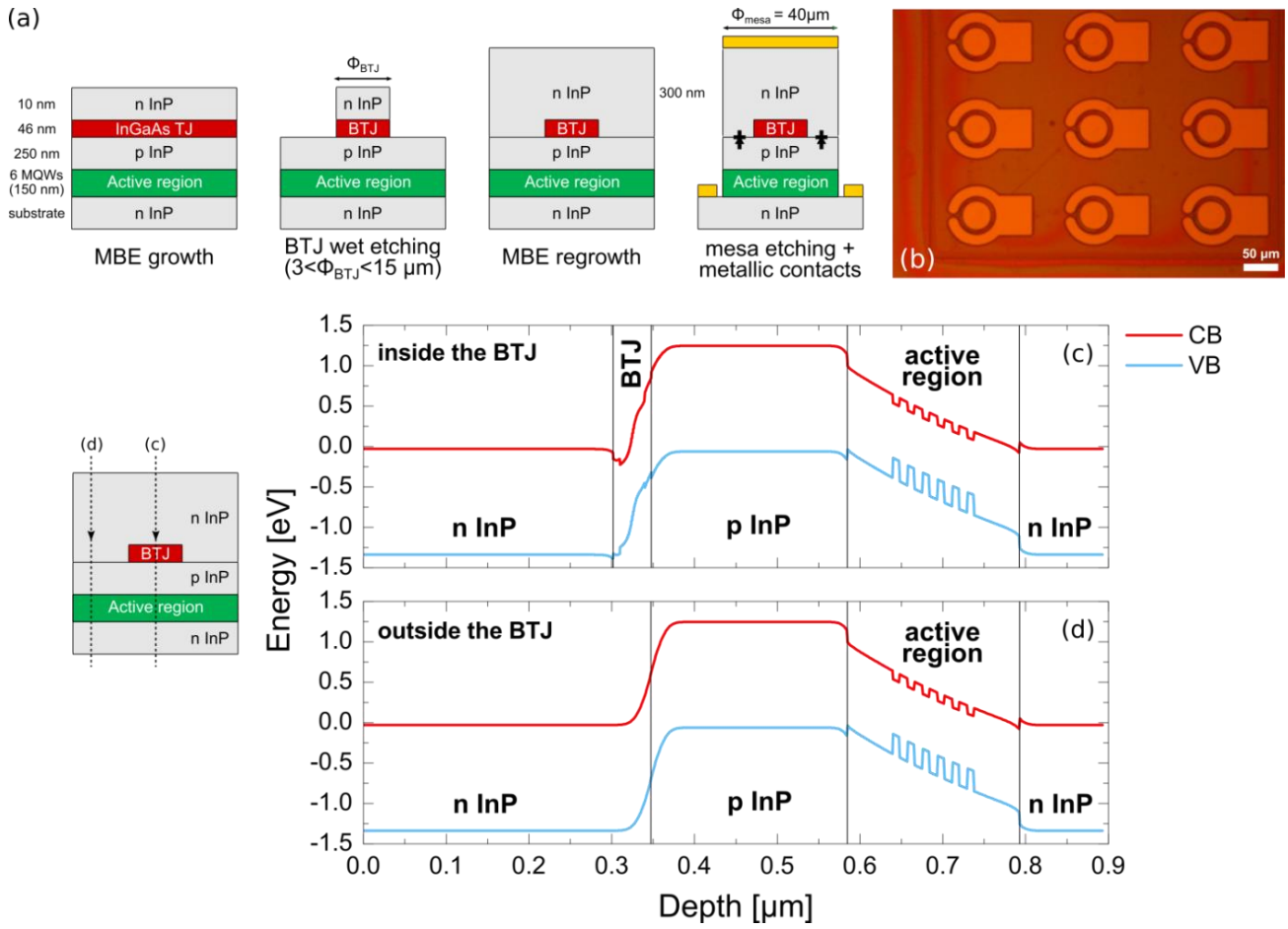


Fig. 2.24 – Sample 6195, InGaAs-BTJs: (a) realization process and (b) microscope photograph of the tested devices. Band diagrams of the structure (c) inside and (d) outside the BTJ.

The experimental  $I$ - $V$  characteristic of a sample integrating a 10  $\mu\text{m}$ -diameter BTJ is shown in Fig. 2.25a.

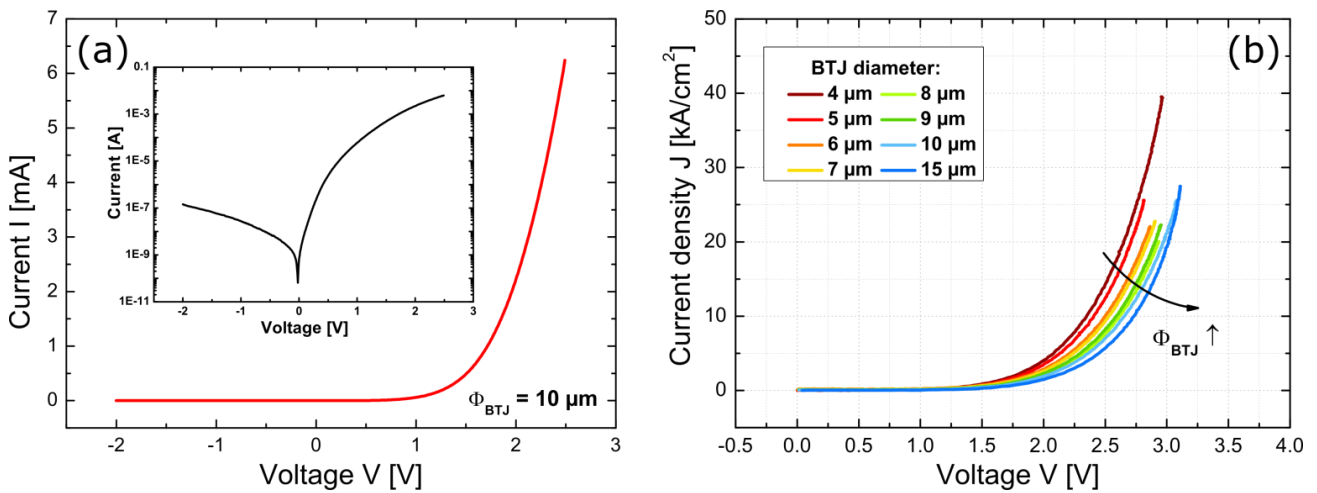


Fig. 2.25 – Electrical characterization of the BTJ-based LEDs: (a)  $I$ - $V$  characteristic of a 10  $\mu\text{m}$ -diameter BTJ sample (the inset shows the same curve in log scale) and (b)  $J$ - $V$  characteristic for different diameters of the BTJ.



The device is conducting in the forward bias regime with a threshold voltage around 1.25 V, while the p-n junction is blocking in the reverse regime, demonstrating that the structure is properly working and has good injection efficiency. We also plotted the  $J$ - $V$  curves of the devices integrating a BTJ with different diameter (Fig. 2.25b), for a voltage ranging from 0 to 3 V. It is worth noting that, independently to the BTJ dimension, the curves are quite similar to each other. This translates into two main considerations:

- a) the quality of the MBE regrowth is good;
- b) the injection surface is truly governed by the dimension of the BTJ (higher current density for smaller BTJ sizes), which confirms again the effectiveness of the InGaAs-BTJ in confining the carriers on small diameters.

From the  $I$ - $V$  curves we were also able to extract the value of the characteristic resistance  $R_s$  and the interface resistance  $R_i$ , which are extrapolated by plotting the resistance of the different BTJs as a function of the inverse of their surface (as shown in Fig. 2.26). The slope of the curve and the intercept with the y-axis provide the value of  $R_s$  and  $R_i$ , respectively. The characteristic resistance of our BTJs have been measured to  $R_s \sim 1 \times 10^{-4} \Omega \cdot \text{cm}^2$ , while the interface resistance value is equal to  $R_s \sim 16 \Omega$ . These values have been obtained for a density current in the range 0.5 - 5  $\text{kA}/\text{cm}^2$ .

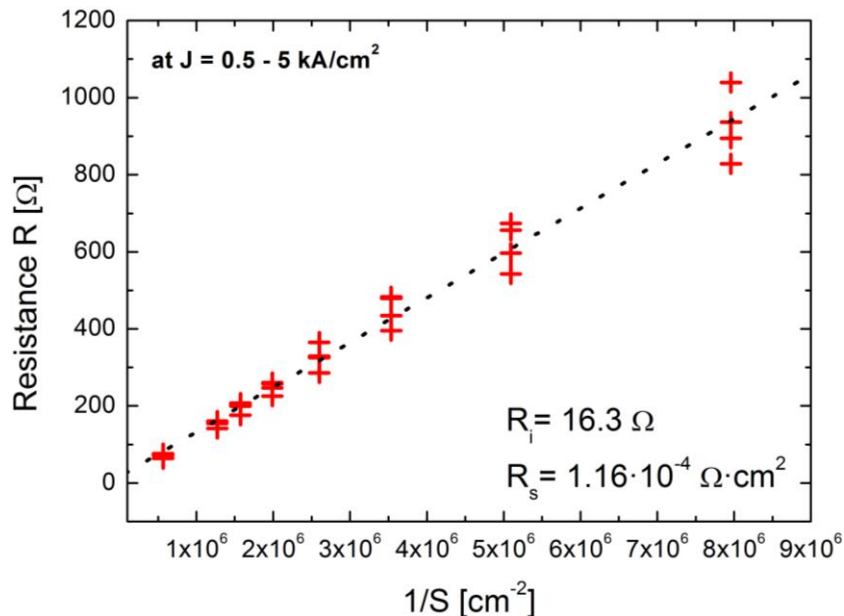


Fig. 2.26– Extrapolation of the characteristic resistance  $R_s$  and interface resistance  $R_i$  of the investigated BTJ (for a current density  $J = 0.5 - 5 \text{ kA}/\text{cm}^2$ ).

The value of the characteristic resistance  $R_s$  measured on such InGaAs-based BTJ is significantly higher than previous reported values obtained on BTJs on InP-based devices emitting around

1.55  $\mu\text{m}$ . Amann group reported a characteristic resistance of  $3 \times 10^{-6} \Omega \cdot \text{cm}^2$  for a n-InGaAs/p-InGaAlAs tunnel junction with delta doping reaching  $1 \times 10^{20} \text{ cm}^{-3}$  at the p-n interface, a total thickness of 32 nm and diameter of 22  $\mu\text{m}$  [Ortsiefer2000]. LPN-CNRS demonstrated that Q<sub>1.4</sub>-based (InGaAsP<sub>1.4 $\mu\text{m}$</sub> ) tunnel junctions can reach good electrical performance as well, with measured characteristic resistances around  $R_s = 5 \times 10^{-6} \Omega \cdot \text{cm}^2$  for tunnel junctions with 35 nm in thickness and diameters ranging from 22  $\mu\text{m}$  to 88  $\mu\text{m}$  [Bousseksou2007]. Here again, a delta doping profile ( $1 \times 10^{20} \text{ cm}^{-3}$ ) was added at the junction interface. In the past, tests on Q<sub>1.4</sub>-based tunnel junctions were also performed at FOTON Institute during J.M. Lamy thesis. In this case a characteristic resistance of  $4.7 \times 10^{-5} \Omega \cdot \text{cm}^2$  was measured for BTJs with diameters ranging from 2  $\mu\text{m}$  to 20  $\mu\text{m}$ , doping levels of  $5 \times 10^{19} \text{ cm}^{-3}$  and total thickness of 50 nm [Lamy2008]. We can additionally notice that characteristic resistance below  $10^{-5} \Omega \cdot \text{cm}^2$  are obtained with tunnel structures whose thickness is  $\leq 35 \text{ nm}$ , and in which delta doping profiles have been used at interfaces. This comparison is summarized in Table 2.7.

**Table 2.7 – Comparison of electrical performance of (B)TJs in 1.55  $\mu\text{m}$ -emitting InP-V(E)CSELs.**

Group	Ref.	(B)TJ composition and doping	(B)TJ diameter	$R_s$ [ $\Omega \cdot \text{cm}^2$ ]
Amann group (WSI)	[Ortsiefer2000]	12 nm n-InGaAs ( $N_d = 3 \times 10^{19} \text{ cm}^{-3}$ ) 20 nm p-InGaAlAs + delta doping at p-n interface	TJ: 4 $\mu\text{m}$ BTJ: 13-22 $\mu\text{m}$	$3 \times 10^{-6}$
LPN-CNRS	[Bousseksou2007]	10 nm n-Q <sub>1.4</sub> ( $N_d = 3 \times 10^{19} \text{ cm}^{-3}$ ) 20 nm p-Q <sub>1.4</sub> ( $N_a = 3 \times 10^{19} \text{ cm}^{-3}$ ) 5 nm p-Q <sub>1.2</sub> buffer ( $N_a = 1 \times 10^{18} \text{ cm}^{-3}$ ) + $10^{20} \text{ cm}^{-3}$ delta doping at p-n interface	22 $\mu\text{m}$ to 88 $\mu\text{m}$ (VECSEL structure)	$5 \times 10^{-6}$
FOTON Institute	[Lamy2008]	25 nm n-Q <sub>1.4</sub> ( $N_d = 5 \times 10^{19} \text{ cm}^{-3}$ ) 25 nm p-Q <sub>1.4</sub> ( $N_a = 5 \times 10^{19} \text{ cm}^{-3}$ ) 10 nm p-Q <sub>1.18</sub> buffer ( $N_a = 5 \times 10^{18} \text{ cm}^{-3}$ )	2 to 20 $\mu\text{m}$	$5 \times 10^{-5}$
FOTON Institute	<b>this work</b> (sample 6195)	8 nm n-Q <sub>1.18</sub> buffer ( $N_d = 1 \times 10^{19} \text{ cm}^{-3}$ ) 15 nm n-Q <sub>1.4</sub> ( $N_d = 1 \times 10^{19} \text{ cm}^{-3}$ ) 15 nm p-Q <sub>1.4</sub> ( $N_a = 1 \times 10^{19} \text{ cm}^{-3}$ ) 8 nm p-Q <sub>1.18</sub> buffer ( $N_a = 1 \times 10^{19} \text{ cm}^{-3}$ )	4 to 15 $\mu\text{m}$	$1 \times 10^{-4}$

It is worth to mention, however, that for our InGaAs-based BTJ, the doping level was not precisely calibrated. It has been targeted to  $N_{a,d} = 10^{19} \text{ cm}^{-3}$ , although it could have probably been lower, somewhere near  $10^{18} \text{ cm}^{-3}$  for both p- and n- sides of the BTJ. This might very easily explain the value of the characteristic resistance measured with our BTJ, which is appreciably higher than the previously reported. Additionally, the value of  $R_s$  measured in our structure comprises the

contribution of the substrate resistance. Taking this into account, a more realistic value of the order of  $\sim 5 \times 10^{-5} \Omega \cdot \text{cm}^2$  can probably be considered. Also, improvements on  $R_s$  can be achieved with higher doping levels, but this implies a low-temperature MBE growth of the BTJ with challenging growth conditions, in order to preserve the crystalline quality of the InGaAs and Q<sub>1.18</sub> layers. We stress again that such a difficult control of the growth parameters on quaternary alloys was one of the reasons which inspired our tests on InGaAs-based BTJ, which were grown at a conventional MBE growth temperature.

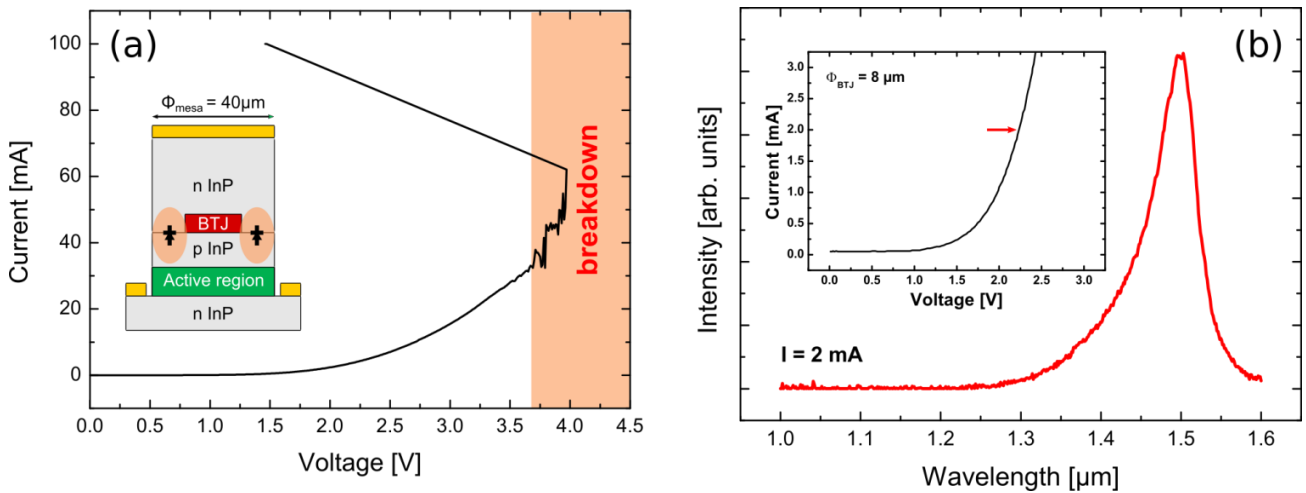


Fig. 2.27 – (a) Measurement of the breakdown voltage (in a 9 μm-diameter BTJ device) and (b) EL spectrum of the InGaAsP MQWs-based active region at 2 mA of injected current (in an 8 μm-diameter BTJ device).

To conclude on the quantitative characterization of the BTJs, we measured a breakdown voltage of  $\sim 3.7 - 4 \text{ V}$  associated to the reversely-biased InP pn-junction surrounding the BTJ (Fig. 2.27a shows an example for a 9 μm-diameter BTJ), that corresponds to a breakdown field of  $E_{break} \sim 8 \cdot 10^5 \text{ V/cm}$ , in agreement with the theoretical value of  $8-10 \times 10^5 \text{ V/cm}$  for InP [Hauser1978]. This also gives an estimation of the maximum current density  $J_{max}$  the device can sustain before the appearance of breakdown, estimated between 51 and 56 kA/cm<sup>2</sup> (for different BTJ diameters in the range 6-15 μm).

We also checked that the temperature rises during the epitaxial regrowth and the device processing steps to realize the BTJ did not impact on the optical performance of the active region. As shown in Fig. 2.27b, the electroluminescence (EL) spectrum (obtained for a current level of 2 mA) is still centered at 1.51 μm, as desired.

## 2.3.2 EP-VCSEL cavity design

### Number of active layers

Conversely to the case of optically-pumped VCSELs, in which three sets have been integrated in the active region of the device, in electrically-injected VCSELs the active region is generally designed to accommodate a single set of MQWs, to avoid the problem of carrier injection in multiple sets. Additionally, increasing the number of active layers composing a set in a RPG structure does not directly translate in a linear increasing of the gain of the structure, because of the saturation of the longitudinal confinement factor  $\Gamma$ . In Fig. 2.28 we plotted the calculated value of  $\Gamma$  with respect to the number of strained MQWs (red dots) contained in the active region of a VCSEL emitting at  $1.55 \mu\text{m}$ , all the MQWs being packed in the same set, which is positioned at a maximum of the internal stationary field (inset of Fig. 2.28). Calculations have been performed by using the TMM model and Eqs. 1.6-1.7 discussed in *Chapter 1*. The result is also compared with a linear evolution which considers that all the QWs are placed at a maximum of the stationary field (black dashed curve).

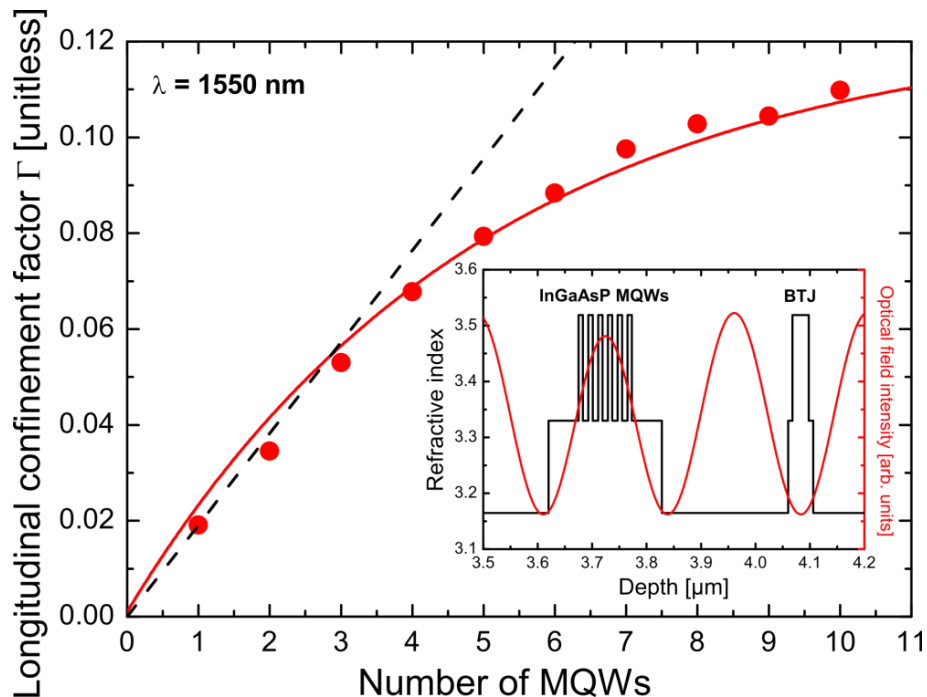


Fig. 2.28 – Longitudinal confinement factor  $\Gamma$  as a function of the number of strained MQWs, in the case of a  $1.55 \mu\text{m}$ -emitting InGaAsP/InP-based EP-VCSEL integrating a single active set and a BTJ (in inset the refractive index profile and the resonant field intensity in the case of 6 strained MQWs, view zoomed on the active region and BTJ). Red dots: simulation results, red solid curve: fitting, black dashed line: linear evolution considering all the QWs placed at a maximum of the stationary field.

According to the result of calculations, we chose to integrate 6 strained MQWs in the active region of our devices. This was a trade-off between an adequate number of active layers and a sufficient gain.

With such a choice, we obtain a cavity with an effective length of 2424 nm (i.e. a  $9\lambda/2$ -long cavity)<sup>4</sup>.

### Optical losses related to the BTJ

In the previous *Section 2.3.1*, we anticipated that the small bandgap of InGaAs (0.74 eV) may be responsible for optical losses at the emission wavelength (1.55  $\mu\text{m}$ , i.e. 0.8 eV) due to fundamental bandgap absorption. However, it is known that the band gap of highly-doped semiconductor increases with respect to that of their intrinsic counterparts because of the Burstein-Moss shift, leading to a change of the absorption edge toward the higher energies [Burstein1954, Moss1954]. This phenomenon has been observed in many semiconductors and it is more pronounced in n-doped than p-doped materials since the density of states effective mass is lower in the conduction band than in the valence band (for those concerned in this work: InP [Lahtinen1986], InGaAs [Munoz2001]). However, direct absorption estimation by ellipsometry measurements would generally require thick layers, which are not easily obtained in practice in the case of heavily-doped InGaAs layers, because of their poor morphological quality. On the other hand, the optical properties extrapolated from these samples would not be representative of the highly-doped thin InGaAs layers used to realize the BTJ.

Concerning a possible used of p- and n-doped InGaAs in 1.55  $\mu\text{m}$ -emitting VCSELs, Xiang et al. showed that, thanks to Burstein–Moss effect, negligible optical absorption at 1.55  $\mu\text{m}$  can be obtained on n-type InGaAs with a donor concentration higher than  $7.7 \times 10^{18} \text{ cm}^{-3}$  [Xiang1999]. In the same work, however, they also showed that high optical absorption (around  $2600 \text{ cm}^{-1}$ ) is still present for p-doped InGaAs with doping concentrations up to  $3.4 \times 10^{19} \text{ cm}^{-3}$ , and therefore p-doped InGaAs is thus not suited for applications at 1.55  $\mu\text{m}$  (or lower). Anyway, it must be mentioned that the authors were investigating a possible use of InGaAs for realizing DBRs at 1.55  $\mu\text{m}$ , which present non-negligible thickness of the  $\lambda/4$  layers, and whose interfaces are placed at the maximum of the resonant field. Thin layers (few nm) of p-doped InGaAs, placed at the antinodes of the resonant field, may present lower values of the linear absorption compared to those announced in the above-mentioned study.

In the past, M.C. Amann's group at Walter Schottky Institute in Munich experimentally demonstrated the operation of 1.55  $\mu\text{m}$ -emitting VCSELs integrating InGa(Al)As-based BTJs, with

---

<sup>4</sup> The VCSEL cavity has an average refractive index of  $n_{avg} = 2.72$  and the penetration length in each DBR is 240 nm.

output performance above 1 mW [Shau2004, Ortsiefer2005, Muller2011], up to the record 7.9 mW in single-mode emission at room temperature for a 1.55  $\mu\text{m}$ -emitting VCSEL [Gründl2013]. In all these cases, the fundamental absorption on the p-side of the BTJ was limited by using p-InGaAlAs (which has a bandgap of 0.83 eV) instead of p-InGaAs, while the n-InGaAs composing the BTJ n-side has negligible fundamental absorption due to the above-mentioned Burstein-Moss shift [Deppe1990a].

In our case, not disposing of Al cells in the GS-MBE system dedicated to the growth of VCSEL structures, both n- and p- sides of the BTJ have been based on the ternary InGaAs. Considering the reduced thickness of the BTJ, and the fact that it is placed at a minimum of the stationary cavity field, it can be interesting to estimate the optical losses introduced on the VCSEL by a fully InGaAs-based BTJ, and the effects of its possible offset with respect to the optimal BTJ position on the cavity (corresponding to a node of the internal standing wave pattern, as shown in Fig. 2.29a), by means of optical simulations based on the TMM.

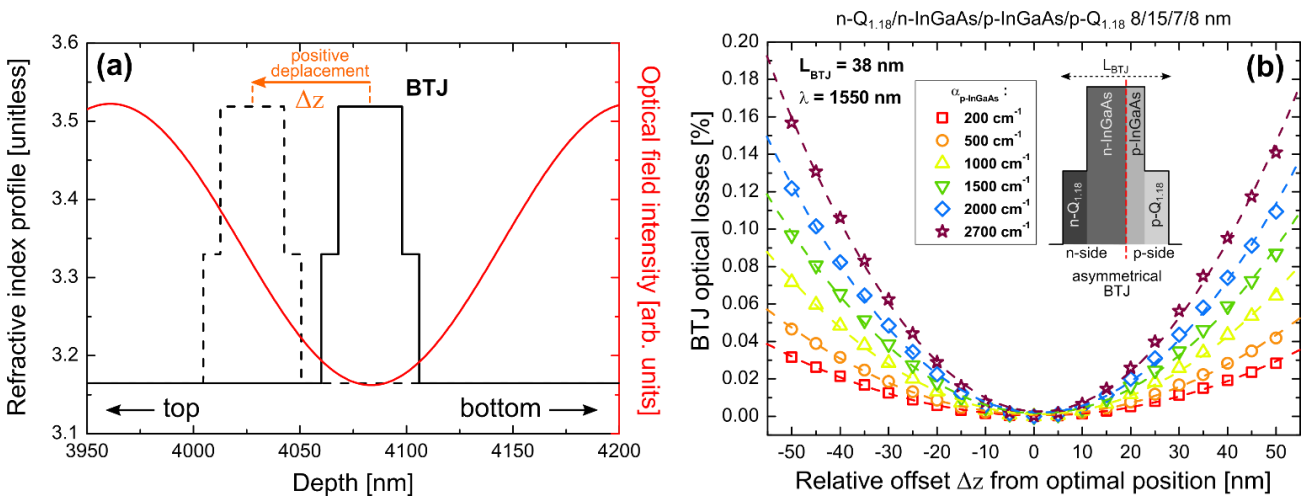


Fig. 2.29 – Calculation of the single-pass optical losses introduced by the InGaAs-BTJ at 1.55  $\mu\text{m}$ : (a) position of the BTJ with respect to a node of the stationary optical field and (b) optical losses with respect to the relative offset  $\Delta z$  from optimal BTJ position for different values of the linear absorption  $\alpha_{p\text{-InGaAs}}$  of the p-doped InGaAs layer composing the BTJ (the absorption of the n-InGaAs has been set to  $\alpha_{n\text{-InGaAs}} = 200 \text{ cm}^{-1}$ ). The composition of the BTJ is: n- $\text{Q}_{1.18}$ /n-InGaAs/p-InGaAs/p- $\text{Q}_{1.18}$  with respective thickness of 8/15/7/8 nm (total thickness  $L_{\text{BTJ}} = 38$  nm).

Fig. 2.29b shows the variation of the single-pass optical losses introduced by the BTJ as a function of the position offset  $\Delta z$  when considering different values for the average linear absorption  $\alpha_{p\text{-InGaAs}}$  of the p-doped InGaAs, ranging from 200  $\text{cm}^{-1}$  (red squares) to the more realistic 2700  $\text{cm}^{-1}$  (violet stars), and a total BTJ thickness of 38 nm (n- $\text{Q}_{1.18}$ /n-InGaAs/p-InGaAs/p- $\text{Q}_{1.18} \rightarrow 8/15/7/8$  nm). We emphasize that the thickness of the p-InGaAs layer (7 nm) has been deliberately set to half the thickness of the n-InGaAs layer (15 nm) to limit as much as possible the

optical losses. For the n-doped InGaAs, a fixed value of  $\alpha_{n\text{-InGaAs}} = 200 \text{ cm}^{-1}$  have been considered for calculations. The optical losses have been calculated by considering an exponential decay given by [Feezell2006]:

$$\delta_{BTJ}[\%] = 100 \left( 1 - e^{-(\alpha_n t_n + \alpha_p t_p) \Gamma_{enh}} \right) \quad (2.3)$$

where  $\alpha_{n,p}$  and  $t_{n,p}$  are the absorption and the thickness of the n- or p- sides of the BTJ, while  $\Gamma_{enh}$  is the gain enhancement factor, as defined in Eq. 1.7.

The results of calculations show that, in any case, the optical losses induced by the BTJ are negligible provided that the BJT is exactly placed on (or very close to) a null of the stationary field ( $\Delta z = 0$ ). More exactly, due to the ‘‘asymmetrical’’ structure of the BTJ (the p-side being half the thickness of the n-InGaAs side), the parabolic curves of the optical losses have the minima around  $\Delta z \sim 3.5 \text{ nm}$  (situation in which the p-InGaAs is exactly place at the minima of the stationary field). The optical losses rapidly grow as the absorption rises, especially for high values of the linear absorption  $\alpha_{p\text{-InGaAs}}$  of the p-InGaAs. This point should be carefully investigated to ensure an optimal operation of VCSEL devices. One method to extrapolate the value of the InGaAs absorption for thin InGaAs layers can be based on cold cavity measurements (similarly to what we have discussed in *Section 2.2.2* in the case of the a-SiN<sub>x</sub> cold cavity), in which the InGaAs-based BTJ is placed inside a high-Q cavity.

To conclude this analysis, although a fully InGaAs-based BTJ could in principle works if properly placed inside the VCSEL cavity, its use can be risky because of natural deviation from nominal thickness of MBE-grown layers composing the VCSEL structure, resulting in a misplaced BTJ, which may introduce unacceptable optical losses. Solutions to this problem can involve the use of carbon instead of beryllium as p-dopant, which improves the dopants’ incorporation and reduces dopant diffusion inside the structure, to attain p-doping levels above  $10^{20} \text{ cm}^{-3}$ . This would allow a further increase of the bandgap of the InGaAs layers to limit its absorption at  $1.55 \mu\text{m}$ , or conversely it would facilitate the doping of the quaternary Q<sub>1.4</sub> (or Q<sub>1.3</sub>) layers, which are almost transparent at  $1.55 \mu\text{m}$  and should be thus preferred to InGaAs (as previously discussed). Please note that this can be also beneficial to improve the electrical performance of the InGaAs-BTJ, as discussed in the previous *Section 2.3.1*.

During the work presented in this manuscript, however, carbon was not available as p-dopant. Only very recently, our lab upgraded the GS-MBE system with a carbon cell for future growth of highly C-doped BTJs, which should ensure better optical and electrical performance.



### 2.3.3 Technological process for electrically-injected VCSELs

The TSHEC process presented in *Section 2.2.3*, and employed to realize optically-pumped VCSELs, has been adapted to the case of electrically-injected devices. The process flow, which will be detailed below, consists in 11 masks levels applied with a conventional photolithography mask aligner, with positive or negative photoresists:

- 1 level for the process of the Si host wafer (wet TMAH etching), as in the OP version;
- 7 pre-bonding levels on the InP wafer;
- 3 post-bonding levels on the bonded InP+Si wafers.

Fig. 2.30 shows the mask for the patterning of the Si wafer (**MASK 1**, Fig. 2.30a) and the elementary cell integrating 17 VCSELs, a test cell and an alignment cell (Fig. 2.30b).

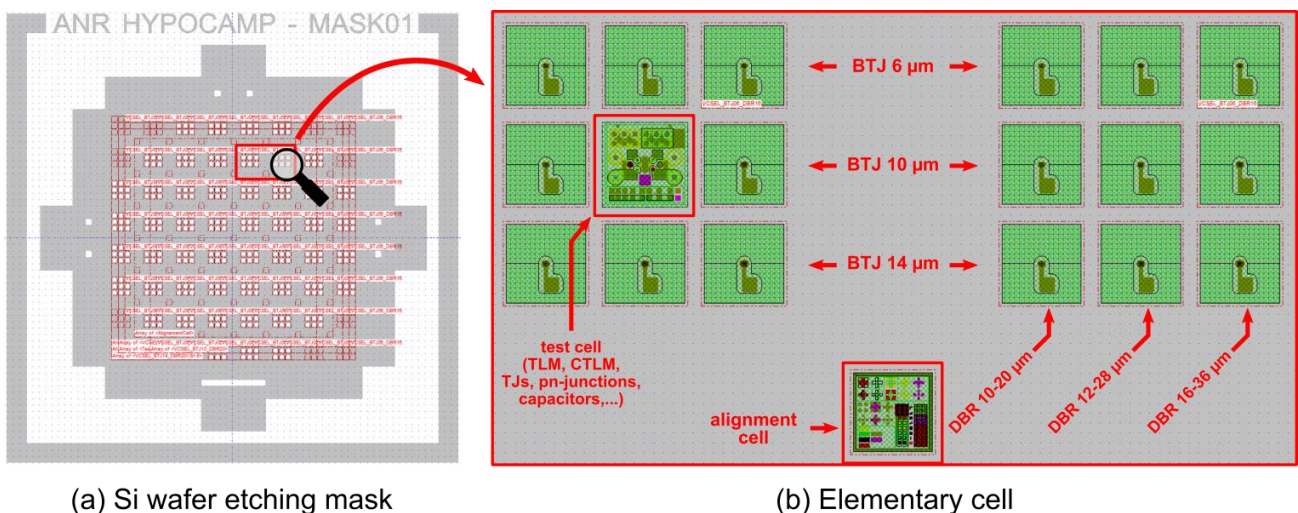


Fig. 2.30 – TSHEC process adapted to EP-VCSELs: (a) mask for Si wafer patterning (**MASK 1**) and (b) elementary cell on InP wafer integrating 17 VCSEL devices with different BTJ and BH-DBR dimensions, a test cell and an alignment cell.

The test cell includes different elements for the electrical characterization of the final devices, such as patterned structures for contact resistivity measurements based on the Transmission Line Method (TLM) and the Circular Transmission Line Method (CTLM), tunnel junctions, pn-junctions, capacitors, etc. The technological flow related to the InP wafer process and VCSELs realization is completely detailed in the following.



### MBE growth of the III-V wafer

As usual, the process starts with the patterning of the Si wafer to realize the matrices of squared vias. The steps (which involves the use of **MASK 1**, see Fig. 2.30a) are the same as in the case of the optically version of the TSHEC process, already described in *Section 2.2.3*.

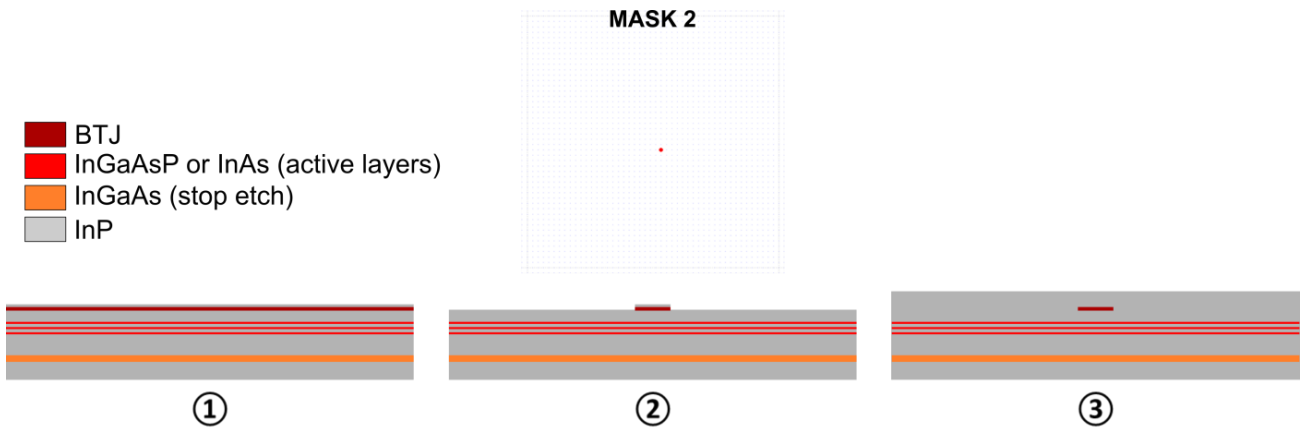


Fig. 2.31 – MBE growth of the III-V structure: (1) epitaxy of the active region and the tunnel junction, (2) patterning of the BTJ (**MASK 2**) and (3) epitaxial regrowth of the n-doped InP layer to form the III-V structure ready to further processing.

The process continues with the MBE growth of an intrinsic InGaAsP-based active region integrating 6 strained MQWs tailored to emit at 1.52  $\mu\text{m}$ , followed by a p-InP layer on an n-doped (001)-oriented InP substrate, in order to form a p-i-n structure. Then the p<sup>++</sup>/n<sup>++</sup> tunnel junction is realized on top of the active region (Fig. 2.31-(1)). The tunnel junction is then patterned by means of a  $\text{H}_3\text{PO}_4 + \text{H}_2\text{O}_2 + \text{H}_2\text{O}$  wet etching procedure, to form a BTJ of three different sizes (**MASK 2**): 6, 10 and 14  $\mu\text{m}$  in diameter (Fig. 2.31-(2)). This step is then followed by the MBE regrowth of a n-doped InP layer, which completes the III-V wafer (Fig. 2.31-(3)).

### Pre-bonding steps

The process of the III-V semiconductor wafer proceeds with the patterning of the VCSELs' mesas using a dry RIE etching with  $\text{CH}_4 + \text{H}_2$  gas mixture (**MASK 3**, Fig. 2.32-(4), next page) and their isolation to individually delimit the devices ( $\text{HCl} + \text{H}_3\text{PO}_4$  chemical wet etching, **MASK 4**, Fig. 2.32-(5)). Then, a Ni/Au/Ge/Ni/Au metallic top n-contact is deposited by e-beam evaporation (**MASK 5**), followed by a rapid thermal annealing (RTA) procedure at 375°C (Fig. 2.32-(6)).

A  $\text{SiN}_x$  passivation layer is deposited by PECVD on the whole wafer (Fig. 2.32-(7)). This layer plays also the role of first (phase-matching) layer of the H-DBR. The passivation layer is then etched away by a RIE procedure, in order to access to the top and bottom contacts (**MASK 6**, Fig. 2.32-(8)).

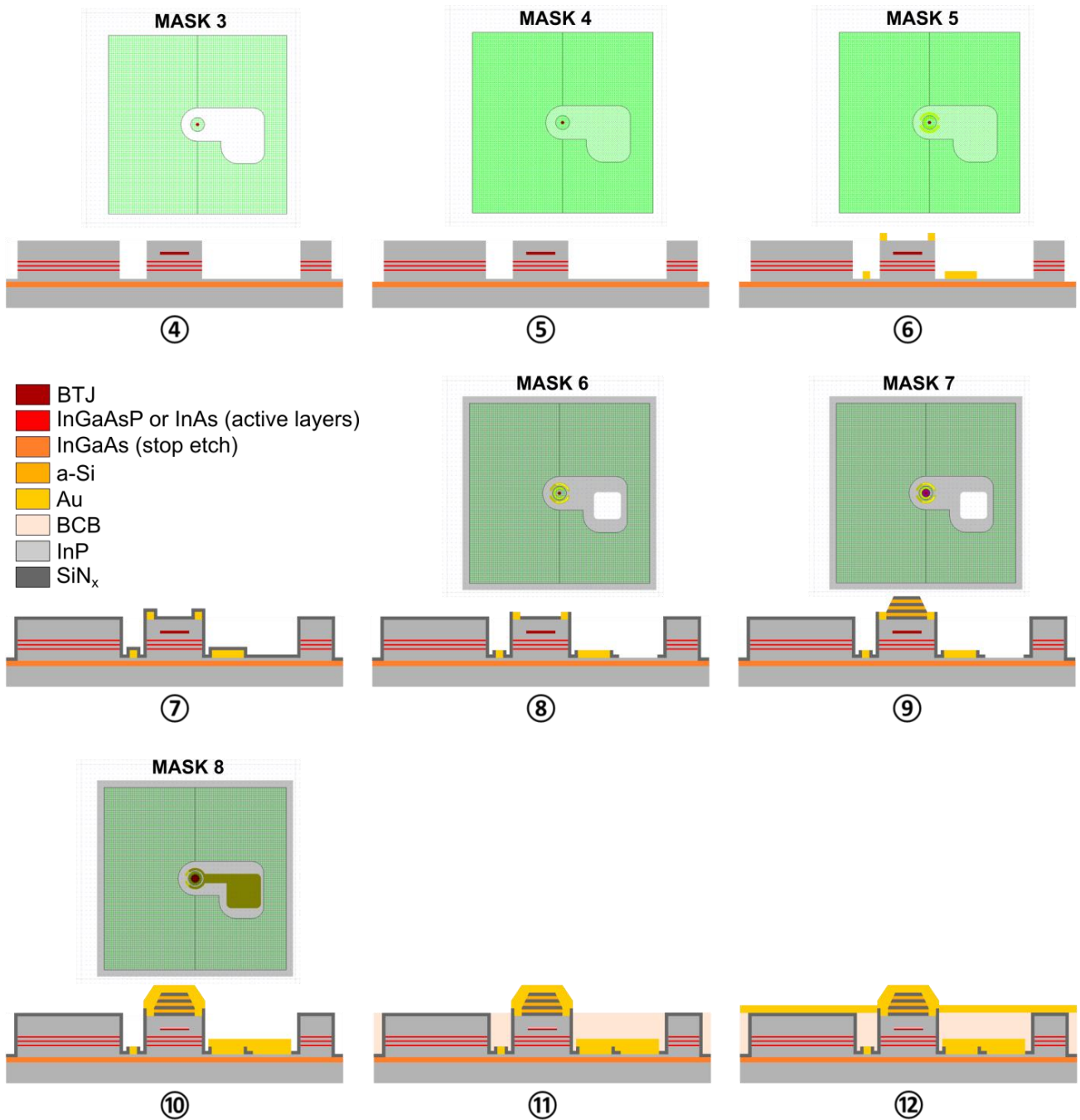


Fig. 2.32 – Pre-bonding steps: (4) mesa delimitation (**MASK 3**) and (5) device isolation (**MASK 4**). (6) Top contact deposition (**MASK 5**) and annealing, (7)  $\text{SiN}_x$  passivation, (8) contact opening (**MASK 6**), (9) bottom BH-DBR deposition and patterning (**MASK 7**), (10) Au deposition (**MASK 8**), (11) BCB planarization and (12) Ti/Au electrode deposition.

Afterwards, the bottom dielectric DBR is deposited by RF sputtering. It consists in 3.5 a-Si/ $\text{SiN}_x$  layers, which are patterned with the RIE system in order to get different reflector sizes (from 10 to 36  $\mu\text{m}$  in diameter), with tilted sidewalls (**MASK 7**, Fig. 2.32-(9)). The bottom reflector is then completed by a 200 nm deposition of Au by RF sputtering to finalize the BH-DBRs (**MASK 8**, Fig. 2.32-(10)), which also acts as a re-growth contact layer for top and bottom contacts. A BCB

planarization step (Fig. 2.32-(11)) anticipates the deposition of a Ti/Au metallic layer (Fig. 2.32-(12)), which acts as electrode for the following electroplating step and also as bottom contact layer.

**Post-bonding steps**

The processed III-V wafer is bonded on the Si patterned substrate by means of a 5 μm-thick BCB layer, according to the TSHEC process previously described, and it is cured on a hot plate at 250°C for 1h under a nitrogen atmosphere (Fig. 2.33-(13)).

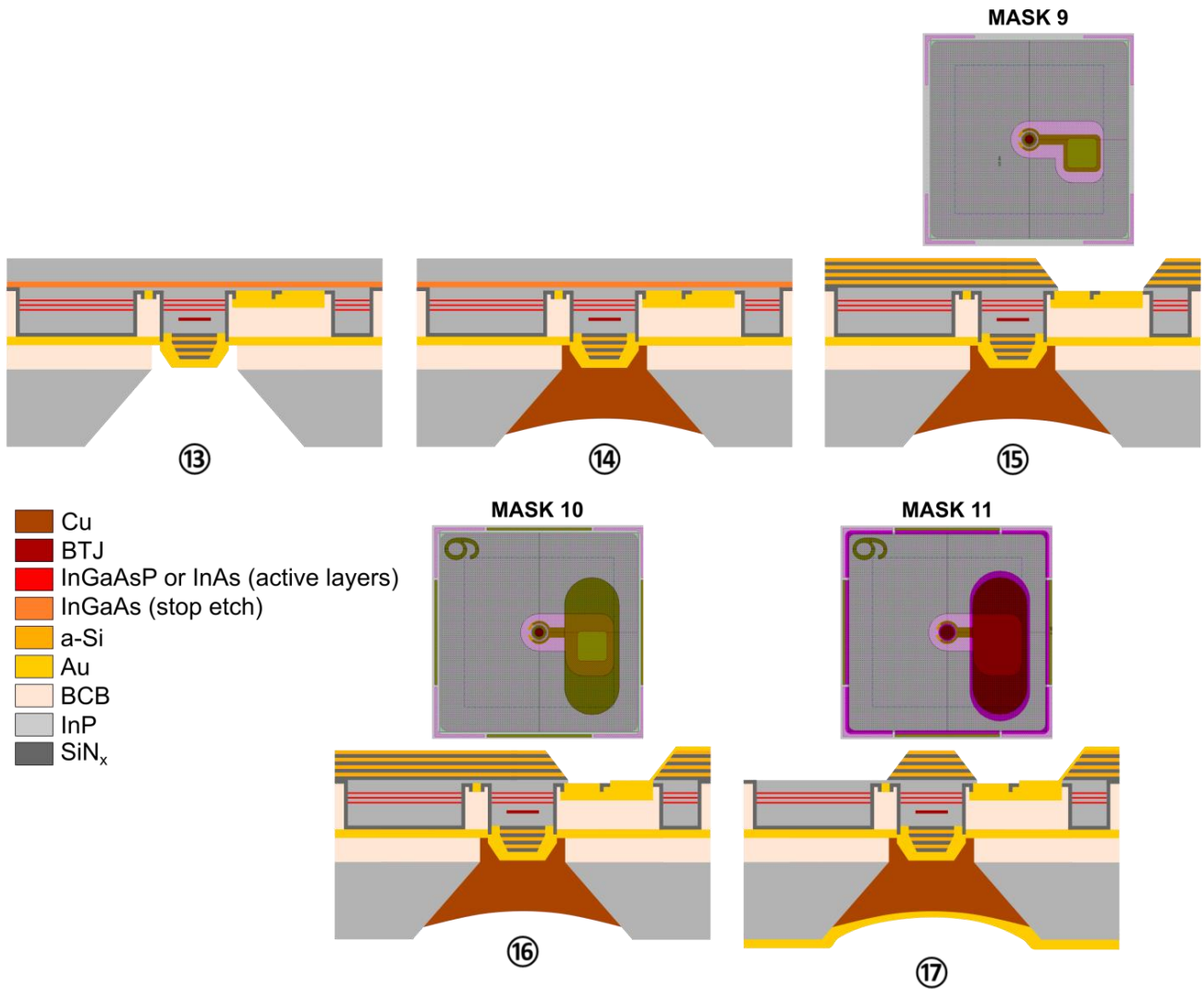


Fig. 2.33 – Post-bonding steps: (13) BCB bonding, (14) Cu electroplating, (15) top DBR deposition and patterning for contact opening (MASK 9), (16) top metallic pad deposition and (17) top DBR patterning (MASK 11).

At this point, an electroplating step is performed, and the Si vias are filled by copper, which act as μ-heat sink and strengthen the mechanical adhesion of the two wafers (Fig. 2.33-(14)), and as bottom electrical contact of the VCSEL as well. A mechanical thinning followed by a chemical etching allows removing the InP substrate and the InGaAs stop-etching layer, and the top dielectric DBR, consisting in 4 a-Si/SiN<sub>x</sub> layers, is deposited by RF sputtering. It is then etched to access to

the top metallic contact (Fig. 2.33-(15)). A metallic pad is then deposited, to bring the contact far from above the InP wafer and improve the mechanical stability when electrical probe contacts will be placed during tests (Fig. 2.33-(16)). The top DBR is eventually patterned, and the bottom (common) Ti/Au contact is finally deposited on the back side of the device (Fig. 2.33-(17)).

### 2.3.4 Preliminary results on EP-VCSEL tests sample

In absence of VCSEL structures devoted to the electrical injection, the process just described has been applied to an InP-based p-i-n diode structure which was originally devoted for edge-emitting laser process. The active region of the sample contains 6 layers of InAs quantum dashes on InP(100), with an emission centered at 1.6  $\mu\text{m}$ . Although this sample was not designed to get a laser emission in the vertical direction, it has been used to realize infrared light-emitting diodes (LEDs) and validate some steps of the EP-VCSEL process.

In particular, we investigated the pre-bonding steps 4-12 (**MASKs 3-8**), as the bonding procedure on the Si platform does not substantially differs from the optically-pumped version of VCSELs. We also skipped the BTJ patterning and regrowth steps, because the structures did not contain any tunnel junction, and because they were already checked during the testing of the BTJs, as detailed in the previous section. Figs. 2.34a<sub>1-6</sub> summarize the steps of the fabrication process applied to the test sample (sample #4820) and Figs. 2.34b,c,d,e show the scanning electron microscope (SEM) characterization.

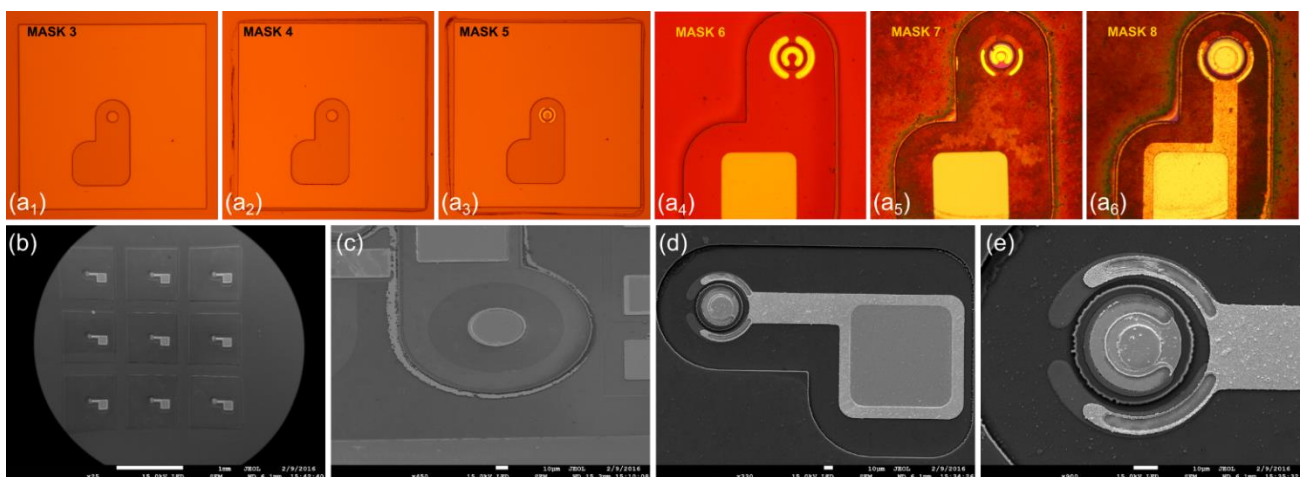


*Fig. 2.34 – (a<sub>1-6</sub>) Optical microscope pictures detailing the pre-bonding process flow (MASKs 3-8). SEM photos of the test sample: (b) a 3x3 matrix, (c) electrical test cell (pn-junction), (d) 26  $\mu\text{m}$ -diameter device and (e) zoom on it.*

The LEDs have been tested on the probe station shown in Fig. 2.35a (next page), dedicated to the characterization of EP-VCSEL devices. The sample has been fixed onto a Peltier cell and contacted by electrical probes, the electroluminescence (EL) has been collected by a stripped multimode fiber



brought close to contact with the sample surface, and sent to an OSA. Fig. 2.35b shows the emission spectra of a LED structure obtained at room temperature for different injected currents (in the range 1-100 mA), and centered on the emission wavelength.

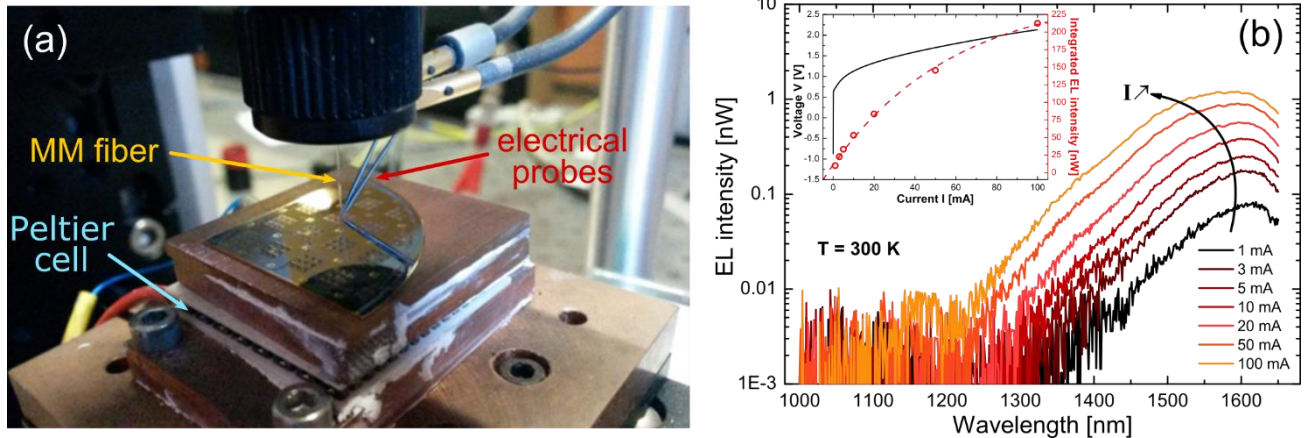


Fig. 2.35 – Measures on LED devices (sample #4820): (a) Test bench used for of the LED characterization and (b) room temperature electro-luminescence intensity vs wavelength for different injected current values (inset shows the evolution of the integrated EL vs current and the LED  $I$ - $V$  characteristic).

The inset of Fig. 2.35b shows the evolution of the integrated EL intensity with respect to the injected current and the  $I$ - $V$  characteristic of the LED. Starting from  $\sim 20$  mA we observe that the integrated intensity begins to saturate.

From the  $I$ - $V$  characteristic, the series resistance has been measured to be  $R_s \sim 125 \Omega$ , which is relatively high. This may be related to the non-optimal doping of the layers composing the structure and in particular to the electrical contacts (metal/semiconductor interfaces). Despite this inconvenient, and waiting for some VCSEL structures, however, these preliminary tests allowed validating some steps of this whole new process devoted to the realization of electrically-pumped devices.

## 2.4 Conclusions

In this chapter we focused on the design of VCSELs based on InP.

In the first part of the chapter we focused our attention on the **thermal management of the devices**. Indeed, in the case of InP-based VCSELs, the main limitations are due to the high thermal resistance of the bottom mirror, which acts as a thermal barrier for the heat flow towards the metal heat-sink. By means of FEM simulations we analyzed different approaches to this problem. Among all of them, **we identified the hybrid metal/dielectric DBR to be the best trade-off** between a simple and fast technological process and a performant thermal behavior. In particular, the thermal

dissipation of the devices can be drastically reduced if a buried hybrid DBRs with a diameter  $\leq 20 \mu\text{m}$  is used.

In parallel, **we developed a new technological process devoted to the realization of InP-based VCSELs.** This process, which has been named “Through Silicon Holes Electroplated Copper” (TSHEC), is described in the second part of the chapter. It relies on the use of benzocyclobutene (BCB) polymer bonding to bond an InP-based VCSEL active region onto a silicon host substrate, through the use of copper-filled vias acting as localized micro-heat sinks. The combination of the TSHEC process and the use of small diameter bottom BH-DBRs allowed demonstrating an **emitted power up to  $\sim 2.5 \text{ mW}$  and threshold as low as  $7 \text{ mW}$  in the case of optically-pumped  $1.55 \mu\text{m}$ -emitting VCSELs.** From thermal characterizations, **we were able to confirm an improved thermal performance** in the case of the devices integrating small-diameter DBRs. For these devices, a significant decrease (-29%) in the thermal resistance was estimated with respect to the case of VCSELs integrating large-area DBRs. The improvements are even more significant (-60%) if compared to the case of large area BCB polymer bonding, as estimated with the FEM analysis.

The third part of the chapter was devoted to the design and the optimization of the basic building blocks for the development of electrically-driven VCSELs, based on the TSHEC process. **We mainly focused on the optimization of the buried tunnel junction.** Thanks to TCAD simulations, we identified InGaAs-based BTJs as possible candidates to be integrated in the current-confinement section of the VCSELs. The TCAD model also allowed improving the tunneling process of the InGaAs-based BTJ by adding a  $\text{Q}_{1.18}$  buffer layer on the p-side of the structure, to decrease the hole barrier at the InP/InGaAs interface. The results of simulations have been experimentally validated on real BTJ structures, which showed fair electrical performance. Anyway, optical absorption at  $1.55 \mu\text{m}$  introduced by the presence of InGaAs (especially the InGaAs layer composing the junction’s p-side) should be experimentally quantified to finally validate the use of InGaAs-based BTJs on InP-VCSELs. For future applications, carbon doping can bring advantages in order to easily reach doping levels above  $10^{20} \text{ cm}^{-3}$ , enabling the use of highly doped quaternary compounds such as  $\text{Q}_{1.4}$ ,  $\text{Q}_{1.3}$  and  $\text{Q}_{1.18}$  with lower optical absorption at  $1.55 \mu\text{m}$ .

**The TSHEC process has been adapted for the electrically-injected version of VCSELs.** The mask set designed for the electrical version of the devices, together with the detailed process, has been described. Due to the lack of dedicated VCSEL structures, the mask set has been successfully tested on LED devices based on quantum dashes-based active regions originally designed for ridge lasers. The preliminary EL characterizations allowed validating some steps of the technological process, while waiting for dedicated VCSEL active regions to be processed.

To summarize, the TSHEC process shows great potential for the hybrid integration of (virtually any) III-V active regions on a Si platform, being simultaneously compatible for a transverse integration of photonic, microelectronic and/or microfluidic devices on the common host substrate. It also avoids stress-induced limitation with respect of standard solutions involving large metallic pseudo-substrates such as Au or Cu, and it has the great advantage to be cost-effective. Moreover, it is fully compatible with both optical pumping and electrical injection schemes. Functionalization through the use of embedded CMOS driving electronics or thermal sensor monitoring in the Si host platform may also be possible, resulting in a versatile solution towards a simplification of the back-end processing and the device packaging steps. Fig. 2.36 shows an artistic image of what can be expected in a future evolution of the TSHEC technology.

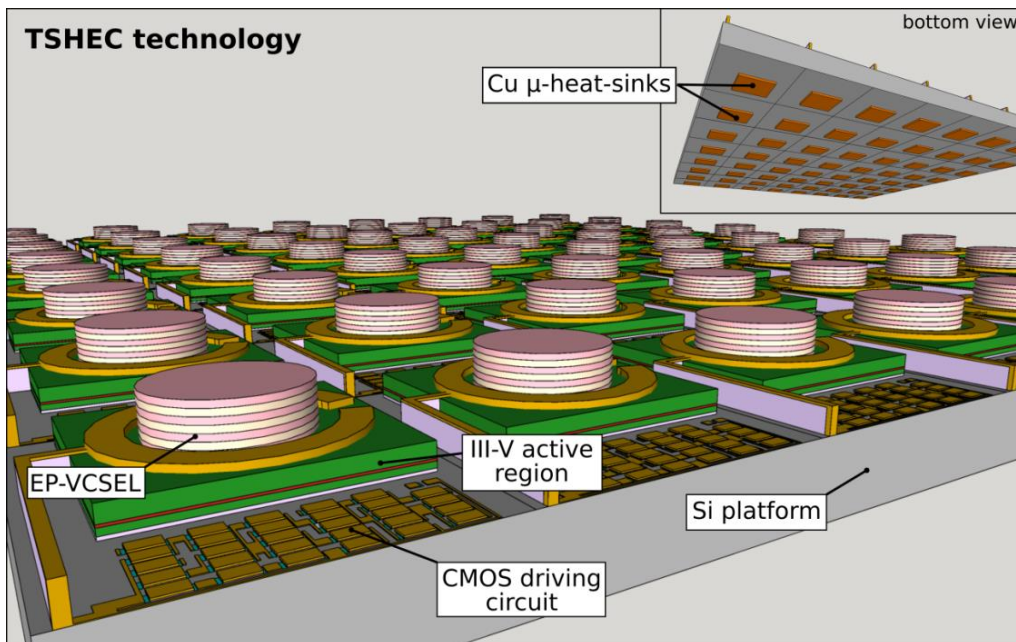


Fig. 2.36 – Artistic view of a CMOS-driven VCSEL array realized by the TSHEC technology.

In the image we recognize a VCSEL array with the III-V active region bonded on the Si platform according to the TSHEC process, and the dedicated CMOS command circuitry in the front of each device.

The development of a hybrid platform for the realization of InP-based vertical-cavity device was also the starting point for the realization of tunable devices based on a new approach involving liquid crystal micro-cells, as it will be discussed in the next *Chapter 3*.

# **Chapter 3**

## ***Monolithic wide-tunable devices based on liquid crystals micro-cells***

<b>3.1 Optical application of tunable devices.....</b>	<b>89</b>
<b>3.2 State-of-the-art of vertical-cavity tunable devices .....</b>	<b>91</b>
3.2.1 Tunable VCSELs .....	92
3.2.2 Tunable filters and photodiodes.....	94
3.2.3 Drawbacks of MEMS-based devices .....	95
<b>3.3 Monolithic approach: the interest of liquid crystals .....</b>	<b>95</b>
3.3.1 Optical properties of liquid crystals .....	96
3.3.2 Working principle of liquid crystals: tuning mechanism.....	98
<b>3.4 Anisotropic gain media: optical and physical properties of self-assembled quantum dashes .....</b>	<b>101</b>
3.4.1 Epitaxial growth .....	102
3.4.2 Polarization properties of QDHs .....	104
3.4.3 Temperature dependence .....	106
3.4.3 Spectral coverage and (modal) gain of QDHs active media .....	107
3.4.4 Summary .....	112
<b>3.5 Devices based on liquid crystal micro-cell technology.....</b>	<b>113</b>
3.5.1 Accomplished results from the past (2006-2014).....	113



*Chapter 3*

3.5.2 The HYPOCAMP project (2014-2019)..... 113

3.5.3 Tunable p-i-n photodiode..... 115

3.5.4 Investigation of a tunable LC-VCSELs: preliminary results..... 121

**3.6 Conclusions ..... 127**

### **3.1 Optical application of tunable devices**

Tunable devices have attracted lot of attention in the last decades, because of their wide range of application. In particular, wavelength-tunable semiconductor sources and detectors are important for the development of compact and versatile optical systems. Such devices cover applications ranging from optical communications, sensors, high-resolution spectroscopy, microwave photonics and biomedical systems. In most cases, large mode-hop-free wavelength tuning is of primarily interests to boost system performance and versatility.

Between all the tunable lasers classes, VCSELs ensures continuous broadband wavelength tuning with inherent longitudinal single-mode emission and high modulation rates. Additionally, as already mentioned in *Chapter 1*, they are also characterized by low power consumption, low production costs, compactness and high degree of scalability. All these peculiarities make VCSELs suitable for integration in optical communication systems or sensing applications requiring tunable functionalities. Moreover, in an extended cavity configuration (such as the one of VECSELs), very narrow laser linewidth and extremely low-noise operation (down to the quantum limit) are obtained. Such characteristics can be successfully employed to realize extremely precise and reliable spectroscopy and metrology systems, or (re)programmable microwave oscillators and filters.

In **optical communications**, tunable lasers have been the subject of extensive research ever since the start of wavelength division multiplexing (WDM) systems, which are now expected to evolve from the actual 2.5 Gbps data rate of the G-PON (Gigabit Passive Optical Networks) architecture to the next-generation 10 Gbps of the WDM-PON architecture, and beyond. This evolution will require lasers with high modulation frequencies at several wavelengths, with an output power of few mW, low power consumption and low realization costs. Tunable VCSELs and reconfigurable wavelength-selective photodiodes (PDs) operating in the 1.3 - 1.55  $\mu\text{m}$  range represent the best candidates to be integrated as low-cost tunable WDM transceivers/receivers for data centers [[Kazovsky2007](#), [Liu2010](#)], fiber-to-the-home (FTTH) applications and multi-service home networks based on single-mode fibers using Coarse WDM (CWDM) [[Guignard2007](#)], providing flexibility and re-configurability for future network provisioning.

**Optical sensors** are also facing an increasing demand on the optical market. On one hand, they are more and more employed in long-distance temperature or strain/deformation/displacement monitoring of civil infrastructures (buildings, bridges, etc.), oil and gas pipelines and transportations (aircrafts, trains, ships and automotive). In these cases, they generally combine a tunable laser and a sensor based on fiber Bragg gratings (FBG), which require laser sources operating at 1.55  $\mu\text{m}$  [[Mizunami2016](#)]. On the other hand, tunable-sources-based optical sensors are also gaining

industrial interests for security and safety issues, environmental monitoring and gas analysis [Schilt2010]. In this context, Tunable Diode Laser Absorption Spectrometry (TDLAS) is nowadays successfully employed for toxic and hazardous in-situ gas detection, such as O<sub>2</sub>, CH<sub>4</sub>, CO, N<sub>2</sub>O, NH<sub>3</sub>, CO<sub>2</sub>, HCl and HBr [Bond2007], or aqueous vapour [Witzel2013]. TDLAS systems provide many advantages with respect to other approaches based on electrochemical or resistive sensors, such as high sensitivity, stability in time and no need for recalibration, and they already integrate near-infrared VCSEL sources in commercially-available products (see Axetris or Vertilas websites [Axetris, Vertilas]). However, this kind of measurements are generally performed at different wavelength (ranging from 1.3 up to 2.3  $\mu\text{m}$ ) depending on the chemical species to be detected, and they require a stable wavelength linewidth ( $< 300 \text{ pm}$ ) to be efficient. For such applications, a simple and robust mode-hop-free tuning mechanism, with a wide emission in the wavelength range of interest would allow increasing the optical sensors efficiencies, as more channels (i.e. gases) could be addressed within a single chip. On the other hand, reconfigurable passive optical devices, such as PDs, can find application as compact micro-spectrometers [Wolffenbuttel2005, Schuler2009] or wavelength-meters [Wu1996], fully integrated on a packaged chip.

**High resolution spectroscopy and metrology** systems based on time-frequency measurements are becoming increasingly used for a large panel of applications, ranging from material characterization to chemical species analysis, up to the fundamental research. Nevertheless, such systems might require high spectral accuracy provided, for instance, by locking a laser source to a very narrow optical reference such as a Doppler-free molecular transition (e.g. acetylene), or an Ultra-Low Expansion (ULE) reference cavity, in order to stabilize the laser wavelength. The high quality of such cavities ( $Q > 10000$ ) implies the use of low-noise and narrow-linewidth ( $< 100 \text{ kHz}$ ) laser sources, in combination with a feedback mechanism to continuously match the laser wavelength with the cavity resonance [Millo2009]. This can be achieved by using single-frequency VECSELs, which lead to a significant reduction of the laser linewidth as well as of the intensity noise, owing to their peculiar operation in the Class-A regime. In contrast with standard VECSELs, which generally provide a single-frequency emission tuned by means of intra-cavity etalon filters, a wavelength-tuning mechanism based on an electro-optic effect will lead to a limited, but extremely fine and continuous tunability of the laser emission. Combined with the intrinsic narrow linewidth and the inherent low frequency drift of VECSELs, such a laser source would be an interesting candidate for ultra-high resolution sub-Doppler spectroscopy and time/frequency metrology.

For what concerns **microwave photonic** applications, the processing of RF signals in the optical domain provides many advantages owing to the higher time-bandwidth factor offered by this technique with respect to full-electronic systems. Microwave photonics approaches have been

shown to be very promising in terms of frequency tunability, reachable frequencies, and filter shaping capabilities, thus overcoming most electronic bottlenecks [Dolfi1997, Capmany2005]. Among the different proposed architectures, photonic filtering of microwave signals using tunable laser sources followed by one or several dispersive delay lines is one of the most versatile approaches, provided that compact and low-cost tunable lasers are used [Polo2003, Taylor2007]. In this framework, tunable VCSELs are again very interesting candidates, as they are very compact (typical VCSELs dimensions are few 100s  $\mu\text{m}^2$ ) and with low costs of fabrication according to the parallel processing of many devices, which allows getting high production yields ( $\sim 100$  VCSELs per  $\text{mm}^2$ ). However, apart from wavelength tunability, the wavelength stability of the laser as well as its relative intensity noise must be compliant with microwave system requirements. A microwave photonic notch filter based on a single-frequency VCSEL device have already been demonstrated in the past [Peng2013], but a fully reconfigurable shape-on-demand microwave filter based on several tunable VCSELs would extend the capabilities of such systems.

In **biomedicine**, tunable sources are again largely employed. Among all the applications, we can refer to optical coherence tomography (OCT) as one of the main representative. This emerging medical imaging technique enables in-situ and real-time sub-surface, micrometer-scale, cross-sectional and 3D imaging of biological tissues in the 750-1400 nm wavelength range. The analysis is performed by measuring the echo time delay and the intensity of backscattered light impinging on the surface of the biological sample. Emerging applications of medical OCT are vast, ranging from the already commercialized ophthalmic and vascular imaging systems, to ongoing clinical investigations in dentistry, dermatology, optical endoscopy, etc. For such applications, tuning ranges of the order of 100 nm with output powers of some tens of mW are generally required for the OCT systems to be effective. In such domain, rapidly-sweep tunable VCSEL devices are again gaining much attention for their optical performance and low price [Grulkowski2012].

### **3.2 State-of-the-art of vertical-cavity tunable devices**

Wide mode-hop free tunability of the emission wavelength can be achieved by producing a change in the optical length of the cavity. To obtain this result, the most used technique is based on the variation of the physical length of the optical resonator. This is typically achieved by thermal or electrostatic actuation of a suspended membrane acting as a movable reflector, usually fabricated by standard processes of the micro electrical-mechanical systems (MEMS) technology. In the case of thermal actuation, the injection of a current on conductive elements in contact with (or close proximity to) the movable mirror causes the thermal expansion (or the deformation) of the

suspended membrane, due to electric resistive heating. This leads to a change in the cavity length of the device. The tuning of the cavity can be also obtained by applying an electric field to produce an electrostatic force between electrical charges, in order to cause the movement of the movable MEMS reflector. In both cases the movable mirror is generally made by dielectrics materials.

One of the main figures of merit of a tunable device is the sweep time  $t_{sweep}$  (or its frequency  $f_{sweep}$ ), i.e. the time needed to tune the cavity on a given wavelength range. Generally, due to the slow dynamics of thermal phenomena, MEMS devices based on such tuning mechanisms (electro-thermal or thermo-optical actuation) suffer from a high inertia that translates in relatively long sweep times, of the order of few ms ( $f_{sweep} < \text{kHz}$ ), while electrostatically-actuated devices are faster, with sweep times of the order of  $\mu\text{s}$  ( $f_{sweep} \sim 100 \text{ kHz}$ ). Concerning the tunable capabilities, both methods have demonstrated to be effective to get a wide tunable range ( $\geq 100 \text{ nm}$ ) at different wavelength, both in the case of VCSELs or Fabry-Pérot (FP) filters and photodiodes (PDs).

### 3.2.1 Tunable VCSELs

An optically-pumped 1060 nm-emitting MEMS-VCSEL with 100 nm continuous tuning range has been reported by Praevium Research Inc. (USA). The device was based on strained InGaAs MQWs active region with a fully oxidized GaAs/ $\text{Al}_x\text{O}_y$  bottom mirror and a suspended dielectric top MEMS mirror, which was electrostatically actuated [Jayaraman2012b]. It is worth to notice that the electrically-injected version of such device was reported few years later, showing a tuning range over 63.8 nm around 1050 nm [John2015] and over 37.7 nm around 850 nm [John2016]. The same group also reported an optically-pumped MEMS-VCSEL based on a similar design, integrating InP-based MQWs, continuously-tunable over 150 nm around 1310 nm [Jayaraman2012a] (Fig. 3.1a, next page). These tunable MEMS-VCSEL sources started to be commercialized by Thorlabs Inc. for OCT applications at 1.3  $\mu\text{m}$  [Thorlabs]. A record of 102 nm tuning range without mode-hopping have been also demonstrated around 1550 nm, employing a MEMS-VCSEL with a thermally-actuated top movable and a bottom hybrid mirror based on dielectric materials, within the collaborative European SUBTUNE project, involving the partnership of several labs including TU Darmstadt and Walter Schottky Institute (Germany) [Gierl2011] (see Fig. 3.1b).

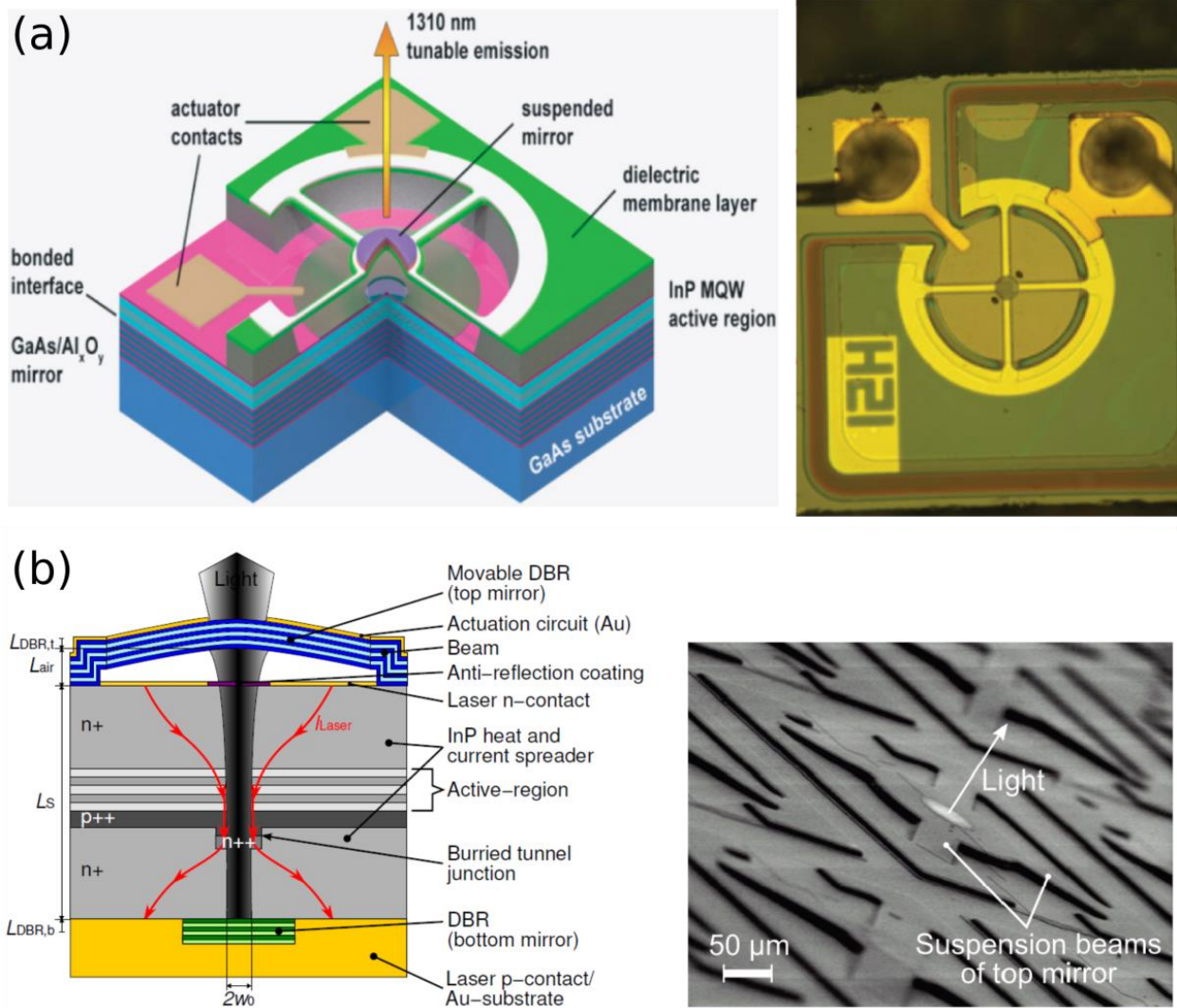


Fig. 3.1 – Cross-section and picture of tunable MEMS-VCSELs based on (a) electrostatic and (b) thermal actuation mechanisms. Reprinted with permission from [Potsaid2012] and [Gierl2011], © SPIE and The Optical Society, respectively.

Table 3.1 summarizes the world record performance of the afore-mentioned devices at different emission wavelengths and for different pumping schemes. To date, these results represent the state-of-the-art in terms of tunable capabilities for MEMS-based VCSELs.

Table 3.1 – State-of-the-art performance of tunable MEMS-VCSELs in the 0.85 - 1.55  $\mu\text{m}$  range.

Emission $\lambda$ [nm]	Pumping scheme	Actuation method	Max tunability range [nm]	Sweep rate $f_{\text{sweep}}$ [kHz]	Max applied voltage/current [V], [mA]	Max $P_{\text{out}}$ [mW]	Ref.
850	EP	electrostatic	37.7	350 – 430	62-76 V	0.67	[John2016]
1050	EP	electrostatic	63.8	240	60 V	0.4	[John2015]
1060	OP	electrostatic	100	500	50 V	1	[Jayaraman2012b]
1310	OP	electrostatic	150	500	56 V	-	[Jayaraman2012a]
1550	EP	thermal	102	1kHz/10nm	25 mA (51 mW)	3.5	[Gierl2011]



### 3.2.2 Tunable filters and photodiodes

Concerning the development of passive tunable components, in the past several works have also been reported. As in the case of VCSELs, tunable FP filters and photodiodes working around 1.55  $\mu\text{m}$  have been based on resonant cavities with micromachined movable semiconductor/air gap interfaces or dielectric-based MEMS-DBRs and suspended membranes. Most of them are based on the electrostatic actuation of the movable reflector. This technique ensures relatively wide tuning ranges ( $> 50$  nm) with applied voltage levels of some tens of volts [Irmer2003, Strassner2005, Yang2014]. The devices based on the electro-thermal actuation can be also performant in terms of narrow linewidth, with maximum achievable tuning ranges as high as 180 nm [Cesar2017] or narrow linewidth as low as 0.2 nm [Halbritter2004], but they generally require high power consumption to work (several hundreds of mW of dissipated power). Some PDs exploiting a thermo-optic mechanism have been also reported, but such devices are characterized by a limited tuning range ( $\sim 5$ -26 nm) and again high power consumptions [Hohlfeld2003, Li2005].

Table 3.2 presents a selection of some demonstrations of passive tunable devices, together with their main performance and actuation method.

**Table 3.2 – Performance of 1.55  $\mu\text{m}$  tunable filters and PDs based on MEMS or movable membranes.**

Device type	Actuation method	Unbiased resonant wavelength $\lambda_0$ [nm]	Tunability range $\Delta\lambda$ [nm]*	Resonance linewidth $\delta\lambda$ [nm]	Applied voltage, current, power	Responsivity [A/W]	Ref.
MEMS filter	electrostatic	1550	-62	0.4	14 V	-	[Spisser1998]
MEMS filter	electrostatic	1470	65	3-5.5	21 V	-	[Strassner2002]
MEMS filter	electrostatic	1600	-140	3-5	3.2 V	-	[Irmer2003]
Si-membrane filter	thermo-optic	1610	5.3	2.7	-	-	[Hohlfeld2003]
MEMS PD	electro-thermal	1540	44	$< 0.2$	250 mW	0.28	[Halbritter2004]
SOI-membrane filter	thermo-optic	1504	26	7	5 V (1.4 W)	-	[Li2005]
MEMS filter	electrostatic	1450	130	$< 0.5$	16 V	-	[Strassner2005]
PC-MOEMS filter	electrostatic	1570	-20	1.5	4 V	-	[Boutami2006]
HCG-MEMS PD	electrostatic	1555	33.5	1.2	6 V	1	[Yang2014]
MEMS PD	electro-thermal	1550	180	0.3	-	0.76	[Cesar2017]

(\*) a negative value means a tuning towards shorter wavelengths when actuation is applied.

### **3.2.3 Drawbacks of MEMS-based devices**

Despite the good tuning performance achieved by optical devices based on movable mirrors or cantilevers, these suffer from some important drawbacks.

First, movable actuators are subjected to external mechanical and acoustic vibrations, thermal fluctuation and intrinsic Brownian motion of the suspended membrane [Huber2004]. All these phenomena contribute in spoiling the spectral performance, especially in the case of active devices such as VCSELs. Indeed, a broadening of the intrinsic laser linewidth from several MHz for a monolithic VCSEL up to 1000 MHz for a tunable MEMS-VCSEL, together with an optical power-dependent dynamic variation of the lasing wavelength (chirp) is systematically observed [Halbritter2007, Paul2016]. For the same reason, long-term reliability of these devices is also questioned. Although it is difficult to find reports about the robustness of MEMS-based VCSELs in the literature, we can expect that a tunable VCSEL based on the mechanical actuation of a movable part as a suspended membrane is not as stable as a monolithic counterpart.

Furthermore, the microfabrication of suspended membranes in MEMS technology is not straightforward to be achieved in practice, because of the technological process to realize the suspended membranes. This can be a limitation for the industrialization of MEMS-based devices, when the throughput yield and the costs become important parameters.

Last but not least, electrostatic (or thermal) actuation of movable membranes generally requires non-negligible driving voltages and high power consumption to achieve wide tuning ranges.

Thus, the development of a technological process for the realization of monolithic and wavelength-tunable devices, insensitive to all the afore-mentioned problems and simultaneously able to guarantee good performance in terms of wide achievable tuning ranges ( $> 50$  nm) with satisfactory sweep frequencies would be very desirable. This can be obtained by exploiting a new approach based on the optical properties of liquid crystals, as explained later in the next section.

## **3.3 Monolithic approach: the interest of liquid crystals**

Monolithic vertical-cavity tunable devices have been proposed some time ago as alternative to MEMS-based devices. In this case, the most investigated approach were based on the thermo-optic tuning of the micro-cavity resonance obtained by the modification of the refractive index of materials composing the device in response to a change in temperature, either realized by cooling or heating the devices with a Peltier cell, or through the Joule effect resulting from the current injection on resistive elements acting as heaters. It becomes quite obvious that tunability of devices



based on such an approach is very limited, because the thermo-optic coefficient of materials employed for their realization does not allow wide excursions. Additionally, the performance (especially in the case of active devices) quickly drop as the temperature rises. For both tunable VCSELs and PDs based on such a method, tunability was limited between 0.6 and 10.5 nm in the case of devices working from 870 nm to 2.3  $\mu\text{m}$  (VCSELs: [Berger1991, Mereuta2008, Boehm2011], PDs: [Wang2006, Lv2008]). Furthermore, the power consumption of these devices is typically of the order of several hundreds of mW, since mA-A current sources are needed to thermally tune them. An alternative solution exploiting quantum confined Stark effect (QCSE) has been also investigated in the past, but again the tunability performance of the devices were limited to few nm in the case of photodiodes integrating GaAs-based MQWs around 850 nm [Wood1985], or 20 nm in the case of AlGaAsSb-based MQWs around 1.8  $\mu\text{m}$  at 110 K [Shi1997]. However, the QCSE approach seems to have produced very little interest in the scientific community.

A promising alternative to the aforementioned approaches would benefit from the integration of a tuning mechanism capable to ensure a large refractive index variation when a moderate driving voltage and ideally no current are applied, which translates in a very low power consumption. Such requirements can be easily fulfilled by exploiting the electro-optic properties of liquid crystals (LC). This approach has been proposed a relatively long time ago and applied to macroscopic passive devices as LC-based tunable Fabry-Pérot filters [Hirabayashi1993, Vogel2003]. More recently, wavelength-tunable ring resonators on silicon-on-insulator platform with a LC cladding have been demonstrated [De Cort2011], together with active devices integrating LC media, to achieve wavelength-tuning in external-cavity lasers (ECTLs) [Sato2007] and VCSELs [Castany2011], or tuning of the polarization state in VCSELs [Xie2012]. However, the combination of LC with micrometric-sized devices to obtain monolithically integrated and wavelength-selective PDs or VCSELs has never been demonstrated up to now.

### 3.3.1 Optical properties of liquid crystals

As the name suggests, a liquid crystal is an intermediate state of matter lying between the liquid and the crystalline states. For that reason, a LC possesses some typical properties of liquids (like fluidity) and some others specific of crystals (like a pseudo-periodic arrangement in one spatial direction, optical and electrical anisotropies, etc.). The physical properties exhibited by LCs are also temperature-dependent, and their phase changes if the temperature is raised or lowered. Fig. 3.2 on next page schematically shows the different phases that are exhibited by LCs.

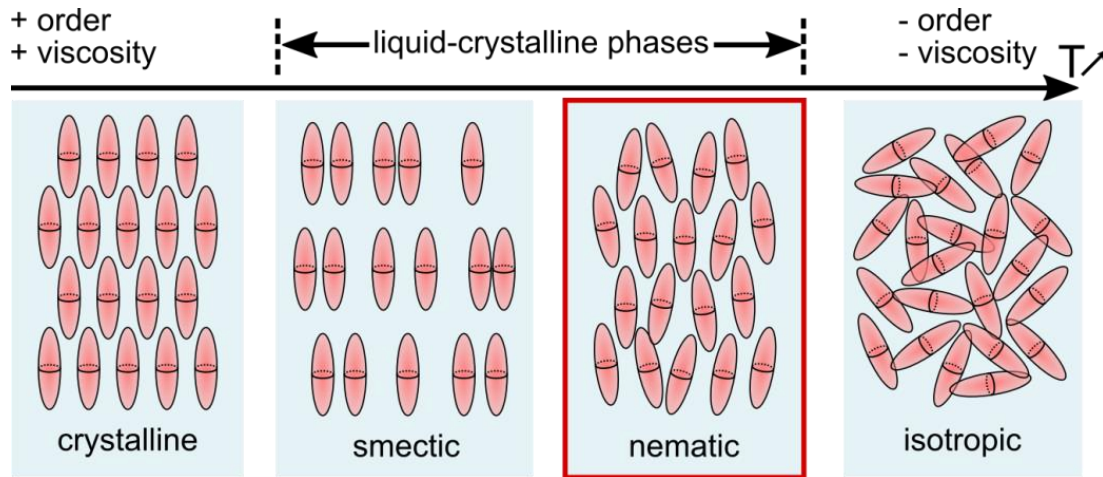


Fig. 3.2 – Schematic image of phase changes and spatial arrangement in liquid crystals as a function of temperature.

In particular, the LCs can be divided into two main groups, depending on their arrangement: the smectic phase, where the LC molecules preserve a precise orientational order and partial positional order, and the nematic phase, in which the molecules have orientational order but no precise position in space. Outside of this range, the molecules are arranged in the crystalline phase (low temperature range), showing the maximum degree of order, or in the isotropic phase (high temperature range), where they do not show any order at all. Throughout these phase changes, the viscosity changes as well, passing from its maximum (crystalline phase) to its minimum (isotropic phase), considered as being water-like. However, the optical properties of LCs not only depend on temperature (and pressure), but also on the state of the liquid crystal (i.e., nematic, smectic, etc.) and the degree of order and the shape of the molecules composing it. In the framework of this study, we will focus the attention on the nematic phase only, which is the most common and simple phase. Independently on the intermediate states (smectic or nematic), LCs share some common properties that can be summarized as:

- the molecules present an anisotropic shape (as elongated rods or disks);
- they also present strong dipoles and are easily polarized by an external electric field, which changes their spatial orientation.

The physical and optical properties of LCs are thus the result of their fluid nature and are mainly based on the spatial arrangement of the molecules and their ability of changing their orientation under the application of an external electric field, causing a change in the optical response of the LC. Particularly, rod-like LCs are uniaxial molecules characterized by a director (the long molecular axis), which determines their optic axis. Thanks to their shape anisotropy, the light propagating across the LC experiences a uniaxial birefringence along that director.

In Fig. 3.3a, the evolution of the ordinary  $n_o$  and extraordinary  $n_e$  indices is represented, as well as the birefringence  $\Delta n = n_e - n_o$ , as a function of the temperature and the wavelength, in the case of the commercially-available E7 nematic LC provided by Merck, which is a well-known and representative mixture<sup>1</sup>. For such a LC, the room temperature (298 K) birefringence at 1550 nm is relatively high and equal to  $\Delta n \approx 0.195$  ( $n_o \approx 1.502$ ,  $n_e \approx 1.697$ ), and the nematic-to-isotropic phase transition occurs around  $T_c = 330$  K. Concerning the absorption of LCs in the wavelength range of interest (i.e. around 1.55  $\mu\text{m}$ ), previous works indicated that it can be considered negligible [Wu1998].

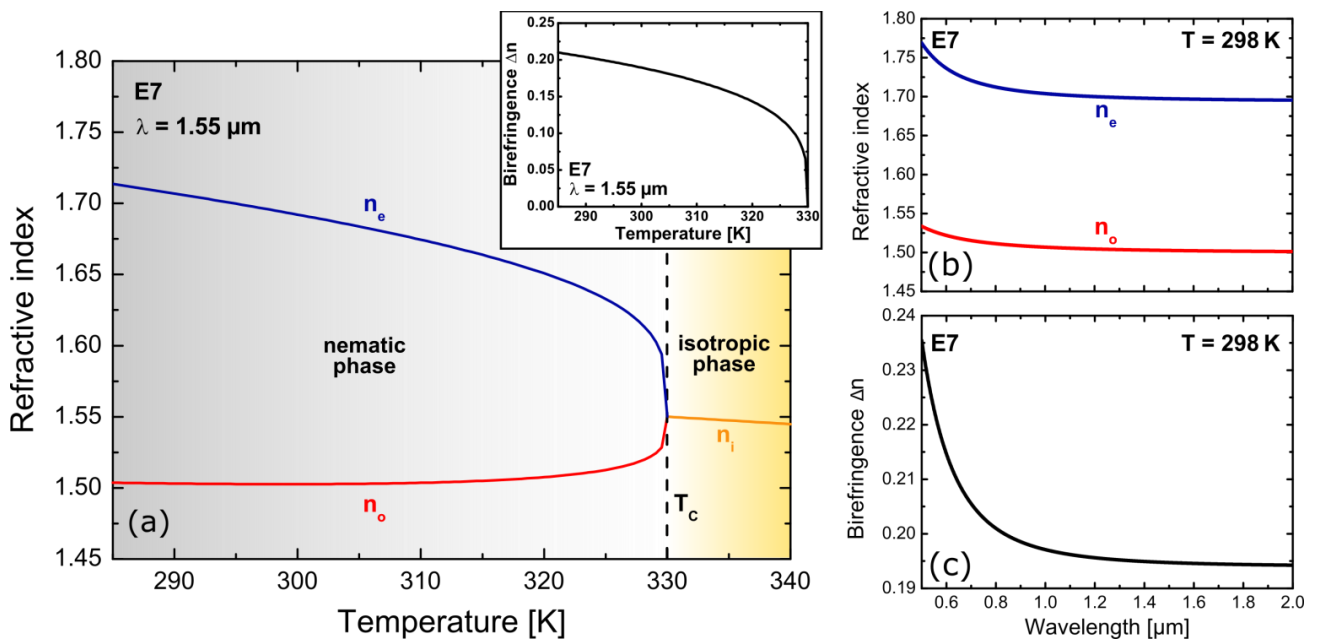


Fig. 3.3 – Optical properties of E7 liquid crystal: ordinary and extraordinary indices as a function of (a) the temperature (nematic-to-isotropic phase transition is also shown, while birefringence vs  $T$  is in inset) and (b) the wavelength. (c) Birefringence as function of the wavelength.

### 3.3.2 Working principle of liquid crystals: tuning mechanism

As a result of the molecules anisotropy, the component of a light beam propagating along the  $z$  direction which is polarized perpendicular to the director of LC molecules ( $y$  direction) always experiences the ordinary index  $n_o$  (ordinary ray,  $E_y$ ), while the component polarized parallel to the director ( $x$  direction) experiences the extraordinary index  $n_e$  (extraordinary ray,  $E_x$ ). This is shown in Fig. 3.4a on next page. If an external electric field  $E_{LC}$  is applied to the LC, the orientation of the molecules follows the field direction, and the extraordinary rays experienced a different effective

<sup>1</sup> The E7 mixture is also known as BL001, it is composed by a mixture of cyanobiphenyls and cyanoterphenols chemical molecules (for example 5CB, 7CB, 80CB, 5CT).

index  $n(\theta)$ , which depends on the orientation of the director of the LC molecules and it is smaller than  $n_e$  (Fig. 3.4b). As the external field further increases, the molecules eventually align along the  $z$  direction. In this case, the effective index  $n(\theta)$  seen by the extraordinary ray becomes nearly equal to the ordinary index  $n_o$  and the medium becomes quasi-isotropic (Fig. 3.4c)<sup>2</sup>.

Relying on what we have just discussed, the approach that involves the use of LCs as intra-cavity tunable mechanism is based on the variation of the effective index inside of a resonant cavity, and it is schematized in Fig. 3.4d in the case of a VCSEL integrating a LC cell of 5  $\mu\text{m}$  in thickness.

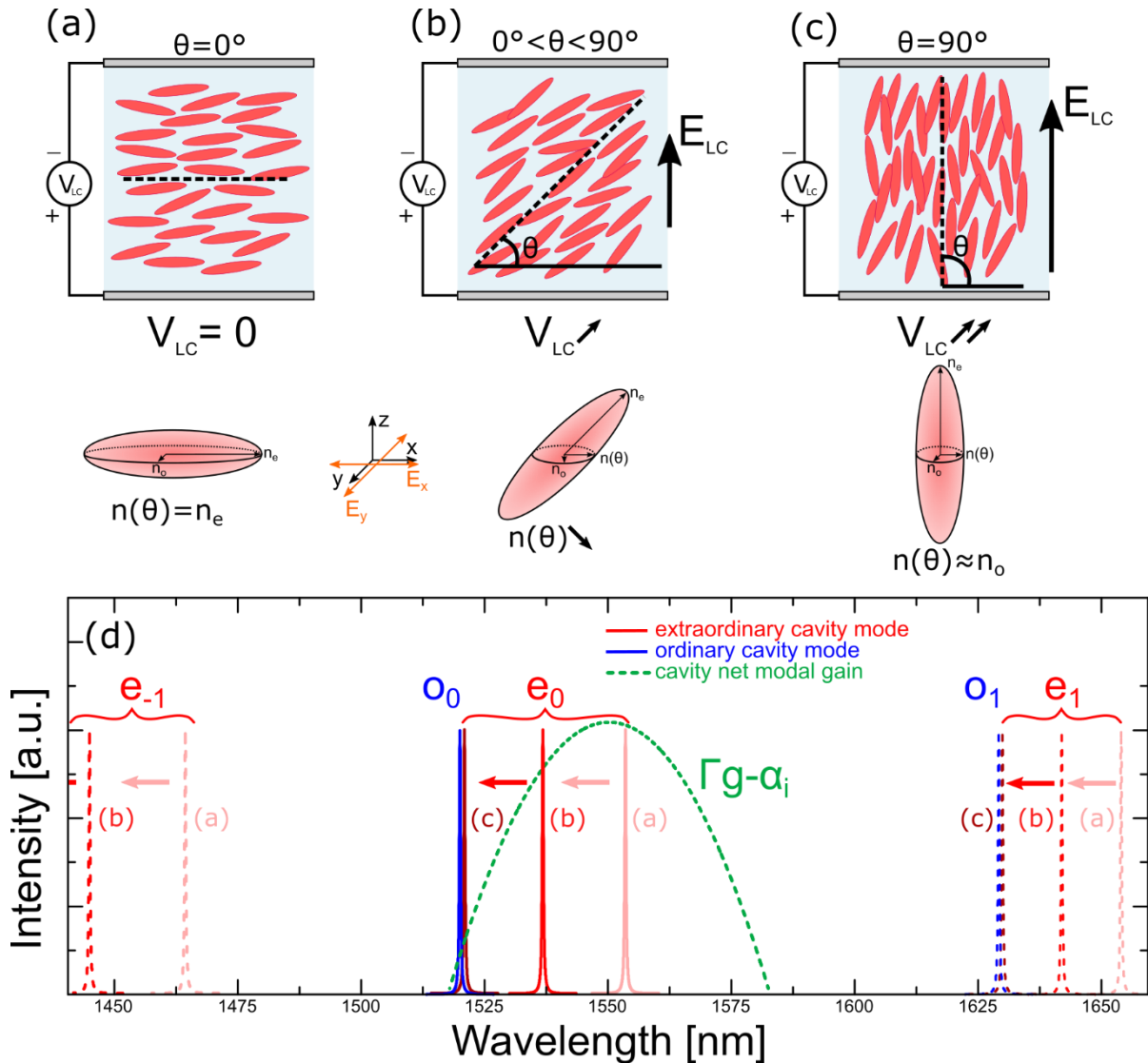


Fig. 3.4 – Optical modulation of a nematic liquid crystal under the application of an external electric field: (a) no field applied, (b) small electric field applied and (c) maximum field applied. The dashed black curve indicates the director (or optical axis) of the LC. (d) Working principle of the tuning mechanism based on the modulation of the optical response of a LC under the application of an AC voltage as the external electric field  $E_{LC}$  increases from a) to c), for a LC thickness of 5  $\mu\text{m}$ .  $o$ =ordinary and  $e$ =extraordinary modes. Solid lines are related to the principal modes of the cavity ( $e_0, o_0$ ), while dashed lines to upper ( $e_1, o_1$ ) or lower ( $e_{-1}, o_{-1}$ ) modes.

<sup>2</sup> The driving voltage signal (and thus the generated electric field) applied to the LC must be an alternating signal with null average DC value, otherwise a DC component would induce a drift of the LC molecules towards one of the electrodes.

The net modal gain of the active region (green dotted curve) is designed to emit at the wavelength of interest (which is around 1550 nm, in our case). The presence of the LC inside the laser cavity translates into the presence of two resonant modes, which are indicated as “o” (ordinary, blue curve) and “e” (extraordinary, red curve) modes. The spectral position of the ordinary and extraordinary modes is mainly determined by the value of the ordinary and extraordinary indices ( $n_o$  and  $n_e$ ), and by the total length of the optical cavity. In particular, since  $n_o < n_e$ , the ordinary mode is placed at a lower wavelength (higher optical frequency). By playing with the length of the cavity, it is possible to place the extraordinary mode somewhere around the peak of the modal gain, while the ordinary mode lies outside. Finally, by applying the external field to the LC, it is possible to tune the cavity resonance associated to the extraordinary mode, which will experience a blueshift towards the smaller wavelengths as the external field is increased ( $n_e$  is decreased), while the ordinary mode stay fixed to its original position.

This effect can be in principle used to realize a monolithic tunable VCSEL device. Obviously, since the ordinary and the extraordinary modes are orthogonally polarized, one direct consequence is that the emission of the VCSEL will be linearly polarized as well. As a consequence, in order to get full benefits of the optical properties of the nematic LCs, the designed active region should fulfill two main requirements:

1. it should have an optical emission over a wide wavelength range, in order to efficiently exploit the large tuning offered by the LCs;
2. the optical emission should be stable and linearly polarized to match the extraordinary axis of the LCs, otherwise the light would be insensitive to the tuning of the extraordinary refractive index, and might lead to a preferential lasing emission of the ordinary mode if it fulfills the gain requirements.

As VCSEL devices based on quantum wells are generally known to suffer from polarization instabilities [**Chang-Hasnain1991, Choquette1994**], these active regions seem not to be the best candidates. An original solution would be to use an active region based on anisotropic quantum nanostructures such as quantum dashes. This kind of nanostructured active medium has been investigated with success by FOTON Institute for a long time now. We will discuss about the physical and optical properties of such a kind of active region in the next section, and we will provide some characterizations which show the quality and performance of quantum dashes, compared to active regions based on conventional strained quantum wells.

### **3.4 Anisotropic gain media: optical and physical properties of self-assembled quantum dashes**

Thanks to their remarkable properties arising from the 3-D carrier confinement, self-organized semiconductor quantum nanostructures like quantum dots or quantum dashes (QDs/QDHs) have attracted increasing attention in the last decades. Their reduced dimensionality leads to atom-like and fully quantized states, with a discrete energy spectrum. Moreover, their physical and optical properties can be precisely tailored by adjusting their composition, shape, or size during the growth process. These intrinsic physical properties allowed the development of low threshold current density, low chirp and high-temperature insensitive laser sources.

Devices integrating QDs-based active region have been early reported in the In(Ga)As/GaAs material system, respectively addressing the 1  $\mu\text{m}$  and 1.3  $\mu\text{m}$  wavelength bands for local area networks applications [Schäfer1999, Huffaker1998, Liu1999]. Due to the high lattice mismatch ( $\sim 7.2\%$ ) between In(Ga)As and GaAs materials, strong nucleation phenomena are promoted, which translate in the spontaneous formation of QD nanostructures. While in principle it is possible to further push their emission towards the long-wavelength range by enlarging the QD size, the realization of efficient QDs GaAs-based sources above 1.3  $\mu\text{m}$  remains still challenging, because of the appearance of stress-induced defects due to the high lattice mismatch in this material system, which compromise the reliability of the devices.

A further extension of the emission wavelength towards the C-band window at 1.55  $\mu\text{m}$  and beyond is achieved by the use of InP substrates, the material system of choice for telecom applications.

However, the growth of quantum nanostructures on InP (and related lattice matched alloys) is more challenging. Indeed, in the InAs/InP system, the lattice mismatch is nearly twofold less ( $\sim 3.2\%$ ) with respect to the previous case, with a consequently slower nucleation rate. Quantum dot and dash growth has been demonstrated by both Metal Organic Chemical Vapor Deposition (MOCVD) and Molecular Beam Epitaxy (MBE) techniques [Reithmaier2005]. However, depending on the growth method, different experimental conditions are needed.

The orientation of the InP substrate has also a strong impact on the morphology of the quantum nanostructures [Stintz2003]. Thanks to their higher surface energy, InP substrates with a (311)B orientation present a higher nucleation rate than conventional (100) orientation, compensating thus the low lattice mismatch, and leading to the formation of a high density of InAs QDs [Fréchengues1999, Li2000]. The use of more conventional oriented substrates, like (001)-oriented InP, more likely results in the growth of QDHs, which are aligned along [1-10] crystallographic direction [Schwertberger2003], with cross section dimensions similar to that of QDs.



As a result of the advantages offered by the quantification of low-dimensional quantum systems in terms of lower threshold current, broader gain response or improved thermal stability with respect to QWs, QDH-based active media have been extensively studied in the past. Most of the contributions presented in the literature are related to edge-emitting and mode-locked lasers or semiconductor optical amplifiers [Lelarge2007, Khan2014], with some works on micrometer-long-cavity VCSELs, for which a well-defined and stable linear state-of-polarization [Lamy2009, Gauthier2012], and a very wide emission over 117 nm around 1.55  $\mu\text{m}$  [Taleb2013] were reported.

In this section, we will discuss some peculiar properties of such InAs QDH gain media on InP, which are a direct consequence of their morphology, such as large size dispersion and spatial anisotropy.

### 3.4.1 Epitaxial growth

The growth of InAs QDHs developed at FOTON Institute is performed by Gas-Source MBE (RIBER 32 system) and is based on the relaxation and subsequently nucleation of a high strained material grown on nominally (001)-oriented InP substrates, according to the Stranski-Krastanow (S-K) method, followed by the formation of elongated nanostructures thanks to the preferred diffusion of adatoms along the [1-10] crystallographic direction, as depicted in Fig. 3.5.

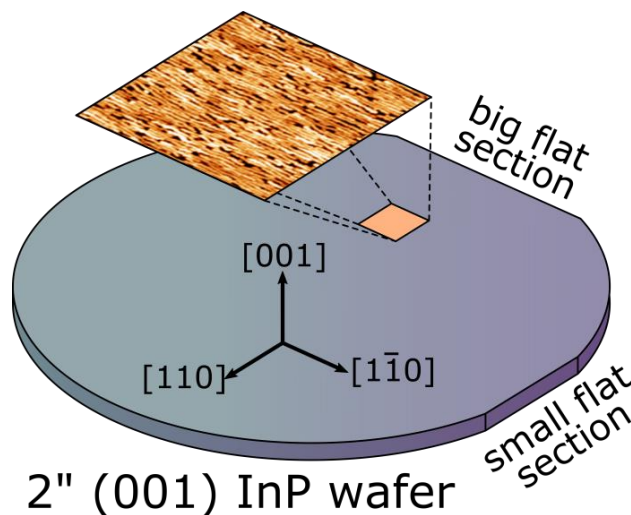


Fig. 3.5 – QDHs alignment with respect to crystallographic directions on a 2-inches nominally (001)-oriented InP substrate.

The size and the density of such nanostructures is a complex process, strongly dependent on several growth parameters (accumulation of strain across the layers, layer thickness, etc.). The reason for such a complex control is mainly due to the small lattice mismatch between the InAs and the

InGaAsP/InP layers. In order to control the height dispersion emitting wavelength of such nanostructures, the so-called “double cap” growth technique has been developed at FOTON Institute [Paranthoën2001].

The number of layers composing the active region is generally higher in the case of nanostructures-based devices, to compensate for the smaller thickness of the active layers. In order to maximize the modal gain of the active region, QDH layers are stacked on top of each other, and grouped into different sets, which are again designed to be located on a maximum of the stationary field of the laser cavity during the device operation. In V(E)CSELs, the modal gain is related to the number of gain layers (SQWs or QDHs), and also to the overlapping of the stationary field with the stacked layers. In the case of the QDH structures, a peculiar attention has been paid to increase the modal gain by stacking nearest QDH layers without suffering from the detrimental effect of the QDH induced strain [Lamy2008, Gauthier2011]. According to previous studies, QDH stacking has been optimized with a reduced 15 nm spacer [Gauthier2011], instead of a conventional 30-40 nm one [Caroff2005].

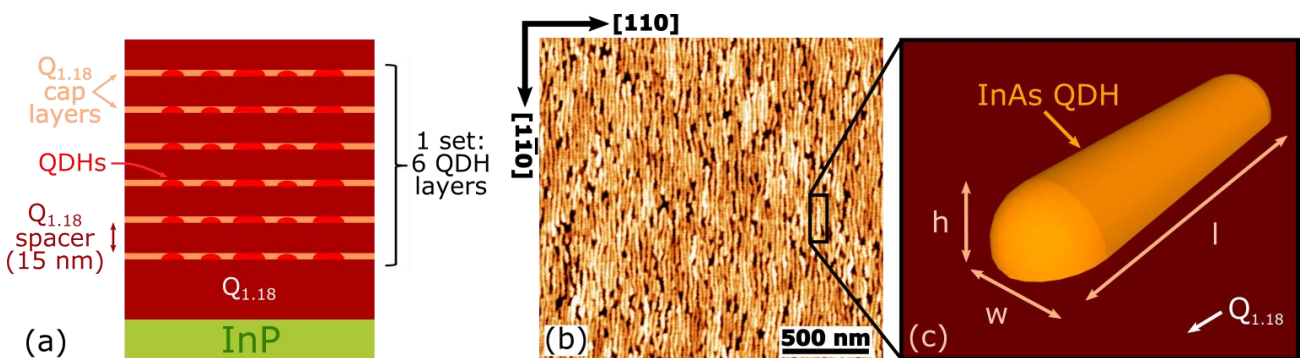


Fig. 3.6 – Quantum dashes stacking and morphology: (a) QDH layers stacking scheme, (b)  $2 \times 2 \mu\text{m}^2$  AFM image of the last uncapped layer from a set of six QDH layers and (c) typical QDH dimensions:  $h = 2.5 \text{ nm}$ ,  $w = 20\text{-}30 \text{ nm}$ ,  $l = 200\text{-}500 \text{ nm}$ .

Fig. 3.6a shows the structure of a set of six layers separated by a 15 nm-thick  $\text{In}_{0.8}\text{Ga}_{0.2}\text{As}_{0.435}\text{P}_{0.565}$   $\text{Q}_{1.18}$  spacer, composing an optimized QDH structure. The AFM image of Fig. 3.6b shows the last uncapped QDH layer related to such a structure. As indicated, the QDHs are preferably oriented along the [1-10] crystalline direction. The average height, width and length of such nanostructures are 2.5 nm, 20-30 nm, and 200-500 nm, respectively (cf. Fig. 3.6c). The typical linear density along the [110] direction (perpendicular to dash alignment) is nearly  $30 \mu\text{m}^{-1}$ . The asymmetry on the shape of QDHs, together with a preferred growth orientation, is the basis of their polarization properties, as further discussed in the next section.



### 3.4.2 Polarization properties of QDHs

Owing to the cylindrical geometry of their cavity, the polarization state of the emitted light in vertical-emitting devices is typically aligned along one of the two orthogonal crystallographic axes of the substrate, i.e. [110] or [1-10] directions for a conventional (001)-oriented InP substrate (see previous Fig. 3.5 for clarity). In the case of VCSELs integrating 2-dimensional isotropic gain media like strained quantum wells (SQWs), if non-polarization-selective elements are used, switching phenomena between the two competing orthogonal polarization eigenstates can occur, leading to polarization instabilities, as widely reported in the literature [[Koyama1991](#), [Choquette1995](#)]. It is not straightforward to control the interplay of these effects during experiments, which can lead to an unpredictable polarization emission and again to switching phenomena during laser operation. In polarization-dependent applications or in experimental setups integrating polarization-sensitive elements, these effects can have a considerable impact.

To avoid the uncertainty of the polarization, without the use of intra-cavity polarization-selective elements (which are generally not easy to implement and may induce unwanted optical losses), the integration of naturally anisotropic gain media with a well-determined state of polarization represents an original approach.

Indeed, the shape anisotropy and the strain of quantum nanostructures like QDHs naturally provides a significant intensity difference between the emitted light aligned along the [110] and [1-10] crystallographic axes [[Musial2012](#)]. To quantify it, a standard procedure is to measure the degree of linear polarization (DOLP) of the photoluminescence intensity through the so-called polarization ratio (PR), which is directly related to the growth quality of quantum dashes layers, and it is defined as

$$PR = \frac{|I_{\parallel} - I_{\perp}|}{|I_{\parallel} + I_{\perp}|} \quad (4.1)$$

where  $I_{\parallel}$  and  $I_{\perp}$  are the peak PL intensities along the two orthogonal crystallographic directions, respectively. In our specific case, we define  $I_{\parallel}$  as the PL intensity in the direction parallel to the QDH alignment, i.e. the [1-10] direction. Consequently,  $I_{\perp}$  is the PL intensity along the [110] direction. Typical values of the  $PR$  for good quality InAs QDHs active media on (001)-oriented substrates are of the order of 20%, with record values as high as 36%, as shown in Fig. 3.7a on the next page.

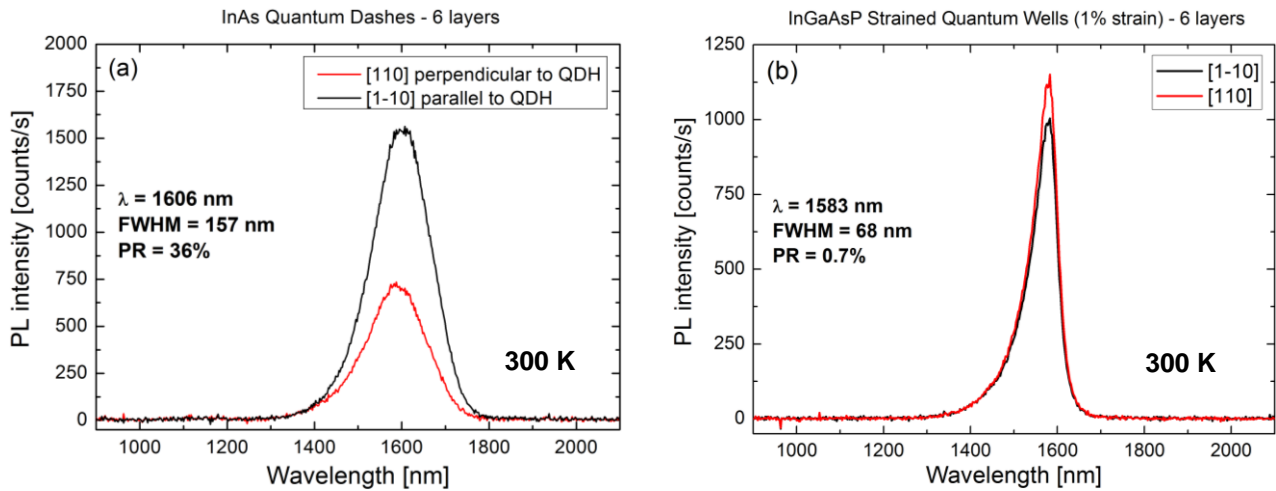


Fig. 3.7 - Normalized room-temperature polarization-resolved PL spectra of (a) InAs QDH-based active regions and (b) InGaAsP SQW-based (6 planes each) on (001)-oriented InP.

In the case of (InGaAsP) strained QWs, due to the isotropy of the 2-dimensional systems in the plane perpendicular to the growth direction, the gain dichroism along the two perpendicular crystallographic directions is generally lower. This translates into a significantly weaker polarization ratio, which ranges from some tenth of % to some % (as presented in Fig. 3.7b), even if this value can be increased by a precise but challenging control of the interface composition of the layers composing the QWs superlattice, as reported in the past [Cortez2000]. The weak polarization anisotropy of strained QWs is not enough to prevent polarization switching phenomena during VCSEL laser operation.

The original approach to integrate InAs QDH nanostructures to control the polarization of the emitted light of a vertical-cavity device has been successfully investigated by FOTON Institute. In 2009 our group demonstrated for the first time a micrometric optically-pumped VCSEL emitting at 1.6  $\mu\text{m}$ , integrating an active region based on three sets of six QDH layers [Lamy2009]. The device showed a stable linear polarization emission along the [1-10] QDH growth direction under a CW pumping, as expected. A later work allowed investigating the behavior of the device when a low frequency modulation was applied to the pump (1  $\mu\text{s}$ -long pulses with 10  $\mu\text{s}$  of repetition period), confirming the effectiveness of QDH active media for the control of the polarization under (low frequency) dynamic operation, unlike a similar device integrating an active region based on SQWs [Gauthier2012]. Benefits deriving from the integration of this anisotropic gain medium could also result in better noise performance and stable emission thanks to the suppression of polarization switching phenomena for these devices, and potentially wider wavelength coverage. The potentiality of QDH media for the realization of broad laser emitters will be discussed in the following.

### 3.4.3 Temperature dependence

The low-dimensionality of QDHs has also consequences in the thermal performance of active regions integrating such elongated nanostructures. In particular, if compared with conventional SQWs, QDHs reveal a less-sensitive behavior with respect to temperature increases in the range of interest for device applications. As already discussed in *Chapter 1*, in the case of vertical-emitting devices the output power is highly dependent on the superposition between the gain curve and the optical field inside the cavity, which defines the resonant mode(s). These two are in turn influenced by the internal operating temperature of the device, but at different rates. The temperature behavior of QDHs can be thus bring a superior performance to the devices, or to mitigate the sensitivity to thermal effects which arise at high pumping rates (i.e. thermal roll-over).

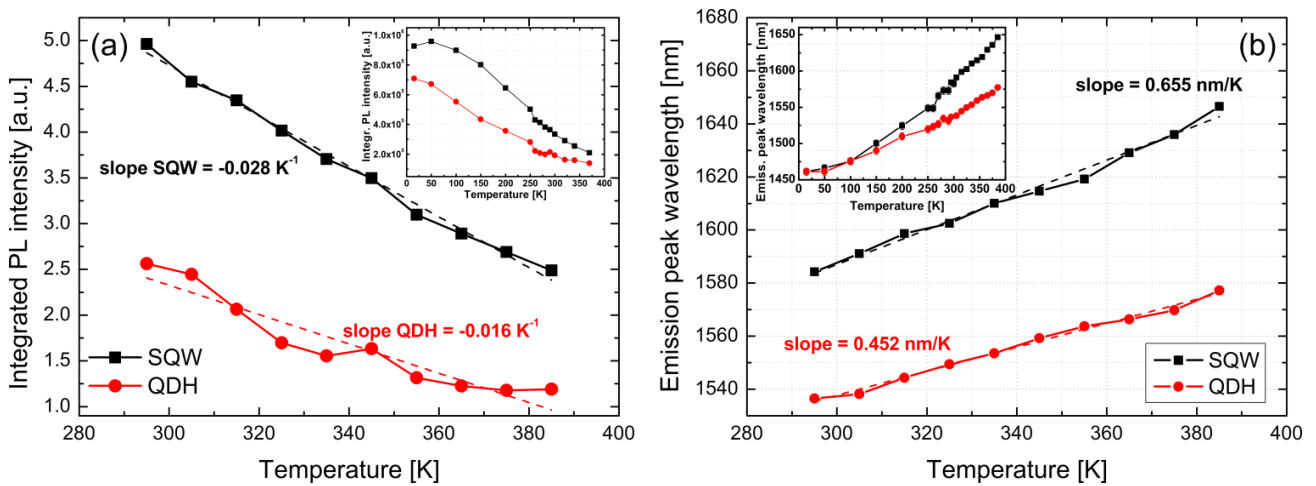


Fig. 3.8 – Evolution of (a) the integrated photoluminescence and (b) the emission wavelength as a function of the temperature in the case of SQWs (black) and QDHs (red). Reproduced from [Taleb2016].

During the thesis of F. Taleb [Taleb2016], the PL temperature behavior of QDH-based active regions has been investigated in the range 15 K - 380 K, and compared to that of SQWs. The potentialities in using QDH-based active regions with respect to SQW-based ones are particularly noticeable by observing the evolution of integrated PL intensity and peak emission wavelength as shown in Fig. 3.8, extracted from [Taleb2016].

As already mentioned in the introduction to the chapter, the high temperature behavior offered by QDHs is quite attractive for semiconductor laser applications, since laser devices typically work in a range between 25°C and 100°C (300 K – 370 K). As shown in Fig. 3.8a, in this range the slope of the integrated PL intensity in the case of QDHs is nearly twofold smaller ( $-0.016 \text{ K}^{-1}$ ) than in the case of SQWs ( $-0.028 \text{ K}^{-1}$ ).

The advantages of QDHs over SQWs in terms of temperature sensitivity are also noticeable with respect to the emission wavelength variation. Fig. 3.8b shows the evolution of the peak wavelength

of the photoluminescence spectrum in the range of interest for laser applications (cf. inset of the figure for the whole temperature range). Again, QDHs are characterized by a slower shift of the peak wavelength, measured to be 0.452 nm/K, in contrast to 0.655 nm/K for the SQWs.

In summary, we highlight that QDHs show a weaker dependence with respect to temperature than what observed with SQWs, both in terms of evolution of the photoluminescence intensity as well as evolution of the emission wavelength. These observations strengthen the idea that low dimension nanostructures like QDHs (or QDs) have potentialities to be integrated on VCSELs and particularly on VECSELs, where the thermal management poses strict limitations on the good operation of devices, and improve their performance at high temperatures.

### **3.4.3 Spectral coverage and (modal) gain of QDHs active media**

The weaker temperature dependence and the control of the polarization of emitted light are not the only advantage of using QDHs active media. The size dispersion of these self-assembled nanostructures gives rise to a wide emission spectrum. In the past, such an active media has been largely employed to realize broad emitting laser sources. Lasing over several tens or hundreds of nanometers around 1.55  $\mu\text{m}$  (and beyond) has been reported in edge emitting devices [Ooi2008, Khan2013] and VCSELs [Taleb2013].

The wide PL spectrum of QDHs resulting from their inhomogeneous broadening might translates in a wide gain, which can be exploited to realize broad emitting VCSEL and VECSEL devices. On the other hand, a wider gain might also imply a more distributed and weaker maximal gain of QDHs with respect to SQWs.

At this point it may be worth to measure the (modal) gain offered by a QDH-based active region, and to compare it with that of a conventional SQW-based one to evaluate their performance. We obtained such an information from the characterization of semiconductor optical amplifier (SOA) and edge-emitting laser (EEL) structures. In both cases, the active region of the devices integrates six SQW or six QDH layers. In this case the samples are emitting at 1.50  $\mu\text{m}$  (SQW) and 1.46  $\mu\text{m}$  (QDH), respectively.

#### **SOAs**

To this aim, we realized multi-sections SOA structures with 7° tilted cavities and different mesa width (ranging from 3 to 10  $\mu\text{m}$ ), according with the technological steps shown in Fig. 3.9 (next page). Each section of the SOA is 1 mm in length and it is separated by 50  $\mu\text{m}$ -long isolation dip from the neighboring sections (resulting in  $\sim 62 \text{ k}\Omega$  resistance). We highlight that, to increase the

modal gain of the structures, it is important that the waveguides of SOAs are collinear to the orientation of the dashes.

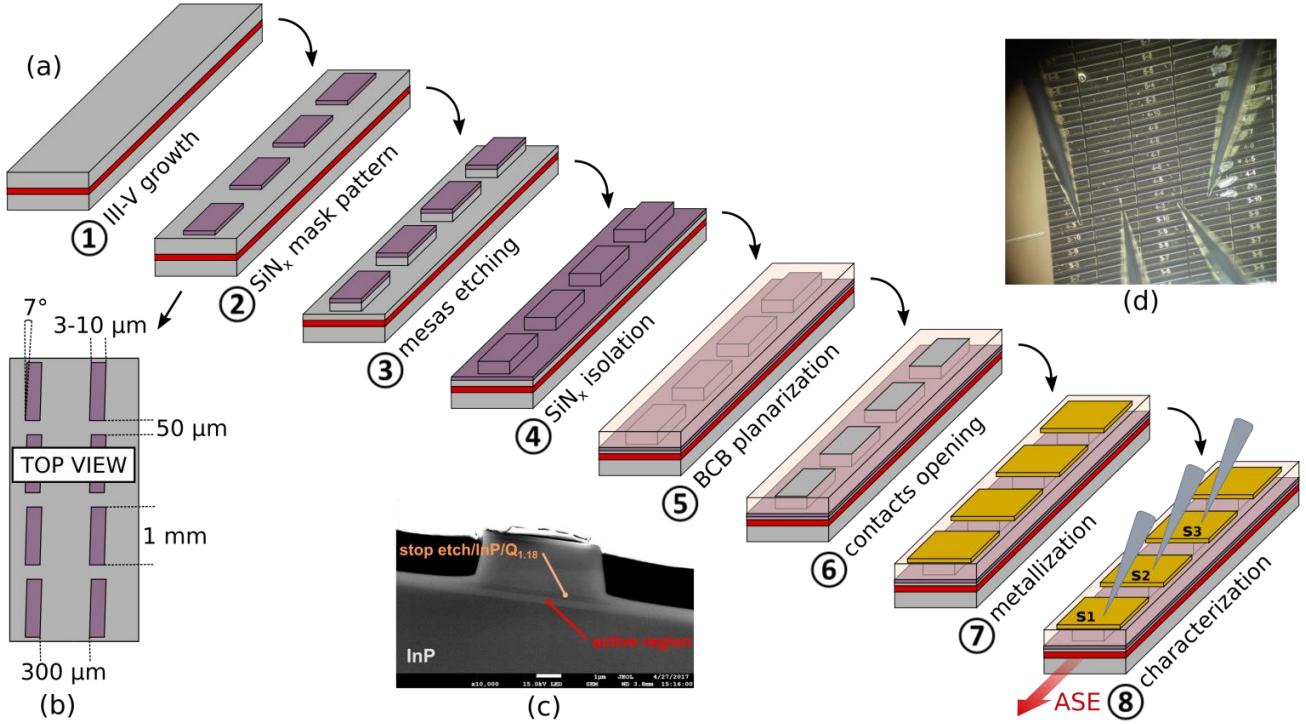


Fig. 3.9 – SOA structures for modal gain measurements: (a) process, (b) top view, (c) device cross section and (d) contacts.

The modal gain measurements in SOA devices have been performed by using the “segmented contact method” [Blood2003]. To perform the measurement, the section 2 is used as the photon source, which is amplified by section 1 (directly polarized) while section 3 is inversely polarized and acts as absorbing section, in order to avoid any unwanted feedback reflection of photons.

The net modal gain ( $\Gamma g_{mat} - \alpha_i$ ) is thus inferred by applying the following relation [Blood2003]:

$$(\Gamma g_{mat} - \alpha_i) = \frac{1}{L} \ln \left[ \frac{I_{meas}(2L)}{I_{meas}(L)} - 1 \right] \quad (3.1)$$

We acquired the amplified spontaneous emission (ASE) spectra  $I_{meas}$  as a function of the wavelength for different values of the density current, and deduced the net modal gain according to the previous formula in the case of SQW- and QDH-based active regions, as shown in Figs. 3.10a,b on next page (curves obtained at room temperature).

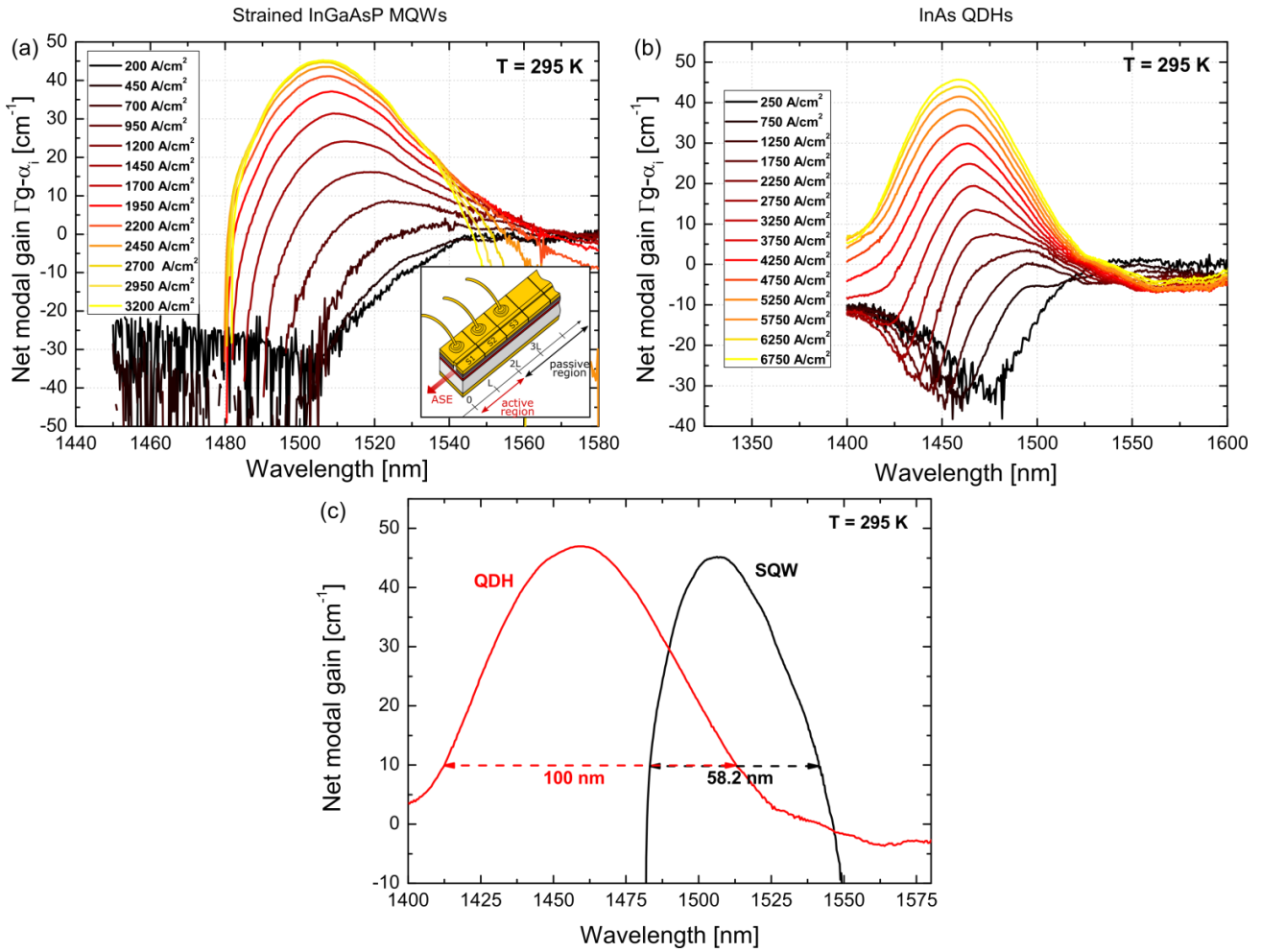


Fig. 3.10 – Evolution of the net modal gain obtained from SOA structures in the case of (a) SQW- and (b) QDH-based active media. (c) Direct comparison between SQW- and QDH-based active regions for current densities of 3.2 and 7.2  $\text{kA/cm}^2$ , respectively.

From these measurements, we deduced a comparable net modal gain, equal to  $\sim 45 \text{ cm}^{-1}$  and  $\sim 46 \text{ cm}^{-1}$  for the SQW-based and QDH-based active region, respectively. In the two cases, the absorption was relatively comparable, and it has been evaluated to  $20 \text{ cm}^{-1}$  (QDHs) and  $10 \text{ cm}^{-1}$  (SQWs), respectively. Fig. 3.10c directly compares the net modal gain of the two structures for which we observe the same value of the modal gain. It is interesting to observe that a wider emission in the case of QDHs is obtained, with a width at  $\Gamma g_{\text{net}} - \alpha_i = 10 \text{ cm}^{-1}$  equal to 100 nm in the case of QDHs, while in the case of SQWs is nearly twofold less, being 58.2 nm.

## EELs

The measurement on EELs allows exactly quantifying the maximum accessible gain which both active regions can provide. The process flow to realize the EELs structures is similar to that presented for SOAs, except for the fact that we used mono-section devices and normal incidence waveguides (i.e. a resonant laser cavity as required by EELs to operate).



In this case, the internal losses  $\alpha_i$ , the internal quantum efficiency  $\eta_i$  and the modal gain  $\Gamma g_{mat}$  have been obtained by data extrapolation from the one-sided output power vs current (P-I) characteristics (Fig. 3.11a,b, next page) related to devices with different cavity lengths (200-1000  $\mu\text{m}$ ) and contact width (3-5  $\mu\text{m}$ ), by considering the two following relations [Coldren2012]:

$$\frac{1}{\eta_{ext}} = \frac{1}{\eta_i} \left( 1 + \frac{\alpha_i}{\ln\left(\frac{1}{R}\right)} L \right) \quad (3.2)$$

$$J = J_{tr} e^{\left( \frac{1}{\Gamma g_{mat}} \left( \alpha_i + \frac{1}{L} \ln\left(\frac{1}{R}\right) - 1 \right) \right)} \quad (3.3)$$

where  $\eta_{ext}$  is the external quantum efficiency,  $R$  is the facet's reflectivity,  $L$  is the cavity length, and  $J_{tr}$  is the transparency density current. We plotted the curves related to Eqs. 3.2 and 3.3 (or rather, its logarithmic linearization) in Fig. 3.11c-f in the case of the SQW- and QDH-based active regions. Table 3.3 summarizes the parameters extrapolated from the EELs measurements on SQW and QDH samples.

**Table 3.3 – Measured and extrapolated parameters for SQW- and QDH-based EELs.**

Active region composition	6× InGaAsP SQWs	6× InAs QDHs
Emission wavelength $\lambda$ [ $\mu\text{m}$ ]	1.50-1.52	1.48-1.51
Threshold current $I_{th}$ [mA]	25-60	30-45
$\Gamma g_{mat}$ [ $\text{cm}^{-1}$ ]	60	35
$\alpha_i$ [ $\text{cm}^{-1}$ ]	19	6
$\eta_i$	0.37	0.38
$J_{\infty}$ [ $\text{A}/\text{cm}^2$ ]	1358	1020

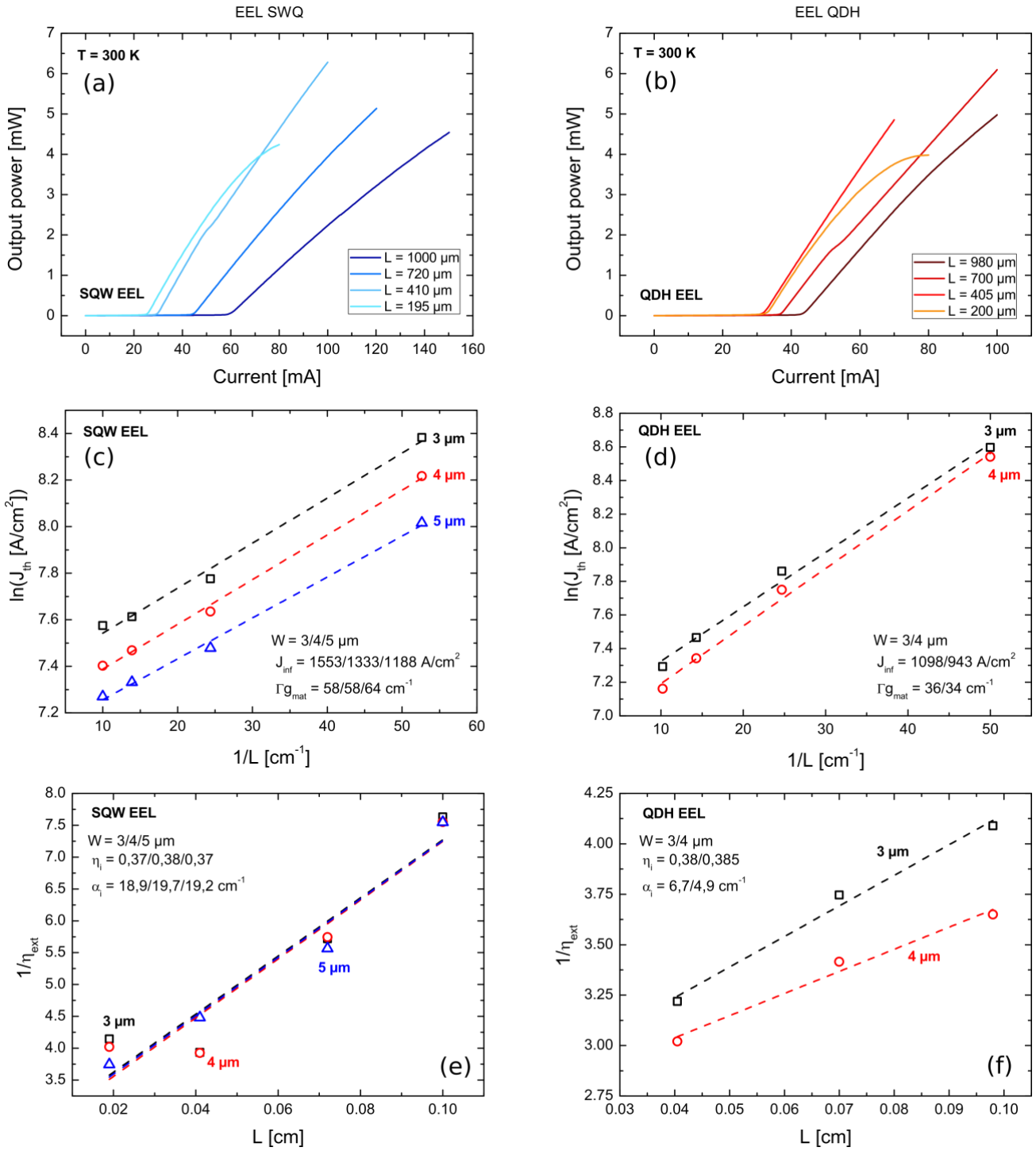


Fig. 3.11 – Gain measurement from EEL structures: parameters extrapolation from output characteristic,  $\ln(J_{th})$  vs  $1/L$  and  $1/\eta_{ext}$  vs  $L$  in the case of (a,c,e) SQW-based and (b,d,f) QDH-based active media. Measurements have been performed at room temperature (300 K).

Comparing these results with those obtained with SOA structures, we observe a more pronounced difference in the value of the net modal gain between SQWs and QDHs, while the internal losses are basically confirmed. However, we can conclude that the characterization of EELs confirmed what expected, i.e. SQW-based active media typically shows higher modal gain with respect to QDH ones. This is mainly due to the smaller quantity of active volume of such nanostructured



active media, both in terms of height and in-plane density. This problem can be partially circumvented by integrating a bigger number of active layers per set. The optimization of the layer number depends on several parameters of the semiconductor structure, such as the laser configuration to be implemented (EELs or VCSELs) and the confinement factor of the designed cavity, as discussed in the previous chapter in the case of a VCSEL active region based on SQWs.

### 3.4.4 Summary

To summarize the comparison between SQW and QDH active media presented in this section, we can conclude that, conversely to the case of a SQW-based active medium, the emission from QDH nanostructures has a well-defined and linear state-of-polarization, which is always aligned according to the quantum dash orientation (i.e. the [1-10] direction).

Also, QDHs show interesting thermal performance compared to SQWs, with a less sensitive decrease of the integrated photoluminescence and a weaker shift of the emission wavelength.

Additionally, due to the size dispersion of the nanostructures, the spectral coverage of QDH media is generally much wider than in the case of SQWs as it has been evidenced by gain measurements. Concerning the maximum achievable net modal gain, QDH-based media show weaker performance with respect to a SQW-based counterpart. This is mostly due to the smaller quantity of active material contained in a QDH-based active region, both in terms of nanostructure height (typical height of QDHs is  $\sim 2.5$  nm) and in terms of in-plane coverage (typical linear density of QDHs along [110] direction is  $\sim 30 \mu\text{m}^{-1}$ ). To compensate for this drawback, a higher number of QDH layers should be integrated in the active region. This can be easily obtained in practice because the average height of the QDH is smaller than that of SQW, so that a bigger number of QDH layers can be packed in the same active set.

According to the characterization we have previously presented, an active region integrating QDH nanostructures seems to be a good candidate to fulfill the requirements for a tunable LC-based VCSEL.

## **3.5 Devices based on liquid crystal micro-cell technology**

### **3.5.1 Accomplished results from the past (2006-2014)**

Concerning the development of LC-based vertical-cavity active devices, significant advances on the integration of LC technology and III-V compounds have been obtained by FOTON Institute and Télécom Bretagne, in the framework of the “Lambda-Access” ANR national project (2007-2011). As a first preliminary result, a 34 nm wavelength tuning range centred at 1.5  $\mu\text{m}$  under pulsed optical pumping was demonstrated from a monolithic device by applying a voltage lower than 3 V on a nematic LC cell integrated inside a VCSEL cavity [**Castany2011**]. This result was the first experimental evidence of the potentialities of using nematic LC cells for the realization of a tunable active device. However, the mode-hop-free tuning range of this first LC-VCSEL was partially limited by a lack of control of the state-of-polarisation on the laser emission.

The aforementioned results were obtained with the use of macroscopic LC-based cells (several  $\text{cm}^2$  in size), which limit the use of these devices in practical applications requiring high degree of integration.

### **3.5.2 The HYPOCAMP project (2014-2019)**

To face the cell miniaturizing issues and develop a full-monolithic and micrometric tunable VCSEL integrating a LC  $\mu$ -cell, in 2014 a partnership of FOTON Institute, LAAS (Toulouse), IMT Atlantique (Brest), and C2N (Marcoussis) join together in the ANR-ASTRID HYPOCAMP<sup>3</sup> project.

The project aimed at developing a new concept of tunable device, compact and robust, potentially low-cost, with a low power consumption, and benefiting from important wavelength accuracy, in agreement with most of the prerequisite for mobile and embedded applications. As already said, the proposed device is based on the integration of a LC electro-optical layer, presenting an important optical index variation, embedded in a vertical-cavity architecture. The potentials of such LC technology enable the realization of completely monolithic devices, with a large wavelength tuning, and without any movable parts. In particular, this last point is expected to increase the reliability of the process, the robustness of the fabricated devices, and more importantly (in the case of active devices) their laser wavelength stability. These entire points make this concept very attractive

---

<sup>3</sup> **HY**brid **P**olarisation controlled and **m**onolithic tunable vertical **C**avity surface emitting **l**asers, for **e**mbedded and **c**om**P**act optical and microwave systems.

compared to the alternative approaches, mainly based on MEMS technology, as explained before in *Section 3.2.3*.

The results, which will be presented in the following, come from this scientific collaboration. The investigated devices were:

1. a passive device, represented by a **tunable p-i-n photodetector** on InP substrate, integrating the LC-based tuning mechanism to realize a micrometric-sized device, enabling a detection around  $1.55\ \mu\text{m}$ . It represents the first micrometric and monolithically integrated device based on such technology, and it was also useful to evidence the proof-of-concept of this technology prior to its integration in active devices.
2. an active device, i.e a **tunable VCSEL** realized on InP substrate and emitting around  $1.55\ \mu\text{m}$ . The final goal is to developed an electrically-injected VCSEL, integrating a  $\mu$ -cell within its laser cavity, to realize a wavelength tuning larger than 50 nm without mode hopping phenomena, a tuning frequency close to 1 kHz, and with a significant improvement in the wavelength stability (linewidth  $< 1\ \text{MHz}$ ).
3. a second active device, a **tunable and ultra-stable VECSEL source** emitting around  $1.55\ \mu\text{m}$ , dedicated to high resolution spectroscopy. It is based on the integration of the LC  $\mu$ -cell within a cm-long cavity, to obtain a shot noise limited laser presenting a narrow laser linewidth ( $\sim 10\ \text{kHz}$ ) and finely tunable over several tens of pm.

LAAS and IMT Atlantique, with the collaboration of C2N, were in charge of the development of the LC-based  $\mu$ -cells technology. In the framework of this PhD manuscript we won't address the technological steps and characterizations which have been developed by our partners. We will just briefly describe the working principle and the architecture of the LC  $\mu$ -cells which have been developed, as it would help the understanding of the operation of the final devices. Concerning these devices, we will thus focus on the technological development and characterizations in which we were directly involved. Additionally, for what concerns the VCSEL devices, at the moment of writing this PhD dissertation the tests are still ongoing, so we will limit to present the basics steps of the development and some simulations we carried out to validate the design of the devices. The main goal of these simulations was to investigate the thermal performance of the structure, as they could have a critical impact on the tuning capability of the device, as discussed later on.

Concerning the development of the tunable VECSEL devices, it will not be presented in this manuscript because preliminary tests showed that the process of LC  $\mu$ -cells developed up to now is not compatible with the operation of external-cavity devices (the presence of LC  $\mu$ -cells imposes

the use of an intra-cavity ITO electrode inside the VECSEL cavity, being responsible of introducing too much optical losses within the VECSEL cavity).

### **3.5.3 Tunable p-i-n photodiode**

The first step toward the realization of a tunable device based on LC technology is obviously represented by the development of the basic block composing the electro-optic tunable mechanism, i.e. the LC-based tunable  $\mu$ -cell. As said, this part has been developed by our partners (LAAS, IMT Atlantique and C2N) and it is composed by a resonant micro-cavity filled by LC molecules (E7 mixture) and defined by two DBR mirrors on each side. In order to maximize the birefringence between the ordinary and extraordinary modes, the molecules of the LC have to be aligned along the same direction. Conventional polymer surface “rubbing” or “brushing” techniques, which are currently applied for standard liquid-crystal displays (LCDs) technology, are not suitable in our case because they induce too many dust particles and surface defects that may prevent the devices from working. Additionally, the non-planar surface of the sample, which presents topographic reliefs greater than 1  $\mu\text{m}$  and mesas with diameters in the range of one hundred  $\mu\text{m}$ , is not suited to implement such simple techniques.

#### **Device architecture**

To overcome these problems, a new method has thus been developed by LAAS and IMT Atlantique. It consists in a localized alignment of the LC molecules thanks to a nanoimprinted subwavelength relief grating (period  $\sim 800$  nm, duty-cycle 50:50 and depth  $\sim 75$  nm) obtained by soft-mold technique on a 600 nm-thick SU-8 layer, which forces the LC molecules to align parallel to the specific direction defined by the relief. The subwavelength period of the relief grating has been also designed to minimize the diffraction losses around 1.55  $\mu\text{m}$ .

Prior to the realization of a tunable PD, the process has validated thanks to the implementation of a Fabry-Pérot micro-filter for light detection around 1.55  $\mu\text{m}$  [Sadani2018], which showed interesting performance. This preliminary LC  $\mu$ -cells FP filter has a nominal cavity length of 5  $\mu\text{m}$ , which is defined by the height of the polymer DF-1005<sup>4</sup> used to realize the walls of the cell, and exhibits a tuning range of 102 nm (limited by the FSR of the cavity) with only 18 V of applied voltage and no current consumption, as well as negligible internal losses, compatible with the

---

<sup>4</sup> DF-1000 is a relatively new and low-cost series of epoxy photosensitive films with different nominal thickness, which are currently used in microfluidics technology. DF-1005 is part of this series, and allows obtaining 5  $\mu\text{m}$ -height films with a great homogeneity in thickness.

measured 0.35 nm spectral linewidth. This last point is crucial for the integration of the LC  $\mu$ -cells inside an optical cavity.

Going further, a second (dedicated) LC  $\mu$ -cell FP filter has been coupled to a MBE-grown InP-based p-i-n structure integrating a 1  $\mu$ m-thick In<sub>0.53</sub>Ga<sub>0.47</sub>As absorbing layer, where the p- and n- contacts were previously deposited, to form a tunable photodiode (as shown on Fig. 3.12a).

The processed sample is a quarter of 2-inch wafer (Fig. 3.12c) integrating 8 different matrices of LC  $\mu$ -cell, each of them composed by 9 devices with different shape (squared or circular) and a photosensitive area ranging from 0.01 mm<sup>2</sup> to 0.3 mm<sup>2</sup>.

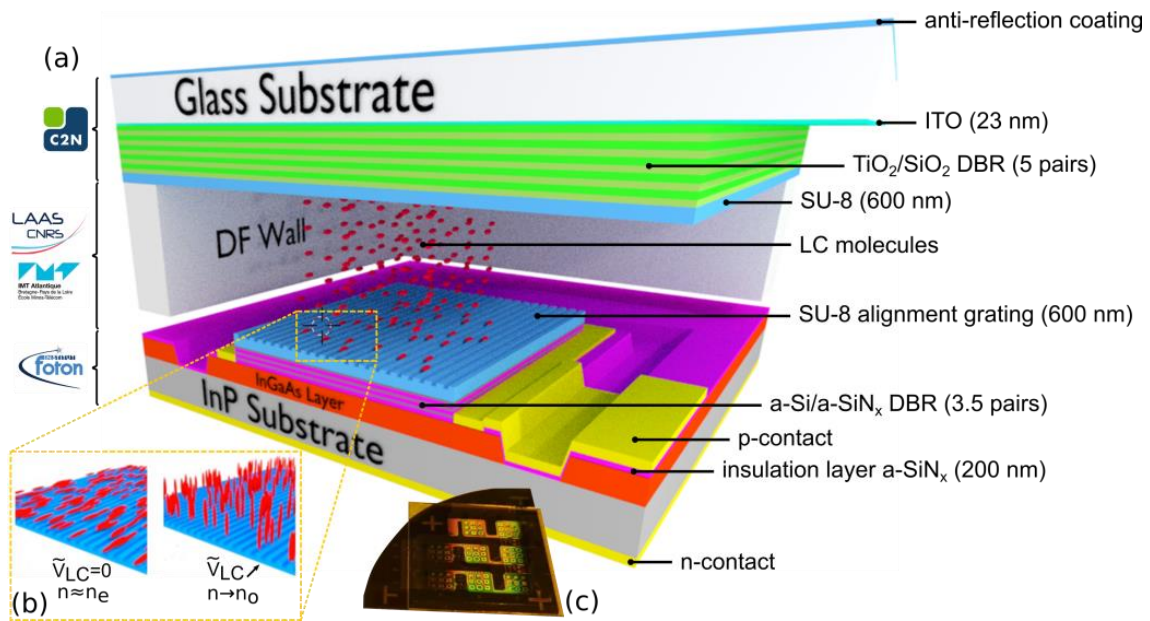


Fig. 3.12 – Tunable p-i-n photodiode based on the LC  $\mu$ -cell: (a) schematic cross-view of the device, (b) alignment of the LC molecules along the SU-8 subwavelength grating and their reorientation with the AC voltage  $V_{LC}$  applied to the  $\mu$ -cell, (c) photograph of a processed quarter of 2-inch wafer with several matrices of PD devices.

The first a-SiN<sub>x</sub> layer (thickness  $t_{a-SiN_x} = 200$  nm) composing the bottom DBR has been deposited by PECVD, for its improved adhesion with the InP substrate with respect with its RF magnetron sputtering counterpart, as stated before. This layer also acts as passivation layer outside of the active area of the PDs.

### Experimental setup

The LC molecules are driven by a pure alternating voltage signal (a square wave) with typical frequency  $f = 2$  kHz, which is applied to the  $\mu$ -cell through the upper indium tin oxide (ITO) contact, while the bottom n-contact is connected to the ground. As a function of the amplitude of the driving signal, the orientation of the LC molecules changes (see Fig. 3.12b) and the optical response of the LC-based filter on top of the active region is modulated (as already discussed in Section 3.3.2). We highlight the fact that, to prevent any particle migration phenomena induced by a

static electric field which can degrade the tunability range and eventually completely prevent the device to be tuned, we systematically verified that no DC component was added to the AC voltage. The device has been characterized with the free-space setup shown in Fig. 3.13.

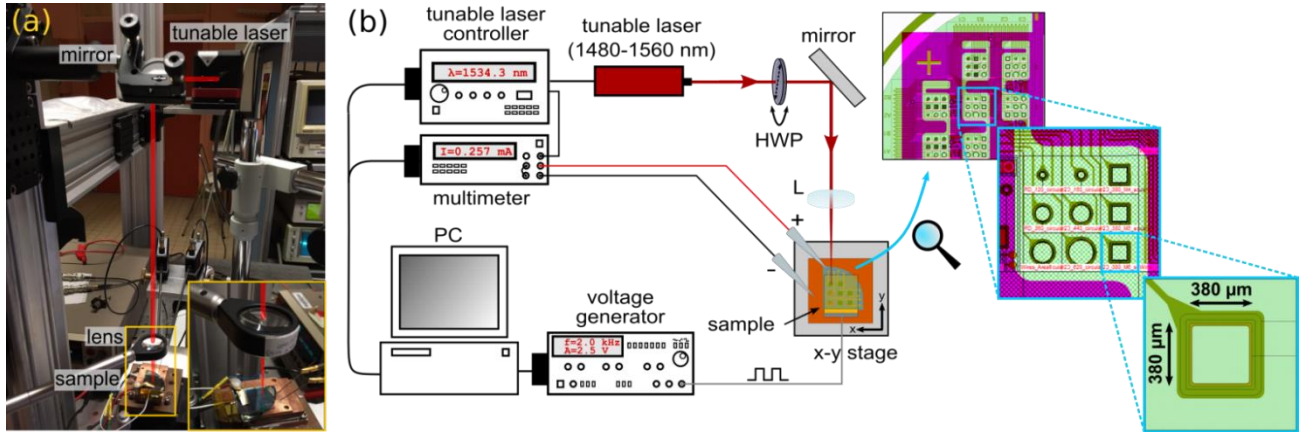


Fig. 3.13 – (a) Picture and (b) scheme of the experimental setup used to characterize the tunable PD (the inset shows a  $3 \times 3$  matrix with photodiodes of different size and the investigated squared  $380 \times 380 \mu\text{m}^2$  PD). HWP: half-wave plate, L: lens.

The sample is placed onto a copper support acting as ground contact, which it is in turn fixed onto an x-y translational stage, to scan the entire surface of the sample and address different devices. An CW linearly-polarized external cavity laser (New Focus Velocity), continuously tunable in the 1480-1560 nm range with a 5 MHz FWHM and a mode-hop free emission, has been used to characterize the sample. The polarization is adjusted with a half-wave plate to exactly match the extraordinary axis of the PD, and finally focused on the sample thanks to a lens with a 40 mm focal length, forming a spot of  $\sim 100 \mu\text{m}$  on the chip surface. Such a spot dimension is sufficiently small to individually address any single PD on the sample. The output power of the tunable laser has been fixed to 2 mW, which reduced to 1.4 mW before arriving on the PD, due to the losses of the optical chain. The PD photo-generated current is then acquired by the contact probes connected to a multimeter and a PC, which also acquires the LC driving signal.

### Tunable photodiode performance

The result of characterization is shown in Fig. 3.14 (next page) in the case of a PD with an active squared surface of  $380 \times 380 \mu\text{m}^2$  (as shown in the inset of the Fig. 3.13b).

Fig. 3.14a shows the I-V characteristic of the p-i-n photodiode in dark conditions and under illumination, when the laser is focused on the active surface of the PD, with an incident power of 1.4 mW at 1527 nm. In such a case, a photocurrent higher than 0.6 mA is generated without any voltage applied to the LC  $\mu$ -cell. In order to characterize the PD response as a function of the LC

voltage, we then fixed the PD voltage to 0 V, and set the incident light to different wavelength (see Fig. 3.14b).

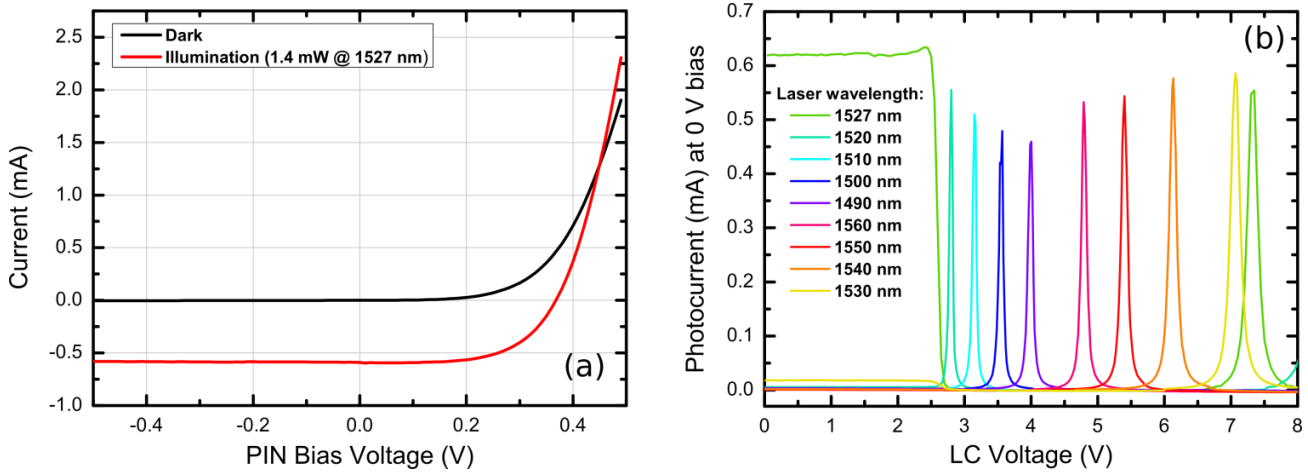


Fig. 3.14 – (a) *I-V* curves of the *p-i-n* photodiode in dark condition and under illumination ( $P_{inc} = 1.4 \text{ mW}$  at 1527 nm) when 0 V are applied to the LC filter. (b) Detected photocurrent as a function of the LC voltage for different laser wavelengths with the PD bias fixed to 0 V.

For the previous value of 1527 nm, we observe 0.62 mA of generated photocurrent in the range 0 - 2 V of applied LC voltage. This nearly constant value of the photocurrent corresponds to a perfect match of the LC filter transmission peak with the 1527nm wavelength of the laser, because the extraordinary index of the LC stays constants over the 0 - 2 V range<sup>5</sup>. For further increasing of the LC voltage, the photocurrent falls to the dark current value ( $\sim 1 \mu\text{A}$ ), before rising again exhibiting a peak at 7.5 V, which correspond to the shift of the adjacent extraordinary mode peak, located at a higher wavelength (above 1600 nm). These measurements, performed for several laser wavelengths, allow obtaining the characteristic of the tunable photodiode on the available spectral range of our tunable laser. A single photocurrent peak is then detected for any different applied voltage within the range 0 - 7 V, confirming the wavelength-selective operation of the tunable PD on a spectral range equal to 80 nm.

The quality factor  $Q$  of the tunable LC-based PD has been then evaluated by acquiring the photocurrent as a function of the incident laser wavelength for different AC voltages applied to the LC  $\mu$ -cell, as shown in Fig. 3.15a (next page). The measurement of the FWHM of each peak lead to an average value of  $\Delta\lambda_{FWHM} = 1.5 \text{ nm}$ , if we exclude the wavelength range  $< 1490 \text{ nm}$ . Such a value of the FWHM gives a measured quality factor  $Q_{meas} = \Delta\lambda_{res}/\Delta\lambda_{FWHM} \sim 1000$ , in good agreement with the expected value ( $Q_{TMM} \sim 1100$  in the range 1500 - 1600 nm).

<sup>5</sup> LC molecules have an initial inertia, and start moving for applied voltages around 2 - 2.5 V.



This also confirms two main points:

- i. the SU-8 sub-wavelength grating used to align the LC molecules does not introduce relevant diffraction losses;
- ii. the absorption of E7 LC molecules around  $1.55 \mu\text{m}$  is negligible.

It is worth to notice that we observe a degradation of the quality factor  $Q$  when the extraordinary mode was approaching the ordinary mode. Investigations to understand the origin of this degradation are still undergoing.

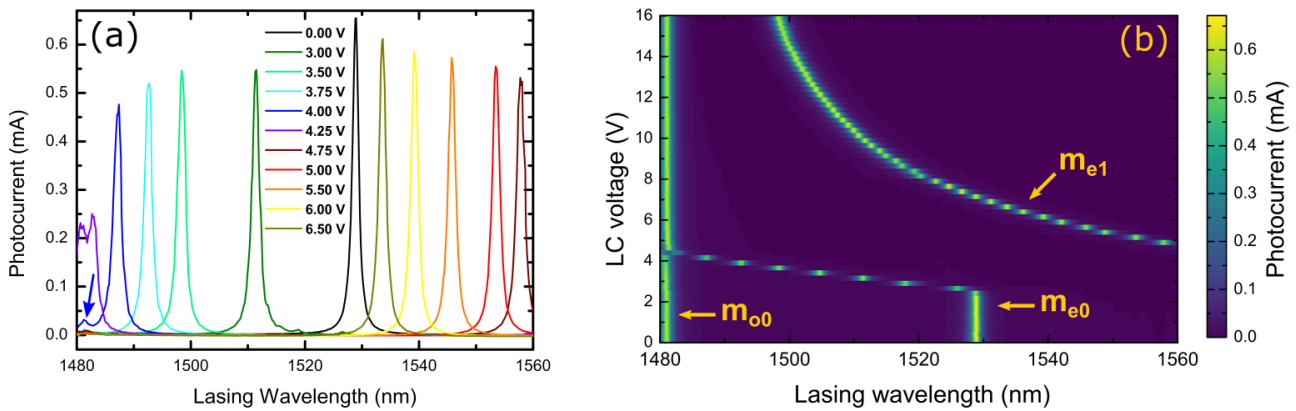


Fig. 3.15 – (a) Photocurrent as a function of the laser wavelength for different applied voltage on the LC  $\mu$ -cell (ranging from 0 V to 6.5 V). (b) Photocurrent mapping as a function of both the applied voltage and the lasing wavelength: the evolution of the ordinary ( $m_{o0}$ ) and extraordinary ( $m_{e0}$  and  $m_{e1}$ ) modes is indicated.

Fig. 3.15b shows the resulting color-scale mapping of the photocurrent intensity, as a function of both the LC voltage and the lasing wavelength. In the map we indicated by  $m_{o0}$  the photocurrent related to the ordinary mode (the fixed line at 1482 nm), obtained by rotating the polarization of the incident light by  $90^\circ$  with respect to the alignment grating thanks to the half-wave plate. Conversely, when the light is aligned parallel to the grating, we observe the photocurrent peaks related to the extraordinary modes ( $m_{e0}$  and  $m_{e1}$  in the figure), which are tuned by applying the AC voltage to the liquid crystals. Again, no tuning is observed for voltage lower than  $\sim 2.5$  V, as previously observed. For what concerns the intensity of the photocurrent of the extraordinary mode, it has been observed an amplitude in the range 0.5 - 0.65 mA on the whole range of measurement, except for a LC voltage equal to 4.25 V. For such a value of the LC voltage the extraordinary mode is close to the ordinary mode position (blue arrow on Fig. 3.15a) and the above-mentioned cross-talk appears, degrading the  $Q$ -factor of the cavity. As a result, the intensity of the photocurrent is decreased and the FWHM is spoiled. Investigations on such a phenomenon are still in progress, in order to identify the cause of the problem and correct it. One possible solution would be to



reduce the thickness of the LC  $\mu$ -cell. This would decrease the useful tuning range of the extraordinary mode, but would allow placing the ordinary mode out of this range. Considering an incident laser power of 1.4 mW on the surface of the chip and excluding the range where cross-talk between the orthogonally-polarized modes occurs (1480 – 1490 nm), the measured intensity of the photocurrent gives responsivity values of 0.35 to 0.46 A/W. These values of responsivity, which is a key figure-of-merit of the photodiode's performance, have been compared with those of a reference PD not integrating any tunable LC  $\mu$ -cell. For this reference device, no DBR layers were obviously deposited on the surface, except for the 200 nm-thick PECVD-SiN<sub>x</sub> isolation layer, which in this case acts as an anti-reflection coating and maximizes the light reaching the absorbing region of the PD. As a consequence, a responsivity in the range 0.57 - 0.64 A/W has been measured. This value of responsivity was expected, and it is consistent with a photodetector's active region integrating a 1  $\mu$ m-thick In<sub>0.53</sub>Ga<sub>0.47</sub>As absorbing layer. The responsivity of the device can be easily increased up to 0.8 or 1 A/W by just simply doubling the thickness of the absorbing layer [Cesar2017]. Additionally, but in a lesser extent, part of the losses is also related to a residual absorption taking places at the ITO layer located outside the  $\mu$ -cavity, which is used as top electrode to tune the filter response and which is significantly absorbent in the near infrared domain. Table 3.4 summarizes the performance obtained by the tunable PD based on the LC  $\mu$ -cell.

**Table 3.4 – Summary of the performance of the LC-based photodiode.**

1.55 $\mu$ m LC-based photodiode performance	
Detection range $\Delta\lambda_{PD}$ (laser limited)	80 nm (1480-1560 nm)
LC AC voltage range	0 - 7 V
Measured cavity $Q$ -factor	$\sim 10^3$
Typical transmission peak $\Delta\lambda_{FWHM}$	1.5 nm
Responsivity (for 1 $\mu$ m-thick absorbing layer)	0.35 - 0.46 A/W
Tunable filter losses	$\sim 2$ dB
Ordinary mode FSR	90 - 101 nm
Extraordinary mode FSR	80 - 88 nm

### 3.5.4 Investigation of a tunable LC-VCSELs: preliminary results

The good performance obtained with the tunable photodiode encouraged us to further pursue on this way and move to the next step of development, which consists in the realization of a tunable VCSEL emitter based on the LC  $\mu$ -cell technology, as schematized on Fig. 3.16. The final device, as conceived, will be electrically-pumped, and would represent a full-monolithic alternative to the MEMS-based tunable VCSEL, with undoubtedly advantages in terms of power consumption and spectral stability of the laser emission, as previously discuss in this chapter.

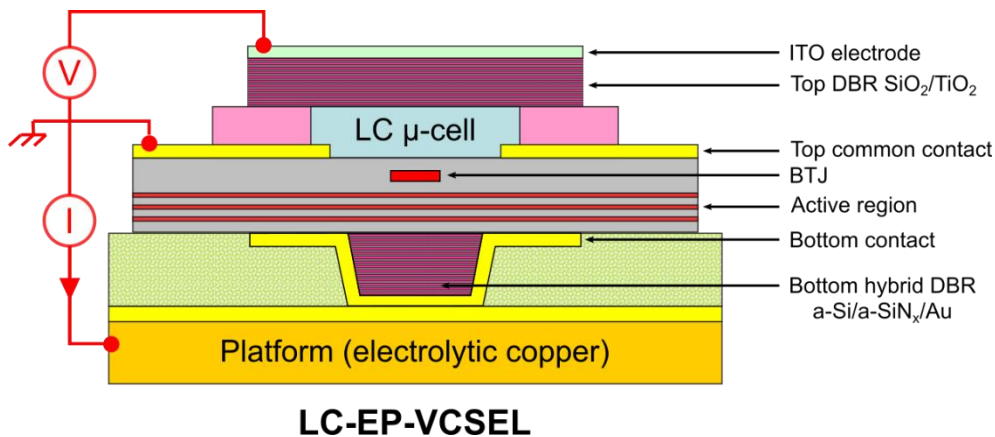


Fig. 3.16 – Schematic cross-section of the investigated tunable EP-VCSEL based on the LC  $\mu$ -cell concept.

#### Thermal modelling

Before proceeding with the technological realization of the device, some peculiar points needed to be investigated. Indeed, concerning the tunable PD, we did not pay attention to the thermal aspects of the device, because of the dissipated power and the corresponding generated heat is limited, and does not represent a big issue for the operation of the PD.

In the case of an active device as a VCSEL integrating a tunable mechanism based on LC, this can no longer be neglected. As discussed in *Chapter 2*, the dissipated power in a VCSEL is significantly higher than a PD. Beside the unwanted limitations arising from a demanding heat management, which limit the intrinsic VCSEL performance in terms of output power and threshold, an non-negligible increase of the device temperature transferred to the LC  $\mu$ -cell can severely affect the optical and physical properties of the LC mixture and locally induce a phase transition from the nematic to the isotropic phase, limiting its tunability efficiency.

In order to investigate the impact of the temperature on the LC performance, we adapted the FEM model we introduced in *Chapter 2* to the case of an EP-VCSEL in which a LC  $\mu$ -cell is inserted in the cavity. The objective here is to estimate the temperature rise on the LC  $\mu$ -cell to identify the best

experimental conditions to ensure proper tuning of the devices or, in other words, the range of dissipated powers for which the tuning mechanism can still properly work.

Fig. 3.17 shows the structure of the device that has been simulated with COMSOL Multiphysics® [Comsol]. Again, for further details on the model the reader is referred to *Appendix B*.

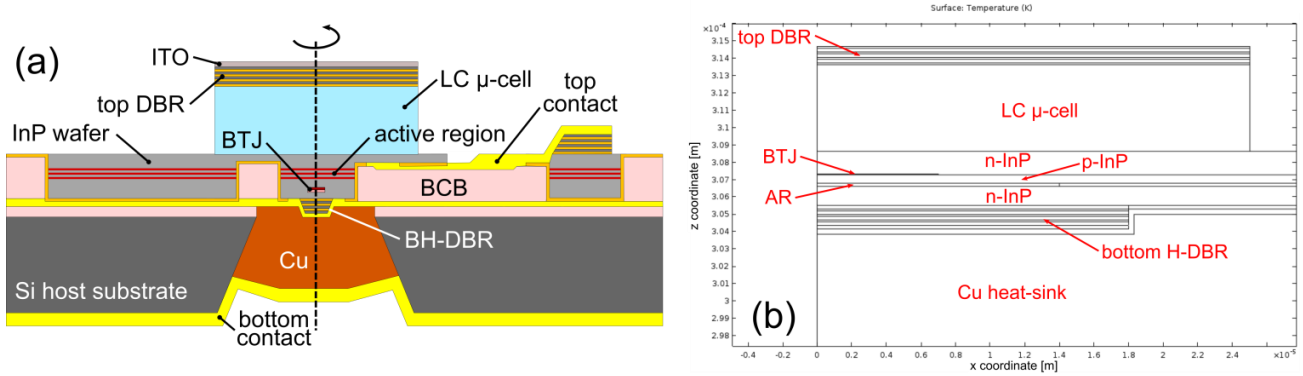


Fig. 3.17 – FEM thermal simulation of the LC-EP-VCSEL: (a) schematic cross-section of the 2D axisymmetric model and (b) definition of the architecture in COMSOL Multiphysics®.

Here we precise that in the model we employed an active region composed by a single set of 6 InGaAsP strained multi-quantum wells (MQW), and an InGaAs-based BTJ. The total dissipated power has been equally divided between the two (active region and BTJ) and the Peltier cell, which is in contact with the bottom surface of the device, has been set to  $T = 20^{\circ}\text{C}$  (293 K). Table 3.5 summarizes the layer composing the LC-EP-VCSEL and the material parameters used in simulations.

**Table 3.5 - Material parameters and thickness of layers used in simulations.**

Layer	Material	Thickness $t$ [nm]	Mass density $\rho$ [Kg/m <sup>3</sup> ]	Heat capacity at constant pressure $C_p$ [J/Kg-K]	Thermal conductivity $k_t$ [W/m-K]
Top DBR (4×)	a-Si	104	2330	703	2,6
	a-SiN <sub>x</sub>	212	3100	350	1
LC μ-cell	E7	5 μm	1700	2000	0,16
InP phase	n-InP	1327	4790	309	69
Active region (6×MQW + barriers)	InGaAsP	208	5000	330	3,5
p-n junction	p-InP	222	4790	309	69
	n-InP	92	4790	309	69
BTJ	InGaAs	46	5500	300	5
Bottom H-DBR (3.5× + Au)	a-Si	104	2330	703	2,6
	a-SiN <sub>x</sub>	212	3100	350	1
	Au	300	19300	129	317
Bonding layer	BCB	5 μm	1050	2180	0,29
Heat-spreader	Cu	200 μm	8960	384	401
Host substrate	Si	300 μm	2329	700	130

Figs. 3.18a,b show the heat flux (white arrows) and the temperature distribution inside the structure. Although the TSHEC architecture seems relatively efficient in removing the heat generated in the active region, we also observe that under certain experimental conditions (such as high dissipated power levels) the LC is partially subjected to a temperature rise. This because the InP top layer (phase layer) is relatively efficient in conducting the heat towards the upper part of the device, as evidenced by the heat color map of Fig. 3.18a. As a consequence, a temperature gradient in the three directions is established. As a function of the amplitude of this thermal gradient, we can have a non-negligible impact on the LC mixture, which basically translates in a local change of the optical properties and, more particularly, in a reduction of the average extraordinary index  $n_e$  of the LC (see Fig. 3.3)<sup>6</sup> up to, in the worst-case scenario, a phase change of LC towards the isotropic phase.

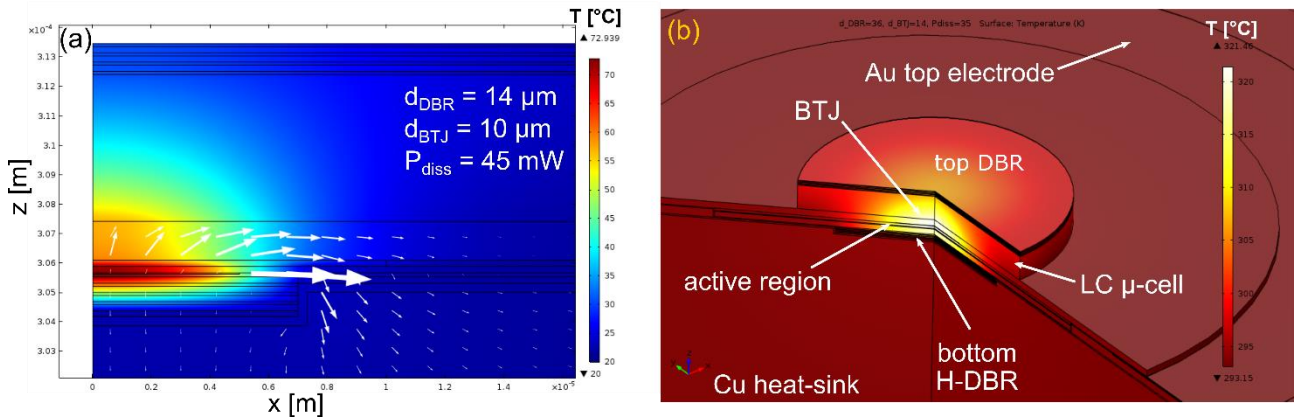


Fig. 3.18 – Result of FEM thermal simulations: map of the internal temperature distribution of the device in (a) 2D and (b) 3D. White arrows in (a) indicates the heat flux.

In order to get a better insight on the thermal behavior of the device, the contribution of different parameters on the thermal heating of the LC  $\mu$ -cell has been estimated. We computed the temperature rise as a function of both the DBR and the BTJ diameter, and the dissipated pump power inside the structure. We consider that half of the power is dissipated in the active region of the VCSEL, while the rest in the BTJ. The results are summarized in Fig. 3.19 on the next page.

<sup>6</sup> The ordinary refractive index  $n_o$  of the LC is less affected by a change in temperature (again, please refer to Fig. 3.3).

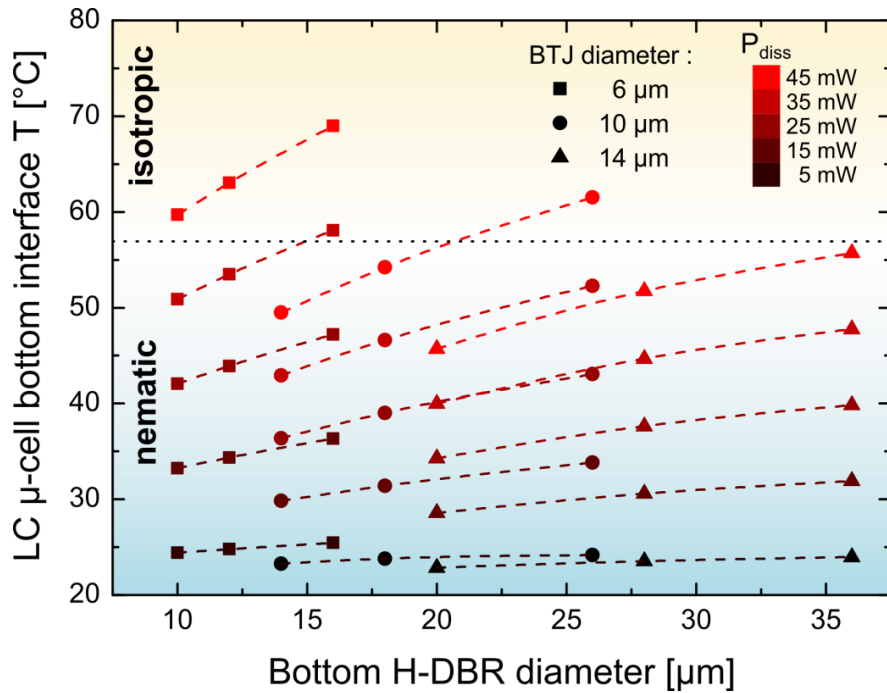


Fig. 3.19 – Results of FEM thermal simulations: temperature of the bottom interface of the LC  $\mu$ -cell as a function of the bottom DBR diameter for various BRJ dimensions. Dotted black line indicates the temperature ( $57^{\circ}\text{C}$ ) for which the E7 LC transition from the nematic (cyan) to the isotropic phase (yellow) occurs.

The first information we can extract from the graph is that, as expected, the temperature rise is higher for large DBRs and small BTJ diameters, and this effect becomes more evident as the pump power increases. More interesting, the figure clearly shows that the temperature of the bottom interface of the  $\mu$ -cell might can exceed the nematic-to-isotropic transition temperature ( $T_c = 57^{\circ}\text{C}$ ) for some combinations of DBR diameter and BTJ dimensions, although most of the points are below this limit. This implies that the LC mixture in contact with the bottom interface of the  $\mu$ -cell would become partially isotropic, while the upper part of the LC mixture which is sufficiently far from the bottom interface would stay in the nematic phase. The final effect on the optical properties of the LC mixture (and thus on the spectral emission of the device) is not straightforward to predict, and at the moment it is still an open question. Anyway, even if this limit is not reached, there are conditions in which the LC molecules experience a relatively large thermal gradient inside the cell, which may limit the effective tuning range achievable by the LC mixture.

For that purpose, experimental inputs might be useful to develop a more exhaustive model which takes into account the heating effects on the optical properties of the LC mixture and on the performance of the devices. It seems, however, that thermal management is a crucial point for the good operation of the LC-based VCSEL. One viable way to partially solve the problem may consist in implementing strategies to limit the heat exchange toward the LC  $\mu$ -cell. One approach might be to deposit a  $\lambda/4$ -thick  $\text{SiN}_x$  anti-reflection (AR) layer on the InP semiconductor, and eventually add or increase the thickness of the SU-8 alignment grating, to thermally decouple the LC from the

semiconductor part. Such approaches have to be tested experimentally, but again FEM simulations can give useful insights on what can be expected in practice.

### **LC-VCSEL process: preliminary tests on 1<sup>st</sup> prototype**

On the basis of the good and promising results obtained with the tunable PD, two different active regions grown on 2-inch wafers have been realized by GS-MBE (samples n. 6133 and 6190). The structures have been designed to be optically-pumped (see Fig. 3.20) in order to simplify the process and quickly adapt the LC  $\mu$ -cell technology in the case of VCSELs. Once the main concept being validated, the goal will be to realize the electrically-injected version of the device.

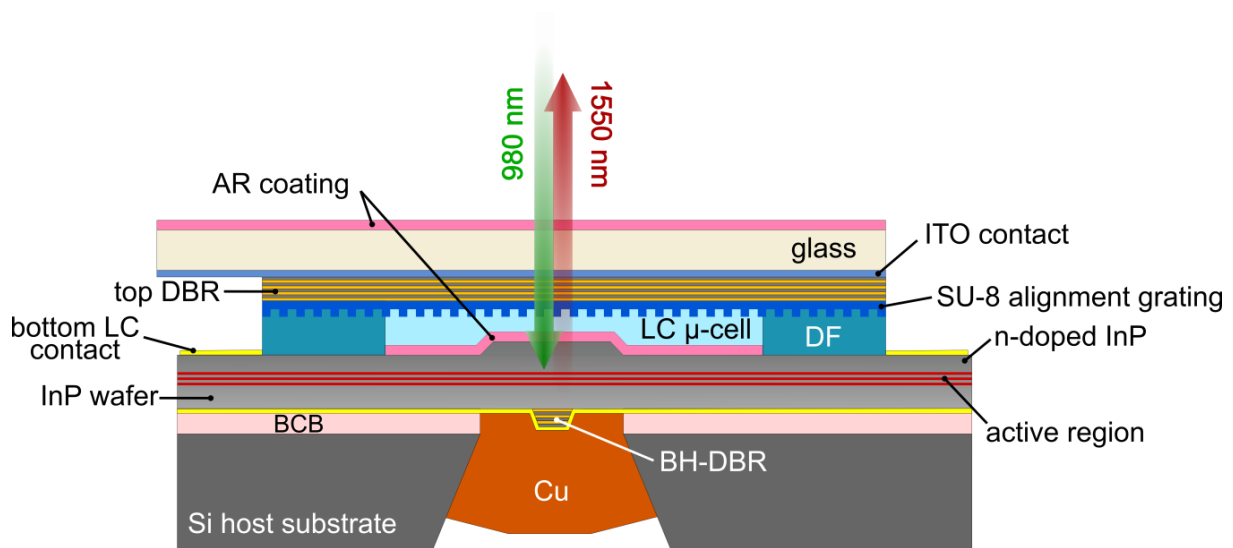


*Fig. 3.20 – Structure of the OP-LC-VCSEL for preliminary tests towards the electrically-injected version.*

In that case we highlight the presence of an n-doped InP layer, which is used to realize the bottom cell electrode instead of a bottom ITO contact, which would not be compatible with laser operation because of the high optical absorption at the emission wavelength which introduces too much optical losses, as discussed before.

Concerning the realization of the active region, due to epitaxial issues the control of the QDH stacked layers with emitted wavelength close to 1.55  $\mu\text{m}$  was rather difficult, and particularly when several sets were stacked on top of each other. Consequently, in QDH structures presenting 3 sets of 6 QDH layers (18 layers in total), the wavelength emission was most of the time centered at 1.6  $\mu\text{m}$  rather than the targeted 1.52  $\mu\text{m}$  (to get VCSEL operating in CW at 1.55  $\mu\text{m}$ ) in optically-pumped structures. As an alternative plan, we decided to growth two different samples: one is entirely based on MQWs, while the second one is a hybrid structure which integrates a first set of QDHs and two more sets of MQWs. In this last structure, the maximal gain is essentially imposed by the SQWs, whereas the QDHs brings the gain anisotropy necessary to clamp the VCSEL output polarization



aligned along the LC extraordinary axis. Fig. 3.21 details the different layers composing the samples. The differences in the two samples are summarized in Table 3.6.

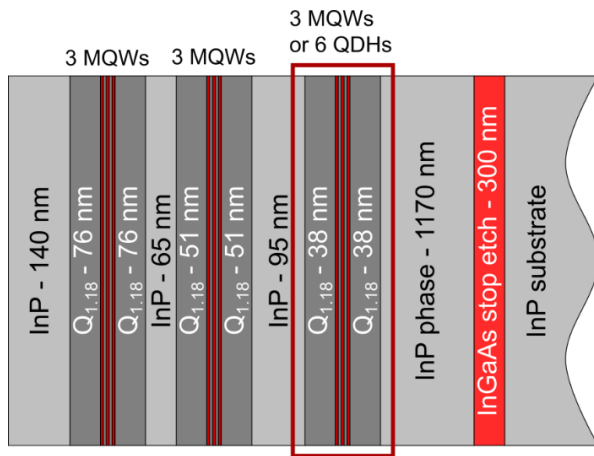


Table 3.6 – Structures parameters.

Sample #	PL emission peak	InP doping	Active region
6133	1.52 $\mu\text{m}$	n-doping ( $10^{17} \text{ cm}^{-3}$ )	3 $\times$ 3 MQWs
6190	1.52 $\mu\text{m}$	n-doping ( $10^{17} \text{ cm}^{-3}$ )	Hybrid: 3 $\times$ 2 MQWs + 6 $\times$ 1 QDHs

Fig. 3.21 – Detailed structure and parameters of samples 6133 and 6190 for the OP-LC-VCSEL prototype process.

From a practical point of view, in the case of the samples without the gain anisotropy, the polarization of the emission should be still ensured by the SU-8 alignment grating, which fixes it along the LC molecules. Fig. 3.22 visually describes the main steps for the realization of the OP-LC-VCSEL prototype:

- ① The active region (in this specific case a quarter of wafer belonging to the sample n. 6133) is bonded onto a Si host substrate according to the TSHEC process introduced in *Chapter 2*;
- ② The LC  $\mu$ -cells are realized, following the process developed for the tunable PD described in the previous chapter;
- ③ The LC electrodes are connected and the OP-LC-VCSEL is ready to be tested.

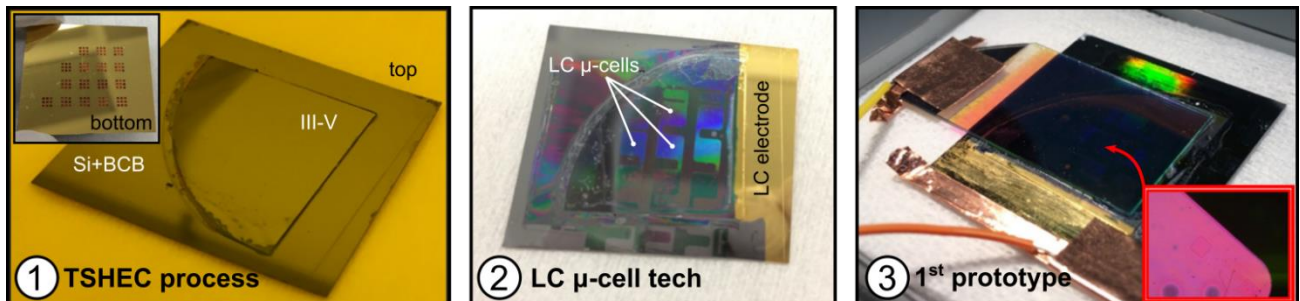


Fig. 3.22 – Different steps for the realization of the 1<sup>st</sup> OP-LC-VCSEL prototype.

At the moment of the writing of this Ph.D. manuscript, experiences are still ongoing, with some preliminary encouraging results. Hopefully, in the short term we would give new and detailed results.

### **3.6 Conclusions**

In this *Chapter 3* we discussed the development of tunable devices in vertical-cavity configuration, with a focus on VCSELs and photodiodes. After an introduction about the main results achieved by MEMS-based technology, which currently represents the main approach for the realization of vertical-cavity tunable devices, we detailed its main drawbacks. Indeed, MEMS are generally subjected to thermal and mechanical vibrations, which limit the spectral performance of the devices. Moreover the realization of micro-suspended cantilevers generally involves demanding and costly technological steps, eventually resulting in low yields. Finally, these devices are generally characterized by non-negligible power consumptions.

In this chapter we **proposed a new and original approach based on the exploitation of the electro-optic properties of liquid crystals, allowing the realization of monolithic, low-cost and low-power consuming devices**. The operating principle to achieve the wavelength tuning thanks to the application of a low AC voltage has been introduced and details on the physical and optical properties of LC have been given, with a focus on the well-known and commercially-available E7 mixture. In particular, the large birefringence offered by such a mixture has been exploited by LAAS and IMT Atlantique to realize a widely tunable Fabry-Pérot filter based on LC  $\mu$ -cells, in the framework of the ANR-ASTRID HYPOCAMP project.

A first proof-of-concept has been validated through the **demonstration of a tunable LC-based photodiode operating around 1.55  $\mu\text{m}$** , which showed a very satisfactory performance. Nevertheless, some improvements are possible. In particular, a cross-talk has been observed when the ordinary and the extraordinary modes are sufficiently close to each other. This has the effect to spoil the spectral performance of the photodiode. Investigations to find the origin of such a phenomenon are ongoing, but one simple method to solve the problem would be to place the ordinary mode outside the accessible wavelength range of the extraordinary mode by choosing an adequate thickness of the LC  $\mu$ -cell.

The results obtained with the tunable photodiode gave momentum for **the development of an active device such as an electrically-injected LC-based VCSEL**. In this case, particular attention should be paid on the choice of the active region. In particular, to efficiently exploit the large tuning range of LCs and obtain a broad tunable device, the gain curve of the active medium should be enough in amplitude and wideness to be used in a tunable VCSEL, together with being linearly polarized, in order to match with the extraordinary axis of the LCs.

For those spectral properties, InAs quantum dashes seem to be the perfect candidates to be integrated in such a LC-based VCSEL. Details on their physical and optical properties have thus



been given. **QDHs are characterized by a well-defined and stable state-of-polarization**, with typical polarization ratios of the order of 20% (or more) as attested by PL comparison with respect to InGaAsP SQWs-based active regions for which polarization ratios of few percent are generally achieved. Moreover, they are quite interesting for their **weaker wavelength shift as a function of the temperature**, which can be exploited to obtain a laser emission less dependent to the evolution of the internal temperature of the device.

Net modal gain measurements on SOA structures confirmed that **QDH structures have a wider spectral emission if compared to that of SQWs** (100 nm vs 58.2 nm for a net modal gain equal to  $10 \text{ cm}^{-1}$ , respectively). On the other hand, measurements on EELs structures showed that **the maximal net modal gain achieved by QDHs is nearly twofold lower if compared to that of SQWs** ( $35 \text{ cm}^{-1}$  vs  $60 \text{ cm}^{-1}$ , respectively). This is most likely due to the fact that the volume of the active material in the case of QDHs is less than in the case of SQWs. To compensate, **a larger number of QDH layers with respect to SQWs needs to be integrated in active regions**.

All the basic blocks developed for the LC-based PD have been the starting point for the **technological development of a LC-based VCSEL**. Very recently, **a first prototype based on a simplified optically-pumped architecture integrating conventional quantum wells has been realized** by using the TSHEC process and the LC  $\mu$ -cell technology. Experiments are currently on going, but some encouraging results are expected.

**Particular attention should be paid on the thermal management of these devices** as well, as suggested by the result of FEM simulations, which indicated that the temperature rise in the active region can be transferred to the LC  $\mu$ -cells. This might ultimately limits the tuning performance of the device, if strategies are not developed. A viable way might consist to thermally decouple the LC micro-cells from the VCSEL active region by using a dielectric layer, eventually coupled with a thicker SU-8 alignment grating.

Due to technical issues, the development of the tunable LC-OP-VECSEL device, which was initially planned, has been suspended. The reason was that preliminary tests to integrate the LC  $\mu$ -cells into a VECSEL cavity showed that the ITO layer used as electrode for driving the LC  $\mu$ -cell was not compatible for an insertion in an external configuration, due to its important optical absorption at the emission wavelength. Solutions involving a doped InP substrate to realize the top LC electrode may represent a viable alternative and are currently under consideration.

Despite this, the development of a QDH-based VECSEL represents the starting point for the realization of a compact tunable low-noise emitter at the telecom wavelength. The next part of the manuscript is thus devoted to the presentation of experimental results related to the realization and characterization of such an OP-QDH-VECSEL.

# **Chapter 4**

## ***VECSELs: basic concepts and advantages***

<b>4.1 Introduction .....</b>	<b>130</b>
<b>4.2. Key elements of a VECSEL .....</b>	<b>131</b>
4.2.1 Composition of the cavity.....	131
4.2.2 Pumping schemes .....	133
<b>4.3 Mode control in VECSELs .....</b>	<b>135</b>
4.3.1 Transverse mode selection for power scaling.....	135
4.3.2 Longitudinal modes.....	139
4.3.3 ...and single-frequency operation .....	140
<b>4.4 Output power .....</b>	<b>143</b>
4.4.1 State-of-the-art in multi-mode emission .....	143
4.4.2 Performance in single-frequency operation .....	147
<b>4.5 VECSEL cavity architectures and applications .....</b>	<b>148</b>
4.5.1 Cavity geometries .....	148
4.5.2 VECSELs applications .....	150
<b>4.6 Optimization guidelines for VECSEL design .....</b>	<b>152</b>
4.6.1 Thermal management in VECSELs .....	153
4.6.2 Resonant vs anti-resonant configurations and confinement factor .....	159
4.6.3 Optimization of laser threshold and output power.....	162
<b>4.7 Conclusions.....</b>	<b>167</b>

## 4.1 Introduction

In the context of this work, a second objective was to integrate a quantum dash-based active region in an extended cavity configuration, in order to realize a Vertical-External-Cavity Surface-Emitting Laser (VECSEL).

VECSELs are a new class of vertical-cavity lasers which are basically composed by a semiconductor gain mirror and an external high-reflective output coupler, to form a relatively long laser cavity (typically some cm in length). Although they may be considered as spatially cumbersome and power consuming optical sources, they present different key properties if compared with other laser technologies. As solid-state lasers, they take advantage of the external cavity, which allows obtaining a good circular and nearly diffraction-limited output beam, together with relatively high output power levels and narrow linewidths, and to obtain new functionalities by the insertion of different intra-cavity elements such as non-linear crystals, filters, saturable absorbers, and so on.

On the other hand, they also benefit from the wide spectral coverage resulting from bandgap engineering and the possibility of electrical injection offered by the use of a semiconductor active region, which are common characteristics of other semiconductor lasers families, as edge-emitting lasers or VCSELs.

Moreover, thanks to the long cavity configuration and the fast carrier dynamic of semiconductors, they can operate in the so-called Class-A regime, which is characterized to an inherently low and flat Relative Intensity Noise response down to the quantum limit, through a wide frequency range. Thanks to all the aforementioned advantages, which make them a versatile laser family, VECSELs are found in many applications, ranging from fundamental to applied physics, up to some commercially-available products.

In this chapter we will briefly address some of the basic operating principles and advantages of VECSELs, the state of the art and the related applications. In a second part we will discuss more in detail some essential rules for the design and the fabrication, with a particular focus on the case of the quantum dash-based VECSEL on InP, emitting in the L-band ( $\sim 1600$  nm), which will be the subject of the subsequent *Chapter 5* of this dissertation.

## 4.2. Key elements of a VECSEL

### 4.2.1 Composition of the cavity

A VECSEL basically consists in two main parts: a **semiconductor chip** fixed on a thermally-controlled heat-sink, and an **external mirror**, which simultaneously defines the laser cavity with the semiconductor chip and acts as output coupler. A simple plane-concave linear cavity is often used, and in most cases the active medium is optically pumped (see Fig. 4.1a, next page).

The VECSEL semiconductor chip (sometimes called  $\frac{1}{2}$ -VCSEL in the literature), which forms the Fabry-Pérot sub-cavity, is typically composed of three main parts, as shown in Fig. 4.1b:

- The **bottom DBR**, which has been directly adopted from the VCSEL technology (cf. *Chapter 1*), consists of a multi-stack of two alternating high and low refractive index layers with a quarter-wave thickness. Its operating principle is exactly the same as in the case of monolithically integrated VCSELs. It is generally designed to have a reflectivity as high as possible, ideally very close to 100%. However, since VECSELS are particularly subjected to thermal heating, a careful design of the DBR must be performed, even more than in the case of VCSELs. This involves the selection of suitable materials, in order to minimize the thermal impedance of the structure. In parallel, a suitable architecture can further improve the heat removal from the active region. We will come back on the thermal optimization of the DBR later in *Section 4.6.1*.
- The **active region**, which provides the gain required to obtain the laser effect and, in the case of optical pumping, it also acts as pump absorbing section. From a practical point of view, the active region of a VECSEL is similar to that of a monolithic VCSEL, and similar design rules are applied in both cases.

Until recently, VECSELS have been only realized by using quantum wells (QWs) based active media, and most of them are still based on such an active layer, since it represents the most performing solution in terms of emitted maximal power. Despite this fact, low-dimensional systems such as quantum dots (QDs) started being employed in the gain section of VECSELS, thanks to their peculiar properties arising from their reduced dimensionality. Further discussions about the design of the active region, together with a state-of-the-art in terms of emitted power (for QWs- and QDs-based VECSELS), will be addressed in the following sections.

- The **spacer** (or window or phase layer), which provides the carrier confinement, preventing carriers from reaching the surface and be lost due to non-radiative recombination processes. The spacer also acts as phase layer. Its thickness is indeed designed in order to have a resonant (or anti-resonant) Fabry-Pérot sub-cavity, according to the specific needs. In the case of aluminum-based devices, it also protects the underlying layers from oxidation. Sometimes an anti-reflection (AR) coating can be deposited on the surface, in order to finely tune the cavity length as desired.

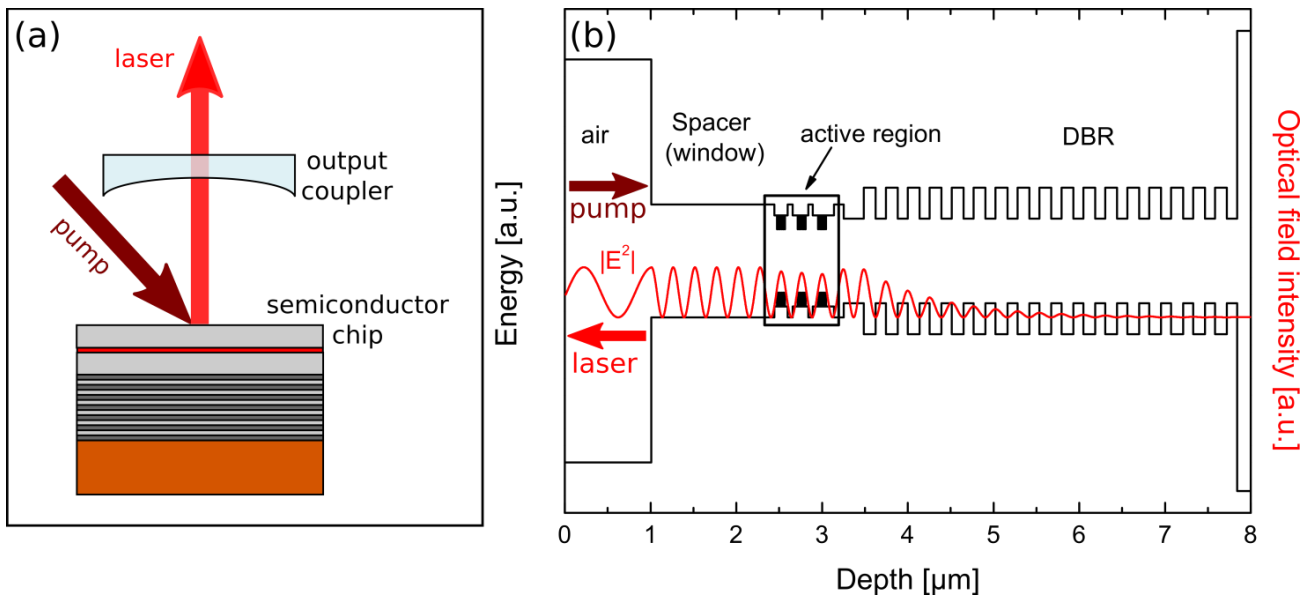


Fig. 4.1 – Example of a VECSEL chip design: (a) semiconductor chip inserted in a two-mirror external linear cavity and (b) band diagram of the different sections (black curve) and resonant optical field intensity at the designed emission wavelength  $\lambda_{\text{laser}}$  (red curve). In this example optical pumping is employed.

The design of the semiconductor chip generally depends on the specific emission wavelength of the device, but from a general point of view it is possible to identify some key rules that are common to all the VECSELs devices. The choice of the targeted emission wavelength also imposes the choice of the particular material system, as already discussed in **Chapter 1**. This choice has a direct impact on the performance of the devices, because of the peculiar properties of each material system. As in the case of VCSELs, GaAs-based VECSELs generally outperforms their counterparts based on other material systems, in terms of maximum emitted power. This is mainly due to the technological maturity and the physical properties of the GaAs systems. Nevertheless, depending on the specific applications, other semiconductors are currently employed to realize VECSEL devices, as InP or GaSb. Table 4.1 (next page) presents an overview of the different III-V semiconductor systems composing the active region and the substrate of demonstrated VECSELs, depending on the specific wavelength range of emission and material system.

**Table 4.1 – Material systems employed for VECSELs.**

Wavelength range [nm]	Active region composition (active layers* / barriers)	Substrate
370-440	InGaN / GaN	sapphire/SiC
640-690	InGaP / AlInGaP	GaAs
650-740	InP QDs/ AlInGaP	GaAs
780-900	GaAs / AlGaAs InAlGaAs / GaAs	GaAs
920-1350	InAs QDs/ InGaAs InGaAs(N) / GaAs InGaAs / GaAs	GaAs
1270-1900	InGaAsP InGaAlAs	InP
1900-2800	InGaAsSb	GaSb

\*the active layers are QWs, if not otherwise specified. Table adapted from [Okhotnikov2010], © 2010 WILEY-VCH.

Concerning the **output coupler**, its reflectivity generally is of the order of 95-99%. In most cases a concave mirror is employed to form a simple linear plane-concave cavity. However, depending on the applications, the cavity configuration can be more complicated. Besides that, the output coupler is also employed to control the transverse profile of the emitted beam. We will address these points later in this chapter.

## 4.2.2 Pumping schemes

VECSELs can be either optically pumped or electrically injected. Depending on these two different excitation schemes, their design can be significantly different, as shown in Fig. 4.2 (next page).

Both approaches present pros and cons, but optical pumping is generally preferred with respect to electrical injection, in the case of such devices. The reason underneath this choice is related to the fact that a homogeneous and confined injection of carriers across a relatively large surface (some hundreds of  $\mu\text{m}$  in diameter), which is common in the case of VECSELs, is relatively easy to achieve with optical pumping. As a result, optically-pumped chips have the advantage to be relatively easy to design and realize with respect to their electrically-pumped version, since they require simpler growing steps and limited cleanroom process.

Conversely, several technological aspects make electrically-injected VECSELs more difficult to realize: an efficient injection of carriers across a wide area typically involves the use of BTJs in combination with thicker doped spreading layers and doped DBRs. Additionally, highly doped layers usually lead to high free carrier absorption and Joule heating, which degrade the laser

threshold and efficiency. Furthermore, in the case of electrical pumping, the uniform injection of carriers is typically limited to areas of few tens of  $\mu\text{m}$  in diameter, which once more limits the maximum emitted power. All these difficulties translate in a significantly lower emitted power levels for the electrically-pumped version, which generally lies in the mW range.

For this reason, up to now the optical pumping scheme continues to be the preferred solution for VECSELS, mainly because it ensures power scaling to the Watt level by simply changing the dimensions of the pumped area, which is clearly not easy to achieve in an electrically-pumped version, since the pumped area is defined by the electrical contacts and the BTJ. Obviously, the advantages of the simple optically-pumped structure are paid by a more complex optical setup, since an external pump module is necessary, making this solution more cumbersome with respect to the electrically-injected counterpart.

However, despite all the technological complications of electrically-injected VECSELS, their development would be a really breakthrough for such a laser technology, because all the advantages inherent to electrically-driven devices like higher compactness, higher power efficiency, faster cavity alignment, etc. To this aim we can cite the works of U. Keller group at ETH Zurich and E. Kapon group at EPFL Lausanne on GaAs-based and InP-based EP-VECSELS, respectively [Pallmann2013, Caliman2013]. Moreover, optical pumping also suffers from some drawbacks in terms of noise behavior, as generally the intensity fluctuations of the pump are transferred to the VECSEL, especially in the low frequency range. This can be a limit in the case of metrological applications requiring high stability.

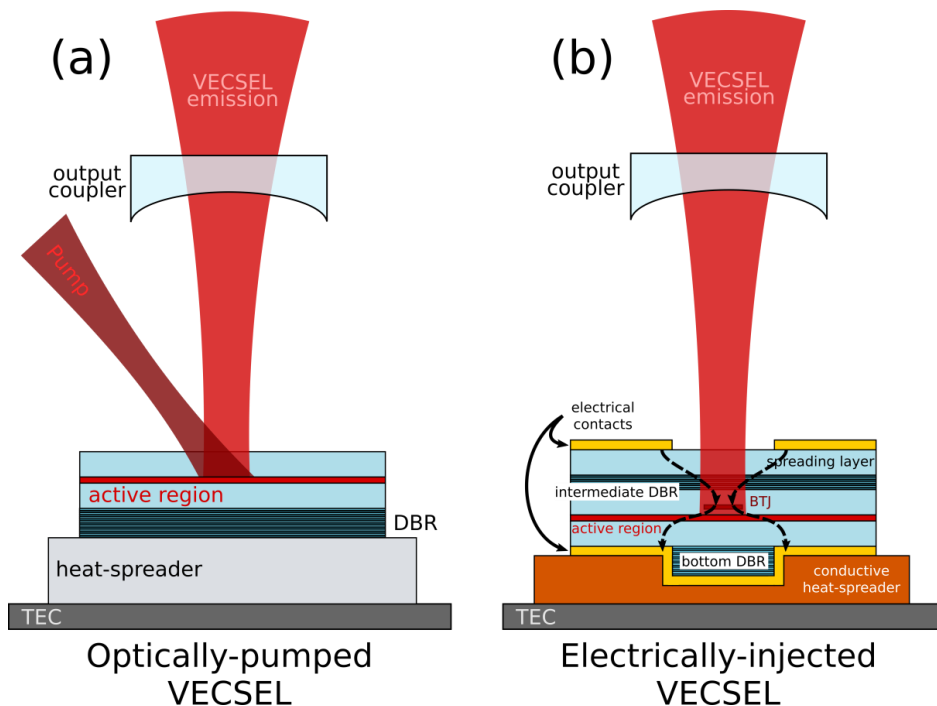


Fig. 4.2 – Excitation architectures in VECSELS: (a) optically-pumping and (b) electrically-injection.



### 4.3 Mode control in VECSELS

We will now describe the main characteristics of VECSELS in terms of mode control, and how to reach a simultaneous (fundamental) single-transverse and single-longitudinal emission regime. When these two conditions are satisfied, and the laser is also operating in a single polarization mode, we refer to this with the expression “single-frequency” operation. Owing to the fact that a single mode is resonant in the cavity, a single-frequency emission also implies a narrower linewidth with respect to the case in which the laser is operating in a multi-mode regime (transverse and/or longitudinal).

Single-frequency lasers are particularly relevant to all optics applications requiring a high degree of spectral purity, such as (but not limited to) fiber-sensing and interferometry, microwave optical carrier generation, spectroscopy and metrology applications, to mention but a few examples.

In this context, the external cavity plays an important role, giving the possibility to select a precise transverse mode by changing the spatial matching between the pump and the cavity spots. Additionally, the external cavity allows the insertion of intra-cavity optical elements. Longitudinal-mode control can be thus achieved thanks to intra-cavity filters, as presented in *Section 4.3.3*.

#### 4.3.1 Transverse mode selection for power scaling

In *Chapter 1* we discussed the main differences between edge-emitting lasers (EELs) and VCSELS. If compared to EELs, VCSELS ensure high quality circular beam profiles, which is a considerable advantage in the case of fiber coupling. Unfortunately, one of the most limiting factors of VCSELS is represented by the low achievable power in single-frequency operation. Indeed, while single-longitudinal mode operation is guaranteed by the micrometric-long cavity, achieving single-transverse mode operation in VCSELS is non-trivial because transverse-mode selection is generally determined by the dimensions of the pumped area (some  $\mu\text{m}$  in diameter) through spectral gain mode filtering and optical index-guiding mechanisms. Non-uniform current injection or thermal lenses phenomena can complicate the mode selection and, in practical cases, these phenomena are generally difficult to forecast and mitigate.

In step-index devices as VCSELS or EELs, because of the index mode-guiding mechanism and the circular geometry, the fundamental and higher transverse modes can be expressed in terms of linearly polarized  $\text{LP}_{mn}$  modes<sup>1</sup>. They are optically confined in the same cylindrical waveguide and have approximately the same transverse spatial extent (see Fig. 4.3a, next page), which may easily

---

<sup>1</sup> The solution to this problem is analogous to the one applied in fiber optics to compute the guided modes in a step-index optical fiber.  $(m,n)$  is the mode-order,  $(0,1)$  being the fundamental mode.

results in higher mode excitation in strong pumping conditions [Michalzik2013]. So that, to prevent the appearance of high-order modes, the pumped region is generally limited to few micrometers in diameter, and the pumping level is kept low. This, in addition to the short length of the active region, limits the maximum achievable single-mode output power to typically few mW.

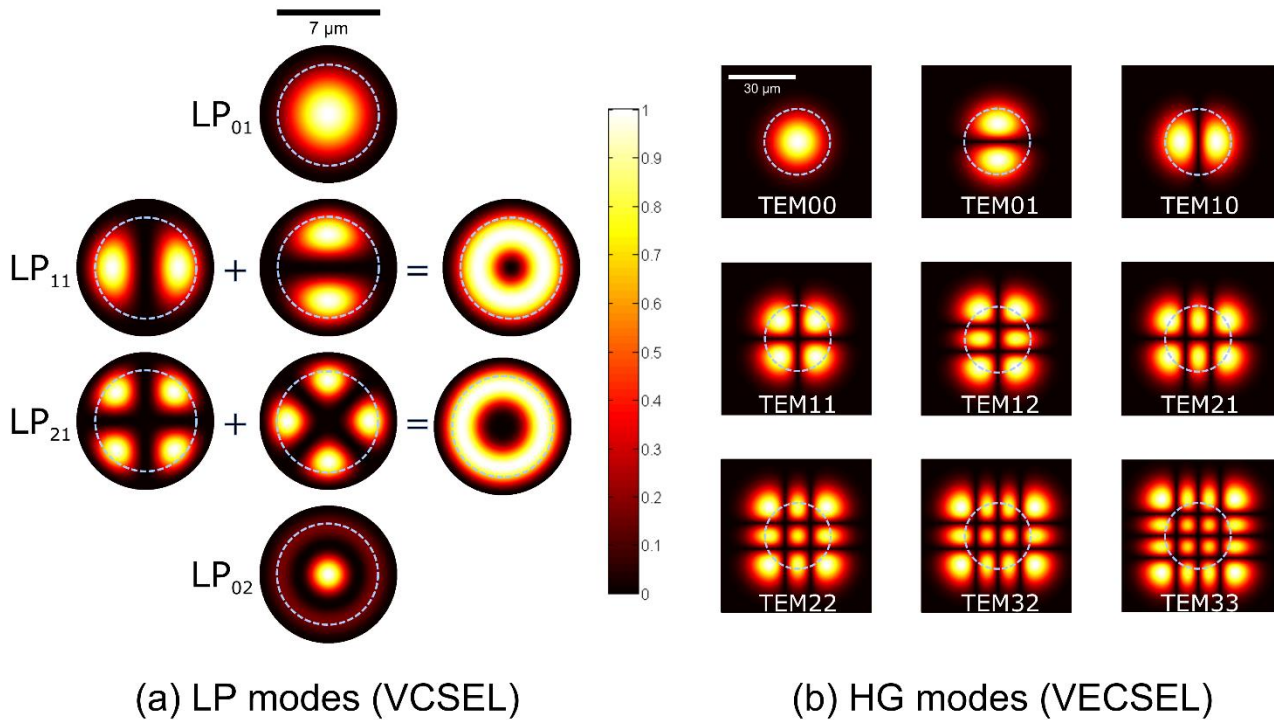


Fig. 4.3 – (a) Computed normalized intensity distribution in the transverse plane for (a) a cylindrical step-index 850 nm-emitting VCSEL for different  $LP_{nm}$  modes with pumped region of  $7\ \mu\text{m}$  in diameter and for (b) HG modes inside a 1550 nm-emitting VECSEL cavity with a waist of  $\omega_0 = 30\ \mu\text{m}$ . Dashed cyan circles show the extent of the fundamental mode in both cases.

The need to increase the maximum emitted power, while simultaneously keeping a good circular fundamental output mode, led to the development of a different approach in which the top DBR of the VCSEL is replaced by a high reflective external output mirror and the cavity is no more at the micrometric scale, but is typically some mm or cm in length. Combining together all those aspects, the concept of VECSEL appeared. The first VECSEL device was demonstrated in a simple and relatively compact linear cavity [Kuznetsov1997], which consists in a plane-concave stable resonator, as the one depicted before in Fig. 4.2a, composed by the optically pumped semiconductor chip mirror at one end and the output coupler at the other.

Because of the semiconductor chip is few  $\mu\text{m}$  in thickness, the external cavity of the VECSEL can be considered almost completely composed by air. So that, the optical modes are no more index-guided but they propagate in free space and are submitted to the laws of the Gaussian optics. The spatial extent between the fundamental Hermite-Gaussian (HG)  $TEM_{00}$  mode and higher HG

$TEM_{mn}$  modes is no more the same, as attested by Fig. 4.3b<sup>2</sup>. It approximately scales with  $\sqrt{n}$ ,  $n$  being the order of the Hermite polynomial [Siegman1986].

This is a key point for achieve power scaling in VECSELS while keeping a fundamental  $TEM_{00}$  mode operation. Indeed, the dimensions of the pumped area are defined by the pump spot on the semiconductor chip surface, while the transverse modes control can be independently provided by the spatial gain filtering, which is obtained by adjusting the position of the external output coupler with respect to the semiconductor chip. This allows optimizing the mode matching between the fundamental  $TEM_{00}$  transverse mode and the pumped region in order to filter all the higher-order  $TEM_{mn}$  modes, which are subjected to optical losses because of a weaker mode matching, as shown in Fig. 4.4a.

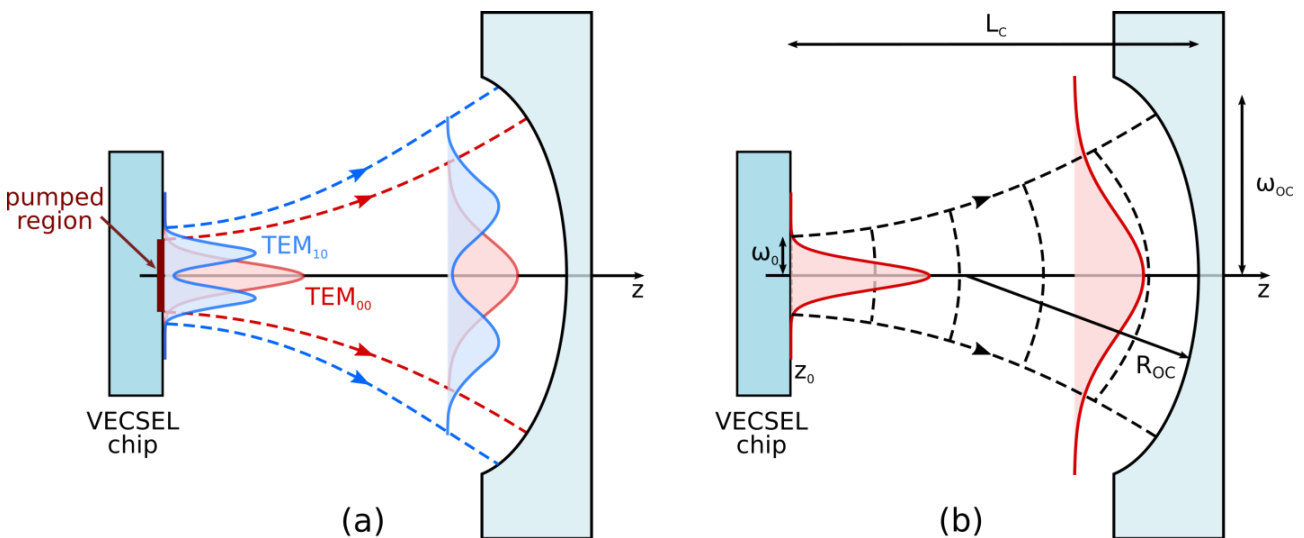


Fig. 4.4 – Gaussian beam propagation inside a plane-concave cavity: (a) transverse mode selection and (b) characteristic quantities of a plane-concave cavity.

In such a way it is possible to increase the optical beam diameter to a precise value, without degradation of the circular emitted beam, provided that the power density is sufficient to get the laser threshold. Consequently, the output power can sensibly increase, since it roughly scales as the area of the pumped region. Using this approach, pumping areas of few hundreds of micrometers can be employed, circumventing the main limitation of monolithic VCSELs.

The scaling of the pumped area not only results in the increasing of the emitted power, but also in the decreasing of the thermal overheating of the semiconductor chip, since now the optical density is lower. This prevents to reach the optical damage of the chip.

<sup>2</sup> Despite their circular geometry, VECSELS generally sustain HG modes (which are typical of a cavity with a rectangular symmetry) rather than Laguerre-Gaussian (LG) modes (typical of a cylindrical cavity). This is due to the fact that small anisotropies (such as an elliptical pumping, slightly tilted surfaces, etc.) can break the circular symmetry and promote HG instead of LG modes.

Since higher-order transverse modes have a larger spatial extent, fundamental-transverse emission can be also forced by using an intra-cavity iris with an appropriate aperture size, in order to introduce diffraction losses for the higher-order modes. The main drawback of this solution is that the output power and the efficiency of the laser are significantly degraded.

For a plane-concave resonator, as the one depicted in Fig. 4.4b, a stable Gaussian TEM<sub>00</sub> mode exists for a cavity length  $L_C$  smaller than the curvature radius  $R_{OC}$  of the spherical output mirror. In this case, the  $1/e^2$  waist of the fundamental mode on the VECSEL chip  $\omega_0$  and on the spherical mirror  $\omega_{oc}$  are given by<sup>3</sup> [Okhotnikov2010]

$$\omega_0 = \sqrt{\frac{\lambda L_C}{\pi} \left( \frac{R_{OC} - L_C}{L_C} \right)^{1/2}} \quad (4.1a)$$

$$\omega_{oc} = \sqrt{\frac{\lambda R_C}{\pi} \left( \frac{L_C}{R_{OC} - L_C} \right)^{1/2}} \quad (4.1b)$$

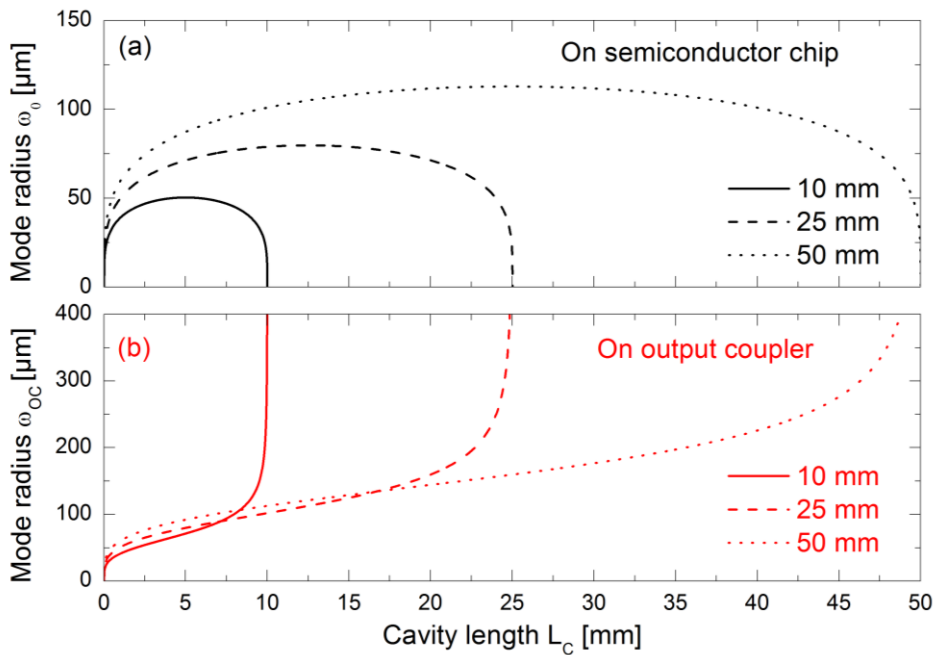


Fig. 4.5 – Calculated TEM<sub>00</sub> mode spot radius vs cavity length (a) on the VECSEL chip and (b) on the output coupler for different values of the radius of curvature  $R_{OC}$  (10, 25 and 50 mm) at  $\lambda = 1.6 \mu\text{m}$ .

The evolution of the two waists as a function of the cavity length is depicted in Fig. 4.5, for different values of the radius of curvature  $R_{OC}$  of the output coupler. These curves have been

<sup>3</sup> These results can be obtained in the framework of ABCD matrix formalism [Kogelnik1965].

obtained by using a MATLAB<sup>®</sup> script based on the ABCD propagation matrix method [Matlab], which is described in *Appendix A*. This script is particularly useful to design more complicated optical cavities (presenting intra-cavity elements) than the simple plane-concave resonator, such as the one of the bi-frequency VECSEL, as it will be presented later in *Chapter 6*.

As shown in the figure, the chip waist has a maximum for a cavity length equal to half the curvature radius, and rapidly vanishes for cavity lengths approaching zero or a length equal to the  $R_{OC}$ . As said before, the chip waist should match with the pump spot size ( $\omega_0 \sim \omega_{pump}$ ), in order to favor the TEM<sub>00</sub> emission and have efficient pumping. The curve thus helps choosing the good radius of curvature and cavity length that ensure the stability and the fundamental mode operation of the VECSEL, for a given pump spot size. In practice, for relatively small pumped areas (i.e.  $\omega_{pump} \sim$  some tens of  $\mu\text{m}$  in radius), the TEM<sub>00</sub> operating region is near the edge of the curve ( $L_C \sim R_{OC}$ ). In this area, small changes in the cavity length translate into large variations of the waist size, so that a fine adjustment of the experimental setup must be performed. In the case of large pumped regions ( $\omega_{pump} \sim$  few hundreds of  $\mu\text{m}$  in radius), fundamental mode matching requires bigger radius of curvature of the output coupler.

### 4.3.2 Longitudinal modes...

Owing to their long cavity, the spacing between two adjacent longitudinal modes of a VECSEL is very small, so that this device intrinsically operates in the multi-longitudinal regime if no filtering mechanisms are employed. The longitudinal modes spacing of a cavity of length  $L_C$  and group index  $n_g$  is related to its free spectral range (FSR), which is defined as

$$\Delta\nu_{FSR} = \frac{c}{2n_g L_C} \quad \Delta\lambda_{FSR} = \frac{\lambda^2}{2n_g L_C} \quad (4.2a,b)$$

for the frequency and wavelength domains, respectively. Here  $c$  is the speed of light in vacuum. The number of longitudinal lasing modes is then limited by the spectral width of the semiconductor medium composing the active region and by the cavity losses.

In the case of VECSELS with cavities of some cm in length, this allows the simultaneous lasing of a large number of longitudinal modes (cf. Fig. 4.6, next page). Generally, standard commercially-available optical spectrum analyzers (OSA) are not sufficiently able to resolve the narrow spacing between the longitudinal modes of a VECSEL. Fabry-Pérot interferometers are thus typically employed to assess if the laser is operating in a single-frequency mode. Electrical spectrum

analyzers (ESA) can be also used in combination with fast photodiodes to reveal the spectral signature of the beating tones between the modes of a multi-frequency laser.

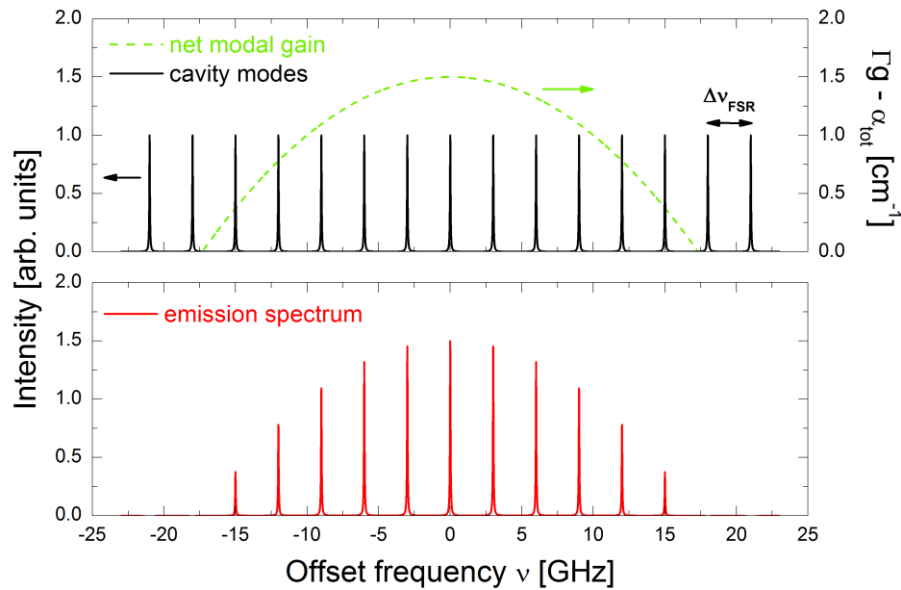


Fig. 4.6 – Schematic illustration of (top) the calculated longitudinal modes of a 50 mm-long cavity ( $\Delta\nu_{FSR} \approx 3$  GHz, i.e. 25.6 pm, in black) at  $\lambda = 1.6 \mu\text{m}$  and the net modal gain (in green). (bottom) The resulting emission spectrum.

As explained at the beginning of this chapter, in the context of the microwave optical signal generation, the spectral purity of the laser sources is one of the main concerns. In order to obtain a single-frequency (i.e. single-transverse and single-longitudinal) operation and avoid the beating resulting from several simultaneously lasing modes, spectral filtering must be employed.

### 4.3.3 ...and single-frequency operation

On the other hand, thanks to the accessible external cavity, single-longitudinal regime can be reached by inserting wavelength-selective elements such as birefringent filters [Zhang2014], gratings [Giet2006, Giet2007] or etalons filters [Baili2014] inside the cavity. In the context of our work, we limit ourselves to the use of etalon filters.

An etalon filter act as an intra-cavity Fabry-Pérot interferometer (see Fig. 4.7a on next page). Its role is to introduce selective losses in order to suppress or strongly attenuate all the modes which are not resonant with respect to its transfer characteristic.

In the general case of non-normal incidence ( $\theta_i \neq 0$ ) of the impinging wave to the surface of the etalon, the transmission of the etalon is thus given by [Koechner1996]:

$$T = \left[ 1 + \frac{4R}{(1-R)^2} \sin^2 \left( \frac{\Delta\varphi_{eta}}{2} \right) \right]^{-1} \quad (4.3)$$

where  $R = \sqrt{R_1 R_2}$  ( $R_1$  and  $R_2$  being respectively the reflectivity of the two faces) and  $\Delta\varphi_{eta}$  is the phase shift for a round-trip inside the cavity, and is given by

$$\Delta\varphi_{eta} = \frac{2\pi}{\lambda} \cdot 2 \cdot n_{eta} \cdot t_{eta} \cdot \cos(\theta_{eta}) \quad (4.4)$$

where  $\lambda$  is the wavelength,  $n_{eta}$  is the refractive index of the material composing the etalon,  $t_{eta}$  is the thickness of the etalon and  $\theta_{eta} = \theta_i/n$  is the angle of refraction in the material.

The transmission  $T$  reaches his maximum ( $T_{max} = 1$ ) when the following condition is satisfied

$$2 \cdot n_{eta} \cdot t_{eta} \cdot \cos(\theta_{eta}) = m\lambda, \quad m = 0, 1, 2, \dots \quad (4.5)$$

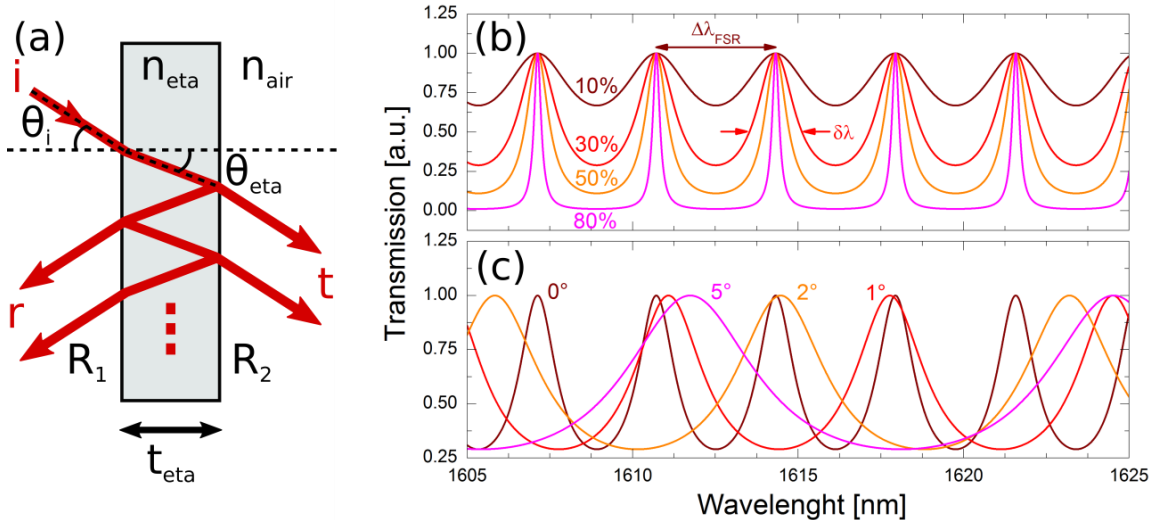


Fig. 4.7 – Working principle of an etalon filter: (a) interferences of a plane wave in a plane-plane cavity transmission characteristic vs wavelength for (b) different values of the reflectivity  $R$  and (c) different angles  $\theta_{eta}$ . The curves are obtained for a 250  $\mu\text{m}$ -thick fused silica etalon ( $n_{eta} \approx 1.44$  at 1.55  $\mu\text{m}$ ).

From Eqs. 4.3 and 4.4, we can clearly see that the transmission depends on the characteristics of the etalon (its reflectivity  $R$ , thickness  $t_{eta}$ , refractive index  $n_{eta}$ , and incident angle  $\theta_i$ ).

Figs. 4.7b,c show the computed transmission of a fused silica etalon with a thickness equal to 250  $\mu\text{m}$ , as a function of the wavelength, for different values of the faces reflectivity and orientation  $\theta_{eta}$ .

Two adjacent peaks of the transmission function are separated by the free spectral range of the etalon, which is equal to<sup>4</sup>

$$\Delta\nu_{FSR,eta} = \frac{c}{2 \cdot n_{eta} \cdot t_{eta} \cdot \cos(\theta_{eta})} \quad (4.6a)$$

or, in the wavelength domain,

$$\Delta\lambda_{FSR,eta} = \frac{\lambda^2}{2 \cdot n_{eta} \cdot t_{eta} \cdot \cos(\theta_{eta})} \quad (4.6b)$$

In the case on normal incidence ( $\theta_i = 0^\circ$ ), the FSR is about 3.6 nm. We can also define the finesse of the etalon as

$$Finesse = \frac{\Delta\lambda_{FSR}}{\delta\lambda} \quad (4.7)$$

where  $\delta\lambda$  is the full width at half maximum of a transmitted peak. The finesse gives a measure of the degree of selectivity of the etalon filter of two adjacent wavelengths.

In the practice, once an etalon filter is selected according to its characteristics (thickness, material and optical properties), it is still possible to tune its response by tilting it, in order to change the path length that the optical wave experiences by passing through, and select a different emission wavelength (as represented in Fig. 4.7c).

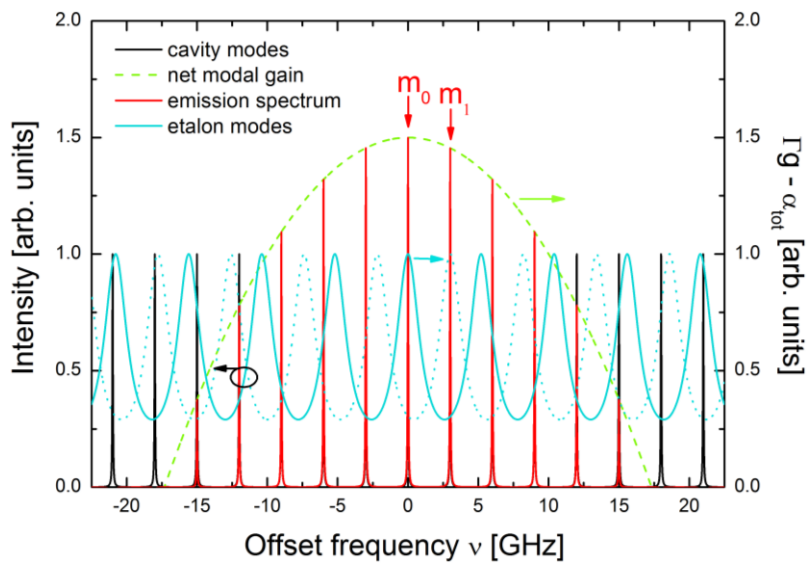


Fig. 4.8 – Mode selection with an intra-cavity etalon filter.

<sup>4</sup> Please note that Eqs. 4.6a,b are the generalization of Eqs. 4.2a,b in the case of non-orthogonal incidence.



Fig. 4.8 shows the schematic principle of mode selection with a Fabry-Pérot etalon filter. The laser cavity is the same as the example depicted in Fig. 4.6, with a *FSR* of 3 GHz. By inserting the etalon filter inside the cavity, we are able to select the  $m_0$  lasing mode which lays on a maximum of the transfer characteristic of the etalon filter (solid cyan curve), while the other  $m_i$  modes are suppressed. By changing the angle of incidence of the etalon (dotted cyan curve), we are able to tune its transmission curve, selecting for instance the  $m_l$  mode. This provides a way to tune the VECSEL emission by changing the etalon orientation.

## 4.4 Output power

### 4.4.1 State-of-the-art in multi-mode emission

As discussed earlier in the chapter, continuous progress in semiconductor materials technology and laser design allowed regular improvements in devices' performance.

Concerning VECSELS, they were originally developed to overcome the key-problem with conventional semiconductor lasers: how to increase the emitted power while preserving high quality circular emission profiles. We saw that this can be achieved thanks to the external cavity configuration of VECSELS, which allows easily increasing both the pump spot and the cavity mode sizes while ensuring the filtering of higher transverse modes as the pumped area is increased, resulting in a power scaling with a preserved TEM<sub>00</sub> beam. Taking into account the thin thickness of the semiconductor chip (some  $\mu\text{m}$  in the case of VECSELS), the heat flow is basically one-dimensional, so that increasing the pumped area also helps in redistributing the heat generated by the pump, especially if appropriate solutions are employed for thermal management (as further discussed in *Section 4.6.1*).

#### Quantum wells-based VECSELS

Starting from the first demonstration of a relatively high power VECSEL ( $> 0.5$  W) [[Kuznetsov1997](#)], lot of effort has been made to further push the performance and the power scaling of these devices, according to different material systems, still attracts lot of interest. Nowadays the available output power range covered by VECSELS is very wide, from tens of mW up to tens of W and beyond, depending on the material system and the emission wavelength range. Fig. 4.9 on next page gives a quick overview of the reported output power achieved by VECSEL technology for different semiconductor material systems and wavelengths ranging from  $0.2 \mu\text{m}$  up to  $2.4 \mu\text{m}$  (the graph is taken from [[Okhotnikov2010](#)] and updated to 2010). If we limit our

attention to the fundamental single-chip configuration (single- or multi-mode emission), maximum output powers have been mainly reported in the 1-40 Watt range from 700 to 2400 nm. Emitted power can be further linearly increased if multi-chip and/or multi-pumping schemes are employed, as proposed by Saarinen et al., Fan et al. and Hunziker et al. [[Saarinen2006](#), [Fan2006](#), [Hunziker2007](#)]. Thanks to high-quality chips, careful design and thermal optimization, more recent results on single-chip devices further pushed the limits towards higher values. For instance, we can quote the work of Heinen et al. from Marburg University, which reported 106 W in multi-transverse mode operation [[Heinen2012a](#)], and which represents the highest reported output power value for a single-chip VECSEL so far. The same group demonstrated up to 23 W in single-frequency operation in 2014 [[Zhang2014](#)]. These two last record results have been obtained at 1  $\mu\text{m}$  using highly-performant InGaAs QWs on GaAs substrates. Indeed, InGaAs QWs benefit from a relatively high gain, and are generally pumped with high-power 808 nm laser diode. In addition, since GaAs-based devices take advantage from thin, thermal efficient and lattice-matched DBRs, they generally show significantly higher output power levels if compared to VECSELs based on InP or GaSb.

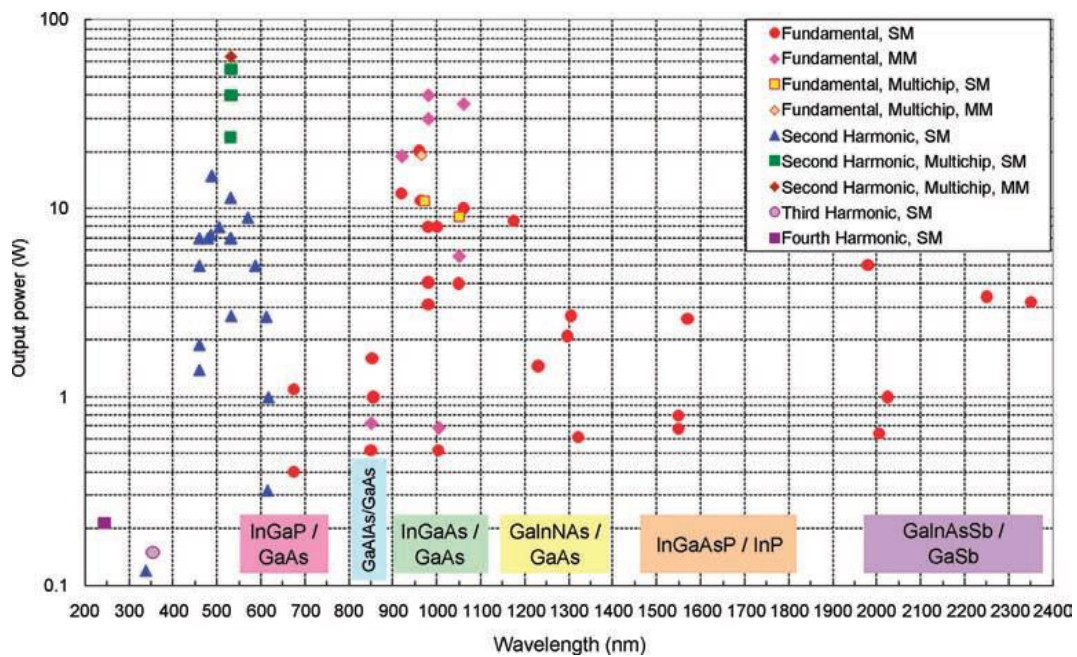


Fig. 4.9 – Reported VECSEL output power vs emission wavelength for different material system (reproduced with permission from [[Okhotnikov2010](#)], © 2010 WILEY-VCH).

The limitations encountered by these last two material systems are mainly due to the lack of thermally efficient compounds for the near or mid-infrared region, so that the thermal conductivity of the materials is relatively low if compared to GaAs-based system. Moreover, as discussed for VCSELs, the lattice-matched materials employed to realize epitaxially-grown DBRs show a low refractive index contrast, so that thick structures are needed to attain high reflectivity values, resulting in thick stacked structures with a high thermal impedance. Nevertheless, in the case of

InP-based VECSELS, the earlier demonstrations of lasing operation involved monolithically grown devices integrating epitaxially-grown lattice-matched InP/InGaAsP DBRs [Symonds2004a, Lindberg2004a, Lindberg2004b, Lindberg2005]. As a result of the poor thermal dissipation of such materials, the emitted power was also relatively low. The need to improve emitted output powers towards the Watt-regime at 1.3  $\mu\text{m}$  and 1.55  $\mu\text{m}$  pushed the development of different strategies to overcome this bottleneck. These solutions encompass the replacement of the already mentioned epitaxially-grown InP/InGaAsP bottom DBR by hybrid dielectric-metallic mirrors [Symonds2004b], or by highly-conductive GaAs/Al(Ga)As reflectors integrated in the VECSEL chip by means of metamorphic growth [Tourenco2007] or wafer fusion techniques [Sirbu2014, Sirbu2015], eventually in combination with the help of high conductive heat-spreader layers (such as diamond) [Lindberg2005, Lyytikäinen2009, Lyytikäinen2011]. DBRs based on GaAs compounds (GaAs/AlGaAs) have been also proposed for VECSEL based on GaSb substrates [Balakrishnan2008]. Thermal management strategies (with a focus on InP-based VECSELS) will be addressed further in detail in *Section 4.6.1*.

To summarize, Table 4.2 presents some of the most important achievements in terms of fundamental continuous wave (CW) emitted power ( $> 100$  mW) and temperature of operation for QWs-based VECSELS covering the 665-2800 nm range, in multi-mode regime. Details about the active region composition (number and type of quantum wells) and emission wavelength are also given. These achievements have been obtained in the GaAs, InP and GaSb material systems.

**Table 4.2 – Best reported CW performance of QW-based VECSEL in multi-mode operation.**

Year	Group(s)	Active region	Substrate	$\lambda$ [nm]	$P_{\text{out}}$ [W]	$T_{\text{op}}$ [°C]	Author (ref.)
2016	Univ. Stuttgart	$\times 20$ InGaP	GaAs	665	2.5	10	[Mateo2016]
2008	ETH Zurich	$\times 7$ InGaAs		960	20.2	-20	[Rudin2008]
2012	Univ. Marburg	$\times 10$ InGaAs		1020	106	0	[Heinen2012a]
2013	Tampere Univ.	$\times 10$ InGaAs		1180	23	0.2	[Leinonen2013]
2017	Tampere Univ. - EPFL	$\times 10$ AlGaInAs	InP	1275	33	-5	[Leinonen2017]
2011	Tampere Univ. - EPFL	$\times 8$ AlGaInAs		1480	4.8	8	[Lyytikäinen2011]
2004	Chalmers Univ.	$\times 20$ InGaAsP		1545	0.78	-33	[Lindberg2004c]
2008	Tampere Univ. - EPFL	$\times 10$ AlGaInAs		1570	2.6	10	[Rautiainen2008]
2012	Tampere Univ. - EPFL	$\times 5$ AlGaInAs		1580	4.6	8	[Rantamäki2012a]
2013	Fraunhofer IAF	$\times ?$ InGaSb	GaSb	2080	8	-15	[Kaspar2013]
2011	Tampere Univ.	$\times 15$ InGaAsSb		2470	0.6	5	[Paajaste2011]
2011	Fraunhofer IAF	$\times 10$ InGaAsSb		2800	0.12	20	[Rösener2011a]

At this point, it is worth to notice that beside the differences inherent to the specific employed material system, the design of the active region and the approaches used for thermal management, the values of the emitted output power reported in the literature highly depend on additional parameters used during the characterization of the devices, such as the choice of the pump spot dimensions, the output coupler reflectivity, the pump wavelength and power or the cooling temperature. It is thus difficult to make a fair comparison between all these different approaches. Anyway, if we focus on InP-based VECSELS emitting around 1.55  $\mu\text{m}$ , InAlGaAs QWs generally shows better performance with respect to InGaAsP QWs.

For the sake of completeness, we mention that fundamental emission from GaN-based VECSELS has also been reported in the UV range, but the power are very limited due to the poor thermal properties and low gain provided by such a material system [Park2003, Debusmann2009, Wunderer2013], and frequency doubling is typically employed to overcome these limitations and access the UV and visible range [Hastie2006, Kim2006].

### Quantum dots-based VECSELS

As this second part of the manuscript deals with the development of a quantum dash-based VECSEL source, it is thus worthwhile to also present the state-of-the-art related to the development of such devices integrating nanostructured active regions. Demonstrations of laser emission with low-dimensional nanostructures VECSELS concern only the case of quantum dot-based devices in the 600-1300 nm range, as presented in the chart of Fig. 4.10.

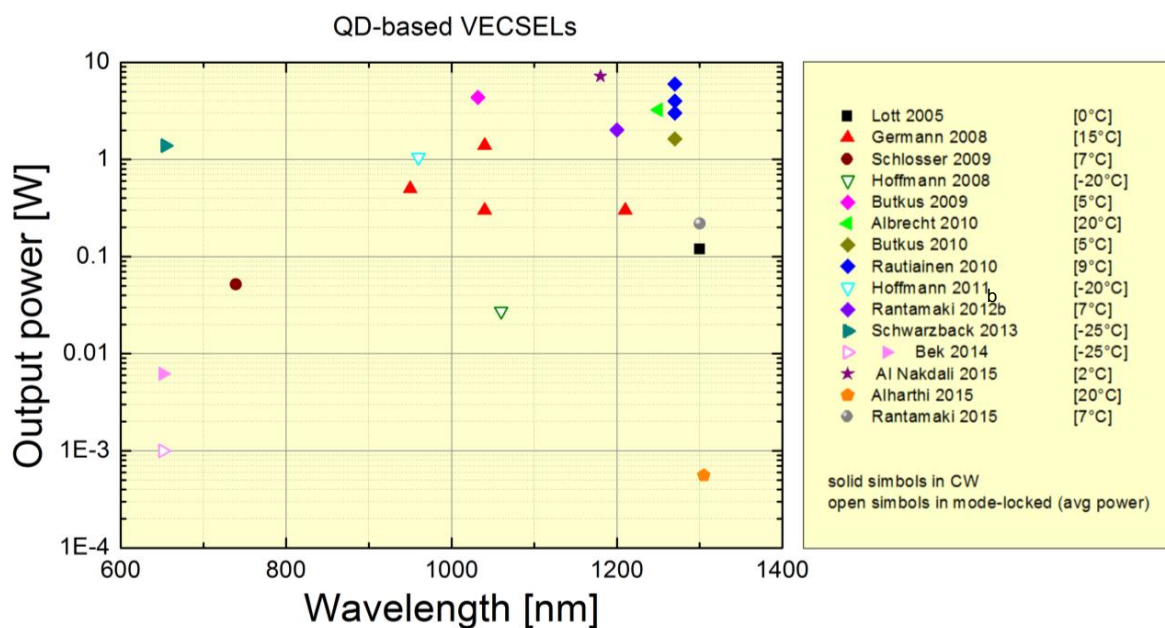


Fig. 4.10 – Reported output power vs emission wavelength of semiconductor nanostructures-based VECSELS. All the results presented in the graph are based on QD devices (most of them grown with Stranski–Krastanov method, and few with sub-monolayer approach). Solid symbols are related to CW operation, open symbols are related to mode-locked operation (average emitted power is given).

The record in terms of emitted power is held by Al Nakdali et al., which in 2015 demonstrate a QD-VECSEL with an active region composed by 39 sets of (InGa)As QDs on GaAs substrate, emitting up to 7.22 W at 1180 nm when cooled at 2°C (4 W at 15°C was also reported) [**Al Nakdali2015**]. When moving towards longer wavelengths, maximum emitted power drop to some hundreds of mW near 1.3  $\mu\text{m}$ . Moreover, QD-based devices generally show lower maximum power levels with respect to the QW-based ones, as attested by the comparison of Figs. 4.9 and 4.10.

Regarding the design of the semiconductor chip for high power generation, most of the reported structures based on QDs integrate a larger number of active layers (between 20 and 40) with respect to the QWs-based counterparts (8 to 15), mainly to compensate for a lower modal gain, directly impacted by the lower amount of active material, as discussed in the previous chapter (typically QD are 3-4 nm high with a 20% surface coverage, whereas QWs are 5-7 nm high with a 100% surface coverage).

Also, most of the reported output power values have been obtained at “low” temperatures (down to -25°C), with few demonstrations at room temperature. In addition, it is worth to notice that such results have been entirely achieved on optically-pumped GaAs-based devices, and to the best of our knowledge no demonstration of a QD nor QDH nanostructures-based VECSEL on an InP substrate has been reported so far.

#### **4.4.2 Performance in single-frequency operation**

As stated before, single-frequency operation is essential for applications such as spectroscopy or metrology, since in such a regime the lasers exhibit very low noise and narrow linewidth.

Owing to the high finesse of the long external cavity, conversely to the case of monolithic integrated VCSELs, sub-MHz linewidths are typically reported for VECSELs, down to the kHz regime. The following Table 4.3 (next page) is an overview of the main achievements obtained for single-frequency OP-VECSEL lasers in terms of maximum output power and linewidth for different emission wavelengths. As we can see, in some works active stabilization schemes were employed (such as Pound-Drever-Hall (PDH), or low frequency integration loops), while in some others the laser linewidth was measured in free-running operation.



**Table 4.3 – Best output power and linewidth of single-freq. VECSELs from different material systems.**

Wavelength [nm]	Output power [W]	Sampling time [ms]	Laser linewidth [kHz]	Cavity length [mm]	Stabilization?	Ref.
678	0.01	-	200	-	-	[Morton2007]
689	0.15	400	~ 10	200	servo locking loop	[Pabœuf2016]
852	0.017	10	< 500	10	< 2 kHz 2-integration stages servo loop	[Cocquelin2009]
1013	23.6	0.1 (1)	88 (407)	140	free-running	[Zhang2014]
1020	15.1	1000	995 (or 4)	-	free-running (or intensity frequency stabilized)	[Laurain2014]
1050	4.6	27	< 75	128	free-running	[Rantamäki2012c]
1180	11	-	-	148	free-running	[Leinonen2013]
1560	1	-	13	320	free-running	[Rantamäki2013]
2000	0.1	0.1	45 (or 9)	-	free-running (or FPI-locking loop)	[Rösener2011b]
2300	1.1	0.1 (1)	20 (30)	280	double PDH locking loop	[Kaspar2013]

## 4.5 VECSEL cavity architectures and applications

### 4.5.1 Cavity geometries

The use of the external configuration, which can be somehow considered a bulky alternative with respect to compact and monolithically integrated semiconductor lasers as edge-emitting or VCSELs, opens the way to a wide variety of device's functionalization. Indeed, VECSELs present the inherent advantage to have an external and accessible cavity which allows the use of different and versatile cavity setups and the insertion of external elements, to further increase the range of possible applications.

From this perspective, different VECSELs architectures are also adapted to different applications. As stated before, earlier demonstrations of VECSEL devices adopted the simple two mirrors plane-concave cavity. Besides that, VECSELs have been also demonstrated with different and more complicated configurations. Fig. 4.11 on next page presents a non-exhaustive overview of the most used cavity architectures [Okhotnikov2010], which are typically combined with intra-cavity optical elements such as the already presented etalons filters or non-linear optical crystals, in order to address different functionalities, sometimes not directly achievable with the conventional two-mirror plane-concave cavity configuration of Fig. 4.11a that we have already introduced. Dual-frequency operation of VECSEL can be for instance achieved by using a birefringent crystal, as depicted in Fig. 4.11b.

Three-mirror V-shaped cavities are frequently employed in combination with semiconductor saturable absorber mirrors (SESAM) to obtain ultra-fast pulses and passive mode-locking (Fig. 4.11c), or for second harmonic generation (SHG) thanks to intra-cavity non-linear crystals (Fig. 4.11d), which permits to reach emission wavelengths which are not directly accessible using conventional semiconductor-based active regions. The same functionalities can be obtained with four-mirror Z-shaped or ring-cavities (Fig. 4.11e,f). More complex multi-pumped multi-chip configurations, such as the ones depicted in Fig. 4.11g,h, have been successfully employed to overcome thermal limitations, which are particularly detrimental for high-power applications, and obtain very high output powers. In this case the power linearly scales as the number of gain chip increases [Saarinen2006, Fan2006], allowing demonstrating power emission beyond 100 Watts.

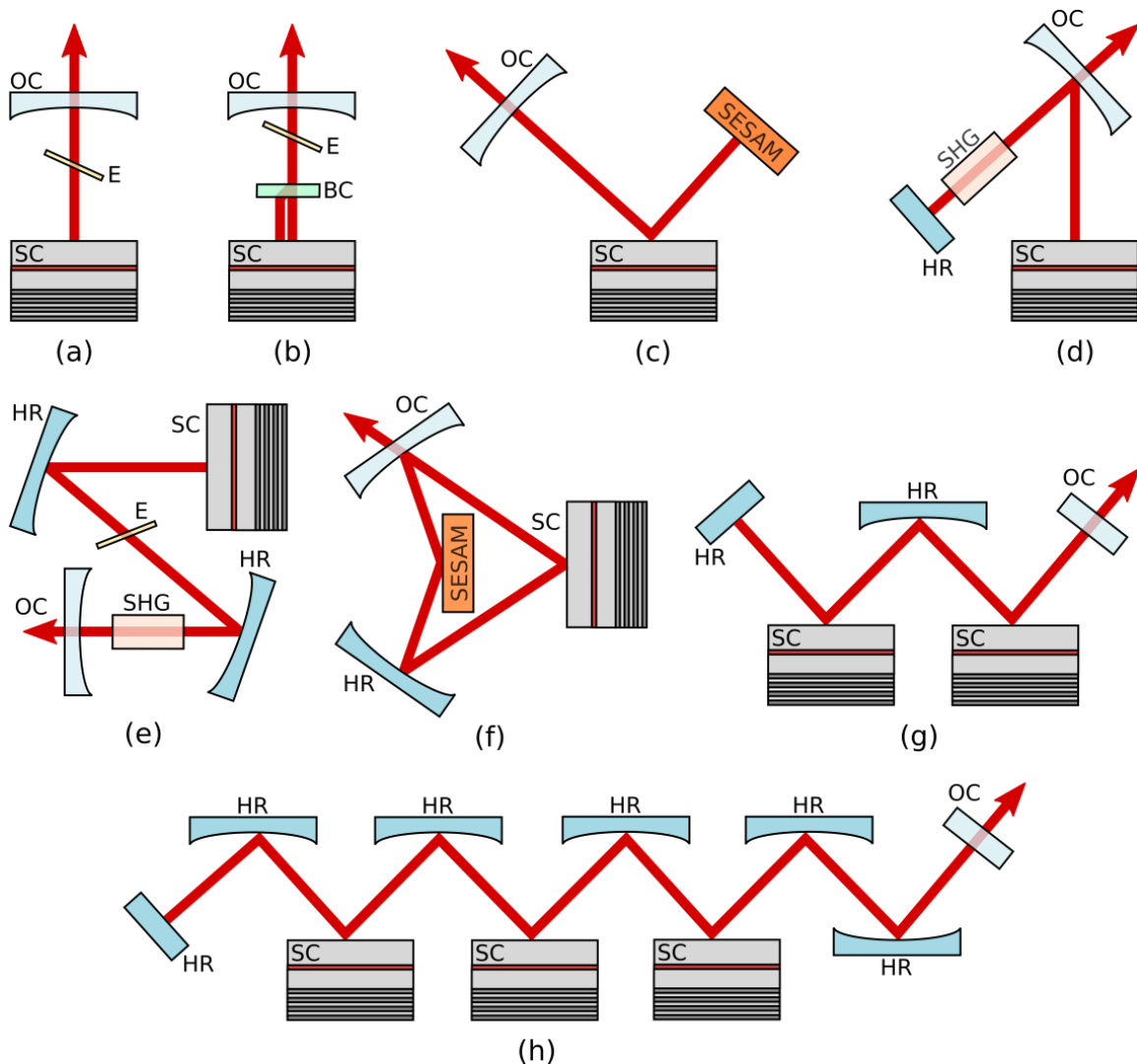


Fig. 4.11 – Schematic overview of the most common VECSEL cavities: two-mirror plane-concave linear cavity (a) general case (eventually in combination with an etalon filter for single-frequency operation) and (b) dual-frequency operation, three-mirror V-shaped cavity for (c) mode-locking or (d) second harmonic generation (SHG), four-mirror (e) Z-shaped cavity (SHG, again) and (f) ring-cavity (mode-locking), (g,h) multi-chip cavity for high-power operation. **OC**: output coupler mirror, **HR**: high-reflective mirror, **SC**: semiconductor chip, **E**: etalon, **BC**: birefringent crystal, **SESAM**: semiconductor saturable absorber mirror, **SHG**: non-linear crystal for second harmonic generation.

## 4.5.2 VECSELs applications

Thanks to their optical properties and to the wavelength versatility already discussed, VECSELs currently found application in a wide range of optical systems, ranging from high-power high-quality laser sources, sensing, ultrafast photonics, biology and medicine, spectroscopy, metrology and microwave photonics. Here follows a brief and non-exhaustive review of this large panel of applications:

1. **High-power and frequency-doubling:** one of the first applications of OP-VECSELs was in high-quality high-power visible optical sources, where Coherent Inc. pioneered their commercial development. One example can be found for instance in RGB TV color projection displays or forensic applications [Chilla2005, Chilla2007]. Yellow/orange multi-watt frequency-doubled VECSELs can also find application in astronomy (guide-star laser sources) and dermatology [Fallahi2008, Berger2012, Kantola2014], as well as biological and medical applications (fluorescence imaging and photodynamic therapy) [Saarinen2015], while 1.55  $\mu\text{m}$ -emitting VECSELs (frequency doubled at 700-800 nm range, Fig. 4.12a) can represent a cheaper and more compact alternative to bulky Ti:Sapphire lasers for atom cooling, bio-photonics and spectroscopy [Rantamäki2012a].
2. **Sensors:** VECSELs can be also employed in sensor-oriented applications. For instance 1.55  $\mu\text{m}$  CW dual-frequency VECSELs have been proposed for fiber sensor based on Brillouin scattering (Fig. 4.12b) [Chaccour2016], while devices emitting in the mid-infrared range ( $> 2 \mu\text{m}$ ) can be employed in gas detection and absorption spectroscopy [Ouvrard2005, Cermak2010], where many atmospheric molecules exhibit peculiar fingerprints.

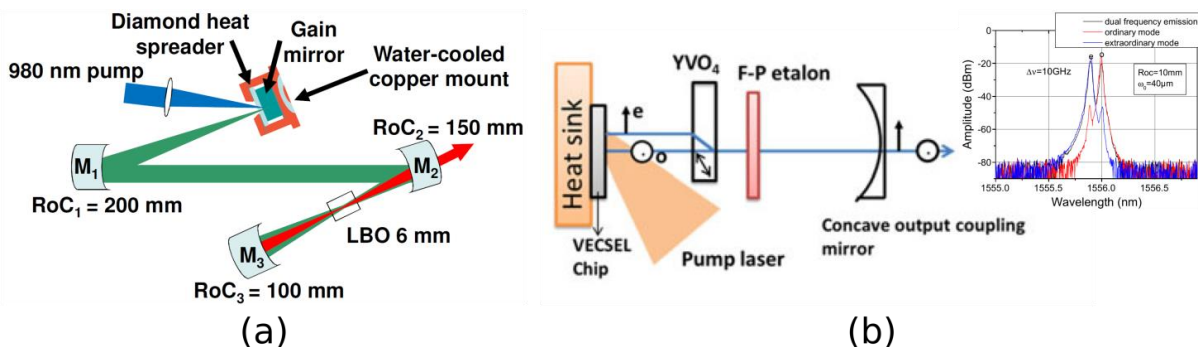


Fig. 4.12 – Examples of (a) frequency-doubled VECSEL setup with an intra-cavity long lithium triborate (LBO) non-linear crystal in a Z-shape cavity configuration (reprinted from [Rantamäki2012a] with permission from OSA) and (b) bi-frequency VECSEL setup in a linear two-mirror cavity (from [Chaccour2016], © 2016 IEEE).



3. **Ultrafast photonics:** in recent years, mode-locked VECSELS integrating SESAM structures have been demonstrated to produce very short pulses, from the picosecond down to the femtosecond regime (Fig. 4.13a) [Klopp2011, Bek2013, Waldburger2016], with W and kW average and peak power respectively [Scheller2012, Wilcox2013], and repetition rates from  $\sim 80$  MHz up to  $\sim 50$  GHz [Butkus2013]. These achievements have been mostly obtained with GaAs-based devices integrating quantum wells active media. It is also worth to notice that recently researchers of the Ultrafast Laser Physics group of ETH Zurich proposed and demonstrate a Mode-locked Integrated eXternal-cavity Surface Emitting Laser (MIXSEL), where the SESAM and the VECSEL gain structure were combined into a single monolithically-grown semiconductor chip [Maas2007, Mangold2013]. Such devices shows very interesting features, being able to produce sub-ps pulses ( $\sim 500$  fs) with repetition rates up to 100 GHz and an average output power  $> 100$  mW [Mangold2014].
4. **Frequency-combs generation and spectroscopy:** ultrafast mode-locked VECSELS have given rise to considerable interest in the generation of optical frequency-combs [Zaugg2014]. As an example, they have been used for heterodyning detection in dual-comb spectroscopy, where two stabilized mode-locked pulse trains share the same laser cavity [Link2015, Link2016]. A quite interesting result involving this kind of optical sources has very recently achieved with the dual-comb spectroscopy of water vapor with a free-running not-stabilized MIXSEL (Fig. 4.13b) [Link2017], which allows avoiding the complexity of the stabilization loops and potentially opens the way to a wide range of industrial application (gas spectroscopy, metrology, etc.).

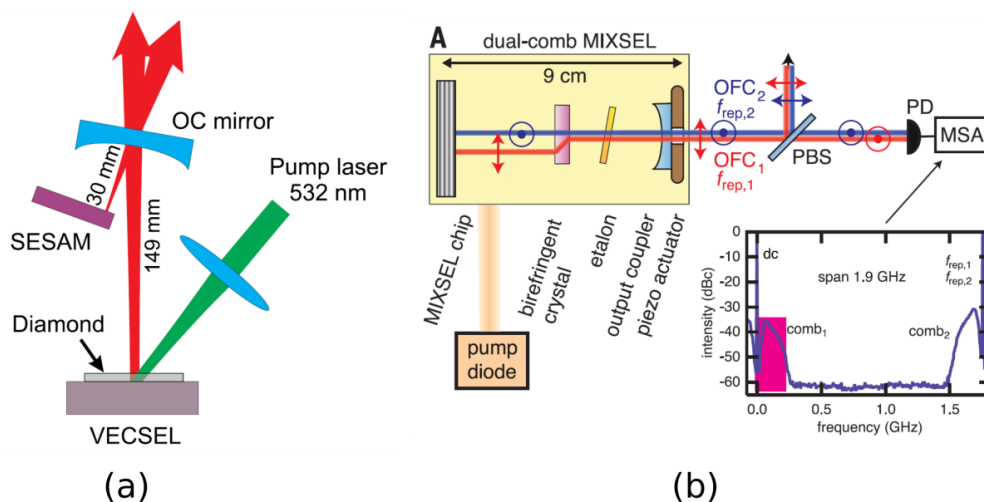


Fig. 4.13 – (a) A typical V-shaped laser cavity configuration of a mode-locked VECSEL (reprinted from [Bek2013] with the permission of AIP Publishing LLC) and (b) the dual-comb MIXSEL used for water vapor spectroscopy in free-running operation (reprinted from [Link2017] with permission from AAAS).

5. **Biology and medicine:** high-peak power short pulses of ultrafast lasers can be fed into highly nonlinear fibers to generate supercontinuum source with a wide optical spectrum covering a large spectral width. Such optical sources are suitable for bio-medical applications, where they can be used in optical high resolution coherence tomography (OCT) for ophthalmology, gastroenterology, dermatology, intra-arterial imaging, and dentistry [Rafailov2014] or in-vivo nonlinear multiphoton microscopy [Aviles-Espinosa2011, Voigt2017].
6. **Metrology and microwave photonics:** thanks to their spectral performance, VECSELS are also well suited for metrology and microwave signal generation. They are employed as narrow linewidth, low-noise optical source for RF optical links and local oscillators in RADAR applications (Fig. 4.14a) [Baili2007, Baili2014], as dual-frequency optical sources for the generation of high purity GHz optical signals at 1  $\mu\text{m}$  [Baili2009b, Pal2010, De2013, De2014a] and 1.55  $\mu\text{m}$  [De2014b, De2015] and THz spectroscopy [Wilcox2006, Mihoubi2008]. Dual-frequency VECSELS have been also employed for the interrogation of stable and precise atomic transitions (frequency references) of Cesium atoms in atomic clocks based on coherent population trapping (Fig. 4.14b) [Dumont2014].

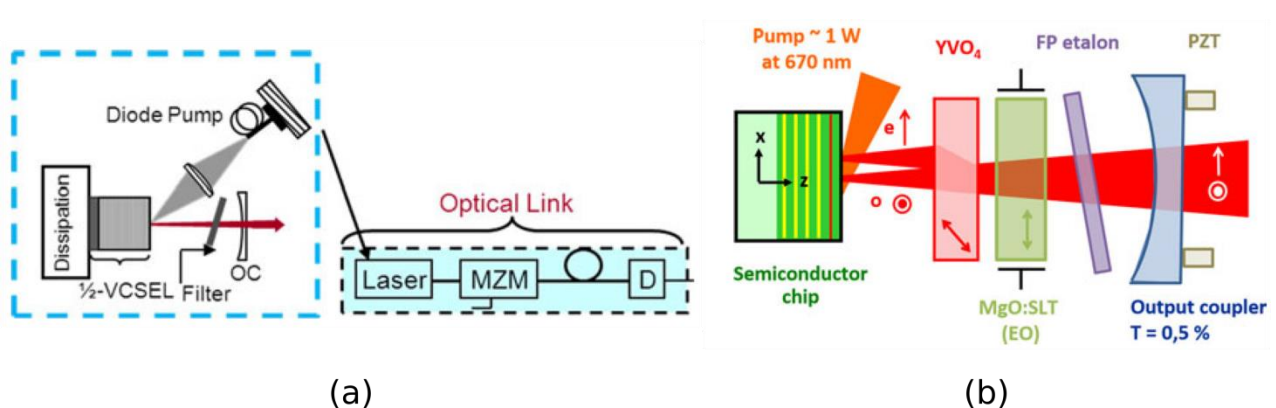


Fig. 4.14 – (a) RF optical link based on low noise optically-pumped VECSEL (from [Baili2014], © 2014 IEEE) and (b) dual-frequency VECSEL source for atomic clock pumping (from [Dumont2014], © 2014 IEEE).

## 4.6 Optimization guidelines for VECSEL design

Having presented the peculiar characteristics and applications of VECSELS, in this section we are going to discuss some useful design modeling which apply for their realization, in the particular case of the optically-pumped version. Although here we will particularly focus on the case of InP-based devices integrating an active region based on quantum nanostructures, most of these rules

are valid in the general case. The results of such modeling have also been a starting point to the realization of the quantum dashes-based VECSEL, which will be the object of the next *Chapter 5*.

### 4.6.1 Thermal management in VECSELS

As already pointed out in the previous sections, because of their reduced thickness, vertical-cavity lasers particularly suffer from thermal heating phenomena. This is especially true in the case of the external cavity arrangement of VECSELS, since the dimension of the pump spot and the incident pump power are significantly larger with respect to the case of micrometric VCSELS, in order to achieve high powers through pump scaling. In both cases, however, the overheating of the active region is responsible for the thermal rollover of the laser and under certain circumstances it may even prevent the device to work at all.

We have already seen in *Section 2.2.2* that the use of a hybrid metal-dielectric DBR (H-DBR), eventually combined with thermally improved architectures, can enhance the performance in the case of monolithic InP-based VCSELS.

In this section, the impact of such a solution will be evaluated in the case of an InP-based VECSELS integrating an InAs/InGaAsP active region, and compared to two different alternatives: the monolithic solution with InP/InGaAsP DBRs and a second structure based on GaAs/Al(Ga)As DBRs. The use of different dissipation schemes will be also tested. The study is basically carried out by using a FEM model (again, the reader can refer to *Appendix B* for details on thermal model). It enables to investigate the thermal behavior of VECSELS in terms of internal heat profile, maximum temperature and heat flow, providing helpful indication to improve heat dissipation through an optimized design of the structure. We will discuss some heat generation mechanisms of semiconductor lasers, which of course apply also in the case of V(E)CSELS. Then, three different heat-sink architectures for thermal management in VECSELS are discussed and compared. Finally, the influence of different bottom DBR compositions is evaluated, in combination with other parameters (such as pump spot size and heat-sink architecture), to identify the optimum design of the laser which will ensure the best thermal performance.

#### Chip architectures for thermal management

As previously discussed, thermal dissipation can seriously limit the performance of VECSELS, regardless of the material system. Generally, in a VECSEL, the issues due to the temperature increase are different with respect to other external-cavity lasers like solid-state-based devices, for two main aspects. Primarily, the limitations to power scaling are due to the absolute temperature

rise in the active region, whereas in the case of solid-state lasers the main problems are due to the temperature gradient (large thermal lensing, stress-induced cracks, etc.). Secondly, in the case of VECSELs the heat density can be very large, up to three orders of magnitude higher than in the solid-state case. This is due to the fact that in both cases the pump spot dimensions are similar, but in a VECSEL, pump absorption takes place in a very limited region (of the order of some  $\mu\text{m}$ ), whereas in the case of diode-pumped solid-state lasers, the active region thickness is on the mm scale, so that the heat load per unit volume is lower.

As previously discussed, given the fact that micrometric-thick active media provide a relatively low gain per photon round-trip, vertical-cavity devices need high reflective DBRs to compensate for the cavity losses. As in the case of VCSELs, materials with a refractive index contrast as high as possible are employed in order to limit the number of pairs  $N$  required to achieve a given reflectivity value and maximize the stop-band interval  $\Delta\lambda_{DBR}$  of the reflector. Also, lattice-matched compounds on the substrate would be generally preferred, to avoid the appearance of stress-induced defect due to significant differences in the lattice parameters of the deposited layers. Finally, thermally performing materials should be employed to minimize the temperature rise in the active region and facilitate the heat flow towards the heat-sink.

From a practical point of view, it is difficult to meet all the previous requirements, and trade-offs are generally made to satisfy optical needs without degrading the thermal impedance of the devices. Table 4.4 compares three lattice-matched semiconductor compounds composing the bottom DBR of VECSEL devices, in terms of materials properties in the 1-2  $\mu\text{m}$  wavelength range. The number of pairs  $N$  has been chosen in order to get 99.7% of theoretical reflectivity for each mirror.

**Table 4.4 – Optical and thermal properties of bottom DBR for different material systems.**

Wavelength [ $\mu\text{m}$ ]	DBR composition	$n_{low} / n_{high}$	$N$	$\Delta\lambda_{DBR}$ [nm]	DBR thickness [ $\mu\text{m}$ ]	$k_{t,L}$ [W/m-K]	$k_{t,V}$ [W/m-K]
1-1.3	GaAs/Al(Ga)As	0.88-0.85	25	108-130	4.1-5.2	70	61
1.55	InGaAsP/InP	0.95	48	46	11.5	38	6-12
2	AlAsSb/GaSb	0.8	21	280	6	20	14

According to Table 4.4, InP-based VECSELs do not benefit from thermally efficient lattice-matched reflectors, as they present low index contrast (the highest ratio between low and high refractive indices  $n_{low}$  and  $n_{high}$  among the three), high thickness and low thermal conductivity. Across the years, several solutions have been investigated in order to identify thermally efficient VECSEL architectures, especially in the case of InGaAsP/InP-based VECSELs. In the perspective to minimize the impact of the heat load, three main configurations are typically adopted. They are

depicted in Fig. 4.15: (a) the as-grown, (b) the thin device and (c) the intra-cavity heat-spreader architectures.

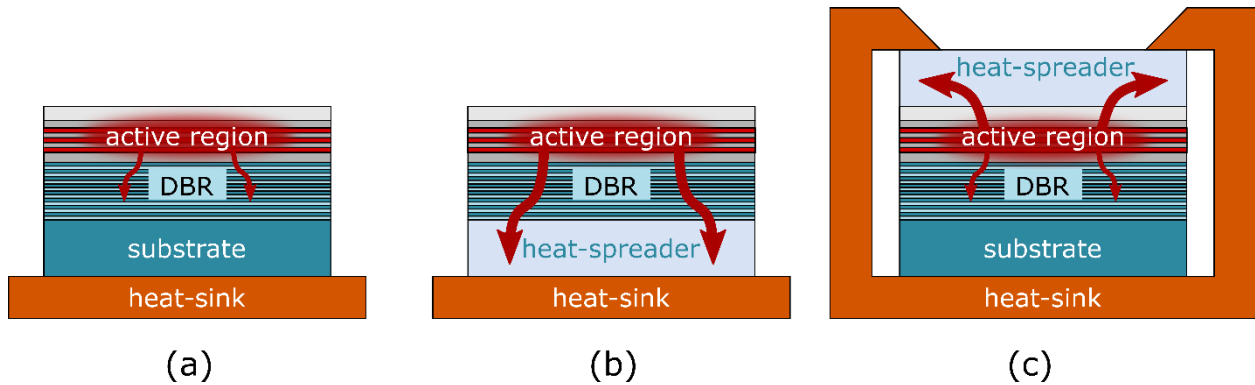


Fig. 4.15 – Different solutions for thermal management in VECSELS: (a) as-grown, (b) thin device and (c) intra-cavity heat-spreader approach.

- As-grown:** the as-grown configuration (Fig. 4.15a) is the simplest approach, since it does not require any further step after the chip growth process. In this case, the VECSEL chip is soldered directly to a high conductive heat-sink (typically Cu) and the heat is removed through the bottom part. In case of the presence of high thermal impedance resulting from the stack of the bottom mirror and the thick substrate, this solution is also the less effective in terms of thermal management. In particular, due to the bad optical and thermal properties of InP material system and related lattice-matched compounds (InGaAsP), such a solution is hardly suitable in the case of VECSELS. It will thus not be further discussed, even if in early works laser operation with relative low power levels has been reported using such a configuration ([Symonds2004a, Lindberg2004a]).
- Thin-device:** the high thermal impedance of the as-grown architecture can be reduced by removing the thick substrate and putting the chip directly in contact with the heat sink, eventually inserting a high conductive heat-spreader in between (typically Cu, SiC or synthetic diamond), as shown in Fig. 4.15b. The effectiveness of this approach relies on the use of DBR presenting low thermal impedance to promote heat removal through the heat-spreader. This solution is particularly suited in the case of GaAs-based devices emitting around 1  $\mu\text{m}$ , which naturally benefits from lattice-matched and thermally efficient GaAs/Al(Ga)As bottom reflectors. Switching from GaAs to InP material system, this approach becomes less effective. An alternative solution has been to replace InP-based as-grown DBR by GaAs based DBR, according to metamorphic growth or wafer bonding techniques of GaAs DBR on InP.

- **Intra-cavity heat-spreader:** the effectiveness of the thin device approach relies on the use of a high thermal conductive bottom mirror. If this cannot be employed (for instance in the case of InP-based device which involves difficult deposition/bonding techniques), an alternative and simple approach consists to bond a high thermally-conductive material on the top surface of the device, in the so-called intra-cavity heat-spreader configuration (Fig. 4.15c). This allows bypassing the thermal barrier represented by the bottom mirror and extracting the heat from the active region towards the upper part of the VECSEL. For this purpose, the most used materials are generally silicon [Lindberg2004b], silicon carbide (SiC) [Hastie2003], or synthetic diamond [Lindberg2004c] grown by Chemical Vapor Deposition (CVD) technique.

We notice that the thin-device configuration can be coupled with the intra-cavity heat-spreader approach to improve thermal dissipation. This allowed demonstrating quite high output power for InP-based VECSELs. For example, we can cite a record of 33 W of emitted power in a 1.3  $\mu\text{m}$ -emitting VECSEL at  $-5^\circ\text{C}$  (23.5 W at  $15^\circ\text{C}$ ) in multi-mode emission [Leinonen2017], or 1 W at 1.56  $\mu\text{m}$  in single-frequency operation at  $15^\circ\text{C}$  (700 mW at  $25^\circ\text{C}$ ) [Rantamäki2013].

### **The InP paradigm: state of the art and thermal modeling**

In the case of VECSELs emitting in the 1.55  $\mu\text{m}$  range, the thermal management is challenging. Indeed, owing to the bad thermal properties of InP-related materials, they show a significantly higher temperature rise with respect to other material systems. Particular attention must be paid in the thermal design of the laser cavity and the bottom mirror, and an efficient heat removal mechanism is even more crucial than in the case of micro-cavity VCSELs.

Although in the context of this work we are not focused on the design of VECSELs for high power applications, an efficient heat management of the devices is anyhow helpful to achieve laser operation, since a high thermal load inside the active region can quickly spoil the laser performance. Additionally, the spectral properties of the VECSEL is also affected by thermal effects with the broadening of the emission spectrum and the drift of the laser linewidth, so that an optimized design of the laser can help limiting these unwanted effects. It is thus interesting to investigate the thermal behavior of the InP-based optically-pumped VECSEL structure, which will be representative of our final device.

To this aim, we use the finite element model (FEM), which is detailed in the *Appendix B* of this manuscript together with the material parameters used in simulations. The model is employed to compute the temperature rise  $\Delta T$  in the active region (with respect to the temperature reference  $T_{ref}$  imposed by the Peltier cell) and to estimate the thermal impedance  $R_{th}$  of the structure, in the case of

a device integrating different DRBs and dissipation schemes. The composition of the semiconductor chip is common to all the structures and is composed by three sets of InGaAsP-based active layers surrounded by InP spacers and a InP window. Such an active region is representative to the one integrated on the grown device<sup>5</sup> (as we will see in *Chapter 6*).

The comparison of the different solutions obtained by this method is useful in order to choose the optimal approach during the VECSEL realization. All three different hybrid-DBR structures integrated in the investigated devices are completed by a gold layer to boost their reflectivity. In particular, they are composed by:

- 48 pairs InP/InGaAsP + 500 nm Au;
- 3.5 pairs a-Si/a-SiN<sub>x</sub> + 500 nm Au;
- 15 pairs GaAs/AlAs + 500 nm Au.

The number of the layers composing the hybrid-DBRs have been chosen in order to have a similar value of the (theoretical) reflectivity, namely 99.7% at  $\lambda = 1.55 \mu\text{m}$ . Each structure has been tested in three different architectures: a thin-device (TD) structure with a 100  $\mu\text{m}$ -thick Cu or CVD diamond heat-spreaders and a structure integrating a 100  $\mu\text{m}$ -thick intra-cavity diamond heat-spreader (ICHS) bonded on a copper heat-sink. Table 4.5 presents the investigated structures and summarizes the composition of each section (again, see *Appendix B* for material parameters used in simulations).

**Table 4.5 – Details of the simulated OP-VECSEL structures.**

Structure*	Active region composition	H-DBR composition	Dissipation scheme and heat-spreader composition	
	3 sets of 3 InGaAsP-based active region (AR) + InP spacers and InP window.  Window: 2 $\mu\text{m}$ AR1: 196 nm spacer1: 143 nm AR2: 146 nm spacer2: 63 nm AR3: 120 nm spacer3: 101 nm	48 pairs InP/InGaAsP + 500 nm Au	TD - 100 $\mu\text{m}$ -thick Cu	
			TD - 100 $\mu\text{m}$ -thick CVD diamond	
			ICHS - 100 $\mu\text{m}$ -thick CVD diamond	
			3.5 pairs a-Si/a-SiN <sub>x</sub> + 500 nm Au	TD - 100 $\mu\text{m}$ -thick Cu
				TD - 100 $\mu\text{m}$ -thick CVD diamond
				ICHS - 100 $\mu\text{m}$ -thick CVD diamond
			15 pairs GaAs/AlAs + 500 nm Au	TD - 100 $\mu\text{m}$ -thick Cu
				TD - 100 $\mu\text{m}$ -thick CVD diamond
				ICHS - 100 $\mu\text{m}$ -thick CVD diamond

(\*) TD and ICCHS are not simultaneously employed.

<sup>5</sup> In the model, the ~ nm-thick active layers are grouped together with the surrounding barriers, in order to avoid unnecessary fine meshes (which are finer as the number of layer increases) and decrease the computational cost.



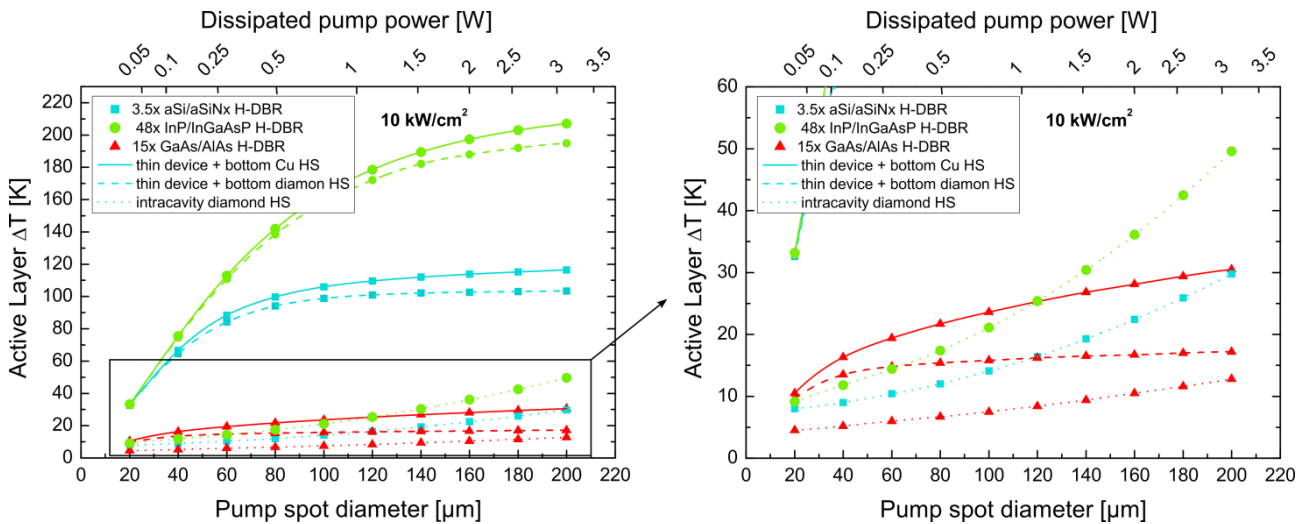


Fig. 4.16 – Temperature rise in the active region of a InP-based OP-VECSEL for different tested architectures. The pump power density has been kept constant to  $10 \text{ kW/cm}^2$ .

The results of the simulation are presented in Fig. 4.16, in the case of a dissipated pump density equal to  $10 \text{ kW/cm}^2$ . As shown by the graphs, the structures integrating poor thermal conductive hybrid-DBRs composed by dielectric a-Si/a-SiN<sub>x</sub> and InP/InGaAsP (cyan and green curves) experience a high thermal load in the active region, especially in the case of the thin-device architecture (solid and dashed lines), as expected. In these cases the temperature rise in the active region exceeds 100 K and 160 K for a 100  $\mu\text{m}$ -diameter spot, respectively. This is mainly due to the fact that the bottom mirror acts as a barrier for the heat flow, and the temperature rises very quickly as the pump spot increases in dimensions. Conversely, the intra-cavity diamond approach (dotted lines) works relatively fine for these structures, allowing a  $\Delta T$  between 10 and 20 K for pump spots which are limited to 100  $\mu\text{m}$  in diameter.

However, the best performance is obtained in the case of the GaAs/AlAs DBR-based devices (red curves). In the case of the thin-device configurations, the temperature rise never exceeds 20-30 K (depending on the composition of the heat-spreader, whereas diamond or Cu), at any pump spot size. The intra-cavity diamond approach outperforms again the other two approaches, with a maximum  $\Delta T$  lower than 15 K, and down to 5 K for small pump spots ( $< 100 \mu\text{m}$  in diameter).

The result of simulations clearly show that GaAs/AlAs DBRs are the best choice to be integrated in InP-based VECSELs, especially if they are used in combination with an intra-cavity diamond heat-spreader and a small pump spot. Nevertheless, the thin device approach gives good results as well, with a temperature rise limited to nearly 15 K for any pump spot size.

**1<sup>st</sup> conclusion**

From thermal simulations we retain that a high-thermally conductive bottom mirror is needed, to efficiently evacuate the heat produced in the active region. Simultaneously, a good optical performance must also be guaranteed. The natural choice is thus to use GaAs/Al(Ga)As-based bottom DBRs, which ensure compliance with both conditions. Additionally to that, the thermal architecture of the device plays a relevant role. The thin-device and the intra-cavity heat-spreader approaches are both adapted to this aim, especially if a high-conductive diamond substrate is employed. Although the ICHS architecture seems to be the most performant (at least for such tested conditions), the thin-device approach simplify the process and, above all, does not introduce unwanted etalon effects.

So that, **we oriented our choice to the integration of a GaAs/Al(Ga)As DBR and the use of a thin-device chip architecture.**

**4.6.2 Resonant vs anti-resonant configurations and confinement factor**

Besides thermal phenomena, which can strongly affect the operation of a VECSEL, its output performance clearly depend on several others parameters. One of them is the value of the material gain  $g_{mat}$ , which is an intrinsic quantity partially dependent on the choice of the particular composition of the active region and on its quality. But the raw material gain is not the only key parameter to assert if the laser will show good optical characteristics in terms of power or threshold. In a vertical-cavity laser (and in a VECSEL in particular), the volume occupied by the gain region is typically few percent of the one occupied by the entire optical mode, and optical losses are also present inside the laser cavity. Therefore, the output characteristic must take into account the net modal gain which is provided to a specific optical mode. This can be done by considering the confinement factor  $\Gamma$ , as discussed in *Chapter 1*. As in the case of VCSELs, the active layers (no matter if QWs, QDHs or QDs) are generally placed at the antinodes of the resonant standing wave, in order to maximize the modal gain of the structure. This is particularly true in the case of applications requiring high emitted power, as frequency doubling for instance.

One can estimate the overlap between the position of the active layers and the resonant electric field maxima by calculating the gain enhancement factor  $\Gamma_{enh}$ , introduced in *Chapter 1* (Eq. 1.7)<sup>6</sup>.

---

<sup>6</sup> In the case of a VECSEL we consider the optical energy stored on the active layers with respect to the total optical energy on the semiconductor sub-cavity of length  $L_{chip}$  (composed by active layers, barriers, confinement layers and DBR), neglecting the external cavity length  $L_c$ .

The gain enhancement factor  $\Gamma_{enh}$  assumes different values depending on the particular design of the sub-cavity which is formed between the DBR and the air. It is interesting to notice that, since the sub-cavity acts as a Fabry-Pérot filter,  $\Gamma_{enh}$  measures the internal field enhancement inside the semiconductor cavity at a given wavelength.

Its filtering characteristic is also strongly dependent on the specific configuration that has been adopted: by acting on the thickness of the layers, it can be possible to design a resonant or an anti-resonant sub-cavity (or more generally any intermediate case between these two extremes). These two configurations are presented in Fig. 4.17, where the optical field intensity inside an InP-based VECSEL emitting around 1.6  $\mu\text{m}$  is plotted for two different wavelengths (1600 and 1630 nm), together with the reflectivity of the structures and the relative computed gain enhancement factor  $\Gamma_{enh}$ .

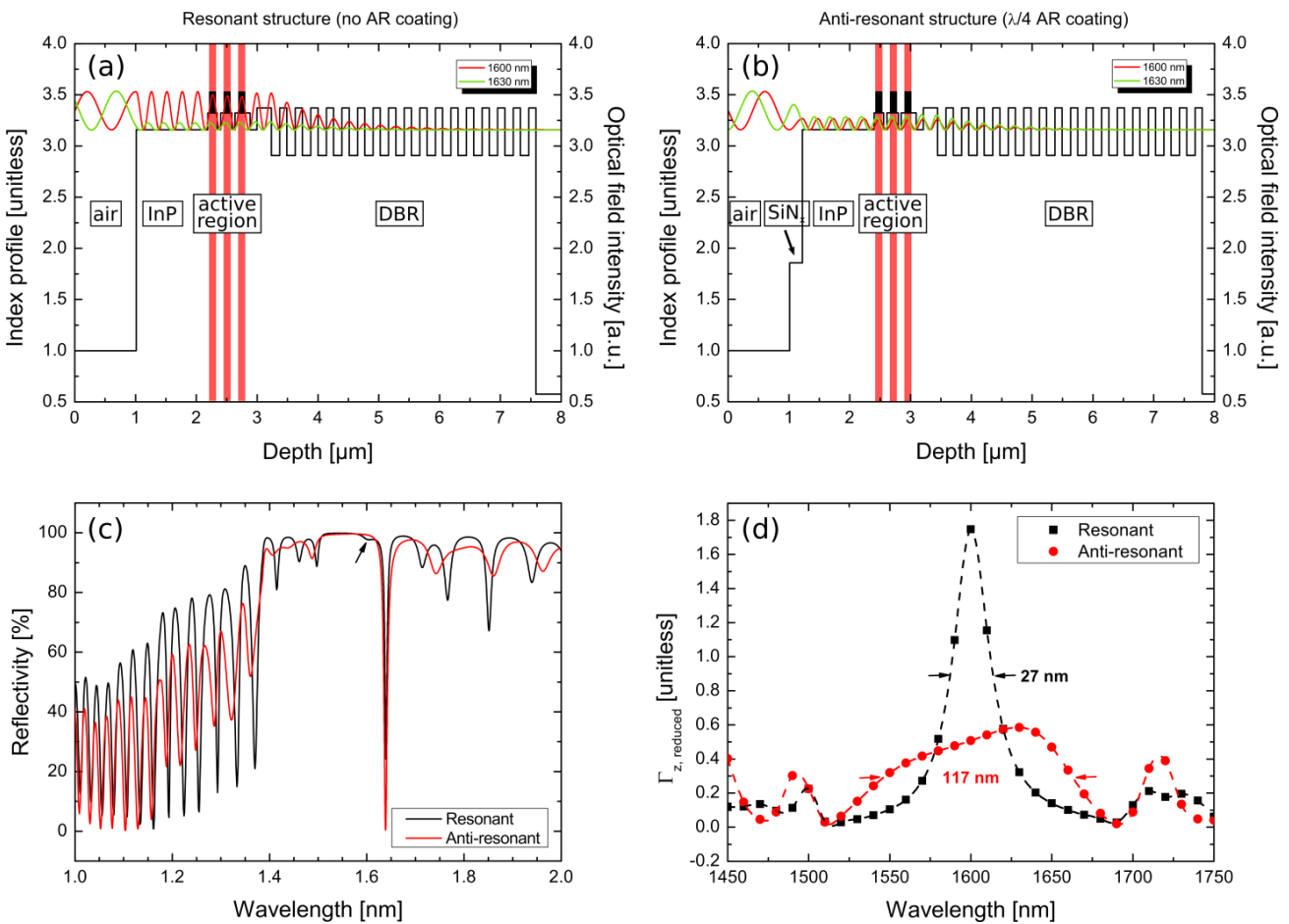


Fig. 4.17 – Resonant vs anti-resonant sub-cavity design: refractive index profiles and calculated optical field intensity (for two different wavelengths) in the case of a (a) resonant and (b) anti-resonant structure, (c) reflectivity spectrum and (d) gain enhancement factor  $\Gamma_{enh}$  calculated for the two configurations.

In the case of the resonant sub-cavity depicted in Fig. 4.17a, the standing wave has a maximum at the semiconductor/air interface and its intensity is enhanced at the designed emission wavelength

$\lambda_{laser} = 1600$  nm. As a result of the micro-cavity resonance, the reflectivity of the chip has a dip around  $\lambda_{laser}$  (black arrow in Fig. 4.17c). Consequently, as shown in Fig. 4.17d,  $\Gamma_{enh}$  has a narrow peaked characteristic (black curve) around the emission wavelength, with a FWHM of 27 nm.

Ideally, its maximum is equal to 2 if all the active layers are exactly placed on the antinodes of the electric field pattern. Anyway, this last problem can be mitigated by post-growth etching steps to adjust the thickness of the semiconductor chip phase layer. Thanks to a high coupling between the standing wave field and the active layers, the resonant configuration guarantees a higher gain per round-trip which results in a lower threshold at the designed emission wavelength. This configuration is thus particularly appropriate for high emission power. Conversely, due to the narrow spectral characteristic of the gain, the maximum achievable spectral coverage is limited, making this solution not suitable for broad tuning applications.

The complementary case is represented by the anti-resonant configuration depicted in Fig. 4.17b, where an anti-reflection coating around the emission wavelength (1600 nm) has been deposited on the surface. In this case, the standing wave has a node at the chip/air interface. In this case the intensity of the standing wave inside the semiconductor structure is dumped in a wide range around the designed emission wavelength, resulting in a weaker coupled internal field. As a result, the micro-cavity effect is not more present in the reflectivity curve of Fig. 4.17c and the gain enhancement factor  $\Gamma_{enh}$  in Fig. 4.17d (red curve) shows a lower and broader characteristic around  $\lambda_{laser}$ , resulting in a structure which is less sensitive to wavelength variations due to micro-cavity tuning, thermal shift or filtering effects introduced by the extended cavity configuration. As a consequence, this solution is more suited to obtain emission in a larger spectral range, but conversely it results in output laser characteristics with higher threshold and lower achievable output power, if compared to the resonant case.

## 2<sup>nd</sup> conclusion

To maximize the sub-cavity enhancement, a resonant design should be preferred. Such a design guarantees a peaked longitudinal confinement factor at the designed emission wavelength. Lower threshold and higher output power are then expected with respect to an anti-resonant configuration, which is better adapted to reach a wider emission, at the expenses of a higher threshold and a lower output power.

To get the best conditions to reach the laser oscillation of our VECSEL, **we choose to use a resonant configuration**, knowing that eventually we will be able to modify it by changing the thickness of the sub-cavity (i.e. by etching the phase layer or depositing an anti-reflection layer).

### 4.6.3 Optimization of laser threshold and output power

This section is devoted to illustrate the basic parameters that influence the VECSEL output power characteristic and laser threshold. In the following, the semiconductor chip will be considered to be optically pumped (as most of VECSELs are) and inserted in a simple two-mirror cavity (DBR + output coupler mirror). As already discussed above, VECSEL characteristics depends on several parameters, some of them related to the specific active region design, i.e. the number of active layers, their composition and thickness, the chip configuration (whether resonant or anti-resonant), DBR reflectivity, etc. Some others depend on other parameters that are specific of the cavity setup, for instance the output coupler transmission, the pump spot dimensions and the incident pump power, to name a few. It can be thus useful to individually investigate their contribution to optimize the VECSEL design, in order to maximize the output characteristic and minimize the laser threshold. In the following, we use a semi-empirical model to obtain information about the interplay between these design parameters. The physical framework behind this model is detailed in *Appendix C*.

These basic design rules contribute to the power scaling of these devices, together with the optimization of the heat management and the increase of the pumped surface. Thanks to that, VECSELs have demonstrated state-of-the-art emitted power up to the multi-watt level on a large range of wavelengths, as already discussed in *Section 4.4*.

In the framework of this model, temperature-induced effects are not taken into account, even they have a critical impact on the laser performance of VECSELs, especially in the case of long-wavelength emitting devices ( $> 1.2\text{-}1.3\ \mu\text{m}$ ). They basically results in a drop of the devices' performance due to the appearance of thermal rollover, as previously discussed.

Table 4.6 (next page) summarizes the typical values of the different parameters that have been used in calculations (if not otherwise specified). Some values of the parameters used in the model have been selected according to typical values of quantum dashes-based structure grown at FOTON Institute, while some others have been chosen according to the experimental conditions and from the scientific literature. The results of simulations helped the design of the VECSEL device which is described in the following chapter.

**Table 4.6 – Value of different parameters for output characteristic and threshold simulations.**

Parameter	Description	Value (typical)
$\lambda_{laser}$	emission wavelength	1600 nm
$\lambda_{pump}$	pump wavelength	975 nm
$\omega_{p1} \times \omega_{p2}$	pump spot semi-minor and semi-major axis (elliptical pump spot is considered)	40 $\mu\text{m} \times 60 \mu\text{m}$ (SM pumping) 72.5 $\mu\text{m} \times 105 \mu\text{m}$ (MM pumping)
$g_0$	(linear) material gain	2000 $\text{cm}^{-1}$
$N_0$	transparency carrier density	$1 \times 10^{18} \text{cm}^{-3}$
$\Gamma_{enh}$	gain enhancement factor $\Gamma_{enh}$	$0 < \Gamma_{enh} < 2$ , depending on chip design
$R_s(\lambda_{laser})$	surface reflectivity (at the emission wavelength)	0.27 (no AR coating) $\sim 0$ (AR coating)
$R_s(\lambda_{pump})$	surface reflectivity (at the pump wavelength)	0.17 (SiN <sub>x</sub> AR coating at $\lambda_{laser}$ )
$N_{active}$	number of active layers	18 (typically)
$L_{active}$	thickness of each active layer	3 nm
$R_{DBR}$	reflectivity of the bottom Distributed Bragg Reflector	0.998 (at the emission wavelength)
$T_{loss}$	round-trip losses transmission factor	0.999
$\eta_{abs}$	pump absorption efficiency of the semiconductor chip	0.8
$A$	Shockley-Read-Hall recombination coefficient	between $1 \times 10^7$ and $2 \times 10^9 \text{s}^{-1}$
$B$	radiative bimolecular coefficient	$(2.5 \pm 0.2) \times 10^{-10} \text{cm}^3 \text{s}^{-1}$
$C$	Auger recombination coefficient	$(1.2 \pm 0.7) \times 10^{-27} \text{cm}^6 \text{s}^{-1}$

SM: single-mode, MM: multi-mode

### Optimization of the number of active layers

Another parameter that can affect the VECSEL's performance is the number of active layers  $N_{active}$  that are integrated in the active region. This has an impact on both the laser threshold and the maximum output power. Generally, there is an optimum value for which the pump threshold and the output power are optimized. Beyond this value, any further increase of the active layers number generally does not translate into a significant improvement of the laser performance.

The rapid decrease of the laser threshold and the consequent improvement of the output power with respect to the increase of the active layers number are generally associated to an increase of the absorption efficiency  $\eta_{abs}$  (i.e. the percentage of the pump power which is absorbed by the active region and contribute to the emission) [Hader2010]. The remaining pump power is typically absorbed by the DBR, contributing to non-radiative losses and thermal heating, which contributes to the unwanted thermal rollover. When the optimum number of active layers is reached, we can consider that the all the impinging pump power is absorbed by the active medium, and keeping increasing  $N_{active}$  do not have any significant impact. On the contrary instead, too many active layers can have the opposite effect, since the bottom QWs are not efficiently pumped, and they starts to absorb light instead amplifying it.

Fig. 4.18a (next page) shows the computed threshold pump power and output power with respect to the number of active layer  $N_{active}$  for different values of the output coupler reflectivity, for an elliptical pump spot size of  $40 \mu\text{m} \times 60 \mu\text{m}$  and a longitudinal confinement factor of  $\Gamma'_z = 1.75$ . The

curves have a minimum for a precise value of  $N_{active}$ , and the value of the minima depends on the reflectivity of the external mirror. For instance, in this example, for a reflectivity  $R = 99.5\%$  of the external mirror, we can expect that the optimum value is around 14 active layers<sup>7</sup>.

A similar tendency can be observed in Fig. 4.18b, in which the output power is plotted as a function of the number of active layers. An increasing of the active layers initially results in a fast increasing of the output power curves, which then reach a maximum. Any further increase of  $N_{active}$  produces a (slight) deterioration of the performance. Again, the optimum number of active media depends on the reflectivity of the output coupler. Higher transmission values of the output coupler result in higher emitted power levels, at the expenses of higher thresholds, while lower transmissions improve the threshold condition. In practice, a trade-off between these two aspects is generally adopted. In this particular example, best results are obtained with  $R=99.5\%$  and a number of active layers included between 18 and 20. By choosing 18 layers, we got a maximum output power of  $\sim 19$  mW and a threshold around 400 mW.

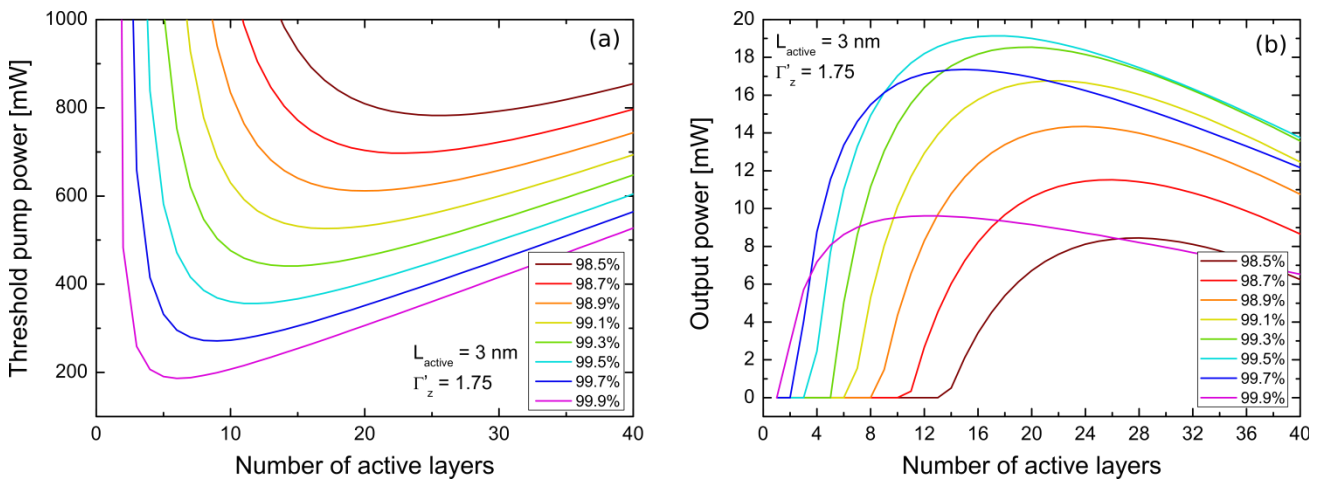


Fig. 4.18 – Computed OP-VECSEL characteristics: (a) threshold pump power and (b) emitted power vs number of active layers  $N_{active}$  for different values of the output coupler reflectivity, in the case of an anti-resonant structure with  $\Gamma_z = 1.75$  and a pump spot size of  $40 \mu\text{m} \times 60 \mu\text{m}$  (semi-axis values). The thickness of the each active layer is 3 nm. The output power curves have been obtained for 1 W incident pump power.

### Resonant vs anti-resonant cavity effects and laser threshold

As discussed in the previous section, the choice of a resonant or anti-resonant configuration has consequences on the value of the longitudinal confinement factor, which in turn has a significant impact on the pump threshold condition. Fig. 4.19 on next page shows the comparison between the two approaches in terms of the pump threshold as a function of the output coupler reflectivity. Following the results of previous simulations, 18 active layers have been considered to be integrated on the semiconductor chip, each of them being 3 nm in thickness. The pump spot size has

<sup>7</sup> This is the standard value of reflectivity of the output couplers which are available at the lab, thus we consider designing the VECSEL active region with respect to this specification.



been fixed to  $40\ \mu\text{m} \times 60\ \mu\text{m}$  (radius dimensions). In the case of the resonant configuration, no anti-reflection coating has been considered (a reflectivity of  $R_s = 27\%$ , which is a typical value for a InP/air interface at  $1600\ \text{nm}$ ) and a gain enhancement factor of  $\Gamma_{enh} = 1.75$  has been calculated. The gain enhancement factor decreases down to  $\Gamma_{enh} = 0.51$  in the case of an anti-resonant configuration, where a quarter-wave anti-reflection coating of  $\text{SiN}_x$  (at the emission wavelength of  $1600\ \text{nm}$ ) has been deposited on the chip surface. The laser threshold of the two structures is thus considerably different, especially if an output coupler with higher transmission value is employed. For a mirror reflectivity of  $R = 99.5\%$ , we especially notice that the threshold of the anti-resonant case is more than twofold higher than the resonant case. Moreover, in the case of the resonant structure, the laser threshold is less sensitive to the output coupler transmission.

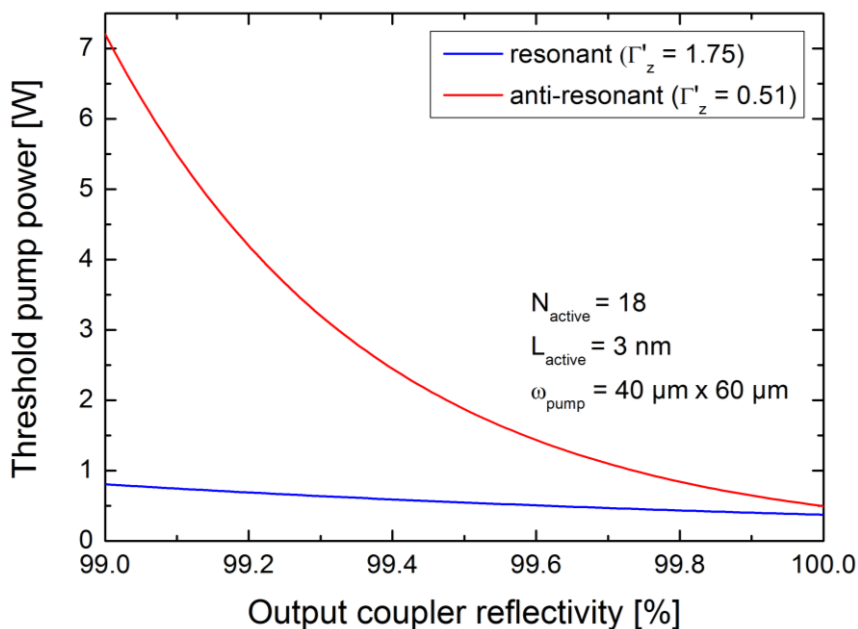


Fig. 4.19 – Comparison of the resonant (blue,  $\Gamma_z = 1.75$ ) and an anti-resonant (red,  $\Gamma_z = 0.51$ ) configuration of a  $1600\ \text{nm}$  emitting OP-VECSEL in terms of computed threshold pump power as a function of the output coupler reflectivity for a device integrating 18 active layers of  $3\ \text{nm}$  each. Pump spot has fixed at  $40\ \mu\text{m} \times 60\ \mu\text{m}$  (radius).

### Output power characteristic

By computing the expected pump threshold  $P_{th}$  and the differential efficiency  $\eta_{diff}$  of the structure, it can be possible to estimate the OP-VECSEL output characteristic as a function of the incident pump power. This can be a starting point to get preliminary information about the choice of the different parameters, in order to roughly optimize the experimental setup, or get an insight about the effect of those choices on the final performance, since those parameters have an interplay on the characteristics of the laser.

As presented in Fig. 4.20, the light-light (LL) curve is dependent on all the parameters that have been previously introduced, but here we mainly focus on the effect of the external mirror

reflectivity. Increasing its transmission leads to a higher external slope efficiency, at the expense of the laser threshold. Anyway, there is again an optimum for which a further increase of the output coupler reflectivity does not translate in a significant improvement of the threshold, whereas the effect on the output power is evident, as it drastically reduces.

In the example of Fig. 4.20, the best trade-off has been obtained for an output coupler reflectivity around 99.5%, this is the value we retain to be the optimum according to these preliminary simulations. The comparison between a resonant versus an anti-resonant (inset of Fig. 4.20) shows the influence of the specific choice configuration in terms of the output characteristic. As discussed above, an anti-resonant structure present significant higher threshold values with respect to a resonant structure (here more than twofold), but it assures a less sensitive structure to thermal or micro-cavity filtering effects, which in some cases may drastically limit (and even prevent) the laser operation of the devices under certain conditions, as already discussed.

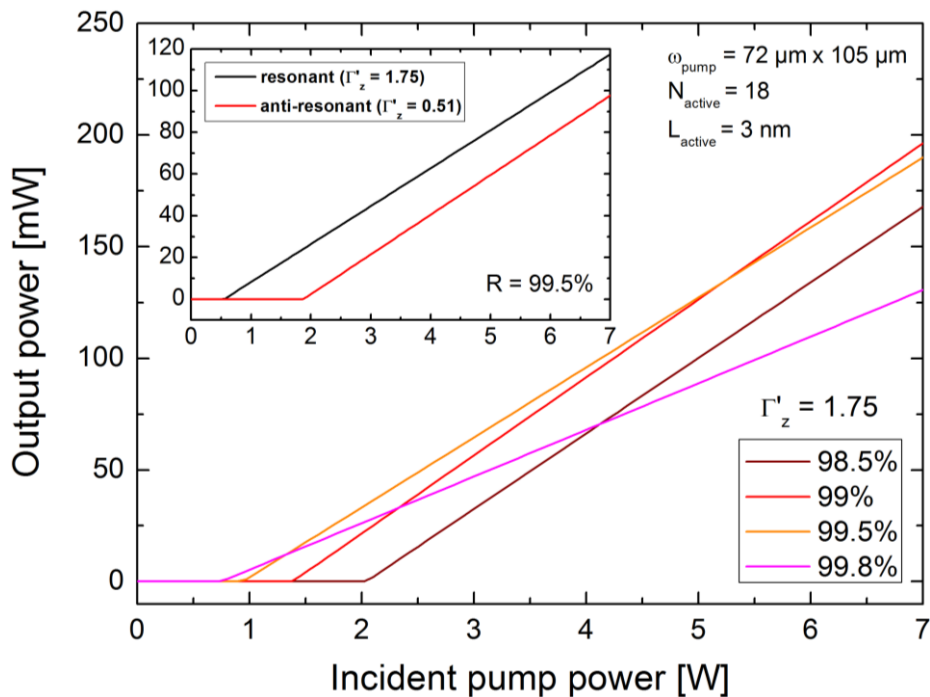


Fig. 4.20 – Computed OP-VECSEL output characteristics for different output coupler reflectivities for  $\Gamma'_z = 1.75$ .  $N_{\text{active}}$  has been set to 18, the pump spot size is  $72 \mu\text{m} \times 105 \mu\text{m}$  (semi-axis). The inset shows the effect of a resonant (black,  $\Gamma'_z = 1.75$ ) or anti-resonant structure (red,  $\Gamma'_z = 0.51$ ) on the laser output for an output mirror with  $R = 99.5\%$ .

Clearly, these basic simulations do not take into account any thermal phenomenon, such as roll-over effect, gain/losses dependences on the temperature or thermal lens induced by refractive index changes, or pumping rate dependence. The model neglects also any multi-transverse/multi-longitudinal effects, and it assumes that the region defined by the pump spot coincides with the (fundamental TEM<sub>00</sub>) cavity mode at the chip surface. Furthermore, any cavity misalignment

(which may lower the matching between the cavity mode and the pump mode) is completely neglected.

### 3<sup>rd</sup> conclusion

The semi-empirical model allows studying the influence of different parameters (number of active layers, chip configuration and output coupler reflectivity) in order to estimate the VECSEL threshold and emitted power. By using the characteristic material parameters listed in Table 4.6, we were able to obtain a starting point for the design of our VECSEL. By following the results of this preliminary study, **we then choose to integrate 18 active layers on our structure to maximize the emitted power and ensure a moderate threshold**, in the case of an **output coupler with reflectivity  $R = 99.5\%$**  (best trade-off  $P_{out}$  vs  $P_{th}$ ). **The study allowed also confirming the choice of the resonant configuration to obtain a low threshold.**

## 4.7 Conclusions

In this chapter we discussed about the peculiarities of vertical-external-cavity surface-emitting lasers.

**The key elements which constitute a VECSEL cavity have been introduced**, and the advantages deriving from the use of an external cavity have been discussed in terms of pump scaling, beam quality and applications. The possibility to easily control the transverse profile of the emission to have a good circular mode profile while keeping high value of the emitted power ( $> W$ ), together with the possibility to functionalize the device through the insertion of intra-cavity elements, contributed to the success of this new class of semiconductor lasers.

Thanks to their versatility, VECSELS have found applications in a wide range of optical systems, some of them (the most significant) have been presented in this introductory chapter. A state-of-the-art in terms laser performance (maximum emitted power and working temperature) has been also presented, in the case of quantum wells- and quantum dots-based devices, for the main III-V semiconductor material systems (GaAs, InP and GaSb).

Finally, **some design rules (mostly focused on the case of InP-based devices) have been discussed**. In particular, according to that study, **we chose:**

- **to adopt a thin-device architecture with GaAs/AlAs-based DBRs to improve the thermal management of the device;**

- **to adopt a resonant configuration in order to promote the lasing of the device at the desired wavelength;**
- **to integrate 18 active layers on our structure to maximize the emitted power and ensure a moderate threshold.**

These rules have been used as a starting point for the design of the optically-pumped quantum dash-based VECSEL, which will be described in the following chapter.

# **Chapter 5**

## ***Development and characterization of a low noise quantum dashes-based VECSEL on InP***

<b>5.1 Introduction .....</b>	<b>170</b>
<b>5.2 Design and realization of the optically-pumped VECSEL based on quantum dash active medium .....</b>	<b>171</b>
5.2.1 Quantum dash active region design and characterization .....	172
5.4.2 GaAs/AlGaAs DBR metamorphic growth and device integration (C2N).....	176
<b>5.3 Characterization of the OP-QDH-VECSEL in multi-mode regime.....</b>	<b>179</b>
5.3.1 Experimental setup.....	179
5.3.2 Spectral emission and output characteristic .....	181
5.3.3 Preliminary conclusion .....	183
<b>5.4 Low noise Class-A single-frequency operation.....</b>	<b>184</b>
5.4.1 Obtaining the low noise Class-A regime .....	184
5.4.2 Realization of the experimental setup .....	187
5.4.3 Estimation of the thermal impedance.....	189
5.4.4 Single-frequency operation .....	191
5.4.5 Static polarization properties of the QDH-VECSEL .....	194
5.4.6 Class-A regime and RIN .....	195
5.4.7 Spectral purity .....	200
<b>5.5 Conclusions.....</b>	<b>203</b>

## 5.1 Introduction

In different material systems, low dimensional nanostructures started to raise interests in the scientific community for their remarkable properties in terms of low threshold and reduced temperature sensitivity [Liu1999, Shchekin2002, Banyoudeh2016], polarization stability [Lamy2009, Gauthier2012], wide spectral coverage [Ooi2008, Taleb2013], narrow linewidth and low noise [Rosales2012, Faugeron2013], ultrafast carrier dynamics [Bhattacharya2000], etc.

For optical generation and remote distribution of wideband microwave or millimeter-wave signals, semiconductor active regions have already demonstrated to bring superior performance. In this case, particular attention must be paid on the spectral purity of the laser source. Indeed, it has been shown that the relative intensity noise (RIN) of the source is generally the main contribution to the noise level of the optical link [Bibey1999], so that it should be kept as low as possible to not spoil the quality of the signals by the additive noise which is naturally introduced. It has been also demonstrated that a semiconductor vertical-cavity surface-emitting laser, when inserted in sufficiently long external cavities to form a VECSEL, can operate in the so-called Class-A regime. This regime is characterized by a very low RIN level, down to the quantum limit (shot noise) [Baili2007], and it does not show resonant phenomena like relaxation oscillations. For such characteristics, VECSELs represent good candidates for the development of ultra-low noise optical sources for the generation of optical carriers in the microwave range, for example.

Besides these advantages, this cavity configuration easily allows to realize dual-frequency emitters by the use of intra-cavity crystals, which lead to the simultaneous oscillation of two orthogonal linearly-polarized modes with different and independently tunable frequencies, for the generation of highly pure GHz and THz radiation by optical mixing of the two modes [De2014b].

In the framework of this thesis, we were therefore interested in investigating the behavior of nanostructured semiconductor active media in an external-cavity configuration, in order to benefit from the long-cavity setup in terms of laser linewidth reduction and enhancement of the noise performance, with the ultimate goal of integration in low-noise and highly tunable optical sources.

*Chapter 5* is thus devoted to present the results of the design, the realization of an optically-pumped VECSEL based on InAs quantum dashes active region on (001)-oriented InP substrate, and its subsequent characterization in terms of output power and spectral characteristics as well as noise behavior.

## 5.2 Design and realization of the optically-pumped VECSEL based on quantum dash active medium

Having presented the optical and thermal properties of InAs quantum dashes active regions in *Chapter 3*, we can now discuss about their integration in a vertical-extended-cavity configuration. In this section we will detail the architecture that we choose for the semiconductor chip composing the optically-pumped quantum dashes-based VECSEL (OP-QDH-VECSEL), and its technological realization. In the next sections, we will present the integration of the final chip in the experimental setups, and its characterization. For the design of the device, we follow the guidelines which have been introduced in the previous *Chapter 4*. For convenience, here we remind the choices that we made:

- the integration of a **bottom DBR based on GaAs/Al(Ga)As**, for its superior thermal and optical properties;
- the use of a **thin-device architecture**, to further improve the thermal extraction without unwanted etalon effects;
- the design of a **resonant structure**, to enhance the cavity effect and obtain a higher output power and a lower threshold condition;
- the **integration of 18 active layers of quantum dashes**, which represents an optimum value to maximize the output power without the degradation of the threshold, in the case of an output mirror with reflectivity  $R = 99.5\%$ .

As depicted in Fig. 5.1 on next page, the VECSEL chip is basically composed by three main parts:

1. The **nanostructures-based active region**, which integrates the InAs quantum dashes layers emitting a  $\lambda = 1.6 \mu\text{m}$ . We choose to group the active layers in 3 sets, each of them containing 6 quantum dashes layers, surrounded by  $\text{In}_{0.8}\text{Ga}_{0.2}\text{As}_{0.435}\text{P}_{0.565}$  barriers on (001)-oriented InP substrate.
2. The **bottom hybrid Distributed Bragg Reflector (H-DBR)**, which will consists in 17 pairs of metamorphically-grown GaAs/AlGaAs layers, centered at the emission wavelength. In order to further reduce the mirror thickness (and thus its thermal impedance  $R_{th}$ ), the DBR will be completed by a 200-nm thick metallic Au layer, to reduce the number of GaAs/AlGaAs pairs while keeping a high value of reflectivity. This mirror is designed to guarantee a theoretical reflectivity of 99.9%;



3. The **bottom highly-conductive heat-spreader**, made by synthetic (CVD-grade) diamond which has an average thermal conductivity  $k_t \sim 1800\text{-}2000$  W/m-K. The heat-spreader, which is fixed to the active chip by means of a metallic Ti/Au bonding layer, allows improving the extraction of the heat from the pumped region towards the Peltier module. The whole thin VECSEL device is then fixed onto a copper heat-sink, which improves the mechanical stability of the chip.

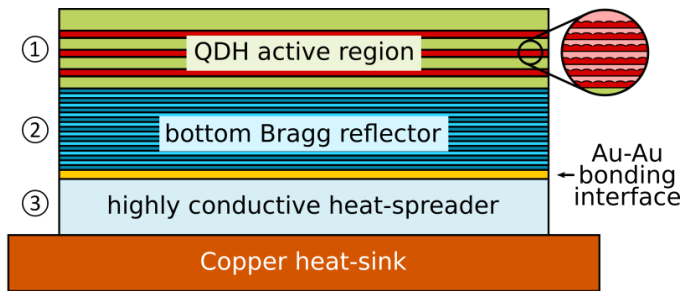


Fig. 5.1 – Design of the OP-QDH-VECSEL composed by the three main parts: (1) active region, (2) GaAs/AlGaAs DBR and (3) diamond heat-spreader.

In the following sections, we detail the design of the active region and the H-DBR.

## 5.2.1 Quantum dash active region design and characterization

### Preliminary considerations

The results of measurements of the modal gain in QDH-based nanostructures active medium presented in *Chapter 3* attested that a larger number of InAs QDH active layers are needed to compensate for the lack of active volume of such nanostructures, compared to the case of InGaAsP SQWs. This was also confirmed by the result of the design simulations based on the semi-empirical model described in the previous chapter, from which we retained the information that around 18 quantum dash layers should compose the active region of our quantum dash-based VECSEL. This result is also in good agreement with respect to the criterion that has been adopted from the previous work of J.M. Lamy on monolithic VCSELs [[Lamy2008](#)]. In this previous work, in order to have a material gain which is comparable to that of a previously designed active region based on conventional lattice-matched  $\text{In}_{0.53}\text{Ga}_{0.43}\text{As}$  quantum wells (QW) on InP, a “rule of thumb” was adopted. This empirical design rule was based on the assumption that the typical height of InAs quantum dashes is around 2.5-3 nm, which correspond to nearly 1/3 of the thickness of standard InGaAsP strained quantum wells (SQWs), which were successfully integrated in a working  $\mu\text{m}$ -long VCSEL emitting at 1.56  $\mu\text{m}$ . In that case, the SQW-based active region was composed by a total number of six SQWs, arranged in 3 sets of 2 SQWs each. Therefore, the number of QDH active layers was set to 18, and they were distributed in 3 sets, each set including 6 QDH planes.

However, this approximation did not consider the longitudinal confinement factor  $\Gamma_z$  nor the inhomogeneous broadening, which is significantly different between a QDH- and a SQW-based active region (~100 nm versus ~60 nm, respectively, as previously seen in **Chapter 3**), so the choice of the number of active layer should also take into account these considerations. It is worth to notice that, consistently with the analysis presented in the previous chapter, this is also the number of active layers needed to maximize the output power of our QDH-VECSEL, while keeping the threshold in an accessible range for commercially-available and cost-effective 980 nm-emitting single-mode pump modules (i.e. 400-500 mW), as presented later in this chapter. Furthermore, this agreement should not surprise, since for monolithic VCSELs most of the times the laser cavity is designed to be resonant, so that we can easily understand this similar result.

## **Design**

With these basic considerations in mind, the quantum dash-based active region (sample QDH-4863) has been designed using the MATLAB<sup>®</sup> simulation routine based on the Transfer-Matrix-Method (TMM), already discussed in **Chapter 1** for the design of the DBRs.

The active region is composed by three sets of six quantum dashes layers grown on a nominally (001)-oriented InP substrate, with an average dash height of 3 nm, consistently with what we have discussed so far. The active region has been designed to have a PL emission at 1.58  $\mu\text{m}$  at room temperature. From our previous experience in monolithic VCSELs, we expect a 20-30 nm redshift of the emission peak during laser operation, due to thermal effects (gain and cavity resonance thermal tuning). Anyway, the redshift extent strongly depends on the internal temperature of the device and the experimental conditions, so that this represents a rough estimation.

The QDH-based active region structure is represented in Fig. 5.2a (next page). Please note that two adjacent quantum dash layers are separated by a 15 nm-thick quaternary alloy layer of  $\text{In}_{0.8}\text{Ga}_{0.2}\text{As}_{0.435}\text{P}_{0.565}$  (Q<sub>1.18</sub>). The thickness of the outer quaternary alloy Q<sub>1.18</sub> layers surrounding each QDH set is chosen to ensure an efficient and balanced pumping through the whole VECSEL structure, in order to guarantee a nearly uniform carrier generation per active set. To this aim, the number of QDHs layers is kept constant for each layer, and the thickness of the outer barriers is increased as the pump penetrates inside the structure, as represented in Fig. 5.2b (next page). In the same figure the pump intensity and the internal optical field intensity (at the lasing wavelength) are plotted.

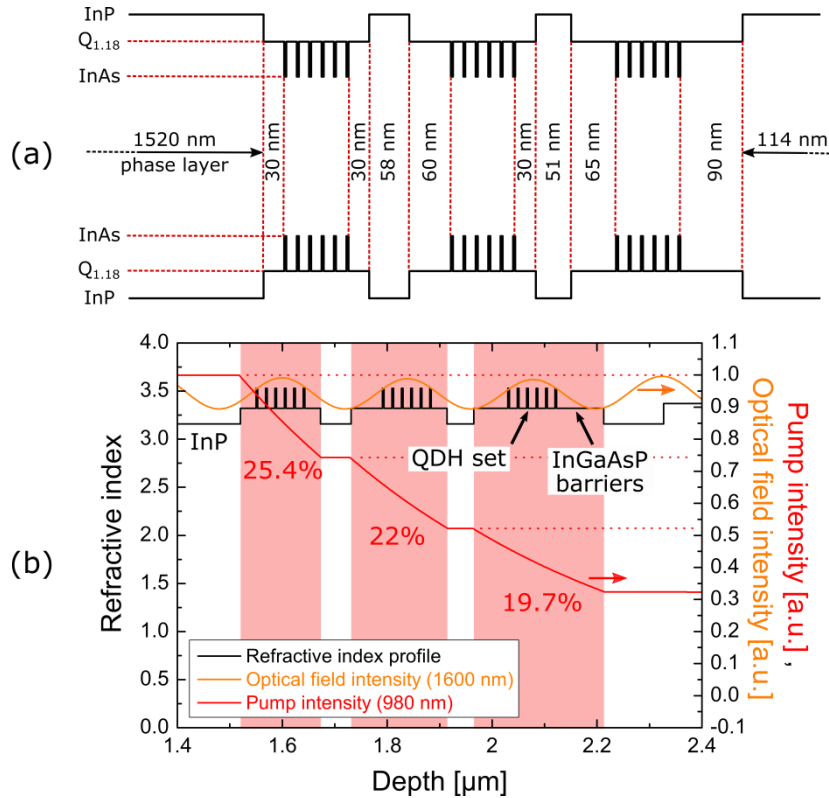


Fig. 5.2 – (a) Design of the active region based on three sets of six quantum dashes layers with InP spacers and  $Q_{1.18}$  barrier thickness. (b) Normalized pump intensity distribution with percentage absorption in each set (red curve) and optical field intensity (orange curve) inside the structure.

At this step, we estimate a single-pass absorption of 25.4%, 22% and 19.7% on the first, second and third QDH set, respectively, for a single-pass total absorption of  $\sim 67\%$ . These values have been calculated by considering an effective absorption coefficient equal to  $\alpha_{eff} = 19000 \text{ cm}^{-1}$  at the pump wavelength<sup>1</sup> ( $\lambda_{pump} = 980 \text{ nm}$ ) for the  $Q_{1.18}$  absorbing layers [Levallois2006a], while the InP layers are transparent in this range. A residual pump reflection due to the bottom DBR can further increase the pump absorption inside the active layers. However, in our case no particular attention has been paid to design the bottom DBR reflectivity at the pump wavelength. We will come back to the DBR design in the next section.

In addition to that, the thickness of each layer is also designed to exactly accommodate the three active sets on the antinodes of the resonant stationary field (orange curve in Fig. 5.2b) inside the sub-cavity formed by the air/InP interface and the bottom DBR. This maximizes the modal gain of the structure thanks to a resonant periodic gain (RPG) configuration, as already discussed in **Chapter 4**. If needed, the InP phase layer can be adjusted by a precise value by post-growth etching steps, in order to compensate for any eventual overgrowth due to MBE thickness tolerances, and to obtain the designed sub-cavity length to match the desired emission wavelength.

<sup>1</sup> This value can be easily justified by considering that the energy levels quantization of InAs QDHs can drastically modify the optical properties of the nanostructures with respect to that of bulk InAs (for which  $\alpha_{InAs} \approx 55000 \text{ cm}^{-1}$  at 980 nm). Additionally, the InAs QDH layers have a negligible thickness with respect to the InGaAsP  $Q_{1.18}$  barriers.

## Growth and characterization

The active region growth is preceded by the calibration of the Gas Source Molecular Beam Epitaxy (GS-MBE) reactor, when the different growth parameters (such as III-V element flux, cells and substrate temperatures, etc.) are verified. To this aim, on the same day of the V(E)CSEL growth, calibration samples are realized. They consist in InGaAs/InP superlattices and a single set of six QDHs. The first one allows getting the on day InP growth rate according to X-ray diffraction (XRD) measurement, when the second one enables to get the on day QDH wavelength emission by photoluminescence characterization. Once the calibration process is successfully completed, the final structure is ready to be grown.

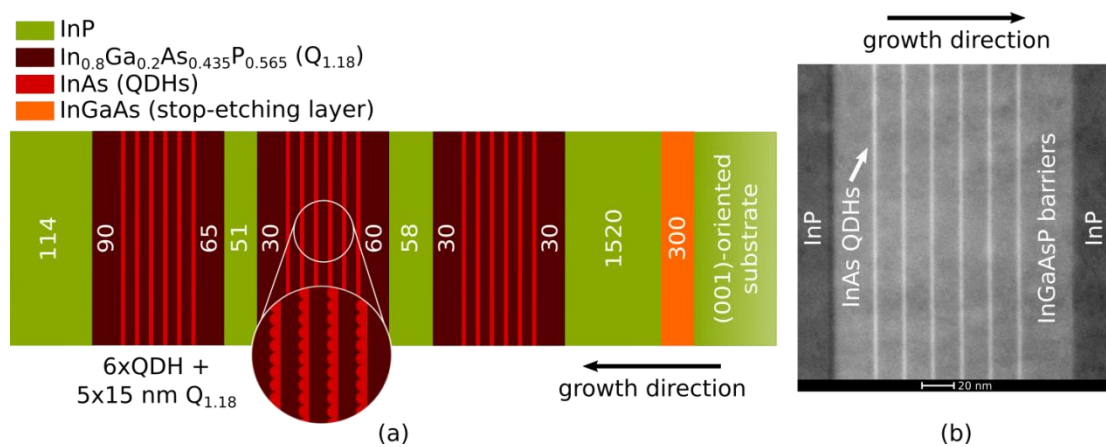


Fig. 5.3 – (a) Structure of the active region realized by GS-MBE on (001)-oriented InP substrate (sample QDH-4863). Layers' thickness is reported in nm. (b) Scanning Transmission Electron Microscopy (STEM) image of the 3<sup>rd</sup> grown set composing the active region, with Energy Dispersive X-Ray Spectroscopy (EDS) analysis of layer composition.

The QDH-based active region of the VECSEL has been grown in reversed order on a (001)-oriented 2-inch InP wafer, following the design presented in the previous section. Its structure is depicted in Fig. 5.3. As discussed in **Chapter 3**, the (001) crystallographic orientation of the InP naturally promotes the growth of InAs QDH along the [1-10] direction.

The growth of the active region begins with a 300 nm-thick InGaAs stop-etching layer, which is used to precisely control the InP substrate removal by chemical etching, during the final steps of the device processing. The growth continues with the deposition of the InP phase layer (nominal thickness of ~ 1520 nm), and the core of the active region, which is composed by the three sets of six InAs QDHs, surrounded by the Q<sub>1.18</sub> InGaAsP barriers, and the InP spacers, as previously explained.

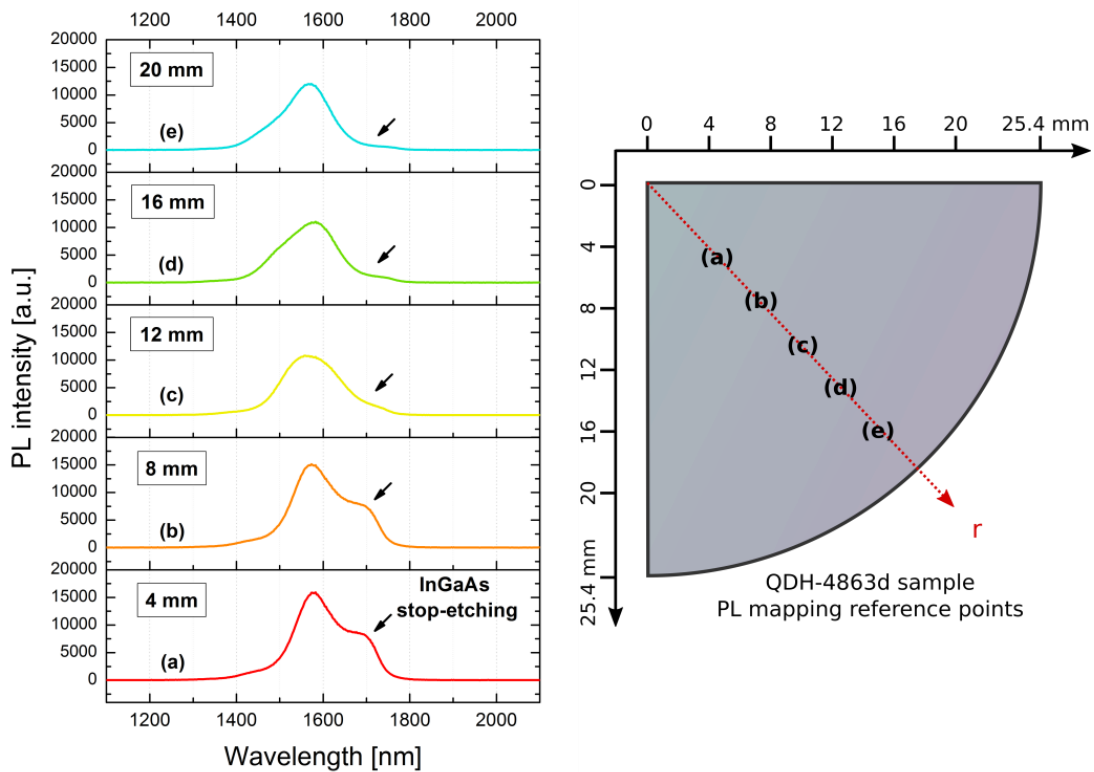


Fig. 5.4 – Room-temperature PL mapping on the sample QDH-4863d for different positions with respect to the center of the 2" wafer. The black arrows indicate the 1.7  $\mu\text{m}$  peak due to the InGaAs stop-etching layer.

The sample has been optically characterized in terms of PL emission, and a room-temperature mapping on a quarter of wafer has been realized. In Fig. 5.4 we reported few spectra at different positions along a line going from the center towards the edge of the wafer. The measurement showed a good uniformity in terms of emission wavelength, which is centered around 1.58  $\mu\text{m}$ . Moreover, a good intensity across the whole surface is observed, with a small decrease in intensity near the edges of the sample and a FWHM between 120 and 140 nm.

The peak around 1.7  $\mu\text{m}$ , clearly visible in curves (a) and (b) is indicated by a black arrow. This peak is related to the presence of the InGaAs stop-etching layer, and it will disappear after the clean-room processing of the sample.

Once the active region has been realized, the bottom reflector can be grown on top of it.

## 5.4.2 GaAs/AlGaAs DBR metamorphic growth and device integration (C2N)

As discussed in Section 4.6.1, the heat management plays an important role on the performance of the devices. This particularly applies in the case of InP-based VECSELs, because of the high dissipated power and the poor thermal properties of the lattice-matched quaternary alloy (InGaAsP) composing the mirror stacking. In the thin device configuration, the one that we chose for our

device, the heat extraction is performed through the bottom DBR, which needs to be thermally efficient to promote the heat extraction through the bottom of the device.

For that purpose, a metamorphic AlGaAs/GaAs DBR has been selected to be grown on the QDH active region.

Once the InP-based active region realized, the sample was sent to Sophie Bouchoule at the Centre de Nanosciences et de Nanotechnologies (C2N) in Marcoussis, to perform the growth of the bottom DBR. In order to compensate for the thermal redshift of the VECSEL emission during laser operation, the mirror has been deliberately designed to be centered at 1600 nm. The choice of the DBR central wavelength has been done by considering a 20 nm offset with respect to the room-temperature PL emission of the active region centered at 1580 nm (as we remember from Fig. 5.4).

We designed a bottom DBR mirror composed by 17 pairs of GaAs/Al<sub>0.97</sub>Ga<sub>0.03</sub>As layers (GaAs: 240 nm, Al<sub>0.97</sub>Ga<sub>0.03</sub>As: 140 nm), completed by a 200 nm of Au layer to boost its reflectivity and limit its thickness. Prior to the DBR growth, a quarter-wave thick InP buffer layer was deposited at the interface, followed by a half-wave thick (480 nm) GaAs buffer layer (see Fig. 5.5a). This structure shows a reflectivity exceeding 99.5% over 142 nm with a maximum theoretical value of 99.9% centered at 1600 nm, as presented in Fig. 5.5b. In practice, because of the growth tolerances and the roughness of the interfaces of the layers, as well as the residual absorption of the materials composing the DBR at the emission wavelength, the reflectivity is generally lower than the theoretical value. Note that the curve of Fig. 5.5b is related to the isolated DBR, in the case of an incident media constituted by undoped InP.

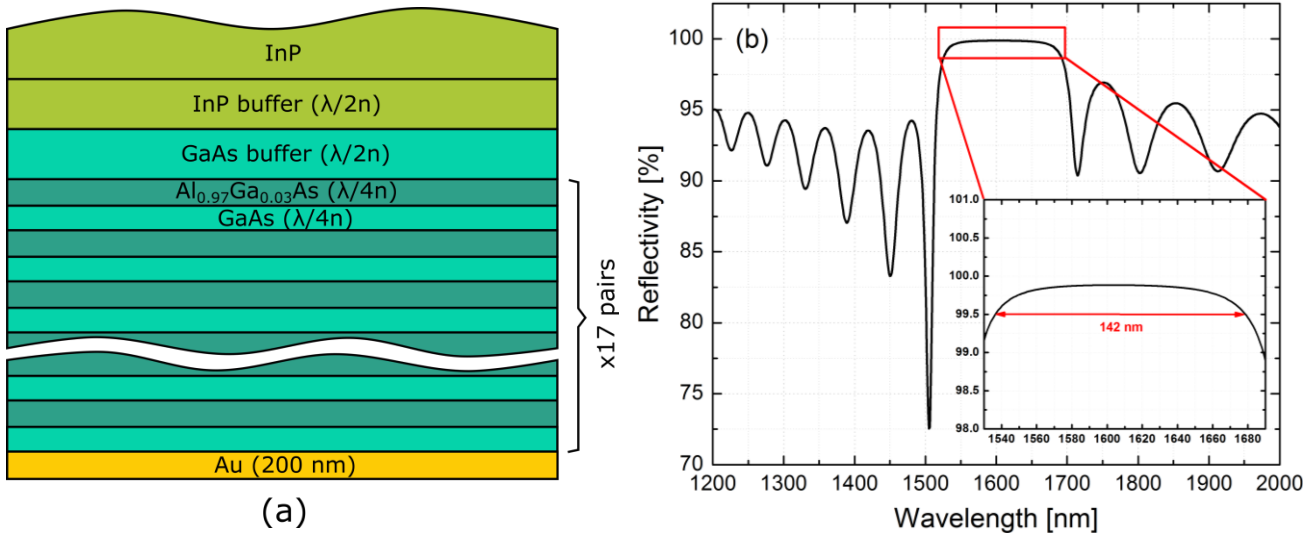


*Fig. 5.5 – (a) Epitaxial structure of the GaAs/Al<sub>0.97</sub>Ga<sub>0.03</sub>As bottom hybrid DBR with the Au metallic layer and (b) the computed reflectivity spectrum.*



The quarter of 2" wafer has been cleaved to form a  $7 \times 7 \text{ mm}^2$  squared sample, and then it has been fixed onto a  $1 \times 1 \text{ cm}^2$  synthetic diamond heat-spreader thanks to an Au-Au metal bonding. To improve the adhesion, a thin Ti layer has been deposited before the gold layers. Prior to any lasing test, the InP substrate has been mechanically polished, and then chemically etched to eliminate the remaining substrate and the InGaAs stop-etching layer. The final thickness of the semiconductor chip is of  $\sim 6 \mu\text{m}$ . To facilitate the manipulation of the device, the whole VECSEL chip has been successively fixed onto a copper mount with a thin thermal grease layer.

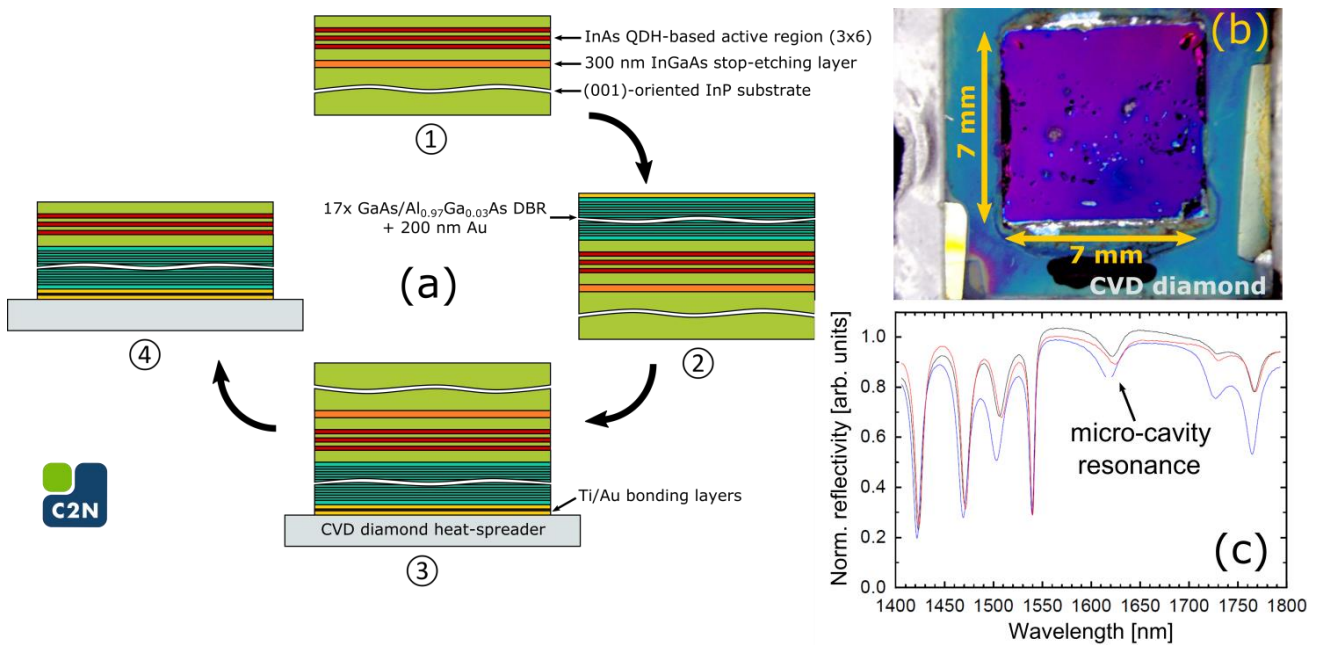


Fig. 5.6 – (a) Processing of the OP-QDH-VECSEL (performed at C2N): ① QDH-based active region growth on (001)-oriented InP substrate, ② Metamorphic growth of the GaAs/Al<sub>0.97</sub>Ga<sub>0.03</sub>As bottom hybrid-DBR with 200 nm-thick Au metallic layer, ③ Dice cleaving and Ti/Au bonding on CVD-grade diamond heat-spreader and ④ Mechanical/chemical removal of the InP substrate. (b) Photograph of the processed chip. (c) Post-processing reflectivity spectrum of the device at three different surface positions.

Fig. 5.6a summarizes the processing of the QDH-VECSEL, performed at C2N. As we can notice from Fig. 5.6b, the processed chip showed some roughness at the surface, which occurred after the CVD diamond bonding and the substrate removal. At this point we were not able to identify the cause, but an optical microscope analysis showed that such roughness is due to the incorporation of some defects into the semiconductor layers. However, part of the semiconductor chip showed a good mirror-like surface, potentially suitable to get lasing operation. A FTIR measurement at different positions on the top surface of the VECSEL revealed the presence of the micro-cavity resonance dip around 1620 nm, as shown in Fig. 5.6c, for three different positions on the semiconductor chip. Once the technological realization was completed, the sample was ready to be used in experiments, as described in the next sections.

## 5.3 Characterization of the OP-QDH-VECSEL in multi-mode regime

### 5.3.1 Experimental setup

The device described in the previous paragraph has been initially characterized in the experimental setup depicted in Fig. 5.7. The purpose of this preliminary test was essentially to investigate the characteristics of the device in terms of maximum output power achievable and wavelength emission, and to check the quality of the sample in terms of surface uniformity.

To this aim, the optically-pumped QDH-VECSEL chip has been assembled with a concave output coupler with a radius of curvature  $R_{oc} = 15$  mm, to form a linear laser cavity. The given nominal reflectivity of the external mirror is  $R = 99.5\%$  at 1550 nm. From a FTIR measurement, we were able to estimate its reflectivity to be  $R = 99.2\%$  at the expected lasing wavelength (i.e. around 1600 nm).

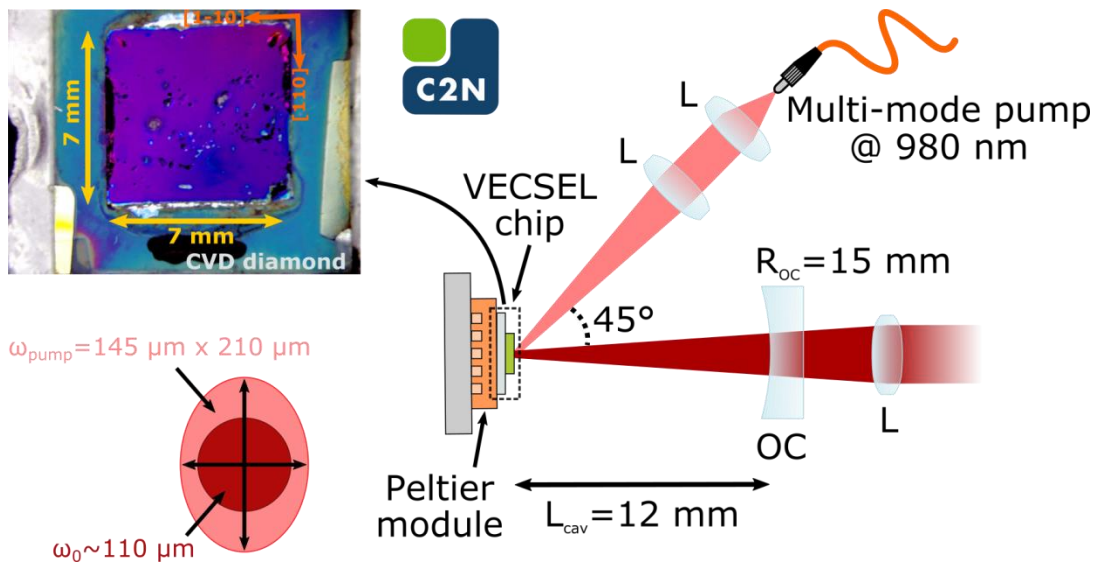


Fig. 5.7 – Scheme of the experimental setup used to characterize the QDH-VECSEL in multi-mode operation, with an image of the chip and the pump and cavity spots' dimensions at the VECSEL surface. Waist dimensions are given in diameter. L: lens,  $L_{cav}$ : cavity length, OC: output coupler,  $R_{oc}$ : output coupler's radius of curvature.

Once the cavity was realized, the active medium has been excited with a commercially-available and non-polarized multi-mode fibered semiconductor pump module, placed at an incidence angle of  $45^\circ$  with respect to the VECSEL cavity axis. The pump module used in this experiment was able to deliver up to 7 W of incident optical power in continuous wave (CW) operation. Its emitted wavelength is around 960 nm just above threshold, and shifts to 973 nm at the maximum emitted power. After the collimating and focusing lenses, the pump forms a spot of  $72 \mu\text{m}$  in radius at the



focusing point, which results in an elliptical spot size of about  $145 \mu\text{m} \times 210 \mu\text{m}$  on the chip surface (minor axis  $\times$  major axis dimensions, respectively), due to the  $45^\circ$  tilt. Once in the active medium, the pump spot becomes nearly circular and equal to  $145 \mu\text{m} \times 149 \mu\text{m}$ , owing to Fresnel refraction. Unfortunately, under such conditions no lasing was observed. Despite all the precautions taken during the design and processing of the device, we suspect a temperature-induced mismatch between the active layers emission peak and the micro-cavity resonance (the two shift at different rates) to be the main cause of the non-operation of the device. The thermal heating due to the incident pump power on the VECSEL surface, in combination with an underestimated thermal impedance, could be at the origin of this mismatch, preventing the VECSEL to reach the lasing threshold. This may be particularly attributed to the resonant design of the VECSEL chip, which is more sensitive to thermal shifts of the resonant dip, which translates into the afore-mentioned mismatch. To solve this problem, a quarter-wave-thick (212 nm)  $\text{SiN}_x$  anti-reflection (AR) coating around the lasing wavelength has been deposited on the top surface of the chip (cf. Fig. 5.8a).

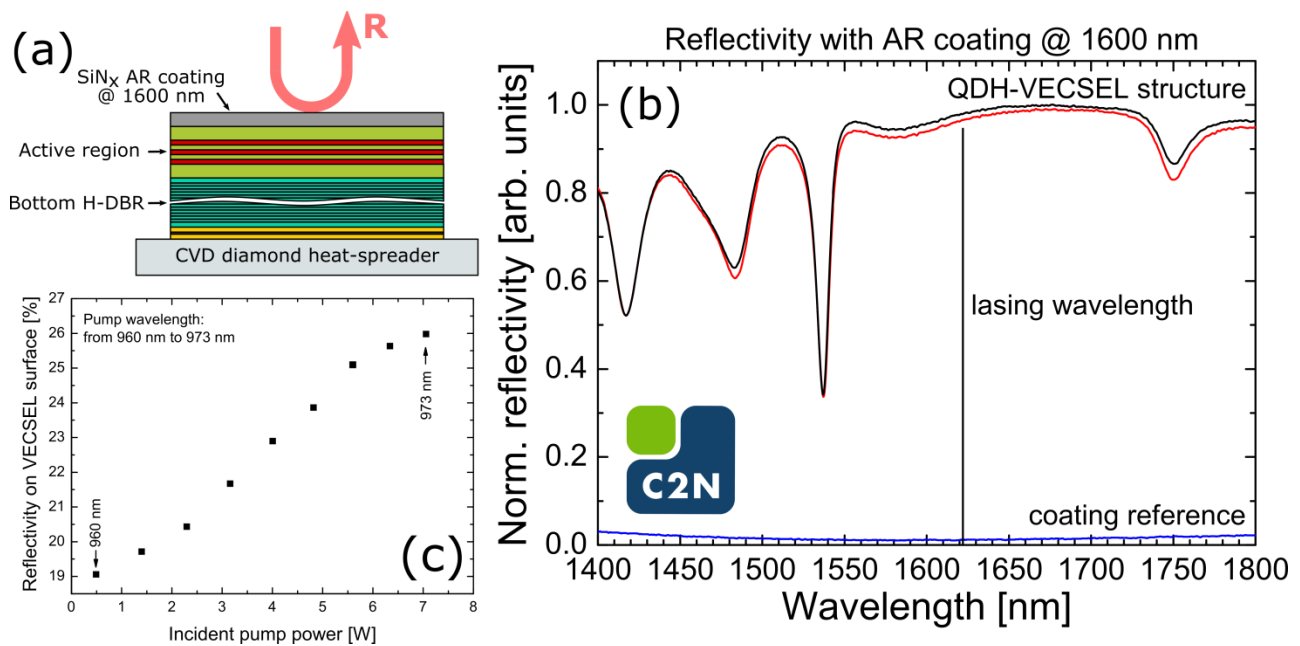
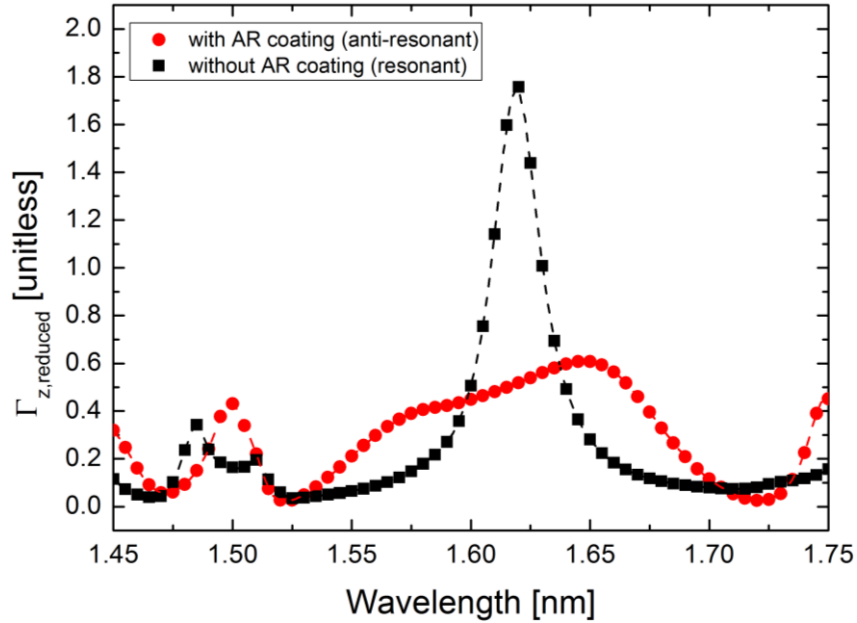


Fig. 5.8 –  $\text{SiN}_x$  AR coating deposition on the QDH-VECSEL top surface: (a) Final structure, (b) FTIR-measured reflectivity spectrum at two different positions across the chip surface and (c) pump reflection vs incident pump power.

After the deposition of the  $\text{SiN}_x$  AR coating, the structure is anti-resonant and the micro-cavity dip at 1620 nm is no more present in the surface reflectivity spectrum (cf. Fig. 5.8b). In these conditions, the pump reflection at the chip surface has been measured to be between 19% and 26% (Fig. 5.8c), depending on the incident pump power on the VECSEL surface. This value is mostly due to the air/ $\text{SiN}_x$  interface and is coherent with the calculated reflection for such a structure, in the case of a  $45^\circ$  angle of incidence. The change of the chip reflectivity with respect to the incident

pump power is mostly due to a redshift of the pump emission from 960 nm to 973 nm, together with a thermal heating which induces a modification of the refractive index of the layers composing the VECSEL structure, as the incident pump power is increased from 0.5 W to 7 W.



*Fig. 5.9 – Computed reduced longitudinal confinement factor of the QDH-VECSEL structure before (black squares) and after (red circles) the deposition of the SiN<sub>x</sub> AR coating.*

Consistently with what discussed in *Section 4.6.3*, the presence of the AR coating now leads to a reduced and nearly constant longitudinal confinement factor  $\Gamma_z$  on a broader wavelength range around the designed emission wavelength, with respect to the as-grown resonant structure (see Fig. 5.9). This in turns translates into a lower but broader value of the modal gain  $\Gamma_z g$  on the wavelength range of interest. The result is that now the laser performance is therefore less sensitive to the wavelength variations due to micro-cavity tuning, thermal-induced wavelength shifts of the resonance dip and the active region peak emission, or filtering effects introduced by the extended cavity configuration, which most likely prevented the VECSEL to reach the lasing condition in previous tests.

### **5.3.2 Spectral emission and output characteristic**

After the deposition of the SiN<sub>x</sub> AR coating, the QDH-VECSEL was able to reach the lasing oscillation in the experimental setup presented above. For the selected pump spot size, the optimal cavity length which maximizes the emitted power of the VECSEL has been found to be equal to 12 mm. For such a length, the waist of the cavity TEM<sub>00</sub> mode at the chip surface is calculated to be

$\omega_0 \sim 55 \mu\text{m}$  in radius (i.e.  $2 \cdot \omega_0 \sim 110 \mu\text{m}$  in diameter). The waist is calculated using the Gaussian beam propagation based on the ABCD matrix method described in **Appendix A**.

Fig. 5.10a shows the output characteristic  $P_{out}$  of the OP-QDH-VECSEL and the measured maximum emitted wavelength as a function of the incident pump power  $P_{inc}$ , for a stage temperature of  $20^\circ\text{C}$ . Under such experimental conditions, the QDH-VECSEL has a threshold pump power around  $P_{th} = 1.3 \text{ W}$  (corresponding to an incident pump density of  $\sim 5.5 \text{ kW/cm}^2$ ), and a maximum emitted power of  $163 \text{ mW}$  at  $7 \text{ W}$  of incident pump power. It is worth noting, however, that the maximum achievable power of the VECSEL is pump-limited, and we expect to get more using a more powerful pump module.

Given the relatively long cavity length (in the cm scale) and due to the lack of any intra-cavity filtering, the VECSEL operates in the multi-longitudinal mode regime, switching from a mono-transverse to a multi-transverse mode emission, for a pump power around  $4 \text{ W}$ . Just above threshold, at  $P_{inc} = 1.8 \text{ W}$ , the QDH-VECSEL emits around  $1611 \text{ nm}$ , as shown in Fig. 5.10b. As the pump is increased, the emission shows a typical redshift attributed to thermal effects, and a broadening related to the appearance of higher-transverse and longitudinal lasing modes, which reach the threshold condition, as attested by Fig. 5.10c.

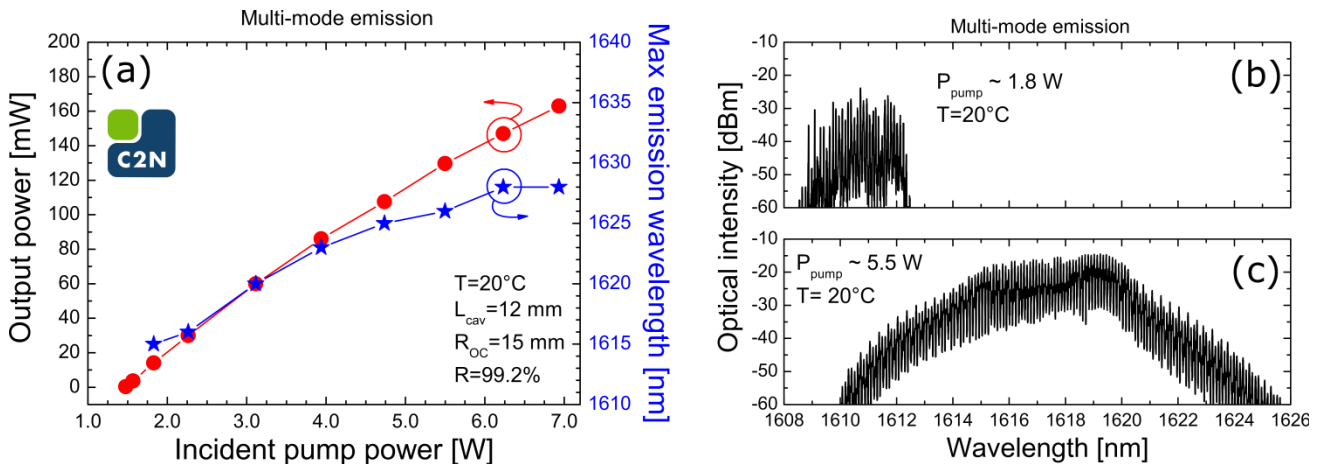


Fig. 5.10 – (a) OP-QDH-VECSEL output power characteristic (red circles) with maximum emitted wavelength (blue stars), and emission spectra (b) near threshold ( $1.8 \text{ W}$ ) and (c) well above threshold ( $5.5 \text{ W}$ ).

Although a direct comparison can be somehow unfair, at this point we would like to stress the fact that our QDH-VECSEL shows a threshold that is at least twofold higher with respect to that of a conventional InGaAsP QW-based VECSEL emitting around  $1.55 \mu\text{m}$  (used as a reference). This comparison has been realized using the same setup and identical experimental conditions (temperature, pump spot size, cavity length, pumping module, etc.). The active region of such a QW-VECSEL integrates 8 SQWs, while the bottom DBR mirror was basically the same (17 pairs of GaAs/AlGaAs), and the semiconductor chip was reported on a diamond substrate. Similarly to

the threshold, the maximum emitted power in the case of the QDH-VECSEL is nearly twofold lower than the one measured for the InGaAsP QW-VECSEL. This worse performance may partially be attributed to the presence of the  $\text{SiN}_x$  anti-reflection coating deposited on the QDH-VECSEL surface, which lowers the longitudinal confinement factor  $\Gamma_z$ , as previously discussed, and to a thermal impedance higher than expected. We will come back to this last point in the following.

During these first lasing tests, we were also interested in characterizing device in terms of lasing uniformity, in order to map the lasing regions across the chip surface. In this case, a quite high dispersion has been observed, with wide non-working areas. Thanks to a near-infrared (NIR) InGaAs CCD camera, it has been possible to identify few lasing points, indicated in Fig. 5.11a with the arrows, and their corresponding output characteristics in Fig. 5.11b. The cause of this relatively large non-homogeneity of lasing across the VECSEL chip is still under investigation, but at present it can be mostly related to a non-uniformity of the thermal impedance of the structure, which is probably higher than expected. We will come back on this last point in the following section.

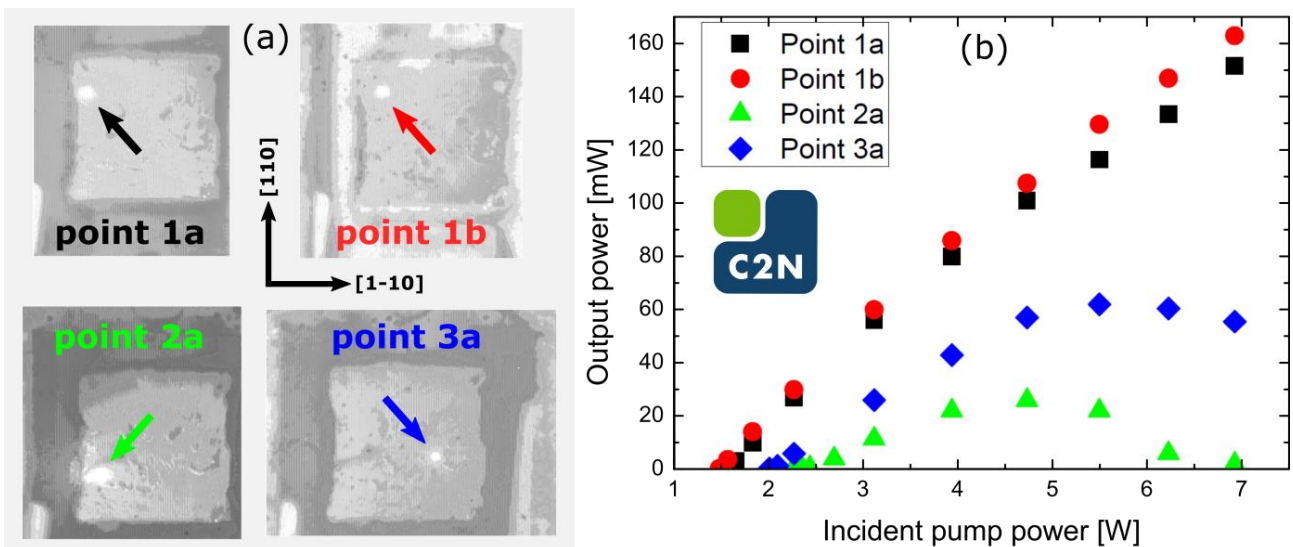


Fig. 5.11 – Mapping on QDH-VECSEL chip surface: (a) lasing positions and (b) corresponding output characteristics.

### 5.3.3 Preliminary conclusion

Despite the relatively high threshold and low output power with respect to a reference sample based on SQW-active region, the results of these first characterizations demonstrate the feasibility to realize a VECSEL on the InP platform which integrates low-dimensional quantum dashes in the active region. To the best of our knowledge, this is the first realization of a nanostructures-based VECSEL in the InP system and emitting beyond  $1.3 \mu\text{m}$ .

The device is able to work in CW operation at ambient temperature, with an emitted power in the 100-mW regime. A future work may consider a new design, where the micro-cavity resonant mode will be exactly matching the gain peak while taking into account for the thermal shift, in order to take advantage of a reduce threshold and a higher output power peculiar of a resonant structure.

## 5.4 Low noise Class-A single-frequency operation

As already discussed in *Chapter 3*, the use of quantum dashes gain medium can result in a better noise performance and stable emission thanks to the suppression of polarization switching effects. Up to now, however, these advantages have been only exploited in the case of monolithic VCSELs, whereas the integration of such quantum dashes has never been tested in an external-cavity arrangement.

In our case, one of the main motivations for the integration of a quantum dash-based active region in a VECSEL cavity was the investigation of such inhomogeneous gain medium as potential candidate for the realization of low noise single- and dual-frequency optical sources at the telecom wavelength.

The intermediate step towards this ambitious goal has been the realization of a quantum dashes-based single-frequency VECSEL, in order to gain insight on the performance of the device in terms of its spectral purity and to validate its Class-A dynamic.

### 5.4.1 Obtaining the low noise Class-A regime

#### Class-A regime

In conventional semiconductor lasers, the lifetime  $\tau_{ph}$  of the photon population inside the laser cavity is generally smaller or comparable to the lifetime  $\tau_c$  of the population inversion of carriers in the active region, which is typically of few ns. Such lasers belong to the Class-B family, and their dynamics can be described by a pair of coupled rate equations (in the case of a single-frequency laser<sup>2</sup>), governing the evolution of the carrier population  $N_c$  and the photon population  $N_{ph}$ . This leads to a second-order frequency response, which is naturally characterized by a resonant behavior, resulting in an excess noise at the relaxation oscillations (RO) frequency. The transfer function  $H(f)$  is of the form [Baili2009a]:

---

<sup>2</sup> The model can be extended to the case in which several modes are oscillating in the laser cavity.

$$H(f) = \frac{RIN_{VECSEL}(f)}{RIN_{pump}(f)} = \frac{\gamma_c^2 \gamma_{ph}^2 r^2}{\left[ \gamma_c \gamma_{ph} (r-1) - (2\pi f)^2 \right]^2 + [2\pi f \gamma_c r]^2} \quad (5.1)$$

In Eq. 5.1,  $\gamma_c$  ( $\gamma_{ph}$ ) is the so-called population (cavity) decay rate, and it is equal to the inverse of the population inversion lifetime  $\gamma_c = 1/\tau_c$  (photon cavity lifetime  $\gamma_{ph} = 1/\tau_{ph}$ ), while  $r$  is the relative pumping rate coefficient, and it is equal to the pump power normalized to the threshold.

Due to the limited length of their cavity (10s-100s of  $\mu\text{m}$ ) which prevents to decouple the dynamic of the two populations, monolithic edge-emitting lasers or VCSELs belong to this class of lasers, and their RO frequencies are typically in the GHz range. Despite their longer cavity, solid-state lasers belong to that family as well, because their long carrier lifetime (of the order of ms) is not sufficient to decouple the two dynamics, although they typically use cm-long cavities. Such systems are thus modeled with a transfer function of the same form of Eq. 5.1.

However, if the photon lifetime  $\tau_{ph}$  is considerably longer than the active medium carrier lifetime  $\tau_c$ , then the laser dynamics can be described by one simple equation, i.e., the one governing the photon dynamic, while the carrier population dynamic is adiabatically neglected, because of its fast evolution in time. This condition leads to the so-called Class-A regime, which is characterized by an overdamped operation typical of a first-order system free of resonant phenomena. In such a case, Eq. 5.1 simplifies in [Baili2009a]:

$$H(f) \approx \frac{\gamma_{ph}^2}{\left[ \gamma_{ph} \left( \frac{r-1}{r} \right) \right]^2 + [2\pi f]^2} \quad (5.2)$$

Such a regime can be achieved if a sufficiently long laser cavity with a limited amount of losses (high-finesse) is employed. In this particular context, VECSELs simultaneously benefit from the ns-scale carrier dynamics of semiconductor lasers and the high-finesse laser cavity. Thanks to the coexistence of these two aspects, which guarantee the respect of the condition  $\tau_{ph} \gg \tau_c$ , Baili et al. have demonstrated, with their pioneering works, that it is possible to exploit the characteristics of VECSELs to realize semiconductor-based Class-A lasers, with laser cavities in the cm-scale range [Baili2008, Baili2009a].

### Relative Intensity Noise and shot noise

Additionally to that, when the laser is operating in the Class-A regime, its Relative Intensity Noise (RIN) is clamped at the shot noise floor, for frequencies higher than the characteristic cut-off frequency  $f_c$ . This level also represents the lowest “classical” achievable noise limit, and it is due to the quantized nature of light. The achievable shot noise level is determined by the maximum output power emitted by the laser source, provided that the saturation of the detector is avoided. From a practical point of view, the RIN can be defined as [Rosencher2002]:

$$RIN(f) = \frac{S_{i_{laser}}(f)}{\langle I_{ph} \rangle^2} \quad (5.3)$$

where  $S_{i_{laser}}(f)$  is the laser contribution to the spectral power density of the detected photocurrent, while  $\langle I_{ph} \rangle$  is the average DC value of the detected photocurrent. RIN is expressed in  $\text{Hz}^{-1}$ . From a practical point of view, the RIN of a laser is typically given in logarithmic scale (unit: dB/Hz):

$$RIN_{dB}(f) = 10 \log(RIN(f)) \quad (5.4)$$

At the shot noise limit  $S_{i_{shot-noise}} = 2q \langle I_{ph} \rangle$  and Eq. 5.3 becomes

$$RIN_{shot-noise}(f) = \frac{S_{i_{shot-noise}}}{\langle I_{ph} \rangle^2} = \frac{2q \langle I_{ph} \rangle}{\langle I_{ph} \rangle^2} = \frac{2q}{\langle I_{ph} \rangle} \quad (5.5)$$

$q$  being the electron charge. Higher detected powers lead to lower shot noise floor values.

In order to reach the low noise regime with our QDH-VECSEL, we will pay attention to simultaneously observe the following conditions:

- i. being transverse single-mode;
- ii. being longitudinal single-mode;
- iii. having a stable state of polarization;
- iv. to maximize the emitted power and the detected photocurrent, without saturating the detector, provided that all the previous conditions are respected.



The first and second conditions are necessary to avoid the appearance of any Mode Partition Noise (MPN) phenomena between coexisting transverse and/or longitudinal modes, which again spoils the noise performance of the optical source [Law1997].

The third condition prevents the appearance of polarization switching phenomena, which degrade the noise characteristic of the laser [Koyama1991]. In our case it is guaranteed by the use of a quantum dashes-based anisotropic gain medium, which presents a stable linear polarization along the [1-10] crystallographic direction, as already discussed in *Chapter 3*.

Finally, the fourth condition is appreciated in order to minimize the shot noise floor of the detected signal, as discussed above.

To this aim, a new experimental setup has been realized: it is described in the following section.

## 5.4.2 Realization of the experimental setup

The experimental setup used to realize the single-frequency QDH-VECSEL is similar to the one used to characterize the device in the multi-mode regime (*Section 5.3.1*). It consists again in a linear plane-concave cavity, formed by the semiconductor chip and the concave output coupler. The semiconductor chip has been mounted on a thermoelectric Peltier cooler by means of a thin layer of thermal grease, and pumped at an incident angle of  $45^\circ$  with respect to the cavity axis (Fig. 5.12a).

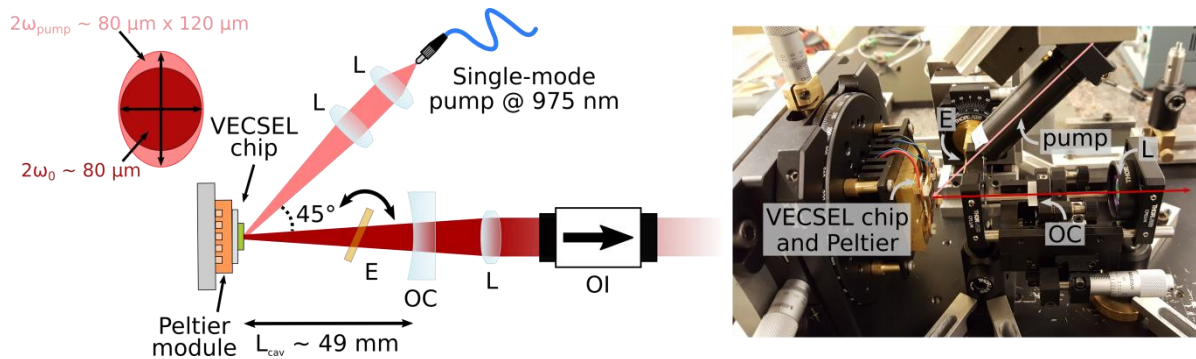


*Fig. 5.12 – (left) Scheme of the experimental setup used to characterize the QDH-VECSEL in single-frequency operation with pump and cavity spots dimensions (in diameter) at the VECSEL surface. (right) Photo of the setup. L: lens,  $L_{cav}$ : cavity length, OC: output coupler, E: etalon filter, OI: optical isolator.*

In such a setup, the active medium is pumped by a butterfly semiconductor laser diode (3SPGroup 2000CHP), able to deliver up to 1 W of maximum power. The emission wavelength of the pump laser is fixed at 975 nm (regardless of the emitted power) by a Fiber-Bragg-Grating (FBG) inserted in a single-mode Polarization-Maintaining-Fiber (PMF) pigtail with a core diameter of  $6.6 \mu\text{m}$ . Fig. 5.12b shows a picture of the cavity setup.

Given the relatively high threshold of such a structure, and the limited output power offered by our pump module, we designed the pumping system such that the incident power density on the chip

surface were sufficiently high to reach the lasing condition, consistently with the geometrical constraints imposed by our setup (lateral size of intra-cavity optical mounts and cavity length). The pump optics are composed by a collimating and focusing plano-convex lenses with focal lengths of  $f_1 = 4.5$  mm and  $f_2 = 50$  mm, respectively. The pump laser has been then focused on the semiconductor chip, placed 40 mm away from the focusing lens  $f_2$ . At this distance, the pump diode forms a spot with a waist of  $\sim 40$   $\mu\text{m}$  in radius, as measured by a Si CCD camera. As discussed before, because of the tilting angle between the pump axis and the VECSEL cavity axis, the pump spot on the semiconductor chip surface is once again elliptical, with dimensions of  $\sim 80$   $\mu\text{m} \times 120$   $\mu\text{m}$  (minor and major axis, respectively). From now on, all the measurements will be obtained with this pump spot dimension, if not otherwise specified.

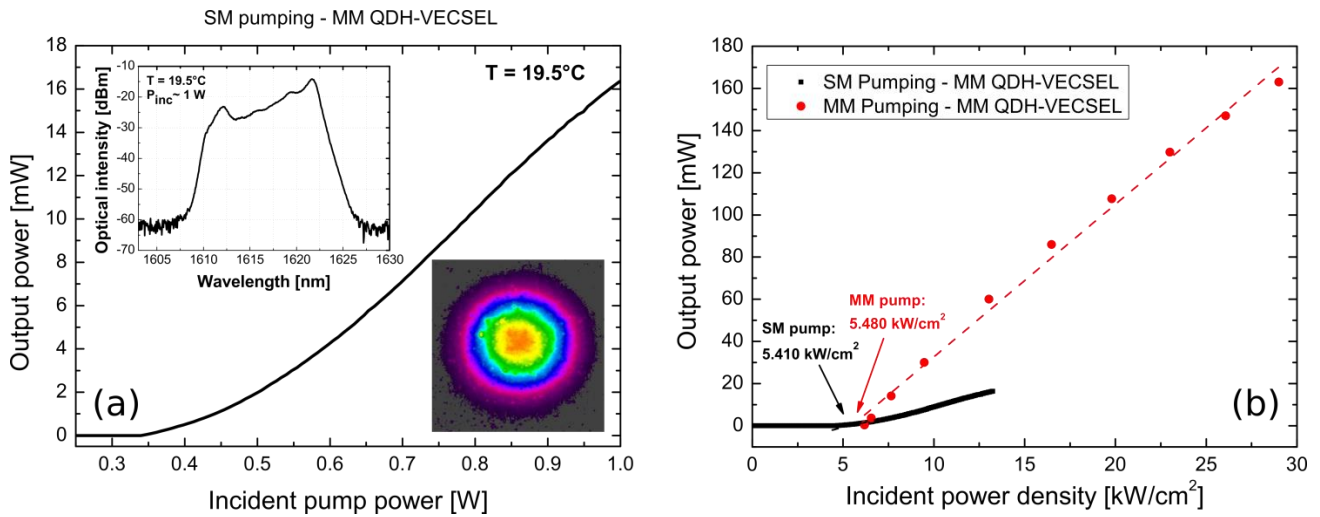


Fig. 5.13 – (Longitudinal) multi-mode emission of the QDH-VECSEL: (a) Output characteristic with optical spectrum and  $TEM_{00}$  beam profile in insets and (b) output power vs incident pump power density at chip surface in the case of the single-mode (black) and multi-mode (red) pump.

Compared to the previous setup, in this case an output coupler with a reflectivity of  $R = 99.5\%$  at 1600 nm and a radius of curvature of  $R_{oc} = 50$  mm has been employed<sup>3</sup>. The cavity length has thus been extended to  $\sim 49$  mm, corresponding to a free spectral range (FSR) of  $\sim 3$  GHz (i.e.  $\sim 26$  pm). The emitted light is then injected in a single-mode fiber for optical analysis (OSA) and/or sent to a large-surface power meter. Without any filtering element inside the cavity, the VECSEL operated in the multi-longitudinal regime, as attested by the optical spectrum in the top inset of Fig.5.13a. At this step we also took care to adjust the cavity length in order to select the fundamental  $TEM_{00}$  transverse mode, while verifying that no higher-order transverse mode was oscillating. We verified this condition by checking the output beam profile with a phosphor-coated camera (bottom inset of Fig. 5.13a). Due to the reduced pumped area with respect to the previous setup, the QDH-VECSEL

<sup>3</sup> The reflectivity of the output coupler at 1600 nm has been experimentally measured with FTIR.

was now able to deliver up to 16.3 mW at  $T = 19.5^\circ\text{C}$  (again pump limited), with a multi-longitudinal mode emission over  $\sim 17$  nm with respect to a center wavelength of 1617 nm. The laser threshold in this configuration has been measured around 350 – 400 mW.

This corresponds approximately to the same value of pump density at threshold measured in the previous setup (namely  $5.4 \text{ kW/cm}^2$ ), as attested by Fig. 5.13b. The slope of the two curves differs by a factor  $\sim 3.2$ , which is consistent with the ratio between the pumped area in the two setups

$$\left( \frac{A_{MM-pump}}{A_{SM-pump}} = \frac{24000 \mu\text{m}^2}{7500 \mu\text{m}^2} = 3.2 \right).$$

By slightly optimizing the dimensions of the pumped area on the chip surface and the cavity length, we were eventually able to extract up to  $\sim 30$  mW at room temperature, with this cavity arrangement.

### 5.4.3 Estimation of the thermal impedance

At this point, we also proceeded to investigate the thermal performance of the device. The experimental setup previously discussed has been used to this aim. Indeed, according to the previous lasing tests in multi-longitudinal operation, the lasing threshold and the maximum emitted power of our VECSEL structure was somehow below expectations, especially if compared to their counterpart based on InGaAsP quantum wells. We already discussed the effect of the  $\text{SiN}_x$  AR coating on the gain enhancement factor  $\Gamma_{enh}$ , which probably limits the performance.

To characterize the thermal behavior of our structure, we estimate its thermal impedance  $R_{th}$ .

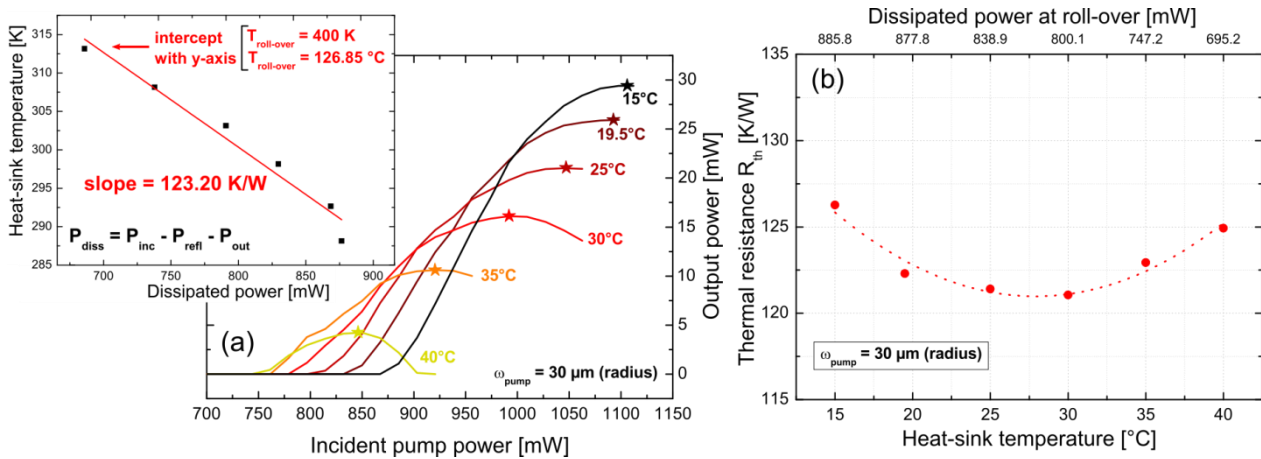


Fig. 5.14 – Estimation of the thermal resistance  $R_{th}$  of the QDH-VECSEL: (a) extrapolation of  $R_{th}$  from measurement according to the method proposed by [Heinen2012b] and (b) thermal resistance at different Peltier temperatures. The stars in (a) indicate the value of the output power at thermal roll-over ( $P_{out,ro}$ ).

Following the method proposed by Heinen et al. [Heinen2012b], we extrapolate  $R_{th}$  directly from the output characteristics. To correctly apply this method, we need to reach the roll-over condition. So that, in order to increase the pump density on the chip surface and be able to observe the

roll-over in the entire temperature range of operation of our VECSEL, we set the pump spot to  $30\ \mu\text{m}$  (radius)<sup>4</sup>, while using the same cavity arrangement described in the previous section.

For each Peltier stage temperature  $T_{hs}$  (in the interval [15°C, 40°C]), we measured the output power at thermal roll-over  $P_{out,ro}$ , as presented in Fig. 5.14a ( $P_{out,ro}$  being indicated by the stars).  $P_{out,ro}$  is related to the heat-sink temperature  $T_{hs}$  by the following expression:

$$T_{hs} = -R_{th}P_{diss,ro} + T_{ro} \quad (5.6)$$

Where  $P_{diss,ro} = P_{inc,ro} - P_{refl,ro} - P_{out,ro}$  is the dissipated power at roll-over, the reflected power  $P_{refl,ro}$  being measured to 17.7% of the incident pump power  $P_{inc,ro}$  (compatible with the presence of the SiN<sub>x</sub> antireflection coating).

Then, by performing a linear regression on the measured data, we are able to calculate the thermal resistance  $R_{th}$  from the inverse of the slope of the fitting line, while the roll-over temperature  $T_{ro}$  (i.e. the active region internal temperature for which we start observing the roll-over) is identified by the intercept with the y-axis, as shown in the inset of Fig. 5.14a. It is equal to  $T_{ro} = 400\ \text{K}$ <sup>5</sup>. We emphasize the fact that such method allows obtaining information on the internal temperature of the device, which is generally not accessible in practice.

From our measurement, we are able to estimate an average thermal resistance of  $R_{th} = 123.2\ \text{K/W}$ . Once we know the roll-over temperature (which is a constant of the VECSEL structure), we are able to obtain the thermal resistance for each applied Peltier temperature. In Fig. 5.14b we plotted the results of each measurement (red points) obtained by the simple relation

$$R_{th} = \frac{-(T_{hs} - T_{ro})}{P_{diss,ro}} \quad (5.7)$$

Those measurements also allowed determining the maximum temperature of operation for the QDH-VECSEL to be 40°C, valid for such pump spot dimensions. Concerning the minimum temperature, we were limited by the experimental conditions which imposed not going down below the dew point (which in our case was around 12°C), to avoid the formation of water moisture on the chip surface.

The value of the thermal impedance of our structure is appreciably higher to the one generally reported in literature for the InP-based quantum-well VECSELs emitting in the  $1.3\ \mu\text{m}$  -  $1.55\ \mu\text{m}$

<sup>4</sup> To do that we used a collimating lens with focus  $f_1 = 6.24\ \text{mm}$  and a focusing lens with  $f_2 = 10\ \text{mm}$ .

<sup>5</sup> This also means that, when the active region reaches 400 K, roll-over appears.

range, which generally are around 40-50 K/W in the case of metamorphic growth DBRs [Tourenco2008, Zhao2012], and 1-10 K/W for wafer fused DBRs [Sirbu2011, Sirbu2014].

The relatively higher thermal impedance of our structure is also directly responsible for the appearance of a thermal lens phenomenon, widely reported in literature in the case of VECSELs [Kemp2006, Laurain2009]. In our case, the effects can be easily observed on the output characteristic of Fig. 5.14a. Indeed, the decrease of the laser threshold as the Peltier temperature increases can be attributed to the presence of a strong gradient of the refractive index profile in the radial direction due to the thermo-optic effect of InP and InGaAsP layers composing the active region ( $dn/dT \sim 2 \cdot 10^{-4} \text{ K}^{-1}$ ) [Melati2016], which induces a strong thermal lens on the semiconductor chip. We also bring the attention to the fact that, since the pump spot on the chip surface was slightly smaller than usual (i.e. the pump density is higher), the thermal lens effects were enhanced.

#### 5.4.4 Single-frequency operation

In order to achieve the longitudinal single-frequency operation of our QDH-VECSEL, a fused silica etalon has been inserted inside the laser cavity, as previously presented in Fig. 5.12. The etalon filter which has been chosen has a thickness of 40  $\mu\text{m}$ , and a squared area of  $5 \times 5 \text{ mm}^2$ . Both facets present an optical coating with a reflectivity  $R = 30\%$  at a normal angle of incidence. Fig. 5.15 (on next page) shows an example of the single-frequency operation of the QDH-VECSEL, obtained employing the aforementioned setup. After the insertion of the etalon, the threshold of the laser increases to  $\sim 750 \text{ mW}$ . In such conditions it was possible to extract a CW maximum output power of 7.9 mW at  $T = 19.5^\circ\text{C}$ , for an incident pump power of 1 W, as attested by Fig. 5.15a.

In order to stabilize the single-frequency emission and avoid any parasitic feedback of the emitted beam towards the VECSEL due to the optical elements along the beam path, we inserted an optical isolator at the fiber entrance. The spectral emission of the VECSEL was now stable and centered at 1610.7 nm, with a side mode suppression ratio (SMSR) over 60 dB (see Fig. 5.15b, next page). The resolution of the OSA employed to acquire the optical spectrum is of 0.08 nm, which is not sufficient to assess the single-frequency operation of our device. We thus analyzed part of the optical signal with a confocal scanning Fabry-Pérot interferometer (FPI) with a FSR = 7 GHz and a finesse of 125, which undoubtedly confirmed the single-frequency operation of the VECSEL<sup>6</sup>, as shown in the inset of Fig. 5.15b. Additionally, we were able to observe a stable single-frequency operation during several tens of minutes, before any eventual appearance of mode hopping

---

<sup>6</sup> In the following, whenever referring to the single-frequency operation of the VECSEL, we implicitly consider that it has always been checked by a FPI measurement.

phenomena, most likely induced by external temperature drifts and/or mechanical vibrations (the experimental setup being not protected against air turbulences and mechanical noise).

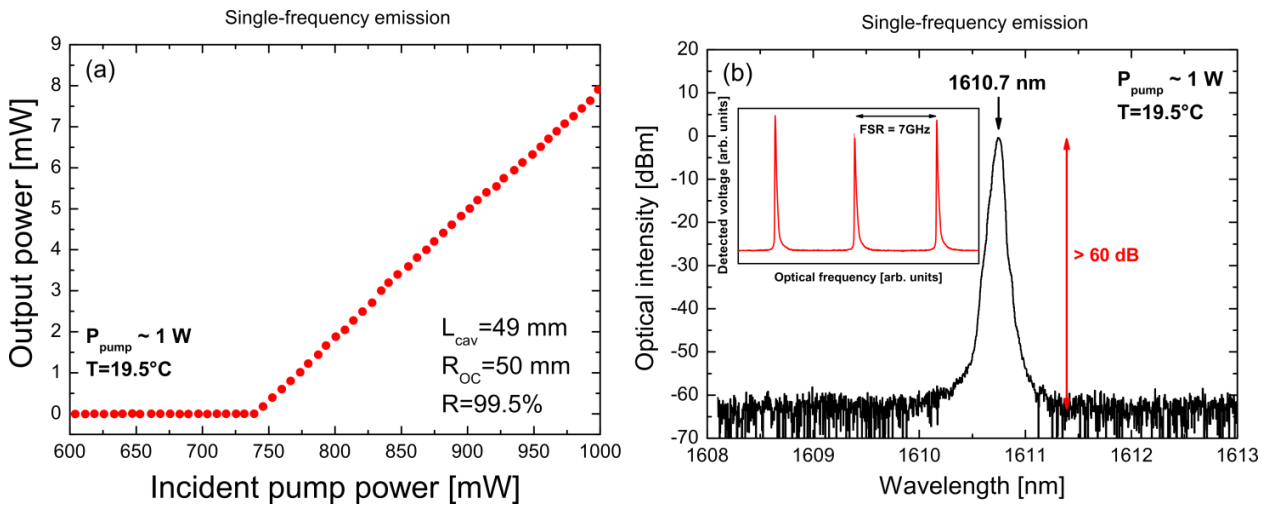


Fig. 5.15 – Single-frequency operation of the QDH-VECSEL: (a) output characteristic and (b) optical spectrum. The single-frequency operation has been checked at the FPI (in inset).

At this point, we were also interested to measure the achievable single-frequency wavelength range of the QDH-VECSEL. The  $40 \mu\text{m}$ -thick intra-cavity etalon filter has been mounted on a rotational support which allowed tuning its transmission characteristic in order to select a precise longitudinal mode. The result of such characterization is shown in Fig. 5.16.

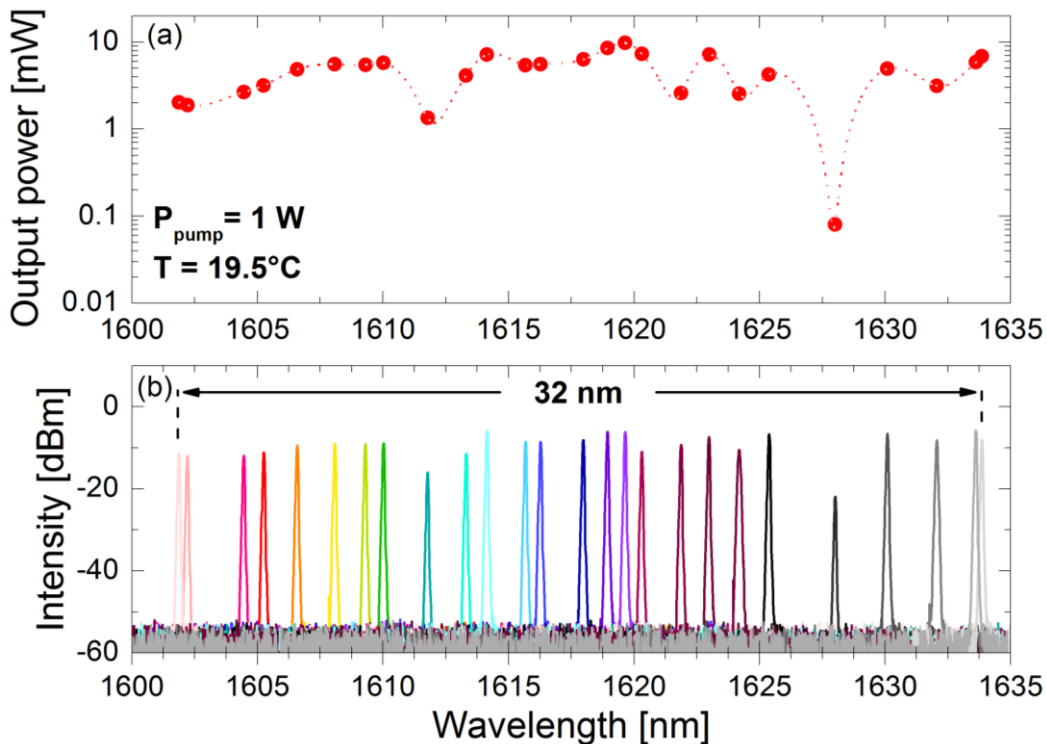


Fig. 5.16 – Wavelength emission range of the QDH-VECSEL in single-frequency mode: (a) emitted power and related (b) emission spectrum.



By finely tuning the optical length of the VECSEL cavity with the etalon filter and the output coupler position, we obtain a broad-band single-frequency emission over  $\Delta\lambda = 32$  nm (1601.8-1633.8 nm) by steps corresponding to the cavity FSR, with an average emitted power mostly in the range 1 - 10 mW, except for a dip around 1628 nm.

The broad-band emission over 32 nm should be compared with previously reported values. Most of the scientific literature concerning broadly tunable single-frequency VECSELs is related to GaSb-based devices. This material system benefits from the high refractive index contrast of AlAsSb/GaSb-based DBRs ( $\Delta n \sim 0.6$ ), which present wide stop bands of  $\sim 300$  nm around  $2 \mu\text{m}$ , as discussed in the previous chapter. For these devices, tuning ranges as high as 75 nm can be obtained with InGaSb-based SQWs (and even more, if several SQW sets designed to emit at different wavelength are employed) [Paajaste2009]. However, achieving a broad emission in InP-based VECSELs is generally not straightforward because of the lack of DBRs with a wide plateau. Despite their good performance in terms of thermal dissipation, GaAs/AlAs DBRs ( $\Delta n = 0.47$  at  $1.55 \mu\text{m}$ ) offer a limited stop-band compared to the above-mentioned AlAsSb/GaSb-based or dielectric-based a-Si/a-SiN<sub>x</sub> DBRs ( $\Delta n = 1.9$ ), the latter unfortunately not suited for their bad thermal conductivity. To draw a fair comparison, we should thus compare our value with some related to InP-devices presenting GaAs-based DBRs, but to the best of our knowledge, no value of tuning range in InP-based VECSELs has been reported so far. Table 5.1 (reproduced from [Okhotnikov2010]) summarizes the best reported values for QW-based VECSELs broad-band tuning ranges, compared with our work (in red).

**Table 5.1 - VECSEL broad tuning ranges for different material systems.**

Material system	Active region	DBR	Emission range (nm)	Tuning (nm)	Ref.
GaAs	InGaP QWs	AlGaAs/AlAs	668-678	10	[Hastie2005]
GaAs	GaAs QWs	AlGaAs/AlAs	830-863	33	[Hastie2003]
GaAs	InGaAs QWs	AlGaAs/AlAs	955-995	40	[Abram2004]
GaAs	InGaAs QWs	AlGaAs/AlAs	1147-1197	50	[Fan2007]
GaAs	GaInNAs QWs	AlAs/GaAs	1163-1193	30	[Vetter2008]
InP	InAs QDHs	GaAs/AlAs	1601-1633	32	our work
GaSb	InGaSb QWs	AlAsSb/GaSb	1925-2002	77	[Paajaste2009]
GaSb	GaInAsSb QWs	AlAsSb/GaSb	2189-2318	129	[Burns2009]



### 5.4.5 Static polarization properties of the QDH-VECSEL

Although linearly polarized, in the case of SQW-based VECSELs, the emission cannot generally be predicted in advance, because of the isotropic nature of the quantum medium: the residual strain on the semiconductor gain chip is in most cases sufficient to force a stable emission along one single linear polarization, which is generally aligned along one crystallographic axis. However, which axis will be the preferred one, is not easy to predict. Such a behavior has been experimentally observed, for instance in the case of a 670 nm-emitting SQW-based VECSEL, where the emission was always orientated parallel to either the major [0-1-1] or minor [0-11] crystal axes [Hastie2005]. Moreover, switching from an axis to the other may occur when the pump power is changed.

Thanks to the gain anisotropy of quantum dashes nanostructures integrated in the active medium, the QDH-VECSEL always shows a stable and linearly polarized emitted light aligned along the elongated direction of the nanostructures ([1-10]), with an orthogonally polarized suppression ratio (OPSR) of 39 dB. This can be observed in Fig. 5.17a, where we reported the two polarization-resolved single-frequency spectra in stationary conditions (CW pumping and emission) related to the // polarization and the  $\perp$  polarization. The spectra have been acquired thanks to a linear film polarizer with a 56 dB extinction ratio placed at the entrance of the optical fiber connected to an OSA with 0.08 nm resolution.

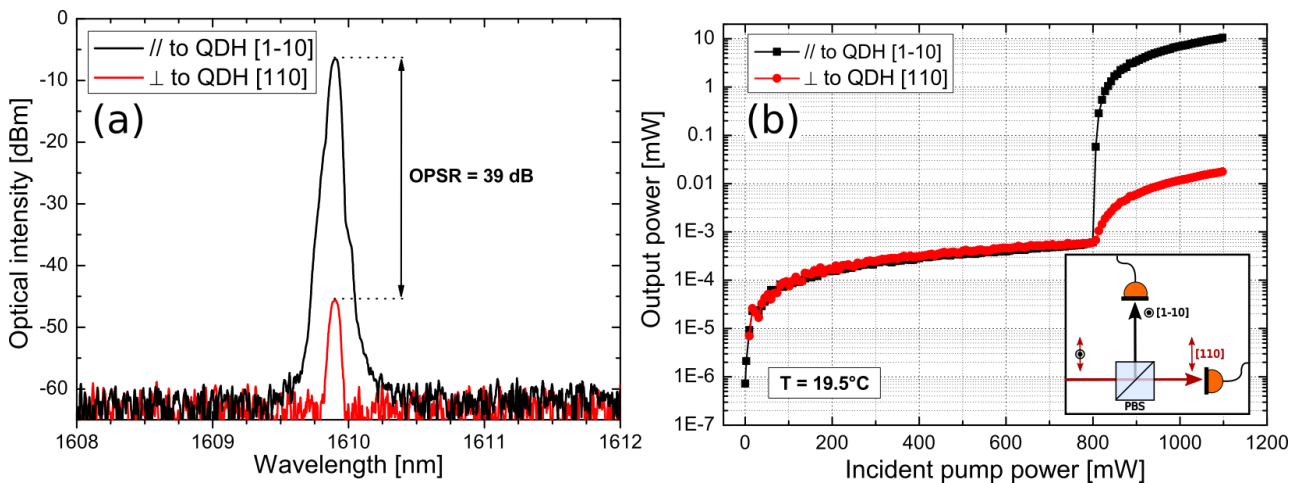


Fig. 5.17 – Polarization-resolved (a) spectra and (b) output characteristics (log scale) for the two orthogonally-aligned polarizations: [1-10] (parallel to quantum dashes, in black) and [110] (perpendicularly to quantum dashes, in red).

In order to check the polarization stability in CW operation, we simultaneously acquired the contributions of the two polarizations to the VECSEL output power with respect to the incident pump power, thanks to a polarizer beam splitter cube. The result of such measurement is shown in Fig. 5.17b. Above threshold, the dominant polarization is the one aligned along the [1-10] direction (parallel to quantum dashes), and we did not observe any polarization-switching, at least in our

range of measurement. In this case, the calculated OPSR of 28 dB at 1.1 W was mainly limited by the extinction ratio ( $\sim 30$  dB at 1550 nm) of the PBS cube used to separate the two polarizations, meaning that the  $\perp$  signal is in fact a residual transmission of the  $\parallel$  signal.

Before concluding this section, we would like to underline the fact that a stable and linearly polarized emission along the [1-10] direction with an OPSR = 30 dB has been already reported in previous work conducted in our laboratory on micrometric-cavity QDH-based VCSELs, both under CW operation [Lamy2009] and low frequency pump modulation ( $f \sim 100$  kHz) [Gauthier2012], and no polarization switching has been observed.

#### **5.4.6 Class-A regime and RIN**

Once realized the single-frequency QDH-VECSEL, whose static performance have been detailed in the previous sections, we were able to investigate its operation as low-noise optical source.

At this stage, it is important to characterize our laser in terms of its RIN characteristic, in order to precisely quantify the level of its noise in the frequency domain, but also, and most importantly, to explore its dynamical behavior which should reveal the Class-A operation of the QDH-VECSEL. We start discussing about the RIN in the low frequency domain (100 kHz-100 MHz), then we will address the frequency domain potentially interesting for RADAR applications (1 GHz-18 GHz).

All the measurements that we are going to discuss have been realized when the VECSEL was operating in free-running mode, i.e. without any servo-locking loop to stabilize its frequency nor intensity or those of the pump diode.

#### **Characterization of RIN in the low frequency range (100 kHz - 100 MHz)**

In order to characterize the RIN of the QDH-VECSEL in the 100 kHz - 100 MHz range, we used the measurement bench depicted in Fig. 5.18 (next page). It consists in a fibered InGaAs fast PIN photodiode (EPITAXX ETX 100 RFC2) with 1.5 GHz bandwidth and responsivity equal to 1 A/W at 1.6  $\mu\text{m}$  ( $\sim 0.68$  A/W at 980 nm), followed by a RF amplifier (MITEQ AU-1332) with an average gain of 54 dB in the 1 kHz - 500 MHz frequency range, and an RF Electrical Spectrum Analyzer (Rohde & Schwarz FSV3) used in AC coupling mode (measurement range  $f = 100$  kHz - 3.6 GHz). The InGaAs photodiode has been charged on a 50  $\Omega$  resistance. To suppress the DC component of the signal, which can damage the ESA, a band-pass filter ( $f_{\text{band-pass}} = 7$  kHz - 23 GHz) has been inserted on its input port. The average DC component is subsequently measured by a digital voltmeter. The exact electrical scheme of the low frequency bench can be found in *Appendix D*. Concerning the QDH-VECSEL cavity, we used the same arrangement described in *Section 5.4.2*.

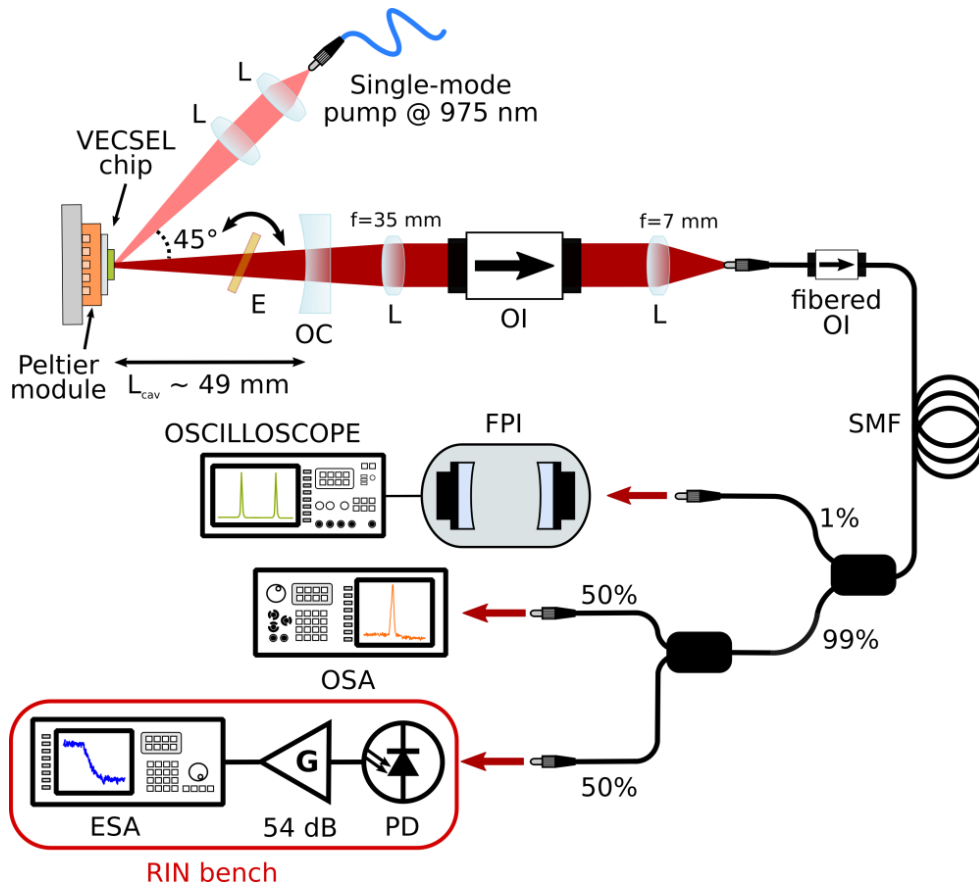


Fig. 5.18 – Experimental setup used to evaluate the RIN characteristic in the 100 kHz-100 MHz frequency range. L: lens,  $L_{cav}$ : cavity length, E: etalon, OC: output coupler, OI: optical isolator, SMF: single-mode fiber, FPI: scanning Fabry-Pérot interferometer, PD: photodiode, G: RF amplifier, OSA/ESA: optical/electrical spectrum analyzer.

The RIN spectra of both the QDH-VECSEL and the pump diode are presented in Fig. 5.19a. These curves have been obtained for a 10 kHz resolution bandwidth (RBW) and an incident pump power of 1 W, i.e. a relative pumping rate coefficient  $r$  equal to 1.39 ( $P_{th}$  being equal to  $\sim 720$  mW). The VECSEL was emitting  $\sim 8$  mW.

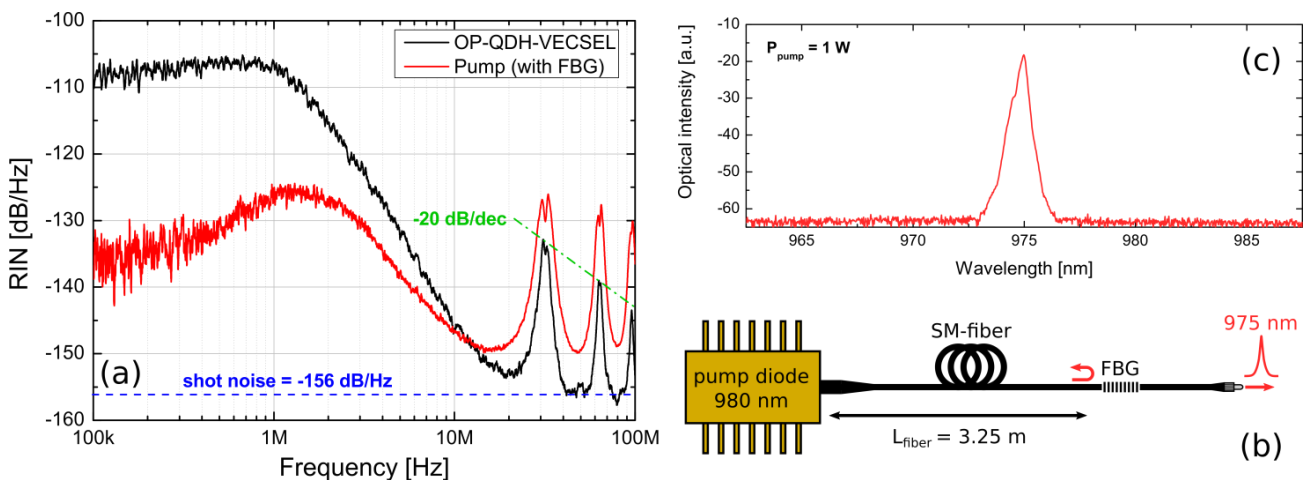


Fig. 5.19 – (a) RIN characteristics of QDH-VECSEL (black) and pump diode (red) in the 100 kHz - 100 MHz range (RBW = 10 kHz, VBW = 10 kHz). Detected photocurrents are 1.25 mA and 0.7 mA for the VECSEL and pump signals, respectively. (b) Scheme of the pump module with the pigtail fiber Bragg grating. (c) Pump emission spectrum at 1 W.

As we can see from the figure, the pump RIN characteristic (in red) exhibits resonant peaks. It turned out that the presence of the resonant peaks is the result of the FBG in the fiber pigtail of the pump laser (Fig. 5.19b), which is used to apply a weak optical feedback to the pump, intended to stabilize its emission wavelength at 975 nm, as attested by Fig. 5.19c. These peaks are replicated at multiples of the inverse of the pump external cavity round-trip time  $\tau_{ext}$ , i.e. the free spectral range  $FSR_{\Delta\nu} = 1/\tau_{ext} = 32$  MHz of the composite cavity of length  $L = 3.25$  m formed by the pump semiconductor laser and the FBG [Nagarajan1993], as checked by inspection (see Fig. 5.19b).

The peaks of the pump are transferred to the OP-QDH-VECSEL RIN characteristic, spoiling the noise behavior, which makes it difficult to assess the transfer function of the QDH-VECSEL, as shown by the black curve of Fig. 5.19a. Nevertheless, despite the presence of the transferred resonant peaks, we observe the filtering action of the VECSEL characteristic on the intensity fluctuations of the pump, which are dumped by the VECSEL transfer function after its cut-off frequency, with a -20dB/dec slope (green dashed line). We can also notice that between the peaks, the RIN characteristic of the VECSEL attains the shot noise floor, which in this case is equal to -156 dB/Hz, for an average detected photocurrent of 1.25 mA.

To recover a clear RIN curve for our VECSEL, the Bragg grating has been removed from the pump fiber. Accordingly, the pump RIN now shows a nearly white noise characteristic over the whole frequency range of interest [Sato1985], with a value of -155 dB/Hz for an average detected photocurrent of 1.26 mA (red curve in Fig. 5.20a). The pump is now multi-mode, and its wavelength is no more fixed, but it is stable enough in terms of intensity to ensure a constant pumping rate over hours. We also checked that the threshold of the VECSEL was not degraded after the modification of the pump fiber.

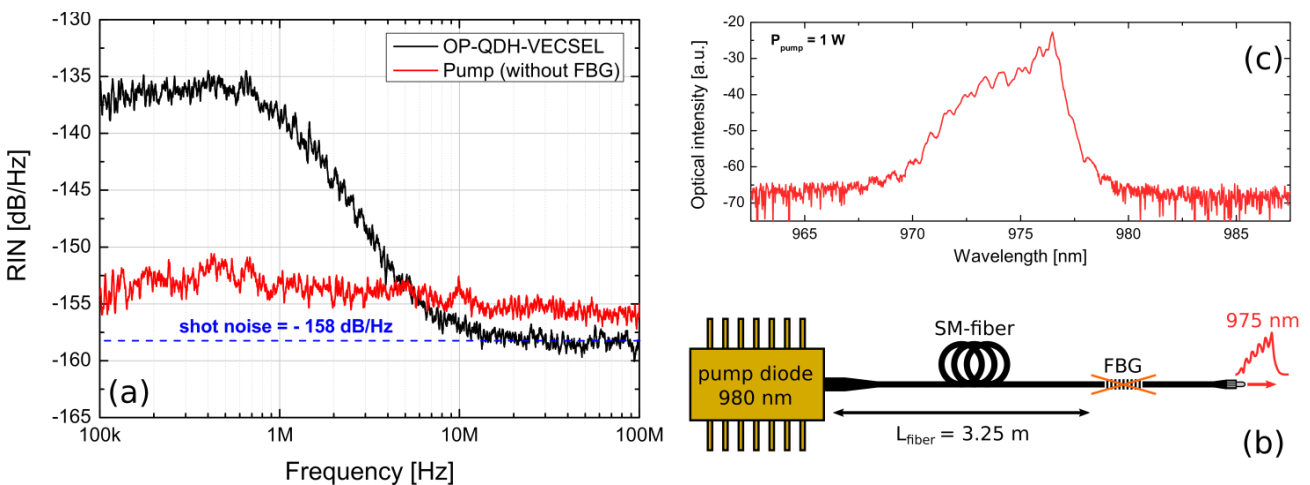


Fig. 5.20 – (a) RIN characteristics of QDH-VECSEL (black) and pump diode (red) in the 100 kHz - 100 MHz range (RBW = 10 kHz, VBW = 10 kHz) after the removal of the FBG from the pump diode fiber. Detected photocurrents are 2 mA and 1.26 mA for the VECSEL and pump signals, respectively. (b) Scheme of the pump module without the pigtail fiber Bragg grating. (c) Pump emission spectrum at 1 W.

After that, the RIN spectrum of the VECSEL becomes smooth and exhibits a first-order low-pass filter characteristic, as shown by the black curve of Fig. 5.20a. The two curves are again obtained for a 1 W of emitted pump power and the same pumping rate  $r$  as before.

The OP-QDH-VECSEL transfer function, which is shown in Fig.5.21, is obtained by dividing the laser RIN by the pump RIN. This is indeed a first-order low-pass filter, with the -20 dB/dec slope previously observed, and it is a clear evidence of the Class-A operation of the QDH-VECSEL. The -3 dB cut-off frequency  $f_{cut-off}$  is found to be about 800 kHz. Concerning the low-frequency part before the cut-off frequency, is essentially dominated by the contribution of the pump intensity noise which is transferred to the VECSEL and amplified, before the filtering action of the Class-A dynamic [Baili2008]. As shown by Fig. 5.20a, the laser RIN decreases above this frequency to reach the shot noise floor at -158 dB/Hz, for an average detected photocurrent of 2 mA.

The QDH-VECSEL transfer function can be fitted by Eq. 5.2, leading to a photon cavity lifetime  $\tau_{ph} = 53$  ns, in agreement with the 0.6% estimated losses per cavity round-trip. We notice that this value is well above the typical carrier lifetime of semiconductor active layers, which is of the order of few ns, as the condition to work as a Class-A laser requires.

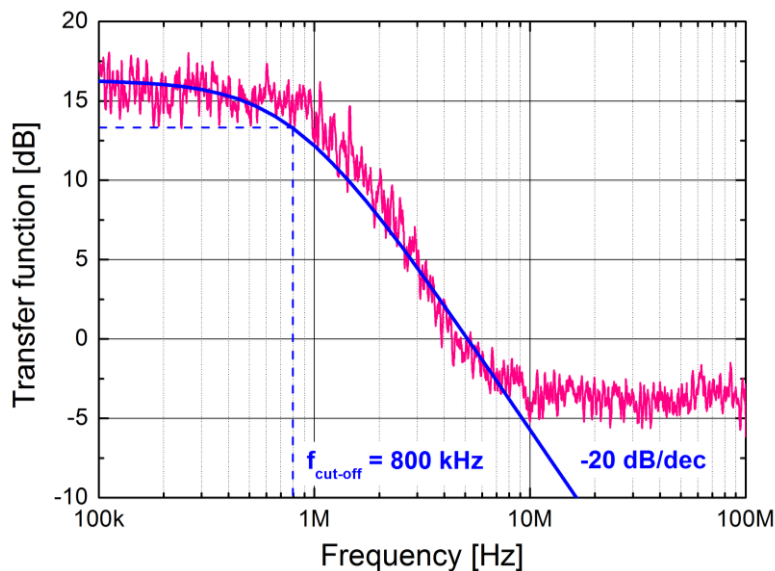


Fig. 5.21 – Transfer function of the OP-QDH-VECSEL.

### Characterization of RIN in the 1 GHz - 18 GHz range

To characterize the RIN of our VECSEL in the range 1 - 18 GHz, we used a different measurement bench. It is composed by:

- an amplification chain with two cascaded RF amplifiers (32 dB B&Z Technologies BZ-00101800-201030-152323 and 35 dB Agile MWT AMT-A0220). A -3 dB attenuator is inserted between the two amplifiers not to saturate the second amplifier. The amplification



chain is thus able to provide an average (measured) gain of 62 dB in the frequency range of interest. The typical noise figure (NF) of the two amplifiers is 1.8 dB and 2.7 dB, respectively;

- a fast InGaAs photodiode (Discovery Semiconductors DSC30S) with 24 GHz bandwidth and responsivity  $\sim 0.75$  A/W at 1600 nm;
- an Aeroflex 3254 electrical spectrum analyzer (frequency range 1 kHz – 26.5 GHz).

The detailed electrical scheme of the acquisition chain can be found in *Appendix D*.

Fig. 5.22 shows the typical RIN characteristic of our VECSEL in this frequency range, acquired with the aforementioned bench, for a pumping rate  $r = 1.39$  and a detected photocurrent of 1 mA. In the figure we reported the value of the shot noise floor (green dashed line) related to the value of the detected photocurrent. As expected, the relaxation oscillations-free regime of our VECSEL, determined by its Class-A operation, translates in a nearly-constant white noise of the RIN characteristic in the investigated range of frequency, except for the appearance of the spurious peaks (indicated by the black arrows in Fig. 5.22). Those peaks are generated by the beating of the VECSEL lasing mode and the residual amplified spontaneous emission at the frequency of the FSR of the laser cavity (we remind being equal to 3 GHz for a 49 mm-long cavity) and its harmonics. The dip on the RIN characteristic observed around 4.7 GHz is related to the gain of the amplification chain, which is plotted in the figure (blue curve) for completeness.

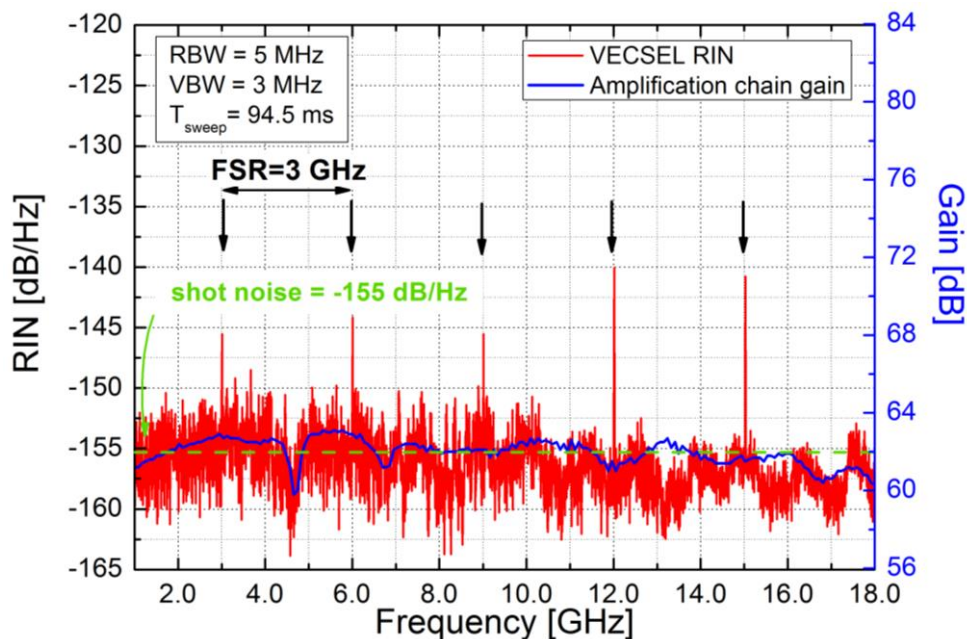


Fig. 5.22 – RIN characteristic of the QDH-VECSEL in the 1GHz-18GHz frequency range (solid red) and related shot noise floor (dashed green). The gain of the amplification chain is plotted as well (solid blue).  
 $RBW = 5$  MHz,  $r = 1.39$ , average detected photocurrent equal to 1 mA.

### 5.4.7 Spectral purity

After having obtained a Class-A VECSEL integrating a QDH-based active region, we are now going to study its spectral purity in terms of laser linewidth and phase noise. Again, the measurements have been performed in free-running mode.

#### Estimation of the laser linewidth

One of the classical methods to measure the linewidth of relatively narrow lasers (as VECSELs are expected to be) is to perform a delayed self-heterodyne measurement. To this aim, an unbalanced Mach-Zehnder interferometer is typically employed.

The setup that we used (which is sketched on Fig. 5.23a) consists in a 80 MHz acousto-optic modulator (AOM) on one arm and a  $L_{delay} = 700$  m delay line on the other arm. Two polarization controllers are employed to turn the polarization of the light in the single-mode fiber as needed.

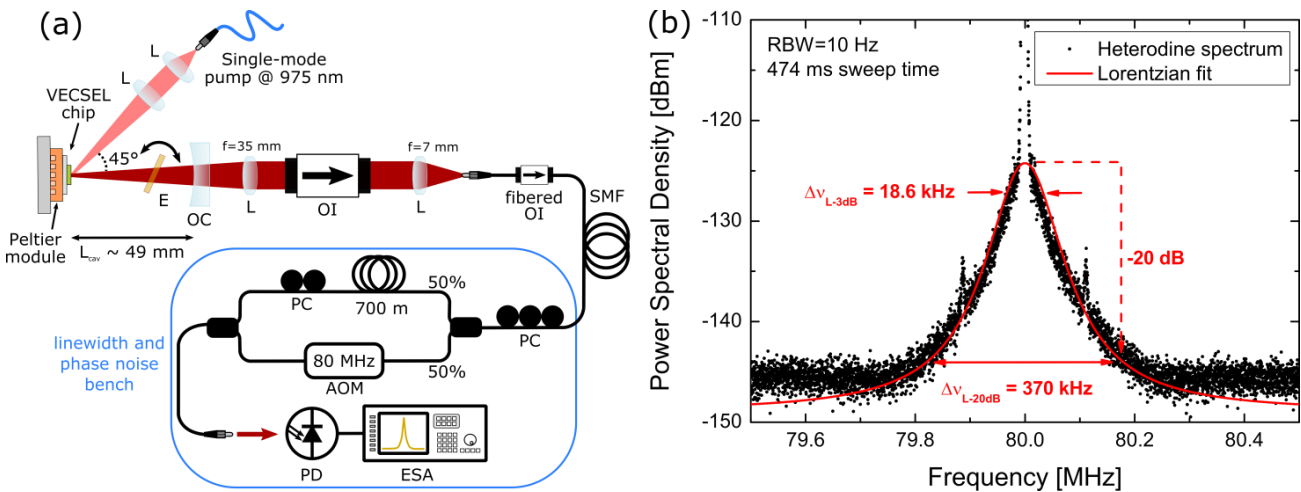


Fig. 5.23 – (a) Delayed self-heterodyne measurement bench based on the unbalanced Mach-Zehnder interferometer and (b) fitted laser linewidth from the autocorrelation spectrum.

*L*: lens,  $L_{cav}$ : cavity length, *E*: etalon, *OC*: output coupler, *OI*: optical isolator, *SMF*: single-mode fiber, *PC*: polarization controller, *AOM*: acousto-optic modulator, *PD*: photodiode, *ESA*: optical/electrical spectrum analyzer.

The injected optical signal is then split in the two arms: the first replica is frequency-shifted at 80 MHz by the AOM, while the second one is retarded in time. For sufficient long delays  $\Delta\tau_{delay}$ , the two replica are completely uncorrelated. However, in our case, the delay<sup>7</sup> introduced in the second arm is equal to  $\Delta\tau_{delay} \sim 3.4 \mu\text{s}$ , which is not enough to completely decorrelate the two signals, as we will see later. The two signals are then recombined and the beating signal is detected

<sup>7</sup> The delay is equal to  $\Delta\tau_{delay} = \frac{L_{opt}}{c} = \frac{L_{delay} n_{SiO_2}}{c}$ , where  $L_{opt}$  is the optical length,  $c$  the speed of light, and  $n_{SiO_2}$  the refractive index of silica fibers at the laser wavelength.



by a fast InGaAs photodiode with 1.5 GHz bandwidth) and analyzed by the Rohde & Schwarz FSV3 ESA. In such conditions, we measured a total incident power of  $\sim 200 \mu\text{W}$  on the photodiode. Fig. 5.23b shows the detected beat tone spectrum at the ESA, obtained for a sweep time of  $T_{\text{sweep}} = 474 \text{ ms}$  and a resolution bandwidth of 10 Hz. The spectral linewidth of our QDH-VECSEL is estimated from this autocorrelation spectrum, assuming the linewidth of our VECSEL has a pure Lorentzian distribution. This hypothesis would be checked afterwards.

In the ideal case of two signals (the frequency-shifted and the delayed replica) having a Lorentzian distribution and being completely uncorrelated, the autocorrelation between the two signals is still a Lorentzian distribution, with a -3 dB full width at half maximum (FWHM) which is twice the linewidth of the original distribution. The presence of the broadened delta function on the autocorrelation spectrum, centered at  $f_{\text{AOM}} = 80 \text{ MHz}$ , is due to the relatively short length of the delay line, which in our case prevents the two signals on the different arms to be completely uncorrelated. However, employing a longer delay line does not solve the problem because the interferometer becomes too sensitive to the environment thermal fluctuations which result in a fluctuation of the delay line length.

Nevertheless, it is still possible to estimate the laser linewidth from two non-completely uncorrelated signals, by fitting the pedestal portion of the autocorrelation profile and considering the FWHM (i.e. the -3 dB linewidth), while ignoring the broadened delta function in the middle of the spectrum [Richter1986]. Additionally, in real cases the heterodyne spectrum of a laser typically has a Voigt profile (resulting from the convolution of a Lorentzian and a Gaussian distribution). The Gaussian contribution to the linewidth is the result of the  $1/f$  noise and length fluctuation due to thermal gradients in the delay line. In principle, the effects of the Gaussian contribution (deriving for example from the contribution of Flicker noise) are more pronounced near the central frequency, and the -3 dB Lorentzian linewidth can be strongly affected.

The wings of our beat note spectrum have been fitted by a pure Lorentzian function, while the two sided spurious peaks appearing at  $\pm 110 \text{ kHz}$  frequency offset are due to the driver electronics of the acousto-optic modulator, and have thus been ignored.

We estimate the Lorentzian linewidth by considering the -20 dB width of the fitted curve which is weakly affected by the Gaussian broadening, and dividing the measured value (370 kHz) by  $2\sqrt{99}$  to recover the -3 dB linewidth value [Chen2015]. The calculations lead to a rough estimated linewidth of 18.6 kHz for our laser. This is a standard value for solid-state lasers and VECSELs with cm-long cavities [Jacobsson2006, Rösener2011b, Rantamäki2013]. We come back to that estimation in the following part, where the frequency noise of our QDH-VECSEL will be presented.

Anyway, a more accurate and direct measurement of the spectral linewidth could be carry out in the future, where the QDH-VECSEL will be injected and servo-locked on a high-finesse and stable Ultra-Low-Expansion (ULE) cavity, employing a Pound-Drever-Hall (PDH) scheme.

### Phase noise and frequency noise

The same self-heterodyne bench has been used to characterize the frequency noise of the QDH-VECSEL. To this aim, the signal provided by the photodiode is demodulated both in phase and in quadrature thanks to the R&S FSV3. The phase noise spectrum of the beating signal is thus numerically reconstructed. Figure 5.24 shows the phase noise of the OP-QDH-VECSEL obtained in free running operation, for an acquisition time of 100 ms (red curve) and 1 s (black curve). The ESA measurement floor is also shown in blue (the dashed line is just a guide for the eyes).

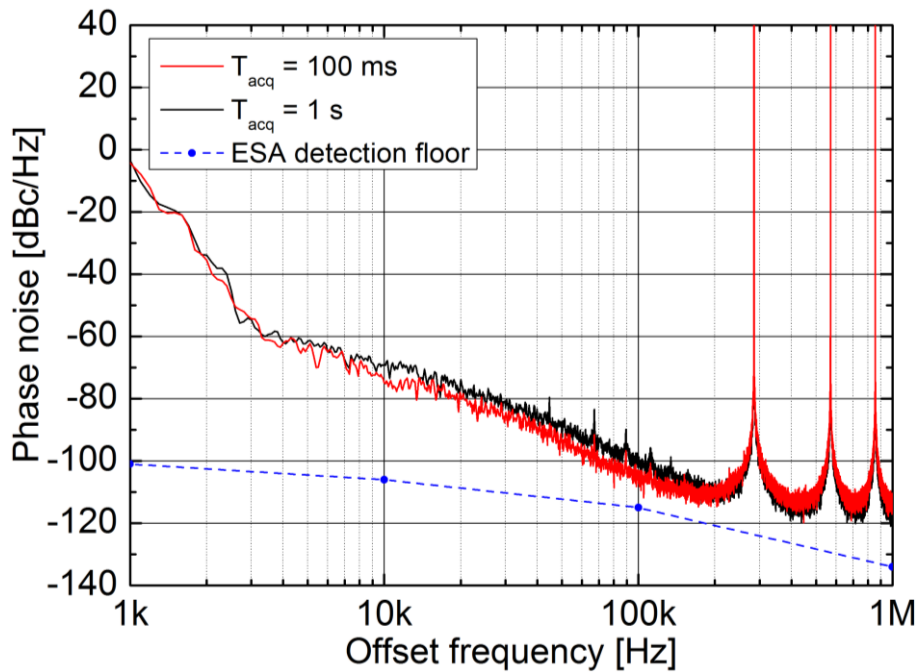


Fig. 5.24 – Phase noise of the QDH-VECSEL in free running operation, for acquisition times of 100 ms (red) and 1 s (black) and a sampling rate of 25 MHz. The ESA measurement floor is indicated with blue dots.

Above 10 kHz frequency offset, the phase noise is below -70 dBc/Hz and reaches -110 dBc/Hz at frequencies above 200 kHz. The peaks lying at 286 kHz (and its harmonics) correspond to the inverse of the self-heterodyne measurement delay time  $\Delta\nu_{\text{delay}} = \frac{1}{\Delta\tau_{\text{delay}}}$  (and its multiples).

It is worthwhile to notice that the spurious peaks at  $\pm 110$  kHz present in the linewidth spectrum are no more visible in the phase noise spectrum, proving that these peaks are related to additive intensity noise introduced by the AOM. The low-frequency excess noise in the low frequency part (below 10 kHz), which in particular induces the broadening of the delta function that was visible in

the linewidth spectrum of Fig. 5.23b, is mostly generated by mechanical vibrations and thermal drifts of the laser emission.

To properly measure the laser linewidth in presence of the Flicker noise at low frequencies, which contributes to the broadening of the delta function around the central frequency of  $f_{AOM} = 80$  MHz as previously discussed, we considered the frequency noise of our VECSEL. To do that, we started from the phase noise and, by taking into account the response of the Mach-Zehnder interferometer, we calculated the frequency noise in the case of 1 s acquisition time. The result is shown in Fig. 5.25. By using the method of the  $\beta$ -separation line proposed by Di Domenico et al. [Di Domenico2010], we measured a linewidth of 5 kHz.

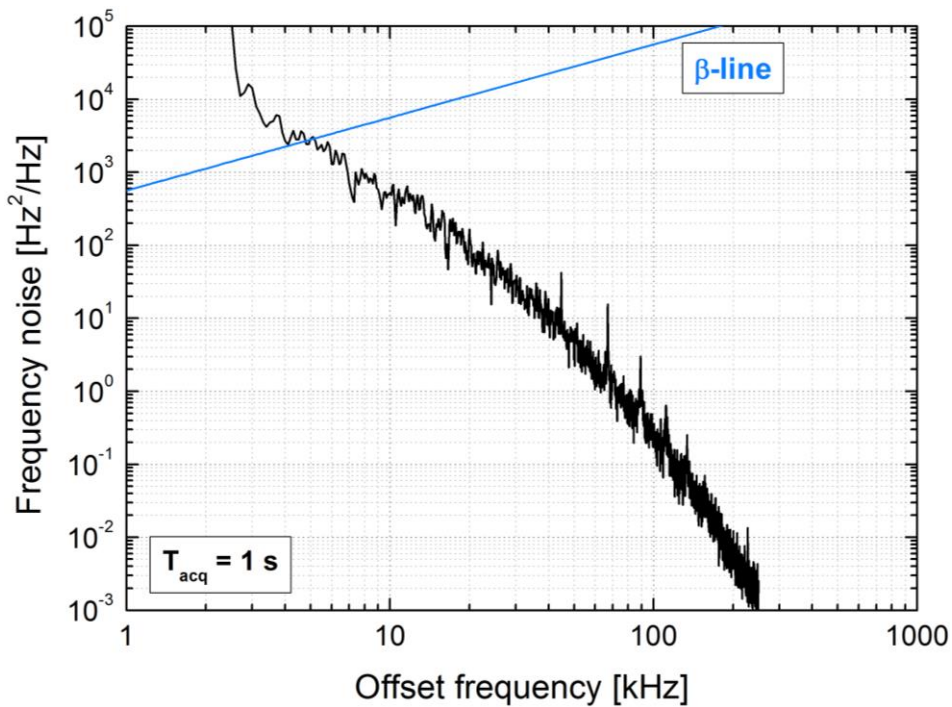


Fig. 5.25 – Frequency noise of the QDH-VECSEL in free running operation, for an acquisition time of 1 s (black curve) and a sampling rate of 25 MHz. The blue line is the  $\beta$ -separation line.

## 5.5 Conclusions

In this chapter we have discussed the design of an optically-pumped VECSEL based on quantum dashes active region, emitting around 1.6  $\mu\text{m}$ , and its technological realization.

The active region has been realized by a GS-MBE reactor, and consists of 18 InAs quantum dash layers, which have been arranged in 3 sets of six layers. The bottom Bragg reflector consists in 17 pairs of GaAs/AlGaAs layers, completed by a gold layer, for a theoretical reflectivity of 99.9%. The semiconductor chip has then fixed on a highly conductive diamond substrate.

During the preliminary tests, no lasing was observed. We suspected a temperature-induced mismatch between the active layers emission peak and the micro-cavity resonance to be the main cause. We solved the issue by depositing a  $\lambda/4$ -thick  $\text{SiN}_x$  anti-reflection coating on the top surface, which helped to weak the thermal shift effect of the gain emission and the micro-cavity resonance. The thermal characterization of the device allowed extrapolating a thermal resistance of  $R_{th} \sim 123 \text{ K/W}$ , which is more than twofold higher than the reference value for InP-based SQW-VECSEL emitting in the  $1.55 \mu\text{m}$  range with metamorphic GaAs-based DBR. This relatively high value may explain the preliminary difficulties in getting laser operation.

The device has been subsequently characterized in two different experimental setups, obtaining a **maximum output power of 163 mW at 20°C in multi-mode operation** in a 12 mm-long cavity.

In single-frequency operation, **the QDH-VECSEL wavelength is tunable across 32 nm** (from 1601.8 nm to 1633.8 nm), **with an average emitted power in the 1-10 mW range**, in a 49-mm long cavity.

Finally, **Class-A operation was demonstrated in a 49-mm long cavity**. From the fitting of the VECSEL transfer characteristic with a first-order function, we were able to calculate a photon cavity lifetime  $\tau_{ph} = 55 \text{ ns}$ , which is well above the active region carrier lifetime  $\tau_c$  (typically few ns). In these conditions, the VECSEL reaches a RIN down to the shot noise limit ( $-158 \text{ dB/Hz}$ , for a detected photocurrent of 2 mA) in the frequency range 10 MHz -18 GHz. Also, **we estimated the laser linewidth in free-running operation to be around 20 kHz, with a delayed self-heterodyne measurement. Measurements according to the  $\beta$ -separation line method allowed refine this estimation, giving a laser linewidth around 5 kHz.** This value needs to be confirmed with the QDH-VECSEL injected on a high-finesse ULE cavity, employing a Pound-Drever-Hall (PDH) servo-locking scheme.

These preliminary results, which demonstrate **the feasibility of low-noise single-frequency VECSEL emitting in the L-band and based on a InP substrate integrating a quantum dash-based active regions**, should be completed by the investigation of such device in dual-frequency operation. With such a purpose in mind, in the next chapter we will discuss the realization of an advanced experimental setup intended to directly investigate the possible dual-frequency operation and in particular the coupling constant measurement of a dual-frequency VECSELs (no matter if QW-, QDH- or QD-based), in a high-coupled regime. From this perspective, preliminary results on a SQW-VECSEL will be provided.

# ***Chapter 6***

## ***Preliminary results on direct coupling constant measurements in dual-frequency VECSELs***

<b>6.1 Introduction .....</b>	<b>206</b>
<b>6.2 Coupling in dual-frequency VECSELs.....</b>	<b>211</b>
6.2.1 Coupling: SQWs vs QDHs/QDs .....	211
6.2.2 Measurement principle of the coupling constant between two laser eigenmodes .....	213
<b>6.3 Direct measurement of the coupling constant in dual-frequency VECSELs ..</b>	<b>215</b>
6.3.1 Development of the experimental setup.....	216
6.3.2 Simultaneous dual-frequency emission between two orthogonally-polarized modes of a SQW-VECSELs.....	219
6.3.3 Preliminary results on direct coupling constant measurement in SQW-VECSELs.....	220
<b>6.4 Conclusions.....</b>	<b>223</b>

## 6.1 Introduction

In the framework of microwave and millimeter-wave photonics and coherent communications systems, semiconductor lasers play a relevant role thanks to their limited costs, small footprint, high reliability and effectiveness in generating highly pure light over a broad frequency range [Seeds2006, Qi2011]. The range of applications of low noise semiconductor optical sources is very wide, involving telecoms, frequency-tunable narrow linewidth sources, microwave or mm-wave carrier signal generation, distribution and detection, radio-over-fiber transmission systems, broadband wireless communications, THz-wave generation, LIDAR-RADAR systems, remote sensing, space telecommunications, metrology, and many others.

Since the generation of microwave or millimeter wave signals in electrical domains involves the use of multi-stage electronic systems, which are bulky and expensive, over the last years semiconductor lasers (especially in the InP material system) have emerged as a key technology for coherent communications systems [Binetti2012] and microwave optical carrier generation [Fandiño2017]. Additionally, microwave photonics has gained momentum thanks to the technological breakthroughs that have been developed across the last decades in InP-based lasers and optical fiber technologies for 1.55  $\mu\text{m}$ -based applications. For instance, optically-carried radio-frequency (RF) signal distribution over silica optical fibers has several advantages if compared to the distribution of electrical signals on classical metallic coaxial cables, such as larger achievable bandwidths, immunity to external electromagnetic interferences, reduced size and weight, parallel signal processing, costs, and sensibly lower losses. Finally, the use of semiconductor materials allows the electrical injection of the devices, contributing on one hand to the reduction of the system dimensions and, on the other hand, to the easy implementation of electronic locking or filtering schemes. This led to the natural development of microwave photonic links for optical signal distribution and detection, which merges the main advantages of both the aforementioned RF microwave systems and optical technologies [Capmany2007, Iezekiel2015].

Over the years, different approaches for the generation of optically-carried RF signals based on semiconductor lasers have been proposed. To name a few: direct [Zhu2018] or external modulation [Qi2005], mode-locking [Lau1988, Bordonalli1996], optical injection schemes [Quirce2012], etc. Although all these techniques can be used to obtain the same result, they suffer from different drawbacks. In the case of direct or external modulation, cumbersome and expensive external RF electrical apparatus are still required and limited modulation depth is achieved.

In this framework, optical heterodyning allows overcoming the intrinsic limitations of the aforementioned modulation schemes.

The generation of RF signals by laser heterodyning is based on the interference of two optical waves ( $E_1$  and  $E_2$ ) having slightly different frequencies ( $\nu_1$  and  $\nu_2$ ) and arbitrary phases ( $\phi_1$  and  $\phi_2$ ):

$$\begin{aligned} E_1(t) &= E_{0,1} \cos(2\pi\nu_1 t + \phi_1) \\ E_2(t) &= E_{0,2} \cos(2\pi\nu_2 t + \phi_2) \end{aligned} \quad (6.1)$$

within the sensitive area of a fast photodetector. The photo-generated current  $I(t)$  at the output of the photodiode is then given by

$$I(t) = \mathcal{R} |E_1(t) + E_2(t)|^2 = \underbrace{\mathcal{R}P_1}_{I_1} + \underbrace{\mathcal{R}P_2}_{I_2} + \underbrace{2\mathcal{R}\sqrt{P_1P_2} \cos[2\pi(\nu_1 - \nu_2)t + (\phi_1 - \phi_2)]}_{I_{RF}} \quad (6.2)$$

where  $\mathcal{R}$  is the photodiode's responsivity and  $P_{1,2}$  the power associated to the two optical modes, respectively. Due to the limited bandwidth of the photodiode, just the RF-component  $I_{RF}$  related to the frequency-difference  $\Delta\nu = \nu_1 - \nu_2$  is converted into electrical signal. In such a way, signals which lay in the GHz to the THz domain can be generated (Fig. 6.1). Obviously, the optical frequency difference must fall within the photodetector's bandwidth, in order to be detected.

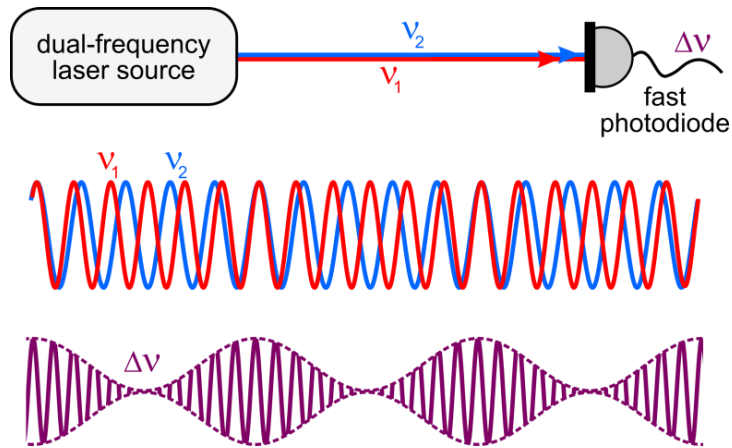


Fig. 6.1 – RF signal generation by laser heterodyning technique: general principle.

Several approaches to realize dual-frequency lasers have been investigated until now in terms of different gain regions (gas, solid-state, doped fibers or semiconductor-based). Although diode-pumped solid-state lasers are attractive in terms of achievable laser power, the fact that semiconductor lasers can be electrically pumped, which translates into a more compact and low-power consumption devices with obvious advantages in terms of system integration, makes the



choice of their use as dual-frequency source particularly promising and attractive. On the other hand, for what concerns the specific architecture of the dual-frequency source, several solutions have been proposed, such as two-laser coupling, composite T cavities, dual-axis cavities, etc.

Table 6.1 summarizes the most significant achievements in coherent dual-frequency lasers obtained so far.

**Table 6.1 – Most significant performance of coherent dual-frequency lasers.**

Refs.	Laser architecture and active region	Cavity design	$\lambda$ (nm)	Average output power	Frequency spacing	Beat-note linewidth	Beat-note Tunability
[Alouini1998]	Solid-state Er:Yb:glass	Two axis	1550	7 mW	DC-2.7 THz	< 10 kHz @ 100 MHz	Yes
[Alouini2001b]	Solid-state Er:Yb:glass	Single axis	1540	10 mW	DC-1.2 GHz	< 10 Hz	Yes
[Rolland2011]	Solid-state Er:Yb:glass	Two axis	1540	2 mW	DC-2 THz	< 1 Hz @ 100 GHz	Yes
[Danion2014]	Solid-state Er:Yb:glass	Two axis	1550	<10 mW	0.1-2.2 THz	30 kHz @ 12 GHz	Yes
[Le Gouët2007]	Solid-state Nd:YAG	Single axis	1064	25 mW	11-124 GHz	Not measured	Yes
[Kim2012]	Semiconductor DFB SQW	Two lasers	1550	15 mW	0.5-2.36 THz	~ 2-3 MHz @ 0.5 THz	Yes
[Van Dijk2011]	Semiconductor SQW coupled DFB/InP	Two axis	1550	-	2-20 GHz	~ 900 kHz @ 10 GHz	Yes
[Bailli2009b, Camargo2012]	Semiconductor VECSEL SQW/GaAs	Two axis	1000 852	20 mW	0.05-8 GHz	4 kHz @ 8 GHz	Yes
[De2014b]	Semiconductor VECSEL SQW/InP	Two axis	1550	100 mW	2.5 and 4.3 GHz	< 10 kHz @ 2-4 GHz	No
[Kervella2015]	Semiconductor SQW coupled DFB/InP	Two axis	1555	-	5-105 GHz	< 30 Hz @ 90 GHz	Yes
[Jiao2012]	Semiconductor mode-locked edge emitting laser QD/InP	Single axis	1550	11 mW	1-2.2 THz	-	Yes
[Akahane2013]	Semiconductor edge emitting laser QD/GaAs	Single axis	1240	2 $\mu$ W	99 GHz	-	No

The optical heterodyning of two phase-locked independent DFB lasers (conditioned an external servo-loop is used to lock the phase between the two lasers, see Fig. 6.2 on next page) or by using two coupled FP or DFB integrated structures has been already demonstrated in the past [Osborne2008, Friederich2010, Van Dijk2011, Kim2012, Carpintero2014, Kervella2015]. T-

cavities have also been used to generate dual-frequency emission with semiconductor lasers in edge-emitting configuration [Lukowski2015, Fedorova2017].

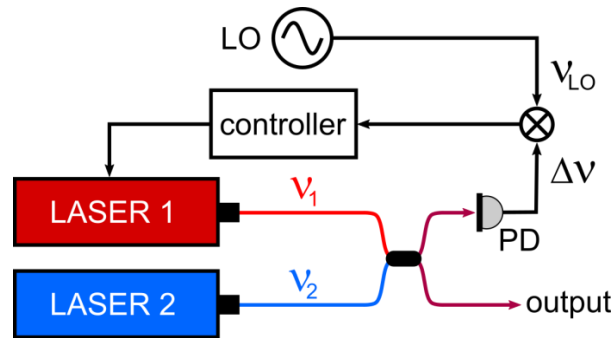


Fig. 6.2 – RF signal generation from two single-frequency (DFB) lasers. LO: reference local oscillator, PD: fast photodiode.

Although these two methods allow generating RF signals in a wide frequency range, they present limited performance in terms of spectral purity. In the case of the short-cavity DFBs, intrinsic high intensity noise due to relaxation oscillation phenomena (Class-B operation) is observed. In the case of two sub-resonators forming the composite T-cavity or two independent DFB lasers, large emission linewidth and high phase noise are expected due to the mechanical fluctuations of the cavity lengths (which are obviously not correlated), resulting in large fluctuations on the frequency difference  $\Delta\nu = |\nu_1 - \nu_2|$ . In applications where spectral purity is critical, these are huge disadvantages.

To improve the spectral performance, laser heterodyning methods of two laser modes sharing the same cavity are thus preferred. In this case, the simultaneous oscillation of two modes inside the same cavity being subjected to the same noise sources (thermal fluctuations, mechanical or acoustical vibrations, etc.), their phase noise is thus highly correlated, and is significantly reduced in the beat-note [De2015]. This configuration could be implemented using a two-longitudinal-frequency laser, but this is generally a non-optimal choice if tunability is desired, because of the limited frequency excursion of the beating signal.

Dual-frequency lasers based on the simultaneous oscillation of two orthogonally-polarized eigenstates are good candidates to simultaneously overcome all these problems. The two eigenstates are emitted by the same cavity, containing a birefringent crystal (e.g. YVO<sub>4</sub>, quartz or calcite) which introduces a phase anisotropy. The two orthogonally-polarized eigenmodes, indicated as ordinary (“o”) and extraordinary (“e”), have different resonance frequencies  $\nu_o$  and  $\nu_e$ , due to the phase anisotropy introduced by the birefringent crystal, and the beat-note signal is thus obtained on the photodiode after a polarizer oriented at 45° at the laser output [Baxter1996, Brunel1997b].

When an electro-optic crystal (introducing an additional phase anisotropy  $\Delta\varphi$ ) is inserted inside the

cavity, the laser becomes a voltage-controlled oscillator at the microwave frequency, and can be efficiently stabilized on a reference signal of a RF local oscillator, using analog [Williams1989, Li2001, Alouini2001b, Brunel2004] or digital [Vallet2007, Rolland2010] optical phase-locked loops (OPLLs), as represented in Fig. 6.3 in the case of a dual-frequency VECSEL. This permits generating and distributing microwave signals of very high spectral purity [Pillet2008, Baili2012, Dumont2014].

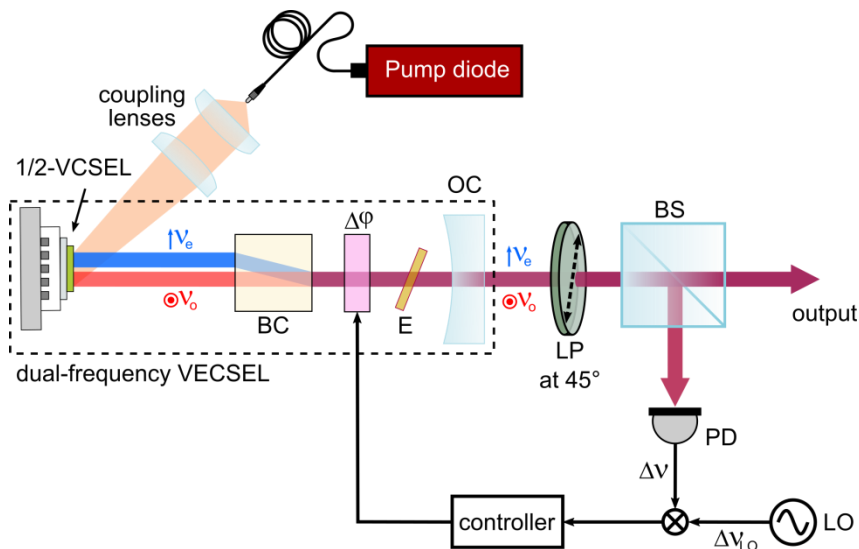


Fig. 6.3 – RF signal generation from a dual-frequency VECSEL with OPLL stabilization. BC: birefringent crystal,  $\Delta\phi$ : electro-optic crystal for additional phase anisotropy, E: etalon, LP: linear polarizer, BS: beam splitter, PD: fast photodiode, LO: reference local oscillator, o,e: ordinary and extraordinary eigenmode (respectively).

VECSELs offer the possibility of Class-A operation, conversely to the case of solid-state lasers, which are inherently Class-B lasers, if dedicated solutions are not implemented [El Amili2014]. On these bases, VECSELs seem the optimal candidates to realize dual-frequency lasers because:

- i. they are inherently low-noise Class-A lasers;
- ii. the extended configuration allows introducing spectral and spatial mode shaping thanks to intra-cavity elements;
- iii. the two orthogonally-polarized eigenmodes are expected to exhibit high correlated phase and intensity noise because they share the same cavity, which leads to a highly pure beating signal through a cancellation (or strong reduction) of these noises;
- iv. they are semiconductor lasers, implying all the afore-mentioned benefits concerning a possible implementation of electrical pumping schemes.

When semiconductors SQWs are used as a gain medium in edge emitting lasers, dual-frequency generation can mainly be obtained using complex architectures, as discussed above. Moreover, even

if coherent emission has been demonstrated with moderate output power (in the mW range), the beat-note linewidth is mainly limited by the important phase noise intrinsically related to the short-cavity length of edge emitting laser design, resulting in linewidth which are of the order of some MHz. Significant improvement are obtained by dual-frequency SQW-VECSELs, which ensure output powers in the 100 mW range, and a beat-note linewidth of the order of the some kHz. On the contrary, coherent dual-frequency laser has been demonstrated with QDs on a single edge emitting laser, showing that such dual-frequency generation may take place within the same active volume (single-axis configuration), in the THz but also in the 100s of GHz frequency difference range. Nevertheless, as previously mentioned, this cavity architecture suffers from important phase noise limitations, resulting in a beat-note linewidth in the MHz range.

## **6.2 Coupling in dual-frequency VECSELs**

### **6.2.1 Coupling: SQWs vs QDHs/QDs**

That being said, the question of the simultaneous oscillation of two laser modes in VECSELs is an important problem that has been only explored in few preceding works, because of the usual “bi-stable” nature of linearly polarized eigenmodes in such lasers. Although robust two-wavelength operation has been demonstrated in SQW-based optically-pumped VECSELs based on different material systems and operating at different wavelengths (852 nm [Dumont2014], 1  $\mu\text{m}$  [Baili2009b], and 1.55  $\mu\text{m}$  [De2014b]), it is important to note that simultaneous oscillation of orthogonally-polarized eigenmodes in such SQW-VECSELs is not a priori guaranteed because of the strong mode competition between them. Indeed, all the demonstrations of bi-frequency SQW-VECSELs so far rely on the intra-cavity spatial separation of the eigenstates on the semiconductor chip side, in order to reduce the cross-coupling inside the active medium and allow their robust simultaneous oscillation inside the laser cavity. Indeed, in contrast to diode-pumped solid-state lasers where both spatial and polarization hole-burning inside the active medium lead to a reduced value of the coupling constant [Brunel1997a, Alouini2000, McKay2007, Schwartz2009], SQW-based devices present a much stronger coupling [Pal2010], and hence often lead to unstable operation. A short off-axis birefringent crystal provides an efficient means to reduce the coupling constant in VECSELs by introducing a spatial separation to get a stable dual-frequency emission [De2014b]. Anyway, from a practical point of view, large spatial separation allow differential noises to appear, which increases the frequency jitter of the beat-note. Thus, spatial separation should be kept as small as possible. On the other hand, it is well known

that the coupling and mode competition have an impact in noise correlations between two modes in Class-A lasers [**Tehrani1978**]. Moreover, a spatial separation makes electrical injection not feasible, when it is one of the main advantages of semiconductors compared to solid-state lasers.

As an alternative to SQW-based gain media, which suffer from mode competition when lasing is performed within the same active volume, nanostructures-based gain media such QDH or QD appears as potential candidates for the generation of coherent dual-frequency lasers. These assumptions mainly come from the fact that these nanostructured gain media present an inhomogeneously broadened density of states (DOS), in opposition to the homogeneously broadened DOS of their SQWs counterpart. As a consequence, QDH/QD-based devices present very unconventional behaviors, such as a negative characteristic temperature ( $T_0$ ) and a very broad laser emission spectrum, as previously discussed on the manuscript. Thanks to these peculiar properties, multimodal emission from a 1.3  $\mu\text{m}$ -emitting InAs/GaAs QDs laser has been related from a collective emission from families in size of QDs [**Sugawara2000**], being (un)coupled between each others as a function of their homogenous linewidth overlapping in the wider inhomogeneously broadened gain curve. Similar results have been obtained with most of all QDH/QD material systems: in 1.16  $\mu\text{m}$ -emitting InGaAs/GaAs QDs [**Djie2007**], 1.3  $\mu\text{m}$ -emitting GaInAsN/GaAs QD [**Miyamoto2003**] and 1.55  $\mu\text{m}$ -emitting InAs/InP QD or QDHs [**Alghoraibi2007**, **Klaime2013**, **Duan2018**].

Also, QD-based lasers present fundamental differences with SQWs-based ones, in terms of carrier dynamics. Above threshold, the QDs gain is not clamped as it is for QWs, as shown for the first time on 1.3  $\mu\text{m}$ -emitting InAs/GaAs QDs [**Markus2003**]. In this case, further increase in the current density leads to simultaneous laser emissions from the QD excited state and ground state. Similar experimental results have been evidenced on other material systems integrating QD-based active media: 1.16  $\mu\text{m}$  InGaAs/GaAs QDs [**Djie2007**] and 1.55  $\mu\text{m}$  InAs/InP QDs [**Platz2005**, **Li2009**].

Based on the intrinsic properties of such low-dimensional nanostructures, there have recently been convincing theoretical and experimental works showing that devices based on QDs are good candidates to produce coherent dual-wavelength operation. Simultaneous two-mode operation over a relatively wide frequency range is theoretically possible, according to [**Chusseau2013**]. In this model, based on realistic parameters for the QD homogeneous and inhomogeneous linewidth, it is shown that stable dual-frequency emission can be possible in the THz frequency range (and lower) both considering uncoupled or coupled QDs. In a more recent theoretical work, Chusseau et al. went further and analytically calculated the coupling constant  $C$  in the case of a QD-based dual-frequency laser [**Chusseau2018**], showing that it only depends on two parameters: one related

to the specific design of the QD-based gain region and the laser, while the second represents the homogeneous broadening of QD emission. In the same work they also showed that always  $C < 1$  for such a QD-based dual-frequency laser.

From an experimental point of view, dual-frequency operation with QD-based devices has only been demonstrated using edge emitting laser structures. In particular, dual-frequency operation was established in different cavity setups, enabling lasing operation on the QD ground state or excited state, with frequency difference tuning from 0.1 up to tens of THz [Grillot2011, Jiao2012, Hurtado2013, Akahane2013, Fedorova2017], covering almost the whole inhomogeneous broadening spectrum of QDs. The two very last cited results ([Akahane2013, Fedorova2017]) are among the most convincing works, showing the high potentialities of QD for coherent dual wavelength emission, from a very large frequency difference in the THz range, down to a narrow frequency difference in the 100s GHz range.

## 6.2.2 Measurement principle of the coupling constant between two laser eigenmodes

The dynamics between two eigenmodes of a laser resonator is governed by the nonlinear coupling constant  $C$ , as originally introduced by Lamb in the case of a gas maser [Lamb1964]. This general model can be also applied to the case of solid-state lasers [Alouini2001a], or VECSELs [Pal2010]. Following his analysis, we can describe the evolution of the intensities of the two optical modes,  $I_1$  and  $I_2$ , by considering the following system of coupled rate equations [Sargent1974]:

$$\frac{\partial I_1}{\partial t} = I_1 (\alpha_1 - \beta_1 I_1 - \theta_{12} I_2) \quad (6.3a)$$

$$\frac{\partial I_2}{\partial t} = I_2 (\alpha_2 - \beta_2 I_2 - \theta_{21} I_1) \quad (6.3b)$$

where  $\alpha_i, \beta_i$  are the net gain and the self-saturation of the  $i^{\text{th}}$  mode, whereas  $\theta_{ij}$  is the cross-saturation between the  $i^{\text{th}}$  mode and the  $j^{\text{th}}$  mode, respectively. In steady-state conditions

$\frac{\partial I}{\partial t} = 0$  and the non-trivial solution of the system of Eqs. 6.3, corresponding to the simultaneous

oscillations of modes 1 and 2, is:

$$I_1 = \frac{(\alpha_1 / \beta_1) - (\theta_{12} / \beta_1)(\alpha_2 / \beta_2)}{1 - C} \quad (6.4a)$$

$$I_2 = \frac{(\alpha_2 / \beta_2) - (\theta_{21} / \beta_2)(\alpha_1 / \beta_1)}{1 - C} \quad (6.4b)$$

$C$  being the Lamb coupling constant.

The values

$$K_{12} = \frac{\theta_{12}}{\beta_1} \quad (6.5a)$$

$$K_{21} = \frac{\theta_{21}}{\beta_2} \quad (6.5b)$$

are the cross-to-self-saturation coefficients. In order to measure the coupling constant  $C$  existing between the two laser eigenstates 1 and 2, we can apply the experimental method developed by our group in the case of a solid-state Nd:YAG [Brunel1997a] or Er:Yb:glass bi-frequency laser [Alouini2001b], and successfully transferred to the case of VECSELs [Pal2010]. It consists in slightly modulating the net gain  $\alpha$  of one eigenmode by introducing weak optical losses, and looking at the evolution of the intensities  $I_1$  and  $I_2$  of the two eigenmodes. This operation is then repeated while the optical losses are applied to the other eigenmode. In such a way, we can directly relate the modulation of  $I_1$  and  $I_2$  to the cross-to-self-saturation coefficients  $K_{12}$  and  $K_{21}$  [Alouini2001b]:

$$K_{12} = \frac{\theta_{12}}{\beta_1} = -\frac{\delta I_1}{\delta I_2} \quad (6.6a)$$

$$K_{21} = \frac{\theta_{21}}{\beta_2} = -\frac{\delta I_2}{\delta I_1} \quad (6.6b)$$

and finally compute the coupling constant  $C$  as [Sargent1974]:

$$C = \frac{\theta_{12}\theta_{21}}{\beta_1\beta_2} = K_{12}K_{21} \quad (6.7)$$

We stress the fact that the frequency of the modulated losses must be chosen sufficiently weak to not perturb the system from its steady-state, in such a way that Eqs. 6.4 still hold.



### **6.3 Direct measurement of the coupling constant in dual-frequency VECSELS**

This section is devoted to the description of the experimental setup which has been conceived and realized in order to exactly measure the value of the coupling constant as a function of the wavelength difference between the two eigenmodes of a dual-frequency VECSEL, the initial goal being to investigate the behavior of the coupling constant in a VECSEL with an anisotropic gain medium such as quantum dashes or quantum dots.

According to what we saw in the previous chapter, the QDH-VECSEL that we realized suffers from a non-negligible overheating which result in a relatively high threshold and low emitted power, if compared to conventional SQW-VECSELS, as already discussed. Although single-frequency operation was demonstrated in such device, any preliminary test in dual-frequency configuration failed, most probably due to the extra optical losses introduced by the intra-cavity elements used to reach the dual-frequency emission, which were sufficient to prevent the QDH-VECSEL from working.

First experiments have thus being performed by using a SQW-VECSEL designed to emit around 1540 nm, which has been provided by E. Kapon's group from the École Polytechnique Fédérale de Lausanne (EPFL, Switzerland) in the framework of a collaborative ANR-FNS international project called IDYLIC<sup>1</sup>. Such a device allowed addressing the following basic points:

1. the validation of the experimental setup;
2. the first direct measurement of the coupling constant without any spatial separation between the eigenstates in the active medium in a dual-frequency SQW-VECSEL, for different value of the wavelength difference between the two modes;
3. the coupling constant measurement on SQW-VECSEL representing also a reference for future coupling constant measurements in the case of QDH- or QD-based VECSELS.

In particular, the second point is of particular importance since this kind of measurement has never been performed up to this moment. Indeed, as discussed previously, dual-frequency emission from SQW-based VECSELS have only been obtained by spatially separating the two orthogonally-polarized eigenstates, thus decreasing the coupling between them. Additionally, as anticipated, it

---

<sup>1</sup> Investigation of quantum Dots within electrically excited vertical and external cavity surface emitting Lasers for the realization of a Coherent and compact dual wavelength laser.

permits to obtain information on a reference sample based on quantum wells, and to compare the results with devices based on different gain media based on quantum dashes and quantum dots active media in future experiments.

### 6.3.1 Development of the experimental setup

As stated above, the VECSEL structure is based on a SQW-based active region on InP substrate. The active region, which has been designed to get laser operation around 1540 nm, integrates 8 compressively strained InGaAlAs QWs, arranged on three different sets according to a 4-2-2 distribution, and then has been wafer-fused to an AlAs/GaAs-based DBR consisting of 19.5 pairs. Both the InP-based active wafer and the GaAs-based DBR wafer were separately grown by MOVPE at EPFL Lausanne (LPN, Laboratory of Physics of Nanostructures). After selective removal of the GaAs substrate, the DBR-side of the wafer has been metalized with Ti/Au. Then, the wafer has been cleaved to obtain  $\sim 3 \times 3$ -mm chips. One of these chips has been subsequently bonded to a metalized  $5 \times 5 \times 0.3$ -mm diamond heat-spreader to form the  $\frac{1}{2}$ -VCSEL chip [Keller2015]. Finally, the InP substrate has been selectively etched. The  $\frac{1}{2}$ -VCSEL has been then characterized using the experimental setup depicted in Fig. 6.4. It consists in two distinct parts: the dual-frequency VECSEL cavity (A) and the analysis part (B).

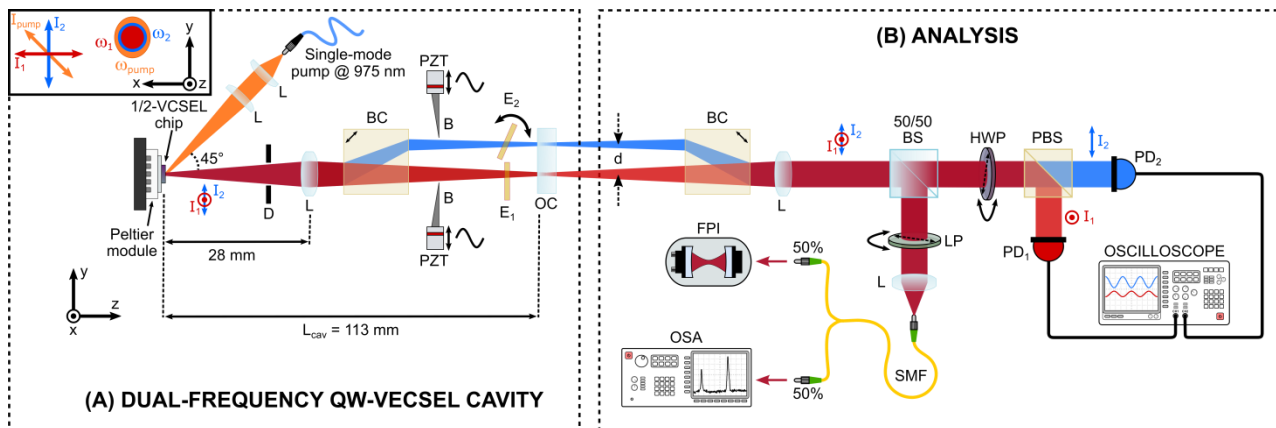


Fig. 6.4 - Experimental setup used to perform the coupling constant measurements with the  $1.54 \mu\text{m}$ -emitting dual-frequency SQW-VECSEL. L: lens, D: diaphragm, BC: YVO4 birefringent crystal, PZT: piezo-actuator, B: razor blade, E: etalon, OC: planar output coupler, BS: beam splitter, LP: linear polarizer, FPI: Fabry-Pérot interferometer, OSA: optical spectrum analyzer, HWP: half-wave plate, PBS: polarizing beam splitter, PD: balanced InGaAs photodiode. Index 1 and 2 are referred to the two orthogonally-polarized eigenmodes  $I_1$  (ordinary) and  $I_2$  (extraordinary).

Concerning the VECSEL cavity, the  $\frac{1}{2}$ -VCSEL chip has then been mounted on a Peltier thermoelectric cooler, whose temperature has been fixed to  $20^\circ\text{C}$  for all the measurements. A linearly-polarized single-mode pigtailed semiconductor diode laser, able to deliver up to 1 W at 980 nm, has

been used to continuously pump the active region of the chip. The pump has been placed at an incident angle of  $45^\circ$  with respect to the VECSEL cavity axis and then focused on the  $\frac{1}{2}$ -VCSEL chip by two lenses, resulting in an elliptical pump spot on the chip surface (ellipticity  $\varepsilon \sim 0.3$ ), which becomes nearly circular on the active region (ellipticity  $\varepsilon \sim 0.03$ ). The polarization of the pump has been oriented to  $45^\circ$  with respect to the x-axis (see inset of Fig. 6.4).

In order to achieve dual-frequency operation, a 10 mm-thick  $\text{YVO}_4$  birefringent crystal cut at  $45^\circ$  from its optical axis has been inserted inside the cavity. However, in our case the  $\text{YVO}_4$  crystal is used to lift the spatial degeneracy outside the active medium. A  $d = 1$  mm separation is thus introduced between the two orthogonally-polarized eigenmodes, which are noted  $I_1$  (ordinary mode, linearly polarized along the x direction) and  $I_2$  (extraordinary mode, linearly polarized along the y direction), as indicated in the Fig. 6.4. Due to the different length of the two arms of the dual-frequency VECSEL, the waists of the two orthogonal eigenmodes on the chip-side slightly differ from each other. They have been calculated to be  $\omega_1 = 30 \mu\text{m}$  and  $\omega_2 = 31 \mu\text{m}$  using the ray transfer matrix method for Gaussian modes propagation (see *Appendix A*) [Kogelnik1966], for a cavity length of 113 mm (see Fig. 6.5), as set in our experimental setup. This relatively long cavity also ensures the Class-A operation of the SQW-VECSEL. The pump dimensions have been then finely adjusted to form a spot with semi-axis dimensions equal to  $32 \mu\text{m} \times 45 \mu\text{m}$  at the semiconductor chip surface (checked by means of a Si-CCD camera). Then the pump spot becomes then nearly circular inside the active medium, with semi-axis dimensions of  $32 \mu\text{m} \times 33 \mu\text{m}$ , owing to Fresnel refraction, as previously said.

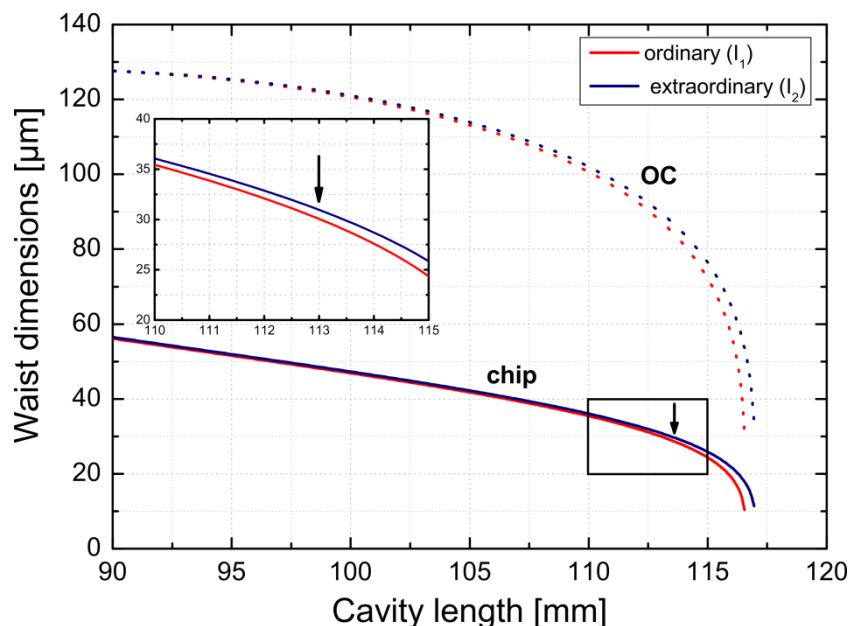


Fig. 6.5 – Radius dimensions of the waist of the ordinary  $I_1$  (red) and extraordinary  $I_2$  (blue) eigenmodes at the semiconductor chip surface and at the output coupler, for different values of the cavity length. In our experiment, we set a cavity length equal to 113 mm (inset shows a zoom of the waist dimensions around that value).

These dimensions ensure that both orthogonally-polarized eigenmodes are efficiently pumped and thus have sufficient gain to simultaneously oscillate when exactly superimposed on the semiconductor chip (see inset of Fig. 6.4). If that were not the case, one of them would experience extra-losses due to inefficient pumping, preventing the mode to reach the threshold condition. Additionally, the dimensions of the pump spot are also set to promote the two eigenmodes to oscillate on the fundamental transverse TEM<sub>00</sub> profile. The fact that the two eigenmodes are perfectly superimposed at the semiconductor chip surface results in an overlap integral close to 100%<sup>2</sup>.

At this point is worth to notice that, according to how the laser resonator architecture and the pumping scheme have been conceived, the two orthogonally-polarized eigenmodes can simultaneously reach the oscillation condition if their separation takes place at the output coupler side of the cavity, i.e. after the YVO<sub>4</sub> birefringent crystal (BC). This condition naturally obliges to close the cavity with a planar output coupler on the side where the two eigenstates are spatially separated, to ensure that both eigenmodes are resonant after one cavity round-trip. The stability of the plane-plane resonator formed is then ensured by a fused silica bi-convex lens with a focal length of  $f = 20$  mm, placed at 28 mm from the VECSEL chip, which ensures that the wavefront of both modes is plane at the output coupler position. To force the single-frequency oscillation of the two eigenmodes, and thus obtain a truly dual-frequency emission, a 100  $\mu\text{m}$ -thick fused silica etalon with a reflectivity  $R_{eta} = 30\%$  on both faces is inserted in each arm. One of the two etalons is mounted on a rotational support (E<sub>2</sub>), which allows independently tuning the emission wavelength of the corresponding eigenmode, while the other is kept fixed (E<sub>1</sub>). A diaphragm is also inserted before the intra-cavity lens in order to eventually filter any residual transverse high-order mode. To limit as much as possible the optical losses, all the intra-cavity elements inserted in the laser resonator are anti-reflection coated at the emission wavelength of the VECSEL. We also selected a planar output coupler with a relatively high reflectivity, namely equal to  $R = 99.5\%$ , to limit its losses and ensure the lasing during the subsequent coupling constant measurements. Two razor blades, mounted on two piezo-actuators which are modulated with a low-frequency varying sinusoidal voltage (typical frequency  $f_{PZT} = 15\text{-}30$  Hz), allow introducing diffraction losses (some tens of percent) on one arm at a time without affecting the other (and vice versa), to modulate the intensity of the two eigenmodes around their nominal steady-state, as it will be further discussed ahead.

---

<sup>2</sup> The overlap is not exactly 100% because of the small waist difference of the two spot profiles, arising from the different cavity length of the two arms.

The analysis part of the experimental setup consists in a second YVO<sub>4</sub> birefringent crystal exactly equivalent to the first one, used to spatially recombine the two eigenmodes. After a collimating lens and a 50/50 beam splitter (BS), part of the signal is coupled into a single-mode fiber and sent to a 10 GHz free spectral range scanning Fabry-Pérot interferometer (FPI) and an optical spectrum analyzer (OSA) for signal analysis. In particular, the FPI is used to systematically monitor the dual-frequency operation of the VECSEL and to check that no mode-hopping occurs during measurements. A linear polarizer, placed before the injection lens, eventually allows discriminating between the two eigenmodes  $I_1$  and  $I_2$ . The remaining part of the signal is sent to a polarizing beam splitter (PBS), which again separates the two eigenmodes towards two balanced InGaAs photodiodes (PD<sub>1</sub> and PD<sub>2</sub>, respectively) connected to a digital oscilloscope through two 50 Ω resistances. A half-wave plate is used to calibrate the response of the two photodiodes. By rotating the half-wave plate, the two polarizations are then switched in the two detection arms and any residual gain/efficiency unbalance between the two detection paths is then taken into account during measurements.

### 6.3.2 Simultaneous dual-frequency emission between two orthogonally-polarized modes of a SQW-VECSELS

If no etalons are present inside the VECSEL cavity, the laser naturally operates in the longitudinal multi-frequency regime, characterized by a wide emission spectrum centered on 1540 nm (see black inset of Fig. 6.6a). In this condition, it exhibits a threshold around 200 mW with a maximum emitted power of 14.7 mW (pump limited, black curve of Fig. 6.6a).

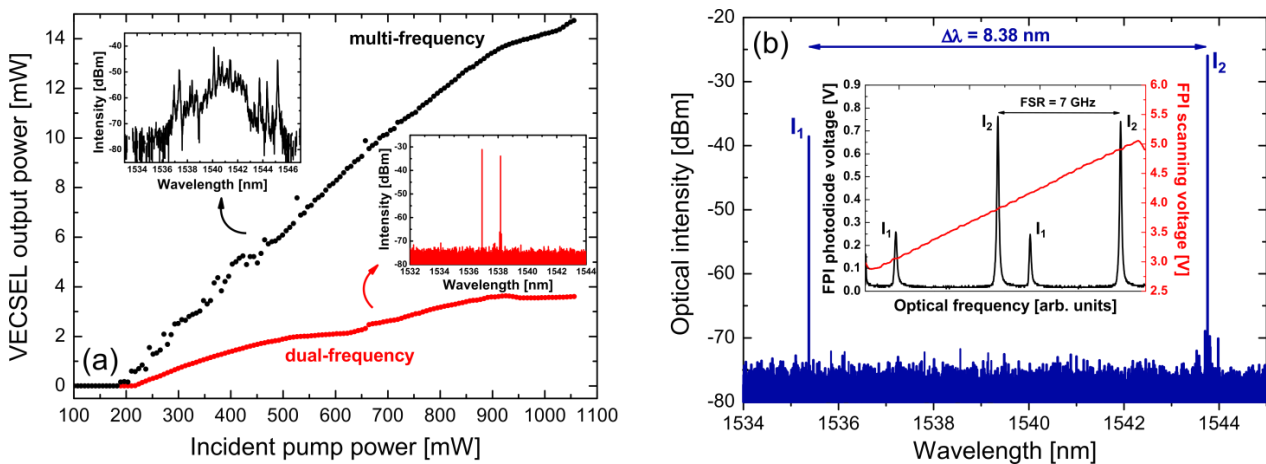


Fig. 6.6 - (a) Typical output characteristics of the SQW-VECSEL as a function of the incident pump power when operating in multi-frequency (black curve) and dual-frequency modes (red curve). Corresponding OSA spectra are shown in insets. (b) Dual-frequency spectrum of  $I_1$  and  $I_2$  eigenmodes, in the case of a wavelength difference  $\Delta\lambda = 8.38$  nm (in inset the finely-resolved FPI spectrum).

The insertion of the two etalons filters on both arms of the cavity forces the VECSEL to oscillate in the dual-frequency regime. As most of the longitudinal lasing modes are suppressed by the optical losses introduced by these two filters (see optical spectrum in red inset), the maximum achievable output power is now significantly reduced to 3.6 mW (red curve in Fig. 6.6a), although the threshold is just slightly increased to 220 mW, confirming that very few additional losses are introduced on the two surviving lasing modes. The truly dual-frequency operation is undoubtedly confirmed by the FPI spectrum shown in the inset of Fig. 6.6b, indicating the simultaneous lasing of the ordinary and extraordinary eigenmodes  $I_1$  and  $I_2$ , which in this specific case are separated by a wavelength difference  $\Delta\lambda = 8.38$  nm around the central emission wavelength, by simply rotating the orientation of the first etalon ( $E_1$ ). It is worth mentioning that the optical losses introduced by the two razor blades on the two polarizations have been carefully balanced in order to get the stable oscillation of the two eigenmodes, as specified in the following paragraph.

### 6.3.3 Preliminary results on direct coupling constant measurement in SQW-VECSELs

Thanks to the spatial separation of 1 mm introduced by the  $\text{YVO}_4$  crystal, it was possible to individually modulate the optical losses of one arm at a time, by modulating the razor blades at 20 Hz around their nominal position. As the modulation period is very long with respect to the characteristic time of the laser (such as the lifetime of photon inside the cavity, the carrier lifetime in the semiconductor and the cut-off frequency of the laser), we can consider that the laser adiabatically follows the evolution of the optical losses and it can be considered as a stationary system.

During the measurements, the incident pump power has been set to 900 mW, corresponding to a pumping rate  $r = 4.15$ . Generally, a stable dual-frequency emission is difficult to maintain over time with a fully superposition of the eigenmodes on the active media, in the case of our SQW-VECSEL. Indeed, thermal fluctuations and mechanical vibrations could also perturb such a balance, resulting in the loss of the dual-frequency operation. This is particularly evident when the movable etalon filter is turned to set the wavelength of mode  $I_2$  (and thus the wavelength difference  $\Delta\lambda$ ), because instabilities appears and the VECSEL eventually switches to single-frequency operation (the weaker mode turns off). This difficulty in reaching a stable dual-frequency emission is also an indication that the coupling constant between the two eigenmodes of our SQW-VECSEL is quite high, probably close to the critical value  $C = 1$ , as expected for QWs-based active media.

Thus, in order to get a simultaneous and stable emission of the two eigenmodes, we finely adjusted the losses of each arm to avoid a potential switching from a dual- to a single-frequency emission. In

particular, we chose a steady nominal position of the razor blade such that we voluntarily introduced sufficient extra optical losses on the strongest  $I_2$  mode<sup>3</sup>, in order to prevent instabilities which could have led to the switching off of the  $I_1$  mode during measurements.

As a result, during the coupling constant measurements the power of the two modes  $I_1$  and  $I_2$  was relatively low, and roughly comprised between 100 and 550  $\mu\text{W}$ , respectively. Additionally, we took care to keep the loss modulation index<sup>4</sup> to a value lower than 10%, in order to not appreciably perturb the dual-frequency operation, nor introducing any significant modification of the spatial profile of the beams.

Figs. 6.7a,b are experimental traces acquired by the oscilloscope and show an example of a coupling measurement between the orthogonally-polarized eigenmodes of the SQW-VECSEL. In this case the wavelength of the extraordinary mode  $I_2$  was set to 1539.5 nm, while that of the ordinary mode  $I_1$  was fixed to 1535.5, giving a wavelength difference equal to  $\Delta\lambda = 4$  nm.

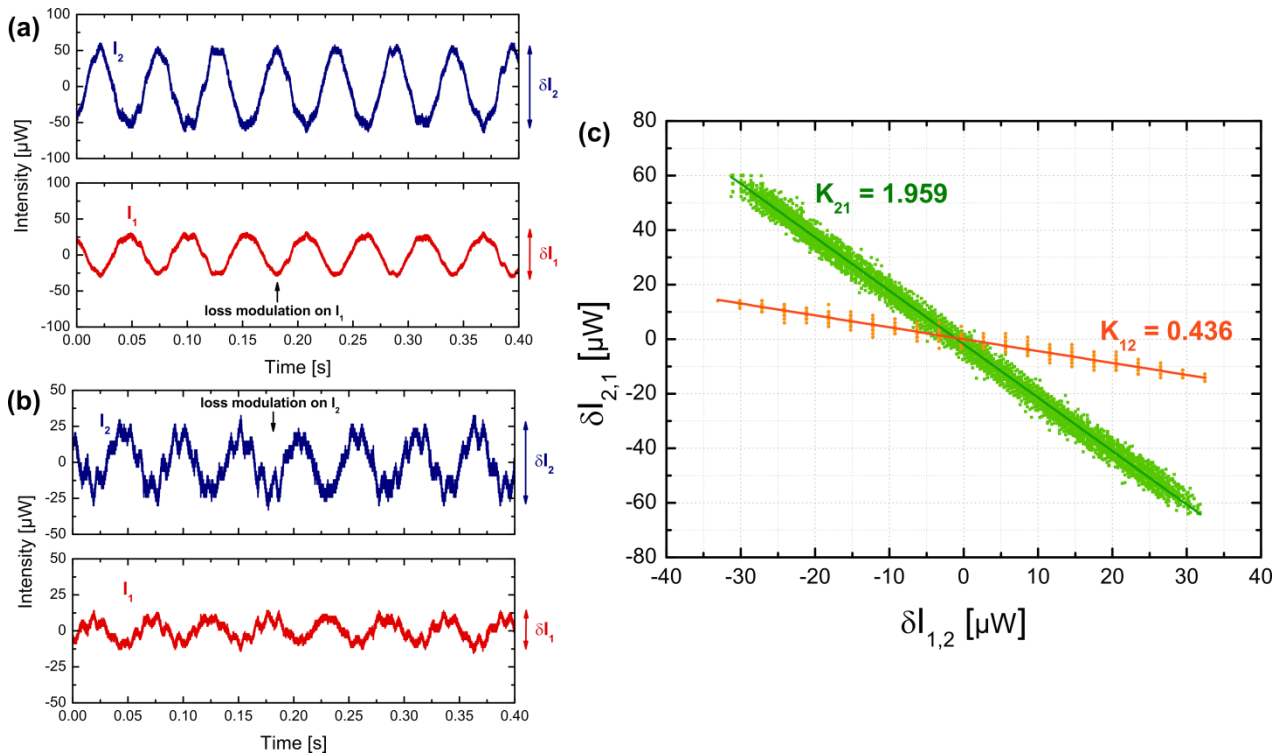


Fig. 6.7 - Evolution of the traces observed at the oscilloscope when the modulation losses are applied to (a) mode  $I_1$  or (b) mode  $I_2$ . The signals have been normalized with respect to their steady value. (c) Relative unmodulated mode intensity versus the relative modulated mode intensity; the absolute value of each slope leads to the value of the respective cross-to-self-saturation ratio  $K_{ij}$ . In this particular case, the wavelength difference  $\Delta\lambda$  was set to 4 nm.

<sup>3</sup> The residual gain dissymmetry between the two eigenmodes is mainly determined by the natural strain of the semiconductor chip as well as the pump induced strain.

<sup>4</sup> The loss modulation index of mode  $i$  is defined as  $MI_i = \frac{\delta I_i}{2} = \tilde{I}_i$ , with  $\tilde{I}_i$  the amplitude variation of the optical intensity around its steady value  $I_i^0$ .



We modulated the optical losses of the ordinary mode and acquired both signals simultaneously, then performed the same for the extraordinary mode. We can notice that the two modes are in antiphase, as expected from Eqs. 6.3. The cross-to-self saturation coefficients  $K_{12}$  and  $K_{21}$  can thus be obtained by plotting the unmodulated signal as a function of the modulated one and by calculating the inverse of the slope of the linear fit on the experimental data, as shown in Fig. 6.7c. In this case we find  $K_{12} = 0.436$  and  $K_{21} = 1.959$ , respectively. The value of the coupling constant is thus equal to  $C = 0.855 \pm 0.012$ .

We repeated the measurements of the coupling constant for different values of the wavelength difference between the two eigenmodes, namely for 2, 6 and 9.8 nm (Fig. 6.8a,b,c). The results of that are summarized in Fig. 6.8c. The error bars of Fig. 6.8c have been obtained by repeating the same measurements over time, and represent the standard deviation around each mean value of  $C$ . As we can see, the different measurement are centered on  $C = 0.843 \pm 0.012$ . We can thus affirm that this value corresponds to the average value of the coupling constant of our SQW-VECSEL.

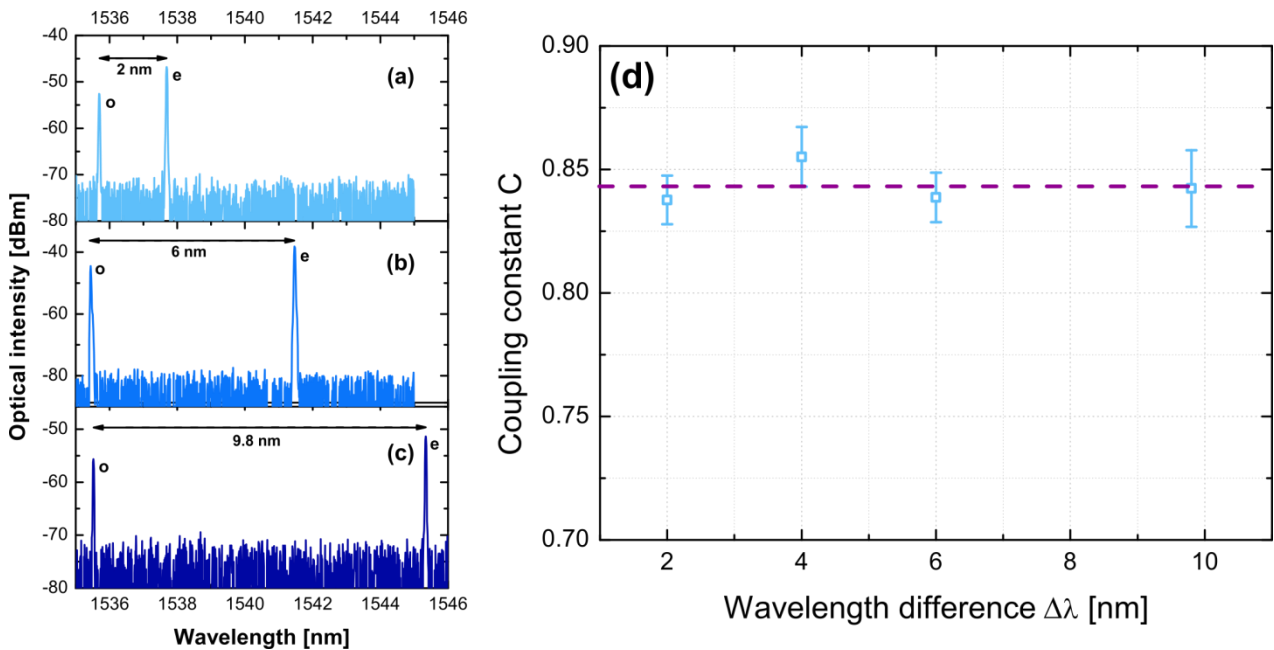


Fig. 6.8 – OSA spectra of the ordinary  $I_1$  and extraordinary  $I_2$  eigenmodes for different wavelength difference  $\Delta\lambda$ : (a) 2 nm, (b) 6 nm, (c) 9.8 nm. (d) Coupling constant  $C$  versus the wavelength difference  $\Delta\lambda$  between the two orthogonally-polarized eigenmodes. Standard deviation is represented by the error bars obtained by repeating the measurements over time. The dashed violet line indicates the averaged value of  $C = 0.843$ .

This value also confirms the fact that in a dual-frequency SQW-VECSEL, the coupling constant between two orthogonally-polarized eigenstates is relatively high, which explains the difficulty to reach and maintain a stable dual-frequency emission. However, we demonstrated the feasibility in reaching the dual-frequency regime in a SQW-VECSEL without any spatial separation of the modes on the semiconductor chip, despite such a high coupling between the two eigenmodes.

Moreover, the results of the coupling constant measurements in an isotropic medium such as SQWs represent a reference for further measurements on QDHs and QDs. At present, the QDH-based VECSEL structure presented in *Chapter 5* does not offer enough gain to perform such experiments. However, the team is pursuing the optimization of both QDH- and QD-based active region with improved gain for future dual-frequency VECSEL operation and coupling constant investigation on such anisotropic gain media.

## 6.4 Conclusions

This chapter was devoted to discuss the preliminary results of the coupling constant measurement on optically-pumped VECSELs. After a brief introduction presenting the advantages of VECSELs as dual-frequency sources, we discussed the benefits of using devices which integrates anisotropic gain media to get dual-frequency regime, such as QD or QDH active regions.

The second part of the chapter was focused to the **description of the experimental setup that has been conceived to directly investigate the coupling between two orthogonally-polarized eigenstates in a dual-frequency VECSEL, as a function of wavelength difference.** This represents a direct method to access to the coupling constant measurement since it does not introduce any spatial separation between the modes on the semiconductor chip, which lowers the value of their coupling. Initially, the setup was conceived to realize such coupling measurements in nanostructured-based (QDH or QD) VECSELs, in order to investigate the benefits related to the anisotropy of such nanostructures. However, since the performance of the QDH-VECSEL available at the moment of the experiences was not sufficient to get lasing in a dual-frequency regime in such a setup, we concentrated our efforts in characterizing a SQW-based VECSEL emitting around 1.54  $\mu\text{m}$ . This allowed validating the experimental setup and the approach and obtaining a measurement reference for future structures with anisotropic gain (QDHs and QDs) which are currently under development.

Beside this, **we also confirmed that a careful balance of the optical losses of the two eigenmodes was required to get a stable dual-frequency emission** with the SQW-VECSEL. This was a first clue that the coupling between orthogonally-polarized eigenmodes is strong on such kind of lasers. Indeed, from direct measurements, it turned out that according to our expectations and previous works on the subject, the coupling constant is relatively high. **We experimentally demonstrated that the average value of this coupling constant is equal to  $C = 0.843 \pm 0.012$ .** **This high value explains why it is not straightforward to achieve a stable dual-frequency emission in VECSELs with homogeneously broadened active medium like SQWs.** This can be related to the isotropic nature of the active medium of the laser. It is known that SQW-based gain

media are subjected to mode competition, which results in switching from dual to single-frequency operation.

For the future, **the setup is ready to perform such experiments in dual-frequency QDH- or QD-VECSELs**, in order to investigate the coupling in such a kind of devices and eventually highlight differences arising from the anisotropic nature of their active regions, as theoretically predicted [**Chusseau2013**] and experimentally demonstrated in few previously reported works on edge-emitting devices [**Grillot2011, Jiao2012, Hurtado2013, Akahane2013, Fedorova2017**]. In summary, the stability of dual-frequency VECSELs might be increased using such a different gain medium, like for instance a QD-based one, as very recently theoretically discussed by Chusseau et al. [**Chusseau2018**].

# ***Conclusions and perspectives***

This Ph.D. dissertation has been focused on the development of InP-based vertical-cavity lasers based on nanostructured active media emitting around the telecom wavelength. Different approaches have been addressed in the manuscript, which is basically divided in two main parts: the first part being devoted to the development and characterization of monolithic micrometric VCSELs, while the second part is focused on the realization of long-cavity VECSELs.

*Chapter 1* was devoted to the presentation of the basic concepts of micrometric-cavity VCSELs. A state-of-the-art of the main approaches adopted to realize such devices has been presented. Then we discussed the main basic blocks composing a VCSEL device, such as the design of the DBR and the laser resonator sections, the different approaches to confine the carriers and control the transverse modes, etc.

In *Chapter 2* we focused on the development of a new technological process to improve the performance of the VCSEL devices. This new approach, which has been called “Through Silicon Holes Electroplated Copper” (TSHEC) process, consists in hybridizing an InP-based active region on a Si host substrate through the use of BCB bonding and localized copper micro-heat-sinks, and it has undoubtedly several advantages, such as: compatibility with conventional low cost processes, the possibility to be applied to different material systems, the possibility to conceive heterogeneous integrated photonic circuits with vertical/horizontal architectures on a Si platform, and thermally improved efficiency, possibility to merge in the same platform optoelectronics (optical sources and detectors), microelectronics (read-out integrated circuits, CMOS driven electronics) and microfluidics (optical functionalization and analysis) components. The process has been validated on an optically-pumped VCSELs emitting at 1.55  $\mu\text{m}$  and it has been proved to bring superior performance of the devices, thanks to the improved thermal dissipation. In particular, we observed a reduction of the VCSEL internal temperature of the devices presenting a reduced BH-DBR diameter ( $d_{\text{BH-DBR}} = 20 \mu\text{m}$ ), together with a lower threshold for such devices, with respect to devices presenting a BH-DBR diameter  $\geq 100 \mu\text{m}$ . The reduction in dimensions of the devices did not imply a reduction in the output performance, as they were able to emit powers well above 2 mW

## *Conclusions and perspectives*

at 16°C, and to operate at temperatures as high as 50°C. These encouraging results pushed towards the next step of development, which consisted in adapting the TSHEC technology to realize electrically-injected VCSELs, with advantages in terms of spatial encumbrance, power consumption, and system integration. For such a reason, we focused on the development of some basic blocks for the electrical injection, in particular on the buried tunnel junction optimization. After a TCAD-based design, we identified a possible candidate structure (compatible with the GS-MBE growth system at FOTON Institute) based on InGaAs, to be integrated in future devices. First tests on realized samples showed that this solution, which employs an n<sup>++</sup>/p<sup>++</sup> InGaAs BTJ with a p<sup>++</sup> Q<sub>1.18</sub> buffer layer, is effective in order to confine the current across a diameter compatible with the VCSEL injection. However, we still have some concerns on such an approach, as the p<sup>++</sup> InGaAs could introduce extra optical losses due to its non-negligible absorption around 1.55 μm, if the BTJ results not exactly accommodated in a minimum of the resonant stationary field of the cavity. To solve this issue, a viable way might be represented by the use of heavily-doped quaternary-based (Q<sub>1.18</sub> or Q<sub>1.4</sub>) BTJs, which have negligible absorption at the emission wavelength due to their sufficiently wide bandgap (> 0.8 eV). This solution will be tested very soon, thanks to the installation of a carbon cell on the GS-MBE system, which allows reaching high value of doping levels thanks to an efficient incorporation of p-dopants on such quaternary alloys. Despite these technological problems, however, we still managed to test an electrically-pumped VCSEL-like structure acting as an infrared-emitting LED, which allowed validating most of the mask levels developed for the electrically-pumped VCSEL. In this perspective, EP-VCSELs based on TSHEC process would be the next step of realization.

Thanks to the result obtained with the TSHEC technology, which has been proven to assure a reliable platform to realize VCSEL devices with good performance, the next step of development has been the integration of a tunable mechanism exploiting the optical properties of liquid crystals to realize monolithically-tunable devices. This has been presented in **Chapter 3**, where we discussed the development of vertical-cavity tunable devices based on a new and original approach based on the integration of liquid crystal-based μ-cells, developed in collaboration with LAAS, IMT Atlantique and C2N. This approach allowed the realization of compact, low-cost and low-power consuming devices, with a first proof-of-concept based on a LC-based photodiode, tunable over 80 nm around 1.55 μm, which showed very satisfactory performance and represent the first demonstration of a device based on such LC μ-cell technology. The results obtained with the tunable photodiode were a first step towards the development of an active device such an electrically-injected LC-based VCSEL, which is indeed based on the TSHEC approach. In the case of a VCSEL, particular attention has been paid on the choice of the active region to be integrated on the device. To efficiently exploit the large optical tuning of LCs and obtain a broad emission, the gain curve of the active medium should be enough in amplitude and

wideness to be used in a tunable VCSEL, together with being linearly polarized, in order to match with the extraordinary axis of the LCs. We thus presented the advantages of QDH-based gain media, which are characterized by a stable and linear state of polarization aligned along the [1-10] crystallographic axis, together with a weaker thermal dependence and a wider emission spectrum with respect to SQW-based active region. A comparative study on InAs QDH and InGaAsP SQW active regions on SOA and edge-emitting lasers structures allowed confirming the broad emission of QDHs with respect to SQWs. However, the study indicated that, to compensate for the smaller volume of active material of QDHs with respect to that of SQWs, a higher number of QDH layers should be integrated in the active region of devices. This must be taken into account during the growth of the active region of the devices.

The basic blocks developed for the LC-based PD have been the starting point for the technological development of a LC-based VCSEL. A first prototype based on a simplified optically-pumped architecture integrating conventional quantum wells has been realized by using the TSHEC process and the LC  $\mu$ -cell technology. Experiments are currently on going with some encouraging results with these LC-OP-VCSELs. Long term perspectives of development may include the possibility to merge the TSHEC and the LC  $\mu$ -cell approaches to couple different optical functionalities (tunable active and passive devices) within the same chip, while keeping low costs and a relatively high level of integration.

On the other hand, preliminary tests showed that the current LC  $\mu$ -cell technology is not suited to be transferred to the case of long-cavity VECSELs, due to the presence of ITO contacts used to drive the LCs. An approach involving a doped InP substrate to realize the top LC electrode might represent a viable alternative to solve the issue and is currently under study.

In *Chapter 4* we introduced the peculiarities of VCSEL devices in external cavity configuration (VECSELs). After having detailed the key elements composing the VECSEL cavity and the advantages arising from long cavity architecture, we presented a state-of-the-art of their development with respect to the main material systems (GaAs, InP and GaSb), for what concerns the SQW-based and the QD-based VECSELs. In the last part we discussed the choice that we adopted to design the optically-pumped QDH-based VECSEL, which has been the subject of the following chapter.

As anticipated, *Chapter 5* deals with the description of the main steps of realization of a QDH-based VECSEL emitting around 1.6  $\mu\text{m}$ , together with its characterization in multi-mode operation as well as low-noise Class-A single-frequency emitter. The VECSEL chip consists in an active region integrating 18 InAs quantum dash layers arranged in 3 sets of 6 layers each, and a monolithically grown 17 pairs GaAs/AlGaAs DBR completed by a gold layer and a diamond heat-spreader. Despite the failure of preliminary lasing tests, which were most probably due to the relatively high thermal impedance of the structure (measured to be  $R_{th} \sim 123 \text{ K/W}$ ) which was the origin of a temperature-induced mismatch

## *Conclusions and perspectives*

between the emission of the active region and the micro-cavity resonance, we managed to get laser operation of the device by the help of a deposited SiN<sub>x</sub> anti-reflection coating on top of the device. In such conditions, the OP-QDH-VECSEL was able to reach a maximum output power of 163 mW at 20°C in multi-mode operation in a 12 mm-long cavity. In single-frequency operation, the QDH-VECSEL wavelength was tunable across 32 nm (from 1601.8 nm to 1633.8 nm), with an average emitted power in the 1-10 mW range, in a 49-mm long cavity. On the same cavity configuration, Class-A operation was demonstrated. In these conditions, we also estimated the laser linewidth in free-running operation to be around 5 kHz. This value of the laser linewidth will be confirmed with the QDH-VECSEL injected on a high-finesse ULE cavity, employing a Pound-Drever-Hall servo-lock scheme. Benefits deriving from the implementation of a finely-tunable mechanism based on LC  $\mu$ -cells would have important consequences for the scientific community. As mentioned, a different approach which is adapted to the case of long-cavity VECSEL is currently under investigation. If implemented, such a LC-QDH-VECSEL would be a good candidate to be integrated on spectroscopy systems based on laser frequency locking on gas absorption lines.

The preliminary results obtained on low-noise single-frequency OP-QDH-VECSEL should be completed by the investigation of such device in dual-frequency operation. With such a purpose **Chapter 6** was devoted to present the design and realization of an advanced experimental setup intended to directly investigate the Lamb coupling constant  $C$  of a dual-frequency VECSELS in a high-coupled regime, with two simultaneously oscillating orthogonally-polarized eigenmodes sharing the same VECSEL cavity. Since the performance of the QDH-VECSEL available at the moment of the experiences were not sufficient to operate in dual-frequency regime, the approach has been validated with a SQW-VECSEL emitting around 1540 nm.

Due to a mismatch of the gain of the two eigenmodes, a careful balance of the optical losses of was required to obtaining a stable simultaneous lasing of the two orthogonally-polarized modes. This is a first indication that the coupling between orthogonally-polarized eigenmodes in a SQW-based active medium is strong. Direct measurements confirmed such a prediction as we experimentally demonstrated that the average value of the Lamb coupling constant  $C$  is equal to  $C = 0.843 \pm 0.012$  for different wavelength difference  $\Delta\lambda$  between the two orthogonally-polarized eigenmodes in the range  $\Delta\lambda = 2$  to 9.8 nm. This high value explains why achieving a stable dual-frequency operation in SQW-VECSELS is challenging.

In the near future, the setup would allow performing such experiments in dual-frequency QDH- or QD-VECSELS, in order to investigate if the inhomogeneous broadening of nanostructured active regions has an impact on the coupling between the two eigenmodes of a dual-frequency VECSEL, as very recently suggested and theoretically discussed by Chusseau et al. [[Chusseau2018](#)]. In this perspective, the stability of dual-frequency VECSELS might be increased



using such a different gain medium, like for instance a QD-based one, and a stable dual-frequency emission without the need of a spatial separation between the eigenmodes would finally permits a true development of electrically-injected dual-frequency VECSELs, which has been prohibitive until now because a separation of the modes implies the use of large pumping areas, which makes the electrical injection of the device unfeasible. This would finally pave the way to the development of compact ultra-stable dual-frequency source, with undoubted advantages for the scientific community.



## ***Appendix A***

***Gaussian beam waist calculation  
based on the ABCD matrices method  
in resonant laser cavities***

### Ray transfer matrices of simple optical elements

The calculation of the cavity waists (Gaussian TEM<sub>00</sub> mode) on the semiconductor chip surface  $\omega_0$  and on the output coupler  $\omega_{OC}$  has been performed by a MATLAB<sup>®</sup> code based on the ABCD matrices method [Kogelnik1965, Kogelnik1966, Siegman1986].

Let's consider a laser cavity with different optical elements inside it. A propagating optical ray inside the cavity can be described by two quantities, the displacement  $x$  from the cavity axis, and its slope  $x'$  with respect to that axis (Fig. A.1a). In the paraxial approximation, each element<sup>1</sup> met by the ray during its propagation can be described by a  $4 \times 4$  ABCD transfer matrix

$$\begin{bmatrix} x_{out} \\ x'_{out} \end{bmatrix} = \underbrace{\begin{bmatrix} A & B \\ C & D \end{bmatrix}}_M \begin{bmatrix} x_{in} \\ x'_{in} \end{bmatrix} \quad (\text{A.1})$$

which relates the output quantities  $(x_{out}, x'_{out})$  with respect to their inputs quantities  $(x_{in}, x'_{in})$  (Fig. A.1b).

Owing to the linearity of the problem, we can simply compute the output quantities with respect to the inputs quantities after  $N$  transformations (i.e. after  $N$  elements), by simply considering the cascade of all the optical elements met by the ray along its path, as represented in Fig. A.1c.

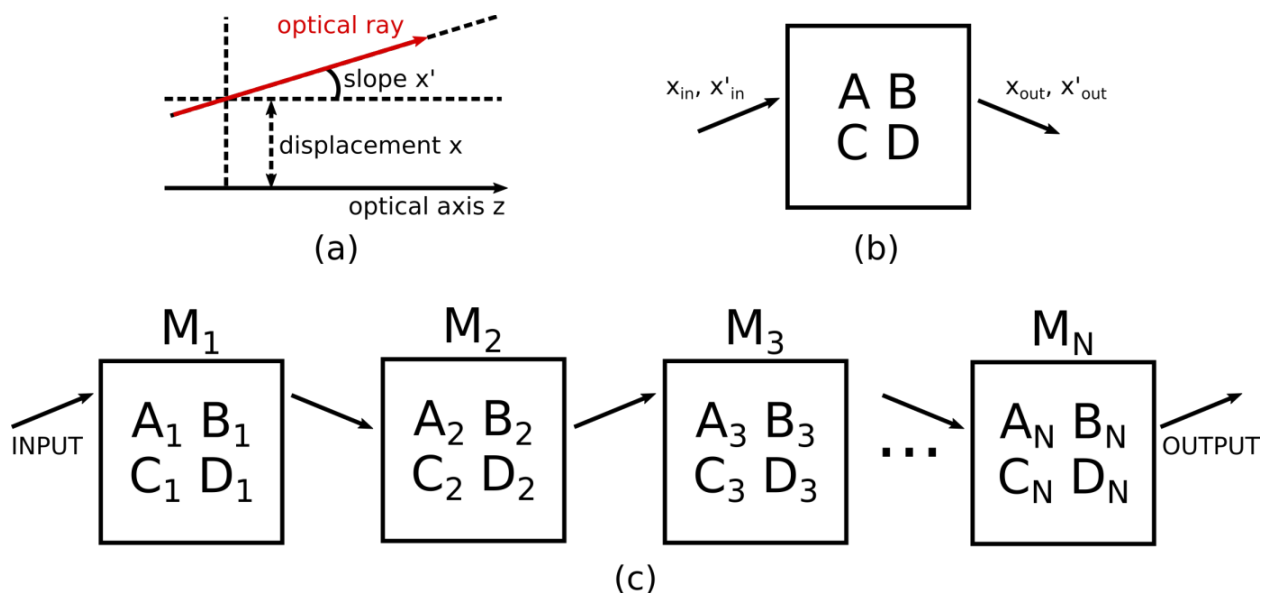


Fig. A.1 – Propagation of optical rays in the paraxial approximation: (a) optical ray quantities, (b) ray transformation after an ABCD matrix describing an optical element and (c) cascade of  $N$  optical elements.

<sup>1</sup> The propagation of the ray across an optical medium with whatever refractive index  $n$  is described with a ABCD matrix as well.

In this case the total ABCD matrix  $M_{tot}$  of the complete transformation chain is given by the multiplication of the single ABCD matrix  $M_i$  of the  $i^{th}$  element

$$M_{tot} = M_N \cdots M_3 M_2 M_1 = \begin{bmatrix} A_{tot} & B_{tot} \\ C_{tot} & D_{tot} \end{bmatrix} \quad (\text{A.2})$$

Fig. A.2 shows the ray transfer matrices of the elementary optical systems used in in calculations.

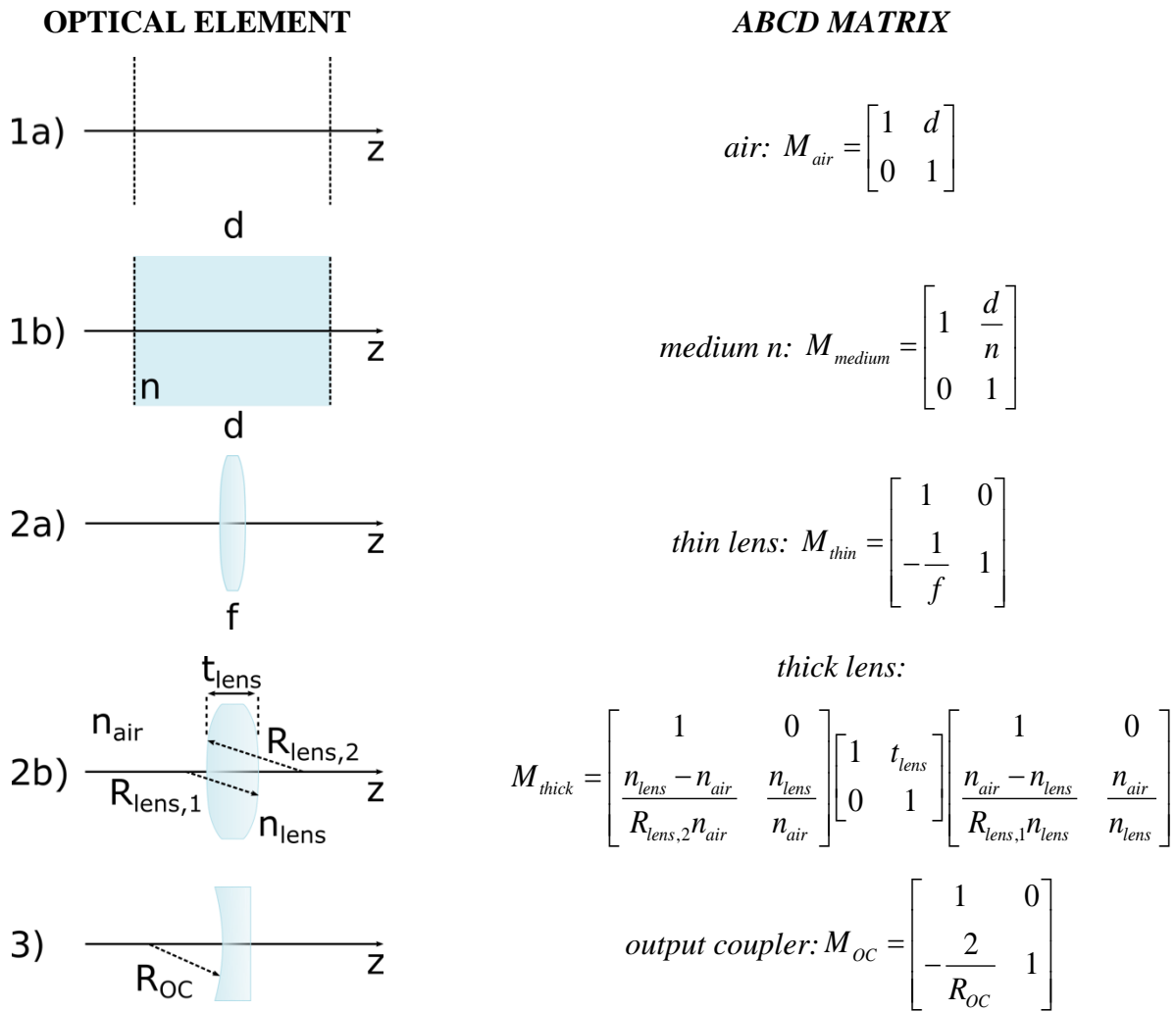


Fig. A.2 – Ray transfer matrices of elementary optical systems.

The waists on the semiconductor chip  $\omega_0$  and on the output coupler  $\omega_{oc}$  can be computed by considering the complex radius  $q(z)$ , which is defined as

$$\frac{1}{q(z)} = \frac{1}{r(z)} - j \frac{\lambda}{\pi \omega^2(z)} \quad (\text{A.3})$$

Appendix A

where  $r(z)$  is the radius of curvature and  $\omega(z)$  the spot size of the Gaussian beam inside the cavity (either  $\omega_0$  or  $\omega_{OC}$ ).

After N optical elements, the complex radius  $q_{in}(z)$  is transformed to

$$q_{out} = \frac{A_{tot}q_{in} + B_{tot}}{C_{tot}q_{in} + D_{tot}} \quad (\text{A.4})$$

In the case of a laser cavity, the stability condition imposes that  $q_{out} = q_{in}$  after a cavity round trip, so that from Eq. A.4 we get

$$q = \frac{-(D_{tot} - A_{tot}) - \sqrt{(D_{tot} - A_{tot})^2 + 4B_{tot}C_{tot}}}{2C_{tot}} \quad (\text{A.5})$$

The Gaussian spot sizes is therefore obtained from Eq. A.3 as

$$\omega = -\sqrt{\frac{\lambda}{\pi \text{Im}(q)}} \quad (\text{A.6})$$

The computed spot size, either on the semiconductor chip surface  $\omega_0$  or the output coupler  $\omega_{OC}$ , depends on the order of multiplication of the matrices, i.e. either we move left→right→left (Fig. A.3a) or right→left→right (Fig. A.3b) with respect to the cavity axis  $z$ .

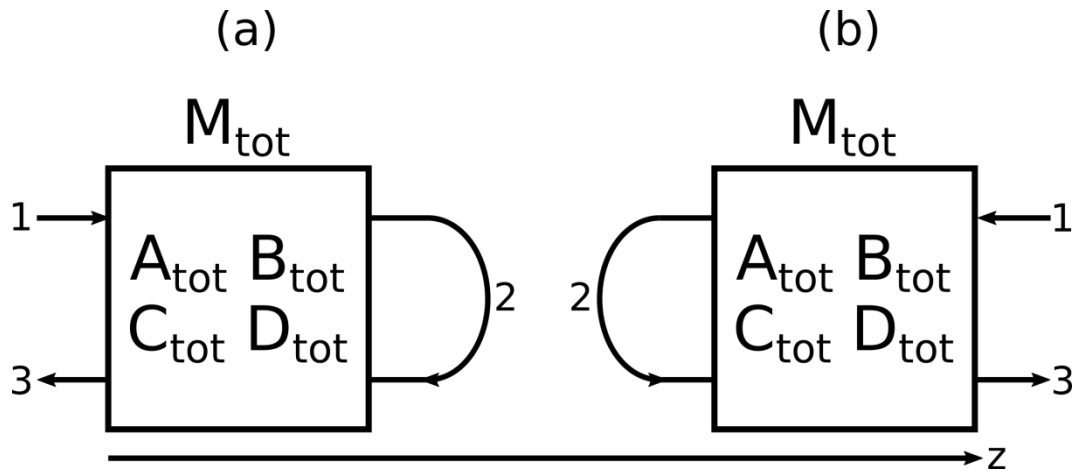


Fig. A.3 – Computation of the spot size on the semiconductor chip surface  $\omega_0$  (left-right-left) or on the output coupler  $\omega_{oc}$  (right-left-right), with respect to the cavity axis  $z$ .

## ***Appendix B***

### ***Modeling heat transfer in V(E)CSELs***



## Heat transfer modeling in V(E)CSELs

Because of its complexity, heat flow in V(E)CSELs cannot be solved in an analytical way. Also, due to the dimensions involved in the problem, numerical approaches must be precisely selected to limit the computational cost. In this particular case, finite element modeling (FEM) software such as COMSOL Multiphysics® or FEMLAB® can be employed to solve the heat transport equation [Pryor2015]. Generally, the structure of a VECSEL is such that the sub-mount dimensions are in the millimeter scale, whereas the pumped area is of the order of tens or hundreds of micrometers and the active region and the mirror layers in the sub-micrometric scale. In the case of VCSELs, pumped areas are sensibly smaller, typically ranging in the tens of micrometers scale, and no diamond heat-spreaders are generally used. Anyway, from a practical point of view, the strategies of simulation that applied for VECSEL still apply for VCSELs. Such a disparity of dimensions imposes a trade-off between a fine analysis of the heat flow, especially in the thinner parts composing the structure (typically the active region and the DBR) and a suitable computational time. To overcome this issue, some reasonable approximations are generally used.

Because of the particular geometry of vertical-cavity lasers, the problem can be simplified in a 2-dimensional one, by considering a circular symmetry with the three cylindrical coordinates ( $r$ ,  $\varphi$ ,  $z$ ) and a rotational axis passing through the center of the device (see Fig. B.1, next page)<sup>1</sup>. In such a case, the heat transfer equation is written as follows [Comsol]

$$\underbrace{\rho C_p \frac{\partial T}{\partial t}}_{\text{transient}} + \underbrace{\rho C_p u \cdot \nabla T}_{\text{convection}} = \underbrace{\nabla \cdot (k_t \nabla T)}_{\text{diffusion}} + \underbrace{Q_s}_{\text{source}} \quad (\text{B.1})$$

where:

- $\rho$  is the mass density;
- $C_p$  is the heat capacity at constant pressure;
- $T$  is the absolute temperature;
- $u$  is the fluid velocity vector;
- $k_t$  is the thermal conductivity;
- $Q_s$  is the heat source.

---

<sup>1</sup> We note that, in the case of the VCSEL devices investigated in this work, the model depicted in Fig. B.1 may be slightly different: the structure is completed by a top DBR, the bottom DBR may be limited in the lateral dimension and the pump area is reduced according to the dimensions of the bottom DBR. The material composition of the DBRs may also be different and no heat-spreader is typically used.

The problem can be further simplified by considering a steady state condition and no fluid flow occurring in solids (i.e. pure conductive phenomena are assumed). So that, eq. B.1 further simplifies in

$$0 = \nabla \cdot (k_t \nabla T) + Q_s \quad (\text{B.2})$$

where only the terms related to diffusion and heat source have survived.

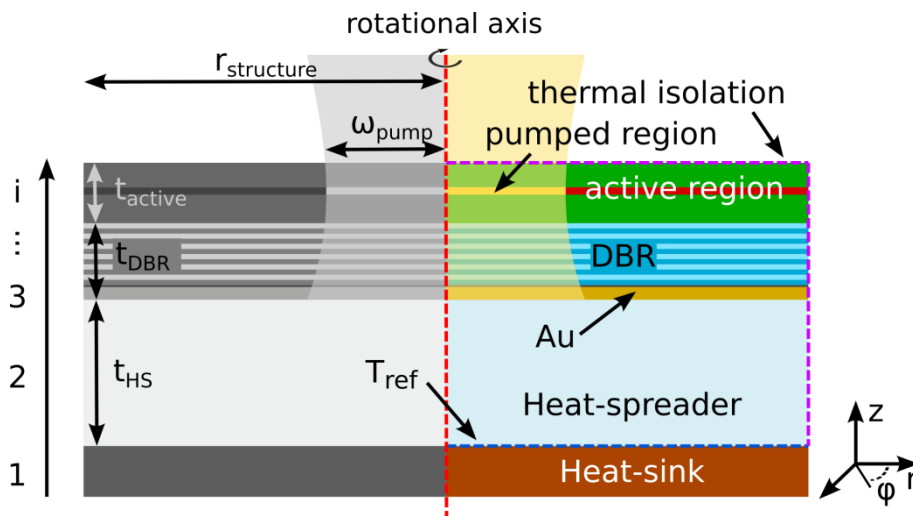


Fig. B.1 – Example of 2D axisymmetric thermal model of an OP-VECSEL. The yellow part in the active region is the pumped area (heat source), whereas the left grayed part is the specular part and it is neglected in the model. Dashed lines are the structure boundaries (red=rotational axis, blue=fixed (Peltier) temperature, violet=thermal isolation). The layers composing the structure are numbered in ascending order from the bottom to the top.

The domains' boundaries are carefully selected as well. The temperature of the blue dashed interface in Fig. B.1 between the heat-spreader and the heat-sink is set to the reference value  $T_{ref}$ , which is fixed by the Peltier module. The upper and the lateral edges of the chip are considered to be thermally insulated (air convection phenomena are neglected, i.e. no heat flow across the top and lateral boundaries), whereas in the radial direction symmetric boundary conditions are set. On the other hand, all the internal interfaces are considered to be perfectly conductive in a first approximation (a more rigorous model should take into account the thermal impedance of the interfaces). Finally, to further improve the computational efficiency, the radius of the device  $r_{structure}$  is kept relatively small, on the order of few hundreds of micrometers), depending on the pump spot dimensions. The lateral dimension of the simulated devices are indeed set to be large enough to ensure that at the lateral edges the temperature is the one imposed by the Peltier cell (i.e. the reference value).

## Appendix B

To properly solve Eq. B.2 and have useful information about the thermal impedance of the device, the thermal properties of the materials, in terms of thermal conductivity  $k_t$ , (+ mass density  $\rho$  and heat capacity  $C_p$  if transient simulations are made) must be known. Table B.1 summarizes all the material parameters (at  $T = 300$  K) used in simulations. Concerning the values of the thermal conductivity, most of them have been found in literature or in the software databases<sup>2</sup>, whereas some others have been measured at the lab using the  $3\omega$  method [Cahill1990] (these are indicated with a \*). This has been necessary since a significant uncertainty exists for the amorphous dielectric materials used in the H-DBR, such as a-Si and a-SiN<sub>x</sub>, or the quaternary alloys InGaAsP composing the active region. Moreover, the software allows taking into account the temperature dependence of these parameters during simulations, improving the reliability of the final result.

**Table B.1 – Room temperature (300 K) material parameters used in thermal simulations.**

Material	$k_t$ [W/m-K]	$\rho$ [Kg/m <sup>3</sup> ]	$C_p$ [J/Kg-K]
a-Si *	2.6	2330	703
a-SiN <sub>x</sub> *	1	3100	350
SiO <sub>2</sub>	1.4	2200	730
TiO <sub>2</sub>	8.5	4249	502
crystalline Si	130	2329	700
GaAs	53	5316	330
Al(Ga)As	84	3810	450
InP	68	4810	310
InGaAsP *	3.5	5000	330
AuIn <sub>2</sub>	162	11300	250
Au	317	19300	130
Cu	400	8700	385
Ti	7.5	4940	710
Ni	60.7	888	460
Al	210	2699	900
AuIn <sub>2</sub>	162	10271	250
ITO	5	6800	-
BCB	0.29	1050	2180
E7 liquid crystal	0.16	1700	2000
SU-8	0.2	1214	1200
silica glass	1.38	2203	703
synthetic Al <sub>2</sub> O <sub>3</sub> (sapphire)	44	398	761
SiC	490	3216	690
synthetic diamond	2000	3200	508

\* thermal conductivity experimentally measured with the  $3\omega$  method at the lab.

<sup>2</sup> For instance, the COMSOL Multiphysics<sup>®</sup> Material Library, MatWeb and the Ioffe Physical-Technical Institute materials databases [Matweb, Ioffe].

Since the layers composing the active region show similar thermal properties, they can be grouped together. In such a way the QWs (or QDHs/QDs) and the absorbing layers are considered to be the heat sources. Again, this allows reducing the computational complexity of the simulations, otherwise too demanding due the high number of layers composing the active region. Conversely, for the Bragg reflector, a distinction must be made. In the case of dielectric-metallic H-DBRs, due to the small number of a-Si/a-SiN<sub>x</sub> layers composing the mirror (3.5 pairs), they have been individually considered. For more complex reflectors involving a higher number of layers (such as InP/InGaAsP- or GaAs/Al(Ga)As-based H-DBRs), they have been grouped together to form a homogeneous layer with a total thickness equal to the sum of each individual layer's thickness, in order to reduce the computational cost. In this latter case, the average thermal conductivity has been considered to be different in the lateral ( $k_{t,L}$ ) and vertical ( $k_{t,V}$ ) directions, according to [Zhao2012, Okhotnikov2010, Lee2009]:

$$k_{t,L} = \frac{\sum_i d_i k_{t,i}}{\sum_i d_i} \quad k_{t,V} = \frac{\sum_i d_i}{\sum_i \frac{d_i}{k_{t,i}}} \quad (\text{B.3a,b})$$

where  $d_i$  and  $k_{t,i}$  are the thickness and the thermal conductivity of the  $i$ -th layer composing the DBR, respectively. The values used in simulation are listed in the following Table B.2 (the 500 nm-thick Au layer is considered separately).

**Table B.2 – Parameters of the multi-stacked InP-based and GaAs-based DBRs used in simulations\*.**

DBR composition	Thickness [ $\mu\text{m}$ ]	$k_{t,L}$ [W/m-K]	$k_{t,V}$ [W/m-K]	$\rho$ [Kg/m <sup>3</sup> ]	$C_p$ [J/Kg-K]
×48 InP/InGaAsP	11.904	36.5	6.8	4905	320
×15 (×17.5) GaAs/Al(Ga)As	4.032 (4.588)	68.9	65.3	4508	394

\* here, DBRs have been designed at 1600 nm. For the 1.55  $\mu\text{m}$ -emitting devices, the thickness of the DBR have been changed accordingly.

Conversely, in the case of the a-Si/a-SiN<sub>x</sub> stack, the thermal conductivity of each layer has been considered to be isotropic, since amorphous materials present the same properties in any direction. Moreover, due to the fact that the complexity of the problem rapidly increases with the number of elements (or subdomains), a standard mesh has been used during simulations, except at the boundaries (i.e. the interfaces between the layers) and in the area defined by the pump spot, where a finer mesh has been considered.

## Appendix B

As mentioned before, the pump laser spot defines the source of thermal heating. The pump absorption, and thus the thermal heat, is considered to be only limited to the active region. In most cases, the pump generally has a Gaussian profile, so that the heat load in the gain region is considered to have the same shape [Kemp2005]. In the simplest case, however, a flat-top heat profile is assumed, so that the heat source is uniformly distributed in the pumped medium along the radial direction. Thus, the (volume) heat load  $Q_{s,i}$  dissipated on the  $i$ -th set is given by

$$Q_{s,i} = \frac{\eta_i P_{diss}}{t_i A_p} \quad (\text{B.4})$$

Here,  $P_{diss}$  is the dissipated pump power (we consider that it is entirely converted into heat),  $\eta_i$  is the heat loading fraction in the  $i$ -th set (in the case of uniform pumping of the sets composing the gain medium, one can assume  $\eta_i = \frac{1}{N_{active}}$ , where  $N_{active}$  is the total number of active sets),  $t_i$  is the thickness of the  $i$ -th set and  $A_p$  is the pump spot area, which for simplicity is assumed to be circular, and related to the pump spot waist  $\omega_{pump}$  at the semiconductor chip surface, as  $A_p = \pi\omega_{pump}^2$ . We can consider  $P_{diss}$  to be equal to the absorbed pump times the quantum defect  $\eta_{def}$ , i.e.

$$P_{diss} = P_{abs}\eta_{def} = P_{abs} \left( 1 - \frac{\lambda_{pump}}{\lambda_{laser}} \right) \quad (\text{B.5})$$

If a more realistic Gaussian radial distribution is assumed for the heat load, eq. B.4 modifies in [Kemp2008]

$$Q_{s,i}(r) = \frac{2\eta_i P_{diss}}{t_i A_p} e^{\left( -2\frac{r^2}{\omega_{pump}^2} \right)} \quad (\text{B.6})$$

Now the dependence of  $Q_{s,i}$  on the radial variable  $r$  is explicit. Eqs. B.4 and B.6 implicitly assume that the heat load is uniformly spread on each set of the active region with respect to the  $z$  direction. To further improve the model, one can eventually take into account the linear (average<sup>3</sup>) absorption  $\alpha_{active}$  in active layers to model the exponential decay of the pump along the vertical direction. In the case of the OP-QDH-VECSEL presented in **Chapter 5**, we estimate  $\alpha_{active} = 19000 \text{ cm}^{-1}$  at the pump

---

<sup>3</sup> In simulations, we consider an average value  $\alpha_{active}$  for each active set of our structures.

wavelength (980 nm), for an active region composed by InGaAsP Q<sub>1.18</sub> quaternary alloy and InAs QDH layers [**Burkhard1982**, **Reid1993**, **Seifert2016**]).

The heat load has now a full dependence on both  $r$  and  $z$  coordinates [**Kemp2005**]:

$$Q_{s,i}(r, z) = \frac{2P_{diss}}{t_i A_p} e^{\left(-2\frac{r^2}{\omega_{pump}^2}\right)} e^{-\alpha_{active}(z_{0,i}-z)} e^{-\sum_j \alpha_j t_j} \quad (\text{B.7})$$

The former exponential is related to the absorption of the  $i$ -th set, while the latter eventually takes into account the absorption of the preceding layers (in our case  $j > i$ , as the pump proceeds from the top to the bottom of the structure). Please note that the heat loading fraction  $\eta_i$  of each  $i$ -th set is no longer useful, as the latter exponential defines the residual power fraction  $P_{diss}$  reaching the  $i$ -th set, after been absorbed by the upper sets.

Slight different but comparable results are obtained according to the different heat load expression which is used in the model, as checked by comparison of the three approaches. From a practical point of view, however, most of times the simple top-heat profile of eq. B.4 can be sufficient to roughly estimate the internal temperature rise  $\Delta T$  of the device under different pumping conditions. Expressions B.4, B.6 and B.7 can be also adapted to model a residual pump absorption in the DBR, by replacing the absorption in the active region  $\alpha_{active}$  with the correspondent value in the DBR,  $\alpha_{DBR}$ . In our case we estimate an effective absorption (mainly related to the GaAs layers) of  $\alpha_{DBR} = 490 \text{ cm}^{-1}$ . This is the average value between the GaAs absorption (around  $1000 \text{ cm}^{-1}$ ) and the AlAs absorption ( $10 \text{ cm}^{-1}$ , negligible), weighted by the thickness of each layer, according to

$$\alpha = \frac{\sum_i \alpha_i t_i}{\sum_i t_i} \quad (\text{B.8})$$

Here the summation is obviously limited to the layers composing the DBR.

From the knowledge of the temperature rise  $\Delta T$  inside the structure it is also possible to estimate the (maximum) thermal resistance of the structure, such as [**Lee2009**, **Zhao2012**]

$$R_{th} = \frac{\Delta T}{P_{diss}} \quad (\text{B.9})$$

The temperature rise  $\Delta T$  is the difference between the maximum temperature  $T_{max}$  localized in the active region and the temperature  $T_{ref}$  of the heat-sink, which is imposed by the Peltier cell (generally set to 289.6 K in simulations).

### Model validation

To validate the approach, the structure presented by Tourennc et al. [Tourennc2008] has been simulated by the proposed model and the results have been compared. The tested device is an OP-VECSEL integrating a 2.5 pairs hybrid PECVD-grade a-Si/a-SiN<sub>x</sub>/Au mirror on a 70  $\mu\text{m}$ -thick silicon carbide (SiC) substrate using AuIn<sub>2</sub> eutectic bonding, as sketched in Fig. B.2a.

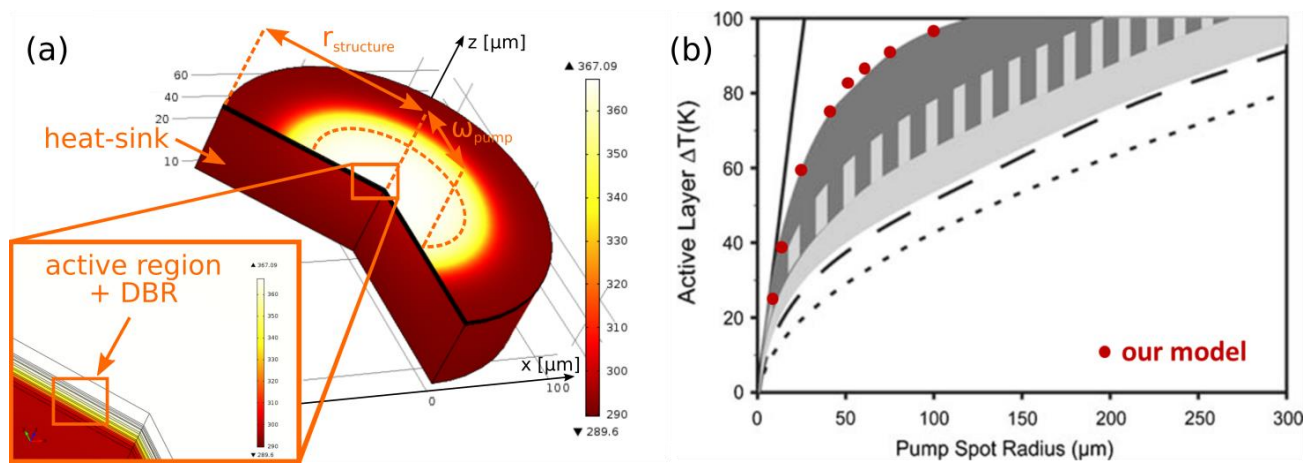


Fig. B.2 – Comparison between our model and the one presented by Tourennc et al. (reprinted from [Tourennc2008] with permission of Springer Nature): (a) simulated OP-VECSEL structure (in this case  $\omega_{pump} = 40 \mu\text{m}$ ,  $r_{structure} = 100 \mu\text{m}$  and  $P_{abs} = 500 \text{ mW}$ ), (b) result comparison.

The temperature rise in the active region is calculated as a function of the pump spot radius, for a fixed absorbed pump power density of  $10 \text{ kW/cm}^2$ . Fig. B.2b shows the comparison with the method presented in this work and the one used by [Tourennc2008] (dark gray area). The results of thermal simulations reveal a good agreement between the two approaches. The small deviations can be related to the difference in the active region composition (in the reference, the QWs are based on InGaAlAs, which has a slightly higher thermal conductivity with respect to InGaAsP, namely  $4.5 \text{ W/m-K}$ ) and to the values of thermal properties of the PECVD dielectric materials used for the hybrid mirror, which slightly differ with respect to their sputtered counterpart. The extension of the dark gray area represents the uncertainty in the temperature rise related to the minimum and maximum values of the thermal conductivity  $k_t$  of a-Si and a-SiN<sub>x</sub>, as pointed out in the article. In our model we have chosen the lower value of the thermal conductivity of the two materials (2.6 and

1 W/m-K, respectively). The other curves of Fig. B.2b (light gray area, long dashes and dots) are related to different VECSEL architectures.

These results show the potentialities of thermal simulations in predicting the increase of the temperature in the active region of a V(E)CSEL during the standard operation. The agreement of the results with respect to experimental measurements and previous scientific works is a clear validation of the approach here presented. In this context, FEM simulations can be useful to test different strategies for thermal management in OP-V(E)CSELs, and then select the best solution which minimizes the thermal budget, in order to prevent (or drastically limit) the effects of the overheating during the laser operation of the device.





## ***Appendix C***

### ***Semi-empirical model for OP-VECSELs threshold and output power estimation***

### VECSEL threshold and output characteristic modeling

In this appendix we will present a simple semi-empirical model that allows estimating the pump threshold and the laser output characteristic of a VECSEL in the continuous wave regime, as a function of several parameters. Some of them are related to the particular material composing the active region (i.e. material gain, recombination coefficients, emission wavelength, etc.), others are relative to the chip design (DBR reflectivity, number of active layers and their thickness, longitudinal confinement factor, etc.) or cavity setup (output coupler reflectivity, pump wavelength and incident power) and so on. The following model is based on the works of [Kuznetsov1999] and [Symonds2003] (see also [Okhotnikov2010]) and has been modified and adapted for the study of InP-based OP-VECSELs presented in this work.

Here, for the material gain  $g_{mat}$  we consider a phenomenological logarithmic dependence from the material gain parameter  $g_0$ , the carrier density  $N$  on the active layers and the transparency carrier density  $N_0$ , such that:

$$g_{mat} = g_0 \ln\left(\frac{N}{N_0}\right) \quad (C.1)$$

At threshold, the gain is equal to the losses and the following condition must hold

$$T_{loss} R_{OC} R_{eff} e^{(2\Gamma g_{th} N_{active} L_{active})} = 1 \quad (C.2)$$

Here  $T_{loss}$  takes into account the round trip losses inside the cavity,  $\Gamma = \Gamma_{xy} \Gamma_z \approx \Gamma_z$  is the confinement factor,  $g_{th}$  the material gain at threshold,  $N_{active}$  the number of the active layers inside the cavity,  $L_{active}$  the thickness of a single active layer,  $R_{OC}$  and  $R_{eff}$  are the output coupler reflectivity and the effective reflectivity of the semiconductor chip, respectively. This last one depends on the particular cavity configuration which has been designed (either resonant or anti-resonant) and it can be calculated by considering that the sub-cavity acts like a Fabry-Perot filter, so that

$$R_{eff} = \frac{(r_{struct} - r_{surface})^2 + 4r_{struct}r_{surface} \sin^2(\varphi)}{(1 - r_{struct}r_{surface})^2 + 4r_{struct}r_{surface} \sin^2(\varphi)} \quad (C.3)$$

where  $\varphi$  is the dephasing associated to the impinging wave (in this context is considered to be zero), and  $r_{struct}$  and  $r_{surface}$  are the semiconductor structure and the chip surface reflectivity, respectively.

The reflectivity of the structure (composed by the DBR and the active region forming the 1/2-VCSEL) takes into account both the effects of the micro-cavity and the DBR, and can be expressed as

$$r_{struct} = \sqrt{R_{struct}} = \sqrt{R_{DBR} e^{(2i\varphi)}} \quad (C.4)$$

When no anti-reflection coating is deposited on top of the chip surface,  $r_{surface}$  is given by the Fresnel relation (in this case, for simplicity at normal incidence):

$$r_{surface} = \sqrt{R_{surface}} = \sqrt{\frac{(n_{air} - n_{semiconductor})^2}{(n_{air} + n_{semiconductor})^2}} \quad (C.5)$$

whereas it is set to zero in the case of a structure with an anti-reflection coating. Fig. C.1 describes the reflectivity of the different sections involved in the computation.

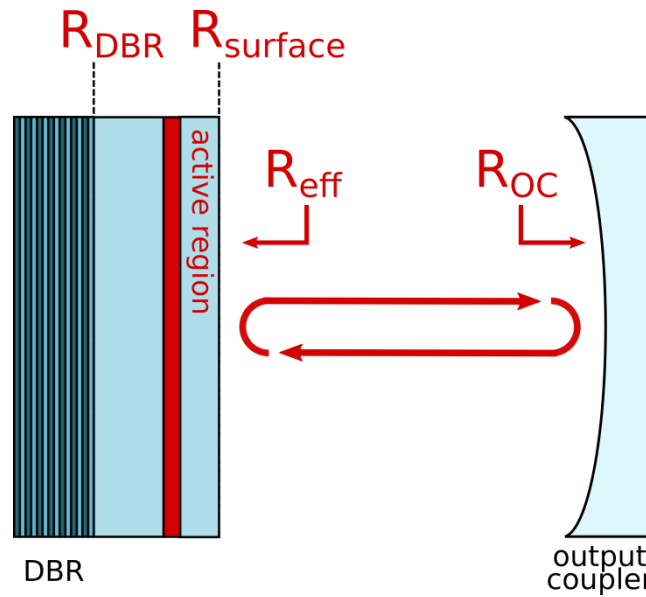


*Fig. C.1 – Definition of VECSEL reflectivities used in the model.*

To calculate the laser threshold, we need to compute the carrier density at threshold, which is given by the following relationship

$$N_{th} = N_0 \left( R_{OC} R_{eff} \right)^{-(2\Gamma_{gth} N_{active} L_{active})^{-1}} \quad (C.6)$$

## Appendix C

So that

$$P_{th} = N_{th} \frac{h\nu_{pump} N_{active} L_{active} A_{pump}}{\eta_{abs} \tau(N_{th})} \quad (C.7)$$

Where  $h$  is the Planck constant,  $\nu_{pump}$  is the pump frequency,  $A_{pump}$  is the pump spot area,  $\eta_{abs}$  the absorption efficiency of the semiconductor structure and  $\tau$  is the carrier lifetime, which depends on the carrier density  $N$  and is given by

$$\tau(N) = \frac{1}{A + BN + CN^2} \quad (C.8)$$

$A$ ,  $B$  and  $C$  being the Shockley-Read-Hall monomolecular, the radiative bimolecular and the Auger recombination coefficients, respectively. Below threshold, the carrier lifetime is computed by using the carrier density given by the following formula

$$N = \frac{\eta_{abs} P_{inc}}{h\nu_{pump} (N_{active} L_{active} A_{pump})} \tau(N) \quad (C.9)$$

where  $P_{inc}$  is the incident pump power on the VECSEL chip. This relationship is replaced by Eq. C.6 when the threshold condition is reached. To finally calculate the output characteristic, we need to further introduce the differential efficiency  $\eta_{diff}$ , which is defined as

$$\eta_{diff} = \eta_{out} \eta_{quant} \eta_{rad} \eta_{abs} \quad (C.10)$$

The different terms composing the differential efficiency are:

- the output efficiency  $\eta_{out} = \frac{\ln(R_{OC})}{\ln(R_{eff} R_{OC} T_{loss})}$  (C.11a)

- the quantum efficiency  $\eta_{quant} = \frac{\lambda_{pump}}{\lambda_{laser}}$  (C.11b)

- the radiation efficiency  $\eta_{rad} = \frac{BN_{th}}{A + BN_{th} + CN_{th}^2}$  (C.11c)

- the absorption efficiency  $0 \leq \eta_{abs} \leq 1$  (C.11d)

Having defined all these parameters, we can then calculate the output power as

$$P_{out} = \eta_{diff} (P_{inc} - P_{th}) \quad (C.12)$$

In the case one is interested to calculate the output power with respect to the net absorbed pump power, the previous relation can be modified in

$$P_{out} = \eta'_{diff} (P_{abs} - P_{th}) \quad (C.13)$$

where  $\eta'_{diff} = \eta_{diff} \frac{(P_{inc} - P_{th})}{(P_{abs} - P_{th})}$ , while  $P_{abs}$  is calculated as

$$P_{abs} = (P_{inc} - P_{refl}) = P_{inc} [1 - R_s(\lambda_{pump})] \quad (C.14)$$

$R_s$  being now evaluated at the pump wavelength  $\lambda_{pump}$ .

This simple model does not take into account any phenomena related to temperature.



## ***Appendix D***

### ***Electrical schemes of RIN measurement benches***



Low-frequency RIN measurement bench (100 kHz – 500 MHz)

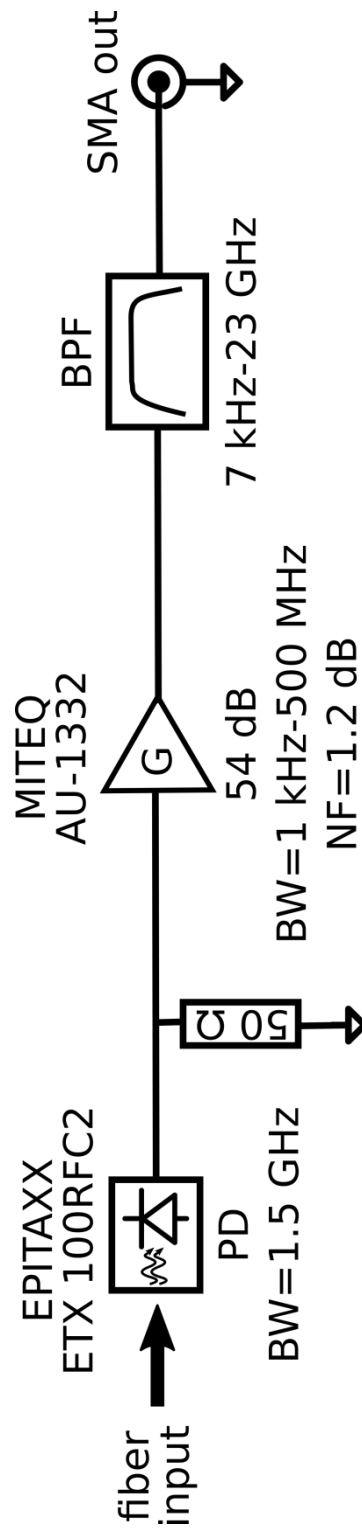


Fig. D.1 - Low-frequency RIN measurement bench in the 100 kHz – 500 MHz frequency range.

High-frequency RIN measurement bench (1 GHz – 18 GHz)

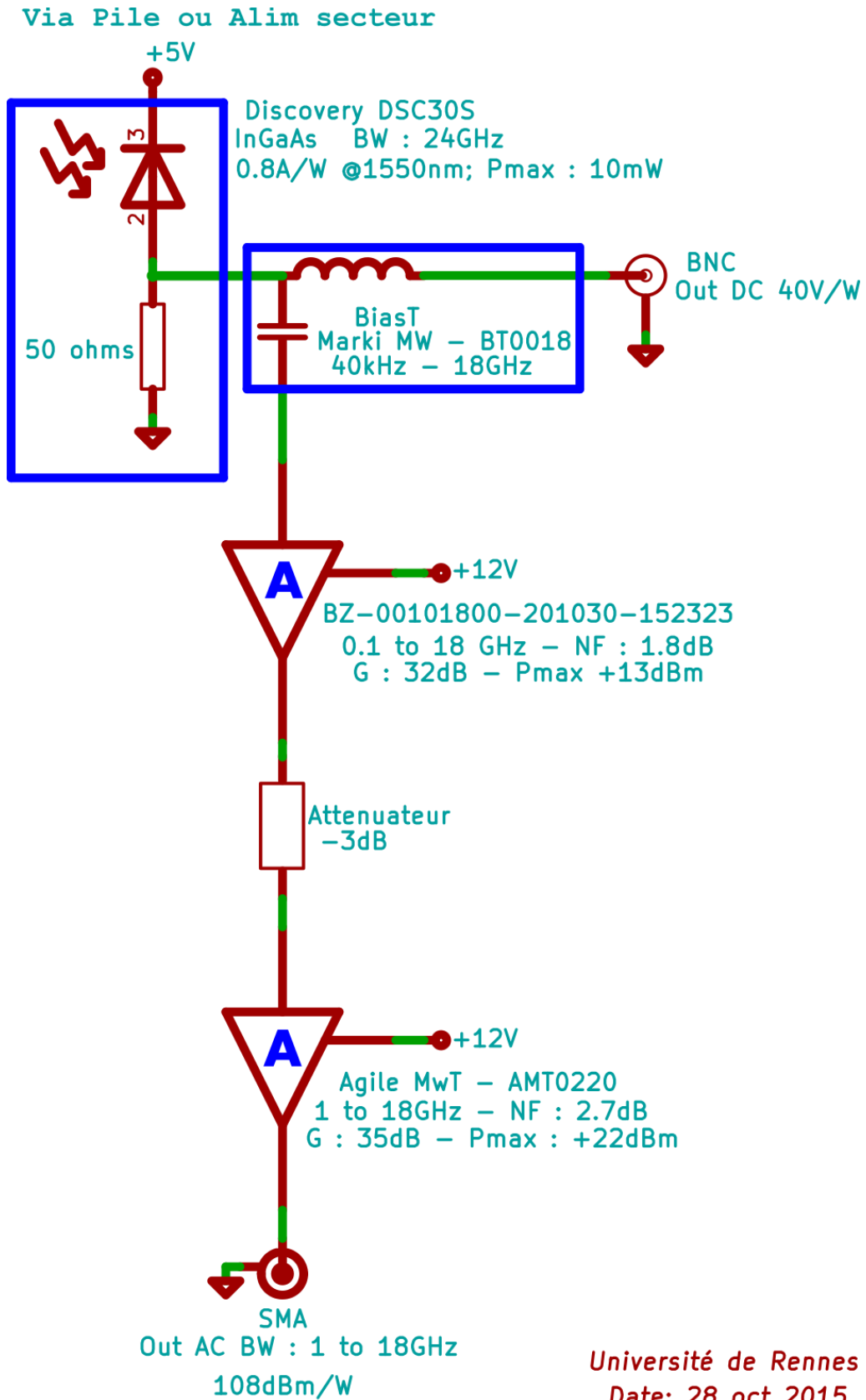


Fig. D.2 - High-frequency RIN measurement bench in the 1 GHz - 18 GHz range frequency range.



# ***Résumé des travaux de thèse***

Ce manuscrit, intitulé “*V(E)CSELS à nanostructures quantiques à 1,55  $\mu\text{m}$  pour les applications à l’optique hyperfréquence et les communications cohérentes*”, présente les résultats obtenus dans le cadre de mes travaux de thèse effectués à l’Institut FOTON, conjointement dans les équipes OHM et DOP. Comme l’intitulé l’indique, ce travaux ont eu comme objectif principal le développement de sources lasers à semi-conducteurs en cavité verticale sur substrat InP, intègrent des régions actives à nanostructure quantiques (plus précisément des bâtonnets quantiques, ou “quantum dashes”, en anglais) et émettent à des longueurs d’onde dites “télécoms”, c’est-à-dire autour de 1550 nm. Les composants investigués dans ce travail sont des dispositifs en cavité micrométrique et monolithique, désignés comme VCSELS (de l’anglais Vertical-Cavity Surface-Emitting Lasers), présentés dans la première partie du manuscrit, et des dispositifs en cavité étendue, ou externe, appelés VECSELS (dont le E signifie External), auxquels la deuxième partie est dédiée. Les applications de ces types de dispositifs sont assez larges, mais dans le cadre des travaux présentés dans ce manuscrit on s’est principalement focalisé sur le développement de ce composants pour des applications aux télécommunications optiques, à la photonique à micro-ondes et aux communications optiques cohérentes.

Le ***Chapitre 1*** présente les caractéristiques de base des lasers semi-conducteurs à cavité verticale, et leurs avantages par rapport à leurs homologues à émission par la tranche. Ce chapitre présente aussi l’état de l’art des VCSELS, la description des briques de base qui composent la cavité résonnante de ces dispositifs et les approches technologiques employés pour obtenir un confinement efficace de porteurs dans ce type de structure, en vue du développement de composants pompés électriquement.

Dans le ***Chapitre 2*** on s’intéresse au problème de la gestion du budget thermique dans les VCSELS, qui représente un des limitations principales pour atteindre des bonnes performances avec ce type de lasers, notamment dans le cas des composants issus de la filière InP, intégrant de

matériaux avec de faibles conductivités thermiques qui limitent la dissipation de la chaleur générée dans leur région active.

En particulier, le point critique pour obtenir une faible impédance thermique est représenté par un bon design du miroir de Bragg inférieur (DBR), essentiellement en termes du choix des matériaux, du nombre de couches et des dimensions latérales, qui permettent de maximiser la dissipation thermique de la chaleur générée dans la zone active. À travers des modèles à éléments finis (FEM), on a étudié différentes approches au problème. Ceux-ci ont permis d'identifier une solution hybride employant des DBRs métal/diélectriques enterrés avec des dimensions latérales optimisées comme étant un bon compromis pour obtenir des bonnes performances thermique, tout en gardant une simple technique de dépôt, compatible avec les procédés technologiques VCSELs développés au laboratoire. La Fig. R.1 montre que le choix des DBRs métal/diélectriques enterrés (BH-DBRs) avec une épaisseur contenue (courbe rouge) présente des avantages notables en terme d'impédance thermique par rapport à des solutions standards qui font recours à des réflecteurs entièrement diélectriques (courbe bleu) ou hybrides avec des larges surfaces (courbe verte). L'étude montre que le recours BH-DBR optimisé est particulièrement efficace si le diamètre du miroir est limité ( $d_{BH-DBR} \leq 20 \mu\text{m}$ ), s'approchant significativement aux performances d'un miroir en GaAs/AlAs, qui représente la référence en termes de performances optiques et thermiques.

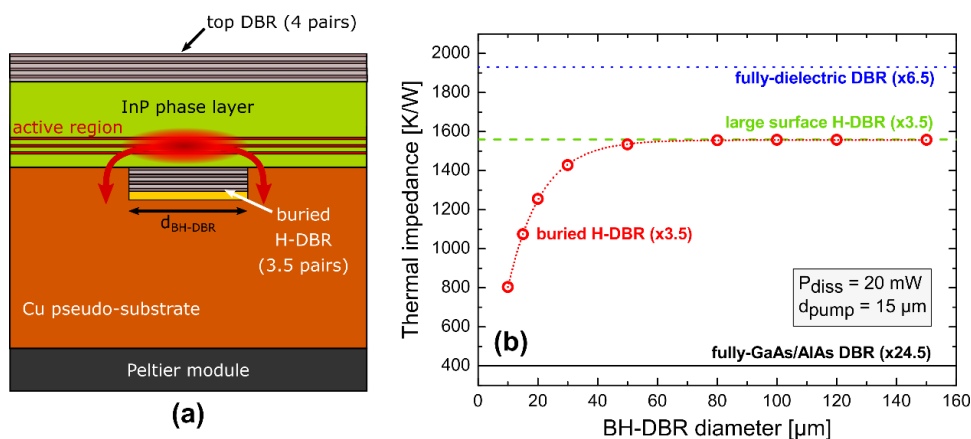


Fig. R.1 – (a) Schéma en section d'un VCSEL intégrant un DBR hybride enterré (BH-DBR) avec 3.5 paires entouré par un pseudo-substrat de cuivre. (b) Résultats de différentes approches étudiés par simulations FEM: calcul de l'impédance thermique en fonction du diamètre du BH-DBR (courbe rouge pointillé) et comparaison avec des solutions employant des DBRs à large surface entièrement diélectrique avec 6.5 paires (courbe bleu pointillé) ou hybrides avec 3.5 paires (courbe vert pointillé). Les miroirs ont été conçus pour avoir une réflectivité de  $R \sim 99.6\%$ .

En parallèle, un nouveau procédé technologique pour la réalisation de VCSELs a été mis au point. Ce procédé, qui a été nommé "Through Silicon Holes Electroplated Copper" (TSHEC), repose sur la technique de collage par résine polymérique BCB (benzocyclobutène). Le BCB est employé pour coller la région active du VCSEL sur un substrat hôte en silicium précédemment structuré pour réaliser de matrices de vias qui sont ensuite remplies par du cuivre déposé avec des techniques de

galvanoplastie, pour enfin former de micro-dissipateurs localisés au niveau de chaque composant. La Fig. R.2a montre le schéma d'un VCSEL en pompage optique émettent à 1.55  $\mu\text{m}$ , obtenu avec cette technique. Le recours conjoint du procédé TSHEC et des BH-DBRs optimisés s'est avéré assez satisfaisant, et il a permis de démontrer de puissance de sortie jusqu'à  $\sim 2.5$  mW (Fig. 2c) avec de seuils lasers si bas que 7 mW (Fig. 2d), dans le cas de VCSEL intègrent une région active à base de 9 puits quantiques InGaAsP.

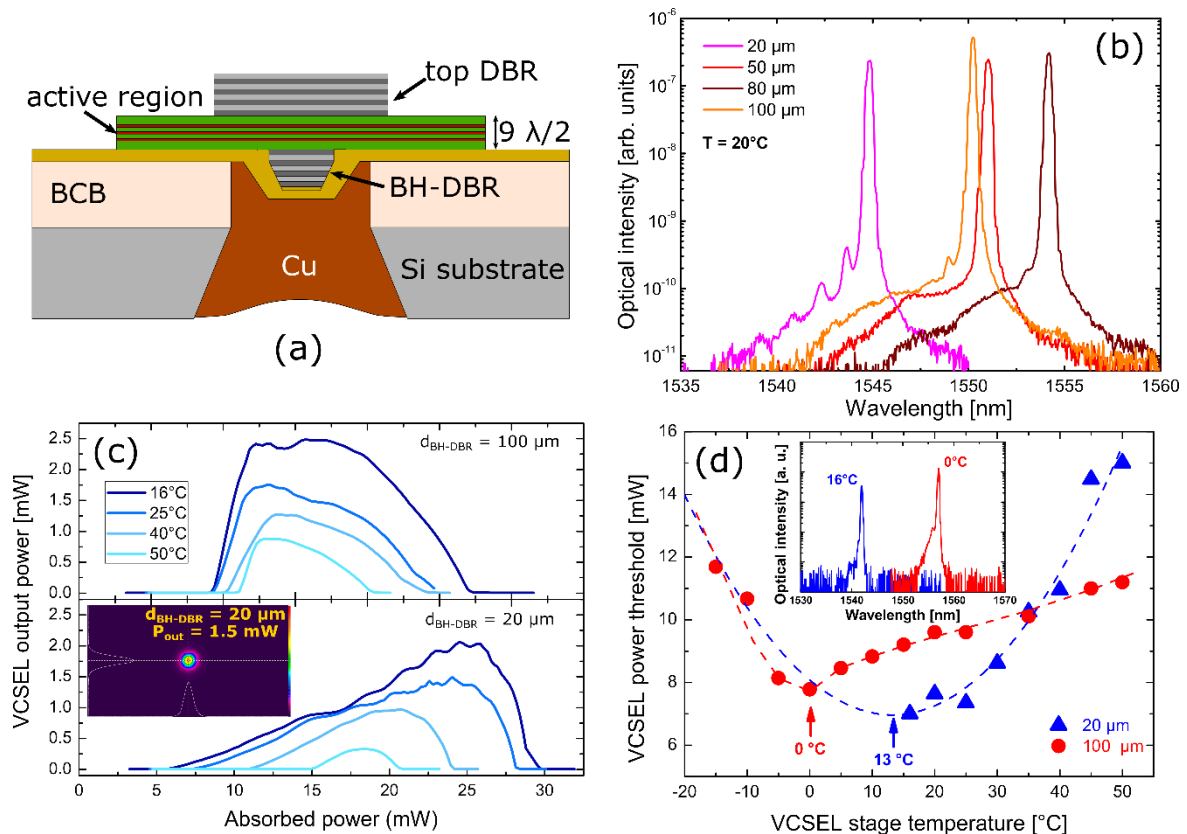


Fig. R.2 – (a) Schéma de dispositifs VCSEL en pompage optique réalisé avec le procédé TSHEC. Caractérisation des composants: (b) spectres d'émission à  $T = 20^\circ\text{C}$ , (c) caractéristique de sortie à différentes températures dans le cas d'un VCSEL intégrant un BH-DBR de 100  $\mu\text{m}$  (haut) ou 20  $\mu\text{m}$  (bas), (d) mesure du seuil laser en fonction de la température dans le cas d'un VCSEL avec BH-DBR de 100  $\mu\text{m}$  (rouge) ou 20  $\mu\text{m}$  (bleu).

Cette approche a aussi permis de démontrer une amélioration nette de l'impédance thermique des composants (-29%), par rapport au cas des VCSELs intégrant des DBR hybrides "plein champ". Cette amélioration est encore plus prononcée (-60%, estimée par simulations FEM) si comparé au cas d'un simple report de la région active sur substrat hôte à l'aide d'un collage par polymère BCB. La dernière partie du chapitre a été consacré à l'optimisation des briques de base pour le développement de VCSELs en pompage électrique basés sur le procédé TSHEC, qui a l'avantage d'être également compatible avec la réalisation de ce type de composant.

On s'est principalement focalisé sur l'optimisation de la jonction tunnel enterré ("Buried Tunnel Junction", ou BTJ, en anglais). A travers de simulations TCAD on a identifié une structure BTJ

basé sur l'alliage ternaire InGaAs en accord de maille sur InP comme possible candidat. Les simulations ont aussi permis d'optimiser le design de la jonction tunnel en ajoutant une couche buffer de quaternaire  $Q_{1.18}$  (InGaAsP avec gap à  $1.18 \mu\text{m}$ ), pour réduire la barrière de potentiel vue par les trous dans le côté p de la jonction et ainsi améliorer le procès d'injection. Ces résultats ont été validés expérimentalement avec de structures BTJ réalisées avec notre bâti d'épitaxie par jets moléculaires à source gazeuse (GS-MBE), qui ont montré de bonnes performances électriques. Cependant, le recours à une BTJ en InGaAs implique une absorption optique relativement élevée à  $1.55 \mu\text{m}$ , qui peut limiter les performances finales des composants VCSELs. Dans l'avenir, une BTJ basée sur des couches quaternaires avec une absorption négligeable à  $1.55 \mu\text{m}$  (comme par exemple le  $Q_{1.4}$ , le  $Q_{1.3}$  ou le  $Q_{1.18}$ ) pourrait s'avérer plus convenable. Cependant, ce type de BTJ nécessite des niveaux de dopage assez élevés ( $N_{a,d} > 10^{19} \text{cm}^{-3}$ ) qui pendant ces travaux de thèse n'étaient pas faciles à atteindre avec le bâti MBE présent au laboratoire (dopage p réalisé avec cellule Béryllium, qui présente des difficultés d'incorporation dans les couches dopées). Pour pallier à cette difficulté, très récemment une cellule Carbone a été installée dans le bâti de croissance, pour permettre une meilleure incorporation des dopants et d'atteindre les niveaux de dopage souhaités. En raison du manque de structures VCSEL dédiées au pompage électrique, le procédé TSHEC a été pu quand même être testé sur des composants électriques tels que des diodes LEDs, basés sur des régions actives à bâtonnets quantiques (QDH) initialement prévues pour la réalisation des lasers à émission par la tranche. Les premières caractérisations avec ces composants ont permis de valider le jeu de masques qui a été conçu pour la réalisation des VCSEL en pompage électrique (Fig. R.3).

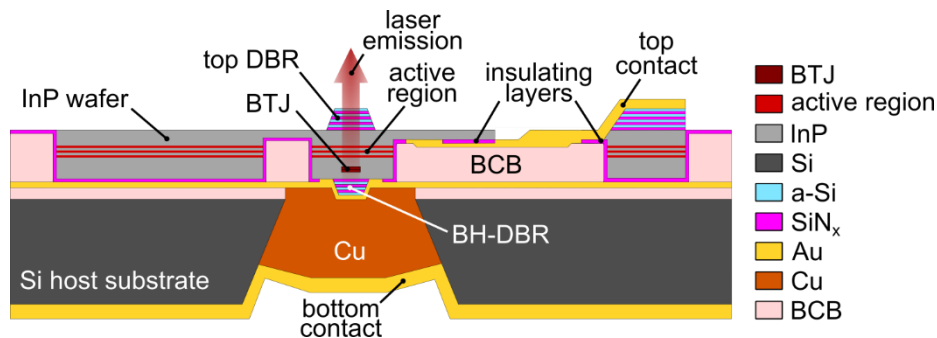


Fig. R.3 – Structure finale envisagée pour le VCSEL en pompage électrique, réalisé avec le procédé TSHEC.

La technologie TSHEC, présenté dans le **Chapitre 2**, a été adaptée pour la réalisation des dispositifs monolithiques accordables en longueur d'onde, comme détaillé dans le **Chapitre 3**. Après avoir introduit les principaux résultats obtenus par la technologie employant des membranes MEMS (de l'anglais Micro-Electrical-Mechanical-Systems), représentant jusqu'au présent la technique d'élection pour la fabrication de dispositifs accordables à cavité verticale, on s'est focalisés sur ses principaux inconvénients. En effet les systèmes MEMS, étant particulièrement

soumis aux fluctuations thermiques et aux vibrations mécaniques externes, présentent des performances spectrales limitées. Pour pallier à cette problématique, nous avons proposé une nouvelle approche originale basée sur l'exploitation des propriétés électro-optiques des cristaux liquides nématiques et sur leur intégration dans de  $\mu$ -cellules au sein de la cavité résonnante des composants à cavité verticale, permettant la réalisation de dispositifs monolithiques accordables, avec un coût contenu et une faible consommation d'énergie.

Une première preuve de concept a été validée par la réalisation d'une photodiode p-i-n accordable sur InP (Fig. R.4), basée sur la dite technologie et fonctionnant autour de 1.55  $\mu\text{m}$ , qui a présenté des performances très satisfaisantes, résumés dans le Tableau R.1. Ces résultats prometteurs, obtenus dans le cadre du projet ANR-ASTRID HYPOCAMP, sont issues de la collaboration entre l'Institut FOTON, le LAAS (Toulouse), l'IMT Atlantique (Brest), and le C2N (Marcoussis).

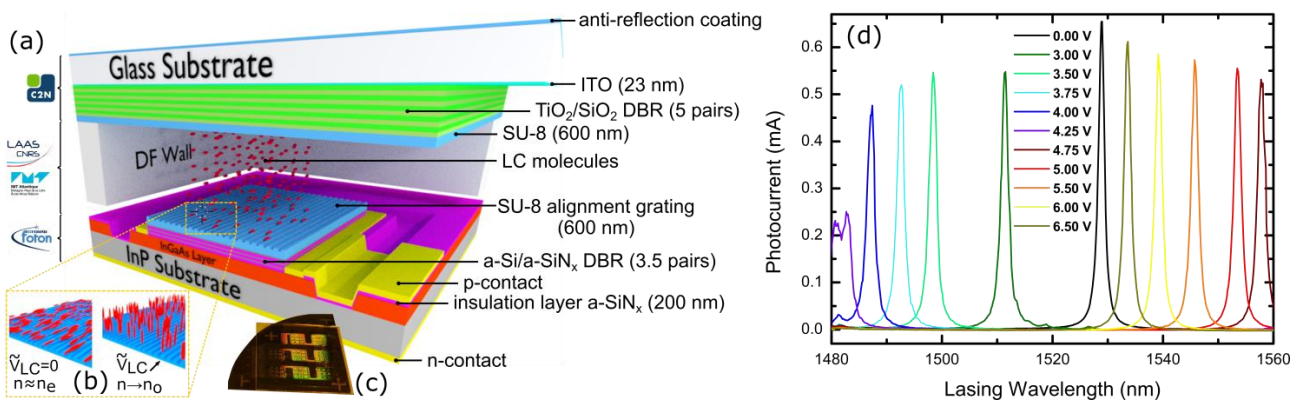


Fig. R.4 – Photodiode p-i-n accordable basée sur la  $\mu$ -cellule à cristaux liquides: (a) structure du composant, (b) orientation des molécules des cristaux liquides avec le réseau d'alignement sub-longueur d'onde en fonction des différentes tensions  $V_{LC}$  appliquées à la  $\mu$ -cellule, (c) photographie d'un quart de plaque de 2 puces avec plusieurs matrices de photodiodes en surface. (d) Photo-courant en fonction de la longueur d'onde pour différentes tension appliqués (entre 0 V et 6.5 V) à la  $\mu$ -cellule à cristaux liquides.

Tableau R.1 – Résumé des performances de la photodiode accordable à cristaux liquides.

Performances	
Plage d'accordabilité $\Delta\lambda_{PD}$ (mesure limité par le laser)	80 nm
Plage de tension AC de pilotage	0 - 7 V
Facteur de qualité $Q$ de la cavité résonnante	$\sim 10^3$
Largeur à mi-hauteur typique du pic de transmission	1.5 nm
Responsivité (pour une couche d'absorption InGaAs d'1 $\mu\text{m}$ d'épaisseur)	0.35 - 0.46 A/W
Pertes optiques	$\sim 2$ dB
Intervalle spectral libre du mode ordinaire	90 - 101 nm
Intervalle spectral libre du mode extraordinaire	80 - 88 nm



Les résultats obtenus avec la photodiode accordable ont permis de valider la technologie des  $\mu$ -cellules à cristaux liquides, et d'envisager le développement de VCSELs accordables en injection électrique qui exploitent ce nouveau approche. Au contraire des composants passifs tels que les photodiodes ou le filtres accordables, dans le cas des VCSELs le choix de la région active joue un rôle primordial pour obtenir l'accordabilité de la longueur d'onde d'émission du laser. En effet, l'accordabilité des cristaux liquides nématiques étant liée au changement de leur indice extraordinaire, il est préférable que la longueur d'onde d'émission soit colinéaire à l'axe extraordinaire des cristaux liquides, pour mieux exploiter toute la plage d'accordabilité offerte par ces derniers. Le recours à des régions actives à base de bâtonnets quantiques permet d'obtenir très facilement cette condition, parce qu'ils présentent une anisotropie de forme leur conférant un état de polarisation linéaire bien défini et exactement déterminé. De plus, grâce à leur large gain, ce type de région active est le candidat idéal pour obtenir un'accordabilité sur une plage spectrale étendue. Dans le chapitre on présente donc les résultats des caractérisations menées sur des régions actives intégrant des bâtonnets quantiques InAs en termes de gain spectral, taux de polarisation et mesures en température, et on les compare avec celles des régions actives conventionnelles basés sur des puits quantiques InGaAsP, pour montrer les avantages que telles régions actives anisotropes confèrent.

Les briques de base développées pour la photodiode accordable ont été le point de départ du développement technologique du VCSEL accordable. Tout récemment, un premier prototype basé sur une architecture simplifiée en pompage optique (OP-LC-VCSEL), intégrant des puits quantiques InGaAsP, a été réalisé en exploitant le procédé TSHEC et la technologie des  $\mu$ -cellules à cristaux liquides (Fig. R.5). Des expériences sont en cours, mais des résultats encourageants sont prochainement attendus.

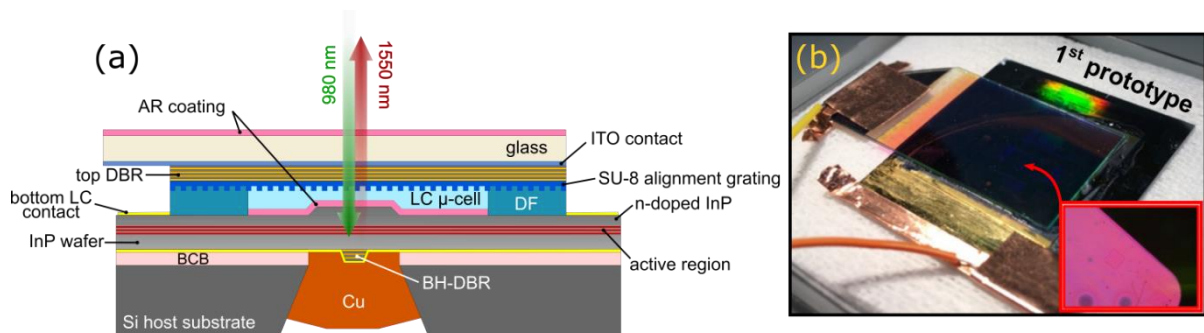


Fig. R.5 – Schéma du OP-LC-VCSEL et photographie du 1<sup>er</sup> prototype réalisé.

Comme mis en évidence par de simulations thermiques FEM, une gestion particulière de la dissipation thermique doit être employée dans ce type de dispositif, pour éviter de dépasser la température critique qui engendre la transition de phase nématique  $\rightarrow$  isotrope, avec des

conséquences néfastes sur les performances optiques des dispositifs (puissance de sortie et plage d'accordabilité fortement limitées).

En raison de problèmes technologiques, le développement d'un dispositif accordable en cavité externe en pompage optique (LC-OP-VECSEL), initialement prévu, a été suspendu. La raison principale étant liée à des tests préliminaires visant à intégrer les  $\mu$ -cellules sur un dispositif VECSEL qui n'ont pas abouti. En particulier, la couche d'ITO utilisée comme électrode de commande des  $\mu$ -cellules à cristaux liquides n'était pas compatible avec une insertion à l'intérieur d'une cavité laser (comme dans le cas d'un VECSEL), en raison d'une très forte absorption optique à la longueur d'onde d'émission. Une approche impliquant un substrat InP dopé pour réaliser l'électrode supérieure pourrait représenter une solution alternative pour pallier à ce type de problématique, mais cela exigera un stade ultérieur de développement qui n'a pas été abordé pendant ces travaux de thèse. Malgré ces problèmes, le développement d'un VECSEL basé sur des QDH InAs sur substrat InP représente le point de départ pour la réalisation d'un émetteur compact et accordable, à faible bruit et aux longueurs d'onde télécom. La suite du manuscrit a été donc consacrée à la présentation de résultats expérimentaux liés à la réalisation et à la caractérisation de l'OP-QDH-VECSEL.

Avant de passer à la description du développement du dit composant, dans le **Chapitre 4** on a discuté les principes de design et les briques de base qui composent une cavité VECSEL, et on a mis en évidence ses particularités par rapport à sa version en cavité monolithique traité dans les chapitres précédents. Dans le quatrième chapitre on discute aussi les enjeux technologiques liés à la gestion du budget thermique dans les VECSELS, qui est encore plus difficile que dans le cas des VCSELS compte tenu des puissances dissipées plus élevées, et qui représente l'un des principaux points critiques pour l'optimisation des performances de tels dispositifs. La dernière partie du chapitre est consacré à la discussion des choix qui ont été considérés pour le design du VECSEL en pompage optique, intégrant une région active à bâtonnets quantiques (OP-QDH-VECSEL) et émettent autour de  $1.6 \mu\text{m}$ , qui représente le sujet du prochain chapitre.

Le **Chapitre 5** est dédié à la description du design, de la réalisation et de la caractérisation de l'OP-QDH-VECSEL (Fig. R.6a, à la page suivante). Dans ce chapitre on détaille la structure de la région active à QDH, consistant en 3 groupes de six plans pour un total de 18 plans d'InAs QDH, et sa réalisation par GS-MBE. On présente aussi le design du DBR hybride inférieur, consistant en 17 paires GaAl/AlGaAs complété par une couche d'or, qui a été réalisé au C2N à Marcoussis avec une croissance métamorphique sur le substrat InP intégrant la région active à QDH. Après avoir été collé sur un substrat de diamant synthétique, le composant a été caractérisé sur deux montages expérimentaux différents : en fonctionnement multi-mode/multi-fréquence (C2N) et en

fonctionnement mono-fréquence (Institut FOTON). Lors des premiers tests, nous avons remarqué l'impossibilité d'obtenir le fonctionnement laser, très probablement à cause d'un décalage spectral entre le pic d'émission de la région active et le pic de résonance de la microcavité induit par une augmentation de la température interne du composant, qui a été partiellement résolu après le dépôt d'une couche antireflet en  $\text{SiN}_x$ . La raison de cet échauffement est liée à une impédance thermique relativement importante, mesurée égale à  $R_{th} \sim 123 \text{ K/W}$ . Cette valeur, environ dix fois plus élevée que dans des VECSEL à puits quantiques à  $1.55 \mu\text{m}$  et intégrant des miroirs en GaAs/AlGaAs, peut facilement expliquer les difficultés observées lors des premiers tests de fonctionnement.

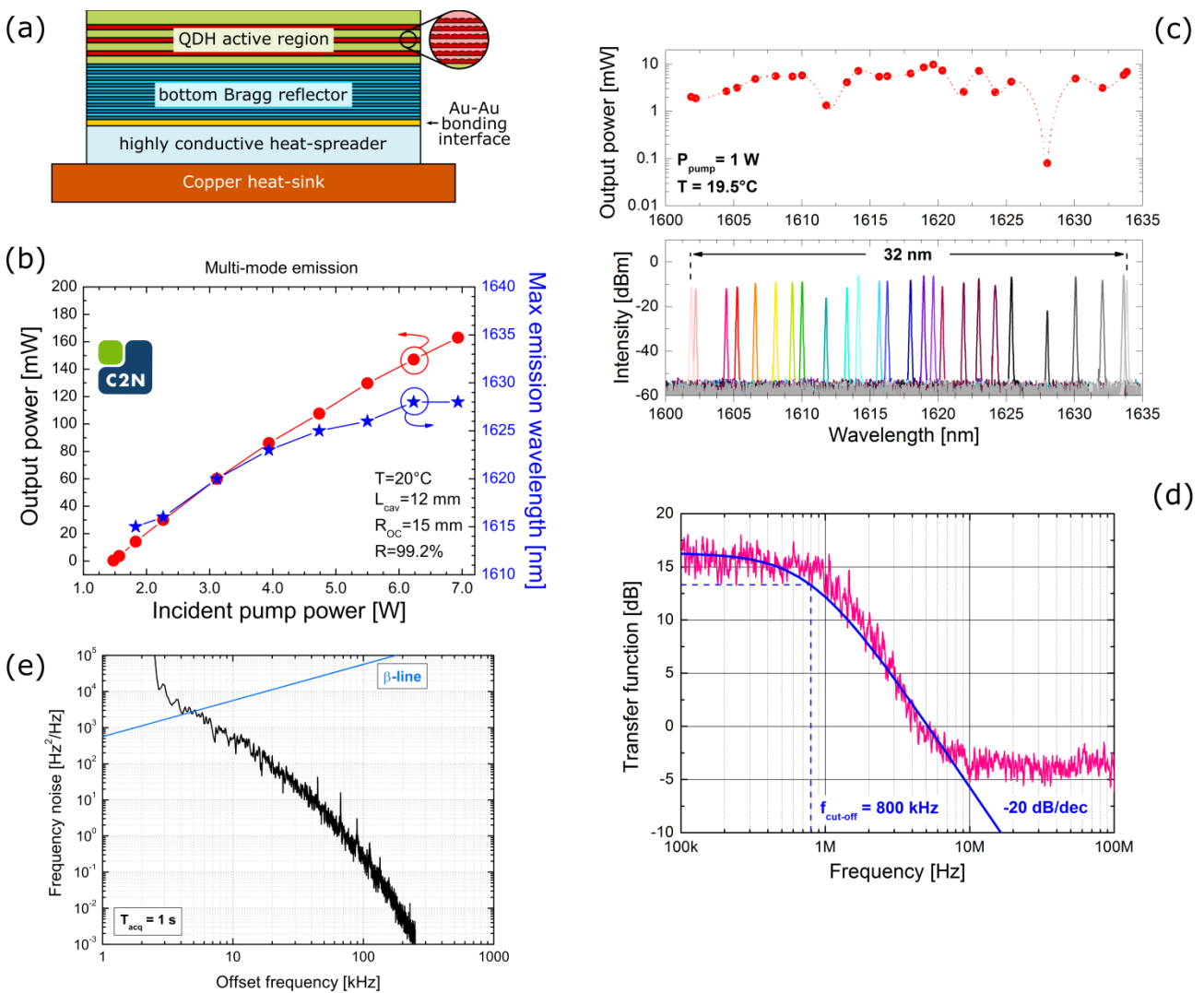


Fig. R.6 – OP-QDH-VECSEL : (a) Structure du composant. (b) caractéristique de sortie et longueur d'onde d'émission en fonction de la puissance de pompe incidente en fonctionnement multi-mode. (c) Puissance de sortie et spectre en fonctionnement mono-fréquence. (d) Fonction de transfert du OP-QDH-VECSEL en fonctionnement Classe-A. (e) Mesure de la largeur de raie avec la méthode de la "β-separation line".

Malgré ces problèmes, une puissance de sortie maximale de 163 mW à  $20^\circ\text{C}$  a été mesurée en fonctionnement multi-mode, dans une cavité de 12 mm de longueur (cf. Fig. R.6b). En fonctionnement mono-fréquence, le VECSEL a montré une émission sur 32 nm (de 1601.8 à

1633.8 nm) avec une puissance de sortie moyenne entre 1 et 10 mW, dans une cavité de longueur égale à 49 mm (Fig. R.6c). Dans cette même configuration, on a confirmé le fonctionnement en Classe-A du VECSEL (Fig. R.6d), avec un niveau de RIN (de l'anglais Relative Intensity Noise) de -158 dB/Hz pour un photo-courant détecté de 2 mA dans la plage de fréquence 10 MHz -18 GHz. Dans ces mêmes conditions on a estimé une largeur de raie autour de 20 kHz, confirmé à 5 kHz par la méthode dite de la “ $\beta$ -separation line” (Fig. R.6e).

Ces résultats représentent la première démonstration à niveau mondial d'un laser VECSEL bas bruit sur InP intégrant des nanostructures quantiques au sein de la région active et émettent à une longueur d'onde télécom. L'étape suivante est représenté par l'investigation de ce type de laser en mode bi-fréquence. Sujet, celui-ci, qui est abordé dans le dernier chapitre du manuscrit.

Dans le *Chapitre 6* on présente les résultats préliminaires des mesures directes qui ont pour but d'investiguer les mécanismes qui règlent le couplage entre deux états propres de polarisation (orthogonaux) dans un VECSEL bi-fréquence. L'approche expérimental, original dans le cas des VECSELs, qui a été conçu et réalisé pour investiguer l'évolution de cette constante de couplage  $C$  (introduite pour la première fois par Lamb dans les cas des masers) est schématisé dans la Fig. R.7.

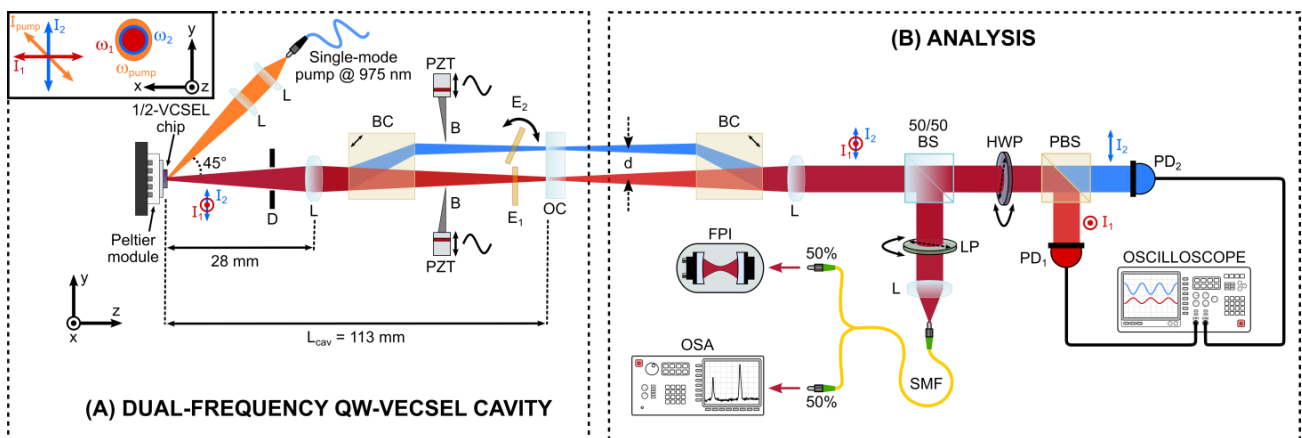


Fig. R.7 – Schéma du setup expérimental employé pour la mesure directe de la constante de couplage  $C$  dans un SQW-VECSEL bi-fréquence.

Ce setup était initialement prévu pour des mesures avec des composants à base de nanostructures quantiques tels que les bâtonnets quantiques (comme l'OP-QDH-VECSEL présenté dans le chapitre précédent) ou les boîtes quantiques. Cependant, du fait que le gain de l'OP-QDH-VECSEL n'était pas suffisant pour opérer en mode bi-fréquence, les mesures ont été d'abord menées sur un VECSEL à base de puits quantiques classiques (SQW-VECSEL) émettant à 1.54  $\mu\text{m}$ , fourni par le groupe de Eli Kapon de l'EPFL (Suisse), dans le cadre du projet internationale ANR-FNS IDYLIC.

Cela a permis dans un premier temps de valider l'approche expérimental, et également d'obtenir des mesures de référence pour des futures campagnes de caractérisation de structures avec de régions actives anisotropes, qui sont en cours de développement à l'Institut FOTON.

Les mesures préliminaires ont révélé un fort couplage entre les deux modes propres orthogonaux, mis en évidence du fait que, pour obtenir le fonctionnement bi-fréquence du SQW-VECSEL, a été nécessaire équilibrer soigneusement les pertes dans les deux bras optiques. Cet approche expérimentale a donc permis de mesurer une valeur moyen de la constante de couplage égale à  $C = 0.843 \pm 0.012$ , pour différents écart en longueur d'onde  $\Delta\lambda$  entre les deux modes (dans la plage 2 à 9.8 nm), comme montré dans la Fig. R.8.

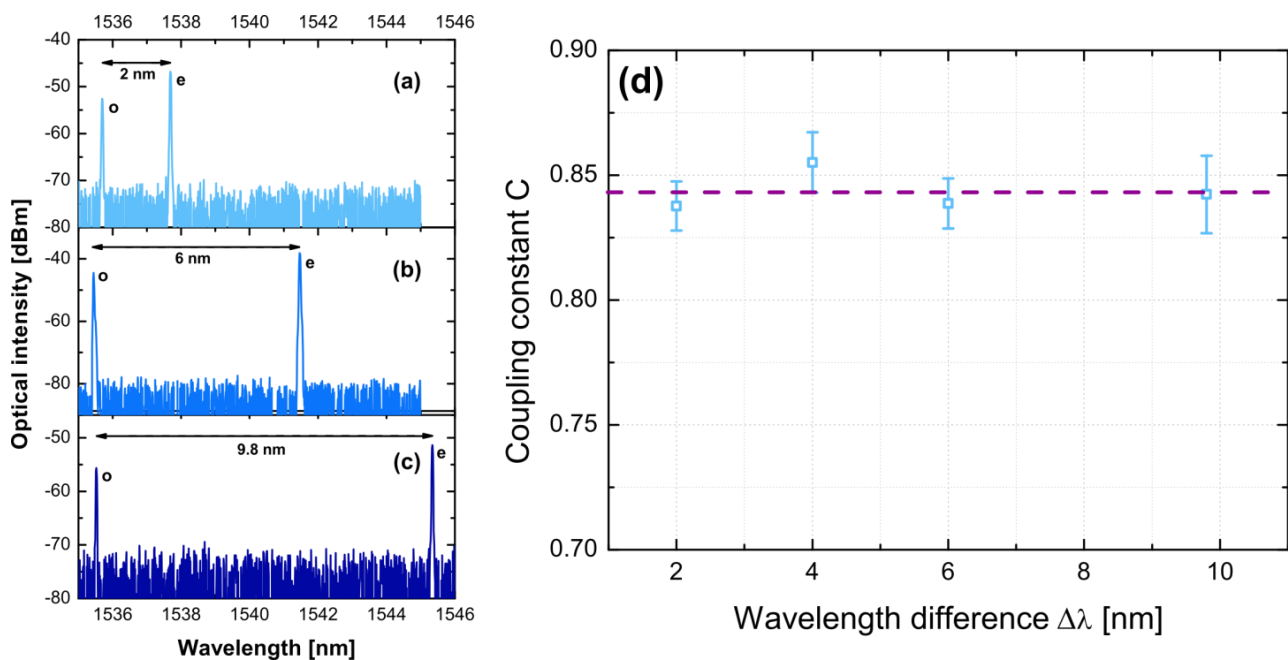


Fig. R.8 – Spectres OSA du mode ordinaire  $I_1$  et extraordinaire  $I_2$  pour différents écarts en longueur d'onde  $\Delta\lambda$ : (a) 2 nm, (b) 6 nm, (c) 9.8 nm. (d) Constante de couplage  $C$  en fonction de  $\Delta\lambda$ . La ligne pointillé violette indique la valeur moyen  $C = 0.843$ .

Cette valeur relativement élevée, qui d'une part était attendue du fait de la nature isotrope de la région active étudiée, confirme le fait que dans un milieu à gain présentant de l'élargissement homogène (comme dans le cas des puits quantiques), l'oscillation bi-fréquence est compliquée à obtenir et elle est soumise à la compétitions entre les deux états propres, comme déjà observé indirectement dans des travaux précédents [Pal2010].

Dans l'avenir, le setup expérimental pourra être utilisé pour répéter ce type d'expériences dans le cas des VECSELs basés sur des régions actives à bâtonnets ou boîtes quantiques, et mettre en évidence les possibles différences dues à l'utilisation de milieux à gain anisotropes, comme très récemment discuté théoriquement par Chusseau et al. [Chusseau2018].

## Bibliography

- [**Abram2004**] R. Abram, M. Schmid, E. Riis, and A. I. Ferguson, "Optically Pumped Vecsels for High Resolution Spectroscopy: the new Ti:Sapphire?," *Laser Spectroscopy: Proceedings of the XVI International Conference* (World of Science Publishing Co. Pte Ltd), 369-372 (2004)
- [**Akahane2013**] K. Akahane, N. Yamamoto, A. Kanno, K. Inagaki, T. Umezawa, T. Kawanishi, T. Endo, Y. Tomomatsu, and T. Yamanoi, "Stable Two-Mode Emission from Semiconductor Quantum Dot Laser," *Appl. Phys. Express* **6**(10), 104001 (2013)
- [**Albrecht2010**] A. R. Albrecht, T. J. Rotter, C. P. Hains, A. Stintz, J. V. Moloney, K. J. Malloy, and G. Balakrishnan, "Multi-watt 1.25  $\mu\text{m}$  quantum dot VECSEL," *Electron. Lett.* **46**(12), 856-857 (2010)
- [**Alghoraibi2007**] I. Alghoraibi, T. Rohel, R. Piron, N. Bertru, C. Paranthoen, G. Elias, A. Nakkar, H. Folliot, A. Le Corre, and S. Loualiche, "Negative characteristic temperature of long wavelength InAs/AlGaInAs quantum dot lasers grown on InP substrates," *Appl. Phys. Lett.* **91**, 261105 (2007)
- [**Alharthi2015**] S. S. Alharthi, E. Clarke, I. D. Henning, and M. J. Adams, "1305-nm Quantum Dot Vertical-External-Cavity Surface-Emitting Laser," *IEEE Photon. Technol. Lett.* **27**(14), 1489-1491 (2015)
- [**Al Nakdali2015**] D. Al Nakdali, M. Gaafar, M. K. Shakfa, F. Zhang, M. Vaupel, K. A. Fedorova, A. Rahimi-Iman, E. U. Rafailov, and M. Koch, "High-Power Operation of Quantum-Dot Semiconductor Disk Laser at 1180 nm," *IEEE Photon. Technol. Lett.* **27**(10), 1128-1131 (2015)
- [**Alias2010**] M. S. Alias, S. Shaari, P. O. Leisher, and K. D. Choquette, "Highly confined and continuous single-mode operation of self-align photonic crystal oxide VCSEL," *Appl. Phys. B* **100**(3), 453-459 (2010)
- [**Alouini1998**] M. Alouini, M. Brunel, F. Bretenaker, M. Vallet, and A. Le Floch, "Dual tunable wavelength Er,Yb:glass laser for terahertz beat frequency generation," *IEEE Photon. Technol. Lett.* **10**(11), 1554-1556 (1998)
- [**Alouini2000**] M. Alouini, F. Bretenaker, M. Brunel, A. Le Floch, M. Vallet, and P. Thony, "Existence of two coupling constants in microchip lasers," *Opt. Lett.* **25**(12), 896-898 (2000)
- [**Alouini2001a**] M. Alouini, "Etude théorique et expérimentale des lasers solides  $\text{Er}^{3+}$  et  $\text{Nd}^{3+}$  : applications des lasers bi-fréquences aux télécommunications optiques et hyperfréquences," Ph.D. dissertation, Université de Rennes 1, Rennes (2001)
- [**Alouini2001b**] M. Alouini, B. Benazet, M. Vallet, M. Brunel, P. Di Bin, F. Bretenaker, A. Le Floch, and P. Thony, "Offset phase locking of Er,Yb:glass laser eigenstates for RF photonics applications," *IEEE Photon. Technol. Lett.* **13**(4), 367-369 (2001)
- [**Anderson1985**] D. A. Anderson, N. Apsley, P. Davies, and P. L. Giles, "Compensation in heavily doped n-type InP and GaAs," *J. Appl. Phys.* **58**(8), 3059 (1985)
- [**Andrejew2016**] A. Andrejew, S. Sprengel, and M.-C. Amann, "GaSb-based vertical-cavity surface-emitting lasers with an emission wavelength at 3  $\mu\text{m}$ ," *Opt. Lett.* **41**(12), 2799-2802 (2016)
- [**Arafin2009**] S. Arafin, A. Bachmann, K. Kashani-Shirazi, and M. C. Amann, "Electrically pumped CW VCSELs at  $\sim 2.6 \mu\text{m}$ ," *Appl. Phys. Lett.* **95**(13), 131120 (2009)



## Bibliography

- [**Aviles-Espinosa2011**] R. Aviles-Espinosa, G. Filippidis, C. Hamilton, G. Malcolm, K. Weingarten, T. Südmeyer, Y. Barbarin, U. Keller, S. Santos, D. Artigas, and P. Loza-Alvarez, “Compact ultrafast semiconductor disk laser: targeting GFP based nonlinear applications in living organisms,” *Biomed. Opt. Express* **2**(4), 739-747 (2011)
- [**Axetris**] Axetris website: <https://www.axetris.com>
- [**Baba1993**] T. Baba, Y. Yogo, K. Suzuki, F. Koyama, and K. Iga, “Near room temperature continuous wave lasing characteristics of GaInAsP/InP surface emitting laser,” *Electron. Lett.* **29**(10), 913-914 (1993)
- [**Babic1992**] D. Babic and S. Corzine, “Analytic expressions for the reflection delay, penetration depth, and absorptance of quarter-wave dielectric mirrors,” *IEEE J. Quantum Electron.* **28**(2), 514-524 (1992)
- [**Babic1995**] D. I. Babic, K. Streubel, R.P. Mirin, N.M. Margalit, J.E. Bowers, E.L. Hu, D.E. Mars, Long Yang, and K. Carey, “Room-temperature continuous-wave operation of 1.54- $\mu$ m vertical-cavity lasers,” in *IEEE Photon. Technol. Lett.* **7**(11), 1225-1227 (1995)
- [**Baili2007**] G. Baili, M. Alouini, D. Dolfi, F. Bretenaker, I. Sagnes, and A. Garnache, “Shot-noise-limited operation of a monomode high-cavity-finesse semiconductor laser for microwave photonics applications,” *Opt. Lett.* **32**(6), 650-652 (2007)
- [**Baili2008**] G. Baili, “Contribution à la réduction du bruit d’intensité relative des lasers à semiconducteurs pour des applications aux RADARs,” Ph.D. dissertation, Université Paris XI, Orsay, (2008)
- [**Baili2009a**] G. Baili, M. Alouini, T. Malherbe, D. Dolfi, I. Sagnes, and F. Bretenaker, “Direct observation of the class-B to class-A transition in the dynamical behavior of a semiconductor laser,” *Europhys. Lett.* **87**(4), 44005 (2009)
- [**Baili2009b**] G. Baili, L. Morvan, M. Alouini, D. Dolfi, F. Bretenaker, I. Sagnes, and A. Garnache, “Experimental demonstration of a tunable dual-frequency semiconductor laser free of relaxation oscillations,” *Opt. Lett.* **34**(21), 3421-3423 (2009)
- [**Baili2012**] G. Baili, G. Pillet, L. Morvan, M. Alouini, D. Dolfi, and I. Sagnes, “Stabilization of a dual-frequency VECSEL free of relaxation oscillations for microwave photonics applications,” *IEEE Photonics Conference 2012*, Burlingame, CA, 2012, pp. 16-17
- [**Baili2014**] G. Baili, L. Morvan, G. Pillet, S. Bouchoule, Z. Zhao, J. Oudar, L. Ménager, S. Formont, F. Van Dijk, M. Faugeron, M. Alouini, F. Bretenaker, and D. Dolfi, “Ultralow Noise and High-Power VECSEL for High Dynamic Range and Broadband RF/Optical Links,” *J. Lightwave Technol.* **32**(20), 3489-3494 (2014)
- [**Balakrishnan2008**] G. Balakrishnan, T. J. Rotter, A. Jallipalli, L. R. Dawson, and D. L. Huffaker, “Interfacial misfit dislocation array based growth of III-Sb active regions on GaAs/AlGaAs DBRs for high-power 2  $\mu$ m VECSELs,” *Proc. SPIE* **6871**, 687111 (2008)
- [**Ballman1983**] A. A. Ballman, A. M. Glass, R. E. Nahory, and H. Brown, “Double doped low etch pit density InP with reduced optical absorption,” *J. Cryst. Growth* **62**(1), 198-202 (1983)
- [**Banyoudeh2016**] S. Banyoudeh, A. Abdollahinia, O. Eyal, F. Schnabel, V. Sichkovskiy, G. Eisenstein, and J. P. Reithmaier, “Temperature-Insensitive High-Speed Directly Modulated 1.55- $\mu$ m Quantum Dot Lasers,” *IEEE Photon. Technol. Lett.* **28**(21), 2451-2454 (2016)
- [**Baxter1996**] G. W. Baxter, J. M. Dawes, P. Dekker, and D. S. Knowles, “Dual-polarization frequency-modulated laser source,” *IEEE Photon. Technol. Lett.* **8**(8), 1015-1017 (1996)

- [**Berger1991**] P. R. Berger, N. K. Dutta, K. D. Choquette, G. Hasnain, and N. Chand, “Monolithically Peltier-cooled vertical-cavity surface-emitting lasers,” *Appl. Phys. Lett.* **59**(1), 117-119 (1991)
- [**Berseth1998**] C.-A. Berseth, A. Schönberg, O. Dehaese, K. Leifer, A. Rudra, and E. Kapon, “Experimental method for high-accuracy reflectivity-spectrum measurements,” *Appl. Opt.* **37**(28), 6671-6676 (1998)
- [**Bhattacharya2000**] P. Bhattacharya, D. Klotzkin, O. Qasaimeh, W. Zhou, S. Krishna and D. Zhu, “High-speed modulation and switching characteristics of In(Ga)As-Al(Ga)As self-organized quantum-dot lasers,” *IEEE J. Sel. Topics Quantum Electron.* **6**(3), 426-438 (2000)
- [**Bek2013**] R. Bek, H. Kahle, T. Schwarzbäck, M. Jetter, and P. Michler, “Mode-locked red-emitting semiconductor disk laser with sub-250 fs pulses,” *Appl. Phys. Lett.* **103**(24), 242101 (2013)
- [**Bek2014**] R. Bek, G. Kersteen, H. Kahle, T. Schwarzbäck, M. Jetter, and P. Michler, “All quantum dot mode-locked semiconductor disk laser emitting at 655 nm,” *Appl. Phys. Lett.* **105**(8), 082107 (2014)
- [**Berger2012**] J. D. Berger, J. L. A. Chilla, S. Govorkov, J. F. P. van Nunen, and A. Y. Lepert, “Towards a practical sodium guide star laser source: design for > 50 watt LGS based on OPSL,” *Proc. SPIE* **8447**, 84470G (2012)
- [**Bibey1999**] M. B. Bibey, F. Deborgies, M. Krakowski, and D. Mongardien, “Very low phase-noise optical links - Experiments and theory,” *IEEE Trans. Microw. Theory Techn.* **47**(12), 2257-2262 (1999)
- [**Binetti2012**] P. R. A. Binetti, M. Lu, E. J. Norberg, R. S. Guzzon, J. S. Parker, A. Sivananthan, A. Bhardwaj, L. A. Johansson, M. J. Rodwell, and L. A. Coldren, “Indium Phosphide Photonic Integrated Circuits for Coherent Optical Links,” *IEEE J. Quantum Electron.* **48**(2), 279-291 (2012)
- [**Blood2003**] P. Blood, G. M. Lewis, P. M. Snowton, H. Summers, J. Thomson, and J. Lutti, “Characterization of semiconductor laser gain media by the segmented contact method,” *IEEE J. Sel. Topics Quantum Electron.* **9**(5), 1275-1282 (2003)
- [**Boehm2011**] G. Boehm, A. Bachmann, J. Roskopf, M. Ortsiefer, J. Chen, A. Hangauer, R. Meyer, R. Strzoda, and M.-C. Amann, “Comparison of InP- and GaSb-based VCSELs emitting at 2.3 $\mu$ m suitable for carbon monoxide detection,” *J. Cryst. Growth* **323**(1), 442-445 (2011)
- [**Bond2007**] T. C. Bond, G. D. Cole, L. L. Goddard, and E. M. Behymer, “Photonic MEMS for NIR in-situ Gas Detection and Identification,” *2007 IEEE Sensors*, Atlanta, GA, 2007, 1368-1371
- [**Bordonalli1996**] A. C. Bordonalli, B. Cai, A. J. Seeds, and P. J. Williams, “Generation of microwave signals by active mode locking in a gain bandwidth restricted laser structure,” *IEEE Photon. Technol. Lett.* **8**(1), 151-153 (1996)
- [**Boucart1999a**] J. Boucart, F. Gaborit, C. Fortin, L. Goldstein, J. Jacquet, and K. Leifer, “Optimization of the metamorphic growth of GaAs for long wavelength VCSELs,” *J. Cryst. Growth* **201–202**, 1015–1019 (1999)
- [**Boucart1999b**] J. Boucart, C. Starck, F. Gaborit, A. Plais, N. Bouche, E. Derouin, J.C. Remy, J. Bonnet-Gamard, L. Goldstein, C. Fortin, D. Carpentier, P. Salet, F. Brillouet, and J. Jacquet, “Metamorphic DBR and tunnel-junction injection: a CW RT monolithic long-wavelength VCSEL,” *IEEE J. Sel. Topics Quantum Electron.* **5**(3), 520-529 (1999)
- [**Bousseksou2007**] A. Bousseksou “Dispositifs semiconducteurs en pompage électrique pour laser en cavité verticale externe émettant à 1,55 micromètres,” Ph.D. dissertation, Université Paris XI, Orsay, (2007)



## Bibliography

- [**Boutami2006**] S. Boutami, B. Ben Bakir, J.-L. Leclercq, X. Letartre, P. Rojo-Romeo, M. Garrigues, P. Viktorovitch, I. Sagnes, L. Legratiet, and M. Strassner, “Highly selective and compact tunable MOEMS photonic crystal Fabry-Perot filter,” *Opt. Express* **14**(8), 3129-3137 (2006)
- [**Brunel1997a**] M. Brunel, M. Vallet, A. Le Floch, and F. Bretenaker, “Differential measurement of the coupling constant between laser eigenstates,” *Appl. Phys. Lett.* **70**(16), 2070-2072 (1997)
- [**Brunel1997b**] M. Brunel, F. Bretenaker, and A. Le Floch, “Tunable optical microwave source using spatially resolved laser eigenstates,” *Opt. Lett.* **22**(6), 384-386 (1997)
- [**Brunel2004**] M. Brunel, F. Bretenaker, S. Blanc, V. Crozatier, J. Brisset, T. Merlet, and A. Poezevara, “High-spectral purity RF beat note generated by a two-frequency solid-state laser in a dual thermo-optic and electro-optic phase-locked loop,” *IEEE Photon. Technol. Lett.* **16**(3), 870-872 (2004)
- [**Bugajski1985**] M. Bugajski and W. Lewandowski, “Concentration-dependent absorption and photoluminescence of n-type InP,” *J. Appl. Phys.* **57**(2), 521-530 (1985)
- [**Burkhard1982**] H. Burkhard, H. W. Dinges, and E. Kuphal, “Optical properties of  $\text{In}_{1-x}\text{Ga}_x\text{P}_{1-y}\text{As}_y$ , InP, GaAs, and GaP determined by ellipsometry,” *J. Appl. Phys.* **53**(1), 655 (1982)
- [**Burns2009**] D. Burns, J.-M. Hopkins, A. J. Kemp, B. Rösener, N. Schulz, C. Manz, K. Köhler, M. Rattunde, and J. Wagner, “Recent developments in high-power short-wave mid-infrared semiconductor disk lasers,” *Proc. SPIE* **7193**, 719311 (2009)
- [**Burstein1954**] E. Burstein, “Anomalous Optical Absorption Limit in InSb,” *Phys. Rev.* **93**(3), 632-633 (1954)
- [**Butkus2009**] M. Butkus, K. Wilcox, J. Rautiainen, O. Okhotnikov, S. Mikhlin, I. Krestnikov, A. Kovsh, M. Hoffmann, T. Südmeyer, U. Keller, and E. Rafailov, “High-power quantum-dot-based semiconductor disk laser,” *Opt. Lett.* **34**(11), 1672-1674 (2009)
- [**Butkus2010**] M. Butkus, J. Rautiainen, O. G. Okhotnikov, S. S. Mikhlin, I. L. Krestnikov and E. U. Rafailov, “1270 nm quantum dot based semiconductor disk lasers,” in *22<sup>nd</sup> IEEE International Semiconductor Laser Conference*, Kyoto, 2010, pp. 71-72, paper P4
- [**Butkus2013**] M. Butkus, E. Viktorov, T. Erneux, C. Hamilton, G. Maker, G. Malcolm, and E. Rafailov, “85.7 MHz repetition rate mode-locked semiconductor disk laser: fundamental and soliton bound states,” *Opt. Express* **21**(21), 25526-25531 (2013)
- [**Cahill1990**] D. G. Cahill, “Thermal conductivity measurement from 30 to 750 K: the  $3\omega$  method,” *Rev. Sci. Instrum.* **61**(2), 802 (1990)
- [**Caliman2011**] A. Caliman, A. Mereuta, G. Suruceanu, V. Iakovlev, A. Sirbu, and E. Kapon, “8 mW fundamental mode output of wafer-fused VCSELs emitting in the 1550-nm band,” *Opt. Express* **19**(18), 16996-17001 (2011)
- [**Caliman2013**] A. Caliman, A. Sirbu, A. Mereuta, K. Pierściński, V. Iakovlev, and E. Kapon, “14XX nm-wavelength electrically-pumped VECSELs fabricated by wafer fusion,” *Opt. Express* **21**(11), 13668-13674 (2013)
- [**Caliman2016**] A. Caliman, A. Mereuta, P. Wolf, A. Sirbu, V. Iakovlev, D. Bimberg, and E. Kapon, “25 Gbps direct modulation and 10 km data transmission with 1310 nm waveband wafer fused VCSELs,” *Opt. Express* **24**(15), 16329-16335 (2016)

- [**Camargo2012**] F. A. Camargo, J. Barrientos, G. Baili, L. Morvan, D. Dolfi, D. Holleville, S. Guerandel, I. Sagnes, P. Georges, and G. Lucas-Leclin, “Coherent Dual-Frequency Emission of a Vertical External-Cavity Semiconductor Laser at the Cesium D<sub>2</sub> Line,” *IEEE Photon. Technol. Lett.* **24**(14), 1218-1220 (2012)
- [**Capmany2005**] J. Capmany, B. Ortega, D. Pastor, and S. Sales, “Discrete-time optical processing of microwave signals,” *J. Lightwave Technol.* **23**(2), 702-723 (2005)
- [**Capmany2007**] J. Capmany and D. Novak, “Microwave photonics combines two worlds,” *Nat. Photon.* **1**, 319-330 (2007)
- [**Caroff2005**] P. Caroff, “Croissance de boîtes quantiques InAs/InP (113B) pour des applications en télécommunications optiques,” Ph.D. dissertation, Institut National des Sciences Appliquées de Rennes, Rennes, (2005)
- [**Carpintero2014**] G. Carpintero, K. Balakier, Z. Yang, R. C. Guzmán, A. Corradi, A. Jimenez, G. Kervella, M. J. Fice, M. Lamponi, M. Chitoui, F. van Dijk, C. C. Renaud, A. Wonfor, E. A. J. M. Bente, R. V. Penty, I. H. White, and A. J. Seeds, “Microwave Photonic Integrated Circuits for Millimeter-Wave Wireless Communications,” *J. Lightwave Technol.* **32**(20), 3495-3501 (2014)
- [**Casey1984**] H. C. Casey Jr. and P. L. Carter, “Variation of intervalence band absorption with hole concentration in p-type InP,” *Appl. Phys. Lett.* **44**(1), 82 (1984)
- [**Castany2011**] O. Castany, L. Dupont, A. Shuaib, J. P. Gauthier, C. Levallois, and C. Paranthoën, “Tunable semiconductor vertical cavity surface emitting laser with an intracavity liquid crystal layer”, *Appl. Phys. Lett.* **98**(16), 161105 (2011)
- [**Cermak2010**] P. Cermak, M. Triki, A. Garnache, L. Cerutti, and D. Romanini, “Optical-Feedback Cavity-Enhanced Absorption Spectroscopy Using a Short-Cavity Vertical-External-Cavity Surface-Emitting Laser,” *IEEE Photon. Technol. Lett.* **22**(21), 1607-1609 (2010)
- [**Cesar2017**] J. Cesar, S. Paul, M. T. Haidar, B. Corbett, A. Chipouline, and F. Küppers, “Surface micromachined MEMS-tunable PIN-photodiodes around 1550-nm,” in *2017 Conference on Lasers and Electro-Optics (CLEO)*, San Jose, CA, 2017, pp. 1-2.
- [**Chaccour2016**] L. Chaccour, G. Aubin, K. Merghem, J. L. Oudar, A. Khadour, P. Chatellier, and S. Bouchoule, “Cross-Polarized Dual-Frequency VECSEL at 1.5  $\mu\text{m}$  for Fiber-Based Sensing Applications,” *IEEE Photon. J.* **8**(6), 1-10 (2016)
- [**Chang2006**] Y. H. Chang, P.C. Peng, W.K. Tsai, G. Lin, F. Lai, R.S. Hsiao, H.P. Yang, H.C. Yu, K.F. Lin, J.Y. Chi, S.C. Wang, and H.C. Kuo, “Single-mode monolithic quantum-dot VCSEL in 1.3  $\mu\text{m}$  with sidemode suppression ratio over 30 dB,” *IEEE Photon. Technol. Lett.* **18**(7), 847-849 (2006)
- [**Chang-Hasnain1990**] C. J. Chang-Hasnain, M. Orenstein, A. Von Lehmen, L. T. Florez, J. P. Harbison, and N. G. Stoffel, “Transverse mode characteristics of vertical cavity surface-emitting lasers,” *Appl. Phys. Lett.* **57**(3), 218-220 (1990)
- [**Chang-Hasnain1991**] C. J. Chang-Hasnain, J. P. Harbison, L. T. Florez, and N. G. Stoffel, “Polarisation characteristics of quantum well vertical cavity surface emitting lasers,” *Electron. Lett.* **27**(2), 163-165 (1991)
- [**Chen2015**] M. Chen, Z. Meng, J. Wang, and W. Chen, “Ultra-narrow linewidth measurement based on Voigt profile fitting,” *Opt. Express* **23**(5), 6803-6808 (2015)

## Bibliography

- [**Chilla2005**] J. L. A. Chilla, H. Zhou, E. Weiss, A. L. Caprara, Q.-Z. Shou, S. V. Govorkov, and M. K. Reed, L. Spinelli, “Blue and green optically pumped semiconductor lasers for display,” Proc. SPIE **5740**, 41 (2005)
- [**Chilla2007**] J. Chilla, Q.-Z. Shu, H. Zhou, E. Weiss, M. Reed, and L. Spinelli, “Recent advances in optically pumped semiconductor lasers,” Proc. SPIE **6451**, 645109 (2007)
- [**Chirovsky1999**] L. M. F. Chirovsky, W. S. Hobson, R. E. Leibenguth, S. P. Hui, J. Lopata, G. J. Zydzik, G. Giaretta, K. W. Goossen, J. D. Wynn, A. V. Krishnamoorthy, B. J. Tseng, J. M. Vandenberg, and L. A. D’Asaro, “Implant-apertured and index-guided vertical-cavity surface-emitting lasers (I2-VCSELs),” IEEE Photon. Technol. Lett. **11**(5), 500-502 (1999)
- [**Choquette1994**] K. D. Choquette and R. E. Leibenguth, “Control of vertical-cavity laser polarization with anisotropic transverse cavity geometries,” IEEE Photon. Technol. Lett. **6**(1), 40-42 (1994)
- [**Choquette1995**] K. D. Choquette, R. P. Schneider, K. L. Lear, and R. E. Leibenguth, “Gain-dependent polarization properties of vertical-cavity lasers,” IEEE J. Sel. Topics Quantum Electron. **1**(20), 661-666 (1995)
- [**Chusseau2013**] L. Chusseau, F. Philippe, P. Viktorovitch, and X. Letartre, “Mode competition in a dual-mode quantum-dot semiconductor microlaser,” Phys. Rev. A **88**, 015803 (2013)
- [**Chusseau2018**] L. Chusseau, A. Vallet, M. Perrin, C. Paranthoën, and M. Alouini, “Lamb mode-coupling constant in quantum-dot semiconductor lasers,” Phys. Rev. B **98**, 155306 (2018)
- [**Cocquelin2009**] B. Cocquelin, D. Holleville, G. Lucas-Leclin, I. Sagnes, A. Garnache, M. Myara, and P. Georges, “Tunable single-frequency operation of a diode-pumped vertical external-cavity laser at the cesium D<sub>2</sub> line,” Appl. Phys. B **95**(2), 315-321 (2009)
- [**Coldren2012**] L. A. Coldren, S. W. Corzine, and M. L. Mašanović, *Diode Lasers and Photonic Integrated Circuits* (John Wiley & Sons Inc., 2012)
- [**CompoundSemiconductor2018**] “Philips Photonics Reaches One Billion VCSEL Milestone” (21 November 2018):  
[https://compoundsemiconductor.net/article/105829/Philips\\_Photonics\\_reaches\\_one\\_billion\\_VCSEL\\_milestone](https://compoundsemiconductor.net/article/105829/Philips_Photonics_reaches_one_billion_VCSEL_milestone)
- [**Comsol**] “COMSOL Multyphysics® website”: <http://www.comsol.com>
- [**Cortez2000**] S. Cortez, O. Krebs, and P. Voisin, “In-plane optical anisotropy of quantum well structures: From fundamental considerations to interface characterization and optoelectronic engineering,” J. Vac. Sci. Technol. B **18**(4), 2232-2241 (2000)
- [**Danion2014**] G. Danion, C. Hamel, L. Frein, F. Bondu, G. Loas, and M. Alouini, “Dual frequency laser with two continuously and widely tunable frequencies for optical referencing of GHz to THz beatnotes,” Opt. Express **22**(15), 17673-17678 (2014)
- [**De2013**] S. De, V. Pal, A. El Amili, G. Pillet, G. Baili, M. Alouini, I. Sagnes, R. Ghosh, and F. Bretenaker, “Intensity noise correlations in a two-frequency VECSEL,” Opt. Express **21**(3), 2538-2550 (2013)
- [**De2014a**] S. De, A. El Amili, I. Fsaifes, G. Pillet, G. Baili, F. Goldfarb, M. Alouini, I. Sagnes, and F. Bretenaker, “Phase Noise of the Radio Frequency (RF) Beatnote Generated by a Dual-Frequency VECSEL,” J. Lightwave Technol. **32**(7), 1307-1316 (2014)

- [**De2014b**] S. De, G. Baili, M. Alouini, J. Harmand, S. Bouchoule, and F. Bretenaker, “Class-A dual-frequency VECSEL at telecom wavelength,” *Opt. Lett.* **39**(19), 5586-5589 (2014)
- [**De2015**] S. De, G. Baili, S. Bouchoule, M. Alouini, and F. Bretenaker, “Intensity- and phase-noise correlations in a dual-frequency vertical-external-cavity surface-emitting laser operating at telecom wavelength,” *Phys. Rev. A* **91**, 053828 (2015)
- [**Debusmann2009**] R. Debusmann, N. Dhidah, V. Hoffmann, L. Weixelbaum, U. Brauch, T. Graf, M. Weyers, and M. Kneissl, “InGaN–GaN Disk Laser for Blue-Violet Emission Wavelengths,” *IEEE Photon. Technol. Lett.* **22**(9), 652-654 (2010)
- [**De Cort2011**] W. De Cort, J. Beeckman, T. Claes, K. Neyts, and R. Baets, “Wide tuning of silicon-on-insulator ring resonators with a liquid crystal cladding,” *Opt. Lett.* **36**(19), 3876–3878 (2011)
- [**Deppe1990a**] D. G. Deppe, N. D. Gerrard, C. J. Pinzone, R. D. Dupuis, and E. F. Schubert, “Quarter-wave Bragg reflector stack of InP-In<sub>0.53</sub>Ga<sub>0.47</sub>As for 1.65  $\mu\text{m}$  wavelength,” *Appl. Phys. Lett.* **56**(4), 315-317 (1990)
- [**Di Domenico2010**] G. Di Domenico, S. Schilt, and P. Thomann, “Simple approach to the relation between laser frequency noise and laser line shape,” *Appl. Opt.* **49**(25), 4801-4807 (2010)
- [**Djie2007**] H. S. Djie, B. S. Ooi, X.-M. Fang, Y. Wu, J. M. Fastenau, W. K. Liu, and M. Hopkinson, “Room-temperature broadband emission of an InGaAs/GaAs quantum dots laser,” *Opt. Lett.* **32**(1), 44-46 (2007)
- [**Dolfi1997**] D. Dolfi, J. Tabourel, O. Durand, V. Laude, J. P. Huignard, and J. Chazelas, “Optical architectures for programmable filtering and correlation of microwave signals,” *IEEE Trans. Microw. Theory Tech.* **45**(8), 1467-1472 (1997)
- [**Duan2018**] J. Duan, H. Huang, K. Schires, P. J. Poole, C. Wang, and F. Grillot, “Temperature dependence of spectral linewidth of InAs/InP quantum dot distributed feedback lasers,” *Proc. SPIE* **10553**, 105530J (2018)
- [**Dudley1994**] J. J. Dudley, D. I. Babić, R. Mirin, L. Yang, B. I. Miller, R. J. Ram, T. Reynolds, E. L. Hu, and J. E. Bowers, “Low threshold, wafer fused long wavelength vertical cavity lasers,” *Appl. Phys. Lett.* **64**(12), 1463 (1994)
- [**Dumont2014**] P. Dumont, F. Camargo, J. M. Danet, D. Holleville, S. Guerandel, G. Pillet, G. Baili, L. Morvan, D. Dolfi, I. Gozhyk, G. Beaudoin, I. Sagnes, P. Georges, and G. Lucas-Leclin, “Low-Noise Dual-Frequency Laser for Compact Cs Atomic Clocks,” *J. Lightwave Technol.* **32**(20), 3817-3823 (2014)
- [**El Amili2014**] A. El Amili, G. Loas, L. Pouget, and M. Alouini, “Buffer reservoir approach for cancellation of laser resonant noises,” *Opt. Lett.* **39**(17), 5014-5017 (2014)
- [**ElectroOptics2018**] “VCSEL Market to be worth \$3.1 billion by 2022” (16 February 2018): <https://www.electrooptics.com/news/vcsel-market-be-worth-31-billion-2022>
- [**Esaki1958**] L. Esaki, “New Phenomenon in Narrow Germanium p-n Junctions,” *Phys. Rev.* **109**(2), 603-604 (1958)
- [**Fallahi2008**] M. Fallahi L. Fan, Y. Kaneda, C. Hessenius, J. Hader, H. Li, J. V. Moloney, B. Kunert, W. Stolz, S. W. Koch, J. Murray, and R. Bedford, “5-W Yellow Laser by Intracavity Frequency Doubling of High-Power Vertical-External-Cavity Surface-Emitting Laser,” *IEEE Photon. Technol. Lett.* **20**(20), 1700-1702 (2008)

## Bibliography

- [**Fan2006**] L. Fan, M. Fallahi, J. Hader, A. R. Zakharian, J. V. Moloney, J. T. Murray, R. Bedford, W. Stolz, and S. W. Koch, "Multichip vertical-external-cavity surface-emitting lasers: a coherent power scaling scheme," *Opt. Lett.* **31**(24), 3612-3614 (2006)
- [**Fan2007**] L. Fan, C. Hessenius, M. Fallahi, J. Hader, H. Li, J.V. Moloney, W. Stolz, S. Koch, J.T. Murray, and R. Bedford, "Highly strained InGaAs/GaAs multiwatt vertical-external-cavity surface-emitting laser emitting around 1170nm," *Appl. Phys. Lett.* **91**(13), 131114 (2007)
- [**Fandiño2017**] J. S. Fandiño, P. Muñoz, D. Doménech, and J. Capmany, "A monolithic integrated photonic microwave filter," *Nat. Photon.* **11**, 124–129 (2017)
- [**Faugeron2013**] M. Faugeron, F. Lelarge, M. Tran, Y. Robert, E. Vinet, A. Enard, J. Jacquet, and F. Van Dijk, "High Peak Power, Narrow RF Linewidth Asymmetrical Cladding Quantum-Dash Mode-Locked Lasers," *IEEE J. Sel. Topics Quantum Electron.* **19**(4), 1101008-1101008 (2013)
- [**Fedorova2017**] K. A. Fedorova, A. Gorodetsky, E. U. Rafailov, "Compact All-Quantum-Dot-Based Tunable THz Laser Source," *IEEE J. Sel. Topics Quantum Electron.* **23**(4), 1-5 (2017)
- [**Feezell2006**] D. Feezell, D. A. Buell, D. Lofgreen, M. Mehta and L. A. Coldren, "Optical Design of InAlGaAs Low-Loss Tunnel-Junction Apertures for Long-Wavelength Vertical-Cavity Lasers," *IEEE J. Quantum Electron.* **42**(5), 494-499 (2006)
- [**Felix1997**] C. L. Felix, W. W. Bewley, I. Vurgaftman, J. R. Meyer, and L. Goldberg, "Midinfrared vertical-cavity surface-emitting laser," *Appl. Phys. Lett.* **71**(24), 3483 (1997)
- [**Francis2005**] D.A. Francis, D. B. Young, J. Walker, A. Verma, D. Gold, and C. Decker, "Monolithic 1310nm buried heterostructure VCSEL using InGaAsP/InP DBR reflectors," *Proc. SPIE* **6013**, 60130A (2005)
- [**Fréchengues1999**] S. Fréchengues, N. Bertru, V. Drouot, B. Lambert, S. Robinet, S. Loualiche, D. Lacombe, and A. Ponchet, "Wavelength tuning of InAs quantum dots grown on (311)B InP," *Appl. Phys. Lett.* **74**(22), 3356-3358 (1999)
- [**Friederich2010**] F. Friederich, G. Schuricht, A. Deninger, F. Lison, G. Spickermann, P. Haring Bolívar, and H. G. Roskos, "Phase-locking of the beat signal of two distributed-feedback diode lasers to oscillators working in the MHz to THz range," *Opt. Express* **18**(8), 8621-8629 (2010)
- [**Gauthier2011**] J.-P. Gauthier, "Réalisation et optimisation de nanostructures à base de semiconducteurs III-V pour les applications de VCSEL accordables," Ph.D. dissertation, Institut National des Sciences Appliquées de Rennes, Rennes, (2011)
- [**Gauthier2012**] J.-P. Gauthier, C. Paranthoën, C. Levallois, A. Shuaib, J.-M. Lamy, H. Folliot, M. Perrin, O. Dehaese, N. Chevalier, O. Durand, and A. Le Corre, "Enhancement of the polarization stability of a 1.55  $\mu\text{m}$  emitting vertical-cavity surface-emitting laser under modulation using quantum dashes", *Opt. Express* **20**(15), 16832-16837 (2012)
- [**Gebretsadik1998**] H. Gebretsadik, K. Kamath, W.-D. Zhou, and P. Bhattacharya, "Lateral oxidation of InAlAs in InP-based heterostructures for long wavelength vertical cavity surface emitting laser applications" *Appl. Phys. Lett.* **72**(2), 135-137 (1998)



- [**Geels1990**] R. S. Geels and L. A. Coldren, "Narrow-linewidth, low threshold vertical-cavity surface-emitting lasers," in *12<sup>th</sup> IEEE International Conference on Semiconductor Laser*, Davos, Switzerland, 1990, pp. 16-17, paper B-1
- [**Germann2008**] T.D. Germann, A. Strittmatter, U.W. Pohl, D. Bimberg, J. Rautiainen, M. Guina, O.G. Okhotnikov, "Quantum-dot semiconductor disk lasers," *J. Cryst. Growth* **310**(23), 5182-5186 (2008)
- [**Geske2004**] J. Geske, K. G. Gan, Y. L. Okuno, J. Piprek, and J. E. Bowers, "Vertical-cavity surface-emitting laser active regions for enhanced performance with optical pumping," *IEEE J. Quantum. Electron.* **40**(9), 1155–1162 (2004)
- [**Gierl2011**] C. Gierl, T. Gruendl, P. Debernardi, K. Zogal, C. Grasse, H. A. Davani, G. Böhm, S. Jatta, F. Küppers, P. Meißner, and M.-C. Amann, "Surface micromachined tunable 1.55  $\mu\text{m}$ -VCSEL with 102 nm continuous single-mode tuning," *Opt. Express* **19**(18), 17336-17343 (2011)
- [**Gierl2014a**] C. Gierl, K. Zogal, S. Paul, and F. Küppers, "Tunable MEMS-VCSEL with >140-nm tuning range using SiO<sub>2</sub>/SiC-based MEMS-DBR," *Proc. SPIE* **9001**, 900107 (2014)
- [**Gierl2014b**] C. Gierl, T. Gründl, S. Paul, K. Zogal, M. T. Haidar, P. Meissner, M.-C. Amann, and F. Küppers, "Temperature characteristics of surface micromachined MEMS-VCSEL with large tuning range," *Opt. Express* **22**(11), 13063-13072 (2014)
- [**Giet2006**] S. Giet, H. D. Sun, S. Calvez, M. D. Dawson, S. Suomalainen, A. Harkonen, M. Guina, O. Okhotnikov, and M. Pessa "Spectral narrowing and locking of a vertical-external-cavity surface-emitting laser using an intracavity volume Bragg grating," *IEEE Photon. Technol. Lett.* **18**(16), 1786-1788 (2006)
- [**Giet2007**] S. Giet, C. Lee, S. Calvez, M. Dawson, N. Destouches, J. Pommier, and O. Parriaux, "Stabilization of a Semiconductor Disk Laser using an intra-cavity High Reflectivity Grating," *Opt. Express* **15**(25), 16520-16526 (2007)
- [**Grillot2011**] F. Grillot, N. A. Naderi, J. B. Wright, R. Raghunathan, M. T. Crowley, and L. F. Lester, "A dual-mode quantum dot laser operating in the excited state," *Appl. Phys. Lett.* **99**, 231110 (2011)
- [**Grulkowski2012**] I. Grulkowski, J. J. Liu, B. Potsaid, V. Jayaraman, C. D. Lu, J. Jiang, A. E. Cable, J. S. Duker, and J. G. Fujimoto, "Retinal, anterior segment and full eye imaging using ultrahigh speed swept source OCT with vertical-cavity surface emitting lasers," *Biomed. Opt. Express* **3**(11), 2733-2751 (2012)
- [**Gründl2013**] T. Gründl, P. Debernardi, M. Müller, C. Grasse, P. Ebert, K. Geiger, M. Ortsiefer, G. Böhm, R. Meyer, and M. C. Amann, "Record Single-Mode, High-Power VCSELs by Inhibition of Spatial Hole Burning," *IEEE J. Sel. Topics Quantum Electron.* **19**(4), 1700913-1700913 (2013)
- [**Guignard2007**] P. Guignard, H. Ramanitra, and L. Guillo, "Home Network based on CWDM Broadcast and Select technology," *33<sup>rd</sup> European Conference and Exhibition of Optical Communication*, Berlin, Germany, 2007, pp. 1-2
- [**Hader2010**] J. Hader, G. Hardesty, T. L. Wang, M. J. Yarborough, Y. Kaneda, J. V. Moloney, B. Kunert, W. Stolz, and S. W. Koch, "Predictive Microscopic Modeling of VECSELs," *IEEE J. Quant. Electron.*, **46**(5), 810-817 (2010)
- [**Haglund2012**] E. Haglund, Å. Haglund, J. S. Gustavsson, B. Kögel, P. Westbergh, and A. Larsson, "Reducing the spectral width of high speed oxide confined VCSELs using an integrated mode filter", *Proc. SPIE* **8276**, 82760L (2012)

## Bibliography

- [**Haidar2018**] M. T. Haidar, S. Preu, J. Cesar, S. Paul, A. S. Hajo, C. Neumeyr, H. Maune, and F. Küppers, “Systematic characterization of a 1550 nm microelectromechanical (MEMS)-tunable vertical-cavity surface-emitting laser (VCSEL) with 7.92 THz tuning range for terahertz photomixing systems,” *J. Appl. Phys.* **123**(2), 023106 (2018)
- [**Halbritter2004**] H. Halbritter, F. Riemenschneider, S. Syguda, C. Dhanavantri, M. Strassner, A. Tarraf, B.R. Singh, I. Sagnes, and P. Meissner, “Tunable and wavelength selective pin photodiode,” *Electron. Lett.* **40**(6), 388-390 (2004)
- [**Halbritter2007**] H. Halbritter, C. Sydlo, B. Kogel, F. Riemenschneider, H. L. Hartnagel, and P. Meissner, “Impact of Micromechanics on the Linewidth and Chirp Performance of MEMS-VCSELs,” *IEEE J. Sel. Topics Quantum Electron.* **13**(2), 367-373 (2007)
- [**Hall1962**] R. N. Hall, G. E. Fenner, J. D. Kingsley, T. J. Soltys, and R. O. Carlson, “Coherent Light Emission From GaAs Junctions,” *Phys. Rev. Lett.* **9**(9), 366-368 (1962)
- [**Hastie2003**] J. E. Hastie, C. W. Jeon, D. Burns, J.-M. Hopkins, S. Calvez, R. Abram, and M. D. Dawson, “A 0.5-W 850-nm Al<sub>x</sub>Ga<sub>1-x</sub>As VECSEL with intracavity silicon carbide heatspreader,” *Proc. SPIE* **5137**, 201 (2003)
- [**Hastie2005**] J.E. Hastie, S. Calvez, M. D. Dawson, T. Leinonen, A. Laakso, J. Lyytikäinen, and M. Pessa, “High power CW red VECSEL with linearly polarized TEM<sub>00</sub> output beam,” *Opt. Express* **13**(1), 77-81 (2005)
- [**Hastie2006**] J.E. Hastie, L.G. Morton, A. J. Kemp, M.D. Dawson, A.B. Krysa, and J.S. Roberts, “Tunable ultraviolet output from an intracavity frequency-doubled red vertical-external-cavity surface-emitting laser,” *Appl. Phys. Lett.* **89**(6), 061114 (2006)
- [**Hauser1978**] J. R. Hauser, “Avalanche breakdown voltages for III-V semiconductors,” *Appl. Phys. Lett.* **33**(4), 351-353 (1978)
- [**Hayashi1995**] Y. Hayashi, T. Mukaihara, N. Hatori, N. Ohnoki, A. Matsutani, F. Koyama, and K. Iga, “Lasing characteristics of low-threshold oxide confinement InGaAs-GaAlAs vertical-cavity surface-emitting lasers,” *IEEE Photon. Technol. Lett.* **7**(11), 1234-1236 (1995)
- [**Heinen2012a**] B. Heinen, T.-L.Wang, M. Sparenberg, A.Weber, B. Kunert, J. Hader, S.W. Koch, J.V. Moloney, M. Koch, and W. Stolz, “106 W continuous-wave output power from vertical-external-cavity surface-emitting laser,” *Electron. Lett.* **48**(9), 516-517 (2012)
- [**Heinen2012b**] B. Heinen, F. Zhang, M. Sparenberg, B. Kunert, M. Koch, and W. Stolz, “On the Measurement of the Thermal Resistance of Vertical-External-Cavity Surface-Emitting Lasers (VECSELs),” *IEEE J. Quantum Electron.* **48**(7), 934-940 (2012)
- [**Higuchi2008**] Y. Higuchi, K. Omae, H. Matsumura, T. Mukai, “Room-temperature CW lasing of a GaN-based vertical-cavity surface-emitting laser by current injection,” *Appl. Phys. Express* **1**(12), 121102 (2008)
- [**Hirabayashi1993**] K. Hirabayashi, H. Tsuda, and T. Kurokawa, “Tunable Liquid-Crystal Fabry-Perot Interferometer Filter for Wavelength-Division Multiplexing Communication Systems,” *J. Lightwave Technol.* **11**(12), 2033–2043 (1993)

- [**Hoffmann2008**] M. Hoffmann, Y. Barbarin, D. J. H. C. Maas, M. Golling, I. L. Krestnikov, S. S. Mikhrin, A. R. Kovsh, T. Südmeyer, and U. Keller, “Modelocked quantum dot vertical external cavity surface emitting laser,” *Appl. Phys. B* **93**(4), 733–736 (2008)
- [**Hoffmann2011**] M. Hoffmann, O. Sieber, V. Wittwer, I. Krestnikov, D. Livshits, Y. Barbarin, T. Südmeyer, and U. Keller, “Femtosecond high-power quantum dot vertical external cavity surface emitting laser,” *Opt. Express* **19**(9), 8108-8116 (2011)
- [**Hofmann2010**] W. Hofmann, “High-Speed Buried Tunnel Junction Vertical-Cavity Surface-Emitting Lasers,” *IEEE Photon. J.* **2**(5), 802-815 (2010)
- [**Hohlfeld2003**] D. Hohlfeld, M. Epmeier, and H. Zappe, “A thermally tunable, silicon-based optical filter,” *Sens. Actuators A-Phys.* **103**(1-2), 93-99 (2003)
- [**Huang2007**] M. C. Y. Huang, Y. Zhou, and C. J. Chang-Hasnain, “A surface-emitting laser incorporating a high-index-contrast subwavelength grating,” *Nature Photonics* **1**, 119–122 (2007)
- [**Huber2004**] D. Huber, P. Corredoura, S. Lester, V. Robbins, and L. Kamas, “Reducing Brownian motion in an electrostatically tunable MEMS laser,” *J. Microelectromech. Syst.* **13**(5), 732-736 (2004)
- [**Huffaker1994**] D. L. Huffaker, D. G. Deppe, K. Kumar, et T. J. Rogers, “Native-oxide defined ring contact for low threshold vertical-cavity lasers,” *Appl. Phys. Lett.* **65**(1), 97-99 (1994)
- [**Huffaker1998**] D. L. Huffaker, G. Park, Z. Zou, O. B. Shchekin, and D. G. Deppe, “1.3  $\mu\text{m}$  room-temperature GaAs-based quantum-dot laser,” *Appl. Phys. Lett.* **73**(18), 2564-2566 (1998)
- [**Hunziker2007**] L. E. Hunziker, Q.-Z. Shu, D. Bauer, C. Ihli, G. J. Mahnke, M. Rebut, J. R. Chilla, A. L. Caprara, H. Zhou, E. S. Weiss, and M. K. Reed, “Power-scaling of optically-pumped semiconductor lasers”, *Proc. SPIE* **6451**, 64510A (2007)
- [**Hurtado2013**] A. Hurtado, I. D. Henning, M. J. Adams, and L. F. Lester, “Dual-mode lasing in a 1310-nm quantum dot distributed feedback laser induced by single-beam optical injection,” *Appl. Phys. Lett.* **102**, 201117 (2013)
- [**Iakovlev2013**] V. Iakovlev, A. Sirbu, Z. Micković, D. Ellafi, G. Suruceanu, A. Mereuta, A. Caliman, and E. Kapon, “Progress and challenges in industrial fabrication of wafer-fused VCSELs emitting in the 1310 nm band for high-speed wavelength division multiplexing applications,” *Proc. SPIE* **8639**, 863904 (2013)
- [**Iezekiel2015**] S. Iezekiel, M. Burla, J. Klamkin, D. Marpaung, and J. Capmany, “RF Engineering Meets Optoelectronics: Progress in Integrated Microwave Photonics,” *IEEE Microw. Mag.* **16**(8), 28-45 (2015)
- [**Ioffe**] Ioffe Physical-Technical Institute database website: <http://www.ioffe.ru/SVA/NSM/Semicond/>
- [**Irmer2003**] S. Irmer, Jürgen Daleiden, Ventzeslav Rangelov, Cornelia Prott, Friedhard Römer, Martin Strassner, Amer Tarraf, and Hartmut Hillmer, “Ultralow biased widely continuously tunable fabry-Perot filter,” *IEEE Photon. Technol. Lett.* **15**(3), 434-436 (2003)
- [**Jacobsson2006**] B. Jacobsson, V. Pasiskevicius, and F. Laurell, “Tunable single-longitudinal-mode ErYb:glass laser locked by a bulk glass Bragg grating,” *Opt. Lett.* **31**(11), 1663–1665 (2006)
- [**Jayaraman2012a**] V. Jayaraman, G. D. Cole, M. Robertson, A. Uddin, and A. Cable, “High-sweep-rate 1310 nm MEMS-VCSEL with 150 nm continuous tuning range,” *Electron. Lett.* **48**(14), 867-869 (2012)



- [**Jayaraman2012b**] V. Jayaraman G.D. Cole, M. Robertson, C. Burgner, D. John, A. Uddin, and A. Cable, "Rapidly swept, ultra-widely-tunable 1060 nm MEMS-VCSELs," *Electron. Lett.* **48**(21), 1331-1333 (2012)
- [**Jayaraman2013**] V. Jayaraman, B. Potsaid, J. Jiang, G. D. Cole, M. E. Robertson, C. B. Burgner, D. D. John, I. Grulkowski, W. Choi, T. H. Tsai, J. Liu, B. A. Stein, S. T. Sanders, J. G. Fujimoto, and A. E. Cable, "High-speed ultra-broad tuning MEMS-VCSELs for imaging and spectroscopy," *Proc. SPIE* **8763**, 87630H (2013)
- [**Jayaraman2018**] V. Jayaraman, S. Segal, K. Lascola, C. Burgner, F. Towner, A. Cazabat, G. D. Cole, D. Follman, P. Heu, and C. Deutsch, "Room temperature continuous wave mid-infrared VCSEL operating at 3.35  $\mu\text{m}$ ," *Proc. SPIE* **10552**, 105520B (2018)
- [**Jiao2012**] Z. Jiao, J. Liu, Z. Lu, X. Zhang, P. J. Poole, P. J. Barrios, D. Poitras, and J. Caballero, "Tunable Terahertz Beat Signal Generation From an InAs/InP Quantum-Dot Mode-Locked Laser Combined With External-Cavity," *IEEE Photon. Technol. Lett.* **24**(6), 518-520 (2012)
- [**John2015**] D. D. John, C. B. Burgner, B. Potsaid, M. E. Robertson, B. Kun Lee, W. Jhon Choi, A. E. Cable, J. G. Fujimoto, and V. Jayaraman., "Wideband Electrically Pumped 1050-nm MEMS-Tunable VCSEL for Ophthalmic Imaging," *J. Lightwave Technol.* **33**(16), 3461-3468 (2015)
- [**John2016**] D. D. John, B. Lee, B. Potsaid, A. C. Kennedy, M. E. Robertson, C. B. Burgner, A. E. Cable, J. G. Fujimoto, and V. Jayaraman, "Single-Mode and High-Speed 850nm MEMS-VCSEL," in *Lasers Congress 2016 (ASSL, LSC, LAC)*, Boston, Massachusetts United State, 2016, paper ATh5A.2
- [**Jung1997**] C. Jung, R. Jager, M. Grabherr, P. Schnitzer, R. Michalzik, B. Weigl, S. Muller, and K.J. Ebeling, "4.8 mW singlemode oxide confined top-surface emitting vertical-cavity laser diodes," *Electron. Lett.* **33**(21), 1790-1791 (1997)
- [**Kantola2014**] E. Kantola, T. Leinonen, S. Ranta, M. Tavast, and M. Guina, "High-efficiency 20 W yellow VECSEL," *Opt. Express* **22**(6), 6372-6380 (2014)
- [**Kaspar2013**] S. Kaspar, M. Rattunde, T. Töpfer, R. Moser, S. Adler, C. Manz, K. Köhler, and J. Wagner, "Recent Advances in 2- $\mu\text{m}$  GaSb-Based Semiconductor Disk Laser—Power Scaling, Narrow-Linewidth and Short-Pulse Operation," *IEEE J. Sel. Topics Quantum Electron.* **19**(4), 1501908-1501908 (2013)
- [**Kaur2014**] K. S. Kaur, J. Missinne, and G. Van Steenberge, "Flip-chip bonding of vertical-cavity surface-emitting lasers using laser-induced forward transfer," *Appl. Phys. Lett.* **104**(6), 061102 (2014)
- [**Kazovsky2007**] L. G. Kazovsky, W. T. Shaw, D. Gutierrez, N. Cheng and S. W. Wong, "Next-Generation Optical Access Networks," *J. Lightwave Technol.* **25**(11), 3428-3442 (2007)
- [**Keller2015**] S. T. Keller, A. Sirbu, V. Iakovlev, A. Caliman, A. Mereuta, and E. Kapon, "8.5 W VECSEL output at 1270 nm with conversion efficiency of 59 %," *Opt. Express* **23**(13), 17437-17442 (2015)
- [**Kemp2005**] A. J. Kemp, G.J. Valentine, J.-M. Hopkins, J.E. Hastie, S.A. Smith, S. Calvez, M.D. Dawson, and D. Burns, "Thermal management in vertical-external-cavity surface-emitting lasers: finite-element analysis of a heatspreader approach," *IEEE J. Quantum Electron.* **41**(2), 148-155 (2005)
- [**Kemp2006**] A.J. Kemp, A.J. Maclean, J.E. Hastie, S.A. Smith, J.-M. Hopkins, S. Calvez, G.J. Valentine, M.D. Dawson, and D. Burns, "Thermal lensing, thermal management and transverse mode control in microchip VECSEL", *Appl. Phys. B* **83**(2), 189 (2006)

- [**Kemp2008**] A.J. Kemp, J.-M. Hopkins, A.J. Maclean, N. Schulz, M. Rattunde, J. Wagner, and D. Burns, "Thermal Management in 2.3- $\mu\text{m}$  Semiconductor Disk Lasers: A Finite Element Analysis," *IEEE J. Quantum Electron.* **44**(2), 125-135, 2008
- [**Kern2013**] A. Kern, A. Al-Samaneh, D. Wahl, and R. Michalzik, "Monolithic VCSEL-PIN Photodiode Integration for Bidirectional Optical Data Transmission," *IEEE J. Sel. Topics Quantum Electron.* **19**(4), 6100313-6100313 (2013)
- [**Kervella2015**] G. Kervella, F. Van Dijk, G. Pillet, M. Lamponi, M. Chtioui, L. Morvan, and M. Alouini, "Optoelectronic cross-injection locking of a dual-wavelength photonic integrated circuit for low-phase-noise millimeter-wave generation," *Opt. Lett.* **40**(15), 3655-3658 (2015)
- [**Khan2013**] M.Z.M. Khan, T.K. Ng, Chi-Sen Lee, P. Bhattacharya, and B. S. Ooi, "Chirped InAs/InP quantum-dash laser with enhanced broad spectrum of stimulated emission," *Appl. Phys. Lett.* **102**(9), 091102 (2013)
- [**Khan2014**] M. Z. M. Khan, T. K. Ng, and B. S. Ooi, "Self-assembled InAs/InP quantum dots and quantum dashes: Material structures and devices", *Prog. Quant. Electron.* **38**(6), 237-313 (2014)
- [**Kim2006**] T. Kim, J. Yoo, K. Kim, S. Lee, S. Lim, G. Kim, J. Kim, S. Cho, J. Lee, and Y. Park, "2 W continuous wave operation of optically pumped blue VECSEL with frequency doubling," *Proc. SPIE* **6132**, 61320K (2006)
- [**Kim2012**] N. Kim, S.-P. Han, H.-C. Ryu, H. Ko, J.-W. Park, D. Lee, M.Y. Jeon, and K. H. Park, "Distributed feedback laser diode integrated with distributed Bragg reflector for continuous-wave terahertz generation," *Opt. Express* **20**(16), 17496-17502 (2012)
- [**Klaime2013**] K. Klaime, R. Piron, F. Grillot, M. Dontabactouny, S. Loualiche, A. Le Corre, K. Yvind, "Systematic investigation of the temperature behavior of InAs/InP quantum nanostructure passively mode-locked lasers," *Proc. SPIE* **8634**, 863407 (2013)
- [**Klopp2011**] P. Klopp, U. Griebner, M. Zorn, and M. Weyers, "Pulse repetition rate up to 92 GHz or pulse duration shorter than 110 fs from a mode-locked semiconductor disk laser," *Appl. Phys. Lett.* **98**(7), 071103 (2011)
- [**Koechner1996**] W. Koechner, *Solid-state laser engineering, 4<sup>th</sup> ed.* (Springer-Verlag Berlin Heidelberg, 1996)
- [**Kogelnik1965**] H. Kogelnik, "On the Propagation of Gaussian Beams of Light Through Lenslike Media Including those with a Loss or Gain Variation," *Appl. Opt.* **4**(12), 1562-1569 (1965)
- [**Kogelnik1966**] H. Kogelnik and T. Li, "Laser Beams and Resonators," *Appl. Opt.* **5**(10), 1550-1567 (1966)
- [**Koyama1989**] F. Koyama, S. Kinoshita, and K. Iga "Room-temperature continuous wave lasing characteristics of a GaAs vertical cavity surface-emitting laser," *Appl. Phys. Lett.* **55**(3), 221-222 (1989)
- [**Koyama1991**] F. Koyama, K. Morito, and K. Iga, "Intensity noise and polarization stability of GaAlAs-GaAs surface emitting lasers," *IEEE J. Quantum Electron.* **27**(6), 1410-1416 (1991)
- [**Kuchta2015**] D. M. Kuchta, A. V. Rylyakov, F. E. Doany, C. L. Schow, J. E. Proesel, C. W. Baks, P. Westbergh, J. S. Gustavsson, and A. Larsson, "A 71-Gb/s NRZ Modulated 850-nm VCSEL-Based Optical Link," *IEEE Photon. Technol. Lett.* **27**(6), 577-580 (2015)

## Bibliography

- [**Kuchta2016**] D. M. Kuchta, T. N. Huynh, F. E. Doany, L. Schares, C. Baks, C. Neumeyr, A. Daly, B. Kögel, J. Rosskopf, and M. Ortsiefer, “Error-Free 56 Gb/s NRZ Modulation of a 1530-nm VCSEL Link,” *J. Lightwave Technol.* **34**(14), 3275-3282 (2016)
- [**Kuznetsov1997**] M. Kuznetsov, F. Hakimi, R. Sprague, and A. Mooradian, “High-power (>0.5-W CW) diode-pumped vertical-external-cavity surface-emitting semiconductor lasers with circular TEM<sub>00</sub> beams,” *IEEE Photon. Technol. Lett.* **9**(8), 1063-1065 (1997)
- [**Kuznetsov1999**] M. Kuznetsov, F. Hakimi, R. Sprague, and A. Mooradian, “Design and characteristics of high-power (>0.5-W CW) diode-pumped vertical-external-cavity surface-emitting semiconductor lasers with circular TEM<sub>00</sub> beams,” *IEEE J. Sel. Topics Quantum Electron.* **5**(3), 561-573 (1999)
- [**Lahtinen1986**] J.A. Lahtinen, “Electroreflectance study of the Burstein-Moss shift in indium phosphide,” *Phys. Rev. B* **33**(4), 2550-2553 (1986)
- [**Lamb1964**] W. E. Lamb, Jr., “Theory of an optical maser,” *Phys. Rev.* **134**(6A), A1429 (1964).
- [**Lamy2008**] J.M. Lamy, “Emetteurs optiques à nanostructures quantiques rapportés sur substrat silicium,” Ph.D. dissertation, Institut National des Sciences Appliquées de Rennes, Rennes, (2008)
- [**Lamy2009**] J. M. Lamy, C. Paranthoën, C. Levallois, A. Nakkar, H. Folliot, J. P. Gauthier, O. Dehaese, A. Le Corre, and S. Loualiche, “Polarization control of 1.6 m vertical-cavity surface-emitting lasers using InAs”, *Appl. Phys. Lett.* **95**(1), 011117 (2009)
- [**Larisch2016**] G. Larisch, P. Moser, J. A. Lott, and D. Bimberg, “Impact of Photon Lifetime on the Temperature Stability of 50 Gb/s 980 nm VCSELs,” *IEEE Photon. Technol. Lett.* **28**(21), 2327-2330 (2016)
- [**Larsson2018**] A. Larsson, E. Simpanen, J.S. Gustavsson, E. Haglund, E.P. Haglund, T. Lengyel, P.A. Andrekson, W.V. Sorin, S. Mathai, M. Tan, and S.R. Bickham, “1060 nm VCSELs for long-reach optical interconnects,” *Opt. Fiber Technol.* **44**, 36-42 (2018)
- [**Lau1988**] K.Y. Lau, “Efficient narrowband direct modulation of semiconductor injection lasers at millimeter wave frequencies of 100 GHz and beyond,” *Appl. Phys. Lett.* **52**(26), 2214 (1988)
- [**Laurain2009**] A. Laurain, M. Myara, G. Beaudoin, I. Sagnes, and A. Garnache, “High power single-frequency continuously-tunable compact extended-cavity semiconductor laser,” *Opt. Express* **17**(12), 9503-9508 (2009)
- [**Laurain2014**] A. Laurain, C. Mart, J. Hader, J. Moloney, B. Kunert, and W. Stolz, “Optical noise of stabilized high-power single frequency optically pumped semiconductor laser,” *Opt. Lett.* **39**(6), 1573-1576 (2014)
- [**Laurand2006**] N. Laurand, S. Calvez, H. D. Sun, M. D. Dawson, J. A. Gupta, and G. C. Aers, “C-band emission from GaInNAsSb VCSEL on GaAs,” *Electron. Lett.* **42**(1), 29-30 (2006)
- [**Law1997**] Y. Law and G.P. Agrawal, “Mode-partition noise in vertical-cavity surface-emitting lasers,” *IEEE Photon. Technol. Lett.* **9**(4), 437-439 (1997)
- [**Lear1994**] K. L. Lear, R. P. Schneider, K. D. Choquette, S. P. Kilcoyne, J. J. Figiel, and J. C. Zolper, “Vertical cavity surface emitting lasers with 21% efficiency by metalorganic vapor phase epitaxy,” *IEEE Photon. Technol. Lett.* **6**(9), 1053-1055 (1994)

- [**Lee1989**] Y. H. Lee, J. L. Jewell, A. Scherer, S. L. McCall, J. P. Harbison, and L. T. Florez, "Room-temperature continuous-wave vertical-cavity single-quantum-well microlaser diodes," *Electron. Lett.* **25**(20), 1377-1378 (1989)
- [**Lee1991**] Y. H. Lee, B. Tell, K. F. Brown-Goebeler, R. E. Leibenguth, and V. D. Mittera, "Deep-red continuous wave top-surface-emitting vertical-cavity AlGaAs superlattice lasers," *IEEE Photon. Technol. Lett.* **3**(2), 108-109 (1991)
- [**Lee2009**] H.K. Lee, Y.M. Song, Y.T. Lee, and J.S. Yu, "Thermal analysis of asymmetric intracavity-contacted oxide-aperture VCSELs for efficient heat dissipation," *Solid-State Electron.* **53**(10), 1086-1091 (2009)
- [**Le Gouët2007**] J. Le Gouët, L. Morvan, M. Alouini, J. Bourderionnet, D. Dolfi, and J.-P. Huignard, "Dual-frequency single-axis laser using a lead lanthanum zirconate tantalate (PLZT) birefringent etalon for millimeter wave generation: beyond the standard limit of tunability," *Opt. Lett.* **32**(9), 1090-1092 (2007)
- [**Leinonen2013**] T. Leinonen, S. Ranta, M. Tavast, R. Epstein, G. Fetzer, Sandalphon, N. Van Lieu, and M. Guina, "High power (23W) vertical external cavity surface emitting laser emitting at 1180 nm," *Proc. SPIE* **8606**, 860604 (2013)
- [**Leinonen2017**] T. Leinonen, V. Iakovlev, A. Sirbu, E. Kapon, and M. Guina, "33 W continuous output power semiconductor disk laser emitting at 1275 nm," *Opt. Express* **25**(6), 7008-7013 (2017)
- [**Lelarge2007**] F. Lelarge, B. Dagens, J. Renaudier, R. Brenot, A. Accard, F. v. Dijk, D. Make, O. L. Gouezigou, J. G. Provost, F. Poingt, J. Landreau, O. Drisse, E. Derouin, B. Rousseau, F. Pommereau, G. H. Duan, "Recent Advances on InAs/InP Quantum Dash Based Semiconductor Lasers and Optical Amplifiers Operating at 1.55  $\mu\text{m}$ ," *IEEE J. Sel. Topics Quantum Electron.* **13**(1), 111-124 (2007)
- [**Levallois2006a**] C. Levallois, "Étude et réalisation de lasers à cavité verticale mono et multi-longueurs d'onde émettant à 1,55  $\mu\text{m}$ ," Ph.D. dissertation, Institut National des Sciences Appliquées de Rennes, Rennes, (2006)
- [**Li2000**] Y.F. Li, F.Q. Liu, B. Xu, X.L. Ye, D. Ding, Z.Z. Sun, W.H. Jiang, H.Y. Liu, Y.C. Zhang, and Z.G. Wang, "Two-dimensional ordering of self-assembled InAs quantum dots grown on (311)B InP substrate," *J. Cryst. Growth* **219**(1), 17-21 (2000)
- [**Li2001**] Yifei Li, A. J. C. Vieira, S. M. Goldwasser, and P. R. Herczfeld, "Rapidly tunable millimeter-wave optical transmitter for lidar-radar," *IEEE Trans. Microw. Theory Tech.* **49**(10), 2048-2054 (2001)
- [**Li2005**] C.B. Li, Y.H. Zuo, B.W. Cheng, R.W. Mao, L. Zhao, W.H. Shi, L.P. Luo, J.Z. Yu, and Q.M. Wang, "Thermally tunable optical filter with crystalline silicon as cavity," *Opt. Commun.* **244**(1-6), 167-170 (2005)
- [**Li2009**] S.G. Li, Q. Gong, Y.F. Lao, H.D. Yang, S. Gao, P. Chen, Y.G. Zhang, S.L. Feng, and H.L. Wang, "Two-color quantum dot laser with tunable wavelength gap," *Appl. Phys. Lett.* **95**, 251111 (2009)
- [**Liau1990**] Z. L. Liau and D. E. Mull, "Wafer fusion: A novel technique for optoelectronic device fabrication and monolithic integration," *Appl. Phys. Lett.* **56**(8), 737-739 (1990)
- [**Lindberg2004a**] H. Lindberg, M. Strassner, J. Bengtsson, and A. Larsson, "InP-based optically pumped VCSEL operating CW at 1550 nm," *IEEE Photon. Technol. Lett.* **16**(2), 362-364 (2004)

## Bibliography

- [**Lindberg2004b**] H. Lindberg, M. Strassner, J. Bengtsson and A. Larsson, “High-power optically pumped 1550-nm VECSEL with a bonded silicon heat spreader,” *IEEE Photon. Technol. Lett.* **16**(5), 1233-1235 (2004)
- [**Lindberg2004c**] H. Lindberg, M. Strassner, E. Gerster and A. Larsson, “0.8 W optically pumped vertical external cavity surface emitting laser operating CW at 1550 nm,” *Electron. Lett.* **40**(10), 601-602 (2004)
- [**Lindberg2005**] H. Lindberg, A. Larsson, and M. Strassner, “Single-frequency operation of a high-power, long-wavelength semiconductor disk laser,” *Opt. Lett.* **30**(17), 2260-2262 (2005)
- [**Link2015**] S. Link, A. Klenner, M. Mangold, C. Zaugg, M. Golling, B. Tilma, and U. Keller, “Dual-comb modelocked laser,” *Opt. Express* **23**(5), 5521-5531 (2015)
- [**Link2016**] S. Link, A. Klenner, and U. Keller, “Dual-comb modelocked lasers: semiconductor saturable absorber mirror decouples noise stabilization,” *Opt. Express* **24**(3), 1889-1902 (2016)
- [**Link2017**] S. M. Link, D. J. H. C. Maas, D. Waldburger, and U. Keller, “Dual-comb spectroscopy of water vapor with a free-running semiconductor disk laser,” *Science* **356**, 1164–1168 (2017)
- [**Linnik2001**] M. Linnik and A. Christou, “Design and performance of a vertical cavity surface emitting laser based on III-V quaternary semiconductor alloys for operation at 1.55  $\mu\text{m}$ ,” *IEEE Trans. Electron Devices* **48**(10), 2228-2237 (2001)
- [**Liu1999**] G. Liu, A. Stintz, H. Li, K. J. Malloy, and L. F. Lester, “Extremely low room-temperature threshold current density diode lasers using InAs dots in  $\text{In}_{0.15}\text{Ga}_{0.85}\text{As}$  quantum well,” *Electron. Lett.* **35**(14), 1163-1165 (1999)
- [**Liu2010**] H. Liu, C. F. Lam, and C. Johnson, “Scaling Optical Interconnects in Datacenter Networks Opportunities and Challenges for WDM,” in *2010 18<sup>th</sup> IEEE Symposium on High Performance Interconnects*, Mountain View, CA, 2010, pp. 113-116
- [**Lo1991**] Y. H. Lo, R. Bhat, D. M. Hwang, M. A. Koza, and T. P. Lee, “Bonding by atomic rearrangement of InP/InGaAsP 1.5  $\mu\text{m}$  wavelength lasers on GaAs substrates,” *Appl. Phys. Lett.* **58**(18), 1961-1963 (1991)
- [**Lott2005**] J. A. Lott, A. R. Kovsh, N. N. Ledentsov and D. Bimberg, “GaAs-Based InAs/InGaAs Quantum Dot Vertical Cavity and Vertical External Cavity Surface Emitting Lasers Emitting Near 1300 nm,” in *2005 Pacific Rim Conference on Lasers & Electro-Optics*, Tokyo, 2005, pp. 160-161, paper CTuJ2-2
- [**Lu2008**] T.-C. Lu, C.-C. Kao, H.-C. Kuo, G.-S. Huang, and S.-C. Wang, “CW lasing of current injection blue GaN-based vertical cavity surface emitting laser,” *Appl. Phys. Lett.* **92**(14), 141102 (2008)
- [**Lukowski2015**] M. Lukowski, C. Hessenius, and M. Fallahi, “Widely Tunable High-Power Two-Color VECSELs for New Wavelength Generation,” *IEEE J. Sel. Topics Quantum Electron.* **21**(1), 432-439 (2015)
- [**Lv2008**] J. Lv, H. Huang, X. Ren, A. Miao, Y. Li, H. Song, Q. Wang, Y. Huang, and S. Cai, “Monolithically Integrated Long-Wavelength Tunable Photodetector,” *J. Lightwave Technol.* **26**(3), 338-342 (2008)
- [**Lyytikäinen2009**] J. Lyytikäinen, J. Rautiainen, L. Toikkanen, A. Sirbu, A. Mereuta, A. Caliman, E. Kapon, and O. Okhotnikov, “1.3- $\mu\text{m}$  optically-pumped semiconductor disk laser by wafer fusion,” *Opt. Express* **17**(11), 9047-9052 (2009)



- [**Lyytikäinen2011**] J. Lyytikäinen, J. Rautiainen, A. Sirbu, V. Iakovlev, A. Laakso, S. Ranta, M. Tavast, E. Kapon, and O. G. Okhotnikov, “High-Power 1.48- $\mu\text{m}$  Wafer-Fused Optically Pumped Semiconductor Disk Laser,” *IEEE Photon. Technol. Lett.* **23**(13), 917-919 (2011)
- [**Ma2017**] Y. J. Ma, Y. G. Zhang, Y. Gu, S. P. Xi, X. Y. Chen, Baolai Liang, Bor-Chau Juang, Diana L. Huffaker, B. Du, X. M. Shao, and J. X. Fang, “Behaviors of beryllium compensation doping in InGaAsP grown by gas source molecular beam epitaxy,” *AIP Advances* **7**(7), 075117 (2017)
- [**Maas2007**] D. J. H. C. Maas, A.-R. Bellancourt, B. Rudin, M. Golling, H. J. Unold, T. Südmeyer, and U. Keller, “Vertical integration of ultrafast semiconductor lasers,” *Appl. Phys. B* **88**(4), 493-497 (2007)
- [**Mangold2013**] M. Mangold, V. Wittwer, C. Zaugg, S. Link, M. Golling, B. Tilma, and U. Keller, “Femtosecond pulses from a modelocked integrated external-cavity surface emitting laser (MIXSEL),” *Opt. Express* **21**(21), 24904-24911 (2013)
- [**Mangold2014**] M. Mangold, C. Zaugg, S. Link, M. Golling, B. Tilma, and U. Keller, “Pulse repetition rate scaling from 5 to 100 GHz with a high-power semiconductor disk laser,” *Opt. Express* **22**(5), 6099-6107 (2014)
- [**Markus2003**] A. Markus, J. X. Chen, C. Paranthoën, and A. Fiore, “Simultaneous two-state lasing in quantum-dot lasers,” *Appl. Phys. Lett.* **82**(12), 1818 (2003)
- [**Masabih2017**] S. Mishkat-Ul-Masabih, J. Leonard, D. Cohen, S. Nakamura, and D. Feezell, “Techniques to reduce thermal resistance in flip-chip GaN-based VCSELs,” *Phys. Status Solidi A*, **214**(8), 1770149 (2017)
- [**Mateo2016**] C. Mateo, U. Brauch, H. Kahle, T. Schwarzbäck, M. Jetter, M. Ahmed, P. Michler, and T. Graf, “2.5 W continuous wave output at 665 nm from a multipass and quantum-well-pumped AlGaInP vertical-external-cavity surface-emitting laser,” *Opt. Lett.* **41**(6), 1245-1248 (2016)
- [**Mathine1996**] D.L. Mathine, H. Nejad, D.R. Allee, R. Droopad, G.N. Maracas, “Reduction of the thermal impedance of vertical-cavity surface-emitting lasers after integration with copper substrates,” *Appl. Phys. Lett.* **69** (4), 463 (1996)
- [**Matlab**] “MatWorks MATLAB® website”: <https://www.mathworks.com/>
- [**Matweb**] Matweb (online materials database) website: <http://www.matweb.com/>
- [**McKay2007**] A. McKay, J. M. Dawes, and J.-D. Park, “Polarisation-mode coupling in (100)-cut Nd:YAG,” *Opt. Express* **15**(25), 16342-16347 (2007)
- [**Melati2016**] D. Melati, A. Waqas, A. Alippi, and A. Melloni, “Wavelength and composition dependence of the thermo-optic coefficient for InGaAsP-based integrated waveguides”, *J. Appl. Phys.* **120**(21), 213102 (2016)
- [**Mereuta2008**] A. Mereuta, V. Iakovlev, A. Caliman, A. Syrbu, A. Rudra, and E. Kapon, “2- $\mu\text{m}$  wavelength range InGa(Al)As/InP-AlGaAs/GaAs wafer fused VCSELs for spectroscopic applications,” in *20<sup>th</sup> International Conference on Indium Phosphide and Related Materials*, Versailles, 2008, pp. 1-3
- [**Mereuta2015**] A. Mereuta, A. Caliman, A. Sirbu, V. Iakovlev, Z. Mickovic, G. Suruceanu, and E. Kapon, “Increasing single mode power of 1.3- $\mu\text{m}$  VCSELs by output coupling optimization,” *Opt. Express* **23**(9), 10900-10904 (2015)

## Bibliography

- [**Michalzik2013**] R. Michalzik, *VCSELs Fundamentals, Technology and Applications of VCSELs* (Springer-Verlag Berlin Heidelberg, 2013)
- [**Mihoubi2008**] Z. Mihoubi, K. Wilcox, S. Elsmere, A. Quarterman, R. Rungsawang, I. Farrer, H. Beere, D. Ritchie, A. Tropper, and V. Apostolopoulos, "All-semiconductor room-temperature terahertz time domain spectrometer," *Opt. Lett.* **33**(18), 2125-2127 (2008)
- [**Millo2009**] J. Millo, D. V. Magalhães, C. Mandache, Y. Le Coq, E. M. L. English, P. G. Westergaard, J. Lodewyck, S. Bize, P. Lemonde, and G. Santarelli, "Ultrastable lasers based on vibration insensitive cavities," *Phys. Rev. A* **79**, 053829 (2009)
- [**Miyamoto2003**] T. Miyamoto, S. Makino, Y. Ikenaga, M. Ohta, F. Koyama, "Wavelength elongation of GaInNAs lasers beyond 1.3  $\mu\text{m}$ ," *IEE Proc. Optoelectron.* **150**(1), 59-63 (2003)
- [**Mizunami2016**] T. Mizunami, T. Yamada, and S. Tsuchiya, "Interrogation of fiber-Bragg-grating temperature and strain sensors with a temperature-stabilized VCSEL," *Opt. Rev.* **23**(5), 703-77 (2016)
- [**Moench2016**] H. Moench, R. Conrads, S. Gronenborn, X. Gu, M. Miller, P. Pekarski, J. Pollmann-Retsch, A. Pruijboom, and U. Weichmann, "Integrated high power VCSEL systems," *Proc. SPIE* **9733**, 97330V (2016)
- [**Morton2007**] L. Morton, H. Foreman, J. Hastie, M. Dawson, and E. Riis, "Actively Stabilised Single-Frequency Red VECSEL," in *Advanced Solid-State Photonics*, OSA Technical Digest Series (CD) (Optical Society of America, 2007), paper WB7
- [**Moss1954**] T.S. Moss, "The Interpretation of the Properties of Indium Antimonide," *Proc. Phys. Soc.* **67**(10), 775-782 (1954)
- [**Muller2011**] M. Muller, W. Hofmann, T. Grundl, M. Horn, P. Wolf, R. D. Nagel, E. Ronneberg, G. Böhm, D. Bimberg, and M.-C. Amann "1550-nm High-Speed Short-Cavity VCSELs," *IEEE J. Sel. Topics Quantum Electron.* **17**(5), 1158-1166 (2011)
- [**Müller2012**] M. Müller Wolf, T. Gründl, C. Grasse, J. Roskopf, W. Hofmann, D. Bimberg, and M.-C. Amann, "Energy-efficient 1.3  $\mu\text{m}$  short-cavity VCSELs for 30 Gb/s error-free optical links," *ISLC 2012 23<sup>rd</sup> International Semiconductor Laser Conference*, San Diego, CA, 2012, pp. 1-2
- [**Munoz2001**] M. Munoz, F.H. Pollak, M. Kahn, D. Ritter, L. Kronik, G.M. Cohen, "Burstein-Moss shift of n-doped  $\text{In}_{0.53}\text{Ga}_{0.47}\text{As}/\text{InP}$ ," *Phys. Rev. B* **63**(23), 233302 (2001)
- [**Musiał2012**] Musiał, P. Kaczmarkiewicz, G. Sęk, P. Podemski, P. Machnikowski, J. Misiewicz, S. Hein, S. Höfling, and A. Forchel, "Carrier trapping and luminescence polarization in quantum dashes," *Phys. Rev. B* **85**, 035314 (2012)
- [**Nagarajan1993**] R. Nagarajan, S. Levy, A. Mar, and J.E. Bowers, "Resonantly enhanced semiconductor lasers for efficient transmission of millimeter wave modulated light," *IEEE Photon. Technol. Lett.* **5**(1), 4-6 (1993)
- [**LabVIEW**] National Instruments LabVIEW® website: "<http://www.ni.com>"
- [**Nakagawa2001**] S. Nakagawa, E. Hall, G. Almuneau, J. K. Kim, D. A. Buell, H. Kroemer, and L. A. Coldren, "1.55- $\mu\text{m}$  InP-lattice-matched VCSELs with AlGaAsSb-AlAsSb DBRs," *IEEE J. Sel. Topics Quantum Electron.* **7**(2), 224-230 (2001)

- [**Nishida2005**] T. Nishida, M. Takaya, S. Kakinuma, and T. Kaneko, "4.2-mW GaInNAs long-wavelength VCSEL grown by metalorganic chemical vapor deposition," *IEEE J. Sel. Topics Quantum Electron.* **11**(5), 958-961 (2005)
- [**Ohiso2002**] Y. Ohiso, H. Okamoto, R. Iga, K. Kishi, and C. Amano, "Single transverse mode operation of 1.55- $\mu\text{m}$  buried heterostructure vertical-cavity surface-emitting lasers," *IEEE Photon. Technol. Lett.* **14**(6), 738-740 (2002)
- [**Okhotnikov2010**] O. G. Okhotnikov, *Semiconductor Disk Lasers* (Wiley-VCH Verlag GmbH & Co. KGaA, 2010)
- [**Ooi2008**] B. S. Ooi, H. Susanto Djie, Y. Wang, C. L. Tan, J. C. M. Hwang, X. M. Fang, J. M. Fastenau, A. W. K. Liu, G. T. Dang, and W. H. Chang, "Quantum Dashes on InP Substrate for Broadband Emitter Applications," *IEEE J. Sel. Topics Quantum Electron.* **14**(4), 1230-1238 (2008)
- [**Orenstein1990**] M. Orenstein, A. C. Von Lehmen, C. Chang-Hasnain, N. G. Stoffel, J. P. Harbison, L. T. Florez, E. Clausen, and J. E. Jewell, "Vertical-cavity surface-emitting InGaAs/GaAs lasers with planar lateral definition," *Appl. Phys. Lett.* **56**(24), 2384-2386 (1990)
- [**Ortsiefer2000**] M. Ortsiefer, R. Shau, G. Böhm, F. Köhler, G. Abstreiter, and M.-C. Amann, "Low-resistance InGa(Al)As Tunnel Junctions for Long Wavelength Vertical-cavity Surface-emitting Lasers" *Jpn. J. Appl. Phys.* **39**(4R), 1727-1729 (2000)
- [**Ortsiefer2005**] M. Ortsiefer, S. Baydar, K. Windhorn, G. Bohm, J. Roskopf, R. Shau, E. Ronneberg, W. Hofmann, and M.-C. Amann, "2.5-mW single-mode operation of 1.55- $\mu\text{m}$  buried tunnel junction VCSELs," *IEEE Photon. Technol. Lett.* **17**(8), 1596-1598(2005)
- [**Osborne2008**] S. Osborne, S. O'brien, E. P. O'reilly, P. G. Huggard, and B. N. Ellison, "Generation of CW 0.5 THz radiation by photomixing the output of a two-colour 1.49  $\mu\text{m}$  Fabry-Perot diode laser," *Electron. Lett.* **44**(4), 296-297 (2008)
- [**Ouvrard2005**] A. Ouvrard, A. Garnache, L. Cerutti, F. Genty, and D. Romanini, "Single-frequency tunable Sb-based VCSELs emitting at 2.3  $\mu\text{m}$ ," *IEEE Photon. Technol. Lett.* **17**(10), 2020-2022 (2005)
- [**Paajaste2009**] J. Paajaste, S. Suomalainen, R. Koskinen, A. Härkönen, M. Guina, and M. Pessa, "High-power and broadly tunable GaSb-based optically pumped VECSELs emitting near 2 $\mu\text{m}$ ," *J. Cryst. Growth* **311**(7), 1917-1919 (2009)
- [**Paajaste2011**] J. Paajaste, R. Koskinen, J. Nikkinen, S. Suomalainen, and O.G Okhotnikov, "Power scalable 2.5  $\mu\text{m}$  (AlGaIn)(AsSb) semiconductor disk laser grown by molecular beam epitaxy", *J. Cryst. Growth* **323**(1), 454-456 (2011)
- [**Pabœuf2016**] D. Pabœuf and J.E. Hastie, "Tunable narrow linewidth AlGaInP semiconductor disk laser for Sr atom cooling applications," *Appl. Opt.* **55**(19),4980-4984 (2016)
- [**Pal2010**] V. Pal, P. Trofimoff, B. Miranda, G. Baili, M. Alouini, L. Morvan, D. Dolfi, F. Goldfarb, I. Sagnes, R. Ghosh, and F. Bretenaker, "Measurement of the coupling constant in a two-frequency VECSEL," *Opt. Express* **18**(5), 5008-5014 (2010)
- [**Pallmann2013**] W. P. Pallmann, C.A. Zaugg, M. Mangold, I. Dahhan, M. Golling, B.W. Tilma, B. Witzigmann, and U. Keller, "Ultrafast Electrically Pumped VECSELs," *IEEE Photon. J.* **5**(4), 1501207-1501207 (2013)



## Bibliography

- [**Paranthoën2001**] C. Paranthoën, N. Bertru, O. Dehaese, A. Le Corre, S. Loualiche, B. Lambert, and G. Patriarche, “Height dispersion control of InAs/InP quantum dots emitting at 1.55  $\mu\text{m}$ ,” *Appl. Phys. Lett.* **78**(12), 1751-1753 (2001)
- [**Park2003**] S.-H. Park, J. Kim, H. Jeon, T. Sakong, S.-N. Lee, S. Chae, Y. Park, C.-H. Jeong, G.-Y. Yeom, and Y.-H. Cho, “Room-temperature GaN vertical-cavity surface-emitting laser operation in an extended cavity scheme”, *Appl. Phys. Lett.* **83**(11), 2121-2123 (2003)
- [**Park2006**] M. R. Park, O. K. Kwon, W. S. Han, K. H. Lee, S. J. Park, and B. S. Yoo, “All-epitaxial InAlGaAs-InP VCSELs in the 1.3-1.6- $\mu\text{m}$  wavelength range for CWDM band applications,” *IEEE Photon. Technol. Lett.* **18**(16), 1717-1719 (2006)
- [**Paul2016**] S. Paul, M. T. Haidar, J. Cesar, M. Malekizandi, B. Kögel, C. Neumeyr, M. Ortsiefer, and F. Küppers, “Far-field, linewidth and thermal characteristics of a high-speed 1550-nm MEMS tunable VCSEL,” *Opt. Express* **24**(12), 13142-13156 (2016)
- [**Peng2013**] P. C. Peng, K. C. Shiu, C. H. Chang, Y. C. Shu, Y. T. Lin, and H. H. Lu, “Vertical-Cavity Surface-Emitting Laser for Tunable Microwave Photonic Filter,” *IEEE J. Sel. Topics Quantum Electron.* **19**(4), 1701605-1701605 (2013)
- [**Pillet2008**] G. Pillet, L. Morvan, M. Brunel, F. Bretenaker, D. Dolfi, M. Vallet, J.-P. Huignard, and A. Le Floch, “Dual-Frequency Laser at 1.5  $\mu\text{m}$  for Optical Distribution and Generation of High-Purity Microwave Signals,” *J. Lightwave Technol.* **26**, 2764-2773 (2008)
- [**Piprek1995**] J. Piprek, H. Wenzel, H.-J. Wuensche, D. Braun, and F. Henneberger, “Modeling light versus current characteristics of long-wavelength VCSELs with various DBR materials,” *Proc. SPIE* **2399**, 605 (1995)
- [**Platz2005**] C. Platz, C. Paranthoën, P. Caroff, N. Bertru, C. Labbé, J. Even, O. Dehaese, H. Folliot, A. Le Corre, S. Loualiche, G. Moreau, J. C. Simon, and A. Ramdane, “Comparison of InAs quantum dot lasers emitting at 1.55  $\mu\text{m}$  under optical and electrical injection,” *Semicond. Scie. Technol.* **20**(5), 459-463 (2005)
- [**Polo2003**] V. Polo, B. Vidal, J. L. Corral, and J. Marti, “Novel tunable photonic microwave filter based on laser arrays and  $N \times N$  AWG-based delay lines,” *IEEE Photon. Technol. Lett.* **15**(4), 584-586 (2003)
- [**Potsaid2012**] B. Potsaid, V. Jayaraman, J. Y. Jiang, A. E. Cable, P. J. S. Heim, I. Grulkowski, and J. G. Fujimoto, “1065nm and 1310nm MEMS tunable VCSEL light source technology for OCT imaging,” *SPIE Newsroom*, 20 August 2012, DOI: 10.1117/2.1201207.004347
- [**Pryor2015**] R.W. Pryor, *Multiphysics Modeling Using COMSOL 5 and MATLAB* (Mercury Learning & Information, 2015)
- [**Pu1999**] R. Pu, C. Duan, and C. W. Wilmsen, “Hybrid integration of VCSEL's to CMOS integrated circuits,” *IEEE J. Sel. Topics Quantum Electron.* **5**(2), 201-208 (1999)
- [**Qi2005**] G. Qi, J. Yao, J. Seregelyi, S. Paquet, and C. Belisle, “Generation and distribution of a wide-band continuously tunable millimeter-wave signal with an optical external modulation technique,” *IEEE Trans. Microw. Theory Techn.* **53**(10), 3090-3097 (2005)
- [**Qi2011**] X. Q. Qi and J. M. Liu, “Photonic Microwave Applications of the Dynamics of Semiconductor Lasers,” *IEEE J. Sel. Topics Quantum Electron.* **17**(5), 1198-1211 (2011)

- [**Quirce2012**] A. Quirce and A. Valle, "High-frequency microwave signal generation using multi-transverse mode VCSELs subject to two-frequency optical injection," *Opt. Express* **20**(12), 13390-13401 (2012)
- [**Rafailov2014**] E. U. Rafailov, *The Physics and Engineering of Compact Quantum Dot-based Lasers for Biophotonics* (Wiley-VCH Verlag GmbH & Co. KGaA, 2014)
- [**Ram1995**] R. J. Ram, J. J. Dudley, J. E. Bowers, L. Yang, K. Carey, S. J. Rosner, and K. Nauka, "GaAs to InP wafer fusion," *J. Appl. Phys.* **78**(6), 4227-4237 (1995)
- [**Rantamäki2012a**] A. Rantamäki, J. Rautiainen, J. Lyytikäinen, A. Sirbu, A. Mereuta, E. Kapon, and O. Okhotnikov, "1 W at 785 nm from a frequency-doubled wafer-fused semiconductor disk laser," *Opt. Express* **20**(8), 9046-9051 (2012)
- [**Rantamäki2012b**] A. Rantamäki, J. Rautiainen, L. Toikkanen, I. Krestnikov, M. Butkus, E. U. Rafailov, and O. Okhotnikov, "Flip Chip Quantum-Dot Semiconductor Disk Laser at 1200 nm," *IEEE Photon. Technol. Lett.* **24**(15), 1292-1294 (2012)
- [**Rantamäki2012c**] A. Rantamäki, A. Chamorovskiy, J. Lyytikäinen, and O. Okhotnikov, "4.6-W Single Frequency Semiconductor Disk Laser With <75-kHz Linewidth," *IEEE Photon. Technol. Lett.* **24**(16), 1378-1380 (2012)
- [**Rantamäki2013**] A. Rantamäki, J. Rautiainen, A. Sirbu, A. Mereuta, E. Kapon, and O. Okhotnikov, "1.56  $\mu\text{m}$  1 watt single frequency semiconductor disk laser," *Opt. Express* **21**(2), 2355-2360 (2013)
- [**Rantamäki2015**] A. Rantamäki, G. Sokolovskii, S. Blokhin, V. Dudelev, K. Soboleva, M. Bobrov, A. Kuzmenkov, A. Vasil'ev, A. Gladyshev, N. Maleev, V. Ustinov, and O. Okhotnikov, "Quantum dot semiconductor disk laser at 1.3  $\mu\text{m}$ ," *Opt. Lett.* **40**(14), 3400-3403 (2015)
- [**Rautiainen2008**] J. Rautiainen, J. Lyytikäinen, A. Sirbu, A. Mereuta, A. Caliman, E. Kapon, and O. Okhotnikov, "2.6 W optically-pumped semiconductor disk laser operating at 1.57- $\mu\text{m}$  using wafer fusion," *Opt. Express* **16**(26), 21881-21886 (2008)
- [**Rautiainen2010**] J. Rautiainen, I. Krestnikov, M. Butkus, E. Rafailov, and O. Okhotnikov, "Optically pumped semiconductor quantum dot disk laser operating at 1180 nm," *Opt. Lett.* **35**(5), 694-696 (2010)
- [**Reddy2003**] M. H. M. Reddy, D. A. Buell, A. S. Huntington, T. Asano, R. Koda, D. Feezell, D. Lofgreen, and L. A. Coldren, "Al<sub>0.95</sub>Ga<sub>0.05</sub>As<sub>0.56</sub>Sb<sub>0.44</sub> for lateral oxide-confinement layer in InP-based devices," *Appl. Phys. Lett.* **82**(9), 1329-1331 (2003)
- [**Redwing1996**] J.M. Redwing, D.A.S. Loeber, N.G. Anderson, M.A. Tischler, and J.S. Flynn, "An optically pumped GaN-AlGaN vertical cavity surface emitting laser," *Appl. Phys. Lett.* **69**(1), 1-3 (1996)
- [**Reid1993**] B. Reid, R. Maciejko, Roman, and A. Champagne, "Absorption and index of refraction for the modeling of InGaAsP/InP photonic devices," *Can. J. Phys.* **71**(9-10), 410-416 (1993)
- [**Reithmaier2005**] J. P. Reithmaier, A. Somers, S. Deubert, R. Schwertberger, W. Kaiser, A. Forchel, M. Calligaro, P. Resneau, O. Parillaud, S. Bansropun, M. Krakowski, R. Alizon, D. Hadass, A. Bilenca, H. Dery, V. Mikhelashvili, G. Eisenstein, M. Gioannini, I. Montrosset, T. W. Berg, M. van der Poel, J. Mørk, and B. Tromborg "InP based lasers and optical amplifiers with wire-/dot-like active regions," *J. Phys. D: Appl. Phys.* **38**, 2088-2102 (2005)

## Bibliography

- [**Richter1986**] L. Richter, H. Mandelberg, M. Kruger, and P. McGrath, "Linewidth determination from self-heterodyne measurements with subcoherence delay times," *IEEE J. Quantum Electron.* **22**(11), 2070-2074 (1986)
- [**Ritter1991**] D. Ritter, R. A. Hamm, M. B. Panish, and M. Geva, "Be doping of InP and GaInAs during metalorganic molecular beam epitaxy," *3rd International Conference on Indium Phosphide and Related Materials (IPRM)*, Cardiff, UK, 1991, pp. 363-366
- [**Rolland2010**] A. Rolland, L. Frein, M. Vallet, M. Brunel, F. Bondu, and T. Merlet, "40-GHz Photonic Synthesizer Using a Dual-Polarization Microlaser," *IEEE Photon. Technol. Lett.* **22**(23), 1738-1740 (2010)
- [**Rolland2011**] A. Rolland, G. Loas, M. Brunel, L. Frein, M. Vallet, and M. Alouini, "Non-linear optoelectronic phase-locked loop for stabilization of opto-millimeter waves: towards a narrow linewidth tunable THz source," *Opt. Express* **19**(19), 17944-17950 (2011)
- [**Rosales2012**] R. Rosales, S. G. Murdoch, R.T. Watts, K. Merghem, A. Martinez, F. Lelarge, A. Accard, L. P. Barry, and A. Ramdane, "High performance mode locking characteristics of single section quantum dash lasers," *Opt. Express* **20**(8), 8649-8657 (2012)
- [**Rosencher2002**] E. Rosencher and B. Vinter, *Optoelectronics* (Cambridge University Press, 2002)
- [**Rösener2011a**] B. Rösener, M. Rattunde, R. Moser, S. Kaspar, T. Töpfer, C. Manz, K. Köhler, and J. Wagner, "Continuous-wave room-temperature operation of a 2.8  $\mu\text{m}$  GaSb-based semiconductor disk laser," *Opt. Lett.* **36**(3), 319-321 (2011)
- [**Rösener2011b**] B. Rösener, S. Kaspar, M. Rattunde, T. Töpfer, C. Manz, K. Köhler, O. Ambacher, and J. Wagner, "2  $\mu\text{m}$  semiconductor disk laser with a heterodyne linewidth below 10 kHz," *Opt. Lett.* **36**(18), 3587-3589 (2011)
- [**Rudin2008**] B. Rudin, A. Rutz, M. Hoffmann, D. Maas, A. Bellancourt, E. Gini, T. Südmeyer, and U. Keller, "Highly efficient optically pumped vertical-emitting semiconductor laser with more than 20 W average output power in a fundamental transverse mode," *Opt. Lett.* **33**(22), 2719-2721 (2008)
- [**Saarinen2006**] E. J. Saarinen, A. Härkönen, S. Suomalainen, and O. G. Okhotnikov, "Power scalable semiconductor disk laser using multiple gain cavity," *Opt. Express* **14**(26), 12868-12871 (2006)
- [**Saarinen2015**] E. Saarinen, J. Lyytikäinen, S. Ranta, A. Rantamäki, A. Sirbu, V. Iakovlev, E. Kapon, and O. Okhotnikov, "750 nm 1.5 W frequency-doubled semiconductor disk laser with a 44 nm tuning range," *Opt. Lett.* **40**(19), 4380-4383 (2015)
- [**Sadani2018**] B. Sadani, B. Boissard, X. Lafosse, T. Camps, J. B. Doucet, E. Daran, C. Paranthoën, C. Levallois, L. Dupont, S. Bouchoule, and V. Bardinal, "Liquid-Crystal Alignment by a Nanoimprinted Grating for Wafer-Scale Fabrication of Tunable Devices," *IEEE Photon. Technol. Lett.* **30**(15), 1388-1391 (2018)
- [**Sargent1974**] M. Sargent, M. O. Scully, and W. E. Lamb Jr., *Laser Physics* (Addison-Wesley, 1974)
- [**Sato1985**] H. Sato, T. Fujita, and K. Fujito, "Intensity fluctuation in semiconductor lasers coupled to external cavity," *IEEE J. Quantum Electron.* **21**(1), 46-51 (1985)
- [**Sato1999**] K. Sato, M. Shikida, T. Yamashiro, K. Asaumi, Y. Iriye, and M. Yamamoto, "Anisotropic etching rates of single-crystal silicon for TMAH water solution as a function of crystallographic orientation," *Sens. Actuator A-Phys.* **73**(1-2), 131-137 (1999)

- [**Sato2007**] K. Sato, K. Mizutani, S. Sudo, K. Tsuruoka, K. Naniwae, and K. Kudo, “Wideband external cavity wavelength tunable laser utilizing a liquid-crystal-based mirror and an intracavity etalon,” *J. Lightwave Technol.* **25**(8), 2226–2232 (2007)
- [**Schäfer1999**] F. Schäfer, J. P. Reithmaier, and A. Forchel, “High-performance GaInAs/GaAs quantum-dot lasers based on a single active layer,” *Appl. Phys. Lett.* **74**(20), 2915-2917 (1999)
- [**Scheller2012**] M. Scheller, T. L. Wang, B. Kunert, W. Stolz, S. W. Koch, and J. V. Moloney, “Passively modelocked VECSEL emitting 682 fs pulses with 5.1W of average output power,” *Electron. Lett.* **48**(10), 588-589 (2012)
- [**Schilt2010**] S. Schilt, K. Zogal, B. Kögel, P. Meissner, M. Maute, R. Protasio, and M.-C. Amann, “Spectral and modulation properties of a largely tunable MEMS-VCSEL in view of gas phase spectroscopy applications”, *Appl. Phys. B* **100**(2), 321-329 (2010)
- [**Schlosser2009**] P. Schlosser, J. Hastie, S. Calvez, A. Krysa, and M. Dawson, “InP/AlGaInP quantum dot semiconductor disk lasers for CW TEM<sub>00</sub> emission at 716 – 755 nm,” *Opt. Express* **17**(24), 21782-21787 (2009)
- [**Schuler2009**] L. P. Schuler, J. S. Milne, J. M. Dell, and L. Faraone, “MEMS-based microspectrometer technologies for NIR and MIR wavelengths,” *J. Phys. D: Appl. Phys.* **42**(13), 133001 (2009)
- [**Schwartz2009**] S. Schwartz, G. Feugnet, M. Rebut, F. Bretenaker, and J.-P. Pocholle, “Orientation of Nd<sup>3+</sup> dipoles in YAG: Experiment and model,” *Phys. Rev. A* **79**, 063814 (2009)
- [**Schwarzrück2013**] T. Schwarzrück, R. Bek, F. Hargart, C. A. Kessler, H. Kahle, E. Koroknay, M. Jetter, and P. Michler, “High-power InP quantum dot based semiconductor disk laser exceeding 1.3 W,” *Appl. Phys. Lett.* **102**(9), 092101 (2013)
- [**Schwertberger2003**] R. Schwertberger, D. Gold, J.P. Reithmaier, and A. Forchel, “Epitaxial growth of 1.55 $\mu$ m emitting InAs quantum dashes on InP-based heterostructures by GS-MBE for long-wavelength laser applications,” *J. Cryst. Growth* **251**(1), 248-252 (2003)
- [**Seeds2006**] A. J. Seeds and K. J. Williams, “Microwave Photonics,” *J. Lightwave Technol.* **24**(12), 4628-4641 (2006)
- [**Seifert2016**] S. Seifert and P. Runge, “Revised refractive index and absorption of In<sub>1-x</sub>Ga<sub>x</sub>As<sub>y</sub>P<sub>1-y</sub> lattice-matched to InP in transparent and absorption IR-region,” *Opt. Mater. Express* **6**(2), 629-639 (2016)
- [**Shamir1998**] N. Shamir, D. Ritter, and C. Cytermann, “Beryllium doped InP/InGaAsP heterojunction bipolar transistors,” *Solid-State Electron.* **42**(11), 2039-2045 (1998)
- [**Shau2001**] R. Shau, M. Ortsiefer, J. Roskopf, G. Bohm, F. Kohler and M. C. Amann, “Vertical-cavity surface-emitting laser diodes at 1.55  $\mu$ m with large output power and high operation temperature,” *Electron. Lett.* **37**(21), 1295-1296 (2001)
- [**Shau2004**] R. Shau, M. Ortsiefer, J. Roskopf, G. Boehm, C. Lauer, M. Maute, and M.-C. Amann, “Long-wavelength InP-based VCSELs with buried tunnel junction: properties and applications,” *Proc. SPIE* **5364**, (2004)
- [**Shchekin2002**] O. B. Shchekin and D. G. Deppe, “1.3  $\mu$ m InAs quantum dot laser with T<sub>o</sub>=161 K from 0 to 80 °C,” *Appl. Phys. Lett.* **80**(18), 3277-3279 (2002)

## Bibliography

- [**Shen2001**] J. L. Shen, C. Y. Chang, H. C. Liu, W. C. Chou, Y. F. Chen, T. Jung, and M. C. Wu, “Reflectivity and photoluminescence studies in Bragg reflectors with absorbing layers,” *Semicond. Sci. Technol.* **16**(7), 548-552 (2001)
- [**Shi1997**] Y. Shi, J. H. Zhao, J. Sarathy, G. H. Olsen, and H. Lee, “Tunable resonant cavity enhanced photodetectors with GaInAsSb/AlGaAsSb multiple quantum well structure grown by molecular beam epitaxy,” *Electron. Lett.* **33**(17), 1498–1499 (1997)
- [**Siegman1986**] A. E. Siegman, *Lasers* (University Science Books, 1986).
- [**Silvaco**] “Silvaco® TCAD website”: <https://www.silvaco.com/>
- [**Sirbu2010**] A. Sirbu, V. Iakovlev, A. Mereuta, A. Caliman, G. Suruceanu, and E. Kapon, “Wafer-fused heterostructures: application to vertical cavity surface-emitting lasers emitting in the 1310 nm band,” *Semicond. Sci. Technol.* **26**(1), 014016 (2010)
- [**Sirbu2011**] A. Sirbu, N. Volet, A. Mereuta, J. Lytikäinen, J. Rautiainen, O. Okhotnikov, J. Walczak, M. Wasiak, T. Czystanowski, A. Caliman, Q. Zhu, V. Iakovlev, and E. Kapon, “Wafer-Fused Optically Pumped VECSELs Emitting in the 1310-nm and 1550-nm Wavebands,” *Advances in Optical Technologies* **2011**, 209093 (2011)
- [**Sirbu2014**] A. Sirbu, K. Pierscinski, A. Mereuta, V. Iakovlev, A. Caliman, Z. Micovic, N. Volet, J. Rautiainen, J. Heikkinen, J. Lytikäinen, A. Rantamäki, O. Okhotnikov, and E. Kapon, “Wafer-fused VECSELs emitting in the 1310nm waveband,” *Proc. SPIE* **8966**, 89660G (2014)
- [**Sirbu2015**] A. Sirbu, A. Rantamaki, V. Iakovlev, A. Mereuta, A. Caliman, N. Volet, J. Lytikäinen, O. Okhotnikov, and E. Kapon, “Recent progress in wafer-fused VECSELs emitting in the 1310nm waveband,” *Proc. SPIE* **9349**, 934907 (2015)
- [**Soda1979**] H. Soda, K. Iga, C. Kitahara, and Y. Suematsu, “GaInAsP/InP Surface Emitting Injection Lasers,” *Jpn. J. Appl. Phys.* **18**(12), 2329 (1979)
- [**Spiga2017**] S. Spiga, W. Soenen, A. Andrejew, D. M. Schoke, X. Yin, J. Bauwelinck, G. Boehm, and M.-C. Amann “Single-Mode High-Speed 1.5- $\mu$ m VCSELs,” *J. Lightwave Technol.* **35**(4), 727-733 (2017)
- [**Spisser1998**] A. Spisser, R. Ledantec, C. Seassal, J. L. Leclercq, T. Benyattou, D. Rondi, R. Blondeau, G. Guillot, and P. Viktorovitch, “Highly selective and widely tunable 1.55- $\mu$ m InP/air-gap micromachined Fabry-Perot filter for optical communications,” *IEEE Photon. Technol. Lett.* **10**(9), 1259-1261 (1998)
- [**Stintz2003**] A. Stintz, T.J. Rotter, and K.J. Malloy, “Formation of quantum wires and quantum dots on buffer layers grown on InP substrates,” *J. Cryst. Growth* **255**(3), 266-272 (2003)
- [**Strassner2002**] M. Strassner, C. Luber, A. Tarraf and N. Chitica, “Widely tunable-constant bandwidth monolithic Fabry-Perot filter with a stable cavity design for WDM systems,” *IEEE Photon. Technol. Lett.* **14**(11), 1548-1550 (2002)
- [**Strassner2005**] M. Strassner, B. Simozrag, S. Bouchoule and I. Sagnes, “Widely tunable and highly selective monolithic Fabry-Perot filter for dense WDM systems,” in *2005 IEEE LEOS Annual Meeting Conference Proceedings*, Sydney, NSW, 2005, pp. 287-288
- [**Sugawara2000**] M. Sugawara, K. Mukai, Y. Nakata, H. Ishikawa, and A. Sakamoto, “Effect of homogeneous broadening of optical gain on lasing spectra in self-assembled In<sub>x</sub>Ga<sub>1-x</sub>As/GaAs quantum dot lasers,” *Phys. Rev. B* **61**, 7595 (2000)



- [**Symonds2003**] C. Symonds, “Laser à semiconducteur en cavité verticale étendue émettant à 1,55  $\mu\text{m}$ , et perspectives pour la génération d’impulsions brèves,” Ph.D. dissertation, Université Paris XI, Orsay, (2003)
- [**Symonds2004a**] C. Symonds, I. Sagnes, J.-L. Oudar, S. Bouchoule, A. Garnache, J. Berggren, and M. Strassner, “Room temperature CW lasing operation of monolithically grown 1.55  $\mu\text{m}$  vertical external cavity surface emitting laser”, *Opt. Commun.* **230**(4), 419-423 (2004)
- [**Symonds2004b**] C. Symonds, J. Dion, I. Sagnes, M. Dainese, M. Strassner, L. Leroy, and J. L. Oudar, “High performance 1.55  $\mu\text{m}$  vertical external cavity surface emitting laser with broadband integrated dielectric-metal mirror,” *Electron. Lett.* **40**(12), 734-735 (2004)
- [**Taleb2013**] F. Taleb, C. Levallois, C. Paranthoën, J.-P. Gauthier, N. Chevalier, M. Perrin, Y. Léger, O. De Sagazan, and A. Le Corre, “ VCSEL Based on InAs Quantum-Dashes With a Lasing Operation Over a 117-nm Wavelength Span”, *IEEE Photon. Technol. Lett.* **25**(21), 2126- 2128 (2013)
- [**Taleb2016**] F. Taleb, “Nouvelles sources lasers massivement accordables pour les applications télécom et les nouveaux capteurs,” Ph.D. dissertation, Institut National des Sciences Appliquées de Rennes, Rennes, (2016)
- [**Tatum2000**] J.A. Tatum, A. Clark, J. K. Guenter, R. A. Hawthorne III, and R. H. Johnson, “Commercialization of Honeywell's VCSEL technology,” *Proc. SPIE* **3946**, 2 (2000)
- [**Tatum2014**] J. A. Tatum, “Evolution of VCSELs,” *Proc. SPIE* **9001**, 90010C (2014)
- [**Tatum2015**] J. A. Tatum, D. Gazula, L. A. Graham, J. K. Guenter, R. H. Johnson, J. King, C. Kocot, G. D. Landry, I. Lyubomirsky, A. N. MacInnes, E. M. Shaw, K. Balemarthy, R. Shubochkin, D. Vaidya, M. Yan, and F. Tang, “VCSEL-Based Interconnects for Current and Future Data Centers,” *J. Lightwave Technol.* **33**(4), 727-732 (2015)
- [**Taylor2007**] J. D. Taylor, L. R. Chen, and X. Gu, “Simple Reconfigurable Photonic Microwave Filter Using an Arrayed Waveguide Grating and Fiber Bragg Gratings,” *IEEE Photon. Technol. Lett.* **19**(7), 510-512 (2007)
- [**Tehrani1978**] M.M- Tehrani, and L. Mandel, “Coherence theory of the ring laser,” *Phys. Rev. A* **17**(2), 677-693 (1978)
- [**Thorlabs**] Thorlabs Inc. MEMS-VCSEL Swept-Wavelength Laser Source at 1.3  $\mu\text{m}$  for OCT system, website page: [https://www.thorlabs.com/newgrouppage9.cfm?objectgroup\\_id=12057](https://www.thorlabs.com/newgrouppage9.cfm?objectgroup_id=12057)
- [**Tian2013**] Z.-N. Tian, L.-J. Wang, Q.-D. Chen, T. Jiang, L. Qin, L.-J. Wang, and H.-B. Sun, “Beam shaping of edge-emitting diode lasers using a single double-axial hyperboloidal micro-lens,” *Opt. Lett.* **38**(24), 5414-5417 (2013)
- [**Tourenco2007**] J.P. Tourenco, S. Bouchoule, A. Khadour, J. Decobert, A. Miard, J.C. Harmand, and J.L. Oudar, “High power single-longitudinal-mode OP-VECSEL at 1.55  $\mu\text{m}$  with hybrid metal-metamorphic Bragg mirror,” *Electron. Lett.* **43**(14), (2007).
- [**Tourenco2008**] J.-P. Tourenco, S. Bouchoule, A. Khadour, J.-C. Harmand, A. Miard, J. Decobert, N. Lagay, X. Lafosse, I. Sagnes, L. Leroy, and J.-L. Oudar, “Thermal optimization of 1.55  $\mu\text{m}$  OP-VECSEL with hybrid metal-metamorphic mirror for single-mode high power operation,” *Opt. Quant. Electron.* **40**(2), 155-165 (2008)

## Bibliography

- [**Vallet2007**] M. Vallet, M. Brunel, and M. Oger, "RF photonic synthesiser," *Electron. Lett.* **43**(25), 1437-1438 (2007)
- [**Van Dijk2011**] F. van Dijk, A. Accard, A. Enard, O. Drisse, D. Make, and F. Lelarge, "Monolithic dual wavelength DFB lasers for narrow linewidth heterodyne beat-note generation," in *2011 International Topical Meeting on Microwave Photonics jointly held with the 2011 Asia-Pacific Microwave Photonics Conf.*, Singapore, 2011, pp. 73-76
- [**Veerabathran2017**] G. K. Veerabathran, S. Sprengel, A. Andrejew, and M.-C. Amann, "Room-temperature vertical-cavity surface-emitting lasers at 4  $\mu\text{m}$  with GaSb-based type-II quantum wells," *Appl. Phys. Lett.* **110**(7), 071104 (2017)
- [**Veerabathran2018**] G. K. Veerabathran, S. Sprengel, A. Andrejew, M.-C. Amann, "Electrically-pumped VCSELs using type-II quantum wells for the mid-infrared," *Proc. SPIE* **10536**, 1053602 (2018)
- [**Vertilas**] Vertilas website: <https://www.vertilas.com/>
- [**Vetter2008**] S. L. Vetter, J.E. Hastie, V.-M. Korpijarvi, J. Puustinen, M. Guina, O. Okhotnikov, S. Calvez, and M.D. Dawson, "Short-wavelength GaInNAs/GaAs semiconductor disk lasers," *Electron. Lett.* **44**(18), 1069-1070 (2008)
- [**Vogel2003**] W. Vogel and M. Berroth, "Tunable liquid crystal Fabry-Perot filters," *Proc. SPIE* **4944**, 293 (2003)
- [**Voigt2017**] F. Voigt, F. Emaury, P. Bethge, D. Waldburger, S. Link, S. Carta, A. van der Bourg, F. Helmchen, and U. Keller, "Multiphoton in vivo imaging with a femtosecond semiconductor disk laser," *Biomed. Opt. Express* **8**(7), 3213-3231 (2017)
- [**Waldburger2016**] D. Waldburger, S. Link, M. Mangold, C. Alfieri, E. Gini, M. Golling, B. Tilma, and U. Keller, "High-power 100 fs semiconductor disk lasers," *Optica* **3**(8), 844-852 (2016)
- [**Wang2006**] W. Wang, X. Ren, H. Huang, X. Wang, H. Cui, A. Miao, Y. Li, and Y. Huang, "Tunable Photodetector Based on GaAs/InP Wafer Bonding," *IEEE Electron Device Lett.* **27**(10), 827-829 (2006)
- [**Wilcox2006**] K. G. Wilcox, F. Rutz, R. Wilk, H. D. Foreman, J. S. Roberts, J. Sigmund, H. L. Hartnagel, M. Koch, and A. C. Tropper, "Terahertz imaging system based on LT-GaAsSb antenna driven by all-semiconductor femtosecond source," *Electron. Lett.* **42**(20), 1159-1160 (2006)
- [**Wilcox2013**] K. Wilcox, A. Tropper, H. Beere, D. Ritchie, B. Kunert, B. Heinen, and W. Stolz, "4.35 kW peak power femtosecond pulse mode-locked VECSEL for supercontinuum generation," *Opt. Express* **21**(2), 1599-1605 (2013)
- [**Wiley1975**] J.D. Wiley, "Chapter 2 Mobility of Holes in III-V Compounds," *Semiconductors and Semimetals*, Vol. 10, pages 91 – 174, (R.K. Willardson and Albert C. Beer Editors, Elsevier, 1975)
- [**Williams1989**] K. J. Williams, L. Goldberg, R. D. Esman, M. Dagenais, and J. F. Weller, "6-34 GHz offset phase-locking of Nd:YAG 1319 nm nonplanar ring lasers," *Electron. Lett.* **25**(18), 1242-1243 (1989)
- [**Wilmsen2001**] C.W. Wilmsen, H. Temkin, L. A. Coldren, *Vertical-Cavity Surface-Emitting Lasers: Design, Fabrication, Characterization, and Applications* (Cambridge University Press, 2001)
- [**Wipiejewski1992**] T. Wipiejewski, K. Panzlaf, E. Zeeb, and K. J. Ebeling, "Submilliamp vertical cavity laser diode structure with 2.2-nm continuous tuning," in *18<sup>th</sup> European Conf. Opt. Comm.*, 1992, PDII-4

- [**Witzel2013**] O. Witzel, A. Klein, C. Meffert, S. Wagner, S. Kaiser, C. Schulz, and V. Ebert, “VCSEL-based, high-speed, in situ TDLAS for in-cylinder water vapor measurements in IC engines,” *Opt. Express* **21**(17), 19951-19965 (2013)
- [**Wolffenbuttel2005**] R. F. Wolffenbuttel, “MEMS-based optical mini- and microspectrometers for the visible and infrared spectral range,” *J. Micromech. Microeng.* **15**(7), S145 (2005)
- [**Wood1985**] T. H. Wood, C. A. Burrus, A. H. Gnauck, J. M. Wiesenfeld, D. A. B. Miller, D. S. Chemla, and T. C. Damen, “Wavelength-selective voltage-tunable photodetector made from multiple quantum wells”, *Appl. Phys. Lett.* **47**(3), 190–192 (1985)
- [**Wu1996**] M. S. Wu, E. C. Vail, G. S. Li, W. Yuen and C. J. Chang-Hasnain, “Widely and continuously tunable micromachined resonant cavity detector with wavelength tracking,” *IEEE Photon. Technol. Lett* **8**(1), 98-100 (1996)
- [**Wu1998**] S.-T. Wu, “Absorption measurements of liquid crystals in the ultraviolet, visible, and infrared,” *J. Appl. Phys.* **84**, 4462 (1998)
- [**Wunderer2013**] T. Wunderer, J. E. Northrup, Z. Yang, M. Teepe, N. M. Johnson, P. Rotella, and M. Wraback, “In-Well Pumped Blue GaN-Based Vertical-External-Cavity Surface-Emitting Lasers”, *Jpn. J. Appl. Phys.* **52**(8S), 08JG11 (2013)
- [**Xiang1999**] N. Xiang, J. Lammasniemi, A.B. Kazantsev, and M. Pessa, “Study of light absorption in n-type and p-type GaInAs and the possibility of making 1.55- $\mu\text{m}$  GaInAs/InP Bragg mirrors,” *J. Mater. Sci.: Mater. Electron.* **10**(4), 255-257 (1999)
- [**Xie2012**] Y. Xie, J. Beeckman, W. Woestenborghs, K. Panajotov, and K. Neyts, “VCSEL with photo-aligned liquid crystal overlay,” *IEEE Photon. Technol. Lett.* **24**(17), 1509–1512 (2012)
- [**Yang1995**] G. M. Yang, M. H. MacDougal, and P. D. Dapkus, “Ultralow threshold current vertical-cavity surface-emitting lasers obtained with selective oxidation,” *Electron. Lett.* **31**(11), 886-888 (1995)
- [**Yang2014**] W. Yang, S. A. Gerke, L. Zhu, C. Chase, Y. Rao, and C. J. Chang-Hasnain, “Long-Wavelength Tunable Detector Using High-Contrast Grating,” *IEEE J. Sel. Topics Quantum Electron.* **20**(6), 178-185 (2014)
- [**Yu2005**] S.F. Yu, *Analysis and Design of Vertical Cavity Surface Emitting Lasers* (John Wiley & Sons Inc., 2005)
- [**Zaugg2014**] C. Zaugg, A. Klenner, M. Mangold, A. Mayer, S. Link, F. Emaury, M. Golling, E. Gini, C. Saraceno, B. Tilma, and U. Keller, “Gigahertz self-referenceable frequency comb from a semiconductor disk laser,” *Opt. Express* **22**(13), 16445-16455 (2014)
- [**Zhang2014**] F. Zhang, B. Heinen, M. Wichmann, C. Möller, B. Kunert, A. Rahimi-Iman, W. Stolz, and M. Koch, “A 23-watt single-frequency vertical-external-cavity surface-emitting laser,” *Opt. Express* **22**(11), 12817-12822 (2014)
- [**Zhao2012**] Z. Zhao, S. Bouchoule, L. Ferlazzo, A. Sirbu, A. Mereuta, E. Kapon, E. Galopin, J. C. Harmand, J. Decobert, and J. L. Oudar, “Cost-Effective Thermally-Managed 1.55- $\mu\text{m}$  VECSEL With Hybrid Mirror on Copper Substrate,” *IEEE J. Quant. Electron.*, **48**(5), 643-650 (2012)
- [**Zhu2018**] N. H. Zhu, Z. Shi, Z. K. Zhang, Y. M. Zhang, C. W. Zou, Z. P. Zhao, Y. Liu, W. Li, and M. Li, “Directly Modulated Semiconductor Lasers,” *IEEE J. Quant. Electron.* **24**(1), 1-19 (2018)





# List of publications and conferences

## Peer-reviewed publications

- [1] **S. Pes**, C. Paranthoën, C. Levallois, N. Chevalier, C. Hamel, K. Audo, G. Loas, S. Bouhier, C. Gomez, J.-C. Harmand, S. Bouchoule, H. Folliot, and M. Alouini, “Class-A operation of an optically-pumped 1.6  $\mu\text{m}$ -emitting quantum dash-based vertical-external-cavity surface-emitting laser on InP”, *Opt. Express* **25**(10), 11760-11766 (2017)  
DOI: [10.1364/OE.25.011760](https://doi.org/10.1364/OE.25.011760)
- [2] F. Taleb, **S. Pes**, C. Paranthoën, C. Levallois, N. Chevalier, O. De Sagazan, A. Le Corre, H. Folliot, and M. Alouini, “Enhancement of VCSEL performances using localized copper bonding through silicon vias”, *IEEE Photonics Technol. Lett.* **29**(13), 1105-1108 (2017)  
DOI: [10.1109/LPT.2017.2703599](https://doi.org/10.1109/LPT.2017.2703599)
- [3] C. Levallois, S. Benattou, B. Boisnard, T. Camps, C. Paranthoën, **S. Pes**, S. Bouchoule, L. Dupont, J.-B. Doucet, M. Alouini, and V. Bardinal, “Liquid crystal-based tunable photodetector operating in the telecom C-band”, *Opt. Express*, **26**(20), 25952-25961 (2018)  
DOI: [10.1364/OE.26.025952](https://doi.org/10.1364/OE.26.025952)
- [4] G. Brévalle, **S. Pes**, C. Paranthoën, M. Perrin, C. Levallois, C. Hamel, A. Mereuta, A. Caliman, E. Kapon, A. Vallet, L. Chusseau, H. Folliot, and M. Alouini, “Direct measurement of the spectral dependence of Lamb coupling constant in a dual frequency quantum well-based VECSEL”, *Opt. Express* **27**(15), 21083-21091 (2019)  
DOI: [10.1364/OE.27.021083](https://doi.org/10.1364/OE.27.021083)
- [5] B. Boisnard, C. Levallois, C. Paranthoën, **S. Pes**, T. Camps, B. Sadani, S. Bouchoule, L. Dupont, M. Alouini, P. Debernardi, and V. Bardinal, “CW operation of a tunable 1550 nm VCSEL integrating liquid-crystals microcells”, submitted to *IEEE Photonics Technol. Lett.*

## Conferences contributions

- [1] **S. Pes**, F. Taleb, C. Paranthoën, C. Levallois, N. Chevalier, M. Alouini, and H. Folliot, “Etudes et caractérisations de V(E)CSELS émettant à 1.55  $\mu\text{m}$  sur InP”, *Optique Bretagne 2015 – 35<sup>ème</sup> Journées Nationales d’Optique Guidée (JNOG’35)*, July 2015, Rennes (France)
- [2] **S. Pes**, C. Paranthoën, C. Levallois, N. Chevalier, H. Folliot, and M. Alouini, “Finely tunable 1.55  $\mu\text{m}$  emitting VeCSELS for embedded and compact optical and microwave systems”, *3<sup>rd</sup> European Workshop on VeCSELS (VeCSELS 2015)*, November 2015, Montpellier (France)
- [3] **S. Pes**, F. Taleb, C. Paranthoën, C. Levallois, N. Chevalier, O. De Sagazan, H. Folliot, and M. Alouini, “Enhancement of VCSEL performances with a new bonding process”, *15<sup>ème</sup> Journées Nano, Micro et Optoélectronique (JNMO 2016)*, May 2016, Les Issambres (France)
- [4] **S. Pes**, F. Taleb, C. Paranthoën, C. Levallois, N. Chevalier, O. De Sagazan, A. Le Corre, H. Folliot, and M. Alouini, “Enhancement of VCSEL performances using a novel bonding process based on localized electroplating copper through Silicon vias”, *9<sup>th</sup> European Workshop on VCSELS (VCSEL Day 2016)*, June 2016, Darmstadt (Germany)
- [5] **S. Pes**, C. Levallois, C. Paranthoën, N. Chevalier, C. Hamel, C. Gomez, J.-C. Harmand, **S. Bouchoule**, H. Folliot, and M. Alouini, “Quantum Dash-based Vertical-External-Cavity Surface-Emitting Laser on InP”,

Compound Semiconductor Week 2017 (CSW 2017) - 29<sup>th</sup> International Conference on Indium Phosphide and Related Materials (IPRM 2017), May 2017, Berlin (Germany)

[6] **S. Pes**, K. Audo, C. Paranthoën, C. Levallois, N. Chevalier, C. Hamel, G. Loas, S. Bouhier, C. Gomez, J.-C. Harmand, S. Bouchoule, H. Folliot, and M. Alouini, “Class-A Operation of InAs Quantum Dash-based Vertical-External-Cavity Surface-Emitting Laser”, Conference on Lasers and Electro-Optics (CLEO 2017), May 2017, San Jose (USA)

[7] C. Levallois, C. Paranthoën, B. Boisnard, T. Camps, B. Sadani, **S. Pes**, S. Bouchoule, L. Dupont, J.-B. Doucet, M. Alouini, and V. Bardinal, “Liquid crystal based tunable PIN-photodiodes for detection around 1.55- $\mu\text{m}$ ”, SPIE Optics + Photonics 2018, Optical Sensing, Imaging, and Photon Counting: From X-Rays to THz, August 2018, San Diego (USA) **[INVITED]**

[8] C. Levallois, B. Boisnard, C. Paranthoën, **S. Pes**, T. Camps, B. Sadani, S. Bouchoule, L. Dupont, M. Alouini, and V. Bardinal, “CW operation of a 1.55- $\mu\text{m}$  VCSEL tunable over 20 nm integrating liquid crystals microcells”, 12<sup>th</sup> European Workshop on VCSELs (VCSEL Day 2019), May 2019, Brussels (Belgium)

[9] G. Brévalle, **S. Pes**, C. Paranthoën, M. Perrin, C. Levallois, C. Hamel, A. Mereuta, A. Caliman, E. Kapon, L. Chusseau, H. Folliot, and M. Alouini, “Mode coupling measurement in dual-frequency quantum well-based VCSEL”, Compound Semiconductor Week 2019 (CSW 2019) - 31<sup>th</sup> International Conference on Indium Phosphide and Related Materials (IPRM 2019), May 2019, Nara (Japan)

## AVIS DU JURY SUR LA REPRODUCTION DE LA THESE SOUTENUE

**Titre de la thèse:**

Nanostructures-based 1,55  $\mu\text{m}$ -emitting Vertical-(External)-Cavity Surface-Emitting Lasers for microwave photonics and coherent communications

**Nom Prénom de l'auteur : PES SALVATORE**

**Membres du jury :**

- Madame SAGNES Isabelle
- Monsieur DOLFI Daniel
- Monsieur GUINA Mircea
- Monsieur CALVEZ Stéphane
- Monsieur FOLLIOU Hervé
- Monsieur PARANTHOEN Cyril
- Monsieur ALOUINI Mehdi

Président du jury : *Isabelle SAGNES*

Date de la soutenance : 26 Septembre 2019

Reproduction de la these soutenue

- Thèse pouvant être reproduite en l'état  
 Thèse pouvant être reproduite après corrections suggérées

Fait à Rennes, le 26 Septembre 2019

Signature du président de jury



Le Directeur,

M'hamed DRISSI



**Titre:** V(E)CSELS à nanostructures quantiques à 1,55  $\mu\text{m}$  pour les applications à l'optique hyperfréquence et les communications cohérentes.

**Mots clés :** V(E)CSELS, bâtonnets quantiques, dispositifs accordables, cristaux liquides, laser bi-fréquence.

**Résumé:** Les travaux de thèse présentés en ce mémoire ont comme objectif principal le développement des sources lasers à semi-conducteurs en cavité verticale sur substrat InP, intégrant des régions actives à nanostructure quantiques, et émettent à des longueurs d'onde "télécom" (1550-1600 nm). Le développement d'un nouveau procédé technologique pour la réalisation de composants VCSEL compacts est détaillé. Ce procédé (nommé TSHEC) a été utilisé pour réaliser des émetteurs VCSELS en pompage optique sur plateforme hôte Si, ayant des performances très satisfaisantes. Ce même procédé a été adapté à la réalisation de VCSELS en pompage électrique, avec une étude préliminaire de la section de confinement électrique basée sur une BTJ en InGaAs, et le développement d'un nouveau jeu de masque dédié. Grâce à la mise au point de la technologie des  $\mu$ -cellules à cristaux liquides réalisé en partenariat avec LAAS, IMT Atlantique et C2N, on a pu adapter

le procédé TSHEC pour la réalisation de dispositifs accordables. Une photodiode accordable autour de 1.55  $\mu\text{m}$  a été réalisée, et des émetteurs VCSELS accordables basés sur la même technologie sont actuellement en cours de développement. Dans ces travaux on a également abordé le développement des VECSELS à base de bâtonnets quantiques InAs et émettent à 1.6  $\mu\text{m}$ . Un premier dispositif a été réalisé et caractérisé en régime multimode et mono-fréquence. Finalement, la réalisation d'un banc expérimental pour la mesure directe de la constante de couplage dans des VECSELS bi-fréquence a été détaillée. Ce banc a permis de quantifier précisément le couplage existant entre deux états propres orthogonaux d'un VECSEL à puits quantiques émettent à 1.54  $\mu\text{m}$ , et prochainement permettra la même étude dans des structures anisotropes, tels quels les bâtonnets quantiques ou les boîtes quantiques, dans le but d'investiguer l'effet de l'élargissement inhomogène présenté par ces milieux à gain en termes de couplage entre modes propres.

**Title:** Nanostructures-based 1.55  $\mu\text{m}$ -emitting Vertical-(External)-Cavity Surface-Emitting Lasers for microwave photonics and coherent communications.

**Keywords :** V(E)CSELS, quantum dashes, tunable devices, liquid crystals, Class-A, bi-frequency lasers.

**Abstract:** The work presented in this dissertation focus on the development of InP-based semiconductor vertical-cavity lasers, based on quantum nanostructures and emitting at the telecom wavelengths (1550-1600 nm). A new technological process for the realization of compact VCSELS is described. This process (named TSHEC) has been employed to realize optically-pumped VCSELS, integrated onto a host Silicon platform, with good performances. The same process has been adapted to develop an electrically-driven version of VCSELS: a preliminary study of the confinement section based on a InGaAs-BTJ is presented, together with the development of a mask set. Thanks to the development of the liquid crystals  $\mu$ -cell technology (in collaboration with LAAS, IMT Atlantique et C2N),

we realized a tunable photodiode at 1.55  $\mu\text{m}$ , and a tunable VCSEL is currently under development. This work also presents the first realization of a 1.6  $\mu\text{m}$ -emitting optically-pumped quantum dashes-based VECSELS, and its characterization in multi-mode and single-frequency regime. Finally, the realization of an experimental setup for the investigation of the coupling between two orthogonal eigenstates of a bi-frequency 1.54  $\mu\text{m}$ -emitting SQW-VECSEL has been conceived and realized. This setup, which allowed the direct quantification of the coupling constant on such a device, in the near future will allow performing the same study on anisotropic structures like quantum dashes or quantum dots, with the objective of studying the inhomogeneous broadening effect observed in these gain regions.